

APRIL 2023

AJNR

VOLUME 44 • PP 357-495

AJNR

AMERICAN JOURNAL OF NEURORADIOLOGY

APRIL 2023
VOLUME 44
NUMBER 4
WWW.AJNR.ORG

THE JOURNAL OF DIAGNOSTIC AND
INTERVENTIONAL NEURORADIOLOGY

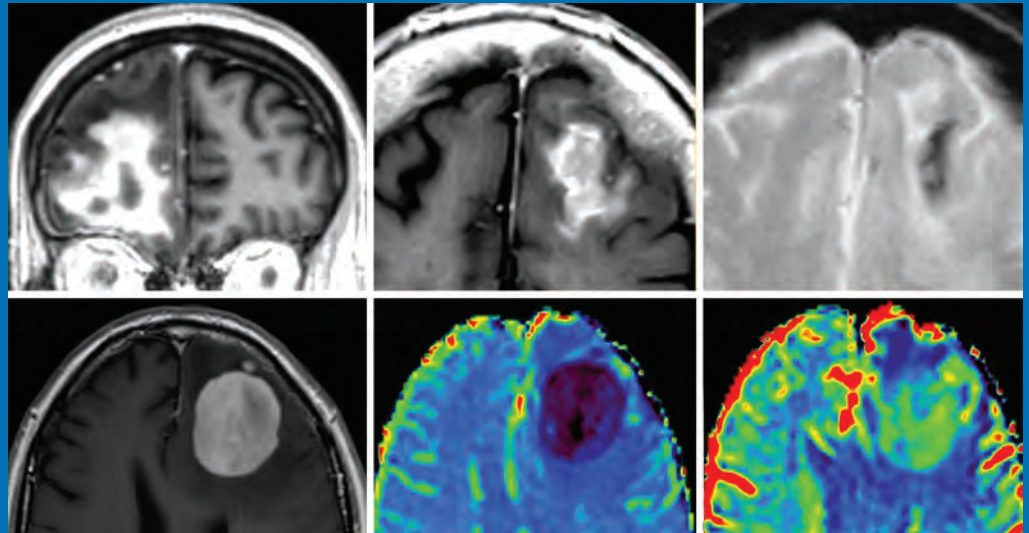
Imaging of CNS lymphoma

Newly recognized CNS tumors from WHO 2021 classification

Stent-assisted coiling in the treatment of unruptured intracranial aneurysms

Incidental MRI findings in research volunteers

Official Journal ASNR • ASFNR • ASHNR • ASPNR • ASSR



FRED™ X™

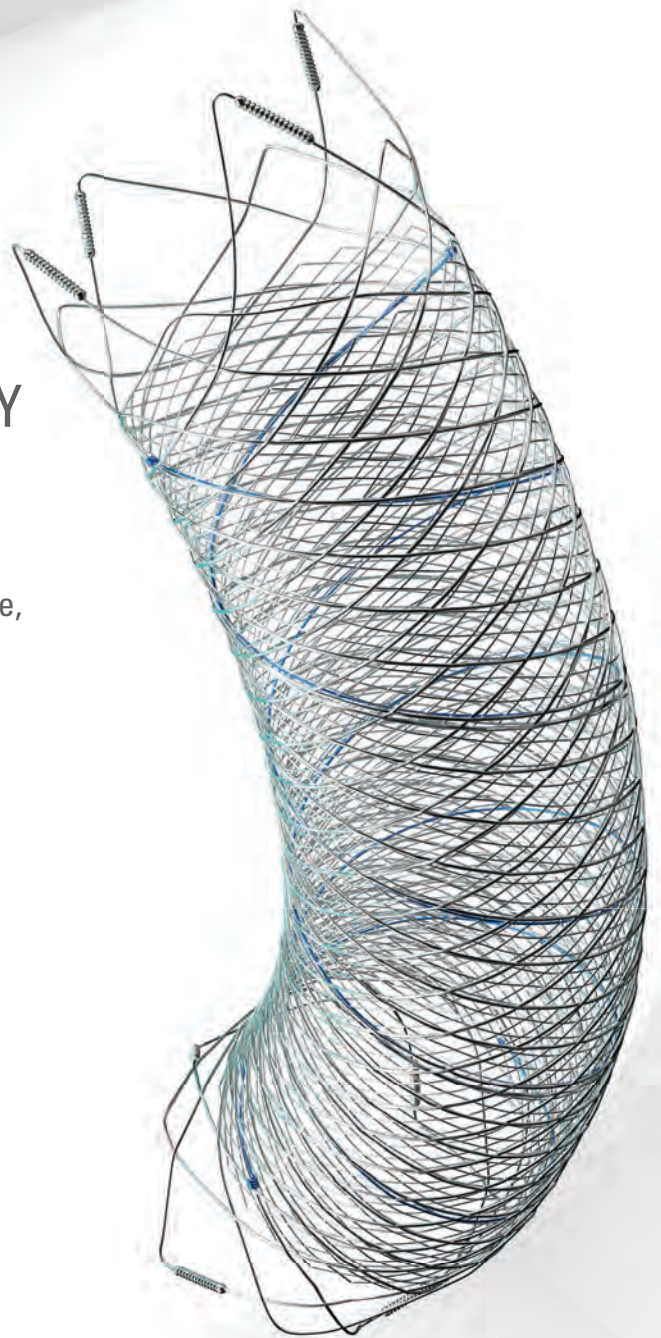
Flow Diverter Stent

THE NEXT ADVANCEMENT IN FLOW DIVERSION TECHNOLOGY

The FRED™ X Flow Diverter features the same precise placement and immediate opening of the FRED™ Device, now with X Technology. X Technology is a covalently bonded, nanoscale surface treatment, designed to:

- **REDUCE MATERIAL THROMBOGENICITY¹**
- **MAINTAIN NATURAL VESSEL HEALING RESPONSE^{2,3,4}**
- **IMPROVE DEVICE DELIVERABILITY AND RESHEATHING¹**

The only FDA PMA approved portfolio with a 0.021" delivery system for smaller device sizes, and no distal lead wire.



For more information, contact your local MicroVention sales representative or visit our website. www.microvention.com

 **MicroVention™**
TERUMO

¹ Data is derived from in vivo and ex vitro testing and may not be representative of clinical performance.

¹ Data on file

² Tanaka M et al. Design of biocompatible and biodegradable polymers based on intermediate water concept. Polymer Journal. 2015;47:114-121.

³ Tanaka M et al. Blood compatible aspects of poly(2-methoxyethylacrylate) (PMEA) – relationship between protein adsorption and platelet adhesion on PMEAs surface. Biomaterials. 2000;21:1471-1481.

⁴ Schiel L et al. X Coating™: A new biopassive polymer coating. Canadian Perfusion Canadienne. June 2001;11(2):9.

Indications for Use: The FRED X System is indicated for use in the internal carotid artery from the petrous segment to the terminus for the endovascular treatment of adult patients (22 years of age or older) with wide-necked (neck width 4 mm or dome-to-neck ratio < 2) saccular or fusiform intracranial aneurysms arising from a parent vessel with a diameter 2.0 mm and 5.0 mm.

Rx Only: Federal (United States) law restricts this device to sale by or on the order of a physician. For Healthcare professionals intended use only.

MICROVENTION, FRED and HEADWAY are registered trademarks of MicroVention, Inc. in the United States and other jurisdictions. Stylized X is a trademark of MicroVention, Inc. © 2022 MicroVention, Inc. MM1222 US 03/22

WEB™ 17

Aneurysm Embolization System

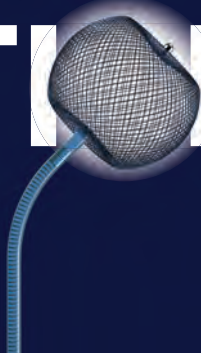
LOWER PROFILE



NEW SIZES



MORE ACCESS OPTIONS



INDICATIONS FOR USE:

The WEB Aneurysm Embolization System is intended for the endovascular embolization of ruptured and unruptured intracranial aneurysms and other neurovascular abnormalities such as arteriovenous fistulae (AVF). The WEB Aneurysm Embolization System is also intended for vascular occlusion of blood vessels within the neurovascular system to permanently obstruct blood flow to an aneurysm or other vascular malformation.

POTENTIAL COMPLICATIONS:

Potential complications include but are not limited to the following: hematoma at the site of entry, aneurysm rupture, emboli, vessel perforation, parent artery occlusion, hemorrhage, ischemia, vasospasm, clot formation, device migration or misplacement, premature or difficult device detachment, non-detachment, incomplete aneurysm filling, revascularization, post-embolization syndrome, and neurological deficits including stroke and death. For complete indications, potential complications, warnings, precautions, and instructions, see instructions for use (IFU provided with the device).

VIA 21, 27, 33 - The VIA Microcatheter is intended for the introduction of interventional devices (such as the WEB device/stents/flow diverters) and infusion of diagnostic agents (such as contrast media) into the neuro, peripheral, and coronary vasculature.

VIA 17,17 Preshaped - The VIA Microcatheter is intended for the introduction of interventional devices (such as the WEB device/stents/flow diverters) and infusion of diagnostic agents (such as contrast media) into the neuro, peripheral, and coronary vasculature.

The VIA Microcatheter is contraindicated for use with liquid embolic materials, such as n-butyl 2-cyanoacrylate or ethylene vinyl alcohol & DMSO (dimethyl sulfoxide).

The device should only be used by physicians who have undergone training in all aspects of the WEB Aneurysm Embolization System procedure as prescribed by the manufacturer.

RX Only: Federal law restricts this device to sale by or on the order of a physician.

For healthcare professional intended use only.



MicroVention Worldwide
Innovation Center PH +1.714.247.8000

35 Enterprise
Aliso Viejo, CA 92656 USA
MicroVention UK Limited PH +44 (0) 191 258 6777
MicroVention Europe, S.A.R.L. PH +33 (1) 39 21 77 46
MicroVention Deutschland GmbH PH +49 211 210 798-0
Website microvention.com



WEB™ and VIA™ are registered trademarks
of Sequent Medical, Inc. in the United States.

©2021 MicroVention, Inc. MM1184 WW 11/2021

LIFE IS FULL OF COMPROMISES.
IT'S TIME TO TAKE A STAND.

NO COMPROMISE

HIGH RELAXIVITY, HIGH STABILITY:^{1,2}
I CHOOSE BOTH.

The individual who appears is for illustrative purposes. The person depicted is a model and not a real healthcare professional. Please see Brief Summary of Prescribing Information including Boxed Warning on adjacent page.

VUEWAY™ (gadopiclenol) solution for injection

Indications

VUEWAY injection is indicated in adults and children aged 2 years and older for use with magnetic resonance imaging (MRI) to detect and visualize lesions with abnormal vascularity in:

- the central nervous system (brain, spine and surrounding tissues),
- the body (head and neck, thorax, abdomen, pelvis, and musculoskeletal system).

IMPORTANT SAFETY INFORMATION

WARNING: NEPHROGENIC SYSTEMIC FIBROSIS (NSF)

Gadolinium-based contrast agents (GBCAs) increase the risk for NSF among patients with impaired elimination of the drugs. Avoid use of GBCAs in these patients unless the diagnostic information is essential and not available with non-contrast MRI or other modalities. NSF may result in fatal or debilitating fibrosis affecting the skin, muscle and internal organs.

- The risk for NSF appears highest among patients with:
 - Chronic, severe kidney disease (GFR < 30 mL/min/1.73 m²), or
 - Acute kidney injury.
- Screen patients for acute kidney injury and other conditions that may reduce renal function. For patients at risk for chronically reduced renal function (e.g. age > 60 years,

hypertension, diabetes), estimate the glomerular filtration rate (GFR) through laboratory testing.

- For patients at highest risk for NSF, do not exceed the recommended VUEWAY dose and allow a sufficient period of time for elimination of the drug from the body prior to any re-administration.

Contraindications

VUEWAY injection is contraindicated in patients with history of hypersensitivity reactions to VUEWAY.

Warnings

Risk of **nephrogenic systemic fibrosis** is increased in patients using GBCA agents that have impaired elimination of the drugs, with the highest risk in patients chronic, severe kidney disease as well as patients with acute kidney injury. Avoid use of GBCAs among these patients unless the diagnostic information is essential and not available with non-contrast MRI or other modalities.

Hypersensitivity reactions, including serious hypersensitivity reactions, could occur during use or shortly following VUEWAY administration. Assess all patients for any history of a reaction to contrast media, bronchial asthma and/or allergic disorders, administer VUEWAY only in situations where trained personnel and therapies are promptly available for the treatment of hypersensitivity reactions, and observe patients for signs and symptoms of hypersensitivity reactions after administration.



MR Suite

IN MRI

INTRODUCING


Vueway™
(gadopiclenol) injection
485.1 mg/mL

HALF THE GADOLINIUM DOSE COMPARED TO OTHER
MACROCYCLIC GBCAs IN APPROVED INDICATIONS.^{1,3-6}
FROM BRACCO, YOUR TRUSTED PARTNER IN MRI.



LIFE FROM INSIDE

Gadolinium retention can be for months or years in several organs after administration. The highest concentrations (nanomoles per gram of tissue) have been identified in the bone, followed by other organs (brain, skin, kidney, liver and spleen). Minimize repetitive GBCA imaging studies, particularly closely spaced studies, when possible.

Acute kidney injury requiring dialysis has occurred with the use of GBCAs in patients with chronically reduced renal function. The risk of acute kidney injury may increase with increasing dose of the contrast agent.

Ensure catheter and venous patency before injecting as **extravasation** may occur, and cause tissue irritation.

VUEWAY may **impair the visualization of lesions** seen on non-contrast MRI. Therefore, caution should be exercised when Vueway MRI scans are interpreted without a companion non-contrast MRI scan.

The most common adverse reactions (incidence \geq 0.5%) are injection site pain (0.7%), and headache (0.7%).

You are encouraged to report negative side effects of prescription drugs to the FDA. Visit www.fda.gov/medwatch or call 1-800-FDA-1088.

Please see BRIEF SUMMARY of Prescribing Information for VUEWAY, including BOXED WARNING on Nephrogenic Systemic Fibrosis.

Manufactured for Bracco Diagnostics Inc. by Liebel-Flarsheim Company LLC - Raleigh, NC, USA 27616.

VUEWAY is a trademark of Bracco Imaging S.p.A.

References: 1. Vueway™ (gadopiclenol) Injection Full Prescribing Information. Monroe Twp., NJ: Bracco Diagnostics Inc.; September 2022. 2. Robic C, Port M, Rousseaux O, et al. Physicochemical and Pharmacokinetic Profiles of Gadopiclenol: A New Macrocytic Gadolinium Chelate With High T1 Relaxivity. *Invest Radiol.* 2019 Aug;54: 475–484. 3. GADAVIST® (gadobutrol) Injection. Full Prescribing Information. Bayer HealthCare Pharmaceuticals Inc. Whippany, NJ; April 2022. 4. DOTAREM® (gadoterate meglumine) Injection. Full Prescribing Information. Guerbet LLC. Princeton, NJ; April 2022. 5. CLARISCAN™ (gadoterate meglumine) injection for intravenous use. Full Prescribing Information. GE Healthcare. Marlborough, MA; February 2020. 6. ProHance® (Gadoteridol) Injection. Full Prescribing Information and Patient Medication Guide. Monroe Twp., NJ: Bracco Diagnostics Inc.; December 2020.

Bracco Diagnostics Inc.
259 Prospect Plains Road, Building H
Monroe Township, NJ 08831 USA
Phone: 609-514-2200
Toll Free: 1-877-272-2269 (U.S. only)
Fax: 609-514-2446
© 2022 Bracco Diagnostics Inc.
All Rights Reserved. US-VW-2200012 10/22

VISIT
VUEWAY.COM
FOR MORE
INFORMATION



Vueway™

(gadopiclenol) injection, for intravenous use

BRIEF SUMMARY: Please see package insert of full prescribing information.

WARNING: NEPHROGENIC SYSTEMIC FIBROSIS (NSF)
Gadolinium-based contrast agents (GBCAs) increase the risk for NSF among patients with impaired elimination of the drugs. Avoid use of GBCAs in these patients unless the diagnostic information is essential and not available with non-contrast MRI or other modalities. NSF may result in fatal or debilitating fibrosis affecting the skin, muscle and internal organs.

- The risk for NSF appears highest among patients with:
 - Chronic, severe kidney disease (GFR <30 mL/min/1.73 m²), or
 - Acute kidney injury.
- Screen patients for acute kidney injury and other conditions that may reduce renal function. For patients at risk for chronically reduced renal function (e.g. age >60 years, hypertension, diabetes), estimate the glomerular filtration rate (GFR) through laboratory testing.
- For patients at highest risk for NSF, do not exceed the recommended Vueway dose and allow a sufficient period of time for elimination of the drug from the body prior to any re-administration [see Warnings and Precautions (5.1) in the full Prescribing Information].

INDICATIONS AND USAGE

Vueway™ (gadopiclenol) is a gadolinium-based contrast agent indicated in adult and pediatric patients aged 2 years and older for use with magnetic resonance imaging (MRI) to detect and visualize lesions with abnormal vascularity in:

- the central nervous system (brain, spine, and associated tissues),
- the body (head and neck, thorax, abdomen, pelvis, and musculoskeletal system).

CONTRAINDICATIONS

Vueway is contraindicated in patients with history of hypersensitivity reactions to gadopiclenol.

WARNINGS AND PRECAUTIONS

Nephrogenic Systemic Fibrosis Gadolinium-based contrast agents (GBCAs) increase the risk for nephrogenic systemic fibrosis (NSF) among patients with impaired elimination of the drugs. Avoid use of GBCAs among these patients unless the diagnostic information is essential and not available with non-contrast MRI or other modalities. The GBCA-associated NSF risk appears highest for patients with chronic, severe kidney disease (GFR <30 mL/min/1.73 m²) as well as patients with acute kidney injury. The risk appears lower for patients with chronic, moderate kidney disease (GFR 30-59 mL/min/1.73 m²) and little, if any, for patients with chronic, mild kidney disease (GFR 60-89 mL/min/1.73 m²). NSF may result in fatal or debilitating fibrosis affecting the skin, muscle, and internal organs. Report any diagnosis of NSF following Vueway administration to Bracco Diagnostics Inc. (1-800-257-5181) or FDA (1-800-FDA-1088 or www.fda.gov/medwatch).

Screen patients for acute kidney injury and other conditions that may reduce renal function. Features of acute kidney injury consist of rapid (over hours to days) and usually reversible decrease in kidney function, commonly in the setting of surgery, severe infection, injury or drug-induced kidney toxicity. Serum creatinine levels and estimated GFR may not reliably assess renal function in the setting of acute kidney injury. For patients at risk for chronically reduced renal function (e.g., age >60 years, diabetes mellitus or chronic hypertension), estimate the GFR through laboratory testing.

Among the factors that may increase the risk for NSF are repeated or higher than recommended doses of a GBCA and the degree of renal impairment at the time of exposure. Record the specific GBCA and the dose administered to a patient. For patients at highest risk for NSF, do not exceed the recommended Vueway dose and allow a sufficient period of time for elimination of the drug prior to re-administration. For patients receiving hemodialysis, physicians may consider the prompt initiation of hemodialysis following the administration of a GBCA in order to enhance the contrast agent's elimination [see Use in Specific Populations (8.6) and Clinical Pharmacology (12.3) in the full Prescribing Information]. The usefulness of hemodialysis in the prevention of NSF is unknown.

Hypersensitivity Reactions With GBCAs, serious hypersensitivity reactions have occurred. In most cases, initial symptoms occurred within minutes of GBCA administration and resolved with prompt emergency treatment.

- Before Vueway administration, assess all patients for any history of a reaction to contrast media, bronchial asthma and/or allergic disorders. These patients may have an increased risk for a hypersensitivity reaction to Vueway.
- Vueway is contraindicated in patients with history of hypersensitivity reactions to Vueway [see Contraindications (4) in the full Prescribing Information].
- Administer Vueway only in situations where trained personnel and therapies are promptly available for the treatment of hypersensitivity reactions, including personnel trained in resuscitation.
- During and following Vueway administration, observe patients for signs and symptoms of hypersensitivity reactions.

Gadolinium Retention Gadolinium is retained for months or years in several organs. The highest concentrations (nanomoles per gram of tissue) have been identified in the bone, followed by other organs (e.g. brain, skin, kidney, liver, and spleen). The duration of retention also varies by tissue and is longest in bone. Linear GBCAs cause more retention than macrocyclic GBCAs. At equivalent doses, gadolinium retention varies among the linear agents with gadodiamide causing greater retention than other linear agents such as gadoxetate disodium, and gadobenate dimeglumine. Retention is lowest and similar

among the macrocyclic GBCAs such as gadoterate meglumine, gadobutrol, gadoteridol, and gadopiclenol.

Consequences of gadolinium retention in the brain have not been established. Pathologic and clinical consequences of GBCA administration and retention in skin and other organs have been established in patients with impaired renal function [see Warnings and Precautions (5.1) in the full Prescribing Information]. There are rare reports of pathologic skin changes in patients with normal renal function. Adverse events involving multiple organ systems have been reported in patients with normal renal function without an established causal link to gadolinium.

While clinical consequences of gadolinium retention have not been established in patients with normal renal function, certain patients might be at higher risk. These include patients requiring multiple lifetime doses, pregnant and pediatric patients, and patients with inflammatory conditions. Consider the retention characteristics of the agent when choosing a GBCA for these patients. Minimize repetitive GBCA imaging studies, particularly closely spaced studies, when possible.

Acute Kidney Injury in patients with chronically reduced renal function, acute kidney injury requiring dialysis has occurred with the use of GBCAs. The risk of acute kidney injury may increase with increasing dose of the contrast agent. Do not exceed the recommended dose.

Extravasation and Injection Site Reactions Injection site reactions such as injection site pain have been reported in the clinical studies with Vueway [see Adverse Reactions (6.1) in the full Prescribing Information]. Extravasation during Vueway administration may result in tissue irritation [see Nonclinical Toxicology (13.2) in the full Prescribing Information]. Ensure catheter and venous patency before the injection of Vueway.

Interference with Visualization of Lesions Visible with Non-Contrast MRI As with any GBCA, Vueway may impair the visualization of lesions seen on non-contrast MRI. Therefore, caution should be exercised when Vueway MRI scans are interpreted without a companion non-contrast MRI scan.

ADVERSE REACTIONS

The following serious adverse reactions are discussed elsewhere in labeling:

- Nephrogenic Systemic Fibrosis [see Warnings and Precautions (5.1) in the full Prescribing Information]
- Hypersensitivity Reactions [see Contraindications (4) and Warnings and Precautions (5.2) in the full Prescribing Information]

Clinical Trials Experience Because clinical trials are conducted under widely varying conditions, adverse reaction rates observed in the clinical trials of a drug cannot be directly compared to rates in the clinical trials of another drug and may not reflect the rates observed in clinical practice.

The safety of Vueway was evaluated in 1,047 patients who received Vueway at doses ranging from 0.025 mmol/kg (one half the recommended dose) to 0.3 mmol/kg (six times the recommended dose). A total of 708 patients received the recommended dose of 0.05 mmol/kg. Among patients who received the recommended dose, the average age was 51 years (range 2 years to 88 years) and 56% were female. The ethnic distribution was 79% White, 10% Asian, 7% American Indian or Alaska native, 2% Black, and 2% patients of other or unspecified ethnic groups.

Overall, approximately 4.7% of subjects receiving the labeled dose reported one or more adverse reactions.

Table 1 lists adverse reactions that occurred in >0.2% of patients who received 0.05 mmol/kg Vueway.

TABLE 1. ADVERSE REACTIONS REPORTED IN >0.2% OF PATIENTS RECEIVING VUEWAY IN CLINICAL TRIALS	
Adverse Reaction	Vueway 0.05 mmol/kg (n=708) (%)
Injection site pain	0.7
Headache	0.7
Nausea	0.4
Injection site warmth	0.4
Injection site coldness	0.3
Dizziness	0.3
Local swelling	0.3

Adverse reactions that occurred with a frequency < 0.2% in patients who received 0.05 mmol/kg Vueway included: maculopapular rash, vomiting, worsened renal impairment, feeling hot, pyrexia, oral paresthesia, dysgeusia, diarrhea, pruritus, allergic dermatitis, erythema, injection site paresthesia, Cystatin C increase, and blood creatinine increase.

Adverse Reactions in Pediatric Patients

One study with a single dose of Vueway (0.05 mmol/kg) was conducted in 80 pediatric patients aged 2 years to 17 years, including 60 patients who underwent a central nervous system (CNS) MRI and 20 patients who underwent a body MRI. One adverse reaction (maculopapular rash of moderate severity) in one patient (1.3%) was reported in the CNS cohort.

USE IN SPECIFIC POPULATIONS

Pregnancy Risk Summary There are no available data on Vueway use in pregnant women to evaluate for a drug-associated risk of major birth defects, miscarriage or other adverse maternal or fetal outcomes. GBCAs cross the human placenta and result in fetal exposure and gadolinium retention. The available human data on GBCA exposure during pregnancy and adverse fetal outcomes are limited and inconclusive (see Data). In animal reproduction studies, there were no adverse developmental effects observed in rats or rabbits with intravenous administration of Vueway during organogenesis (see Data). Because of the potential risks of gadolinium to the fetus, use Vueway only if imaging is essential during pregnancy and cannot be delayed. The estimated background risk of major birth defects and miscarriage for the indicated population(s) are unknown. All pregnancies have a background risk of birth defect, loss, or other adverse outcomes. In the U.S. general population, the estimated background risk of major birth defects and miscarriage in clinically recognized pregnancies is 2% to 4% and 15% to 20% respectively. Data Human Data Contrast enhancement is visualized in the placenta and fetal tissues after maternal GBCA administration. Cohort studies and case reports on exposure to GBCAs during pregnancy have not reported a clear association between GBCAs and adverse effects in the exposed neonates. However, a retrospective cohort study comparing pregnant women who had a GBCA MRI to pregnant women who did not have an MRI reported a higher occurrence of stillbirths and neonatal deaths in the group receiving GBCA MRI. Limitations of this study include a lack of comparison with non-contrast MRI and lack of information about the maternal indication for MRI. Overall, these data preclude

a reliable evaluation of the potential risk of adverse fetal outcomes with the use of GBCAs in pregnancy.

Animal Data Gadolinium Retention: GBCAs administered to pregnant non-human primates (0.1 mmol/kg on gestational days 85 and 135) result in measurable gadolinium concentration in the offspring in bone, brain, skin, liver, kidney, and spleen for at least 7 months. GBCAs administered to pregnant mice (2 mmol/kg daily on gestational days 16 through 19) result in measurable gadolinium concentrations in the pups in bone, brain, kidney, liver, blood, muscle, and spleen at one-month postnatal age.

Reproductive Toxicology: Animal reproduction studies conducted with gadopiclenol showed some signs of maternal toxicity in rats at 10 mmol/kg and rabbits at 5 mmol/kg (corresponding to 52 times and 57 times the recommended human dose, respectively). This maternal toxicity was characterized in both species by swelling, decreased activity, and lower gestation weight gain and food consumption.

No effect on embryo-fetal development was observed in rats at 10 mmol/kg (corresponding to 52 times the recommended human dose). In rabbits, a lower mean fetal body weight was observed at 5 mmol/kg (corresponding to 57 times the recommended human dose) and this was attributed as a consequence of the lower gestation weight gain.

Lactation Risk Summary There are no data on the presence of gadopiclenol in human milk, the effects on the breastfed infant, or the effects on milk production. However, published lactation data on other GBCAs indicate that 0.01% to 0.04% of the maternal gadolinium dose is excreted in breast milk. Additionally, there is limited GBCA gastrointestinal absorption in the breast-fed infant. Gadopiclenol is present in rat milk. When a drug is present in animal milk, it is likely that the drug will be present in human milk (see Data). The developmental and health benefits of breastfeeding should be considered along with the mother's clinical need for Vueway and any potential adverse effects on the breastfed infant from Vueway or from the underlying maternal condition. Data In lactating rats receiving single intravenous injection of [¹⁵²Gd]-gadopiclenol, 0.3% and 0.2% of the total administered radioactivity was transferred to the pups via maternal milk at 6 hours and 24 hours after administration, respectively. Furthermore, in nursing rat pups, oral absorption of gadopiclenol was 3.6%.

Pediatric Use The safety and effectiveness of Vueway for use with MRI to detect and visualize lesions with abnormal vascularity in the CNS (brain, spine, and associated tissues), and the body (head and neck, thorax, abdomen, pelvis, and musculoskeletal system) have been established in pediatric patients aged 2 years and older.

Use of Vueway in this age group is supported by evidence from adequate and well-controlled studies in adults with additional pharmacokinetic and safety data from an open-label, uncontrolled, multicenter, single dose study of Vueway (0.05 mmol/kg) in 80 pediatric patients aged 2 to 17 years. The 80 patients consisted of 60 patients who underwent a CNS MRI and 20 patients who underwent a body MRI [see Adverse Reactions (6.1) and Clinical Pharmacology (12.3) in the full Prescribing Information].

The safety and effectiveness of Vueway have not been established in pediatric patients younger than 2 years of age.

Geriatric Use Of the total number of Vueway-treated patients in clinical studies, 270 (26%) patients were 65 years of age and over, while 62 (6%) patients were 75 years of age and over. No overall differences in safety or efficacy were observed between these subjects and younger subjects.

This drug is known to be substantially excreted by the kidney, and the risk of adverse reactions to this drug may be greater in patients with impaired renal function. Because elderly patients are more likely to have decreased renal function, it may be useful to monitor renal function.

Renal Impairment in patients with renal impairment, the exposure of gadopiclenol is increased compared to patients with normal renal function. This may increase the risk of adverse reactions such as nephrogenic systemic fibrosis (NSF). Avoid use of GBCAs among these patients unless the diagnostic information is essential and not available with non-contrast MRI or other modalities. No dose adjustment of Vueway is recommended for patients with renal impairment. Vueway can be removed from the body by hemodialysis [see Warnings and Precautions (5.1, 5.3, 5.4) and Clinical Pharmacology (12.3) in the full Prescribing Information].

OVERDOSAGE

Among subjects who received a single 0.3 mmol/kg intravenous dose of gadopiclenol (6 times the recommended dose of Vueway), headache and nausea were the most frequently reported adverse reactions. Gadopiclenol can be removed from the body by hemodialysis [see Clinical Pharmacology (12.3) in the full Prescribing Information].

PATIENT COUNSELING INFORMATION Advise the patient to read the FDA-approved patient labeling (Medication Guide).

Nephrogenic Systemic Fibrosis Inform the patient that Vueway may increase the risk for NSF among patients with impaired elimination of the drugs and that NSF may result in fatal or debilitating fibrosis affecting the skin, muscle and internal organs.

Instruct the patients to contact their physician if they develop signs or symptoms of NSF following Vueway administration, such as burning, itching, swelling, scaling, hardening and tightening of the skin; red or dark patches on the skin; stiffness in joints with trouble moving, bending or straightening the arms, hands, legs or feet; pain in the hip bones or ribs; or muscle weakness [see Warnings and Precautions (5.1) in the full Prescribing Information].

Gadolinium Retention Advise patients that gadolinium is retained for months or years in brain, bone, skin, and other organs following Vueway administration even in patients with normal renal function. The clinical consequences of retention are unknown. Retention depends on multiple factors and is greater following administration of linear GBCAs than following administration of macrocyclic GBCAs [see Warnings and Precautions (5.3) in the full Prescribing Information].

Injection Site Reactions Inform the patient that Vueway may cause reactions along the venous injection site, such as mild and transient burning or pain or feeling of warmth or coldness at the injection site [see Warnings and Precautions (5.5) in the full Prescribing Information].

Pregnancy Advise pregnant women of the potential risk of fetal exposure to Vueway [see Use in Specific Populations (8.1) in the full Prescribing Information].

Rx only

US Patent No. 10,973,934
Manufactured for Bracco Diagnostics Inc. by Liebel-Flarsheim Company LLC
- Raleigh, NC, USA 27616.
Toll Free: 1-877-272-2269 (U.S. only)
Revised November 2022

AJNR

AMERICAN JOURNAL OF NEURORADIOLOGY

APRIL 2023
VOLUME 44
NUMBER 4
WWW.AJNR.ORG

Publication Preview at www.ajnr.org features articles released in advance of print. Visit www.ajnrblog.org to comment on AJNR content and chat with colleagues and AJNR's News Digest at <http://ajnrdigest.org> to read the stories behind the latest research in neuroimaging.

357 **PERSPECTIVES** *J.S. Ross*

REVIEW ARTICLES

 358 **Imaging of Lymphomas Involving the CNS: An Update-Review of the Full Spectrum of Disease with an Emphasis on the World Health Organization Classifications of CNS Tumors 2021 and Hematolymphoid Tumors 2022** *A. Pons-Escoda, et al.* **ADULT BRAIN**

  367 **Newly Recognized CNS Tumors in the 2021 World Health Organization Classification: Imaging Overview with Histopathologic and Genetic Correlation** *R.K. Rigsby, et al.* **ADULT BRAIN**

LEVEL 1 EBM EXPEDITED PUBLICATION

    381 **Stent-Assisted Coiling in the Treatment of Unruptured Intracranial Aneurysms: A Randomized Clinical Trial** *W. Boisseau, et al.* **INTERVENTIONAL**

RADIOLOGY-PATHOLOGY CORRELATION

390 **Radiology-Pathology and Surgical Correlation in Astroblastoma** *F. Sprenger, et al.* **PEDIATRICS**

GENERAL CONTENTS

  396 **MR Imaging Signs of Gadolinium Retention Are Not Associated with Long-Term Motor and Cognitive Outcomes in Multiple Sclerosis** *A. Scaravilli, et al.* **ADULT BRAIN**

403 **Clinical Profiles and Patterns of Neurodegeneration in Amyotrophic Lateral Sclerosis: A Cluster-Based Approach Based on MR Imaging Metrics** *G. Milella, et al.* **ADULT BRAIN**

  410 **Comparison between Dual-Energy CT and Quantitative Susceptibility Mapping in Assessing Brain Iron Deposition in Parkinson Disease** *Y. Chen, et al.* **ADULT BRAIN**

  417 **Incidental Findings from 16,400 Brain MRI Examinations of Research Volunteers** *P.A. Rowley, et al.* **ADULT BRAIN**

  424 **Phenotyping Superagers Using Resting-State fMRI** *L.L. de Godoy, et al.* **FUNCTIONAL**

AJNR (Am J Neuroradiol ISSN 0195–6108) is a journal published monthly, owned and published by the American Society of Neuroradiology (ASNR), 820 Jorie Boulevard, Oak Brook, IL 60523. Annual dues for the ASNR include approximately 19% for a journal subscription. The journal is printed by Intellicor Communications, 330 Eden Road, Lancaster, PA 17601; Periodicals postage paid at Oak Brook, IL and additional mailing offices. Printed in the U.S.A. POSTMASTER: Please send address changes to American Journal of Neuroradiology, P.O. Box 3000, Denville, NJ 07834, U.S.A. Subscription rates: nonmember \$452 (\$530 foreign) print and online, \$320 online only; institutions \$520 (\$594 foreign) print and basic online, \$1029 (\$1103 foreign) print and extended online, \$380 online only (basic), \$825 online only (extended); single copies are \$35 each (\$40 foreign). Indexed by PubMed/MEDLINE, BIOSIS Previews, Current Contents (Clinical Medicine and Life Sciences), EMBASE, Google Scholar, HighWire Press, Q-Sensei, RefSeek, Science Citation Index, SCI Expanded, ReadCube, and Semantic Scholar. Copyright © American Society of Neuroradiology.

I am a global citizen.
I am patient-centered care.
I am committed to health equity.
I am a teacher.
I am a life-long learner.
I am determined.
I am curious.
I am a collaborative team player.
I am a volunteer.
I am ASNR.

Don't miss out on the tools, resources and relationships you've come to rely on. Log in and renew your ASNR membership today! www.asnr.org

EDITOR-IN-CHIEF

Jeffrey S. Ross, MD

Professor of Radiology, Department of Radiology,
Mayo Clinic College of Medicine, Phoenix, AZ

SENIOR EDITORS

Harry J. Cloft, MD, PhD

Professor of Radiology and Neurosurgery,
Department of Radiology, Mayo Clinic College of
Medicine, Rochester, MN

Christopher G. Filippi, MD

Professor and Alice Ettinger-Jack R. Dreyfuss
Chair of Radiology,
Tufts University School of Medicine,
Radiologist-in-Chief
Tufts University Medical Center, Boston, MA

Thierry A.G.M. Huisman, MD, PD, FICIS, FACR

Radiologist-in-Chief and Chair of Radiology, Texas
Children's Hospital,
Professor of Radiology, Pediatrics, Neurosurgery,
and OBGYN, Baylor College of Medicine,
Houston, TX

Yvonne W. Lui, MD

Associate Professor of Radiology,
Chief of Neuroradiology,
New York University School of Medicine,
New York, NY

C.D. Phillips, MD, FACR

Professor of Radiology, Weill Cornell Medical
College, Director of Head and Neck Imaging,
New York-Presbyterian Hospital, New York, NY

Lubdha M. Shah, MD, MS

Professor of Radiology and Director of Spine
Imaging, University of Utah Department of
Radiology and Imaging Sciences, Salt Lake City, UT

STATISTICAL SENIOR EDITOR

Bryan A. Comstock, MS

Senior Biostatistician,
Department of Biostatistics,
University of Washington, Seattle, WA

ARTIFICIAL INTELLIGENCE DEPUTY EDITOR

Peter D. Chang, MD

Assistant Professor-in-Residence,
Departments of Radiological Sciences,
Computer Sciences, and Pathology,
Director, Center for Artificial Intelligence in
Diagnostic Medicine (CAIDM),
University of California, Irvine, Irvine, CA

EDITORIAL BOARD

Ashley H. Aiken, Atlanta, GA

Matthew D. Alexander, Salt Lake City, UT

Lea M. Alhilali, Phoenix, AZ

Jason W. Allen, Atlanta, GA

Mohammed A. Almekhlafi, Calgary, Alberta,
Canada

Niranjan Balu, Seattle, WA

Matthew J. Barkovich, San Francisco, CA

Joachim Berkefeld, Frankfurt, Germany

Karen Buch, Boston, MA

Judah Burns, New York, NY

Danielle Byrne, Dublin, Ireland

Federico Cagnazzo, Montpellier, France

Gloria C. Chiang, New York, NY

Daniel Chow, Irvine, CA

Kars C.J. Compagne, Rotterdam, The Netherlands

Yonghong Ding, Rochester, MN

Birgit Ertl-Wagner, Toronto, Ontario, Canada

Aaron Field, Madison, WI

Nils D. Forkert, Calgary, Alberta, Canada

Frank Gaillard, Melbourne, Australia

Joseph J. Gemmete, Ann Arbor, Michigan

Brent Griffith, Detroit, MI

Michael J. Hoch, Philadelphia, PA

Joseph M. Hoxworth, Phoenix, AZ

Raymond Y. Huang, Boston, MA

Susie Y. Huang, Boston, MA

Ferdinand K. Hui, Honolulu, HI

Christof Karmonik, Houston, TX

Gregor Kasprian, Vienna, Austria

Timothy J. Kaufmann, Rochester, MN

Hillary R. Kelly, Boston, MA

Toshibumi Kinoshita, Akita, Japan

Ioannis Koktzoglou, Evanston, IL

Stephen F. Kralik, Houston, TX

Luke Ledbetter, Los Angeles, CA

Franklin A. Marden, Chicago, IL

Markus A. Möhlenbruch, Heidelberg, Germany

Mahmud Mossa-Basha, Morrisville, NC

Renato Hoffmann Nunes, Sao Paulo, Brazil

Sam Payabvash, New Haven, CT

Johannes A.R. Pfaff, Salzburg, Austria

Eike I. Piechowiak, Bern, Switzerland

Laurent Pierot, Reims, France

Alexander R. Podgorsak, Chicago, IL

Eytan Raz, New York, NY

Jeff Rudie, San Diego, CA

Paul M. Ruggieri, Cleveland, OH

Fatih Seker, Heidelberg, Germany

Maksim Shapiro, New York, NY

Timothy Shepherd, New York, NY

Mark S. Shiroishi, Los Angeles, CA

Neetu Soni, Rochester, NY

Ashok Srinivasan, Ann Arbor, MI

Jason F. Talbott, San Francisco, CA

Anderanik Tomasian, Los Angeles, CA

Fabio Triulzi, Milan, Italy

Arastoo Vossough, Philadelphia, PA

Richard Watts, New Haven, CT

Elysa Widjaja, Toronto, Ontario, Canada

Ronald Wolf, Philadelphia, Pennsylvania

Shuang Xia, Tianjin, China

Leonard Yeo, Singapore

Woong Yoon, Gwangju, South Korea

David M. Yousem, Evergreen, CO

Carlos Zamora, Chapel Hill, NC

Chengcheng Zhu, Seattle, WA

EDITORIAL FELLOW

Alexandre Boutet, Toronto, Ontario, Canada

SPECIAL CONSULTANTS TO THE EDITOR

AJNR Blog Editor

Neil Lall, Denver, CO

Case of the Month Editor

Nicholas Stence, Aurora, CO

Case of the Week Editors

Matylda Machnowska, Toronto, Ontario, Canada

Anvita Pauranik, Calgary, Alberta, Canada

Classic Case Editor

Sandy Cheng-Yu Chen, Taipei, Taiwan

Health Care and Socioeconomics Editor

Pina C. Sanelli, New York, NY

Physics Editor

Greg Zaharchuk, Stanford, CA

Podcast Editor

Kevin Hiatt, Winston-Salem, NC

Twitter Editor

Jacob Ormsby, Albuquerque, NM

Official Journal:

American Society of Neuroradiology

American Society of Functional Neuroradiology

American Society of Head and Neck Radiology

American Society of Pediatric Neuroradiology

American Society of Spine Radiology

Founding Editor

Juan M. Taveras

Editors Emeriti

Mauricio Castillo, Robert I. Grossman,

Michael S. Huckman, Robert M. Quencer

Managing Editor

Karen Halm

Assistant Managing Editor

Laura Wilhelm

Executive Director, ASNR

Mary Beth Hepp

AJNR *go green*

***AJNR* urges American Society of Neuroradiology members to reduce their environmental footprint by voluntarily suspending their print subscription.**

The savings in paper, printing, transportation, and postage directly fund new electronic enhancements and expanded content.

The digital edition of *AJNR* presents the print version in its entirety, along with extra features including:

- Publication Preview
- Case Collection
- Podcasts
- The *AJNR* News Digest
- The *AJNR* Blog

It also reaches subscribers much faster than print. An electronic table of contents will be sent directly to your mailbox to notify you as soon as it publishes.

Readers can search, reference, and bookmark current and archived content 24 hours a day on www.ajnr.org.

ASNR members who wish to opt out of print can do so by using the *AJNR* Go Green link on the *AJNR* Website (<http://www.ajnr.org/content/subscriber-help-and-services>). Just type your name in the email form to stop print and spare our ecosystem.

In Planning for Brain Metastases Treatment, Imaging may be the Missing Link in Cost Containment¹

When faced with a patient presenting with metastatic brain cancer, determining whether to use up-front stereotactic radiosurgery (SRS) vs. first treating with whole brain radiotherapy (WBRT) is a significant clinical decision.

WBRT: The whole story on cognitive impairment

While whole brain radiotherapy (WBRT) has been the main treatment option for many years, experts agree that it often results in cognitive deterioration and a negative impact on quality of life. This mental decline has a devastating impact on patients and their families and adds ongoing costs for the healthcare systems managing these symptoms.

Using WBRT instead of SRS in some patients is estimated to decrease the total costs of brain metastasis management, though with increased toxicity.

SRS: Fewer side effects but greater risk of missed tumors

The cost of upfront SRS is the greatest contributor to cost of brain metastasis management.¹ SRS is often more expensive than WBRT. What's more, multiple applications of SRS can increase the cost of treatment greatly.

Stereotactic radiosurgery (SRS) has far fewer side effects, but upfront use of SRS is expensive and can carry the risk of missed tumors, requiring repeat procedures such as salvage SRS.¹

Number of lesions and lesion size are key factors to be considered when determining the treatment plan for these patients. It follows that increased diagnostic information and accuracy could be beneficial in directing the proper therapy and improving overall long-term patient outcomes and containing costs. Getting the diagnosis right the first time is crucial to ensure proper treatment begins quickly, and high cost/high stakes procedures such as SRS need precise surgical planning.

What does optimal visualization mean for outcomes and cost?

For surgical planning with SRS, radiologists need the best visualization achievable to accurately count the number and size of the lesions. These metrics are the key predictors of the need for SRS,¹ WBRT, or a combination of both.

By selecting the ideal contrast agent and equipment protocols, neuroradiologists can identify the proximate numbers of metastases for upfront treatment and reduced salvage treatment occurrences.

The role of radiology

As medical care for oncology patients continues to evolve, it will be increasingly important to assess the cost of various interventions given the often-limited life expectancy of cancer patients, the rising costs of cancer therapy, and the increasing prevalence of cancer in an aging population.

Through seeing all the tumors and tumor borders as clearly as technology allows, radiology can play a part in ensuring that proper treatment can begin quickly,

while containing costs through optimized patient care. Efforts to carefully manage treatment approaches require improvements in protocol design, contrast administration in imaging, and utilizing multimodal imaging approaches.

In this era of precision medicine, radiology departments' contribution to this improved standard of care will have significant short and long-term implications by reducing cost of care, providing a more proximate diagnosis, and ensuring optimal patient outcomes. ■



Getting the diagnosis right the first time is crucial to ensure proper treatment begins quickly.

Reference: 1. Shenker, R. F., McTyre, E. R., Taksler, D et al. Analysis of the drivers of cost of management when patients with brain metastases are treated with upfront radiosurgery. *Clin Neurol Neurosurg.* 2019 Jan;176:10-14.



The ASNR Career Center

The Go-To Job Site for Neuroradiology Employers and Job Seekers

For Job Seekers

- Access to an expanded network of jobs via the National Healthcare Career Network
- Confidential resume posting
- Professional online profile

For Employers

- Employer resources to help you recruit top talent
- Multiple pricing options, including free Fellowship listings
- Resume search

Start here: careers.asnr.org



The Helix nebula (NGC 7293) is a poorly named "planetary nebula" located in the constellation of Aquarius, and sometimes referred to as the "Eye of Sauron." Planetary nebulas have nothing to do with planets and were erroneously named because they seemed to resemble gas-giant planets with the equipment of the time (circa 1824). The dying of a star causes the ejection of its outer gaseous layers and leaves behind a white dwarf star (center of the eye). This image was acquired as a series of 96 5-minute exposures (8 hours) using red, green, and blue filters. The telescope was a 12.5" Ritchey-Chretien telescope, f/9 on a Paramount ME mount situated in Australia. The camera was an Apogee Alta U16 CCD with Astrodon filters. The images were processed using PixInsight, Photoshop, and Topaz Labs Adjust AI and DeNoise AI.

Jeffrey S. Ross, Mayo Clinic, Phoenix, Arizona

Imaging of Lymphomas Involving the CNS: An Update-Review of the Full Spectrum of Disease with an Emphasis on the World Health Organization Classifications of CNS Tumors 2021 and Hematolymphoid Tumors 2022

 A. Pons-Escoda,  P. Naval-Baudin,  R. Velasco,  N. Vidal, and  C. Majós



ABSTRACT

SUMMARY: Lymphomas of the CNS are the second most frequent primary brain malignancy in adults after gliomas. Presurgical suspicion of lymphoma greatly impacts patient management. The radiologic features of this tumor have been widely covered in the literature for decades, but under current classifications, mainly corresponding to the most common presentations of the most frequent type: primary diffuse large B-cell lymphoma of the CNS. Nevertheless, rarer presentations of this specific lymphoma and of other World Health Organization lymphoma subtypes with different imaging features are rarely treated. Moreover, important advances in imaging techniques, changing epidemiologic factors with relevant impact on these tumors (eg, immunodeficiency/dysregulation), and recent updates of the World Health Organization Classification of CNS Tumors 2021 and Hematolymphoid Tumors 2022 may have rendered some accepted concepts outdated. In this article, the authors aim to fulfill a critical need by providing a complete update-review, emphasizing the latest clinical-radiologic features of the full spectrum of lymphomas involving the CNS.

ABBREVIATIONS: ALK+/ALK- = anaplastic lymphoma kinase positive and negative; CLIPPERS = chronic lymphocytic inflammation with pontine perivascular enhancement responsive to steroids; DLBCL = diffuse large B-cell lymphoma; EBV = Epstein-Barr virus; MALT = mucosa-associated lymphoid tissue; NK = natural killer; PSR = percentage of signal recovery; WHO = World Health Organization

Lymphomas of the CNS are the second most frequent primary brain malignancy in adults after gliomas, accounting for 7% of all malignant tumors.¹ A presurgical suspicion of this tumor will greatly impact patient management. Corticoids should be avoided before a definitive diagnosis is made, and prompt biopsy is recommended to prioritize chemoradiotherapy instead of tumor resection, such as in the case of suspected glioblastoma.^{2,3}

The radiologic features of these tumors have been widely covered in the literature in recent decades. Imaging characteristics of lymphomas may be considered typical, leading to a potential misunderstanding of this tumor as a straightforward presurgical suspicion. Nevertheless, this is often far from the reality in daily practice. In fact, the typical appearance of lymphomas is currently almost exclusively related to the most common presentations of

the most frequent type: primary diffuse large B-cell lymphoma (DLBCL) of the CNS, negative for Epstein-Barr virus (EBV). If rarer presentations of this specific lymphoma or other specific subtypes with different characteristic imaging features are considered, the complexity increases, and it becomes a great mimicker with a challenging differential diagnosis. Also, important advances in imaging techniques, dynamic changes in epidemiologic factors with relevant impact on these tumors (eg, immunodeficiency/dysregulation), and recent changes in the World Health Organization (WHO) classifications of CNS² and hematolymphoid⁴ tumors may have rendered some well-accepted concepts of the disease outdated.⁵⁻⁸

The Research Ethics Committee of the Hospital Universitari de Bellvitge approved this article for publication (PR348/22).

WHO Classification of Tumors, 5th Edition

Insights. Some basic concepts regarding WHO classifications need to be understood for an optimally up-to-date comprehension of lymphomas in the CNS. First, these tumors fall between two 5th edition WHO classifications: the CNS² and the hematolymphoid.⁴ Second, despite impressive advances in molecular pathology, the mainstay in lymphomas remains histology of biopsy specimens; this differs greatly from other brain tumors such as gliomas, for which molecular pathology is vital. Nevertheless, clinically relevant pathogenesis, mutation profiles, and genetic drivers have been characterized in recent years. Recurrent mutations frequently

Received December 6, 2022; accepted after revision January 19, 2023.

From the Radiology (A.P.-E., P.N.-B., C.M.) Pathology Departments (N.V.), Hospital Universitari de Bellvitge, Barcelona, Spain; Neurooncology Unit (A.P.-E., R.V., N.V., C.M.), Institut d'Investigació Biomèdica de Bellvitge, Barcelona, Spain; and Institute of Neurosciences and Department of Cell Biology, Physiology and Immunology (R.V.), Universitat Autònoma de Barcelona, Barcelona, Spain.

This work was partially supported by a grant from the Instituto de Salud Carlos III (PI20/00360) to Carles Majós and Albert Pons-Escoda.

Please address correspondence to Albert Pons-Escoda, MD, Radiology Department, Institut de Diagnòstic per la Imatge, Hospital Universitari de Bellvitge, C/Feixa Llarga SN, L'Hospitalet de Llobregat, 08907, Barcelona, Spain; e-mail: albert.pons.idi@gencat.cat; @PonsEscoda

 Indicates open access to non-subscribers at [www.ajnr.org](http://dx.doi.org/10.3174/ajnr.A7795)
<http://dx.doi.org/10.3174/ajnr.A7795>

activate the B-cell receptor, toll-like receptor, and NF- κ B pathways, and alterations in genes involved in chromatin structure and modification, cell-cycle regulation, and immune recognition are common. *MYD88* and *CD79B* mutations may be of clinical interest because they can be detected in several body fluids (plasma and CSF), potentially assisting in disease-monitoring under treatment and in minimally-invasive initial diagnosis. Also, knowledge of genetically activated pathways, tumor immune microenvironment, and expression of immune-response biomarkers may point to specific treatment targets. Finally, lymphoma classifications include clinical factors, especially regarding the immune status of patients, which plays an essential role in tumor classification with important treatment implications.^{2,4}

Updates. Thus, some changes may be identified in the updated WHO Classifications of CNS Tumors 2021 and Hematolymphoid Tumors 2022, first in CNS immunodeficiency-associated lymphoma. Whereas the prior CNS classification included a heterogeneous group of diseases primarily defined by the patient immunodeficiency setting, currently, it is exclusively defined as DLBCL and EBV positive (both essential criteria) lymphoma.² Moreover, the current spectrum of immunodeficiency includes immune-dysregulation according to the hematolymphoid classification, in which immunocompromised settings without a fully demonstrable immunodeficiency, such as immunosenescence (among others), are included.^{2,4}

Next, a change in terminology is recommended in the upcoming hematolymphoid classification, representing a paradigm shift. Currently, the type of immunodeficiency-associated lymphoma is not first determined by the immunodeficiency/dysregulation setting, as in the previous classification (eg, AIDS-related DLBCL). Instead, it is defined primarily by the tumor histology with the so-called 3-part nomenclature, composed of the following: 1) histologic lesion, 2) oncogenic virus status, and 3) immunodeficiency background of the patient (eg, DLBCL, EBV-positive, and autoimmune setting).⁴ This integrated nomenclature allows the grouping of specific types of immunodeficiency-associated lymphomas (such as DLBCL EBV-positive), despite the underlying immunodeficiency/dysregulation, to better define the unique shared pathogenetic mechanisms.^{4,9,10}

On the other hand, lymphomatoid granulomatosis is no longer considered an immunodeficiency-associated entity. It occurs exclusively in immunocompetent patients, and in the case of an underlying immunodeficiency, it should be considered a subtype of a polymorphic lymphoproliferative disorder.⁴

Also, according to the WHO classification of hematolymphoid tumors, the term primary CNS lymphoma may be considered imprecise, and it is no longer recommended for referring specifically to primary DLBCL of the CNS,⁴ which is the currently preferred term.^{2,4}

Finally, some tumors do not differ in their specific histology but rather in their precise location. This is because in the new WHO hematolymphoid classification, primary DLBCL of the CNS is classified together with DLBCL of the vitreoretina and of the testes of immunocompetent patients as primary DLBCL of immune-privileged sites. All these entities arise in so-called immune sanctuaries created by their anatomic and functional immune regulatory

barriers (eg, the blood-brain barrier). However, large B-cell lymphomas occurring in the dura (dural lymphoma) or inside the brain vessels (intravascular lymphoma) escape these immune privileges and are, therefore, classified separately.^{2,4}

With all these upgraded concepts in mind, the authors aim to provide a complete update-review of imaging features of the full spectrum of lymphomas involving the CNS, mainly based on those entities included in the 5th edition WHO Classification of Tumors of the CNS 2021.² Primary DLBCL of the CNS, immunodeficiency-associated CNS lymphoma, lymphomatoid granulomatosis, intravascular large B-cell lymphoma of the CNS, mucosa-associated lymphoid tissue (MALT) lymphoma of the dura, other low-grade B-cell lymphomas of the CNS, anaplastic large-cell lymphoma (anaplastic lymphoma kinase positive and negative [ALK+/ALK-]), and T-cell and natural killer (NK)/T-cell lymphoma are discussed. Finally, the clinical-radiologic entity “lymphomatosis cerebri” and secondary lymphomas are also reviewed.

Imaging of CNS Lymphomas

Primary DLBCL of the CNS. Primary DLBCL of the CNS corresponds to 80%–85% of all CNS lymphomas, occurs almost always in immunocompetent patients, is EBV-negative, and is of unknown etiology.² The term primary CNS lymphoma may be considered imprecise, and it is no longer recommended by the WHO classification of hematolymphoid tumors⁴ for referring specifically to primary DLBCL of the CNS, which is the currently preferred term.^{2,4}

It usually appears as single or multiple (30%–35%) parenchymal lesions, located supratentorially (>80%), with a particular affinity for the basal ganglia, periventricular regions, midline, and corpus callosum (\approx 45%). It is also frequent in brain hemispheres (\approx 40%), rarely found in the posterior fossa, and exceptionally in the spinal cord (Fig 1).² Associated leptomeningeal or subependymal enhancement is characteristic, but an exclusive presentation of the disease in this location may raise suspicion of secondary lymphoma. The typical perivascular histologic pattern also carries a characteristic perivascular enhancement on imaging (Fig 1). Parenchymal lesions are most frequently solid and homogeneous, but their presentation can range from well-defined expansive to ill-defined infiltrative lesions.^{2,5-7,11}

Notably, these lesions are frequently hyperattenuating on NCCT,^{2,5-7,11} which is important to keep in mind because CT is the first-line radiologic examination and suspicion at this point may lead to corticoid avoidance (Fig 1). If administered, corticoids can complicate subsequent imaging and histologic diagnosis.^{2,3,12}

Regarding specific tumor MR imaging features, lymphoma typically appears hypointense on T2WI with marked diffusion restriction on DWI. Nevertheless, a T2-blackout effect consisting of a persistent hypointensity on $b = 1000$ images due to very low T2 signal may lead to misinterpretation. Thus, ADC map hypointensity might be more reliable than $b = 1000$ hyperintensity in assessing actual diffusion restriction.^{2,5-7,11} NCCT hyperattenuation, low T2 signal, and diffusion restriction correlate with high cellularity on histology, with Ki-67 proliferation indexes usually above 90% (Fig 1).¹³

Historically, the presence of hemorrhage or signs of necrosis on preoperative imaging in immunocompetent patients have been considered a factor arguing strongly against a diagnosis of lymphoma.¹⁴ However, the histologic appearance of tumor

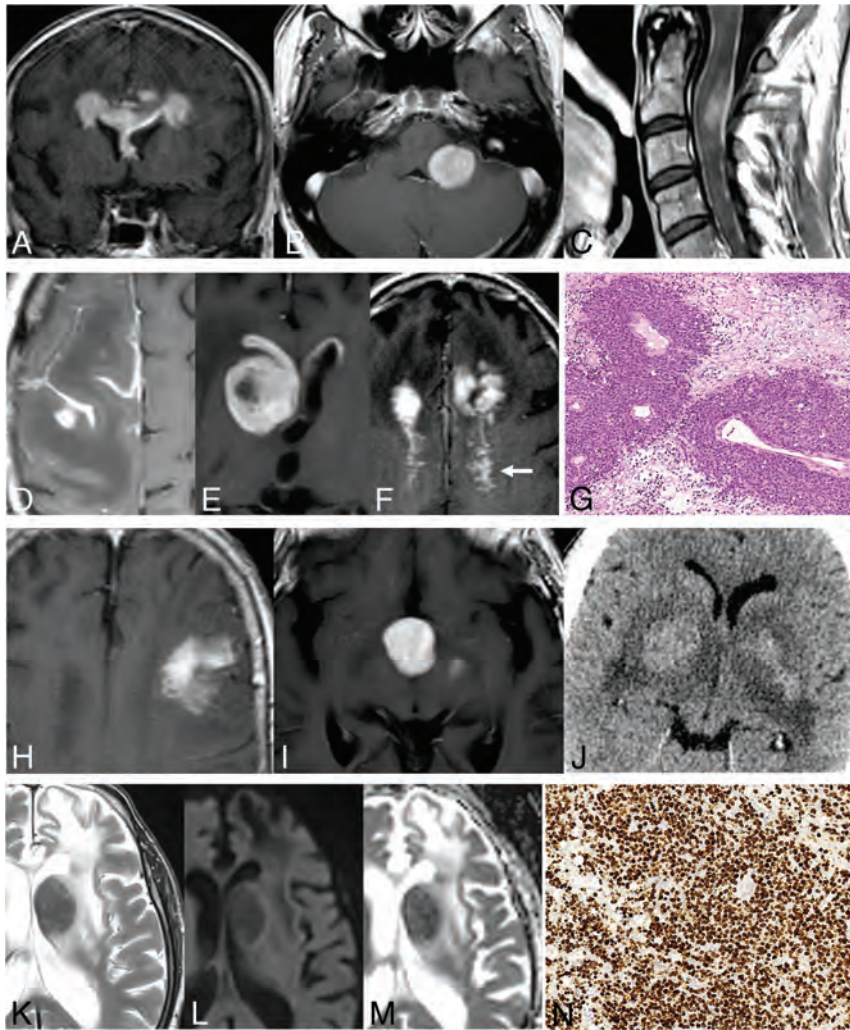


FIG 1. Primary DLBCLs of the CNS, EBV-negative. A–C: Usual deep, periventricular, corpus callosum, and midline location (A); a rare location in the posterior fossa (B); and exceptional in the spinal cord (C). D–G: Parenchymal lesions with associated characteristic leptomeningeal (D), subependymal (E), and perivascular (arrow, F) enhancement patterns. Histologic hematoxylin-eosin stain (original magnification $\times 20$) shows highly cellular, perivascular accumulation of lymphoma cells (G). H–J: Mass lesion with ill-defined infiltrative (H) or well-defined expansive (I) margins. Hyperattenuated lesions on NCCT (J). K–N: Deep T2 hypointensity of a lesion (K) with a T2-blackout effect at $b = 1000$ image (L) but a low signal of actual diffusion restriction on the ADC map (M). Ki-67 proliferation index by immunohistochemistry (original magnification $\times 20$) exceeding 90% (N).

samples frequently includes hemorrhagic tumors with central necrosis.² Accordingly, recent literature reports the presence of hemorrhage on imaging in up to 50% of patients evaluated with SWI (20% with T2WI) and heterogeneous or ring enhancement (usually associated with necrosis) in up to 10%–15% of cases.^{3,15} Therefore, the authors discourage this classic assumption and believe that a certain degree of hemorrhage and heterogeneous or ring enhancements does not rule out suspicion of lymphoma, considering other imaging features as well (Fig 2).

Regarding quantitative imaging techniques beyond DWI, ¹H-MR spectroscopy and DSC-PWI, included in consensus recommendations for imaging CNS lymphoma,¹⁶ have shown promising results for presurgical diagnosis. Attention must be paid to pulse-sequence parameters (TE, TR, flip angle), prebolus usage, and leakage corrections for DSC-PWI, but in general terms, this

tumor shows low-to-intermediate CBV, a high percentage of signal recovery (PSR), and characteristic time-intensity curve morphology.^{7,17,18} Lower CBV values in lymphomas have paradoxically been related to a worse prognosis of survival.¹⁹ ¹H-MR spectroscopy can also reinforce a presurgical suspicion in basically 2 ways: Short TE depicts much lower mIns (described as a glial marker) than that associated with enhancing non-necrotic astrocytoma (ie, grade 3), and long TE shows much lower mobile lipids (associated with necrosis) than glioblastoma or metastasis (Fig 2).²⁰

Brain FDG-PET may play a role in the presurgical differentiation of lymphoma and other malignant brain tumors such as glioblastoma and metastasis because most lymphoma lesions are highly FDG-avid, with homogeneous uptake.¹⁶

As an additional comment on primary DLBCL of the CNS, it has been reported that “sentinel” inflammatory lesions, which may disappear after anti-inflammatory treatment, can precede the diagnosis of lymphoma by up to 2 years,²¹ so attention must be paid to the patient’s history of prior inflammatory brain lesions (Fig 3).

Immunodeficiency-Associated CNS Lymphoma. According to the latest WHO classification, the immunodeficiency-associated CNS lymphoma subtype specifically corresponds to primary DLBCL of the CNS, EBV-positive. Indeed, large B-cell histology and lymphotropic EBV tissue-positivity are currently the essential diagnostic criteria

for immunodeficiency-associated lymphoma of the CNS.² It represents 8%–10% of all primary CNS lymphomas. Despite being considered an infrequent entity, this is the second most frequent type of primary lymphoma of the CNS. Its clinical context has changed during recent decades. Whereas in the 1990s, AIDS due to HIV was the leading cause, currently and especially in more developed countries, other causes predominate, such as post transplant status, autoimmune disease, and iatrogenesis.^{22–28} This shift in the mechanisms of immunodeficiency and other developments in patient monitoring as well as in imaging techniques have also resulted in a change in the main differential diagnoses to consider. Currently, therefore, glioblastoma or metastases are more likely than opportunistic infections, in contrast to previous decades.^{8,29,30}

Morphologic imaging of this lymphoma is quite characteristic, and the opposite of that of the “typical” CNS lymphoma. It can

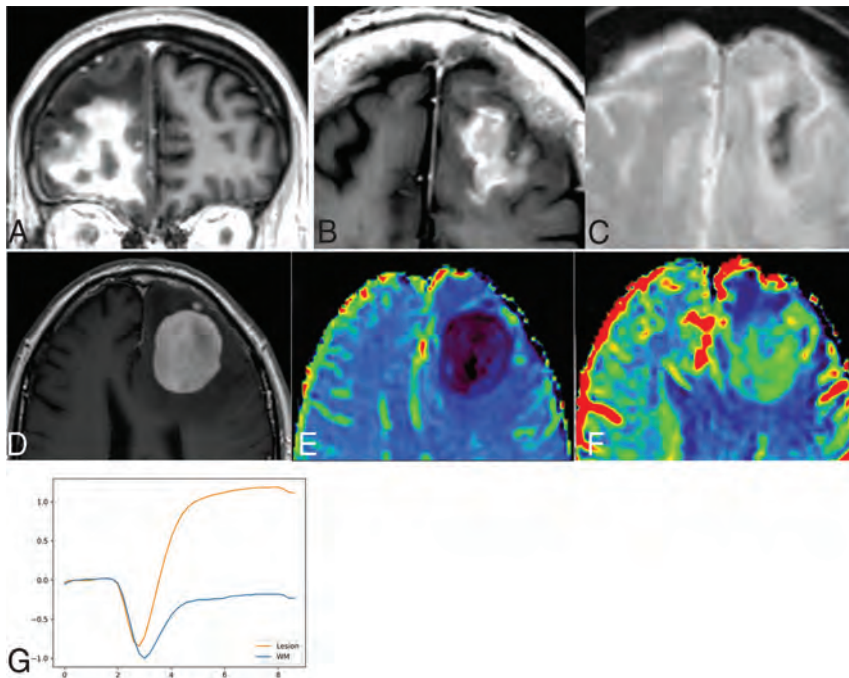


FIG 2. A–C: Primary DLBCLs of the CNS, EBV-negative, with imaging signs of central necrosis (A) and tumoral hemorrhage (B and C). D–G: DSC-PWI features of a left frontal primary DLBCL of the CNS, EBV-negative (D). Low-to-intermediate CBV on noncorrected (E) and corrected (F) color maps. Characteristic lymphoma DSC-PWI time-intensity curve morphology with ascending-part of the curve recovering signal intensity far above the baseline (high PSR) (G).

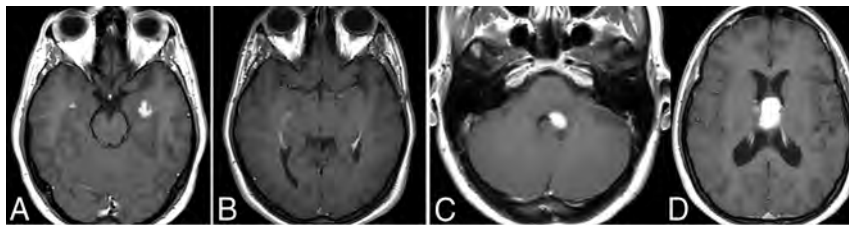


FIG 3. Sentinel inflammatory lesions preceding primary DLBCL of the CNS. Two enhancing periventricular temporal lesions were detected in a patient (A). A biopsy was obtained, and histopathology showed an inflammatory infiltrate without evidence of neoplasia. The lesions disappeared on further imaging controls during the following 2 years (B). In a subsequent MR imaging control, new masslike lesions reappeared (C and D). A biopsy of the new lesions yielded the final histopathologic diagnosis of primary DLBCL of the CNS.

be deep or hemispheric, with a slightly greater tendency to multiplicity. It is almost constantly highly necrotic with ring enhancement and intermediate-to-prominent signs of hemorrhage. T2WI and DWI signal patterns are both variable and inconsistent. In summary, it is a tumor that differs from the typical appearance of lymphoma and, rather, presents more like the main differential diagnoses, which are glioblastoma and metastasis.^{8,29,30} A characteristic T2WI heterogeneous hypointensity of the nonenhancing “necrosis,” not corresponding to blood products or mineralization, has recently been suggested in these tumors, in contrast to the usual hyperintense T2 signal of nonhemorrhagic necrosis in other tumors (Fig 4).⁸

While conventional imaging is often insufficient to reach a presurgical diagnosis of this challenging entity, quantitative imaging, especially DSC-PWI, can provide diagnostic clues. Indeed,

the perfusion features of this lymphoma follow those of low-to-intermediate CBV, high PSR, and the characteristic time-intensity curve morphology when depicting an ROI in the solid parts of tumors (Fig 4).⁸ Finally, the ¹H-MR spectroscopy pattern seems of low value for presurgical characterization as lymphoma because this tumor has prominent mobile lipids overlapping with necrotic glioblastomas or metastasis.²⁰

In conclusion, we suggest that in dealing with a necrohemorrhagic tumor, potential immunodeficiency/dysregulation of the patient must be thoroughly examined. If this cannot be ruled out, DLBCL EBV-positive should be considered, and careful DSC-PWI assessment can provide a presurgical diagnostic clue.

Lymphomatoid Granulomatosis. According to the new WHO classification of hematolymphoid tumors, lymphomatoid granulomatosis is a lymphoproliferative disorder with large atypical EBV-positive B-cells, T-cell infiltration, and tissue necrosis occurring exclusively in immunocompetent patients.⁴ Previously, it was included in the group of immunodeficiency-associated entities, but currently, the identification of an underlying immunocompromised status rules out lymphomatoid granulomatosis, and it should instead be considered a subtype of a polymorphic lymphoproliferative disorder in the setting of immunodeficiency/dysregulation.⁴ Lymphomatoid granulomatosis is a very rare entity that exceptionally occurs primarily in the CNS, though CNS involvement is

usually secondary. It represents a spectrum of lymphoid disease graded from 1 to 3, with corresponding degrees of aggressiveness from indolent to very aggressive.^{2,4}

On imaging, typical findings are those of secondary lymphoma with frequent subependymal or leptomeningeal involvement and perivascular enhancement. Occasionally, it may be angiocentric and angiodestructive, resembling intravascular lymphoma. When there is isolated CNS involvement, it usually corresponds to grade 3 disease, and brain biopsy demonstrates DLBCL EBV-positive,^{2,4} in which case imaging findings may consist of masslike lesions with hemorrhage and necrosis.^{2,4,31,32}

In the recent literature, lymphomatoid granulomatosis has been correlated with chronic lymphocytic inflammation with pontine perivascular enhancement responsive to steroids (CLIPPERS). Some authors hypothesize that this entity is a kind of a sentinel

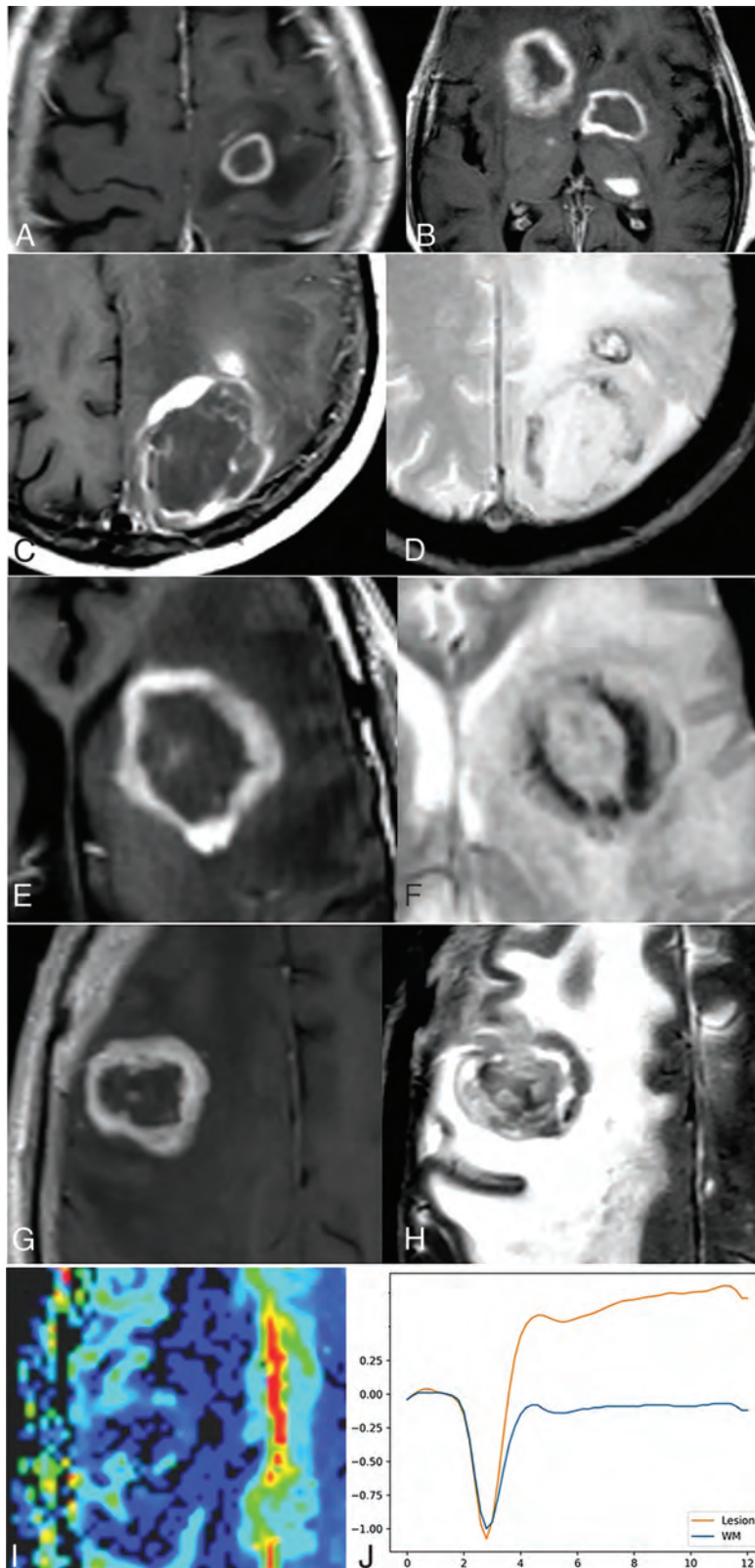


FIG 4. Primary DLBCLs of the CNS, EBV-positive (immunodeficiency/dysregulation-associated). Single (A) and multiple (B) lesions with prominent necrosis (C and E) and tumoral hemorrhage (D and F). Heterogeneous deep T2 hypointensity (H) of the nonenhancing central content (G) of lesions, so-called necrosis. Low-intermediate CBV on the corrected color map (I) and DSC-PWI time-intensity curve with high PSR (J), also very characteristic of this lymphoma subtype.

lesion, while others postulate that CLIPPERS may be an inflammatory response to lymphomatous tumor cells, responding to corticosteroids preceding the definitive tumor recurrence.^{33,34}

Intravascular Large B-Cell Lymphoma of the CNS. Intravascular large B-cell lymphoma of the CNS is defined by the selective proliferation of malignant B large-tumor cells within the brain vessels, particularly small- to medium-sized blood vessels, without or with minimal parenchymal extension. The tumor cells may occlude vessels causing patched bleeding and ischemia. Also, it is not exceptional for some tumor cells to extravasate beyond the vessels, focally reaching brain parenchyma. Regarding clinical presentation, strokelike symptoms are typical, though not always present.³⁵

The main phenomena detected on imaging are ischemic and hemorrhagic lesions, which usually suggest the differential with vasculitis, emboli, or hypercoagulability. The ischemia-like lesions appear dynamic and evanescent between near-in-time imaging follow-ups. Furthermore, those possible tumor cells that extravasate beyond the vessels may focally reach the brain parenchyma, forming tumor islands that can appear as enlarging areas of parenchymal enhancement.^{2,36} Morphologic imaging features on these enhancing islands may be helpful for presurgical suspicion because they can express the signal characteristics of typical lymphoma. In addition, ependymal and leptomeningeal enhancement may also be present.^{36,37} Advanced imaging features may include a tumoral pattern on ¹H-MR spectroscopy with high Cho to NAA ratios, as well as a characteristic DSC-PWI pattern with shortened MTT (differing from ischemic lesions), low-to-intermediate CBV, high PSR, and the characteristic time-intensity curve morphology of lymphomas in the CNS.^{7,18,20}

In summary, this entity should be kept in mind whenever encountering MR imaging with hemorrhage and multiple dynamic ischemic lesions on T2WI and DWI, enlarging parenchymal enhancement, and possible associated leptomeningeal or subependymal disease (Fig 5).^{36,37}

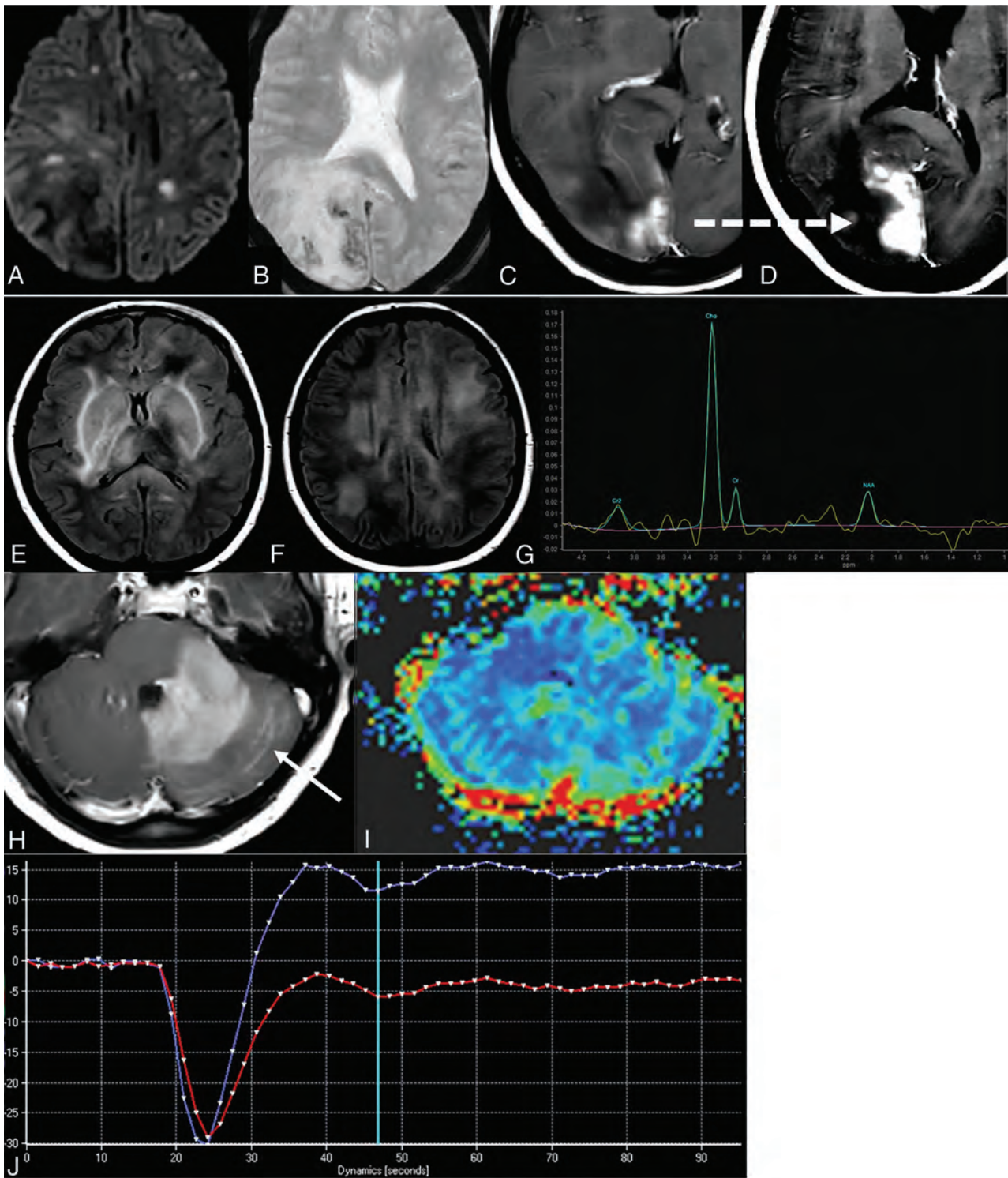


FIG 5. Intravascular lymphoma (A–D). Acute patched ischemia-like lesions on DWI (A), hemorrhages (B), and an area of enhancement (C), which grows on the subsequent few days of imaging control (D). Dashed arrow in C–D indicates the growth of the same enhancing-lesion in few days. DLBCL following a lymphomatosis cerebri pattern (E–J): extensive, patched, bilateral, and diffuse FLAIR hyperintensity on the basal ganglia (E) and white matter (F), with an area of enhancement in the left cerebellum (H) and associated leptomeningeal disease (arrow in H). Intermediate CBV in DSC-PWI color maps (I) and characteristic high PSR and time-intensity curve morphology (J). Tumoral pattern on ¹H-MR spectroscopy at long TE with a high Cho-to-NAA ratio (H) and absent mIns at the short TE (not shown), helpful in the differential diagnosis with nontumoral entities and gliomatosis cerebri, respectively.

MALT Lymphoma of the Dura. Lymphomas arising primarily in the dura are rare ($\approx 1\%$) and usually correspond to MALT lymphoma. Occasionally, large B-cell lymphoma may also be primarily dural. Etiology and underlying associations are unknown.^{2,38}

On conventional imaging, they appear as extra-axial lesions with a wide dural base, soft attachment angles, and a possible CSF cleft between the lesion and brain parenchyma. In addition, edema or brain tissue infiltration can occur. They usually appear

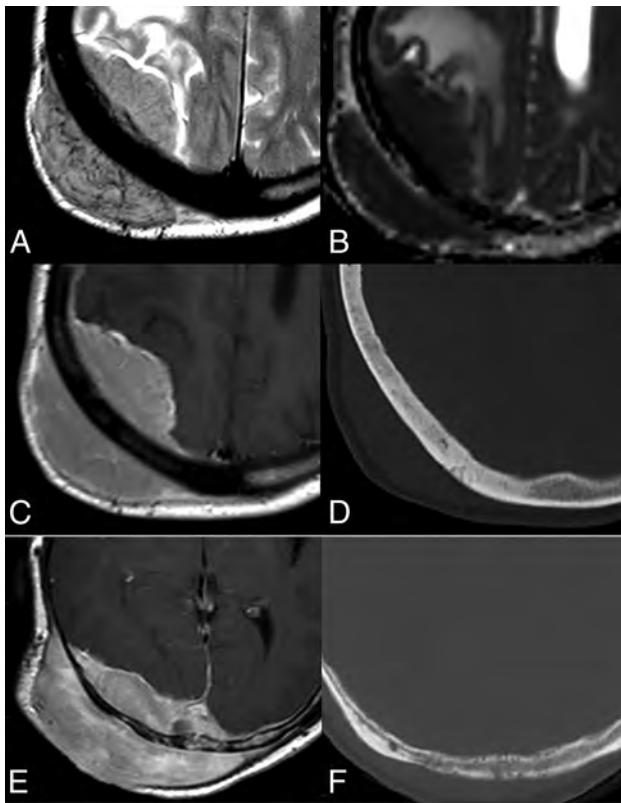


FIG 6. Dural lymphomas. MALT dural lymphoma (A–D) with extra-axial lesion features such as a CSF cleft (A) and a wide-implantation dural base with soft marginal angles (C), as well as T2-hypointensity (A) and diffusion restriction (B). Almost normal calvarial bone; only subtle sclerosis seen (D), despite the great soft-tissue component on both sides of the diploe (A–C). Similar imaging features with minimal bone destruction and a subtle permeative pattern (F) in comparison with the prominent soft-tissue component (E) in another diffuse large B-cell dural lymphoma (E and F).

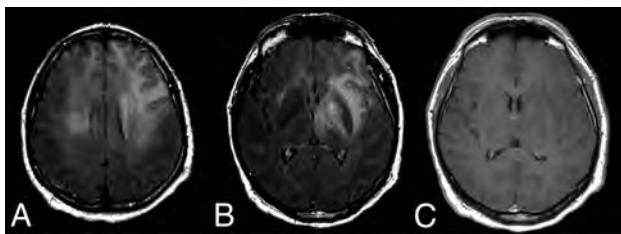


FIG 7. NK/T-cell lymphoma presenting with a lymphomatosis cerebri radiologic pattern (A–C). Patched and diffuse, bilateral and asymmetric, deep and subcortical, hyperintense lesions on FLAIR (A and B) without contrast enhancement (C).

homogeneous, NCCT hyperattenuated, T2WI hypointense, and with restricted diffusion; however, these features overlap with those of the most frequent extra-axial tumor in adults, meningioma (Fig 6).^{39,40}

Regarding advanced imaging, ¹H-MR spectroscopy can be of help for the differential diagnosis because meningiomas characteristically present with alanine, metastases present abundant mobile lipids, and the rarer solitary fibrous tumors (formerly termed hemangiopericytoma) show a high myo-inositol peak.³⁹

A clue for the presurgical suspicion of this tumor is provided by a characteristic pattern of bone infiltration or transdiploic extension. Characteristically, lymphoma presents as an extensive soft-tissue mass without bone destruction (normal bone to subtle permeative patterns) (Fig 6). This pattern is explained by the extension of tumor cells through Haversian canals. It differs from what is seen in meningiomas with hyperostosis or in plasmacytoma or metastasis with aggressive lytic destruction.³⁹

Other Low-Grade B-Cell Lymphomas of the CNS, Anaplastic Large Cell Lymphoma ALK+/ALK–, T-Cell and Natural Killer (NK)/T-Cell Lymphoma. The CNS WHO classification 2021 includes low-grade B-cell lymphoma of the CNS, ALK+/ALK–, T-Cell, and NK/T-cell lymphoma classified as miscellaneous, rare lymphomas in the CNS.² They represent a heterogeneous group of tumors with scarce evidence of concrete imaging findings. While low-grade B-cell lymphomas may occasionally appear as lymphoma-like lesions, other very different radiologic appearances are described, such as resembling edema, glial tumor, meningioma, and gliosis.⁴¹ Regarding anaplastic large-cell and T-cell or NK/T-cell lymphomas, some authors postulate that they may resemble lymphoma or lymphomatosis cerebri on imaging, with other nonspecific presentations also possible (Fig 7). In summary, very heterogeneous imaging presentations, occasionally resembling lymphoma, can be seen in this heterogeneous group of exceptional entities.^{41–43}

Lymphomatosis Cerebri. Lymphomatosis cerebri corresponds to a clinical-radiologic pattern that is not included as a concrete histopathologic WHO entity. It may be observed in the context of different histologic lymphoma subtypes, but in most cases, it corresponds to primary DLBCL of the CNS. The typical clinical presentation is a subacute onset of dementia, cognitive impairment, and personality changes.^{44,45}

It consists of a nonenhancing or scarcely-enhancing (30%) T2-FLAIR hyperintense infiltration of brain tissue. It is usually located in white matter regions, with different distributions ranging from focal to patched or diffuse. The main differential includes gliomatosis cerebri (also considered a radiologic pattern and not a WHO entity) and inflammatory and toxic-metabolic diseases. Of note, in this form of CNS lymphoma, brain lesions may be highly variable and change between near-in-time follow-up scans.^{44–47}

In line with what was detailed in the intravascular lymphoma section, the detection of a tumoral pattern on ¹H-MR spectroscopy without relevant amount of mIns (potential glial marker present in gliomatosis) in abnormal areas of T2-FLAIR hyperintensity, as well as the above-described characteristic DSC-PWI pattern in the possible enhancing lesions, supports presurgical suspicion^{46,47} (Fig 5).

Secondary Lymphomas of the CNS. Secondary lymphoma refers to the CNS spread of lymphoma that originated elsewhere. It may be as an isolated recurrence or as a synchronic systemic disease with an overall incidence of around 5%–10% in patients with systemic lymphomas, usually non-Hodgkins. Its occurrence is directly correlated with pathologic aggressiveness and ranges from <3% in the indolent, less-aggressive histologies to as high as 50% in the very aggressive ones such as Burkitt lymphoma.⁴⁸

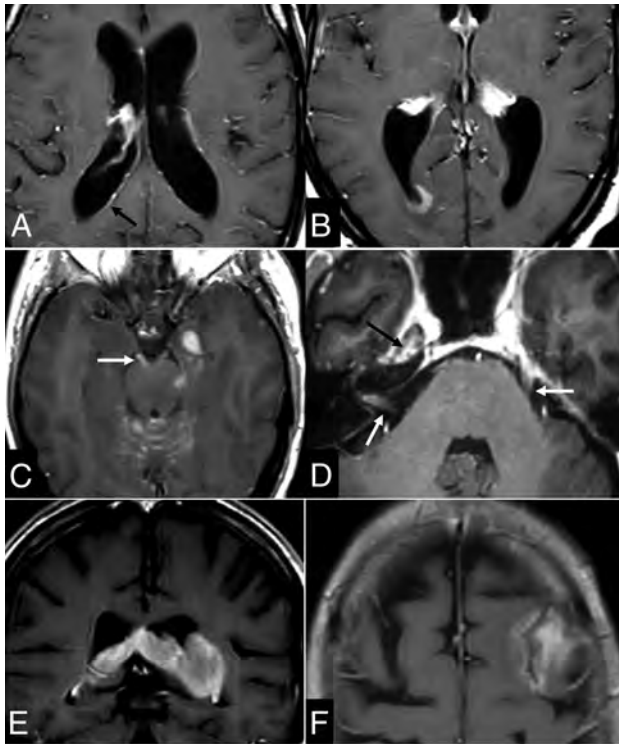


FIG 8. Imaging findings in secondary lymphomas of the CNS. *A–B:* Thin subtle linear (*arrow* in *A*) and nodular (*B*) subependymal enhancements. *C–D:* Prominent leptomeningeal disease along the superior vermis and cerebellar folia and third cranial nerve (*arrow* in *C*) as well as inside the right internal auditory canal—cranial nerves VII and VIII—and along the trigeminal nerve in the right Meckel cave and the left cisternal segment (*arrows* in *D*). Associated parenchymal mass in the left temporal lobe (*C*). *E–F:* Secondary lymphomas presenting as predominant intraparenchymal lesions with associated adjacent subependymal (*E*) and leptomeningeal (*F*) disease.

Although historically, it has been thought that secondary lymphomas presented with leptomeningeal involvement in a high proportion of cases (around 70%¹¹); more recent data differ, suggesting parenchymal involvement in 40%–60%, leptomeningeal in 20%–30%, and both in 10% (Fig 8).^{49,50} This higher proportion of parenchymal involvement in secondary lymphoma is important to consider in the radiologic interpretation because it is non-specific for differentiation from primary CNS lymphoma, in which parenchymal lesions are almost constant.¹¹ Despite these differing disease distributions, imaging can frequently overlap, and differentiation between primary and secondary must rely on other staging examinations, such as a PET/CT scan, bone marrow aspiration, testicular sonography, vitreal examination, and the patient's history of systemic lymphoma.^{48,50}

CONCLUSIONS

The classification of CNS lymphomas is evolving. The radiologist plays a key role in the initial management of lymphomas, and a failure to suggest the possibility of this diagnosis on initial imaging may have a negative clinical impact. For this reason, the radiologist needs to be aware of the full spectrum of imaging presentations of CNS lymphoma. In this sense, we note some key points:

- 1) Primary DLBCLs of the CNS present as homogeneous lesions, hyperdense on NECT, T2 hypointense, and with restricted diffusion. The presence of a certain degree of hemorrhage or signs of necrosis should not rule out their presurgical diagnosis.
- 2) Immunodeficiency-associated lymphomas (primary DLBCLs of the CNS, EBV-positive) appear as necrohemorrhagic tumors in potentially immunocompromised hosts. Special attention must be paid to the features of DSC-PWI, which may provide findings that suggest lymphoma.
- 3) Dural lymphoma should be suspected when a disproportionate soft-tissue mass without relevant bone destruction is identified in an extra-axial transdiploic tumor.
- 4) Intravascular lymphoma and lymphomatosis cerebri may be evolutive diagnoses of suspicion when dynamically changing T2-FLAIR areas of signal abnormality (and hemorrhage in intravascular lymphoma) are found. Also, attention must be paid to leptomeningeal and subependymal enhancement.
- 5) DSC-PWI and ¹H-MRS provide clues of great help in the differential diagnosis for each lymphoma subtype.
- 6) Secondary lymphomas often appear as parenchymal lesions. Isolated leptomeningeal or subependymal disease is characteristic but apparently less prevalent than formerly assumed.

ACKNOWLEDGMENTS

We thank CERCA Programme/Generalitat de Catalunya for institutional support.

Disclosure forms provided by the authors are available with the full text and PDF of this article at www.ajnr.org.

REFERENCES

1. Miller KD, Ostrom QT, Kruchko C, et al. **Brain and other central nervous system tumor statistics, 2021.** *CA Cancer J Clin* 2021;71:381–406 CrossRef Medline
2. World Health Organization. **Central Nervous System Tumors.** *WHO Classification of Tumours Online.* 5th ed. <https://tumourclassification.iarc.who.int/welcome/>. Accessed January 16, 2023
3. Velasco R, Mercadal S, Vidal N, et al; GELTAMO and GENOSEN Group. **Diagnostic delay and outcome in immunocompetent patients with primary central nervous system lymphoma in Spain: a multicentric study.** *J Neurooncol* 2020;148:545–54 CrossRef Medline
4. World Health Organization. **Hematolymphoid Tumours.** *WHO Classification of Tumours Online.* 5th ed. <https://tumourclassification.iarc.who.int/welcome/>. Accessed January 16, 2023
5. Tang YZ, Booth TC, Bhogal P, et al. **Imaging of primary central nervous system lymphoma.** *Clin Radiol* 2011;66:768–77 CrossRef Medline
6. Mansour A, Qandeel M, Abdel-Razeq H, et al. **MR imaging features of intracranial primary CNS lymphoma in immune competent patients.** *Cancer Imaging* 2014;14:1–9 CrossRef Medline
7. Pons-Escoda A, Garcia-Ruiz A, Naval-Baudin P, et al. **Presurgical identification of primary central nervous system lymphoma with normalized time-intensity curve: a pilot study of a new method to analyze DSC-PWI.** *AJNR Am J Neuroradiol* 2020;41:1816–24 CrossRef Medline
8. Pons-Escoda A, Garcia-Ruiz A, Naval-Baudin P, et al. **Diffuse large B-cell Epstein-Barr virus-positive primary CNS lymphoma in non-AIDS patients: high diagnostic accuracy of DSC perfusion metrics.** *AJNR Am J Neuroradiol* 2022;43:1567–74 CrossRef Medline
9. Cree IA. **The WHO Classification of Haematolymphoid Tumours.** *Leukemia* 2022;36:1701–02 CrossRef Medline
10. Li W. *The 5(th) Edition of the World Health Organization Classification of Hematolymphoid Tumors.* In: Li W, ed. Brisbane (AU) 2022

11. Haldorsen IS, Espeland A, Larsson E-M. **Central nervous system lymphoma: characteristic findings on traditional and advanced imaging.** *AJNR Am J Neuroradiol* 2011;32:984–92 CrossRef Medline
12. Deckert M, Brunn A, Montesinos-Rongen M, et al. **Primary lymphoma of the central nervous system: a diagnostic challenge.** *Hematol Oncol* 2014;32:57–67 CrossRef Medline
13. Brunn A, Nagel I, Montesinos-Rongen M, et al. **Frequent triple-hit expression of MYC, BCL2, and BCL6 in primary lymphoma of the central nervous system and absence of a favorable MYC(low)BCL2 (low) subgroup may underlie the inferior prognosis as compared to systemic diffuse large B cell lymphomas.** *Acta Neuropathol* 2013;126:603–05 CrossRef Medline
14. Jhaveri MD. **Chapter 173: diffuse large B-cell lymphoma.** In: Jhaveri MD, Osborn AG, Salzman KL. *Diagnostic Imaging: Brain*. 4th ed. Elsevier; 2020:602–06
15. Sakata A, Okada T, Yamamoto A, et al. **Primary central nervous system lymphoma: is absence of intratumoral hemorrhage a characteristic finding on MRI?** *Radiol Oncol* 2015;49:128–34 CrossRef Medline
16. Barajas RF, Politi LS, Anzalone N, et al. **Consensus recommendations for MRI and PET imaging of primary central nervous system lymphoma: guideline statement from the International Primary CNS Lymphoma Collaborative Group (IPCG).** *Neuro Oncol* 2021;23:1056–71 CrossRef Medline
17. Lee MD, Baird GL, Bell LC, et al. **Utility of percentage signal recovery and baseline signal in DSC-MRI optimized for relative CBV measurement for differentiating glioblastoma, lymphoma, metastasis, and meningioma.** *AJNR Am J Neuroradiol* 2019;40:1145–450 CrossRef Medline
18. Xing Z, You RX, Li J, et al. **Differentiation of primary central nervous system lymphomas from high-grade gliomas by rCBV and percentage of signal intensity recovery derived from dynamic susceptibility-weighted contrast-enhanced perfusion MR imaging.** *Clin Neuroradiol* 2014;24:329–36 CrossRef Medline
19. Valles FE, Perez-Valles CL, Regalado S, et al. **Combined diffusion and perfusion MR imaging as biomarkers of prognosis in immunocompetent patients with primary central nervous system lymphoma.** *AJNR Am J Neuroradiol* 2013;34:35–40 CrossRef Medline
20. Mora P, Majós C, Castañer S, et al. **1H-MRS is useful to reinforce the suspicion of primary central nervous system lymphoma prior to surgery.** *Eur Radiol* 2014;24:2895–905 CrossRef Medline
21. Hussein L, Saleh A, Reifenberger G, et al. **Inflammatory demyelinating brain lesions heralding primary CNS lymphoma.** *Can J Neurol Sci* 2012;39:6–10 CrossRef Medline
22. Levine AM. **Lymphoma complicating immunodeficiency disorders.** *Ann Oncol* 1994;5(5 Suppl 2):29–35 CrossRef Medline
23. Gandhi MK, Hoang T, Law SC, et al. **EBV-associated primary CNS lymphoma occurring after immunosuppression is a distinct immunobiological entity.** *Blood* 2021;137:1468–77 CrossRef Medline
24. Mahale P, Shiels MS, Lynch CF, et al. **Incidence and outcomes of primary central nervous system lymphoma in solid organ transplant recipients.** *Am J Transplant* 2018;18:453–61 CrossRef Medline
25. Verdu-Bou M, Tapia G, Hernandez-Rodriguez A, et al. **Clinical and therapeutic implications of Epstein-Barr virus in HIV-related lymphomas.** *Cancers (Basel)* 2021;13:5534 CrossRef Medline
26. Kaulen LD, Karschnia P, Dietrich J, et al. **Autoimmune disease-related primary CNS lymphoma: systematic review and meta-analysis.** *J Neurooncol* 2020;149:153–59 CrossRef Medline
27. Mancuso S, Carlisi M, Santoro M, et al. **Immunosenescence and lymphomagenesis.** *Immun Ageing* 2018;15:1–7 CrossRef Medline
28. Barosi G. **An immune dysregulation in MPN.** *Curr Hematol Malig Rep* 2014;9:331–39 CrossRef Medline
29. Suh CH, Kim HS, Lee SS, et al. **Atypical imaging features of primary central nervous system lymphoma that mimics glioblastoma: utility of intravoxel incoherent motion MR imaging.** *Radiology* 2014;272:504–13 CrossRef Medline
30. Sauter A, Faul C, Bitzer M, et al. **Imaging findings in immunosuppressed patients with Epstein Barr virus-related B cell malignant lymphoma.** *Am J Roentgenol* 2010;194:W141–49 CrossRef Medline
31. Patsalides AD, Atac G, Hedge U, et al. **Lymphomatoid granulomatosis: abnormalities of the brain at MR imaging.** *Radiology* 2005;237:265–73 CrossRef Medline
32. Tateishi U, Terae S, Ogata A, et al. **MR imaging of the brain in lymphomatoid granulomatosis.** *AJNR Am J Neuroradiol* 2001;22:1283–90 Medline
33. De Graaff HJ, Wattjes MP, Rozemuller-Kwakkel AJ, et al. **Fatal B-cell lymphoma following chronic lymphocytic inflammation with pontine perivascular enhancement responsive to steroids.** *JAMA Neurol* 2013;70:915–18 CrossRef Medline
34. Dang YL, Kok HK, McKelvie PA, et al. **Chronic lymphocytic infiltration with pontine perivascular enhancement responsive to steroids (CLIPPERS) and its association with Epstein-Barr virus (EBV)-related lymphomatoid granulomatosis: a case report.** *BMC Neurol* 2021;21:80 CrossRef Medline
35. Fonkem E, Dayawansa S, Stroberg E, et al. **Neurological presentations of intravascular lymphoma (IVL): meta-analysis of 654 patients.** *BMC Neurol* 2016;16:9 CrossRef Medline
36. Baehring JM, Henchcliffe C, Ledezma CJ, et al. **Intravascular lymphoma: magnetic resonance imaging correlates of disease dynamics within the central nervous system.** *J Neurol Neurosurg Psychiatry* 2005;76:540–44 CrossRef Medline
37. Yamamoto A, Kikuchi Y, Homma K, et al. **Characteristics of intravascular large B-cell lymphoma on cerebral MR imaging.** *AJNR Am J Neuroradiol* 2012;33:292–96 CrossRef Medline
38. Quinn ZL, Zakharia K, Schmid JL, et al. **Primary dural diffuse large B-cell lymphoma: a comprehensive review of survival and treatment outcomes.** *Clin Lymphoma Myeloma Leuk* 2020;20:e105–12 CrossRef Medline
39. Pons Escoda A, Naval Baudin P, Mora P, et al. **Imaging of skull vault tumors in adults.** *Insights Imaging* 2020;11:23 CrossRef Medline
40. Smith AB, Horkanyne-Szakaly I, Schroeder JW, et al. **From the Radiologic Pathology Archives: mass lesions of the dura—beyond meningioma, radiologic-pathologic correlation.** *Radiographics* 2014;34:295–312 CrossRef Medline
41. Jahnke K, Schilling A, Heidenreich J, et al. **Radiologic morphology of low-grade primary central nervous system lymphoma in immunocompetent patients.** *AJNR Am J Neuroradiol* 2005;26:2446–54 Medline
42. Magaki S, Satyadev R, Chen Z, et al. **Central nervous system ALK-negative anaplastic large cell lymphoma with IRF4/DUSP22 rearrangement.** *Brain Tumor Pathol* 2022;39:25–34 CrossRef Medline
43. Menon MP, Nicolae A, Meeke H, et al. **Primary CNS T-cell lymphomas: a clinical, morphologic, immunophenotypic, and molecular analysis.** *Am J Surg Pathol* 2015;39:1719–29 CrossRef Medline
44. Izquierdo C, Velasco R, Vidal N, et al. **Lymphomatosis cerebri: a rare form of primary central nervous system lymphoma: analysis of 7 cases and systematic review of the literature.** *Neuro Oncol* 2016;18:707–15 CrossRef Medline
45. Hatanpaa KJ, Fuda F, Koduru P, et al. **Lymphomatosis cerebri: a diagnostic challenge.** *JAMA Neurol* 2015;72:1066–67 CrossRef Medline
46. Li L, Rong JH, Feng J. **Neuroradiological features of lymphomatosis cerebri: a systematic review of the English literature with a new case report.** *Oncol Lett* 2018;16:1463–74 CrossRef Medline
47. Yu H, Gao B, Liu J, et al. **Lymphomatosis cerebri: a rare variant of primary central nervous system lymphoma and MR imaging features.** *Cancer Imaging* 2017;17:26 CrossRef Medline
48. Nagpal S, Glantz MJ, Recht L. **Treatment and prevention of secondary CNS lymphoma.** *Semin Neurol* 2010;30:263–72 CrossRef Medline
49. Ferreri AJM, Doorduijn JK, Re A, et al; International Extranodal Lymphoma Study Group (IELSG). **MATRIX-RICE therapy and autologous haematopoietic stem-cell transplantation in diffuse large B-cell lymphoma with secondary CNS involvement (MARIETTA): an international, single-arm, phase 2 trial.** *Lancet Haematol* 2021;8:e110–21 CrossRef Medline
50. Bobillo S, Khwaja J, Ferreri AJM, et al. **Prevention and management of secondary central nervous system lymphoma.** *Haematologica* 2022. Nov 17 CrossRef Medline

Newly Recognized CNS Tumors in the 2021 World Health Organization Classification: Imaging Overview with Histopathologic and Genetic Correlation

R.K. Rigsby, P. Brahmbhatt, A.B. Desai, G. Bathla, B.A. Ebner, V. Gupta, P. Vibhute, and A.K. Agarwal



ABSTRACT

SUMMARY: In 2021, the World Health Organization released an updated classification of CNS tumors. This update reflects the growing understanding of the importance of genetic alterations related to tumor pathogenesis, prognosis, and potential targeted treatments and introduces 22 newly recognized tumor types. Herein, we review these 22 newly recognized entities and emphasize their imaging appearance with correlation to histologic and genetic features.

ABBREVIATIONS: AT/RT = atypical teratoid/rhabdoid tumor; cIMPACT-NOW = Consortium to Inform Molecular and Practical Approaches to CNS Tumor Taxonomy-Not Official WHO; GFAP = glial fibrillary acidic protein; MAPK = mitogen-activated protein kinase; NEC = not elsewhere classified; NOS = not otherwise specified; PFA and PFB = posterior fossa ependymoma groups A and B; WHO = World Health Organization; WHO CNS5 = *World Health Organization Classification of Tumors of the Central Nervous System*, fifth edition; IDH = isocitrate dehydrogenase

The World Health Organization (WHO) published the *World Health Organization Classification of Tumors of the Central Nervous System*, fifth edition (WHO CNS5),¹ WHO CNS5 builds on the fourth edition, published in 2016, and the recommendations of the Consortium to Inform Molecular and Practical Approaches to CNS Tumor Taxonomy-Not Official WHO (cIMPACT-NOW),² which produced 7 updates between 2018 and 2020.³⁻⁹

The continued discovery of pathologically relevant molecular markers, along with an improved understanding of secondary alterations in tumor biology and clinical course, has led to recognition of 22 new tumor types, in addition to nomenclature changes to the existing classification. Three provisional entities are included, which appear clinicopathologically distinct but await additional studies before full acceptance.¹

Despite the increasing realization of the altered molecular profile and clinical course, the imaging data on the newly recognized entities remain scarce, mostly confined to case reports and small case series.¹⁰⁻¹² Herein, we present a consolidated review of the WHO CNS5 new tumor types with emphasis on the

common imaging findings. A brief review of the general changes to the tumor taxonomy, nomenclature, and grading system is also presented.

Immunohistochemistry and Molecular Markers

Basic histology has been the backbone of previous WHO classifications of >100 known CNS tumors. Under these classifications, however, there was marked interobserver variability and poor differentiation of tumors with diverse biologic behavior. Immunohistochemistry provided major insights into the cellular markers of tumor phenotype and stronger correlations with tumor behavior, resulting in improved standardization. This information has been in routine use for more than a decade with continual improvements and discovery of new immunohistochemical stains. In 2016, for the first time, molecular markers were used in addition to histology for the classification of CNS tumors. WHO CNS5 makes a substantial addition of specific genetic markers to immunohistochemistry and histology. Epigenetic markers, particularly alterations in DNA methylation, have also been added. These have proved immensely valuable not only for diagnosis but also for prognosis and treatment guidance.

During the past decade, DNA methylation profiling has emerged as a powerful tool for research, which has started making its way into the classification system. At present, it can assess the methylation status of 850,000 cytosine-guanine sites across the human genome with huge data sets matched through standardized controls, providing great precision in tumor identification. Using these techniques, the German Cancer Research Center and Heidelberg University have provided a reference cohort for almost

Received November 2, 2022; accepted after revision December 14.

From the Department of Radiology (R.K.R., P.B., A.B.D., V.G., P.V., A.K.A.), Mayo Clinic, Jacksonville, Florida; Department of Radiology (G.B.), Mayo Clinic, Rochester, Minnesota; and Department of Laboratory Medicine and Pathology (B.A.E.), Mayo Clinic, Rochester, Minnesota.

Please address correspondence to Amit K. Agarwal, MBBS, MD, Department of Radiology, Mayo Clinic, 4500 San Pablo Rd S, Jacksonville, FL 32224; e-mail: Agarwal.Amit@mayo.edu

Indicates open access to non-subscribers at www.ajnr.org

Indicates article with online supplemental data.

<http://dx.doi.org/10.3174/ajnr.A7827>

all known tumor entities (www.molecularneuropathology.org). Machine learning tools can easily and accurately match a sample cohort with the references in the data base.^{13,14} At present, 4 of the newly recognized tumors use unique methylation profiles as part of their defining characteristics (high-grade astrocytoma with piloid features, diffuse glioneuronal tumor with oligodendroglioma-like features and nuclear clusters, and posterior fossa ependymoma, groups A and B [PFA and PFB]).

Tumor Taxonomy and Nomenclature

WHO CNS5 recognizes the variability in the need for molecular marker-based diagnoses. Some tumors have molecular characteristics that enable a complete diagnosis, whereas other tumors do not require a molecular approach for diagnosis. Thus, the current hybrid taxonomy is thought to represent an intermediate stage preceding even more precise future classifications. The only pertinent changes to the current taxonomy are “type” replacing “entity” and “subtype” replacing “variant.”¹

WHO CNS5 attempts to make nomenclature more consistent and simpler per the 2019 cIMPACT-NOW Utrecht meeting recommendations.⁹ WHO CNS5 uses simplified tumor names and only includes location, age, or genetic modifiers with established clinical utility. Nevertheless, the nomenclature changes are not uniformly applied because several historical terms are deeply ingrained in the literature (eg, medulloblastoma, myxopapillary ependymoma, pleomorphic xanthoastrocytoma), and name changes could be substantially disruptive to clinical care and scientific experiments. Gene and protein nomenclature has been updated to bring consistency across other existing guidelines.

CNS Tumor Grading

Two noteworthy changes to the grading system include the use of Arabic instead of Roman numerals and the use of tumor grades within types. For example, anaplastic astrocytoma, which was WHO grade III, is no longer a tumor type. Rather, an isocitrate dehydrogenase (IDH)-mutant tumor is now categorized as grade 2, 3, or 4 based on a combination of histologic and molecular information. Both changes ensure more nomenclature uniformity across classification systems of non-CNS tumors. Additionally, the use of tumor grades within types allows more flexibility, while at the same time emphasizing biologic similarity within tumor types.¹

Not Otherwise Specified and Not Elsewhere Classified

Not otherwise specified (NOS) implies a lack of or failure to obtain available molecular, histologic, or genetic information, which limits making a specific diagnosis. Not elsewhere classified (NEC) refers to cases in which the diagnostic testing has been successful but the results do not readily conform to a standard diagnosis under WHO CNS5. Both modifiers are primarily meant to alert the oncologist to either a lack of complete work-up (NOS) or lack of a standard diagnosis despite adequate work-up (NEC).

Bone and Soft-Tissue Tumors

WHO CNS5 attempts to align the classification of mesenchymal nonmeningothelial tumors with the WHO classification of bone and soft-tissue tumors. Tumors that overlapped both classification systems but were rarely encountered in the CNS (eg, leiomyoma)

were removed.¹ Additionally, 3 newly recognized mesenchymal tumors were added to WHO CNS5: intracranial mesenchymal tumor, FET-CREB fusion-positive, *CIC*-rearranged sarcoma, and primary intracranial sarcoma, *DICER1*-mutant.¹

The following sections describe the WHO CNS5 newly described tumor types and are summarized in the Online Supplemental Data. For a general review of WHO CNS5, the readers are referred to an excellent review by Osborn et al.¹⁵

Diffuse Astrocytoma, MYB- or MYBL1-Altered

This WHO grade 1 tumor is 1 of 4 low-grade pediatric tumors that require molecular differentiation from one another due to their similar, nonspecific, low-grade histologic characteristics.¹ The defining feature of this tumor is structural variation, such as fusion, rearrangements, or amplification, involving *MYB* or *MYBL1*, which are transcriptional regulators for cellular proliferation and differentiation.¹⁶ IDH and H3 are wild-type by definition.⁶ The median age at diagnosis is 5 years (range, 0–26 years), and there is no sex predilection.¹⁷ Reflecting the histopathology, the imaging features are nonspecific but typical of a low-grade glioma with an infiltrative, heterogeneously T2-hyperintense, nonenhancing, non-diffusion-restricting mass. The cerebral cortex is the most common location, followed by supratentorial white matter/deep gray nuclei, then the brainstem (Fig 1).¹⁷

Polymorphous Low-Grade Neuroepithelial Tumor of the Young

Polymorphous low-grade neuroepithelial tumor of the young is another of the 4 types of pediatric low-grade tumors and is definitionally WHO grade 1.¹ It is a glial tumor with oligodendrocytic features, frequent calcifications, and an infiltrative growth pattern. It is characterized by strong CD34 immunostaining and mitogen-activated protein kinase (MAPK) pathway alterations, specifically involving *FGFR* or *BRAF*.¹⁸ The most specific alteration appears to be *FGFR2-CTNNA3* fusion.¹⁶ The median age at diagnosis is 15.5 years (range, 5–57 years), with a slight female predominance (male/female ratio, 1:1.7), and epilepsy is the most common presentation (87%).¹⁹ The tumor is located supratentorially, almost always cortically or subcortically, with two-thirds in the temporal lobe. Prominent dense calcifications are classic, with calcifications occurring in 83% of cases. Typical tumors are well-circumscribed, solid, and cystic, T1- and T2-signal variable, T2-FLAIR hyperintense, and nonenhancing or mildly enhancing (Fig 2).¹⁹

Diffuse Low-Grade Glioma, MAPK Pathway–Altered

Diffuse low-grade glioma is another of the low-grade pediatric tumors. While not yet assigned a WHO grade, histologically, it behaves like a WHO grade 2 tumor with an oligodendroglial, astrocytic, or mixed pattern with infiltrative growth and typical low-grade cellular features.¹⁶ Numerous molecular alterations can activate the oncogenic MAPK pathway. More common alterations involve *FGFR1* and *BRAF*; less common alterations involve *NTRK1/2/3*, *MET*, *FGFR2*, and *MAP2K1*. *IDH1/2* and *H3F3s* mutations and *CDKN2A* homozygous deletions must be absent.¹⁶ This tumor commonly presents with epilepsy in the pediatric population and occasionally in adults. While there is a paucity of

literature on the radiologic findings of this tumor, given its histopathologic similarity to the other pediatric low-grade tumors, it is presumed that the imaging findings are also similar. A T2-FLAIR and T2-hyperintense, nonenhancing, cortical, temporal lobe mass is demonstrated (Fig 3).

Diffuse Hemispheric Glioma, H3 G34-Mutant

Diffuse hemispheric glioma is a high-grade pediatric-type tumor, definitionally WHO grade 4.^{1,20} Histopathologic features are similar to those of either glioblastoma or what was previously called a primitive neuroectodermal tumor. The glioblastoma-type tumors are malignant, hypercellular gliomas with astrocytic differentiation, high mitotic rates, microvascular proliferation, and necrosis. The defining molecular feature of this tumor is a missense mutation of *H3F3a*, which codes for histone H3, causing arginine or less commonly valine to be substituted for the normal glycine 34 (when numbered using the legacy nomenclature, which does not include the initiating methionine in the numbering).^{1,20} There is a strong association with *ATRX* and *TP53* mutations. *PDGFRA* amplification is associated with the glioblastoma morphology. *CCND2* amplification is associated with the primitive neuroectodermal tumor morphology.^{1,20} The median age at diagnosis is 15.8 years (interquartile range, 13–22 years), with a slight male predominance (male/female ratio, 1.5:1).²¹ The frontal and parietal lobes are the most common locations with frequent abutment of leptomeningeal or ependymal surfaces. Margins may be sharp or ill-defined. Most tumors are hyperdense,

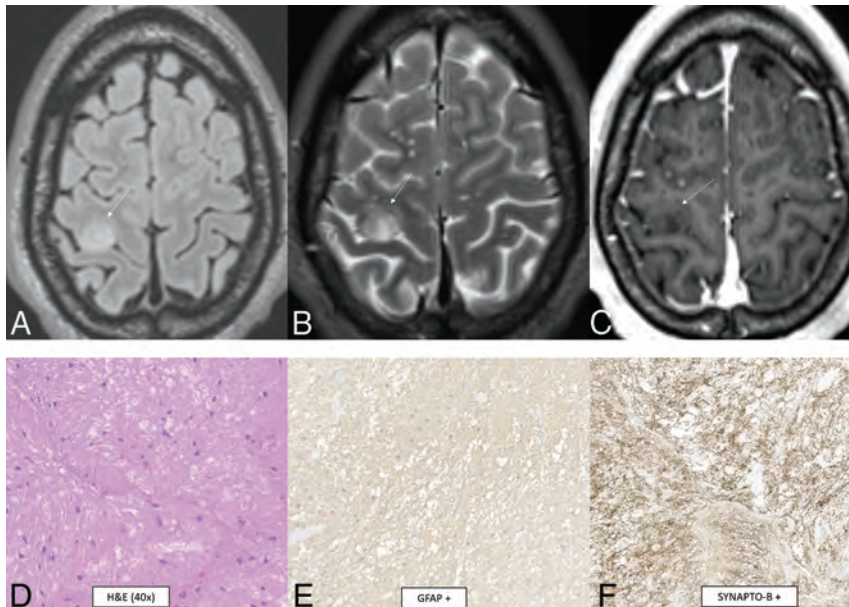


FIG 1. Diffuse astrocytoma, *MYB*- or *MYBL1*-altered. A cortical T2 FLAIR (A) and T2 (B) hyperintense mass is noted within the right precentral gyrus (arrows) with low T1 signal and no enhancement (C). Histopathology reveals mildly hypercellular white matter with vaguely hypocellular areas and atypical glial cells (D), which are positive for GFAP (E) and synaptophysin (F). Chromosomal microarray analysis revealed a gain of 8q13.1q21.3, disrupting *MYBL1*. This is a WHO grade 1 tumor.

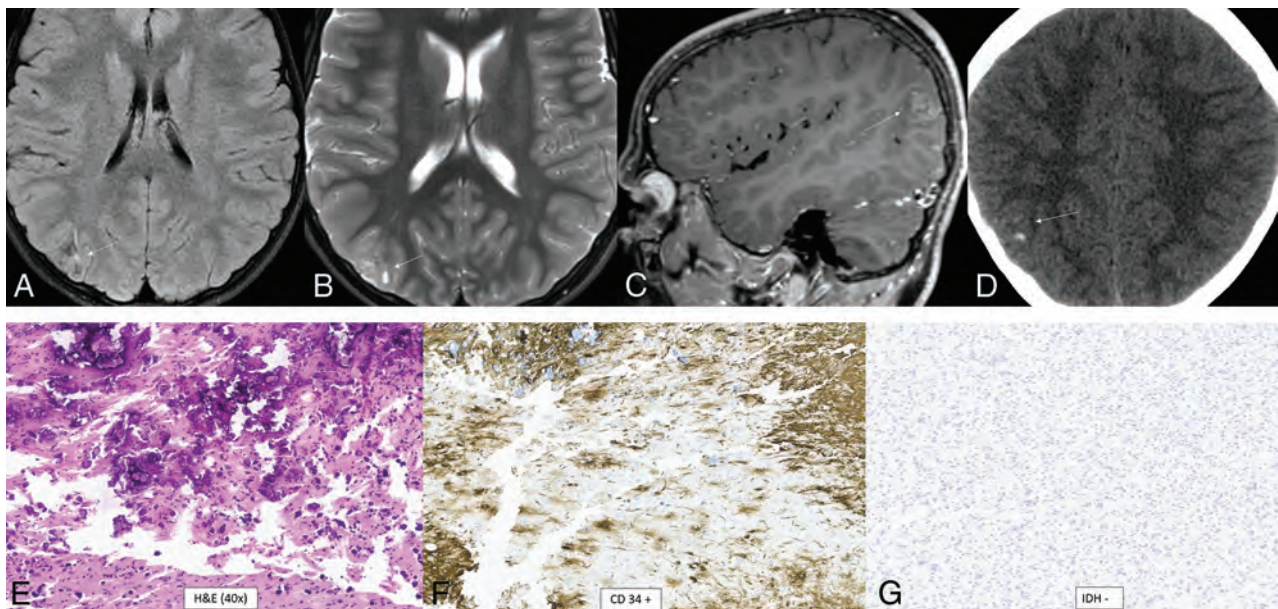


FIG 2. Polymorphous low-grade neuroepithelial tumor of the young. It is a cortical/subcortical mass on T2-FLAIR (A) and T2-weighted images (B) with a cystic (“bubbly”) appearance, some suppression of fluid signal on the FLAIR image, and faint heterogeneous enhancement (C) within the right inferior parietal lobule (arrows). CT shows faint specks of calcification within the lesion (D). Histology demonstrates a relatively well-demarcated low-grade neuroepithelial tumor with prominent dystrophic calcification (E). Tumor cells have oligodendroglial-like morphology and are strongly positive for CD34 (F), with low proliferative activity. Immunohistochemical stain is negative for IDH1 R132H (G) and positive for OLIG2. Chromosomal microarray identified loss of 10q21.3q26.13 disrupting *CTNNA3* and *FGFR2*, representing a *FGFR2-CTNNA3* fusion.

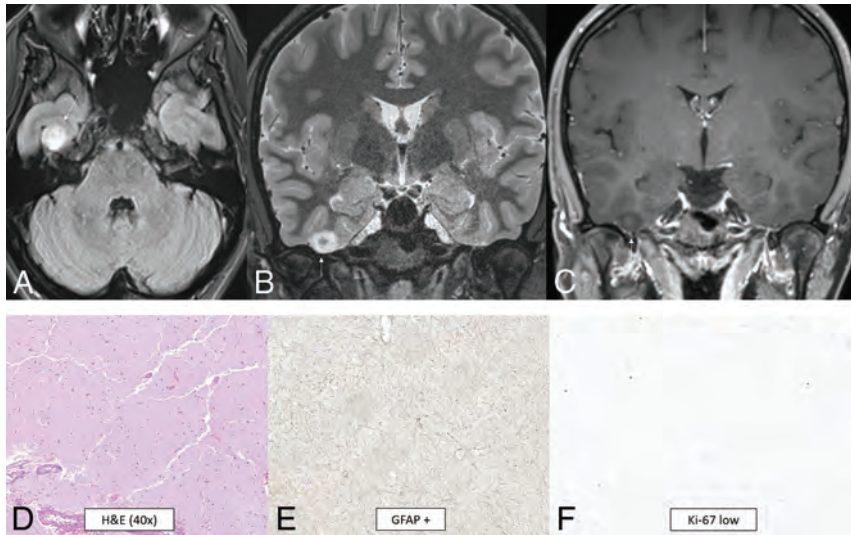


FIG 3. Diffuse low-grade glioma, MAPK pathway–altered. A cortical T2-FLAIR (A) and T2-hyperintense mass (B) is noted within the right fusiform gyrus (arrows) with low T1 signal and no enhancement (C). A histologic section shows a diffusely infiltrating glioma of low cellularity with no mitotic activity, microvascular proliferation, or necrosis (D). Immunohistochemical staining is positive for GFAP (E) and shows a low Ki-67 proliferation index (F). Targeted next-generation sequencing identified a *QKI-NTRK2* fusion, suggestive of MAPK pathway alteration.

T1-hypointense, T2-hyperintense, enhancing, and diffusion-restricting. In adults, there may be no or only faint enhancement, in which case diffusion restriction is more helpful in assessing aggressiveness.²² Tumoral hemorrhage and necrosis can be seen and occasionally calcification (Fig 4).²³

Diffuse Pediatric-Type High-Grade Glioma, H3 Wild-Type and IDH Wild-Type

Diffuse pediatric-type high-grade glioma is another of the 4 pediatric high-grade glioma types. It does not have an assigned WHO grade or a single defining molecular or genetic feature.¹ About half of tumors previously classified as “pediatric glioblastoma” demonstrate mutations of histone 3 or uncommonly *IDH1/2*. The remaining heterogeneous tumors now fall under this new classification. The 3 recognized subtypes are characterized by *MYCN*, *PDGFRA*, and *EGFR* amplifications with numerous coexisting genetic abnormalities described.²⁴ The *MYCN* subtype has high cellularity and mitosis, spindle, and epithelioid cell components; necrosis; and microvascular proliferation.^{25,26} The median age at diagnosis is 8–11 years (range, 2–18 years).²⁴ There is no sex predilection overall, but there is a slight male predominance for the *EGFR* subtype (male/female ratio, 1.6:1).²⁴ The location is usually supratentorial, with the posterior fossa approaching 20% of cases, depending on subtype.²⁴ The *MYCN* subtype classically shows a solid, enhancing, diffusion-restricting, well-margined temporal lobe mass abutting the meninges with tumoral necrosis, rare hemorrhage, and no calcifications.^{25,26} A tumor in the pons has greater enhancement and diffusion restriction compared with a diffuse midline glioma, H3 K27-altered.²⁵ Figure 5 demonstrates a less-typical case without enhancement of the primary tumors.

Infant-Type Hemispheric Glioma

Infant-type hemispheric glioma is a pediatric-type, diffuse, high-grade glioma that has not yet been assigned a specific WHO grade.

The hallmark of this tumor is receptor tyrosine kinase gene fusions of *ALK*, *ROS1*, *NTRK1/2/3*, or *MET*.¹ *NTRK3* fusion has also been described in congenital mesoblastic nephroma and congenital fibrosarcoma, implying that such genetic alterations are tied to age-related mechanisms.²⁷ Most of these tumors show high-grade histologic features.²⁷ Histopathology shows hypercellularity, astrocytic differentiation, necrosis, microvascular proliferation, and nuclear pleomorphism.²⁸ The median age at diagnosis is 2.8 months (range, 0.0–12.0 months) with no sex predilection. Overall median survival is 1.9 years.²⁷ The tumors are almost always located in the cerebral hemispheres.²⁷ Imaging data are scarce, but tumors tend to be large with solid and prominent cystic components, intratumoral hemorrhage, and enhancement.^{29–31} Leptomeningeal disease has been reported.³⁰

High-Grade Astrocytoma with Piloid Features

High-grade astrocytoma with piloid features is a circumscribed astrocytic glioma that has not yet been assigned a WHO grade but behaves like WHO grade 3 or 4.^{8,15} A hallmark of this tumor is its unique methylation profile.³² The most common genetic abnormalities are *cdkn2A/B* deletion, MAPK pathway alteration (affecting *NF1*, *BRAF*, and *FGFR1*), and *ATRX* mutation or loss of expression. Histologically, tumors tend to show moderate cellularity, glioblastoma-like foci, moderate nuclear pleomorphism, a moderate mitotic rate, lack of necrosis, vascular hypertrophy, and infiltrative growth.³² Most occur in the posterior fossa (74%), usually in the cerebellum, followed by supratentorial then spinal locations. The median age is 41.5 years, with occurrence from pediatrics to the elderly and no sex predilection.³² There appears to be an association with neurofibromatosis type 1.³³ Tumors tend to be T1-hypointense-to-isointense, T2-hyperintense, heterogeneously enhancing, non-diffusion-restricting, and non-necrotic with sharp or ill-defined margins (Fig 6).¹²

Diffuse Glioneuronal Tumor with Oligodendroglioma-Like Features and Nuclear Clusters (Provisional Type)

Diffuse glioneuronal tumor with oligodendroglioma-like features and nuclear clusters is a provisional tumor that has not yet been assigned a WHO grade. The hallmark of this tumor is its unique methylation profile.³⁴ Additionally, monosomy 14 is seen in almost all cases. Histologically, the tumors tend to have oligodendroglioma-like perinuclear haloes, clear cell morphology, vascular growth, nuclear clusters resembling “pennies on a plate,” moderate-to-high cellularity, and infiltrative growth.³⁴ Calcifications have been reported.³⁵ The median age is 9 years (range, 2–75 years), and there is no sex predilection.³⁴ Location is usually in the cerebral hemispheres, more commonly in the temporal lobe.³⁴ A typical tumor is solid and cystic, T1-hypointense, T2-hyperintense, and

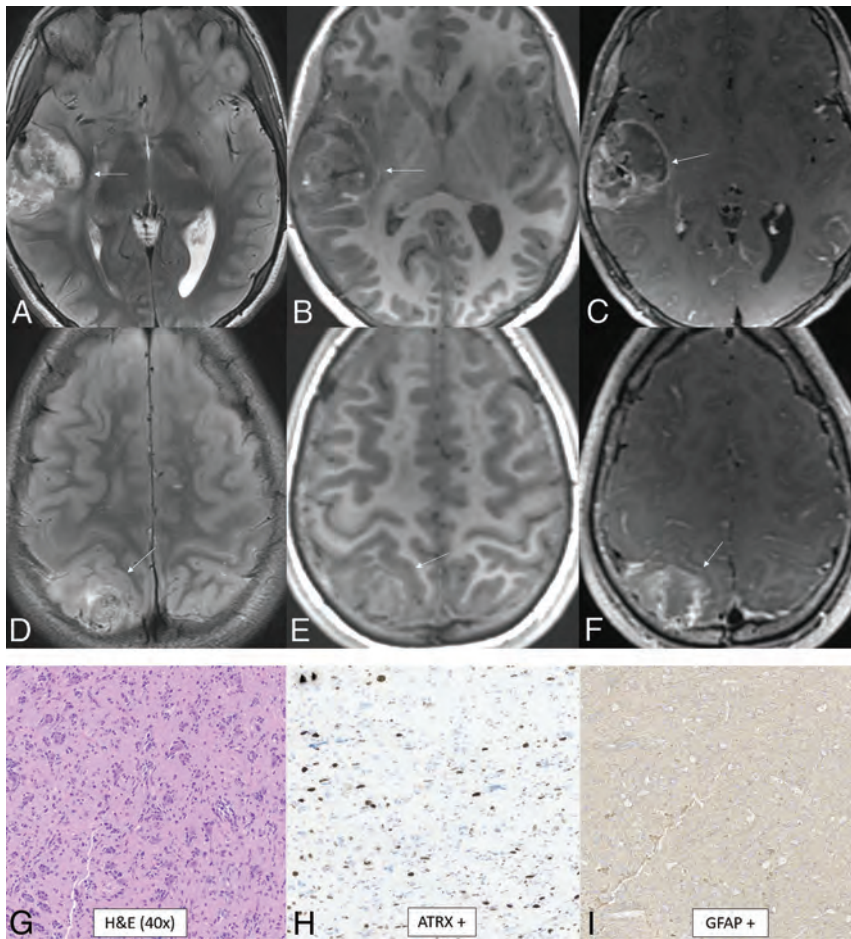


FIG 4. Diffuse hemispheric glioma, H3 G34-mutant. Multifocal masses are seen in the right temporal and parietal lobes. The temporal mass shows heterogeneously increased T2 signal (A), heterogeneously low T1 signal with a few foci of T1-hyperintense hemorrhage (B), and heterogenous enhancement (C, arrows). The parietal mass shows similar signal characteristics with heterogeneous T2-FLAIR hyperintensity (D), T1-hypointensity (E), and enhancement (F, arrows). The histologic section reveals an infiltrating glioma with astrocytic morphology (G). Glioma cells are positive for ATRX (H) and GFAP (I) stains and negative for IDH1 R132H and OLIG2. There was a high Ki-67 proliferation index of up to approximately 20%. This immunophenotype suggested a mutation of H3 G34, warranting further genomic evaluation. Next-generation sequencing revealed a somatic mutation in *H3-3A* (also known as *H3F3A*). Currently, there are no clinically approved therapies specifically targeting *H3-3A* mutations.

nonenhancing-to-minimally enhancing with calcifications and without adjacent edema (Fig 7).³⁵

Myxoid Glioneuronal Tumor

Myxoid glioneuronal tumor is a benign WHO grade 1 tumor that shows low-grade oligodendrocyte-like tumor cells with a myxoid-/mucin-rich stroma on histology. A fine capillary network is sometimes present along with neurocytic rosettes. Glial fibrillary acidic protein (GFAP) and OLIG2 are positive. The defining feature is a *PDGFRA* p.K385 mutation. Abnormalities in *FGFR1*, *IDH1/2*, *BRAF*, *MYB*, and *MYBL1* are absent.^{36,37} Data are limited, but in the largest described series, the median patient age was 23.6 years (range, 6–65 years) with no sex predilection.³⁸ These tumors have a propensity for the septum pellucidum.^{36,38} A typical mass is well-defined, lobulated, T1-hypointense, T2-hyperintense, nonenhancing, non-diffusion-restricting, and without surrounding edema.

T2-FLAIR shows relative hypointensity centrally and hyperintensity peripherally (Fig 8). There is no elevated CBF. Larger lesions can appear L-shaped and have mass effect, which can mimic high-grade tumors.^{36–39}

Multinodular and Vacuolating Neuronal Tumor

Most of the multinodular and vacuolating neuronal tumors are WHO grade 1 tumors that have a *MAP2K1* mutation, but *FGFR2-ZMYND11* translocations and *BRAF*, *DEPDC5*, *SMO*, *TP53*, *PIK3CA*, and *CIC* mutations can also occur.^{16,40} Histologically, there are multiple, discrete, and coalescent nodules with immature neuronal cells and round vesicular nuclei. Pericellular eccentric vacuolization with prominent nucleoli and eosinophilic cytoplasm are seen. There is no mitosis, perivascular lymphocytic infiltration, microcalcification, or oligodendroglia-like cells. OLIG2, α -internexin, and synaptophysin are positive.⁴⁰ The median age is 41 years (range, 8–63 years), and there is a slight female predominance (male/female ratio, 1:1.4).⁴¹ The tumor presents as cluster of variably-sized nodules in the subcortical ribbon and superficial subcortical white matter following the gyral contour. The frontal then parietal, occipital, and temporal lobes are the most common locations.^{41,42} The tumors are T1 iso- to hypointense, T2-hyperintense, nonenhancing, non-diffusion-restricting, and without mass effect, calcification, hemorrhage, or surrounding edema (Fig 9).^{41–44}

Supratentorial Ependymoma, YAP1 Fusion-Positive

Supratentorial ependymomas, which are WHO grade 2 or 3, are associated with many different mutations with *YAP1* fusions accounting for only 7% of all supratentorial ependymomas.³⁰ Within this group, *YAP1-MAMLD1*, and *YAP1-FAM11B* fusions are common.^{45–48} Histologically, bipolar spindle cells with elongated processes are seen among blood vessels. Perivascular anuclear zones form perivascular pseudorosettes, and some cells have cytoplasmic vacuolization. Neoplastic nuclei are moderate in size and round-to-ovoid with speckled chromatin. Rosenthal fibers are seen in the zone surrounding the tumor.^{46,47} Irregular cells resembling tancytes are visualized. GFAP, S-100, and vimentin are positive.^{45–47} Data are limited, but the reported median age is 1.4 years (range, 0–51 years) with most patients younger than 4 years of age and almost all younger than 9 years of age. There is a female predominance (male/female ratio, 1:3).⁴⁵ Location is

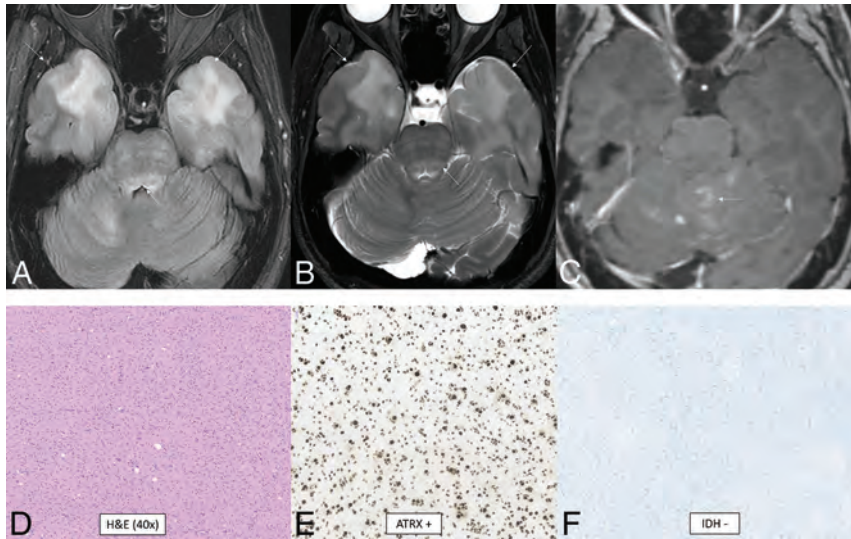


FIG 5. Diffuse pediatric-type high-grade glioma, H3 wild-type and IDH wild-type. MR images demonstrate diffusely infiltrating masses in the bilateral temporal lobes with mild mass effect, T2-FLAIR (A) and T2-hyperintensity (B, anterior arrows), and no enhancement (C). There is additional T2-FLAIR and T2-hyperintensity in the dorsal pons and posterior fossa leptomeningeal enhancement (posterior arrows). Histology reveals a high-grade diffusely infiltrating astrocytoma with high mitotic activity (D). The tumor shows ATRX retention (E) and wild-type IDH status (F) on immunohistochemical stains. Whole-genome methylation analysis showed a match to diffuse pediatric-type high-grade glioma. The tumor was H3 wild-type and IDH wild-type and had a *TERT* promoter mutation, which was identified on the neuro-oncology targeted next-generation sequencing panel.

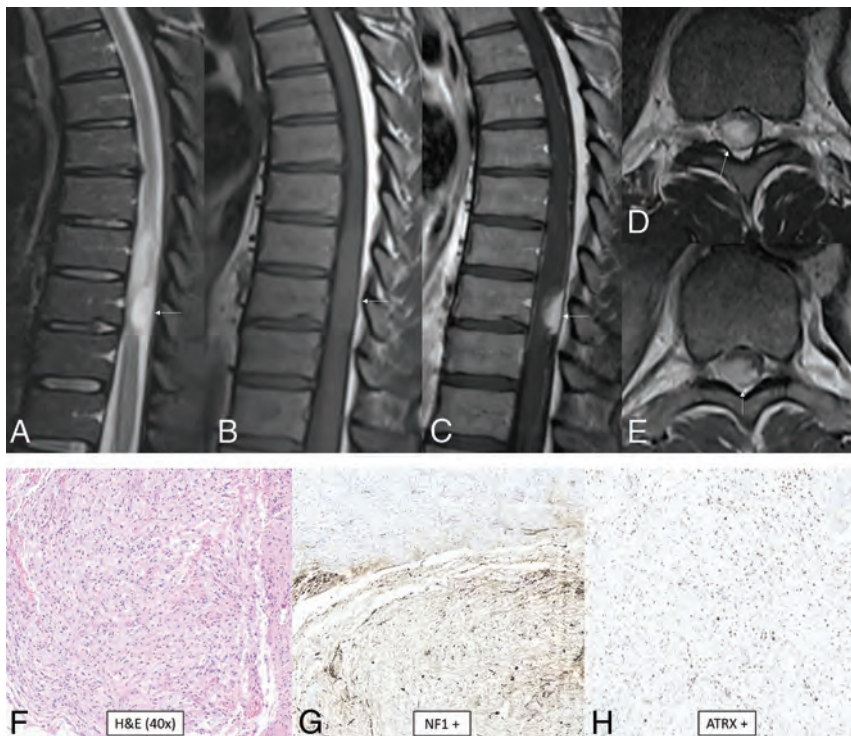


FIG 6. High-grade astrocytoma with piloid features. MR images demonstrate an eccentric T2-hyperintense mass (A) along the posterior thoracic cord with low T1 signal (B) and avid enhancement (C–E, arrows). Surrounding intramedullary T2-hyperintensity represents edema and/or tumor infiltration. Histology reveals an astrocytoma with piloid morphology (F), having NFI (G) and ATRX (H) mutations in association with *CDK2NA/B* homozygous deletion. Whole-genome methylation profiling showed a match to high-grade astrocytoma with piloid features. Most of these tumors occur intracranially.

within the lateral ventricles or in the brain parenchyma adjacent to them.³⁰ For extraventricular, supratentorial ependymomas in general, the frontal and temporal lobes are the most common locations.⁴⁶ A typical tumor is mixed density, solid and cystic, well-margined, T1 iso- to hypointense, T2 iso- to hyperintense, enhancing, and diffusion-restricting with calcifications. Internal hemorrhage can occur.^{46,48,49}

Posterior Fossa Ependymoma, Group PFA

Posterior fossa ependymomas are divided into groups PFA and PFB. PFA is a WHO grade 2 or 3 tumor characterized by loss of H3 K27 trimethylation due to *EZH2* overexpression.^{50–52} PFA tumors are further divided into PFA-1 and PFA-2 based on the specific mutation present. PFA-1 has *HOX* mutations while PFA-2 has *EN2* and *CNPY1* mutations.^{9,50–52} Histology demonstrates well-differentiated cells with ependymal rosettes and perivascular pseudorosettes. Dystrophic calcification, hemorrhage, myxoid degeneration, and metaplasia can also be seen. GFAP and S-100 are positive, and OLIG2 is negative.⁵³ The median age is 3 years (range, 0–51 years) with most patients younger than 9 years of age.⁴⁵ There is a slight male predominance (male/female ratio, 1.8:1). Overall survival at 5 and 10 years of age is 68% and 56%, respectively.⁴⁵ PFAs account for nearly 90% of all posterior fossa ependymomas.³⁰ Tumors arise from the roof of the fourth ventricle or the cerebellopontine cistern, can traverse the foramina of Luschka or Magendie, and can encase cranial nerves and vessels.^{52,53} The typical imaging appearance shows calcification, cystic change, T1 iso- to hypointensity, T2-hyperintensity, and heterogeneous enhancement. Hemorrhage and diffusion restriction can be present.^{52,53}

Posterior Fossa Ependymoma, Group PFB

PFB is a WHO grade 2 or 3 tumor characterized by increased H3 K27 trimethylation.^{50–52} PFB ependymomas also arise from the fourth ventricle but more commonly from the floor as opposed to the roof. In comparison with PFA, PFB

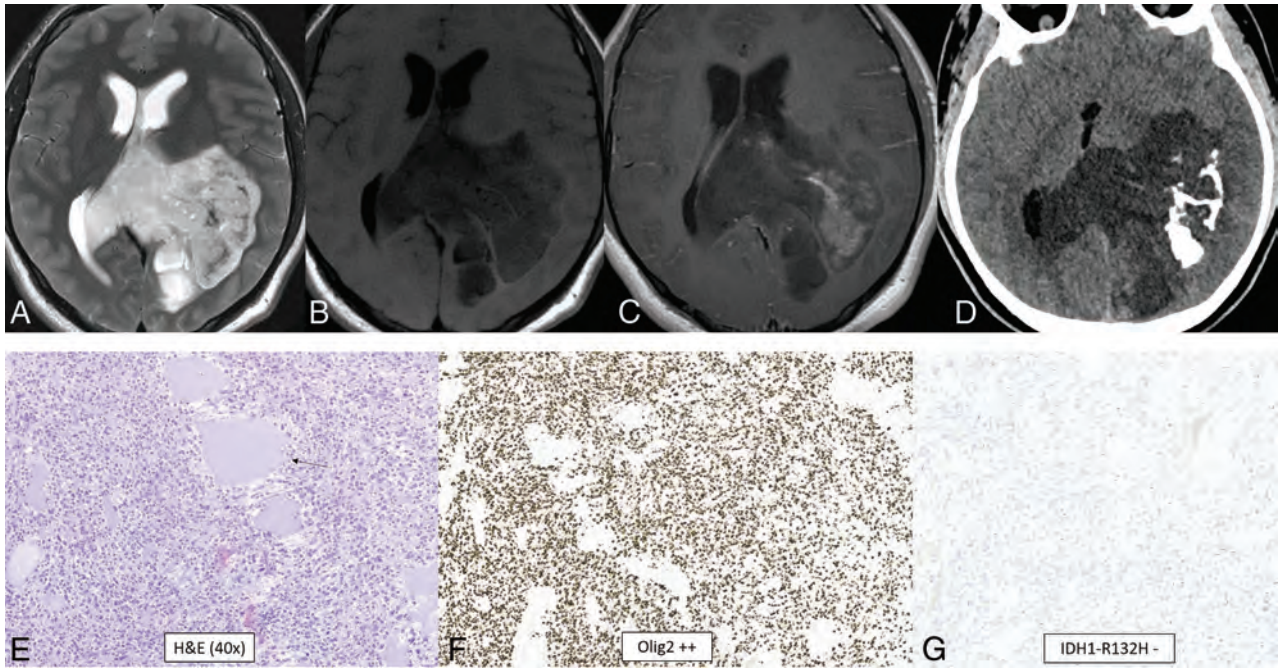


FIG 7. Diffuse glioneuronal tumor with oligodendroglioma-like features and nuclear clusters (provisional type). CT and MR images demonstrate a large well-circumscribed mass centered at the left atrium with involvement of the left parietal lobe and transcalsal extension to the right hemisphere. The tumor shows T2-hyperintensity (A), T1-hypointensity (B), patchy heterogeneous enhancement (C), and dense calcification (D). The histologic section demonstrates a highly cellular infiltrating glioma with oligodendroglioma-like microcyst formation (arrow, E) and extensive calcification. The tumor cells show moderate, clear cytoplasm and round-to-elongated, irregular, and hyperchromatic nuclei with high mitotic activity. The tumor cells are diffusely positive for OLIG2 (F) and negative for IDH1 R132H (G) and H3 K27M by immunohistochemistry. Whole-genome methylation analysis confirmed the final integrated diagnosis of diffuse glioneuronal tumor with oligodendroglioma-like features and nuclear clusters.

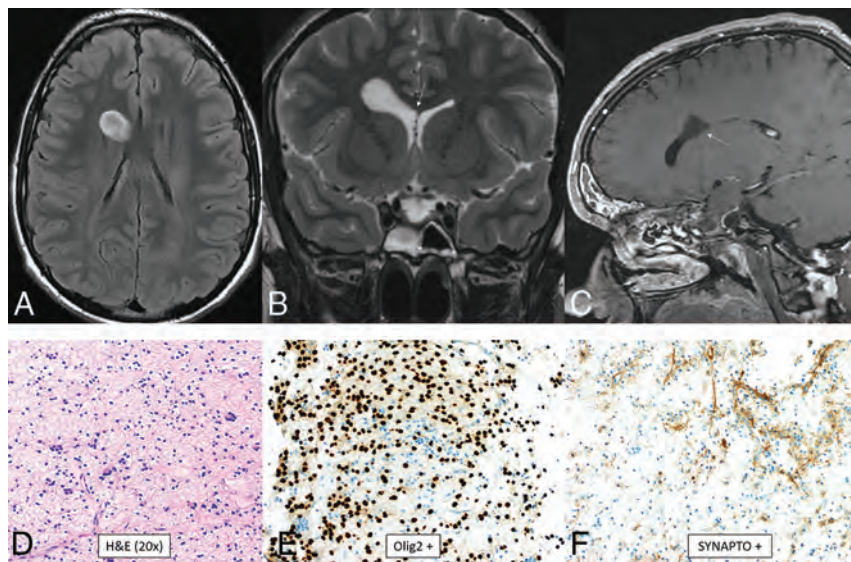


FIG 8. Myxoid glioneuronal tumor. MR imaging shows a mass in the right frontal horn region with peripheral T2-FLAIR hyperintensity and relative central T2-FLAIR hypointensity (A), which is slightly hypointense to CSF on the T2-weighted image (B), approaches the septum pellucidum (arrow, B), and does not enhance (C). There is no adjacent edema. Histology shows an oligodendroglioma-like appearance with moderate cellularity and uniform round nuclei with a circumferential arrangement around delicate vessels (D). Immunohistochemical staining is positive for OLIG2 (E), synaptophysin (F), and GFAP and negative for NeuN. This tumor has a *PDGFRA* p.K385 mutation and lacks *FGFR1* abnormalities. Dysembryoplastic neuroepithelial tumor is a histologic mimic but has a mutation of *FGFR1*.

tumors more commonly occur in adolescents and young adults.^{30,54} On the basis of supplemental data from the largest reported series, the overall median age is 27.5 years (range, 1–72 years) with no sex predilection, though there are age and sex differences among PFB subtypes.⁵⁵ Prognosis is substantially better than for PFA, with overall survival at 5 and 10 years being 100% and 88%, respectively.⁴⁵ The histology and immunohistochemistry findings are similar to those of PFA. The imaging findings are also similar; however, compared with PFA tumors, PFB tumors tended to be more cystic, less calcified, and less enhancing.⁵⁴

Spinal Ependymoma, MYCN-Amplified

Spinal ependymoma is a rare, aggressive tumor of the spinal cord.^{56,57} While not yet assigned a specific WHO grade, its histologic features are usually WHO grade 3 but can be WHO grade 2.^{56,58} Its defining feature is amplification of *MYCN*, which has been implicated as

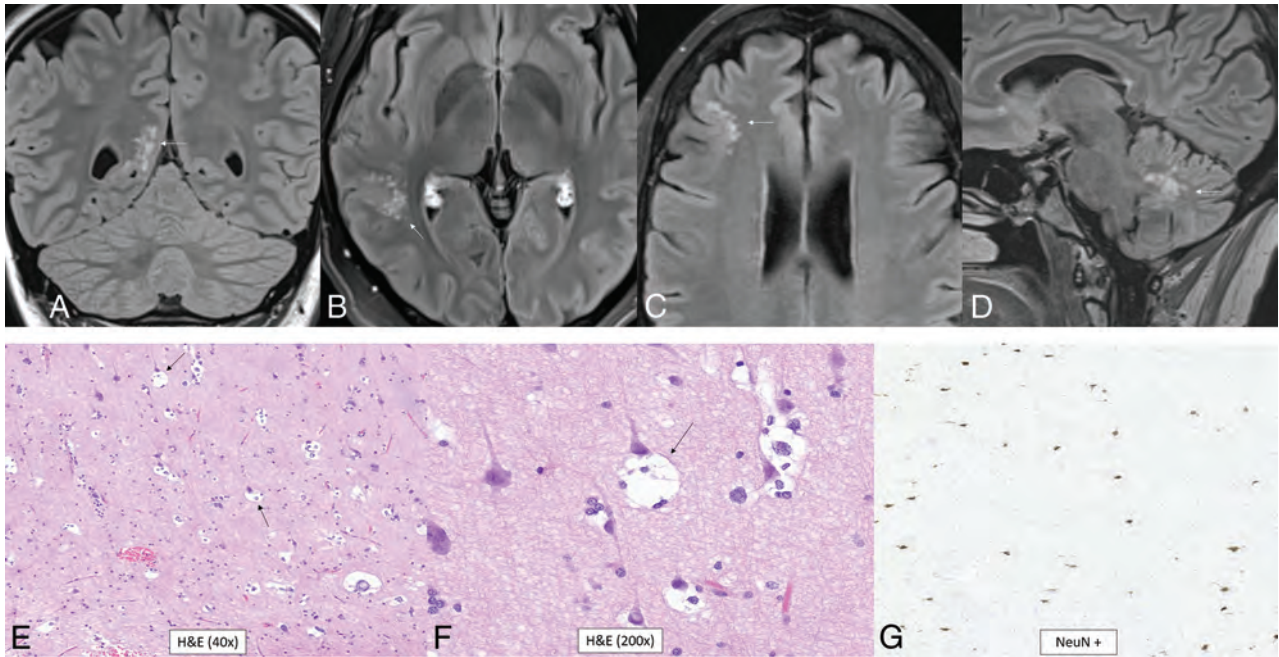


FIG 9. Multinodular and vacuolating neuronal tumor. Four different patients with pathology-proved (A, and E–G) and radiologic (B–D) diagnoses. T2-FLAIR images show small, subcortical clusters of hyperintense nodules with no edema or mass effect (A–D, arrows). Histology shows “neuronal” tumor cells with eosinophilic cytoplasm (E), multiple intracytoplasmic vacuoles that markedly enlarge the cytoplasm (arrows, E and F), and perineuronal satellitosis. There is positive *NeuN* staining of the viable normal scattered pyramidal neurons with negative staining of the tumor cells (G).

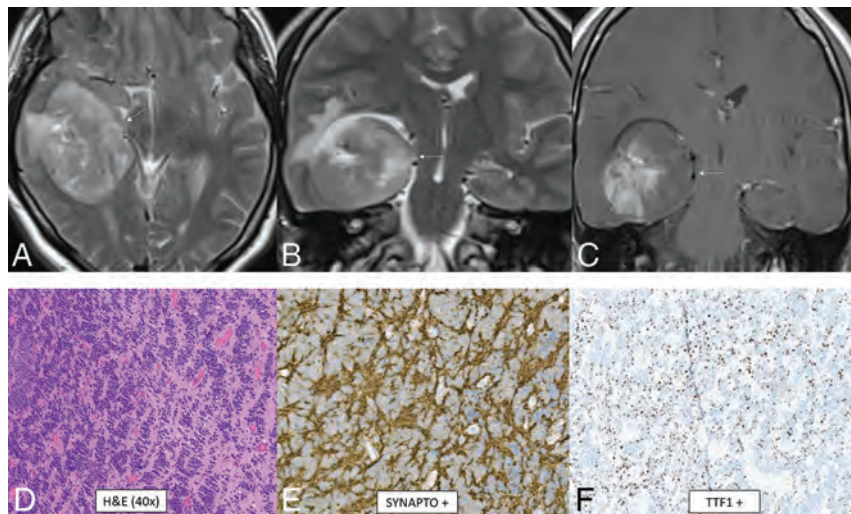


FIG 10. CNS neuroblastoma, *FOXR2*-activated. MR images show a large cortical and subcortical well-circumscribed expansile mass in the right temporal lobe involving the hippocampus (arrows) with T2-hyperintensity (A and B) and patchy enhancement (C). Histology shows a highly cellular infiltrating neuroepithelial neoplasm with a complex pattern, including an undifferentiated and extensive spongioblastoma pattern with brisk mitotic activity (D). On immunohistochemistry, the tumor shows divergent differentiation with expression of synaptophysin (E), OLIG2, and TTF1 (F). Whole-genome methylation profiling indicated a match to CNS neuroblastoma, *FOXR2*-activated.

the driver of its aggressive behavior.⁵⁶ Histologically, this tumor is anaplastic with marked cellular atypia and nuclear hyperchromasia. Prominent pink nucleoli, necrosis, mitosis, and glomeruloid vascular proliferation are common. GFAP and EMA are positive.^{56,58} While data are limited, the reported median age is

32 years (range, 12–56 years) with no sex predilection.⁵⁸ These tumors can grow to be large and cause spinal canal widening. A typical tumor is well-demarcated, iso- to hyperdense, T1 iso- to hypointense, and T2 iso- to hyperintense. Enhancement is variable. A hemosiderin rim (“cap sign”) may form from tumoral hemorrhage.^{30,56,59,60}

Cribriform Neuroepithelial Tumor (Provisional Type)

Cribriform neuroepithelial tumor is a benign tumor that has not yet been assigned a WHO grade. It is defined by a large, heterozygous deletion in *SMARCB1*, which is also seen in atypical teratoid/rhabdoid tumor (AT/RT).^{30,61,62} The key histologic features of cribriform neuroepithelial tumor are the presence of cribriform strands, ribbons, and nuclei with dense chromatin. Cells lack prominent nucleoli, and the cytoplasm is slightly eosinophilic and ill-defined. In more compact areas, small lumina may be seen with true rosettes.^{61,63,64} Tyrosinase, EMA, vimentin, MAP2C, and synaptophysin are positive.^{61,65,66} While data are limited, the reported median age is 1.7 years (range, 0.8–10.8 years) without a definite sex predilection.⁶⁵ The location is intraventricular or within the brain parenchyma adjacent to the

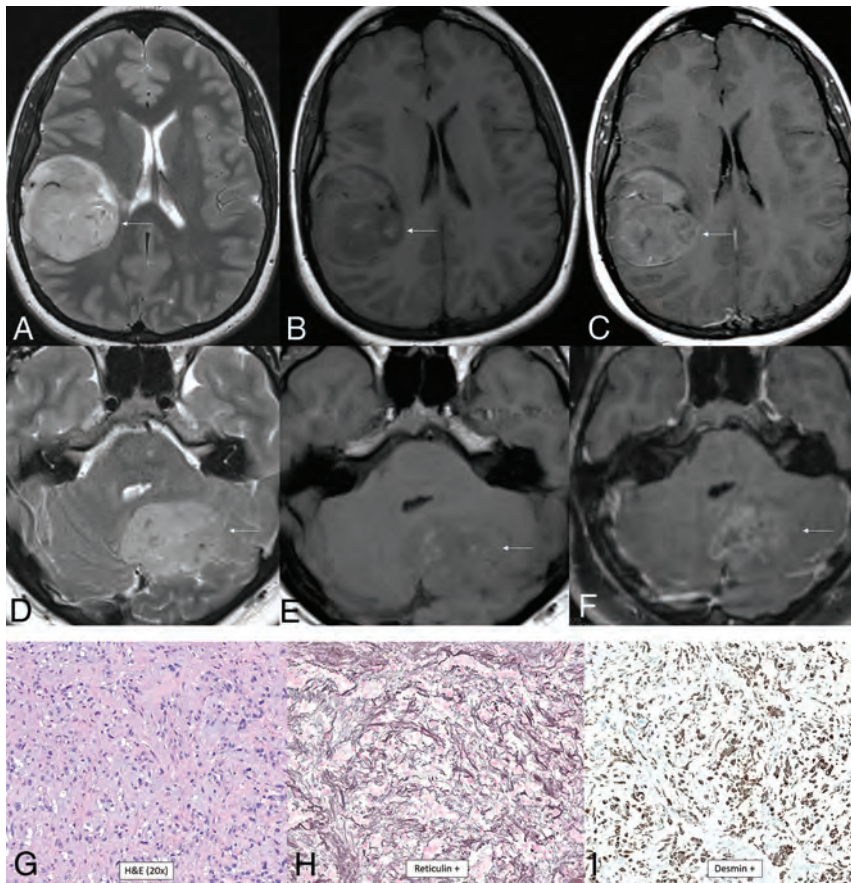


FIG 11. CNS tumor with *BCOR* internal tandem duplication. In 1 patient (A–C), there is a large well-circumscribed mass in the right posterior frontal lobe with heterogeneous T2-hyperintensity and prominent intratumoral vessels (A), heterogeneous T1-hypointensity (B), and enhancement (C, arrows). In a different patient (D–F), there is similar signal and morphology of a mass centered in the left cerebellar hemisphere on the T2-weighted (D), T1-weighted (E), and T1-weighted post-contrast (F) images (arrows). Histology from the first patient is characterized by relatively uniform nuclei, perivascular arrangement of tumor cells (rosette formation), and necrosis without microvascular proliferation (G). Immunohistochemical stains demonstrate OLIG2 positivity (H) and consistent NeuN positivity (I). Next-generation sequencing identified a frameshift mutation in *BCOR*, and chromosomal microarray demonstrated a segmental chromosomal loss disrupting *BCOR*.

ventricles. Tumors have been described in the lateral, third, and fourth ventricular regions without a clear predilection for 1 of these 3 locations.⁶⁵ Imaging typically reveals a large mass with T1-hypointensity, T2-hyperintensity, heterogeneous enhancement, and diffusion restriction.

CNS Neuroblastoma, FOXR2-Activated

CNS neuroblastoma is a highly malignant embryonal tumor without an official WHO grade. These tumors have variable chromosomal rearrangements or mitochondrial DNA insertions converging on *FOXR2*, leading to overexpression.^{67,68} *FOXR2* binds to and stabilizes MYC and MYCN proteins and therefore promotes MYC-related transcriptional activities, leading to increased cellular proliferation and tumorigenesis.^{67,68} Histology shows a small-cell tumor, embryonal architecture, a high proportion of neuropil, neurocytic cell, or ganglion cell differentiation, and, frequently, vascular pseudorosettes and nuclear palisades.⁶⁷ OLIG2 and synaptophysin are positive.⁶⁷ The median age is 4.5 years (range, 1.4–16 years) without a sex predilection.⁶⁹ In the largest

described series, tumors were large and supratentorial with invariable involvement of the deep white matter and frequent invasion of the cortex (80%) as well as a ventricular ependymal surface (64%).⁶⁹ The frontal lobe was the most common location, though involvement of multiple regions was common. Typical tumors were multilobulated, solid, and cystic/necrotic, T2-hyperintense, enhancing, and diffusion-restricting (Fig 10). Calcification or hemorrhage was present in approximately 40% of tumors. Calvarial remodeling was present in nearly half of cases and occurred more frequently with larger tumors.

CNS Tumor with *BCOR* Internal Tandem Duplication

CNS tumor with *BCOR* internal tandem duplication is a high-grade tumor that has not yet been assigned a specific WHO grade. Histologically, it is a compact tumor containing spindle and oval cells with fine chromatin with a well-demarcated border with adjacent brain parenchyma.^{67,70} Perivascular pseudorosettes with an ependymoma-like appearance and an intervening anuclear zone are prominent.⁶⁷ Peripheral calcified palisading necrosis is typically present. Tumors often demonstrate fibrillary processes and contain dense capillary networks.^{67,70} GFAP and S-100 are negative, and *BCOR*, OLIG2, and NeuN are positive.⁶⁷ Data are limited, but the reported median age is 1.8 years (range, 1.2–7.6 years) with a female predominance (male/female ratio, 1:2.3).⁷⁰ Location can be supratentorial or infratentorial, but dural abutment is common. A typical tumor is large, solid, centrally necrotic, iso- to hypodense, T2-hyperintense, diffusion-restricting, and mildly enhancing. Calcification or blood products are sometimes present at the border of the necrotic region. Large intratumoral macroscopic vessels may be present (Fig 11).⁷⁰

Desmoplastic Myxoid Tumor of the Pineal Region, SMARCB1-Mutant

Desmoplastic myxoid tumor is a tumor of the pineal region without a specific WHO grade that has a mutation in *SMARCB1*, resulting in a loss of function, similar to AT/RT.^{71,72} Histologically, there is no brisk mitotic activity or necrosis, typically seen in AT/RT. These tumors have a variable myxoid morphology combined with spindled and epithelioid cells embedded within a densely collagenized stroma. CD34 is positive, and INI1 is negative.⁷¹⁻⁷³ Unlike AT/RT, this tumor more commonly occurs in adults (median age, 40 years; range, 15–61 years).¹⁵ Data are limited,

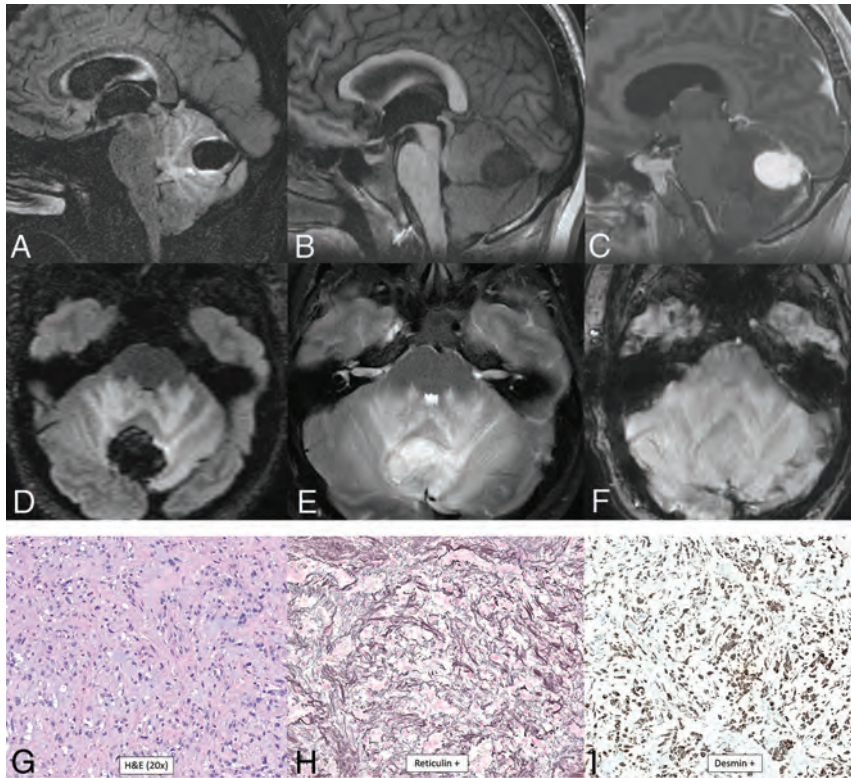


FIG 12. Intracranial mesenchymal tumor, FET-CREB fusion-positive (provisional type). Sagittal (A–C) and axial (D–F) MR images demonstrate a lobulated circumscribed mass along the superior vermis. The mass is markedly T2-FLAIR hypointense (A and D), T1-hypointense (B), homogeneously enhancing (C), and T2-hyperintense (E), with marked surrounding vasogenic edema. There is a lack of hypointensity within the tumor on the susceptibility-weighted image (F). Histology demonstrates a mesenchymal neoplasm with low-grade features (G), with staining positive for reticulin (H) and desmin (I), markers of connective tissue and muscle, respectively. The marked T2-FLAIR hypointensity corresponding to the area of homogeneous enhancement is an atypical appearance.

but there does not appear to be a sex predilection.⁷² On imaging, there is variable T1 signal, T2 intermediate signal, and enhancement.^{71,73} Large tumors can compress the cerebral aqueduct and cause obstructive hydrocephalus.⁷¹

Intracranial Mesenchymal Tumor, FET-CREB Fusion-Positive (Provisional Type)

Intracranial mesenchymal tumor is a group of rare mesenchymal CNS tumors without an assigned WHO grade. Intracranial angiomatoid fibrous histiocytomas and intracranial myxoid mesenchymal tumors have now been combined into this group because both have an in-frame genetic fusion of a FET RNA-binding protein (EWSR1 or FUS) to a CREB transcription factor (ATF1, CREB1, or CREM).⁷⁴ Histology is variable and may show solid nodules of epithelioid or spindled cells with a syncytial growth pattern, pseudoangiomatous spaces, a fibrous pseudocapsule, prominent pericapsular lymphoplasmacytic infiltrates, or mucin-rich stroma.⁷⁴ Desmin, CD99, and EMA are positive, and skeletal and smooth muscle markers, S-100, GFAP, and OLIG2 are negative.⁷⁴ The median age is 17 years (range, 4–70 years) with a female predominance (male/female ratio, 1:2.2).⁷⁴ Location is typically extra-axial, most commonly along the cerebral convexities but can be intraventricular or infratentorial.¹⁵ A dural tail and

calvarial involvement may be present. A typical tumor is well-circumscribed, lobulated, and cystic and solid with T2 and T2-FLAIR hyperintensity and enhancement. Internal blood products may be present. Extensive adjacent vasogenic edema is common (Fig 12).¹⁵

CIC-Rearranged Sarcoma

CIC-rearranged sarcoma is a highly aggressive WHO grade 4 round cell mesenchymal neoplasm that is one of the most common and best characterized subgroups of “Ewing-like sarcomas”⁷⁵ and is predominantly extracranial.⁷⁶ These tumors are characterized by CIC rearrangements with multiple fusion partners identified (*DUX4*, *FOXO4*, *LEUTX*, *NUTM1*, *NUTM2A*).^{75,76} The *CIC-NUTM1* fusion pair appears to have a greater predilection for the CNS.^{67,75} Histologically, they are small, round cell tumors, but in contrast to Ewing sarcoma, they exhibit distinctive nucleoli in cells with vesicular nuclei, variable epithelioid morphology occasionally with clear cytoplasm, focal myxoid change and cell spindling, and reduced uniformity of nuclei size and shape.^{75,76} CD99, ETV4, and WT1 are positive.^{75,76} Data are limited for *CIC*-rearranged sarcoma of the CNS, but cases have been reported in both pediatric and adult patients.^{77,78} Location is

anywhere along the neuroaxis.^{79,80} A typical tumor is extra-axial, solid, variably lobulated; T2 iso- to hyperintense; and homogeneously or heterogeneously enhancing (Fig 13). Peritumoral edema can be present.⁸¹

Primary Intracranial Sarcoma, DICER1-Mutant

Primary intracranial sarcoma is a highly malignant tumor, associated with familial *DICER1* syndrome and occasionally neurofibromatosis type 1.^{15,82,83} A specific WHO grade has not yet been assigned. There are several other *DICER1*-associated tumors in and outside the CNS.⁸² *DICER1* encodes a protein that facilitates activation of an RNA-induced silencing complex. Disruption of this pathway leads to altered protein expression, activation of the NRAS variants, inactivation of TP53, and copy number alternations.⁸² Histologically, there is high cellularity, brisk mitotic activity, intratumoral hemorrhage, some areas of fascicular spindle cells, and embryonic-type tissues, which may have rhabdomyoblastic differentiation.^{82,83} Coalescence of cells into “organoid” formations has been observed.⁸² PAS, α -1 antitrypsin, and desmin are positive, with patchy-to-complete loss of H3K27me.^{82,83} The median age is 6.0 years (range, 2.0–17.5 years) without a sex predilection.⁸⁴ Tumors are presumed to arise from mesenchymal progenitor cells located within the

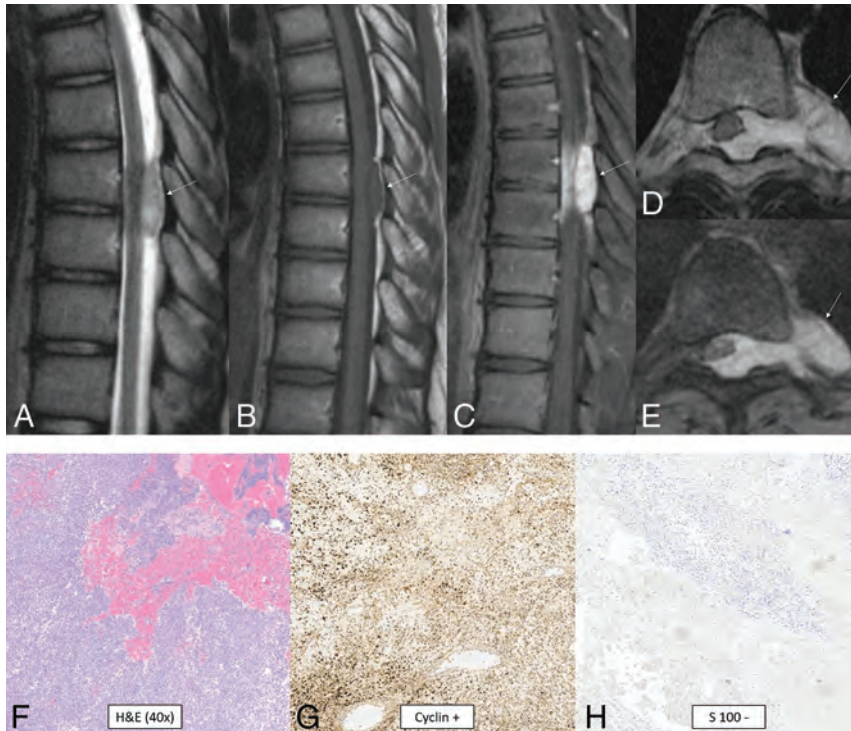


FIG 13. *CIC*-rearranged sarcoma. MR images reveal a small well-circumscribed peridural mass in the midthoracic region (arrows). The mass is T2-hyperintense (A), T1-isointense (B), and avidly enhances (C–E). The tumor extends through the left neural foramen into the paraspinous space and also exerts moderate mass effect on the cord, displacing it to the right (D and E). Histology reveals small, round, sarcomatous cells (F) with molecular stains of neoplastic cells positive for cyclin (G), calretinin, WTI (focal), and CD99 (patchy) and negative for S-100 (H), CK, EMA, desmin, and synaptophysin. Fluorescence in situ hybridization showed a balanced rearrangement of the *CIC* locus in 91% (181/200) of the nuclei.

meninges or perivascular spaces⁸³ and thus can present as intra-axial or extra-axial masses. Intra-axial masses tend to be peripheral and within the cerebral hemispheres.^{82–86} The typical appearance is hyperdense, T2 iso- to hypointense, diffusion-restricting, and enhancing, with intratumoral hemorrhage and peritumoral edema.^{82–85,87}

Pituitary Blastoma

Pituitary blastomas are rare WHO grade 4 embryonal tumors of the adenohypophysis associated with *DICER1* mutations.^{15,85,88} Histologically, these tumors resemble the embryonic pituitary gland and are composed of blastema-like cells, epithelial glands with rosettes resembling primitive Rathke-type epithelia, and large secretory epithelial cells that express hormones such as adrenocorticotropic hormone or rarely growth hormone.^{85,89} In the largest reported series, the median age was 11 months (range, 2–24 months) with a slight female predilection (male/female ratio, 1:1.4),⁹⁰ though a case in a young adult has been described.⁸⁹ The most common clinical presentation is an infant with Cushing syndrome, ophthalmoplegia, and/or diabetes insipidus.⁸⁵ The imaging appearance is variable, ranging from a small pituitary mass to a large heterogeneous solid and cystic mass mimicking a macroadenoma.⁸⁹ Internal calcification has been reported in 1 case.⁸⁹

CONCLUSIONS

The 2021 version of the WHO CNS tumor classification includes terminology updates reflecting more accurate understanding of tumorigenesis as well as the presentation of 22 newly recognized tumors, which were reviewed here. This edition furthers the growing movement away from purely histologic diagnoses and toward molecular diagnoses, increasing the emphasis on specific genetic mutations and DNA methylation-based classification. Because this classification system improves standardization in diagnosis and facilitates targeted treatments, it will continue to grow and adapt on the basis of new understanding of molecular alterations and tumor pathogenesis.

Disclosure forms provided by the authors are available with the full text and PDF of this article at www.ajnr.org.

REFERENCES

- Louis DN, Perry A, Wesseling P, et al. **The 2021 WHO Classification of Tumors of the Central Nervous System: a summary.** *Neuro Oncol* 2021;23:1231–51 CrossRef Medline
- Louis DN, Aldape K, Brat DJ, et al. **cIMPACT-NOW (the Consortium to Inform Molecular and Practical Approaches to CNS Tumor Taxonomy): a new initiative in advancing nervous system tumor classification.** *Brain Pathol* 2017;27:851–52 CrossRef Medline
- Louis DN, Wesseling P, Paulus W, et al. **cIMPACT-NOW update 1: not otherwise specified (NOS) and not elsewhere classified (NEC).** *Acta Neuropathol* 2018;135:481–84 CrossRef Medline
- Louis DN, Giannini C, Capper D, et al. **cIMPACT-NOW update 2: diagnostic clarifications for diffuse midline glioma, H3 K27M-mutant and diffuse astrocytoma/anaplastic astrocytoma, IDH-mutant.** *Acta Neuropathol* 2018;135:639–42 CrossRef Medline
- Brat DJ, Aldape K, Colman H, et al. **cIMPACT-NOW update 3: recommended diagnostic criteria for “Diffuse astrocytic glioma, IDH-wildtype, with molecular features of glioblastoma, WHO grade IV.”** *Acta Neuropathol* 2018;136:805–10 CrossRef Medline
- Ellison DW, Hawkins C, Jones DT, et al. **cIMPACT-NOW update 4: diffuse gliomas characterized by MYB, MYBL1, or FGFR1 alterations or BRAF(V600E) mutation.** *Acta Neuropathol* 2019;137:683–87 CrossRef Medline
- Brat DJ, Aldape K, Colman H, et al. **cIMPACT-NOW update 5: recommended grading criteria and terminologies for IDH-mutant astrocytomas.** *Acta Neuropathol* 2020;139:603–08 CrossRef Medline
- Louis DN, Wesseling P, Aldape K, et al. **cIMPACT-NOW update 6: new entity and diagnostic principle recommendations of the cIMPACT-Utrecht meeting on future CNS tumor classification and grading.** *Brain Pathol* 2020;30:844–56 CrossRef Medline
- Ellison DW, Aldape KD, Capper D, et al. **cIMPACT-NOW update 7: advancing the molecular classification of ependymal tumors.** *Brain Pathol* 2020;30:863–66 CrossRef Medline
- Aboian MS, Solomon DA, Felton E, et al. **Imaging characteristics of pediatric diffuse midline gliomas with histone H3 K27M mutation.** *AJNR Am J Neuroradiol* 2017;38:795–800 CrossRef Medline

11. Chen Y, Tian T, Guo X, et al. **Polymorphous low-grade neuroepithelial tumor of the young: case report and review focus on the radiological features and genetic alterations.** *BMC Neurol* 2020;20:123 CrossRef Medline
12. Bender K, Perez E, Chirica M, et al. **High-grade astrocytoma with piloid features (HGAP): the Charite experience with a new central nervous system tumor entity.** *J Neurooncol* 2021;153:109–20 CrossRef Medline
13. Capper D, Jones DTW, Sill M, et al. **DNA methylation-based classification of central nervous system tumours.** *Nature* 2018;555:469–74 CrossRef Medline
14. Priesterbach-Ackley LP, Boldt HB, Petersen JK, et al. **Brain tumour diagnostics using a DNA methylation-based classifier as a diagnostic support tool.** *Neuropathol Appl Neurobiol* 2020;46:478–92 CrossRef Medline
15. Osborn AG, Louis DN, Poussaint TY, et al. **The 2021 World Health Organization Classification of Tumors of the Central Nervous System: what neuroradiologists need to know.** *AJNR Am J Neuroradiol* 2022;43:928–37 CrossRef Medline
16. Bale TA, Rosenblum MK. **The 2021 WHO Classification of Tumors of the Central Nervous System: an update on pediatric low-grade gliomas and glioneuronal tumors.** *Brain Pathol* 2022;32:e13060 CrossRef Medline
17. Chiang J, Harreld JH, Tinkle CL, et al. **A single-center study of the clinicopathologic correlates of gliomas with a MYB or MYBL1 alteration.** *Acta Neuropathol* 2019;138:1091–92 CrossRef Medline
18. Huse JT, Snuderl M, Jones DT, et al. **Polymorphous low-grade neuroepithelial tumor of the young (PLNTY): an epileptogenic neoplasm with oligodendroglioma-like components, aberrant CD34 expression, and genetic alterations involving the MAP kinase pathway.** *Acta Neuropathol* 2017;133:417–29 CrossRef Medline
19. Kurokawa M, Kurokawa R, Capizzano AA, et al. **Neuroradiological features of the polymorphous low-grade neuroepithelial tumor of the young: five new cases with a systematic review of the literature.** *Neuroradiology* 2022;64:1255–64 CrossRef Medline
20. Korshunov A, Capper D, Reuss D, et al. **Histologically distinct neuroepithelial tumors with histone 3 G34 mutation are molecularly similar and comprise a single nosologic entity.** *Acta Neuropathol* 2016;131:137–46 CrossRef Medline
21. Crowell C, Mata-Mbembwa D, Bennett J, et al. **Systematic review of diffuse hemispheric glioma, H3 G34-mutant: Outcomes and associated clinical factors.** *Neurooncol Adv* 2022;4:vdac133 CrossRef Medline
22. Picart T, Barrिताult M, Poncet D, et al. **Characteristics of diffuse hemispheric gliomas, H3 G34-mutant in adults.** *Neurooncol Adv* 2021;3:vdab061 CrossRef Medline
23. Kurokawa R, Baba A, Kurokawa M, et al. **Neuroimaging features of diffuse hemispheric glioma, H3 G34-mutant: a case series and systematic review.** *J Neuroimaging* 2022;32:17–27 CrossRef Medline
24. Korshunov A, Schrimpf D, Ryzhova M, et al. **H3-/IDH-wild type pediatric glioblastoma is comprised of molecularly and prognostically distinct subtypes with associated oncogenic drivers.** *Acta Neuropathol* 2017;134:507–16 CrossRef Medline
25. Tauziède-Espariat A, Debily MA, Castel D, et al. **An integrative radiological, histopathological and molecular analysis of pediatric pontine histone-wildtype glioma with MYCN amplification (HGG-MYCN).** *Acta Neuropathol Commun* 2019;7:87 CrossRef Medline
26. Tauziède-Espariat A, Debily MA, Castel D, et al. **The pediatric supratentorial MYCN-amplified high-grade gliomas methylation class presents the same radiological, histopathological and molecular features as their pontine counterparts.** *Acta Neuropathol Commun* 2020;8:104 CrossRef Medline
27. Guerreiro Stucklin AS, Ryall S, Fukuoka K, et al. **Alterations in ALK/ROSI/NTRK/MET drive a group of infantile hemispheric gliomas.** *Nat Commun* 2019;10:4343 CrossRef Medline
28. Clarke M, Mackay A, Ismer B, et al. **Infant high-grade gliomas comprise multiple subgroups characterized by novel targetable gene fusions and favorable outcomes.** *Cancer Discov* 2020;10:942–63 CrossRef Medline
29. Olsen TK, Panagopoulos I, Meling TR, et al. **Fusion genes with ALK as recurrent partner in ependymoma-like gliomas: a new brain tumor entity?** *Neuro Oncol* 2015;17:1365–73 CrossRef Medline
30. McNamara C, Mankad K, Thust S, et al. **2021 WHO classification of tumours of the central nervous system: a review for the neuroradiologist.** *Neuroradiology* 2022;64:1919–50 CrossRef Medline
31. Fang Y, Wang YZ, Wei X, et al. **Infant-type hemispheric glioma in a Chinese girl: a newly defined entity.** *Fetal Pediatr Pathol* 2023;42:114–22 CrossRef Medline
32. Reinhardt A, Stichel D, Schrimpf D, et al. **Anaplastic astrocytoma with piloid features, a novel molecular class of IDH wildtype glioma with recurrent MAPK pathway, CDKN2A/B and ATRX alterations.** *Acta Neuropathol* 2018;136:273–91 CrossRef Medline
33. Lucas CG, Sloan EA, Gupta R, et al. **Multiplatform molecular analyses refine classification of gliomas arising in patients with neurofibromatosis type 1.** *Acta Neuropathol* 2022;144:747–65 CrossRef Medline
34. Deng MY, Sill M, Sturm D, et al. **Diffuse glioneuronal tumour with oligodendroglioma-like features and nuclear clusters (DGONC): a molecularly defined glioneuronal CNS tumour class displaying recurrent monosomy 14.** *Neuropathol Appl Neurobiol* 2020;46:422–30 CrossRef Medline
35. Pickles JC, Mankad K, Aizpurua M, et al. **A case series of diffuse glioneuronal tumours with oligodendroglioma-like features and nuclear clusters (DGONC).** *Neuropathol Appl Neurobiol* 2021;47:464–67 CrossRef Medline
36. Solomon DA, Korshunov A, Sill M, et al. **Myxoid glioneuronal tumor of the septum pellucidum and lateral ventricle is defined by a recurrent PDGFRA p.K385 mutation and DNT-like methylation profile.** *Acta Neuropathol* 2018;136:339–43 CrossRef Medline
37. Zamora C, Castillo M. **From dysembryoplastic neuroepithelial tumors to myxoid glioneuronal tumors, a new entity.** *AJNR Am J Neuroradiol* 2021;42:E77–78 CrossRef Medline
38. Lucas CG, Villanueva-Meyer JE, Whipple N, et al. **Myxoid glioneuronal tumor, PDGFRA p.K385-mutant: clinical, radiologic, and histopathologic features.** *Brain Pathol* 2020;30:479–94 CrossRef Medline
39. Narvaez EO, Inada BS, de Almeida P, et al. **Myxoid glioneuronal tumour - report of three cases of a new tumour in a typical location and review of literature.** *BJR Case Rep* 2021;7:20200139 CrossRef Medline
40. Choi E, Kim SI, Won JK, et al. **Clinicopathological and molecular analysis of multinodular and vacuolating neuronal tumors of the cerebrum.** *Hum Pathol* 2019;86:203–12 CrossRef Medline
41. Nunes RH, Hsu CC, da Rocha AJ, et al. **Multinodular and vacuolating neuronal tumor of the cerebrum: a new “Leave Me Alone” lesion with a characteristic imaging pattern.** *AJNR Am J Neuroradiol* 2017;38:1899–904 CrossRef Medline
42. Buffa GB, Chaves H, Serra MM, et al. **Multinodular and vacuolating neuronal tumor of the cerebrum (MVNT): a case series and review of the literature.** *J Neuroradiol* 2020;47:216–20 CrossRef Medline
43. Alizada O, Ayman T, Akgun MY, et al. **Multinodular and vacuolating neuronal tumor of the cerebrum: Two cases and review of the literature.** *Clin Neurol Neurosurg* 2020;197:106149 CrossRef Medline
44. Turan A, Tatar IG, Hekimoglu A, et al. **Advanced magnetic resonance imaging findings of multinodular and vacuolating neuronal tumor.** *Turk Neurosurg* 2021;31:725–30 CrossRef Medline
45. Pajtler KW, Witt H, Sill M, et al. **Molecular classification of ependymal tumors across all CNS compartments, histopathological**

- grades, and age groups. *Cancer Cell* 2015;27:728–43 CrossRef Medline
46. Sun S, Wang J, Zhu M, et al. **Clinical, radiological, and histological features and treatment outcomes of supratentorial extraventricular ependymoma: 14 cases from a single center.** *J Neurosurg* 2018;128:1396–402 CrossRef Medline
 47. Wang J, Wang L, Fu L, et al. **Supratentorial ependymoma with YAP1:FAM118B fusion: a case report.** *Neuropathology* 2021;41:133–38 CrossRef Medline
 48. Wang X, Han F, Lv Y, et al. **Supratentorial extraventricular ependymomas: imaging features and the added value of apparent diffusion coefficient.** *J Comput Assist Tomogr* 2021;45:463–71 CrossRef Medline
 49. Jabeen S, Konar SK, Prasad C, et al. **Conventional and advanced magnetic resonance imaging features of supratentorial extraventricular ependymomas.** *J Comput Assist Tomogr* 2020;44:692–98 CrossRef Medline
 50. Mariet C, Castel D, Grill J, et al. **Posterior fossa ependymoma H3 K27-mutant: an integrated radiological and histomolecular tumor analysis.** *Acta Neuropathol Commun* 2022;10:137 CrossRef Medline
 51. Pajtler KW, Wen J, Sill M, et al. **Molecular heterogeneity and CXorf67 alterations in posterior fossa group A (PFA) ependymomas.** *Acta Neuropathol* 2018;136:211–26 CrossRef Medline
 52. Sabin ND, Hwang SN, Klimo P Jr, et al. **Anatomic neuroimaging characteristics of posterior fossa type a ependymoma subgroups.** *AJNR Am J Neuroradiol* 2021;42:2245–50 CrossRef Medline
 53. Smith AB, Smirniotopoulos JG, Horkanyne-Szakaly I. **From the radiologic pathology archives: intraventricular neoplasms: radiologic-pathologic correlation.** *Radiographics* 2013;33:21–43 CrossRef Medline
 54. Yonezawa U, Karlowee V, Amatya VJ, et al. **Radiology profile as a potential instrument to differentiate between posterior fossa ependymoma (PF-EPN) group A and B.** *World Neurosurg* 2020;140:e320–27 CrossRef Medline
 55. Cavalli FMG, Hubner JM, Sharma T, et al. **Heterogeneity within the PF-EPN-B ependymoma subgroup.** *Acta Neuropathol* 2018;136:227–37 CrossRef Medline
 56. Raffeld M, Abdullaev Z, Pack SD, et al. **High level MYCN amplification and distinct methylation signature define an aggressive subtype of spinal cord ependymoma.** *Acta Neuropathol Commun* 2020;8:101 CrossRef Medline
 57. Swanson AA, Raghunathan A, Jenkins RB, et al. **Spinal cord ependymomas with MYCN amplification show aggressive clinical behavior.** *J Neuropathol Exp Neurol* 2019;78:791–97 CrossRef Medline
 58. Ghasemi DR, Sill M, Okonechnikov K, et al. **MYCN amplification drives an aggressive form of spinal ependymoma.** *Acta Neuropathol* 2019;138:1075–89 CrossRef Medline
 59. Celano E, Salehani A, Malcolm JG, et al. **Spinal cord ependymoma: a review of the literature and case series of ten patients.** *J Neurooncol* 2016;128:377–86 CrossRef Medline
 60. Koeller KK, Rosenblum RS, Morrison AL. **Neoplasms of the spinal cord and filum terminale: radiologic-pathologic correlation.** *Radiographics* 2000;20:1721–49 CrossRef Medline
 61. Hasselblatt M, Oyen F, Gesk S, et al. **Cribiform neuroepithelial tumor (CRINET): a nonrhabdoid ventricular tumor with INI1 loss and relatively favorable prognosis.** *J Neuropathol Exp Neurol* 2009;68:1249–55 CrossRef Medline
 62. Tauziède-Espariat A, Guerrini-Rousseau L, Puget S, et al. **A novel case of cribiform neuroepithelial tumor: a potential diagnostic pitfall in the ventricular system.** *Pediatr Blood Cancer* 2021;68:e29037 CrossRef Medline
 63. Arnold MA, Stallings-Archer K, Marlin E, et al. **Cribiform neuroepithelial tumor arising in the lateral ventricle.** *Pediatr Dev Pathol* 2013;16:301–07 CrossRef Medline
 64. Pawel BR. **SMARCB1-deficient tumors of childhood: a practical guide.** *Pediatr Dev Pathol* 2018;21:6–28 CrossRef Medline
 65. Johann PD, Hovestadt V, Thomas C, et al. **Cribiform neuroepithelial tumor: molecular characterization of a SMARCB1-deficient non-rhabdoid tumor with favorable long-term outcome.** *Brain Pathol* 2017;27:411–18 CrossRef Medline
 66. Ruland V, Hartung S, Kordes U, et al. **Choroid plexus carcinomas are characterized by complex chromosomal alterations related to patient age and prognosis.** *Genes Chromosomes Cancer* 2014;53:373–80 CrossRef Medline
 67. Sturm D, Orr BA, Toprak UH, et al. **New brain tumor entities emerge from molecular classification of CNS-PNETs.** *Cell* 2016;164:1060–72 CrossRef Medline
 68. Li X, Wang W, Xi Y, et al. **FOXR2 interacts with MYC to promote its transcriptional activities and tumorigenesis.** *Cell Rep* 2016;16:487–97 CrossRef Medline
 69. Tietze A, Mankad K, Lequin MH, et al. **Imaging characteristics of CNS neuroblastoma-FOXR2: a retrospective and multi-institutional description of 25 cases.** *AJNR Am J Neuroradiol* 2022;43:1476–80 CrossRef
 70. Cardoen L, Tauziède-Espariat A, Dangouloff-Ros V, et al. **Imaging features with histopathologic correlation of CNS high-grade neuroepithelial tumors with a BCOR internal tandem duplication.** *AJNR Am J Neuroradiol* 2022;43:151–56 CrossRef Medline
 71. Matsumura N, Goda N, Yashige K, et al. **Desmoplastic myxoid tumor, SMARCB1-mutant: a new variant of SMARCB1-deficient tumor of the central nervous system preferentially arising in the pineal region.** *Virchows Arch* 2021;479:835–39 CrossRef Medline
 72. Thomas C, Wefers A, Bens S, et al. **Desmoplastic myxoid tumor, SMARCB1-mutant: clinical, histopathological and molecular characterization of a pineal region tumor encountered in adolescents and adults.** *Acta Neuropathol* 2020;139:277–86 CrossRef Medline
 73. Wang YE, Chen JJ, Wang W, et al. **A case of desmoplastic myxoid tumor, SMARCB1 mutant, in the pineal region.** *Neuropathology* 2021;41:37–41 CrossRef Medline
 74. Sloan EA, Chiang J, Villanueva-Meyer JE, et al. **Intracranial mesenchymal tumor with FET-CREB fusion-A unifying diagnosis for the spectrum of intracranial myxoid mesenchymal tumors and angiomatoid fibrous histiocytoma-like neoplasms.** *Brain Pathol* 2021;31:e12918 CrossRef Medline
 75. Sbaraglia M, Righi A, Gambarotti M, et al. **Ewing sarcoma and Ewing-like tumors.** *Virchows Arch* 2020;476:109–19 CrossRef Medline
 76. Kallen ME, Hornick JL. **The 2020 WHO Classification: what's new in soft tissue tumor pathology?** *Am J Surg Pathol* 2021;45:e1–e23 CrossRef Medline
 77. Yoshida A, Goto K, Kodaira M, et al. **CIC-rearranged sarcomas: a study of 20 cases and comparisons with Ewing sarcomas.** *Am J Surg Pathol* 2016;40:313–23 CrossRef Medline
 78. Le Loarer F, Pissaloux D, Watson S, et al. **Clinicopathologic features of CIC-NUTM1 sarcomas, a new molecular variant of the family of CIC-fused sarcomas.** *Am J Surg Pathol* 2019;43:268–76 CrossRef Medline
 79. Donahue JE, Yakirevich E, Zhong S, et al. **Primary spinal epidural CIC-DUX4 undifferentiated sarcoma in a child.** *Pediatr Dev Pathol* 2018;21:411–17 CrossRef Medline
 80. Song K, Huang Y, Xia CD, et al. **A case of CIC-rearranged sarcoma with CIC-LEUTX gene fusion in spinal cord.** *Neuropathology* 2022;42:555–62 CrossRef Medline
 81. Hu W, Wang J, Yuan L, et al. **Case report: a unique case of pediatric central nervous system embryonal tumor harboring the CIC-LEUTX fusion, germline NBN variant and somatic TSC2 mutation: expanding the spectrum of CIC-rearranged neoplasia.** *Front Oncol* 2020;10:598970 CrossRef Medline
 82. Kamihara J, Paulson V, Breen MA, et al. **DICER1-associated central nervous system sarcoma in children: comprehensive clinicopathologic and genetic analysis of a newly described rare tumor.** *Mod Pathol* 2020;33:1910–21 CrossRef Medline

83. Lee JC, Villanueva-Meyer JE, Ferris SP, et al. **Primary intracranial sarcomas with DICER1 mutation often contain prominent eosinophilic cytoplasmic globules and can occur in the setting of neurofibromatosis type 1.** *Acta Neuropathol* 2019;137:521–25 CrossRef Medline
84. Diaz Coronado RY, Mynarek M, Koelsche C, et al. **Primary central nervous system sarcoma with DICER1 mutation-treatment results of a novel molecular entity in pediatric Peruvian patients.** *Cancer* 2022;128:697–707 CrossRef Medline
85. de Kock L, Priest JR, Foulkes WD, et al. **An update on the central nervous system manifestations of DICER1 syndrome.** *Acta Neuropathol* 2020;139:689–701 CrossRef Medline
86. Leelatian N, Goss J, Pastakia D, et al. **Primary intracranial sarcoma, DICER1-mutant presenting as a pineal region tumor mimicking pineoblastoma: case report and review of the literature.** *J Neuropathol Exp Neurol* 2022;81:762–64 CrossRef Medline
87. Rashidi A, Luna LP, Rodriguez F, et al. **Teaching NeuroImages: intracranial DICER1-associated spindle cell sarcoma in a child.** *Neurology* 2020;95:e2176–77 CrossRef Medline
88. Shih RY, Schroeder JW, Koeller KK. **Primary tumors of the pituitary gland: radiologic-pathologic correlation.** *Radiographics* 2021;41:2029–46 CrossRef Medline
89. Chhuon Y, Weon YC, Park G, et al. **Pituitary blastoma in a 19-year-old woman: a case report and review of literature.** *World Neurosurg* 2020;139:310–13 CrossRef Medline
90. Liu AP, Kelsey MM, Sabbaghian N, et al. **Clinical outcomes and complications of pituitary blastoma.** *J Clin Endocrinol Metab* 2021;106:351–63 CrossRef Medline

Stent-Assisted Coiling in the Treatment of Unruptured Intracranial Aneurysms: A Randomized Clinical Trial

W. Boisseau, T.E. Darsaut, R. Fahed, B. Drake, H. Lesiuk, J.L. Rempel, J.-C. Gentric, J. Ognard, L. Nico, D. Iancu, D. Roy, A. Weill, M. Chagnon, J. Zehr, P. Lavoie, T.N. Nguyen, and J. Raymond



ABSTRACT

BACKGROUND AND PURPOSE: Stent-assisted coiling may improve angiographic results of endovascular treatment of unruptured intracranial aneurysms compared with coiling alone, but this has never been shown in a randomized trial.

MATERIALS AND METHODS: The Stenting in the Treatment of Aneurysm Trial was an investigator-led, parallel, randomized (1:1) trial conducted in 4 university hospitals. Patients with intracranial aneurysms at risk of recurrence, defined as large aneurysms (≥ 10 mm), postcoiling recurrent aneurysms, or small aneurysms with a wide neck (≥ 4 mm), were randomly allocated to stent-assisted coiling or coiling alone. The composite primary efficacy outcome was “treatment failure,” defined as initial failure to treat the aneurysm; aneurysm rupture or retreatment during follow-up; death or dependency (mRS > 2); or an angiographic residual aneurysm adjudicated by an independent core laboratory at 12 months. The primary hypothesis (revised for slow accrual) was that stent-assisted coiling would decrease treatment failures from 33% to 15%, requiring 200 patients. Primary analyses were intent to treat.

RESULTS: Of 205 patients recruited between 2011 and 2021, ninety-four were allocated to stent-assisted coiling and 111 to coiling alone. The primary outcome, ascertainable in 203 patients, was reached in 28/93 patients allocated to stent-assisted coiling (30.1%; 95% CI, 21.2%–40.6%) compared with 30/110 (27.3%; 95% CI, 19.4%–36.7%) allocated to coiling alone (relative risk = 1.10; 95% CI, 0.7–1.7; $P = .66$). Poor clinical outcomes (mRS > 2) occurred in 8/94 patients allocated to stent-assisted coiling (8.5%; 95% CI, 4.0%–16.6%) compared with 6/111 (5.4%; 95% CI, 2.2%–11.9%) allocated to coiling alone (relative risk = 1.6; 95% CI, 0.6%–4.4%; $P = .38$).

CONCLUSIONS: The STAT trial did not show stent-assisted coiling to be superior to coiling alone for wide-neck, large, or recurrent unruptured aneurysms.

ABBREVIATIONS: CA = coiling alone; DSMC = Data and Safety Monitoring Committee; RR = relative risk; SAC = stent-assisted coiling; UIA = unruptured intracranial aneurysm

The use of stents for the treatment of unruptured intracranial aneurysms (UIAs) was first approved in the United States in 2002 as a Humanitarian Device Exemption. The initial indication was to mechanically assist the coiling of wide-neck (≥ 4 mm) aneurysms not amenable to endovascular or surgical treatment.^{1,2} Subsequently, clinical usage has expanded to all types of aneurysms.^{3–12} While coiling is strictly an intrasaccular treatment, stents are deployed in the artery bearing the aneurysm.

Antiplatelet regimens are therefore necessary to prevent arterial thromboembolic complications, rendering the use of stents problematic in recently ruptured aneurysms.¹³ There may be benefits to the use of stent-assisted coiling (SAC), in addition to mechanically preventing coil protrusion into the parent artery during the coiling procedure, which may improve the long-term angiographic results of endovascular treatments such as a flow-diverting effect^{14–16} or better healing due to the provision of a scaffold for neointimal closure of the neck.¹⁷ However, these potential benefits were not observed in experimental models.¹⁸ Whether SAC increases procedural risks or improves long-term angiographic results has not been convincingly shown despite

Received January 25, 2023; accepted after revision February 16.

From the Department of Radiology (W.B., D.I., D.R., A.W., J.R.), Service of Neuroradiology, Centre Hospitalier de l'Université de Montréal, Montreal, Québec, Canada; Department of Surgery (T.E.D.), Division of Neurosurgery and Department of Radiology and Diagnostic Imaging (J.L.R.), University of Alberta Hospital, Mackenzie Health Sciences Centre, Edmonton, Alberta, Canada; Departments of Neurology (R.F.) and Neurosurgery (B.D., H.L.), University of Ottawa, the Ottawa Hospital, Ottawa, Ontario, Canada; Department of Radiology (J.-C.G., J.O.), University Hospital of Brest, Brest, France; Departement of Radiology (L.N.), Service of Interventional Neuroradiology, Centre Hospitalo-universitaire de Saint-Etienne, Saint-Etienne, France; Department of Mathematics and Statistics (M.C., J.Z.), Pavillon André-Aisenstadt, Montreal, Québec, Canada; Department of Neurosurgery (P.L.), Centre Hospitalier Universitaire de Québec-Université Laval, Québec, Canada; and Departments of Neurology (T.N.N.) and Radiology (T.N.N.), Boston Medical Center, Boston, Massachusetts.

Please address correspondence to Jean Raymond, MD, Centre Hospitalier de l'Université de Montréal (CHUM), Department of Radiology, Room D03.5462b, Montreal, Québec, Canada H2X 0C1; e-mail: jean.raymond@umontreal.ca

Indicates open access to non-subscribers at www.ajnr.org

Indicates article with online supplemental data.

Evidence-Based Medicine Level 1.

<http://dx.doi.org/10.3174/ajnr.A7815>

multiple case series and meta-analyses published during 20 years.³⁻¹² A randomized trial comparing the results of coiling with or without stent placement has never been published.

The Stenting in the Treatment of Aneurysm Trial (STAT) was launched in 2011 to provide a clinical research context for the use of SAC in UIAs.¹⁹ The trial compared a policy of coiling alone (CA) versus the use of a self-expandable stent (any stent, not a flow diverter) in addition to the coiling procedure. The primary hypothesis of the trial was that in patients with aneurysms prone to recurrence, SAC would decrease the proportion of patients reaching “treatment failure,” a composite clinical and angiographic primary outcome measure that included aneurysmal rupture or retreatment during follow-up or a recurrent or residual aneurysm on follow-up angiography at 12 months. We here report the final results of the trial.

MATERIALS AND METHODS

This report follows the Consolidated Standards of Reporting Trials (CONSORT) recommendations.²⁰ STAT was an investigator-led, multicenter randomized controlled trial integrated into clinical practice. The trial proposed randomized allocation to SAC or CA in patients eligible for both options. There were 4 participating centers (Montreal, Ottawa, and Edmonton in Canada, and Brest in France). All sites received institutional review board approval. The protocol was published,¹⁹ and the trial was registered at <http://www.clinicaltrials.gov> number NCT01340612.

Patients

All patients were 18 years of age or older with a life expectancy of at least 2 years. Patients had at least 1 UIA prone to recurrence, defined and categorized at the time of registration before randomization as a large (≥ 10 mm) aneurysm (STAT-1), a recurrent aneurysm after previous coiling (STAT-2), or a wide-neck (≥ 4 mm) aneurysm of < 10 mm (STAT-3). There were few exclusion criteria: 1) absolute contraindications to endovascular treatment, anesthesia, or the use of dual antiplatelet regimens; 2) the presence of other aneurysms requiring treatment during the same session; 3) the presence of an associated cerebral arteriovenous malformation; 4) recently ruptured aneurysms (< 3 months); and 5) the presence of a recurring, previously stented aneurysm. Screening logs of all potentially eligible patients with UIAs were not required per protocol. All patients signed an informed consent form.

Randomization and Masking

SAC or CA was randomly allocated (1:1) using a Web-based platform assuring concealment of the allocation. The randomized allocation was stratified according to the STAT1-3 subgroups and minimized for the type of coils to be used (platinum or second generation). Patients, interventionists, and outcome assessors were not blinded to treatment assignment.

Interventions and Follow-up Tests and Visits

Coiling with or without stent placement was performed according to standards of practice, with the patient under general anesthesia. Antiplatelet and anticoagulation regimens and testing for platelet inhibition were prescribed according to routine practice at each

site. Details regarding the endovascular technique; type of coils; use of adjunctive techniques such as balloon remodeling (routine in STAT centers for large or wide-neck aneurysms); whether the stent was deployed before or following coiling; the use of multiple stents; and posttreatment medical management decisions were left to the discretion of the treating physicians. A stent could be used as a bailout maneuver in patients allocated to CA if this was judged appropriate by the treating physician, to ensure the safety of patients. Similarly, the physician could choose not to use the stent in patients allocated to SAC when it was judged impossible or dangerous at the time of the procedure.

Follow-up tests and visits were limited to those considered clinically indicated, such as neurologic examinations, brain imaging studies, and a functional assessment according to the mRS score at discharge, 1 month, and 12 (± 3) months. Follow-up angiography (invasive or noninvasive) at 12 (± 3) months was considered standard of practice.

Data capture and management through secure servers (MedSciNet; <https://medscinet.com/about.aspx>) were in compliance with good clinical practice requirements. Case report forms were simple, and the data collected were parsimonious, to facilitate completion by care personnel, because no financial compensation was provided to participating centers.

Primary and Secondary Outcome Measures

The primary end point of the 2011 protocol was the incidence of angiographic recurrences at 12 (± 3) months, defined as the following: 1) an angiographic recurrence of the lesion, as judged by an independent core lab (composed of 2 raters) according to a previously published classification;²¹ 2) an episode of intracranial bleeding; or 3) retreatment of the same lesion by endovascular or surgical means during the follow-up period.¹⁹ Furthermore, the protocol stipulated that “recurrences would be recorded (present or absent) as they are discovered, at the follow-up assessment (12 \pm 3 months), as clinical symptoms appear at any time, or at time of death.”¹⁹

Because this definition lacked precision and may not be ascertainable in some patients, the primary outcome was modified in July 2021, after consulting with the Data and Safety Monitoring Committee (DSMC) but before any data examination, to be in line with other endovascular trials.²²⁻²⁴ Two other components have been added to the composite primary outcome, treatment failure (initial treatment failure using any device and treatment- or aneurysm-related death or dependency precluding follow-up angiography). If the coiling procedure was not feasible, for example due to coil instability, the physician had the option of using a stent, a use that was not considered a failure of the initial treatment (but was counted as a crossover in “as-treated analyses”). One primary poor outcome was attributed per patient. When a patient met > 1 of the criteria, the following hierarchical order was prespecified to classify the patient for final analyses: death or mRS 3-5 (from any cause within 30 days of the intervention and from related causes during follow-up) $>$ aneurysm rupture during follow-up $>$ retreatment during follow-up $>$ initial treatment failure (defined as the inability to perform endovascular treatment) $>$ major recurrence or residual aneurysm at imaging follow-up (3-12 months) as adjudicated by an independent core

laboratory of 2 neuroradiologists blinded to treatment groups and according to a previously validated classification.^{25,26}

Secondary outcomes included the individual components of the composite primary outcome: the mRS score at discharge and 12 months posttreatment; the success in occluding the aneurysm at the end of the procedure; perioperative complications (ischemic strokes and intracranial hemorrhages within 31 days of the intervention and during follow-up); angiographic results at 12 months; length of hospital stay (number of days); discharge disposition (home, other hospital, rehabilitation facility; death); and retreatment of the index aneurysm at any time.

Hypotheses and Number of Patients

The 2011 protocol planned for the recruitment of 600 patients.¹⁹ This number was based on 2 hypotheses: The primary efficacy hypothesis was that SAC would decrease angiographic recurrences by 20% at 12 months and a total sample size of 536 patients would allow the detection of such a difference with a power of 80% and an error of 0.0125 (to account for subgroup analyses for the 3 main categories of lesions: large, wide neck, and recurrent aneurysms). The secondary safety hypothesis was that the use of intracranial stent placement would not double the number of dead or dependent patients (mRS > 2) from 6% to 12% at 12 months. In July 2021, before any knowledge of the data, the steering committee (SC), in agreement with the DSMC, dropped the safety hypothesis and modified the primary efficacy hypothesis: SAC was hypothesized to decrease treatment failures from 33% to 15%, which would require approximately 200 patients (88 patients per group; power of 80% and α of 5%, plus 10% to account for crossovers and losses to follow-up). Details are provided in the Online Supplemental Data.

Trial Interruption

On August 31, 2021, after a blinded examination of interim results, the DSMC recommended trial continuation. However, in September 2021, ten years after the recruitment of the first patient, the SC decided to finalize and report the trial.

Statistical Analyses

Blinded data were examined at prespecified intervals by an independent DSMC, composed of an interventional neurologist, a dual-trained neurosurgeon, and a statistician; but no hypothesis testing was performed.

Descriptive statistics on demographic variables and preoperative data are provided to compare the 2 groups at baseline. Means, SDs, medians, and ranges are presented for quantitative variables, and frequency tables for categoric variables. Primary safety and efficacy outcomes are described using percentages and 95% CIs. The intent-to-treat analyses for the primary efficacy hypothesis were performed on available observations. The relative risks (RRs and 95% CIs) were estimated using a generalized estimating equation with a binomial distribution and a log-link function. The groups were not different with respect to risk factors for poor outcomes, and no adjustments for residual confounding factors were made.

The analyses of interaction between prespecified subgroups of interest and treatment were made by adding subgroup variables and interaction in generalized estimating equation models. Patient

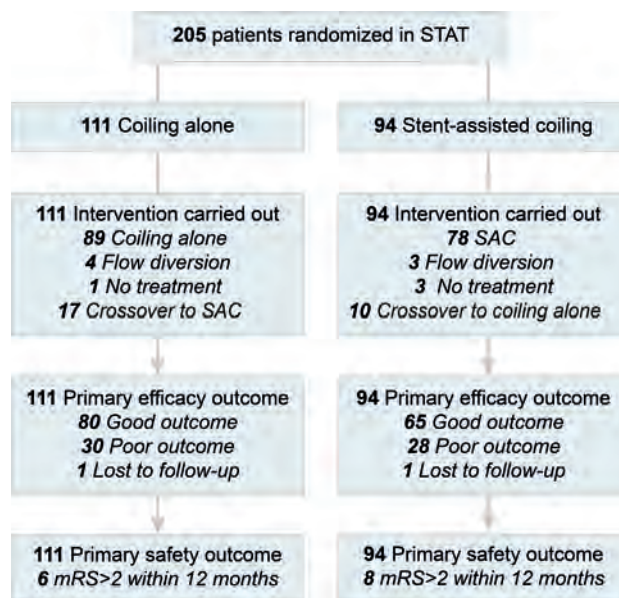


FIG 1. STAT participant flow CONSORT diagram.²⁰

and aneurysm subgroups were examined as prespecified in 2011, regardless of the results of tests for interaction. Subgroup results according to STAT 1–3 categories indicated at the time of registration, according to aneurysm size (<10 mm or \geq 10 mm), neck size (<4 mm or \geq 4 mm), and location (posterior circulation and anterior circulation subdivided into carotid, anterior cerebral artery, and MCA aneurysms) are reported. As-treated exploratory analyses (defined as coiling with or without any attempt or use of stent placement, regardless of treatment allocation) are also provided. We also explored what results would have been if complete occlusion (rather than the combination of complete and near-complete occlusion) had been used as the criterion for a good angiographic outcome. One adverse event is reported per patient. When a patient had >1 event, we used the most severe to categorize the patient. Analyses were performed using SAS software, Version 9.4 (SAS Institute) and SPSS, Version 26 (IBM) with a significance level of 5%.

Roles of the Sponsor and Funding Source

The trial was sponsored by the Center Hospitalier de l'Université de Montréal. The sponsor had no part in the study design, data collection, analysis, or reporting and no access to the data or source documents. The corresponding author had full access to all the data and had final responsibility for the decision to submit for publication. There was no funding source for this study.

RESULTS

Between August 2011 and August 2021, we recruited 205 patients: Ninety-four were assigned to SAC, and 111 to CA. For each group, the number of participants who were randomly assigned, received intended treatment, and were analyzed for the primary outcome is illustrated in the trial profile (Fig 1).

The baseline patient and aneurysm characteristics are shown in Table 1. Groups were comparable: Ninety-two (44.9%) patients had small wide-neck aneurysms (STAT-3); 75 (36.6%), a recurrent

Table 1: Patient and index aneurysm characteristics

Characteristics	CA (n = 111)	SAC (n = 94)	Total (n = 205)
Patient			
Age at treatment (mean) (SD) (yr)	58.6 (10.4)	58.0 (8.8)	58.3 (9.7)
Female (No.) (%)	77 (69.4)	65 (69.1)	142 (69.3)
STAT type lesion			
STAT-1: unruptured aneurysm, never treated, with a dimension of ≥ 10 mm (No.) (%)	21 (18.9)	17 (18.1)	38 (18.5)
STAT-2: major recurrent aneurysm after previous coiling, but no previous stent placement (No.) (%)	41 (36.9)	34 (36.2)	75 (36.6)
STAT-3: small (<10 mm), wide-neck (≥ 4 mm) aneurysm (No.) (%)	49 (44.1)	43 (45.7)	92 (44.9)
Pretreatment mRS score (No.) (%)			
0	84 (75.7)	70 (74.5)	154 (75.1)
1	21 (18.9)	20 (21.3)	41 (20.0)
2	5 (4.5)	2 (2.1)	7 (3.4)
3	1 (0.9)	1 (1.1)	2 (1.0)
4	0	1 (1.1)	1 (0.5)
Presentation			
Symptomatic	4 (3.6)	4 (4.3)	8 (3.9)
Additional aneurysm to a previously ruptured and treated one	13 (11.7)	6 (6.4)	19 (9.3)
Incidental finding	94 (84.7)	84 (89.4)	178 (86.8)
Index aneurysm location (No.) (%)			
Anterior circulation			
Ophthalmic/paraophthalmic	7 (6.3)	3 (3.2)	10 (4.9)
Posterior communicating/anterior choroidal	7 (6.3)	13 (13.8)	20 (9.8)
Carotid terminus	6 (5.4)	1 (1.1)	7 (3.4)
MCA bifurcation/M1	18 (16.2)	14 (14.9)	32 (15.6)
Anterior communicating/A1	40 (36.0)	25 (26.6)	65 (31.7)
Distal ACA	0	2 (2.1)	2 (1.0)
Posterior circulation			
PCA	0	3 (3.2)	3 (1.5)
Basilar terminus	24 (21.6)	23 (24.5)	47 (22.9)
SCA	3 (2.7)	5 (5.3)	8 (3.9)
Basilar trunk	2 (1.8)	0	2 (1.0)
Vertebrobasilar junction	2 (1.8)	2 (2.1)	4 (2.0)
PICA	2 (1.8)	3 (3.2)	5 (2.4)
Index aneurysm maximal external size (mean) (SD) (range) (mm)			
	9.2 (6.4)	9.2 (5.9)	9.2 (6.1)
	(2–50)	(3–35)	(2–50)
<10 (No.) (%)	74 (66.7)	63 (67.0)	137 (66.8)
≥ 10 (No.) (%)	37 (33.3)	31 (33.0)	68 (33.2)
Index aneurysm neck size (mean) (SD) (range) (mm)			
	4.4 (2.2)	4.1 (1.6)	4.3 (1.9)
	(2–20)	(2–9)	(2–20)
Aneurysm neck ≥ 4 mm (No.) (%)			
	72 (64.9)	58 (61.7)	130 (63.4)

Note:—ACA indicates anterior cerebral artery; PCA, posterior cerebral artery; SCA, superior cerebellar artery.

aneurysm (STAT-2); and 38 (18.5%), a large aneurysm (STAT-1). The most frequent locations were the anterior communicating artery (65; 31.7%), basilar bifurcation (47; 22.9%), and MCA bifurcation (32; 15.6%).

Seventeen of 111 patients (15.3%) allocated to CA underwent SAC, while 10/94 (10.6%) patients allocated to SAC were treated with CA. Technical details regarding treatment for both groups are provided in the Online Supplemental Data. In 4 patients from STAT-2, residual aneurysms were judged too small for any treatment (3 in the SAC arm and 1 in the CA arm). Seven patients were treated with flow diverters (3 in the SAC arm and 4 in the CA arm). Patients allocated to SAC were initially treated with a single ($n = 64$) or 2 ($n = 14$) stents. Stents were delivered before coiling in 20/78 (25.6%) and after coiling in 58/78 (74.4%) patients.

The primary outcome is available for 203/205 patients (99%), with 1 patient missing in each group (Fig 1 and Tables 2 and 3). Treatment failure occurred in 28/93 patients allocated to SAC (30.1%; 95% CI, 21.2%–40.6%) compared with 30/110 (27.3%; 95% CI, 19.4%–36.7%) allocated to CA (RR = 1.10; 95% CI, 0.7–

1.7; $P = .66$). Details of each component of the primary outcome in the intent to treat analysis are provided in Table 2.

There were no incidences of aneurysm rupture during follow-up. Three patients were retreated (all in the SAC group). Angiographic results at 12 months accounted for most of the primary outcome adjudications (185/203; 91%). Follow-up vascular imaging studies, available in 198 patients (96.6%), were performed by MRA in 135 (68.2%), by catheter angiography in 59 (29.8%), and by CTA in 4 (2%) patients. More patients were followed by catheter angiography in the SAC group (37.2%) than in the CA group (21.6%) (Table 3). The mean time of angiographic follow-up was 14.8 (SD, 9.5) months for patients allocated to SAC, and 13.5 (SD, 5.2) months for patients allocated to CA. The mean time of the follow-up mRS evaluation was 15.3 (SD, 8.0) months for SAC and 15.7 (SD, 10.5) months for CA.

Results for predefined subgroups of interest are illustrated in the forest plot (Fig 2), even though none of the interaction tests were significant.

Poor clinical outcomes (mRS > 2) in the intent to treat analysis are detailed in Table 4. A poor clinical outcome (mRS > 2) occurred in 8/94 patients allocated to SAC (8.5%; 95% CI, 4.0%–16.6%) compared with 6/111 (5.4%; 95% CI, 2.2%–11.9%) with CA

Table 2: Primary outcome in intent-to-treat analysis

Intent-to-treat analysis 1-year outcome ^a	CA (n = 111)	SAC (n = 94)
Treatment failure (composite) (No.) (%)	30 (27.3)	28 (30.1)
Clinical		
mRS 6	2 (1.8)	3 (3.2)
mRS 3–5	3 (2.7)	3 (3.2)
Intracranial hemorrhage	0	0
Retreatment	0	3 (3.2)
Angiographic		
Immediate failure	3 (2.7)	1 (1.1)
Residual aneurysm (core lab)	22 (19.8)	18 (19.4)
Missing primary outcome	1 (0.9)	1 (1.1)

^aRR = 1.10; 95% CI, 0.71–1.71; P = .656.

Table 3: Secondary outcomes in intent-to-treat analysis

	CA (n = 111)	SAC (n = 94)	RR (95% CI)	P Value
Hospitalization			0.78 (0.48–1.28)	.325
Patients hospitalized for >3 days (No.) (%)	30 (27.3)	20 (21.3)		
Discharge location (No.) (%)			1.18 (0.35–3.96)	.788
Home	106 (95.5)	89 (94.7)		
Other than home	5 (4.5)	5 (5.3)		
Other hospital	1 (0.9)	0		
Rehabilitation center	2 (1.8)	2 (2.1)		
Death	2 (1.8)	3 (3.2)		
mRS at discharge (No.) (%)			1.18 (0.35–3.96)	.788
0	84 (75.7)	69 (73.4)		
1	17 (15.3)	16 (17.0)		
2	5 (4.5)	4 (4.3)		
3	2 (1.8)	1 (1.1)		
4	1 (0.9)	0 (0.0)		
5	0 (0.0)	1 (1.1)		
6	2 (1.8)	3 (3.2)		
1-Year mRS (No.) (%)			1.17 (0.43–3.22)	.761
0	66 (60.0)	54 (57.4)		
1	30 (27.3)	26 (27.7)		
2	7 (6.4)	7 (7.4)		
3	1 (0.9)	2 (2.1)		
4	2 (1.8)	0 (0.0)		
5	1 (0.9)	0 (0.0)		
6	3 (2.7)	5 (5.3)		
Missing mRS data	1 (0.9)	0		
Time of 1-year mRS assessment (mean) (SD) (mo)	15.7 (10.5)	15.3 (8.0)		
Morbidity and mortality at 1 year (mRS > 2). (No.) (%)	6 (5.4%)	8 (8.5%)		
Retreatment of index aneurysm during follow-up (No.) (%)	0	3 (3.2)		
Immediate angiographic outcome			0.97 (0.42–2.23)	.936
Complete occlusion (No.) (%)	67 (60.4)	55 (58.5)		
Residual neck (No.) (%)	33 (29.7)	30 (31.9)		
Residual saccular aneurysm (No.) (%)	11 (9.9)	9 (9.6)		
Angiographic outcome at 1 year (core lab) (Detailed results in Online Supplemental Data)				
Complete occlusion (No.) (%)	38 (34.2)	42 (44.7)		
Residual neck (No.) (%)	43 (38.7)	24 (25.5)		
Residual saccular aneurysm (No.) (%)	27 (24.3)	24 (25.5)		
1-year imaging not available ^a (No.) (%)	3 (2.7)	4 (4.3)		
Time of 1-year imaging assessment (mean) (SD) (mo)	13.5 (5.2)	14.8 (9.5)		
Follow-up vascular imaging ^a (No.) (%)	108 (97.3)	90 (95.7)		
MRA (No.) (%)	82 (73.9)	53 (56.4)		
Catheter angiography (No.) (%)	24 (21.6)	35 (37.2)		
CTA (No.) (%)	2 (1.8)	2 (2.1)		

^aThree deaths in the CA group, 4 deaths in the SAC group. For 1 patient in the SAC group (who died 298 days after treatment), the 1-year imaging was adjudicated using the 3-month follow-up angiogram.

(RR = 1.6; 95% CI, 0.6–4.4; P = .38). Five deaths were related to treatment complications (2 in the CA and 3 in the SAC arms). Deaths unrelated to the aneurysm or treatment (and not included in the primary outcome measure) were reported in 3 patients (1 in the CA and 2 in the SAC groups). Details of poor clinical outcomes at any time point are provided in the Online Supplemental Data.

Adverse events occurred in 25/94 (26.6%) patients with SAC and 23/111 (20.7%) with CA (RR = 1.28; 95% CI, 0.78–2.11; P = .323). Cerebrovascular ischemic and hemorrhagic events occurred in 21/94 (22.3%) patients with SAC, and in 18/111 (16.2%) with CA (RR = 1.38; 95% CI, 0.78–2.43; P = .268). Complication rates according to subgroups of interest are provided in the Online Supplemental Data. The test of interaction was significant for aneurysm size (P = .02): complications were more frequent in patient with aneurysms <10 mm allocated to SAC than in those allocated to CA (RR 2.0 ± 0.69 95% CI 1.0–3.9; P = .04).

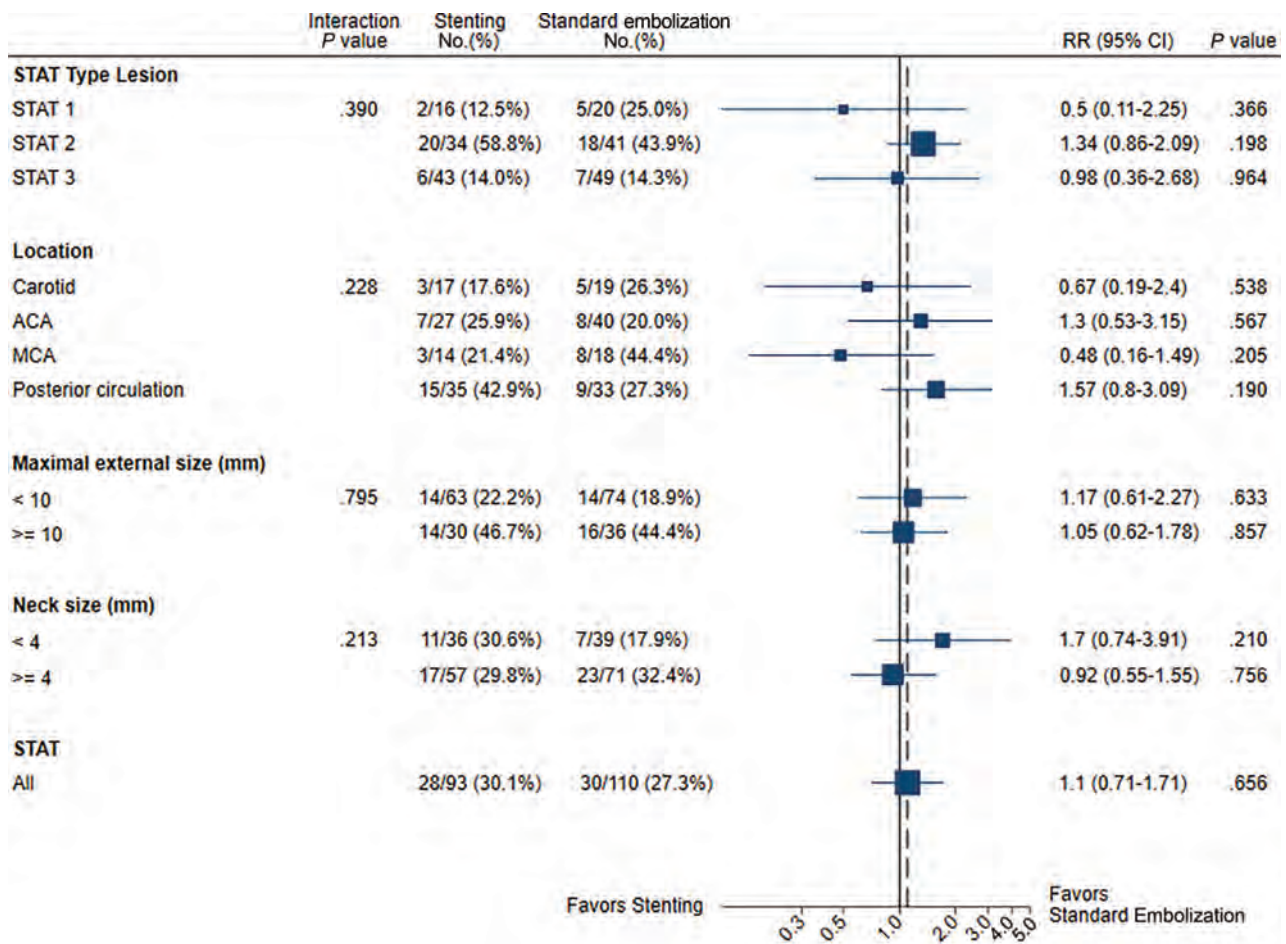


FIG 2. Subgroup analysis of the primary outcome at 1 year. ACA indicates anterior cerebral artery.

Table 4: Clinical outcomes (mRS > 2 at 12 months) in intent-to-treat analysis

Intent to treat	CA (n = 111)	SAC (n = 94)
Death (No.) (%)	3 (2.7)	5 (5.3%)
Related	2	3
Unrelated	1	2
mRS 3–5 (No.) (%)	3 (2.7)	3 (3.2)
Total (No.) (%)	6 (5.4)	8 (8.5)

Results for the secondary outcomes in the intent-to-treat analyses are detailed in Table 3. Secondary outcomes (immediate and 12 month angiographic outcomes, days of hospitalization, discharge disposition, mRS at discharge and at 12 months) were similar between groups. Angiographic results at 12 months were similar (RR 1.1; 95% CI 0.66–1.71; $P = .789$). Changing the definition of a good angiographic outcome as a complete occlusion did not change results (Online supplemental data).

As-treated analyses included 198/205 patients (97%; seven patients treated with flow diverters were excluded). The primary outcome (treatment failure) occurred in 27/102 patients treated with SAC (26.5%; 95% CI, 18.4%–36.3%) compared with 29/94 (30.8%; 95% CI, 21.9%–41.3%) treated with CA (RR = 0.86; 95% CI, 0.55–1.34; $P = .498$). Details of each component of the primary outcome are provided in Table 5.

Predefined as-treated subgroup analyses of the primary outcome are detailed and illustrated in the forest plot (Online Supplemental Data). There were no significant interactions, and subgroup results were similar.

In as-treated analyses, all-cause death or dependency at 1 year occurred in 10 of 104 (9.6%) SAC patients and in 4 of 94 CA patients (4.3%) (RR = 2.26; 95% CI, 0.73–9.96; $P = .156$) (Table 6). Other secondary outcomes (Online Supplemental Data) (immediate angiographic outcomes, days of hospitalization, discharge disposition, and mRS at discharge and at 12 months) were similar between groups.

As-treated angiographic results at 12 months, categorized as the presence of a residual aneurysm or not, were not significantly different (RR = 0.77; 95% CI, 0.48–1.2; $P = .300$). SAC was significantly better than CA in as-treated analyses when “complete occlusion” was used as the definition of a good angiographic outcome (RR = 0.74; 95% CI, 0.59–0.94; $P = .012$) (Online Supplemental Data).

Adverse events (any severity) occurred in 34/104 (32.7%) patients who underwent SAC, compared with 12/94 (12.8%) patients with CA (RR = 2.56; 95% CI, 1.41–4.65; $P = .002$). Details are provided in the Online Supplemental Data. Ischemic and hemorrhagic events were more frequent in patients who underwent SAC (30/104 [28.8%]) compared with 7/94 (7.4%) patients who received CA (RR = 3.87; 95% CI, 1.79–8.40; $P = .001$).

Table 5: Primary outcome in as-treated analysis

As-treated analysis 1-year outcome ^a	CA (n = 94)	SAC (n = 104)
Treatment failure (composite) (No.) (%)	29 (30.9)	27 (26.0)
Clinical		
mRS 6	1 (1.1)	4 (3.9)
mRS 3–5	3 (3.2)	3 (3.1)
Intracranial hemorrhage	0	0
Retreatment	0	3 (3.2)
Angiographic		
Immediate failure	3 (3.3)	1 (1.1)
Residual aneurysm (core lab)	22 (25.3)	16 (17.6)
Missing primary outcome	0	2 (1.9)

^a RR = 0.86; 95% CI, 0.55–1.34; P = .498.

Table 6: Clinical outcomes (mRS > 2 at 12 months) in as-treated analysis

As-treated	CA (n = 94)	SAC (n = 104)
Death (No.) (%)	1 (1.1)	7 (6.7)
Related	1	4
Unrelated	0	3
mRS 3–5 (No.) (%)	3 (3.2)	3 (2.9)
Total (No.) (%)	4 (4.3)	10 (9.6)

DISCUSSION

The Problem of Residual Aneurysms after Coiling

Residual or recurrent aneurysms after coiling occur in 10%–33% of patients.^{27,28} In ruptured aneurysms, they have been associated with a persistent risk of subarachnoid hemorrhage.^{27,28} In UIAs, they are more likely to occur in large, wide-neck, and recurrent aneurysms.²³ In the context of a preventive treatment against ruptures, recurrences lead to a number of clinical consequences, such as routine angiographic surveillance of nearly all patients and retreatment in 5%–15%²⁹ (even up to 25% of patients at 10 years in some series).³⁰ Potentially more effective coils have been developed with varying but mostly disappointing results,^{31–36} particularly for large and recurrent aneurysms.²³

Stent Placement and Residual Aneurysms

The use of SAC, originally designed to treat otherwise untreatable aneurysms, has expanded in the hope of decreasing the risk of recurrences.^{3,6–8,10–12,37–40} This hypothesis has never been tested in a randomized trial. Previous studies,^{3–10} including systematic reviews and meta-analyses,^{11,12} have shown diverging results. Some studies have reported that aneurysms treated with SAC were less prone to recurrence,^{3,5,8,10–12} while other studies did not show such an effect.^{4,6,7,9} Higher treatment-related risks of mortality and morbidity were shown in some reports,^{3,7,11} but not in others.^{4–6,8,10} Many studies reported significant baseline differences between the groups being compared, most often with characteristics that could favor SAC (ie, a high proportion of unruptured sidewall aneurysms and shorter follow-up time).^{3–5} Thus, after 20 years, we still lack reliable evidence regarding the risks and potential benefits of adding a stent to a coiling procedure in patients with UIAs eligible for both options. It is in this context of uncertainty that STAT was launched in 2011.

The Choice of Primary Outcome

The primary end point of STAT was a composite that included clinical and angiographic outcome measures. Although the main goal

of UIA treatment is to prevent future ruptures, these are rare events.^{22–24} Using death or disability from rupture during follow-up would necessitate the recruitment of thousands of patients followed for a long time. Most clinicians rely on angiographic results to assess the efficacy of treatment, and most endovascular trials have used angiographic outcomes as primary end points.^{22–24} The residual aneurysm cutoff category was chosen to judge treatment failure because it has been shown to be more repeatable, and its clinical significance more constant than other categories.²⁵ The clinical criteria included in the composite primary outcome measure ensured that a patient becoming dependent or dying because of a treatment-related complication (or because the treatment was clinically ineffective) would not count as a good outcome. However, clinical outcomes weighed little in the final comparison between treatments, which was driven mainly by angiographic results.

Primary Outcome Results

STAT did not show a large benefit of SAC over CA for the treatment of UIAs. This was true for patients with large (STAT-1), recurrent (STAT-2), or wide-neck aneurysms (STAT-3). The trial was only powered to show a large effect (a decrease in the failure rate from 33% to 15%). We cannot exclude that with the inclusion of a larger number of patients, a more modest but still clinically significant benefit could have been demonstrated.

In STAT, a substantial number of crossovers diluted the contrast between treatments. The classic way of analyzing results (intent to treat) remains clinically appropriate for practical reasons. First, many crossovers, such as bailout stent placement in patients with coil protrusion and parent vessel or branch occlusion (in the CA group) or failure to catheterize the branch necessary to land the stent (in the SAC group), were inevitable. Second, the goal of the trial was to assess the role of stent placement to intentionally improve the results of endovascular treatment. Perhaps the groups being compared could have been more precisely defined as SAC (if possible) versus CA plus bailout stent placement (only if necessary).

From an explanatory or mechanistic perspective, it is worth looking at the as-treated results: Does stent placement have the potential to improve the angiographic results of coiling?

Only by redefining a good angiographic outcome as a complete occlusion and only by looking at as-treated analyses could SAC be shown superior to CA (Online Supplemental Data). The clinical significance of this finding remains questionable, but it may be a signal in favor of the capacity of stent placement to improve angiographic results of coiling in the long term. This capacity may come at a cost in terms of complications: As-treated analyses also showed complications to be more frequent with SAC, particularly for small aneurysms. Although in some of these cases, complications occurred when stents were being used as a rescue strategy (ie, a technical complication had already occurred), thromboembolic complications with stent placement remain a concern.

Safety of Treatments

The overall morbidity and mortality of patients treated in STAT were within the range of our initial estimate (between 6% and 12%). Safety end points were similar between the 2 groups in intent-to-treat analyses, but the trial was underpowered to draw

any conclusions about the safety of SAC over CA. The upper limit of the 95% CI of the risk ratio of 4.4 cannot exclude SAC being associated with a large increase in initial or long-term neurologic deficits compared with CA. Cerebrovascular ischemic and hemorrhagic events in STAT were relatively high compared with previous registries^{6,7} and meta-analysis.¹¹ However, those comparisons are not valid, and aneurysms randomized in STAT were typically larger and many were difficult to treat by any and all methods.

Trial Limitations

Before we examine the potential impact on clinical practice, we must review the trial limitations. Only 4 centers participated, which limits the generalizability of results. Although STAT is the only randomized controlled trial comparing SAC and CA, the number of patients remains small. The introduction of flow diverters likely directed many patients with difficult aneurysms to other clinical trials.²² The original plan was to recruit 40–50 centers, but the lack of financial support deterred many potential centers from participating. As many as 600 patients would have been necessary to exclude the possibility that SAC would double the risk of death or dependency. Yet, safety is of primary importance when a preventive treatment is offered to mostly asymptomatic individuals. Many advanced SAC techniques, such as X or Y stent placement, were not frequently used, and trial results cannot be applied to these treatments. Most stents were braided stents (83%), and results may not apply to other types of stents. There were a substantial number of crossovers, diluting the contrast between groups in the intent-to-treat analyses. The 12-month follow-up period was relatively short. This may not have given enough time for some recurrences to become apparent. Clinical outcome assessments were not blinded, and core laboratory adjudications could not be masked to the presence of artifacts caused by stents. Death or dependency accounted for a relatively small number of poor outcomes in both groups (5-versus-6 patients, including 2-versus-3 deaths). Thus, potential bias from lack of blinding of mRS clinical assessors is unlikely to have significantly affected results. There were some disparities in follow-up imaging modalities between groups. However, because only residual aneurysms, readily identified by any imaging technique, were considered in the adjudication of the primary outcome, this potential bias is unlikely to have affected the results. Finally, the trial was conducted during 10 years. Indications, devices, techniques, and clinical expertise have evolved over such a long period.

Potential Implications for Practice and Future Research

STAT results do not apply to patients excluded by protocol, such as those with ruptured aneurysms. They do not apply to most small UIAs because only patients at high risk for recurrence (with large, wide-neck, or recurrent aneurysms) were eligible. Patients judged untreatable without stent placement, a subjective notion, were also excluded by definition.

For patients with UIAs treatable by both options, the trial showed no large benefit of a policy of stent placement in addition to coiling. In addition, the trial raises concerns regarding potential thromboembolic complications. This was particularly true for patients with small aneurysms at low risk of rupture, for whom

the crucial question remains: Should they be offered preventive treatment at all?⁴¹

The use of stents for the treatment of UIAs is an example of the failure of our community to use randomized trials to safely introduce innovations in neurovascular care.² We must find ways to integrate clinical research into practice to optimize care in real time.⁴² Future trials on SAC should probably be integrated into ongoing randomized clinical trials.^{41,43,44}

CONCLUSIONS

STAT did not show SAC to be superior to CA for wide-neck, large, or recurrent unruptured aneurysms. More randomized data are needed to determine the role of SAC in the treatment of aneurysms.

Disclosure forms provided by the authors are available with the full text and PDF of this article at www.ajnr.org.

REFERENCES

1. U.S. Department of Health and Human Services; US Food & Drug Administration. **Humanitarian Device Exemption (HDE)**. <https://www.accessdata.fda.gov/scripts/cdrh/cfdocs/cfhde/hde.cfm?id=H02000>
2. December 5, 2022; Accessed on September 12, 2022
3. Raymond J, Darsaut TE. **Stenting for intracranial aneurysms: how to paint oneself into the proverbial corner**. *AJNR Am J Neuroradiol* 2011;32:1711–13 CrossRef Medline
4. Piotin M, Blanc R, Spelle L, et al. **Stent-assisted coiling of intracranial aneurysms**. *Stroke* 2010;41:110–15 CrossRef Medline
5. Hwang G, Park H, Bang JS, et al. **Comparison of 2-year angiographic outcomes of stent- and nonstent-assisted coil embolization in unruptured aneurysms with an unfavorable configuration for coiling**. *AJNR Am J Neuroradiol* 2011;32:1707–10 CrossRef Medline
6. Chalouhi N, Jabbour P, Singhal S, et al. **Stent-assisted coiling of intracranial aneurysms: predictors of complications, recanalization, and outcome in 508 cases**. *Stroke* 2013;44:1348–53 CrossRef Medline
7. Chung EJ, Shin YS, Lee CH, et al. **Comparison of clinical and radiologic outcomes among stent-assisted, double-catheter, and balloon-assisted coil embolization of wide neck aneurysms**. *Acta Neurochir (Wien)* 2014;156:1289–95 CrossRef Medline
8. Hetts SW, Turk A, English JD, et al; Matrix and Platinum Science Trial Investigators. **Stent-assisted coiling versus coiling alone in unruptured intracranial aneurysms in the Matrix and Platinum Science Trial: safety, efficacy, and mid-term outcomes**. *AJNR Am J Neuroradiol* 2014;35:698–705 CrossRef Medline
9. Liu YQ, Wang QJ, Zheng T, et al. **Single-centre comparison of procedural complications, clinical outcome, and angiographic follow-up between coiling and stent-assisted coiling for posterior communicating artery aneurysms**. *J Clin Neurosci* 2014;21:2140–44 CrossRef Medline
10. Ozretić D, Radoš M, Pavliša G, et al. **Long-term angiographic outcome of stent-assisted coiling compared to non-assisted coiling of intracranial saccular aneurysms**. *Croat Med J* 2015;56:24–31 CrossRef Medline
11. Consoli A, Vignoli C, Renieri L, et al. **Assisted coiling of saccular wide-necked unruptured intracranial aneurysms: stent versus balloon**. *J Neurointerv Surg* 2016;8:52–57 CrossRef Medline
12. Feng MT, Wen WL, Feng ZZ, et al. **Endovascular embolization of intracranial aneurysms: to use stent(s) or not? Systematic review and meta-analysis**. *World Neurosurg* 2016;93:271–78 CrossRef Medline
13. Phan K, Huo YR, Jia F, et al. **Meta-analysis of stent-assisted coiling versus coiling-only for the treatment of intracranial aneurysms**. *J Clin Neurosci* 2016;31:15–22 CrossRef Medline
14. Bodily KD, Cloft HJ, Lanzino G, et al. **Stent-assisted coiling in acutely ruptured intracranial aneurysms: a qualitative, systematic review of**

- the literature. *AJNR Am J Neuroradiol* 2011;32:1232–36 CrossRef Medline
14. Baráth K, Cassot F, Fasel JH, et al. **Influence of stent properties on the alteration of cerebral intra-aneurysmal haemodynamics: flow quantification in elastic sidewall aneurysm models.** *Neurol Res* 2005;27 Suppl 1:S120–28 CrossRef Medline
 15. Hirabayashi M, Ohta M, Rüfenacht DA, et al. **Characterization of flow reduction properties in an aneurysm due to a stent.** *Phys Rev E Stat Nonlin Soft Matter Phys* 2003;68:021918 CrossRef Medline
 16. Lieber BB, Gounis MJ. **The physics of endoluminal stenting in the treatment of cerebrovascular aneurysms.** *Neurol Res* 2002;24(Suppl 1):S33–42 CrossRef Medline
 17. Lopes D, Sani S. **Histological postmortem study of an internal carotid artery aneurysm treated with the Neuroform stent.** *Neurosurgery* 2005;56:E416; discussion E416 CrossRef Medline
 18. Raymond J, Darsaut TE, Bing F, et al. **Stent-assisted coiling of bifurcation aneurysms may improve endovascular treatment: a critical evaluation in an experimental model.** *AJNR Am J Neuroradiol* 2013;34:570–76 CrossRef Medline
 19. Darsaut TE, Raymond J; STAT Collaborative Group. **The design of the STenting in Aneurysm Treatments (STAT) trial.** *J Neurointerv Surg* 2012;4:178–81 CrossRef Medline
 20. Boutron I, Altman DG, Moher D, et al; CONSORT NPT Group. **CONSORT Statement for Randomized Trials of Nonpharmacologic Treatments: A 2017 Update and a CONSORT Extension for Nonpharmacologic Trial Abstracts.** *Ann Intern Med* 2017; 167:40–47 CrossRef Medline
 21. Roy D, Milot G, Raymond J. **Endovascular treatment of unruptured aneurysms.** *Stroke* 2001;32:1998–2004 CrossRef Medline
 22. Raymond J, Darsaut TE, Guilbert F, et al. **Flow diversion in aneurysms trial: the design of the FIAT study.** *Interv Neuroradiol* 2011; 17:147–53 CrossRef Medline
 23. Raymond J, Klink R, Chagnon M, et al. **Hydrogel versus bare platinum coils in patients with large or recurrent aneurysms prone to recurrence after endovascular treatment: a randomized controlled trial.** *AJNR Am J Neuroradiol* 2017;38:432–41 CrossRef Medline
 24. White PM, Lewis SC, Gholkar A, et al; HELPS Trial Collaborators. **Hydrogel-coated coils versus bare platinum coils for the endovascular treatment of intracranial aneurysms (HELPS): a randomised controlled trial.** *Lancet* 2011;377:1655–62 CrossRef Medline
 25. Benomar A, Farzin B, Gevry G, et al. **Noninvasive angiographic results of clipped or coiled intracranial aneurysms: an inter- and intraobserver reliability study.** *AJNR Am J Neuroradiol* 2021;42:1615–20 CrossRef Medline
 26. Benomar A, Farzin B, Volders D, et al. **Angiographic results of surgical or endovascular treatment of intracranial aneurysms: a systematic review and inter-observer reliability study.** *Neuroradiology* 2021;63:1511–19 CrossRef Medline
 27. Raymond J, Guilbert F, Weill A, et al. **Long-term angiographic recurrences after selective endovascular treatment of aneurysms with detachable coils.** *Stroke* 2003;34:1398–403 CrossRef Medline
 28. Byrne JV, Sohn MJ, Molyneux AJ, et al. **Five-year experience in using coil embolization for ruptured intracranial aneurysms: outcomes and incidence of late rebleeding.** *J Neurosurg* 1999;90:656–63 CrossRef Medline
 29. Ferns SP, Sprengers ME, van Rooij WJ, et al. **Coiling of intracranial aneurysms: a systematic review on initial occlusion and reopening and retreatment rates.** *Stroke* 2009;40:e523–29 CrossRef Medline
 30. Lecler A, Raymond J, Rodriguez-Régent C, et al. **Intracranial aneurysms: recurrences more than 10 years after endovascular treatment—a prospective cohort study, systematic review, and meta-analysis.** *Radiology* 2015;277:173–80 CrossRef Medline
 31. van Rooij WJ, de Gast AN, Sluzewski M. **Results of 101 aneurysms treated with polyglycolic/polylactic acid microfilament Nexus coils compared with historical controls treated with standard coils.** *AJNR Am J Neuroradiol* 2008;29:991–96 CrossRef Medline
 32. White PM, Raymond J. **Endovascular coiling of cerebral aneurysms using “bioactive” or coated-coil technologies: a systematic review of the literature.** *AJNR Am J Neuroradiol* 2009;30:219–26 CrossRef Medline
 33. Molyneux AJ, Clarke A, Sneade M, et al. **Cerecyte coil trial: angiographic outcomes of a prospective randomized trial comparing endovascular coiling of cerebral aneurysms with either Cerecyte or bare platinum coils.** *Stroke* 2012;43:2544–50 CrossRef Medline
 34. McDougall CG, Johnston SC, Gholkar A; et al; MAPS Investigators. **Bioactive versus bare platinum coils in the treatment of intracranial aneurysms: the MAPS (Matrix and Platinum Science) trial.** *AJNR Am J Neuroradiol* 2014;35:935–42 CrossRef Medline
 35. Bendok BR, Abi-Aad KR, Ward JD, et al; Heat Study Investigators. **The hydrogel endovascular aneurysm treatment trial (HEAT): a randomized controlled trial of the second-generation hydrogel coil.** *Neurosurgery* 2020;86:615–24 CrossRef Medline
 36. Raymond J, Ghostine J, van Adel BA, et al. **Does increasing packing density using larger caliber coils improve angiographic results of embolization of intracranial aneurysms at 1 year: a randomized trial.** *AJNR Am J Neuroradiol* 2020;41:29–34 CrossRef Medline
 37. Chalouhi N, Jabbour P, Gonzalez LF, et al. **Safety and efficacy of endovascular treatment of basilar tip aneurysms by coiling with and without stent assistance: a review of 235 cases.** *Neurosurgery* 2012;71:785–94 CrossRef Medline
 38. Yang H, Sun Y, Jiang Y, et al. **Comparison of stent-assisted coiling vs coiling alone in 563 intracranial aneurysms: safety and efficacy at a high-volume center.** *Neurosurgery* 2015;77:241–47; discussion 247 CrossRef Medline
 39. Hong Y, Wang YJ, Deng Z, et al. **Stent-assisted coiling versus coiling in treatment of intracranial aneurysm: a systematic review and meta-analysis.** *PLoS One* 2014;9:e82311 CrossRef Medline
 40. Jahshan S, Abila AA, Natarajan SK, et al. **Results of stent-assisted vs non-stent-assisted endovascular therapies in 489 cerebral aneurysms: single-center experience.** *Neurosurgery* 2013;72:232–39 CrossRef Medline
 41. Darsaut TE, Desal H, Cognard C, et al. **Comprehensive Aneurysm Management (CAM): an all-inclusive care trial for unruptured intracranial aneurysms.** *World Neurosurg* 2020;141:e770–77 CrossRef Medline
 42. Darsaut TE, Raymond J. **Ethical care requires pragmatic care research to guide medical practice under uncertainty.** *Trials* 2021; 22:143 CrossRef Medline
 43. Raymond J, Januel AC, Iancu D, et al. **The RISE trial: a randomized trial on intra-saccular Endobridge devices.** *Interv Neuroradiol* 2020;26:61–67 CrossRef Medline
 44. Darsaut TE, Keough MB, Boisseau W, et al. **Middle Cerebral Artery Aneurysm Trial (MCAAT): A randomized care trial comparing surgical and endovascular management of MCA aneurysm patients.** *World Neurosurg* 2022;160:e49–54 CrossRef Medline

Radiology-Pathology and Surgical Correlation in Astroblastoma

F. Sprenger, E.B. da Silva Jr, M.S. Cavalcanti, and B.C. de Almeida Teixeira

ABSTRACT

SUMMARY: Astroblastoma is a rare astrocytic glial neoplasm that affects mainly young girls, peaking between 10 and 30 years of age, with low- and high-grade manifestations. Imaging characteristics are well-described, but histopathologic and, more recently, molecular analysis is fundamental to establish the diagnosis, now based on *MNI* alterations. We describe a case with typical imaging and histologic features of an *MNI*-altered astroblastoma.

ABBREVIATIONS: 5-ALA = 5-aminolevulinic acid; AT/RT = atypical teratoid/rhabdoid tumor; GFAP = glial fibrillary acidic protein; k^{trans} = volume transfer constant

A 9-year-old girl with a previous diagnosis of high-functioning autism spectrum disorder presented with a 2-day history of headache, vomiting, and sleepiness. On the first day of symptoms, she was seen at a pediatric emergency department and discharged with anesthesia. Due to progressive worsening and unresponsiveness to medication, she was referred to a neurologic tertiary facility. The clinical examination showed a preserved consciousness level and no focal neurologic deficits or signs of meningeal irritation. Blood work had no relevant findings. MR imaging was performed to rule out intracranial pathology.

Imaging

MR imaging showed a large, well-circumscribed intra-axial heterogeneous mass in the right frontal lobe (Fig 1). The lesion had an eccentric, solid component isointense to gray matter on T1 and T2, with intense heterogeneous enhancement due to multiple, small, nonenhancing cysts within the solid portion, giving the lesion a bubbly appearance.

Larger cystic areas were observed on the periphery of the lesion with an intermediate signal on FLAIR and hyperintensity on T2. Foci of hypointensity on SWI and hyperintensity on the filtered phase were also seen and interpreted as punctate calcifications.

A slight perilesional FLAIR hyperintensity was present and attributed to vasogenic edema. There was small mass effect, with a little, leftward, midline shift and right lateral ventricle compression.

Advanced sequences demonstrated foci of intensely restricted diffusion ($ADC = 861 \times 10^{-6} \text{ mm}^2/\text{s}$), suggesting high cellularity, increased relative CBV (1.8 \times), and increased volume transfer constant (k^{trans}) (0.170). MR spectroscopy showed increased Cho/Cr and Cho/NAA ratios (6.98 and 2.26, respectively), suggesting cellular membrane breakdown with neuronal depletion and a prominent lipid-lactate peak, inferring necrosis (Fig 2).

The above-mentioned findings suggested an aggressive primary supratentorial neoplasm, like high-grade astrocytoma, ependymoma, and embryonal tumor, mainly atypical teratoid/rhabdoid tumor (AT/RT). Despite its rarity and nonspecific manifestations, overlapping with characteristics of the above-mentioned tumors, astroblastoma was also considered, given the patient's age, the peripheral polymorph cysts, the solid enhancing portion with a bubbly appearance, and the well-circumscribed margins.

Neuraxis evaluation showed no additional lesions, and the patient underwent surgical resection 3 days after presentation at the tertiary center.

Operative Report

The patient was submitted to 5-aminolevulinic acid (5-ALA)-assisted microscopic near-total resection via frontal craniotomy. Perilesional thin-walled cysts were initially evacuated. The solid portion of the lesion was soft and heterogeneous, with an intense 5-ALA fluorescence and was resected with its capsule. The surgical cavity had faint 5-ALA positivity (Fig 3).

Intraoperative histopathologic examination showed a small-cell neoplasm with pseudorosettes, initially suggesting ependymoma.

Received September 7, 2022; accepted after revision February 17, 2023.

From the Department of Radiology (F.S., B.C.d.A.T.), Hospital de Clínicas da Universidade Federal do Paraná, Curitiba, Brazil; Department of Neurosurgery (E.B.d.S.), Instituto de Neurologia de Curitiba, Curitiba, Brazil; and Neopath Patologia Diagnóstica (M.S.C.), Curitiba, Brazil.

Please address correspondence to Flávia Sprenger, MD, Department of Radiology, Rua General Carneiro, 181, Curitiba, Paraná, Brazil, 80060-900; e-mail: flaviasprenger@gmail.com

<http://dx.doi.org/10.3174/ajnr.A7824>

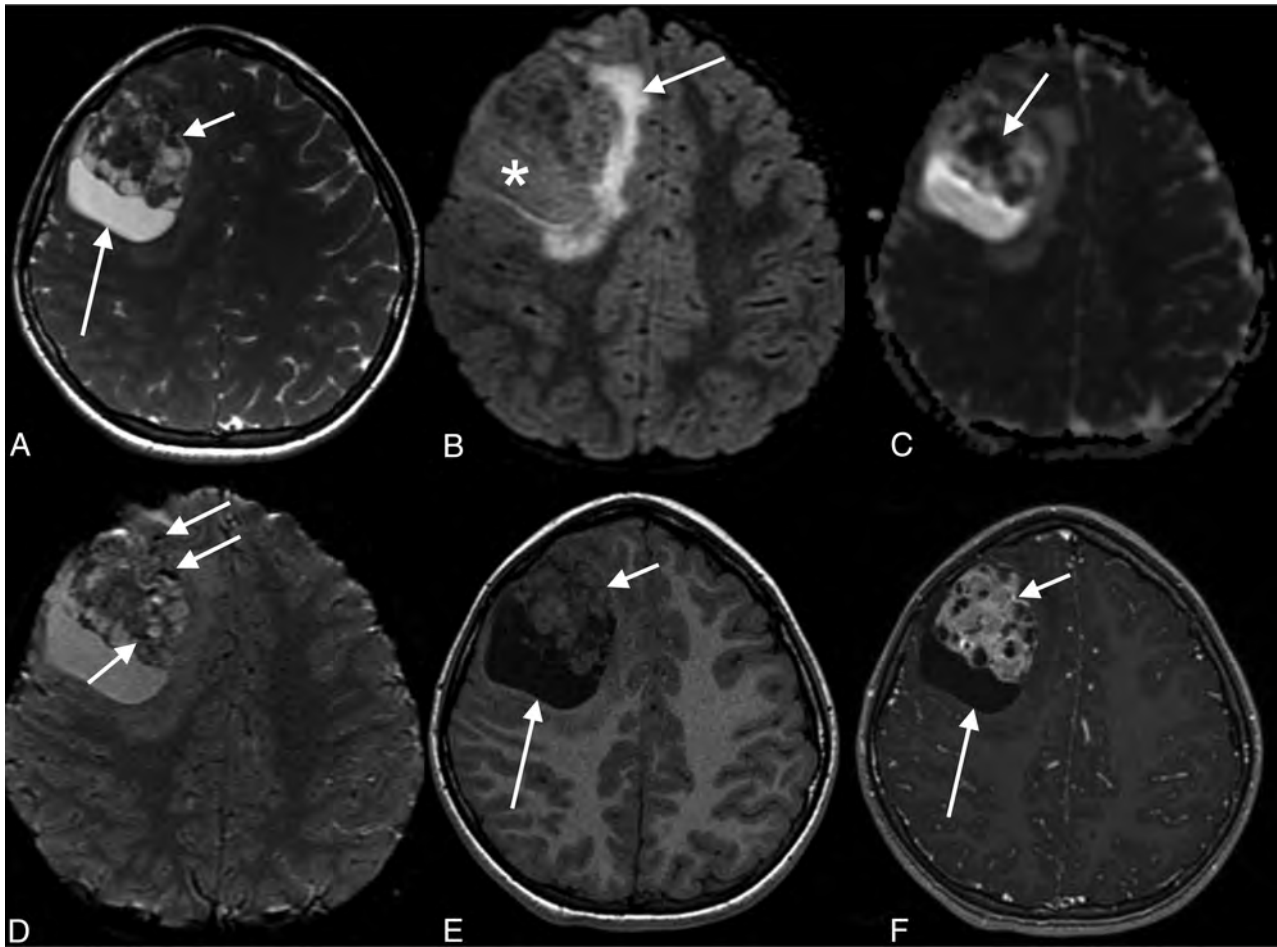


FIG 1. MR images and tumor characterization on multiple sequences. A, Axial T2 image shows the right frontal solid-cystic mass, with large peripheral cysts (*long arrow*) and an eccentric bubbly-appearing solid component (*short arrow*). B, Axial FLAIR demonstrates that the signal intensity of the content of the peripheral cyst is not suppressed (*asterisk*), as well as mild perilesional edema (*arrow*). C, ADC map shows foci of intensely restricted diffusion on the anterior and solid aspect of the lesion (*arrow*). D, Axial SWI demonstrates foci of marked hypointensity (*arrows*), corresponding to punctate calcifications according to the filtered phase signal (not shown). E, Axial T1 image demonstrates an isointense to gray matter heterogeneous solid portion (*short arrow*) with a hypointense large peripheral cyst (*long arrow*). F, Axial T1 postgadolinium image shows intense heterogeneous enhancement of the solid part, with multiple small permeating cysts, giving the tumor a bubbly aspect (*short arrow*). The large peripheral cysts show no enhancement (*long arrow*).

Pathology: Astroblastoma

Grossly, the tumor was fragmented and was tan and soft, with an identifiable cystic membrane.

Histopathologic examination showed solid sheets and pseudopapillae of rhabdoid cells oriented radially toward vessels, forming astroblastic pseudorosettes (Fig 5). Findings also included necrosis and easily recognizable mitoses (up to 4 mitoses/10 high power fields).

Immunohistochemistry was positive for glial fibrillary acidic protein (GFAP) antibody, epithelial membrane agent, and D2-40 (podoplanin), with a Ki-67 index of 25%. Integrase interactor 1 (*INI-1/SMARCB1*) expression was retained. The final diagnosis was astroblastoma. *MNI* profiling was not possible due to limited availability.

Pathologic differential diagnosis is challenging, especially with ependymomas, because they also present with perivascular pseudorosettes. Astroblastic pseudorosettes, however, have distinct columnar, tapered, or cuboid cell borders oriented radially around a hyalinized vessel. On the other hand, ependymal pseudorosettes

have unclear cell borders within a fibrillary perivascular area.¹ Supratentorial ependymomas also tend to have infiltrative margins, not seen in our case, and *RELA*-fused tumors show *LICAM* positivity on immunohistochemistry.

High-grade astrocytomas present as infiltrating astrocytic neoplasm with fibrillar glial processes, necrosis, and microvascular proliferation. Immunohistochemistry is positive for isocitrate dehydrogenase 1 (*IDH1*).² These morphologic differences ruled out this diagnosis in our case.

Angiocentric glioma, gemistocytic astrocytomas, and glioblastomas can also present with focal areas of perivascular pseudorosettes and their infiltrative characteristics. Therefore, astroblastoma diagnosis should be reserved for well-circumscribed gliomas in which the gliovascular characteristic is the main finding.³

AT/RT has variable patterns of histopathologic and immunostaining, consisting of rhabdoid cells, in addition to a small, blue, round cell component, and variable foci of mesenchymal or epithelial differentiation. Immunohistochemistry is usually positive for vimentin and epithelial membrane agent, and characteristically,

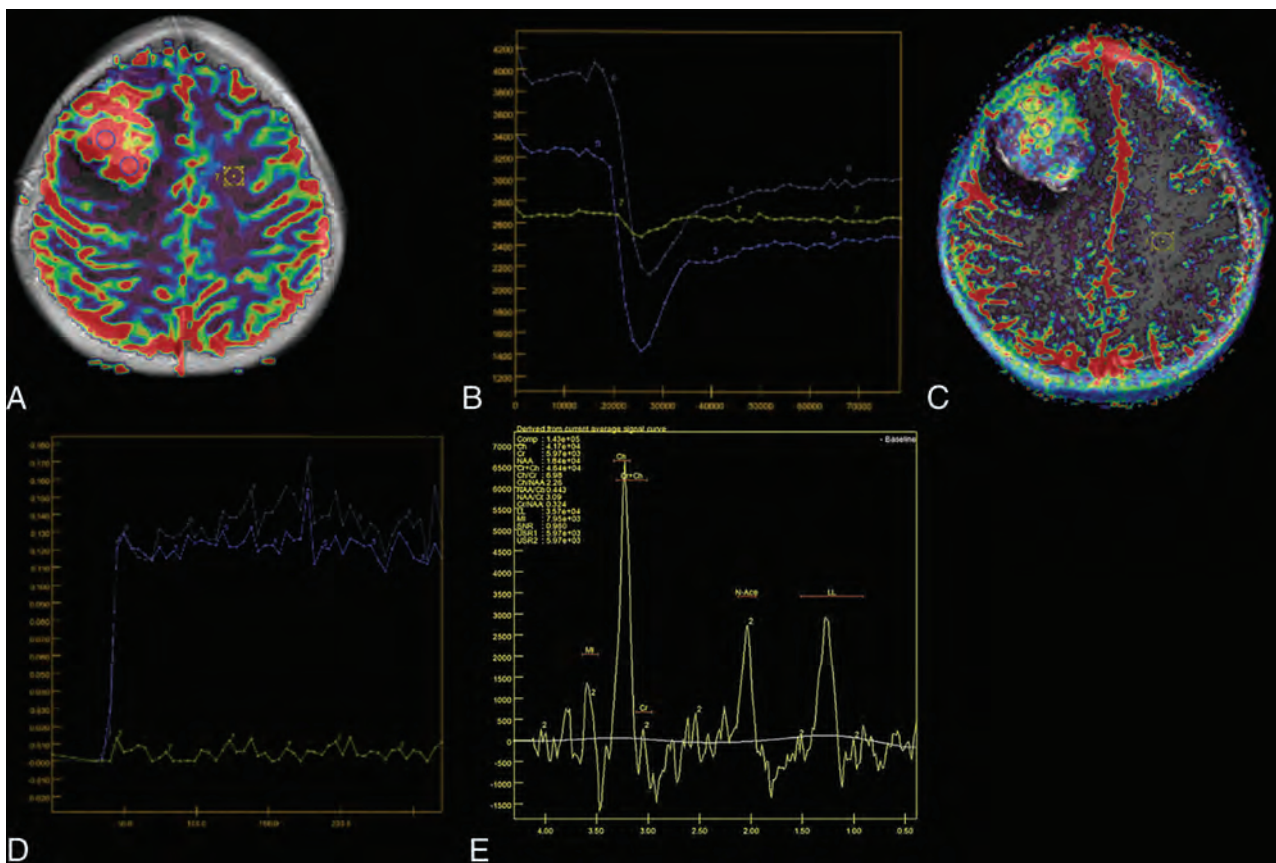


FIG 2. Advanced MR imaging features. *A* and *B*, Axial relative CBV map and curves, respectively, show intensely increased perfusion ($1.8\times$) within the solid part of the tumor, raising suspicion for a high-grade lesion. *C* and *D*, T1 perfusion K^{trans} map and curves, respectively, demonstrate intensely increased permeability and K^{trans} values in the enhancing portion of the lesion (0.170), suggesting increased capillary permeability. *E*, Proton spectroscopy shows an increased Cho peak, with increased Cho/Cr and Cho/NAA ratios, inferring cellular proliferation, as well as an increased lipid-lactate peak, suggesting anaerobiosis. LL indicates lipid lactate; USRI/2, Muon spin rotation; N-ace, N-acetylaspartate; MI, myoinositol.

there is a loss of either *INI-1/SMARCB1* or *SMARCA4*, the defining feature of this entity.⁴

DISCUSSION

Astroblastoma is a rare circumscribed astrocytic glial neoplasm, representing $<3\%$ of all gliomas, affecting mainly the cerebral hemispheres with a peak incidence between 10 and 30 years of age. Some series describe a higher prevalence in female patients.^{3,5,6} Its biologic behavior ranges from indolent to aggressive lesions, and a World Health Organization grade has not yet been attributed.¹

Historically, astroblastomas were initially described by Bailey and Cushing in 1924,⁷ but their histopathologic and molecular features overlapping with diffuse astrocytomas, pleomorphic xanthoastrocytomas, and ependymomas have led to decades of confusion. It has been described as a stage of glioma dedifferentiation, a fiber-producing astrocytoma, or rare tancytes or ependymal astrocyte neoplasm. The term itself is confusing because they are not notoriously astrocytic nor blastic. Only recently, assisted by molecular advances, their reliable diagnostic criteria have been established.^{3,5,6} Recent genetic profiling of high-grade neuroepithelial tumors revealed that many of the lesions with recurrent *MNI* mutations had histologic features of astroblastoma.⁸

The *MNI* gene, located in chromosome 22, is involved in meningioma and myeloid leukemia pathogenesis, and its rearrangements can be detected through DNA methylation. In addition to astroblastoma, many central nervous system primary tumors may express *MNI* alterations, like circumscribed and diffuse gliomas. Recently, this molecular signature has been attributed to the latter for more accurate diagnosis, but further research is needed to establish the ways these rearrangements act in astroblastoma and how it differs from manifestations in similar neuroepithelial tumors.⁹⁻¹²

Therefore, astroblastoma still shows molecular heterogeneity, with no exclusivity of *MNI* mutations in all cases, with most being classifiable within the *MNI* or *BRAF* DNA methylation groups.⁹ Despite minor heterogeneity, *MNI* alterations have become the defining feature of this condition in the 2021 World Health Organization CNS tumor classification, which is now called *MNI*-altered astroblastoma.¹⁰

Imaging usually reveals a supratentorial peripherally located solid-cystic mass with little or no vasogenic edema and rarely adjacent parenchyma infiltration (Figure 4). A bubbly aspect is frequently seen due to multiple cysts. Calcifications are seen in most cases, more commonly in a punctate pattern within the solid part. The solid component is usually isointense on T1 and T2/

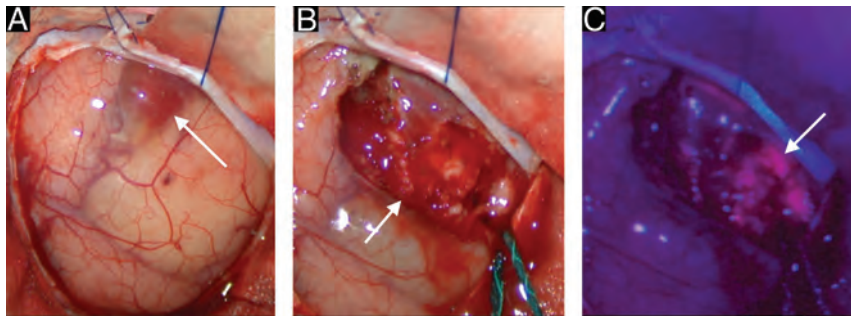


FIG 3. Intraoperative surgical microscope images. A, External view of the tumor demonstrates its peripheral cystic areas (arrow). B, Solid portion of the lesion after the cyst evacuation (arrow). C, The solid aspect of the tumor under blue light demonstrates its intense 5-ALA fluorescence (arrow).



FIG 4. The schematic representation of astroblastoma consists of a hemispheric heterogeneous lesion with a lobulated solid and eccentric component and peripheral larger cysts. Note the faint perilesional edema, disproportional to the size of the lesion.

FLAIR, with a heterogeneous gadolinium enhancement and intermediate ADC values ranging from 1190 to $1250 \times 10^{-6} \text{ mm}^2/\text{s}$. Cystic areas are hyperintense on fluid-sensitive sequences and show facilitated diffusion. No MR imaging features can help differentiate indolent and malignant astroblastomas. Atypical presentations include solid masses with central necrosis and an irregularly rimmed cyst.^{3,6,13,14}

Imaging differential diagnosis includes supratentorial ependymomas, astrocytomas, and AT/RT.

YAPI fusion-type ependymoma also presents as a heterogeneous mass with cystic areas. However, it is more prevalent among younger children, usually younger than 3 years of age. Due to its fibrillary components and infiltrative nature, perilesional edema and microinvasion are significantly more evident in ependymomas than in astroblastomas.^{6,15}

High-grade astrocytomas manifest less frequently in children but also have imaging features that overlap with astroblastoma because presentation may also demonstrate a heterogeneous supratentorial mass. Similar to ependymomas, mass effect and

perilesional infiltration are more striking in astrocytomas compared with astroblastomas.¹⁶

AT/RT may also present as large supratentorial heterogeneous masses, with a peak incidence in younger children around 3 years of age. Imaging demonstrates solid-cystic masses, with frequent hemorrhage and intensely restricted diffusion, in contrast to astroblastoma. Leptomeningeal dissemination is also frequent in AT/RT but not expected in astroblastoma.⁴

Macroscopically, astroblastomas present as well-circumscribed solid-cystic masses with a bubbly appearance secondary to cystic degeneration.

Microscopic features include elongated eosinophilic cells with GFAP-positive processes oriented radially from the cell body toward a usually hyalinized vessel, resembling ependymal perivascular pseudorosettes, but with a tapering or columnar aspect. Immunohistochemistry shows positivity for epithelial membrane agent and D2-40. GFAP, *OLIG2*, and *S-100* are often positive to variable extents (Fig 5).³

Histologic features that indicate an aggressive biologic behavior include increased mitotic activity, palisading necrosis, high cellularity, vascular proliferation, and a high Ki-67 index. Higher Ki-67 indexes are also related to prognosis and survival rates, with a cutoff of 4%.¹

A primary histopathologic differential diagnosis includes high-grade astrocytomas, supratentorial ependymomas, atypical teratoid/rhabdoid tumors, and gemistocytic astrocytoma and these are better discussed in the previous session (See Pathology: Astroblastoma).

Treatment relies on gross surgical resection whenever possible. Low-grade lesions with satisfactory excision are usually followed up. Patients with incomplete resection or high-grade features in histology usually undergo adjuvant radiation and systemic chemotherapy with temozolomide.^{12,17}

Our patient had an excellent postoperative evolution, and 6-month control imaging shows no signs of recurrence. However, the multidisciplinary team opted for isolated adjuvant surgical cavity radiation due to faint 5-ALA surgical cavity positivity, necrosis, and mitotic activity. Systemic chemotherapy was not initiated.

Due to its rarity and imprecise imaging and histopathologic features, misdiagnosis is frequent. The ensemble of nonspecific features is the key. Astroblastoma should be remembered when this set of features is present, especially in a young female patient with a large, well-circumscribed hemispheric solid-cystic lesion.

Case Summary

- Astroblastoma is a rare intra-axial and hemispheric neoplasm typically present in adolescents and young adults.
- Imaging findings are not specific and include a heterogeneous mass with peripheral cysts and a solid bubbly-appearing component, overlapping with other tumors that affect children and young patients.

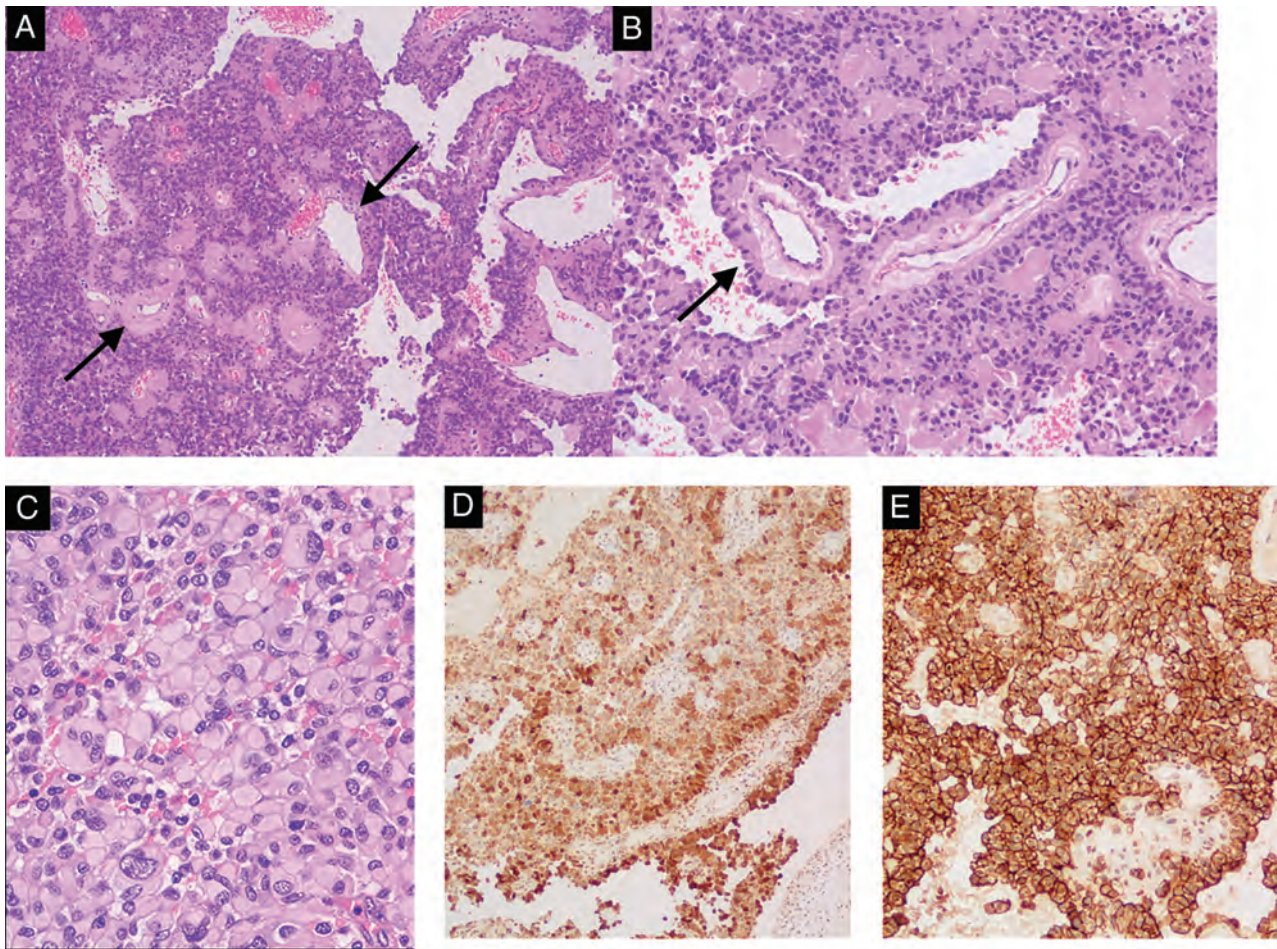


FIG 5. Pathologic findings of astroblastoma. *A*, The lesion was composed of solid sheets and pseudopapillae, with prominent hyalinized vessels (arrows), H&E, original magnification $\times 100$. *B*, Tumor cells have well-defined cytoplasmic borders, a columnar aspect radially arranged around the hyalinized blood vessels, forming astroblastic pseudorosettes (arrow), H&E, original magnification $\times 100$. *C*, Tumor shows rhabdoid features consisting of large cells with abundant eosinophilic cytoplasm and eccentric nuclei, H&E, original magnification $\times 100$. Tumor cells are diffusely positive for GFAP (*D*, immunohistochemistry, original magnification $\times 100$) and D2-40 (*E*, immunohistochemistry, original magnification $\times 200$).

- Pathologic differentiation from ependymoma can be challenging because both show perivascular rosettes. Subtle morphologic features can help differentiate astroblastic from ependymal pseudorosettes.
- Recently, *MNI* gene alterations have come to define this condition, which is now entitled *MNI*-altered astroblastoma.
- The main imaging differential diagnoses include high-grade astrocytomas, AT/RT tumors, and supratentorial ependymoma.
- Prognosis varies according to the presence of high-grade histologic findings, which also dictate adjuvant therapy.

Disclosure forms provided by the authors are available with the full text and PDF of this article at www.ajnr.org.

REFERENCES

1. Lehman NL, Hattab EM, Mobley BC, et al. **Morphological and molecular features of astroblastoma, including BRAFV600E mutations, suggest an ontological relationship to other cortical-based gliomas of children and young adults.** *Neuro Oncol* 2017;19:31–42 CrossRef Medline
2. Ichimura K, Narita Y, Hawkins CE. **Diffusely infiltrating astrocytomas: pathology, molecular mechanisms and markers.** *Acta Neuropathol* 2015;129:789–808 CrossRef Medline
3. Hammas N, Senhaji N, Alaoui Lamrani MY, et al. **Astroblastoma: a rare and challenging tumor—a case report and review of the literature.** *J Med Case Rep* 2018;12:102 CrossRef Medline
4. Zin F, Cotter JA, Haberler C, et al. **Histopathological patterns in atypical teratoid/rhabdoid tumors are related to molecular sub-group.** *Brain Pathol* 2021;31:12967 CrossRef Medline
5. Brat DJ, Hirose Y, Cohen KJ, et al. **Astroblastoma: clinicopathologic features and chromosomal abnormalities defined by comparative genomic hybridization.** *Brain Pathol* 2000;10:342–52 CrossRef Medline
6. Port JD, Brat DJ, Burger PC, et al. **Astroblastoma: radiologic-pathologic correlation and distinction from ependymoma.** *AJNR Am J Neuroradiol* 2002;23:243–47 Medline
7. Bailey P, Cushing H. *Classification of the Tumors of the Glioma Group.* Philadelphia, Pa: Lippincott;1926:83–84;133–136
8. Wood MD, Tihan T, Perry A, et al. **Multimodal molecular analysis of astroblastoma enables reclassification of most cases into more specific molecular entities.** *Brain Pathol* 2018;28:192–202 CrossRef Medline
9. Lehman NL, Usabalieva A, Lin T, et al. **Genomic analysis demonstrates that histologically-defined astroblastomas are molecularly heterogeneous and that tumors with MNI rearrangement exhibit the most favorable prognosis.** *Acta Neuropathol Commun* 2019;7:42 CrossRef Medline
10. Louis DN, Perry A, Wesseling P, et al. **The 2021 WHO Classification of Tumors of the Central Nervous System: a summary.** *Neuro Oncol* 2021;23:1231–51 CrossRef Medline

11. Saini M, Jha AN, Tangri R, et al. **MN1 overexpression with varying tumor grade is a promising predictor of survival of glioma patients.** *Hum Mol Genet* 2021;29:3532–45 CrossRef Medline
12. Petruzzellis G, Alessi I, Colafati GS, et al. **Role of DNA methylation profile in diagnosing astroblastoma: a case report and literature review.** *Front Genet* 2019;10:391 CrossRef Medline
13. Bell JW, Osborn AG, Salzman KL, et al. **Neuroradiologic characteristics of astroblastoma.** *Neuroradiology* 2007;49:203–09 CrossRef Medline
14. Kurokawa R, Baba A, Kurokawa M, et al. **Neuroimaging of astroblastomas: a case series and systematic review.** *J Neuroimaging* 2022;32:201–12 CrossRef Medline
15. Santosh V, Mangalore S, Aryan S, et al. **Imaging characteristics of supratentorial ependymomas: study on a large single institutional cohort with histopathological correlation.** *Asian J Neurosurg* 2015;10:276–81 CrossRef Medline
16. Okamoto K, Ito J, Takahashi N, et al. **MRI high-grade astrocytic tumors: early appearance and evolution.** *Neuroradiology* 2002;44:395–402 CrossRef Medline
17. Mallick S, Benson R, Venkatesulu B, et al. **Patterns of care and survival outcomes in patients with astroblastoma: an individual patient data analysis of 152 cases.** *Childs Nerv Syst* 2017;33:1295–302 CrossRef Medline

MR Imaging Signs of Gadolinium Retention Are Not Associated with Long-Term Motor and Cognitive Outcomes in Multiple Sclerosis

A. Scaravilli, M. Tranfa, G. Pontillo, F. Falco, C. Crisculo, M. Moccia, S. Monti, R. Lanzillo, V. Brescia Morra, G. Palma, M. Petracca, E. Tedeschi, A. Elefante, A. Brunetti, and S. Cocozza



ABSTRACT

BACKGROUND AND PURPOSE: The long-term impact of gadolinium retention in the dentate nuclei of patients undergoing administration of serial gadolinium-based contrast agents is still widely unexplored. The aim of this study was to evaluate the impact of gadolinium retention on motor and cognitive disability in patients with MS during long-term follow-up.

MATERIALS AND METHODS: In this retrospective study, clinical data were obtained from patients with MS followed in a single center from 2013 to 2022 at different time points. These included the Expanded Disability Status Scale score to evaluate motor impairment and the Brief International Cognitive Assessment for MS battery to investigate cognitive performances and their respective changes with time. The association with qualitative and quantitative MR imaging signs of gadolinium retention (namely, the presence of dentate nuclei T1-weighted hyperintensity and changes in longitudinal relaxation R1 maps, respectively) was probed using different General Linear Models and regression analyses.

RESULTS: No significant differences in motor or cognitive symptoms emerged between patients showing dentate nuclei hyperintensity and those without visible changes on T1WIs ($P = .14$ and 0.92 , respectively). When we tested possible relationships between quantitative dentate nuclei R1 values and both motor and cognitive symptoms, separately, the regression models including demographic, clinical, and MR imaging features explained 40.5% and 16.5% of the variance, respectively, without any significant effect of dentate nuclei R1 values ($P = .21$ and 0.30 , respectively).

CONCLUSIONS: Our findings suggest that gadolinium retention in the brains of patients with MS is not associated with long-term motor or cognitive outcomes.

ABBREVIATIONS: BICAMS = Brief International Cognitive Assessment for MS; BVMT = Brief Visuospatial Memory Test; CVLT California Verbal Learning Test; DD = disease duration; DN = dentate nuclei; DMT = disease-modifying therapy; EDSS = Expanded Disability Status Scale; GBCA = gadolinium-based contrast agent; Gd = gadolinium; GLM = General Linear Model; GMV = gray matter volume; SDMT = Symbol Digit Modalities Test; qMRI = quantitative MRI

The role of gadolinium-based contrast agents (GBCAs) in neuroradiologic clinical practice is unquestionable. Nevertheless, during the past years, possible consequences of their repeat administration have been reported.¹ Since 2014, an increased interest in brain gadolinium (Gd) retention has emerged, especially for those patients undergoing multiple GBCA administrations during their

life.² This scenario applies to patients with malignancies³ as well as inflammatory conditions such as MS for whom contrast administration is recommended at the time of diagnosis⁴ and often repeated during clinical relapses and to monitor the effectiveness of disease-modifying therapy (DMT) and subclinical disease activity (particularly when previous studies for comparison are not available) or when opportunistic CNS infections are suspected.⁵

From a radiologic standpoint, brain Gd retention results in the development of a T1WI hyperintensity detectable on conventional imaging at the level of deep gray matter structures, with particular reference to the globus pallidus and, mostly, the dentate nuclei (DN). Several ex vivo and preclinical models have confirmed this finding, linking the development of such modifications to the number of previous GBCA administrations⁶ and, in particular, to linear compounds,⁷ to the point that the use of some Gd chelates has been restricted since 2017.⁸

However, while a large body of evidence supports the relationship between GBCA administration and development of

Received September 6, 2022; accepted after revision February 4, 2023.

From the Departments of Advanced Biomedical Sciences (A.S., M.T., G.P., E.T., A.E., A.B., S.C.), Electrical Engineering and Information Technology (G.P.), and Neurosciences and Reproductive and Odontostomatological Sciences (F.F., C.C., M.M., R.L., V.B.M., M.P.), University of Naples "Federico II," Naples, Italy; Institute of Biostructure and Bioimaging (S.M.), National Research Council, Naples, Italy; Institute of Nanotechnology (G.P.), National Research Council, Lecce, Italy; and Department of Human Neurosciences (M.P.), Sapienza University of Rome, Rome, Italy.

A. Scaravilli and M. Tranfa contributed equally to this work.

Please address correspondence to Giuseppe Pontillo, MD, Department of Advanced Biomedical Sciences, University "Federico II," Via Pansini, 5, 80131, Naples, Italy; e-mail: giuseppe.pontillo@unina.it; @NeuroN_Lab

 Indicates article with online supplemental data.
<http://dx.doi.org/10.3174/ajnr.A7807>

T1WI hyperintensity,^{2,3,6,9} the clinical impact of Gd deposition is still underexplored, and available investigations provide conflicting results. Indeed, no significant association has emerged between cumulative Gd exposure and the development of parkinsonism in a population study.¹⁰ In MS, while there seems to be no association between DN hyperintensity and worsening of motor symptoms,¹¹ Gd retention has been associated with cerebellar dysarthria and lower verbal fluency scores.^{12,13} So far, to the best of our knowledge, only 1 study has explored long-term clinical outcomes of Gd deposition in a small cohort of patients with MS evaluated at different time points during follow-up.¹²

Given this background, the aim of this study was to expand the current knowledge about the possible clinical impact of Gd accumulation in the brain, using MS as a model of a chronic condition with multiple exposures to GBCA. To accomplish this aim and investigate the presence of a delayed GBCA toxicity in patients with MS, we evaluated the long-term effects of GBCA retention on motor worsening, cognitive performance, and cognitive worsening during a 7-year follow-up period.

MATERIALS AND METHODS

Compliance with Ethical Standards

This study was approved by the local ethics committee (Carlo Romano Ethical Committee of the University of Naples “Federico II”, Approval no. 209/13) in accordance with the ethical standards of the institutional research committee and with the 1964 Helsinki Declaration and its later amendments. Written informed consent was obtained from each patient before enrollment.

Participants

This retrospective analysis was conducted on the same group of 74 patients with relapsing-remitting MS described in a previous work.¹⁴ Inclusion and exclusion criteria, as well as information about the number and type of previous GBCA administrations, were also reported in previously published works.^{11,14} All MR images used in the current analysis were acquired between 2013 and 2015. Given that these MR images were obtained before 2017, when the use of linear GBCA was limited by international agencies such as the European Medicines Agency, in some of these patients, a linear GBCA was administered (with a proportion of around 26% of linear GBCA, 45/175). Overall, a mean number of 6 GBCAs (range, 1–15) had been administered before the index MR imaging analyzed in the current work, all with the recommended standard doses.

Of 74 patients, 32 (43.2%) had concomitant comorbidities (cardiovascular comorbidities, $n = 11$; autoimmune comorbidities, $n = 11$; psychiatric comorbidities, $n = 7$; digestive system comorbidities, $n = 6$; neurologic comorbidities, $n = 5$; metabolic comorbidities, $n = 3$; respiratory comorbidities, $n = 3$; genitourinary comorbidities, $n = 1$; musculoskeletal comorbidities, $n = 1$).

In line with expert consensus opinions and international guidelines on the use of MR imaging for disease monitoring,¹⁵ all patients underwent a yearly brain MR imaging with Gd from the time of diagnosis onward until the recent change in monitoring recommendations.¹⁶

With reference to motor evaluation, 11 patients were lost to follow-up, leading to a final cohort of 63 subjects. All patients

fulfilled the 2010 revision of the McDonald criteria at the time of MS diagnosis. The Expanded Disability Status Scale (EDSS) scores were obtained by experienced neurologists (V.B.M. and R.L, both with >25 years of experience) within 1 week from the baseline MR imaging and after a mean follow-up of 7.6 (SD, 0.6) years. Changes in the EDSS score (Δ EDSS) were calculated, in line with a previous study,¹¹ as the subtraction of EDSS score on follow-up from the baseline EDSS score, defining motor worsening if a subject showed a Δ EDSS of ≥ 1 (for a baseline EDSS ≤ 5.5) or ≥ 0.5 (for a baseline EDSS > 5.5).

Although cognitive evaluations were not routinely performed at the time of the baseline MR imaging and from 2020 to 2022 due to practice modifications related to the pandemic, the Brief International Cognitive Assessment for MS (BICAMS) battery¹⁷ for most enrolled subjects (65/74, 87.8%) was collected by an experienced neuropsychologist (F.F., with >10 years of experience) after a mean follow-up of 4.6 (SD, 1.0) years and in a subset of 32 patients also after 7.5 (SD, 0.7) years from baseline MR imaging.

Briefly, the BICAMS includes the Symbol Digit Modalities Test (SDMT) to assess attention and processing speed, the California Verbal Learning Test (CVLT) to assess episodic verbal learning and memory, and the Brief Visuospatial Memory Test (BVMT) to assess visuospatial memory. Corresponding z scores were estimated according to previous works.^{18,19} Patients were defined as cognitively impaired if they showed at least 1 of the z score values of equal or less than -1.5 .²⁰ For the ancillary analysis, cognitive worsening with time was defined by a Δ BICAMS of equal or less than -0.5 , calculated as a subtraction of the mean zBICAMS at 7.5 years from the mean zBICAMS at 4.6 years.

Finally, the number of new relapses and disease duration (DD) were collected as additional clinical variables.

MR Imaging Data Acquisition and Analysis

A complete description of MR imaging data acquisition and analysis is available in a previous work.¹⁴ Briefly, MR imaging signs of Gd retention were qualitatively evaluated on unenhanced T1WIs, recording the presence of a visible bilateral hyperintensity affecting both DN (Fig 1). A quantitative MR imaging (qMRI) analysis of GBCA accumulation was achieved through the calculation of qMRI maps according to previous works^{21,22} and automatically extracting mean R1 values after the placement of 2 irregular bilateral ROIs on the axial section with the best representation of the DN (Fig 2).¹⁴

Finally, hyperintense lesions were detected and segmented on FLAIR images with a semiautomatic approach (Jim7; Xinapse Systems) to obtain lesion load volumes and for the inpainting procedure.²³ By means of FSL SIENAX (<http://fsl.fmrib.ox.ac.uk/fsl/fslwiki/SIENAX>), the T1WI volumes were processed to extract gray matter volume (GMV), normalized for the corresponding V-scaling factor, as a measure of cortical atrophy.

Statistical Analysis

To evaluate possible differences in terms of age and DD between stable and motor or cognitively worsened patients, we performed

an independent 2-samples *t* test, while differences in terms of sex were tested through a χ^2 test.

Possible differences in terms of Δ EDSS between patients with and without DN hyperintensity, along with possible differences of DN R1 values between stable and motor-worsened patients, were probed via the General Linear Model, accounting for potential confounding factors (age, sex, MS phenotype, DMT, GMV, lesion load, DD, and new relapses). Furthermore, the possible relationship between Δ EDSS and DN R1 values was tested via hierarchical multiple linear regression analysis, including clinical and demographic variables (sex, age, MS phenotype, DMT, DD, and new relapses) in the first block and MR imaging variables in the second one. For the cognitive evaluation, possible differences in terms of *z* scores of each BICAMS battery test between patients with and without DN hyperintensity, along with possible differences of DN R1 values between stable and cognitively worsened subjects, were tested using a GLM similar to the one previously described for the motor analyses. A similar hierarchical multiple linear regression analysis was also performed to test the possible

relationship between BICAMS test *z* scores and clinical, demographic, and MR imaging variables.

Finally, the same analyses were also performed to compare Δ BICAMS between patients with and without DN hyperintensity and probe the possible relationship between DN R1 and the development of cognitive worsening or between Δ BICAMS and DN R1 values.

Methods and subsequent results of an additional subanalysis evaluating possible differences in terms of DN R1 values among subjects undergoing DMT changes with time are reported in the Online Supplemental Data.

All statistical analyses were performed by S.C. using the Statistical Package for the Social Sciences (Version 25.0; IBM), with a *P* = .05 set to indicate a statistically significant difference in the between-group comparison and regression analyses.

RESULTS

A complete list of demographic and clinical information of the studied population for motor and cognitive data is available in Tables 1 and 2, respectively.

At baseline, 73/74 patients (98.7%) were in treatment with a DMT: fingolimod, *n* = 17; natalizumab, *n* = 28; interferon β -1a, *n* = 20; interferon β -1b, *n* = 7; and glatiramer acetate, *n* = 1). During a follow-up period of >7 years, 27.0% (17/63) of patients did not undergo therapeutic switches, whereas the remaining patients switched therapy once (55.5%, 35/63) or more (17.5%, 11/63) than once (natalizumab, *n* = 20; fingolimod, *n* = 14; cladribine,

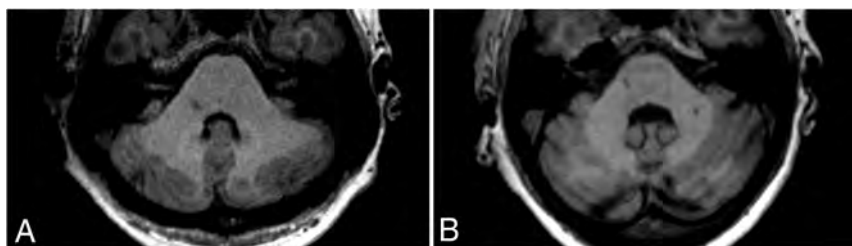


FIG 1. Selected axial slices of unenhanced T1WI at the level of the DN. An example of increased (A) and absent (B) DN T1WI hyperintensity in 37- and 54-year-old female patients, both receiving a similar number of Gd administrations across time (*n* = 15 and *n* = 12, respectively) but a different molecule (gadopentetate dimeglumine and gadobutrol, respectively).

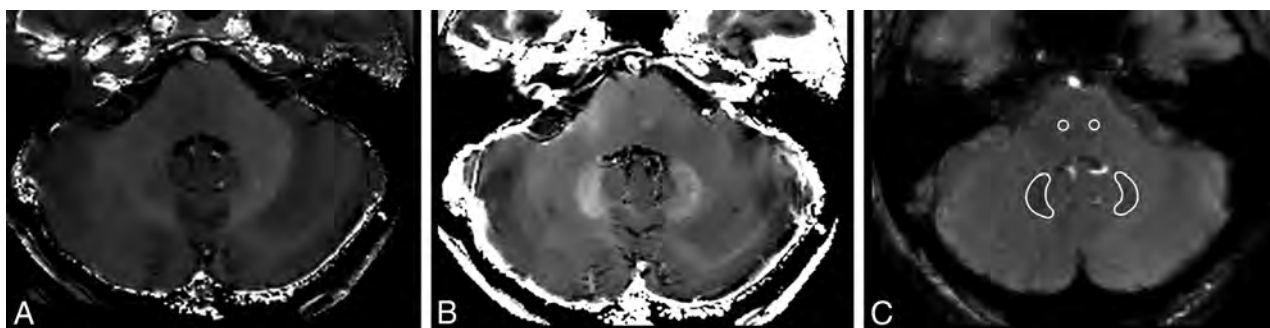


FIG 2. Representative axial R1 (A) and R2* (B) maps at the level of the DN in a 28-year-old healthy male control. C, DN and brainstem ROI positioning on the flow-compensated gradient-echo sequence ($TE_2 = 22.14$ ms, $\theta = 20^\circ$) used to obtain qMRI maps.

Table 1: Demographic and motor clinical variables of the subjects included in this study^a

Motor Examination	Baseline (<i>n</i> = 74)	Follow-Up (<i>n</i> = 63)
Age (mean) (range) (yr)	36.1 (SD, 10.1) (21–62)	44.4 (SD, 10.4) (28–69)
Sex (M/F)	27:47	26:37
DD (mean) (yr)	9.8 (SD, 6.8)	18.3 (SD, 7.0)
EDSS (median) (range)	3.0 (1.5–6.5)	2.5 (1.0–7.5)
Follow-up time from baseline (mean) (yr)	NA	7.6 (SD, 0.6)
Δ EDSS (mean)	NA	–0.3 (SD, 0.9)
Clinical progression (progressed/stable)	NA	6/57

Note:—NA indicates not applicable.

^a Motor worsening was defined if a subject showed a Δ EDSS ≥ 1 (for baseline EDSS ≤ 5.5) or ≥ 0.5 (for baseline EDSS > 5.5).

$n = 8$; ocrelizumab, $n = 5$; alemtuzumab, $n = 4$; interferon β -1a, $n = 3$; dimethyl fumarate, $n = 3$; interferon β -1b, $n = 2$; siponimod, $n = 1$; and peginterferon β -1a, $n = 1$).

With reference to motor performances, 6 of 63 patients (9.5%) showed a motor worsening at follow-up, with 4 of these patients converting to a secondary-progressive course. Stable and worsened patients did not differ in terms of age ($P = .39$) or sex ($P = .91$), while a significant difference in DD ($P = .04$) emerged. When we compared subjects showing DN hyperintensity at baseline with patients without any detectable change on unenhanced T1WI, no significant difference emerged in terms of Δ EDSS ($P = .14$) (Fig 3A). Similarly, no significant difference was found in terms of DN R1 between stable subjects and patients showing motor worsening ($P = .15$) (Fig 3B).

When we tested for a possible relation between DN R1 values and Δ EDSS, the regression model with clinical and demographic variables explained only 24.0% of the variance of Δ EDSS, whereas adding to the model lesion load and GMV increased the explained variance by 16.5% (40.5%, $P = .005$). When we evaluated

independent predictors, the only significant effect was identified for GMV ($P = .04$), without any significant effect of DN R1 values in explaining the Δ EDSS variance ($P = .21$) (Fig 4A).

With reference to cognitive performances, 40 of 65 patients (61.5%) presented with cognitive impairment at a mean of 4.6 years of follow-up. These subjects did not differ from cognitively preserved patients in terms of age ($P = .87$), sex ($P = .44$), and DD ($P = .37$). Similarly, no significant differences were observed between patients with and without DN hyperintensity on MR imaging in terms of BICAMS z score ($P = .92$) or its individual components ($P = .96$ for the SDMT; $P = .41$ for the BVMT; $P = .53$ for the CVLT) (Fig 5A). Finally, the group of patients with cognitive impairment was not different in terms of mean DN R1 values ($P = .26$) compared with cognitively preserved subjects (Fig 5B).

When we investigated the relation between DN R1 values and BICAMS scores, the model explained 16.5% of the variance, without a significant effect of DN R1 in explaining BICAMS z scores ($P = .30$) or its components ($P = .40$ for the SDMT; $P = .24$ for the BVMT; $P = .61$ for the CVLT).

Finally, in the subset of patients with follow-up examinations available at 7.5 years, 5 of 32 patients (15.6%) showed cognitive worsening. These subjects were not different in terms of age ($P = .96$), sex ($P = .60$), DD ($P = .19$), or R1 values ($P = .18$) compared with stable patients. Similarly, there were no significant differences in terms of Δ BICAMS between patients with and without DN hyperintensity on MR imaging ($P = .27$) and no significant effect of DN R1 values in explaining the Δ BICAMS variance ($P = .28$) (Fig 4B).

Table 2: Demographic and cognitive clinical variables of the subjects included in this study^a

Cognitive Examination	First Follow-Up ($n = 65$)	Second Follow-Up ($n = 32$)
Age (mean) (range) (yr)	36.5 (SD, 10.1) (21–62)	45.9 (SD, 10.5) (29–61)
Sex (M/F)	26:39	13:19
DD (mean) (yr)	15.0 (SD, 7.1)	18.6 (SD, 7.7)
SDMT z score (mean)	-1.3 (SD, 1.2)	-1.1 (SD, 1.1)
BVMT z score (mean)	-0.9 (SD, 1.5)	-0.6 (SD, 1.4)
CVLT z score (mean)	-0.6 (SD, 1.4)	-0.4 (SD, 1.5)
BICAMS z score (mean)	-0.9 (SD, 1.1)	-0.7 (SD, 1.0)
FU time from baseline (mean) (yr)	4.6 (SD, 1.0)	7.5 (SD, 0.7)
Δ BICAMS (mean)	NA	-0.3 (SD, 0.8)
Cognitive impairment (impaired/preserved)	40/25	NA
Cognitive progression	NA	5/32 (15.6%)

Note:—FU indicates follow-up.

^aCognitive impairment at the first time point was defined if a subject showed at least one of the z score values of equal or less than -1.5. Cognitive worsening at second time point was defined in case of Δ BICAMS equal or less than -0.5.

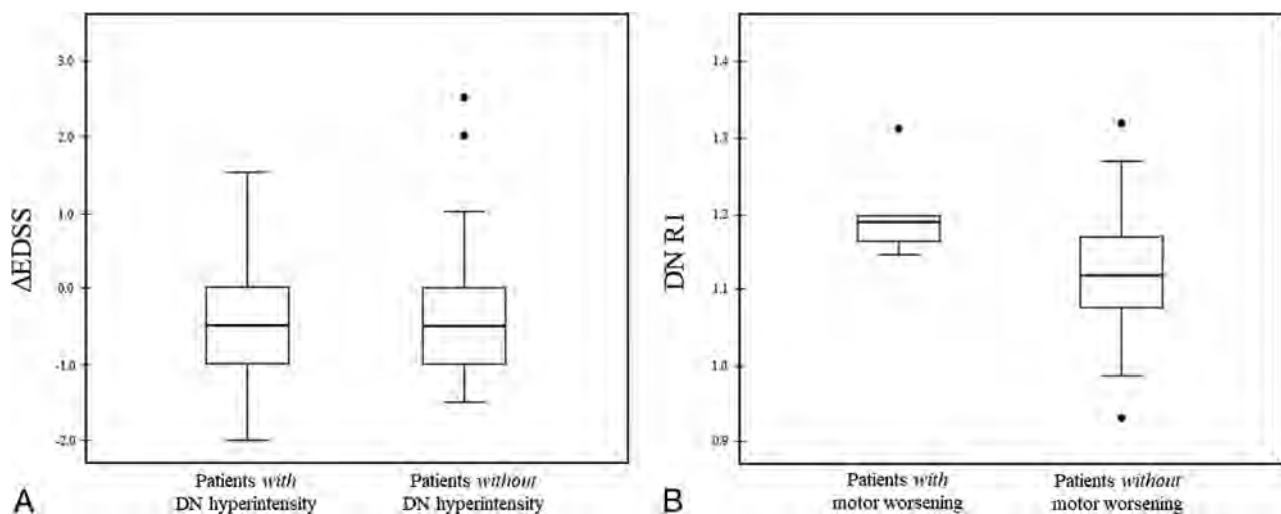


FIG 3. Boxplots showing Δ EDSS (A) and DN R1 values (B) of patients with and without a DN hyperintensity on unenhanced T1WI and motor worsening, respectively. Motor worsening was defined if a subject showed a Δ EDSS ≥ 1 (for baseline EDSS ≤ 5.5) or ≥ 0.5 (for baseline EDSS > 5.5). R1 values are expressed as s^{-1} .

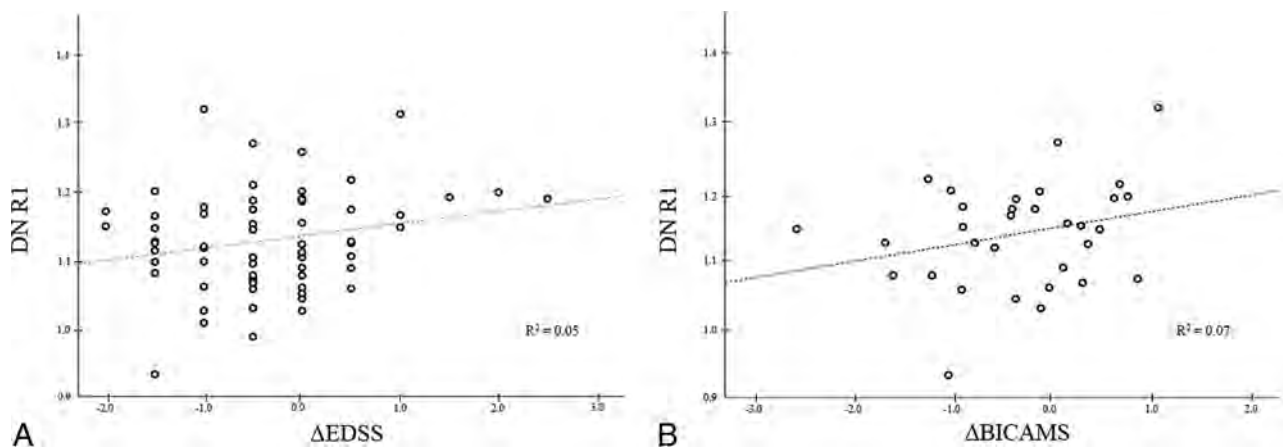


FIG 4. Scatterplots showing the absence of a significant relation between DN R1 values and Δ EDSS (A) and Δ BICAMS (B), respectively. R1 values are expressed as s^{-1} .

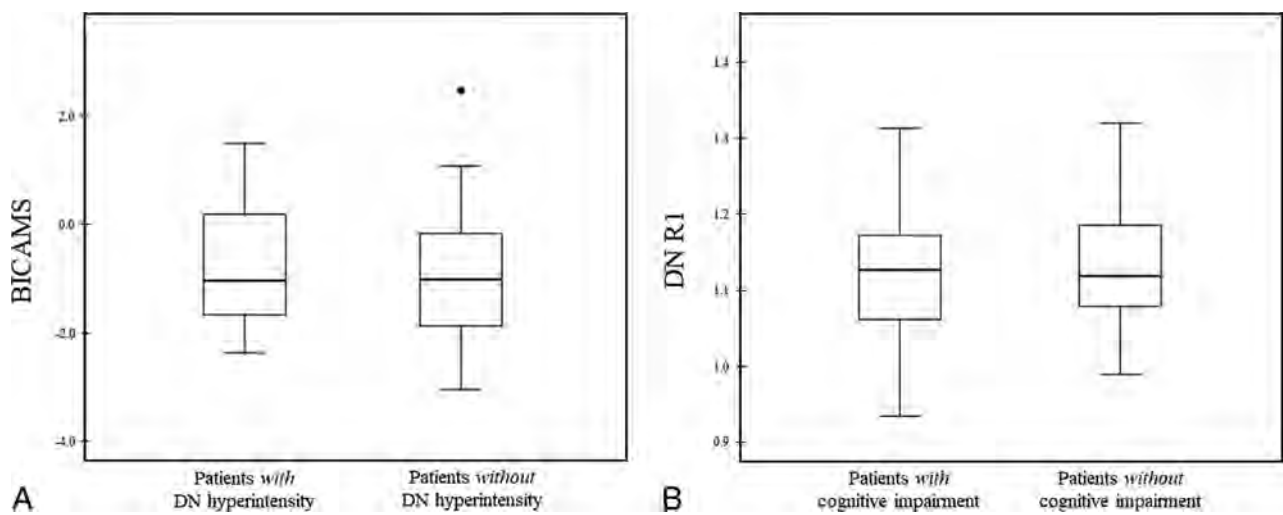


FIG 5. Boxplots showing BICAMS (A) and DN R1 values (B) of patients with and without DN hyperintensity on unenhanced T1WI and cognitive impairment, respectively. Cognitive impairment was defined if a subject showed at least 1 of the z score values equal or less than -1.5 . R1 values are expressed as s^{-1} .

DISCUSSION

A significant body of literature regarding Gd accumulation in tissues of patients with normal renal function has been published.^{2,3,6,9} Given that brain Gd retention occurs mainly in the DN,^{2,3,6,9} we investigated whether qualitative and quantitative MR imaging signs of Gd accumulation in this region would correlate with clinical changes with time.

With reference to motor performance, we found no significant difference in terms of DN R1 between stable and motor-worsened patients, in line with previous studies showing no significant association between GBCA exposure and the development of parkinsonism.¹⁰ Similarly, a case series in patients with glioblastoma multiforme²⁴ who received at least 50 GBCA injections during 10 years did not identify any clinical impairment possibly related to Gd deposition. Additionally, our results expand findings from previous cross-sectional and short-term longitudinal studies in MS, reporting no association between motor disability and DN Gd deposition.^{11,25,26} Overall, these results are in line with the hypothesis of an absence of direct damage affecting the DN due to Gd

deposition, given that this structure plays a key role in the physiology of the motor control loop²⁷ and its involvement should, therefore, result in the development of harmful and disruptive motor symptoms similar to those observed in animal models in which direct damage to this structure has been induced.²⁸

Exploring the cognitive counterpart of Gd retention, we did not find a significant association between cognitive impairment and mean DN R1 values, also in line with findings in most of the available literature.^{29,30}

However, 2 studies in patients with MS^{12,25} previously reported a possible association between Gd retention and lower verbal fluency performance. One study¹² observed an association between high signal DN intensity and low verbal fluency performances, and it might be tempting to quickly settle this matter by indicating, in the obvious advantages of qMRI, the most plausible explanation for these differences. Indeed, the same authors²⁵ failed to confirm this association when evaluating quantitative R1 values. Nevertheless, in this same latter study, a mild correlation between poor information-processing speed (as measured by the SDMT)

and DN R1 values²⁵ was identified. Here, after analyzing a group of patients with MS with similar demographic and clinical features and a similar quantitative approach, we were not able to confirm this finding. These discrepancies across studies might be explained by several factors, and we fully agree that MS pathology might be confounding the results.²⁵ Here, to address this issue and although we acknowledge that overcorrection might be a possible pitfall in statistical analysis,³¹ we have considered many known confounders that might account for changes in the SDMT results and failed to find any significant associations between SDMT and DN R1 values.

This result, corroborated by the absence of other significant associations within the cognitive domains assessed by the BICAMS, strengthens the hypothesis of an absence of a significant clinical impact of Gd retention in the brain, in line with recent preclinical observations showing no behavioral alterations in mice that developed T1WI hyperintensity on MR imaging after multiple injections of linear GBCA.³² Although the role of the cerebellum in language is well-recognized,³³ verbal fluency tasks seem to be more related to the lateral portion of the hemispheres rather than the DN itself,³³ as also confirmed by a coordinate-based activation likelihood estimation meta-analysis on brain activation during both phonemic and semantic verbal fluency tasks.³⁴ Furthermore, given the above-mentioned role of the DN as a main relay of several different motor and cognitive loops, it seems very unlikely that among all the functions that might have been affected by Gd retention, only verbal fluency, which is characterized by a complex interplay of a variety of cognitive functions and brain areas,³⁵ could have been involved. Similar considerations also apply to the correlation between increased DN T1WI hyperintensity and mild dysarthria observed in a different study,¹³ because dysarthria is usually related to hemispheric damage, with a preponderant right lateralization.³⁶

Finally, we acknowledge that different from the motor analysis in which GMV proved to be an independent predictor of disability, we did not identify any MR imaging predictor of cognitive impairment. A possible explanation of this result should be researched in a more profound and prominent involvement of other brain areas, such as the deep gray matter,³⁷⁻³⁹ in explaining the development of cognitive deficits in MS.

This study has some limitations. As previously discussed, due to its retrospective nature, we were not able to investigate some features, such as dysarthria or verbal fluency, which could have been of interest; a direct investigation of the correlation between qMRI changes affecting the DN and verbal fluency or dysarthria is, therefore, warranted. Another limitation is the relatively low number of patients investigated, which might have limited the sensitivity toward smaller effect sizes as well as preventing us from performing a subgroup analysis comparing linear and macrocyclic GBCAs. Nevertheless, this represents a trade-off for the use of qMRI evaluation, that in change provides more accurate evaluation of Gd retention compared with qualitative conventional MR imaging.

CONCLUSIONS

Although characterized by these limitations, our results suggest that Gd accumulation, indirectly assessed via qualitative and

qMRI parameters, is not associated with detectable clinical correlates in terms of global motor and cognitive worsening in MS.

Disclosure forms provided by the authors are available with the full text and PDF of this article at www.ajnr.org.

REFERENCES

1. Gulani V, Calamante F, Shellock FG, et al; International Society for Magnetic Resonance in Medicine. **Gadolinium deposition in the brain: summary of evidence and recommendations.** *Lancet Neurol* 2017;16:564–70 CrossRef Medline
2. Kanda T, Ishii K, Kawaguchi H, et al. **High signal intensity in the dentate nucleus and globus pallidus on unenhanced T1-weighted MR images: relationship with increasing cumulative dose of a gadolinium-based contrast material.** *Radiology* 2014;270:834–41 CrossRef Medline
3. Quattrocchi CC, Mallio CA, Errante Y, et al. **Gadodiamide and dentate nucleus T1 hyperintensity in patients with meningioma evaluated by multiple follow-up contrast-enhanced magnetic resonance examinations with no systemic interval therapy.** *Invest Radiol* 2015;50:470–72 CrossRef Medline
4. Wattjes MP, Ciccarelli O, Reich DS, et al. **2021 MAGNIMS-CMCS-NAIMS consensus recommendations on the use of MRI in patients with multiple sclerosis.** *Lancet Neurol* 2021;20:653–70 CrossRef Medline
5. Brisset JC, Kremer S, Hannoun S, et al. **New OFSEP recommendations for MRI assessment of multiple sclerosis patients: special consideration for gadolinium deposition and frequent acquisitions.** *J Neuroradiol* 2020;47:250–58 CrossRef Medline
6. Errante Y, Cirimele V, Mallio CA, et al. **Progressive increase of T1 signal intensity of the dentate nucleus on unenhanced magnetic resonance images is associated with cumulative doses of intravenously administered gadodiamide in patients with normal renal function, suggesting dechelation.** *Invest Radiol* 2014;49:685–90 CrossRef Medline
7. Robert P, Lehericy S, Grand S, et al. **T1-weighted hypersignal in the deep cerebellar nuclei after repeated administrations of gadolinium-based contrast agents in healthy rats: difference between linear and macrocyclic agents.** *Invest Radiol* 2015;50:473–80 CrossRef Medline
8. **FDA Drug Safety Communication: FDA evaluating the risk of brain deposits with repeated use of gadolinium-based contrast agents for magnetic resonance imaging (MRI).** May 18, 2017. <https://www.fda.gov/drugs/drug-safety-and-availability/fda-drug-safety-communication-fda-evaluating-risk-brain-deposits-repeated-use-gadolinium-based>. Accessed December 1, 2022
9. McDonald RJ, McDonald JS, Kallmes DF, et al. **Intracranial gadolinium deposition after contrast-enhanced MR imaging.** *Radiology* 2015;275:772–82 CrossRef Medline
10. Welk B, McArthur E, Morrow SA, et al. **Association between gadolinium contrast exposure and the risk of parkinsonism.** *JAMA* 2016;316:96–98 CrossRef Medline
11. Cocozza S, Pontillo G, Lanzillo R, et al. **MRI features suggestive of gadolinium retention do not correlate with Expanded Disability Status Scale worsening in multiple sclerosis.** *Neuroradiology* 2019;61:155–62 CrossRef Medline
12. Forslin Y, Shams S, Hashim F, et al. **Retention of gadolinium-based contrast agents in multiple sclerosis: retrospective analysis of an 18-year longitudinal study.** *AJNR Am J Neuroradiol* 2017;38:1311–16 CrossRef Medline
13. Kühn I, Maschke H, Großmann A, et al. **Dentate-nucleus gadolinium deposition on magnetic resonance imaging: ultrasonographic and clinical correlates in multiple sclerosis patients.** *Neurol Sci* 2022;43:2631–39 CrossRef Medline
14. Tedeschi E, Palma G, Canna A, et al. **In vivo dentate nucleus MRI relaxometry correlates with previous administration of gadolinium-based contrast agents.** *Eur Radiol* 2016;26:4577–84 CrossRef Medline
15. Wattjes M, Rovira À, Miller D, et al. **Evidence-based guidelines: MAGNIMS consensus guidelines on the use of MRI in multiple**

- sclerosis—establishing disease prognosis and monitoring patients. *Nat Rev Neurol* 2015;11:597–606 CrossRef Medline
16. Wattjes MP, Ciccarelli O, Reich DS, et al; Magnetic Resonance Imaging in Multiple Sclerosis study group; Consortium of Multiple Sclerosis Centres; North American Imaging in Multiple Sclerosis Cooperative MRI Guidelines Working Group. **MAGNIMS-CMSC-NAIMS consensus recommendations on the use of MRI in patients with multiple sclerosis.** *Lancet Neurol* 2021;20:653–70 CrossRef Medline
 17. Benedict RH, Amato MP, Boringa J, et al. **Brief International Cognitive Assessment for MS (BICAMS): international standards for validation.** *BMC Neurol* 2012;12:55 CrossRef Medline
 18. Goretti B, Niccolai C, Hakiki B, et al. **The Brief International Cognitive Assessment for Multiple Sclerosis (BICAMS): normative values with gender, age and education corrections in the Italian population.** *BMC Neurol* 2014;14:171 CrossRef Medline
 19. Coccozza S, Pontillo G, Russo C, et al. **Cerebellum and cognition in progressive MS patients: functional changes beyond atrophy?** *J Neurol* 2018;265:2260–66 CrossRef Medline
 20. Meijer KA, van Geest Q, Eijlers AJC, et al. **Is impaired information processing speed a matter of structural or functional damage in MS?** *Neuroimage Clin* 2018;20:844–50 CrossRef Medline
 21. Borrelli P, Palma G, Tedeschi E, et al. **Improving signal-to-noise ratio in susceptibility weighted imaging: a novel multicomponent non-local approach.** *PLoS One* 2015;10:e0126835 CrossRef Medline
 22. Palma G, Tedeschi E, Borrelli P, et al. **A novel multiparametric approach to 3D quantitative MRI of the brain.** *PLoS One* 2015;10:e0134963 CrossRef Medline
 23. Battaglini M, Jenkinson M, De Stefano N. **Evaluating and reducing the impact of white matter lesions on brain volume measurements.** *Hum Brain Mapp* 2012;33:2062–71 CrossRef Medline
 24. Vymazal J, Krámská L, Brožďová H, et al. **Does serial administration of gadolinium-based contrast agents affect patient neurological and neuropsychological status? Fourteen-year follow-up of patients receiving more than fifty contrast administrations.** *J Magn Reson Imaging* 2020;51:1912–13 CrossRef Medline
 25. Forslin Y, Martola J, Bergendal Å, et al. **Gadolinium retention in the brain: an MRI relaxometry study of linear and macrocyclic gadolinium-based contrast agents in multiple sclerosis.** *AJNR Am J Neuroradiol* 2019;40:1265–73 CrossRef Medline
 26. Zivadinov R, Bergsland N, Hagemeier J, et al. **Cumulative gadolinium administration leads to brain gadolinium deposition in early MS.** *Neurology* 2019;93:e611–23 CrossRef Medline
 27. Middleton FA, Strick PL. **Basal ganglia and cerebellar loops: motor and cognitive circuits.** *Brain Res Brain Res Rev* 2000;31:236–50 CrossRef Medline
 28. Vilis T, Hore J. **Effects of changes in mechanical state of limb on cerebellar intention tremor.** *J Neurophysiol* 1977;40:1214–24 CrossRef Medline
 29. Mallio CA, Quattrocchi CC, Rovira À, et al. **Gadolinium deposition safety: seeking the patient's perspective.** *AJNR Am J Neuroradiol* 2020;41:944–46 CrossRef Medline
 30. Mallio CA, Piervincenzi C, Gianolio E, et al. **Absence of dentate nucleus resting-state functional connectivity changes in nonneurological patients with gadolinium-related hyperintensity on T(1)-weighted images.** *J Magn Reson Imaging* 2019;50:445–55 CrossRef Medline
 31. Lee PH. **Should we adjust for a confounder if empirical and theoretical criteria yield contradictory results? A simulation study.** *Sci Rep* 2014;4:6085 CrossRef Medline
 32. Akai H, Miyagawa K, Takahashi K, et al. **Effects of gadolinium deposition in the brain on motor or behavioral function: a mouse model.** *Radiology* 2021;301:409–16 CrossRef Medline
 33. Murdoch BE. **The cerebellum and language: historical perspective and review.** *Cortex* 2010;46:858–68 CrossRef Medline
 34. Wagner S, Sebastian A, Lieb K, et al. **A coordinate-based ALE functional MRI meta-analysis of brain activation during verbal fluency tasks in healthy control subjects.** *BMC Neurosci* 2014;15:19 CrossRef Medline
 35. Patterson J. Verbal fluency. In: Kreutzer JS, DeLuca J, Caplan B, eds. *Encyclopedia of Clinical Neuropsychology.* Springer-Verlag; 2011:2603–06
 36. Ackermann H, Hertrich I. **The contribution of the cerebellum to speech processing.** *J Neurolinguistics* 2000;13:95–116 CrossRef
 37. Pontillo G, Penna S, Coccozza S, et al. **Stratification of multiple sclerosis patients using unsupervised machine learning: a single-visit MRI-driven approach.** *Eur Radiol* 2022;32:5382–91 CrossRef Medline
 38. Houtchens MK, Benedict RH, Killiany R, et al. **Thalamic atrophy and cognition in multiple sclerosis.** *Neurology* 2007;69:1213–23 CrossRef Medline
 39. Petracca M, Pontillo G, Moccia M, et al. **Neuroimaging correlates of cognitive dysfunction in adults with multiple sclerosis.** *Brain Sci* 2021;11:346 CrossRef Medline

Clinical Profiles and Patterns of Neurodegeneration in Amyotrophic Lateral Sclerosis: A Cluster-Based Approach Based on MR Imaging Metrics

G. Milella, A. Introna, D.M. Mezzapesa, E. D'Errico, A. Fraddosio, M. Ucci, S. Zoccollella, and I.L. Simone

ABSTRACT

BACKGROUND AND PURPOSE: The previous studies described phenotype-associated imaging findings in amyotrophic lateral sclerosis (ALS) with a prior categorization of patients based on clinical characteristics. We investigated the natural segregation of patients through a radiologic cluster-based approach without a priori patient categorization using 3 well-known prognostic MR imaging biomarkers in ALS, namely bilateral precentral and paracentral gyrus cortical thickness and medulla oblongata volume. We aimed to identify clinical/prognostic features that are cluster-associated.

MATERIALS AND METHODS: Bilateral precentral and paracentral gyri and medulla oblongata volume were calculated using FreeSurfer in 90 patients with amyotrophic lateral sclerosis and 25 healthy controls. A 2-step cluster analysis was performed using precentral and paracentral gyri (averaged pair-wise) and medulla oblongata volume.

RESULTS: We identified 3 radiologic clusters: 28 (31%) patients belonged to “cluster-1”; 51 (57%), to “cluster 2”; and 11 (12%), to “cluster 3.” Patients in cluster 1 showed statistically significant cortical thinning of the analyzed cortical areas and lower medulla oblongata volume compared with subjects in cluster 2 and cluster 3, respectively. Patients in cluster 3 exhibited significant cortical thinning of both paracentral and precentral gyri versus those in cluster 2, and this latter cluster showed lower medulla oblongata volume than cluster 3. Patients in cluster 1 were characterized by older age, higher female prevalence, greater disease severity, higher progression rate, and lower survival compared with patients in clusters 2 and 3.

CONCLUSIONS: Patients with amyotrophic lateral sclerosis spontaneously segregate according to age and sex-specific patterns of neurodegeneration. Some patients with amyotrophic lateral sclerosis showed an early higher impairment of cortical motor neurons with relative sparing of bulbar motor neurons (cluster 3), while others expressed an opposite pattern (cluster 2). Moreover, 31% of patients showed an early simultaneous impairment of cortical and bulbar motor neurons (cluster 1), and they were characterized by higher disease severity and lower survival.

ABBREVIATIONS: ALS = amyotrophic lateral sclerosis; ALSFRS-r = ALS Functional Rating Scale-Revised; CS = control subjects; IQR = interquartile range; MOv = medulla oblongata volume; ODI = onset-to-diagnosis interval; ParaCT = paracentral gyrus; PreCT = precentral gyrus

Amyotrophic lateral sclerosis (ALS) is a fatal neurodegenerative disease known for its extremely heterogeneous natural course.¹ Early identification of patients characterized by a faster disease progression rate is one of the primary goals in the field of motor neuron diseases to provide correct information about prognosis, care needs, and support services.

Several staging systems were previously proposed to stratify patients according to the phase of the disease and cognitive

profiles and to identify prognostic factors.²⁻⁷ The feasibility of these staging systems has been proved in both trials and the clinical setting, by successfully allocating patients into specific disease categories. Several standard procedures have been proposed to guarantee interrater reliability in assessing the correct staging.^{8,9} However, until now, clinical staging still requires the careful consideration of observed clinical parameters and relies invariably on the interpretation of reported symptoms and other potentially subjective factors. Therefore, several quantitative biomarkers,^{10,11} beyond clinical parameters, have been proposed to correctly distinguish subgroups of patients according to different prognoses.

Among different “dry biomarkers,”¹² MR imaging has progressively acquired greater relevance to assess *in vivo* the extent of CNS damage in patients with ALS, given its accessibility and non-invasiveness. A recent review stated that the most disease-sensitive

Received September 20, 2022; accepted after revision February 20, 2023.

From the Neurology Unit (G.M., A.I., D.M.M., E.D., A.F., M.U., I.L.S.), Department of Basic Medical Sciences, Neurosciences and Sense Organs, University of Bari “Aldo Moro,” Bari, Italy; and Azienda Sanitaria Locale Bari (S.Z.), San Paolo Hospital, Bari, Italy.

Please address correspondence to Isabella Laura Simone, MD, Neurology Unit, Department of Basic Medical Sciences, Neurosciences and Sense Organs, University of Bari “Aldo Moro”; Piazza Giulio Cesare II, 70124 Bari, Italy; e-mail: isabellalaura.simone@uniba.it

<http://dx.doi.org/10.3174/ajnr.A7823>

MR imaging patterns are located in motor regions.¹³ Specifically, disease severity (expressed as ALS Functional Rating Scale-Revised [ALSFRS-r] score) and progression rate correlated with the mean cortical thickness of the motor area,¹⁴⁻¹⁸ extramotor areas (eg, paracentral lobules),^{17,19} and medulla oblongata volume (MOv).¹⁹⁻²¹ These MR imaging metrics have also been proposed as predictive biomarkers of survival.^{20,22}

Nonetheless, most imaging studies validated MR imaging metrics by describing phenotype-, genotype-, or stage-associated radiologic profiles²³⁻²⁵ in a priori selected clinical categorizations (eg, spinal or bulbar onset, fast and slow progressors, prevalent upper or lower motor neuron impairment). An alternative interesting approach was recently performed by Bede et al,²⁶ which used cluster analysis of pooled imaging data and subsequent analysis of cluster-associated clinical characteristics. Using a large unsegregated MR imaging data set and 74 MR imaging metrics, the authors found that patients with ALS spontaneously segregated in 2 clusters mainly according to 3 specific areas, namely superior lateral temporal and superior and inferior frontal gyri. The 2 clusters exhibited different frontotemporal impairment on MR imaging and the prevalence of *C9orf72* mutation carriers. In line with this study, Tan et al²⁷ found that patients with ALS could be divided into 3 subgroups (pure motor neuron; orbitofrontal and temporal involvement; posterior cingulate cortex, parietal white matter temporal operculum and cerebellum) using a connectome-based clustering algorithm among 68 cortical regions, 15 subcortical structures, and all the white matter tracts between these latter regions.

Different from these latter studies, we restricted our cluster-based analysis to MR imaging metrics identified as core features of disease severity and survival in ALS by previous reports, namely cortical thickness of the precentral gyrus (PreCT)²² and paracentral gyrus (ParaCT)²² and MOv.²⁰ Thus, we aimed to identify the clinical and prognostic features of the different radiologic clusters.

MATERIALS AND METHODS

Ethics Approval

We confirm that we have read AJNR's position on issues involved in ethical publication and affirm that this report is consistent with those guidelines. Ethics approval was waived by the local ethics committee, considering that all the procedures being performed were part of the routine care (study No. 6778).

Population

A total of 90 incident patients with ALS referred to our ALS tertiary center between 2018 and 2020 were consecutively recruited at the time of diagnosis. A careful diagnostic work-up was performed to exclude ALS-mimicking diseases. All patients met the criteria for clinically definite, probable, or possible ALS according to the El Escorial-revised criteria.⁴ Exclusion criteria included prior cerebrovascular events, traumatic brain injury, neurosurgical procedures, as well as neoplastic, paraneoplastic, or neuroinflammatory comorbidities.

None of the patients fulfilled the criteria for ALS and frontotemporal dementia according to the Strong criteria.⁵

Demographic characteristics and clinical data have been registered and collected by experienced neurologists of the ALS team. We recorded the following demographic and clinical variables: age at symptom onset, sex, onset-to-diagnosis interval (ODI), age at diagnosis (corresponding to the first neurologic clinical evaluation), site of symptom onset, and clinical phenotype.¹

All patients were functionally evaluated using the ALSFRS-r.²⁸ The progression rate was calculated using the following formula: $(48 - \text{ALSFRS-r}) / \text{disease durations (months)}$.²⁹

Longitudinal clinical evaluations were performed at 4- to 6-month intervals, and data regarding death or tracheostomy were recorded. The censoring date was set at March 31, 2022. Tracheostomy or death (if it occurred) were considered as a composite outcome.

Control subjects (CS) consisted of 25 subjects, not affected by inflammatory, autoimmune, and vascular or neurodegenerative diseases, without a family history of ALS and without abnormal findings on brain MR imaging.

MR Imaging Acquisitions

All participants underwent MR imaging on a 1.5T MR imaging scanner (Philips) at Azienda Ospedaliero Universitaria Policlinico of Bari. Specifically, patients with ALS underwent MR imaging at the time of diagnosis, concurrent with their first neurologic evaluation. Routine T1-, T2-weighted, and FLAIR sequences were performed to exclude other causes of focal or diffuse brain damage, including lacunar and extensive cerebrovascular lesions. 3D structural MR imaging was acquired using a T1-weighted MPRAGE sequence (TR/TE/flip angle = 25.00 ms/4.60 ms/30.00°, FOV = 240 mm, matrix = 256 × 256, voxel size = 0.93 × 0.93 × 1.0 mm³).

Cortical Thickness Analysis and Volumetric Analysis

FreeSurfer software, Version 7.1 (<http://surfer.nmr.mgh.harvard.edu>) was used to assess cortical thickness. Processing steps included correction for magnetic field inhomogeneity, alignment to a specific atlas,³⁰ skull removal, and segmentation of voxels into GM, WM, and CSF. Cortical thickness was then calculated on the basis of the shortest distance of 2 surfaces: the interface between GM and WM and the pial surface. The anatomic labels of the Desikan-Killiany atlas³¹ were used to calculate average cortical thickness in the precentral and paracentral cortical regions in the left and right cerebral hemispheres separately.

MOv was obtained using the FreeSurfer tool "segmentBS.sh."³² Segmentation (<https://surfer.nmr.mgh.harvard.edu/fswiki/BrainstemSubstructures>) was conducted using a robust and accurate Bayesian algorithm, relying on a probabilistic atlas of the brainstem and neighboring anatomic structures implemented in FreeSurfer.³² Additionally, from each preprocessed T1-weighted data set, total intracranial volume was calculated using FreeSurfer. Raw volumetric values of the medulla oblongata were corrected for the total intracranial volume using the residual method.³³

Statistical Analysis. The bilateral PreCT and ParaCT were averaged pair-wise and, together with MOv, were included in the 2-step cluster analysis. The choice of using the left and right precentral and paracentral cortical thicknesses averaged pair-wise is

consistent with previous studies that showed that cortical atrophy in these latter regions occurred early and bilaterally, especially in patients with ALS with bulbar-onset³⁴ and, irrespective of the side of first limb weakness, in patients with ALS with spinal onset.³⁵ Furthermore, because interhemispheric asymmetry was found in healthy subjects,³⁶ the inclusion of MR imaging metrics belonging to both the right and left hemispheres could have biased the entire analysis by finding clusters that are subject-related and not disease-related. Therefore, we included the pair-wise average precentral and paracentral cortical thickness, to provide an overall measure of cortical atrophy, as performed elsewhere.^{22,26}

Both cortical thickness and volumetric measures were minimum-maximum normalized to a 0–1 scale, to account for different measurements scales. The 2-step cluster analysis was performed using the Euclidean distance measure. The number of clusters was not fixed a priori, and the Bayesian information criterion was used to determine the number of clusters. On the basis of cluster membership of individual patients, cluster sizes were determined and silhouette analyses were run using the STATS CLUS SIL extension of SPSS (IBM).²⁶

ANCOVA was performed to evaluate differences in MR imaging metrics between the following groups: first, between CS and each radiologic ALS cluster and then among patients with ALS belonging to different clusters. In the analysis, PreCT and ParaCT and MOv were included as dependent variables, and study groups as categorical independent variables. Age at the first neurologic evaluation (time of diagnosis) and sex were considered potential confounding factors,³⁷ and they were used as covariates.

Demographic and clinical variables of the entire ALS population and of each cluster patient were reported as median (along with interquartile range [IQR]) or frequencies (percentages) for continuous and categorical variables, respectively. Group differences in the demographic and clinical variables were evaluated using a Mann-Whitney *U* test for continuous variables and the χ^2 or Fisher exact test for categorical variables.

To evaluate the different prognoses of each cluster, we dichotomized all patients with ALS into long and short survivors using the 2-step cluster analysis.³⁸ Categorical variables (reaching or not reaching the end point) and continuous variables (time elapsed between symptoms onset and censoring date or end points) were included in the model. Logistic regression was used to test the different percentages of short and long survivors in each cluster. The results were reported as OR and 95% CI. Last, Kaplan-Meier survival curves were used to illustrate the distribution of survival, and log-rank tests were used to test for differences among different radiologic clusters.

RESULTS

Clinical and Demographic Characteristics of the ALS Population and CS

The median age at symptom onset was 57 years, and the median ODI was 10 months. The spinal onset of disease was more frequent than bulbar onset (74% and 26%, respectively). Sixty-eight patients (76%) were classified as classic ALS phenotypes.¹ Twenty-two (24%) patients were classified as having “definite ALS” according to the El Escorial-revised criteria.⁴ Sixty-five (72%) patients reached the composite outcome (tracheostomy or death)

at the censoring date. The estimated median survival time from symptom onset to combined outcome was 47 months (Table).

CS were sex- and age-matched to patients with ALS with a median age of 54 years (IQR = 45–57 years) and a male-to-female ratio of 14:11 (56% male and 44% female).

MR Imaging Metrics

Two-step cluster analysis identified 3 distinct clusters of anatomic disease burden distribution: among all patients with ALS, 28 (31%) belonged to cluster 1; 51 (57%), to cluster 2; and 11, (12%) to cluster 3. The silhouette coefficient of 0.6 indicates reasonable cohesion and separation according to Kaufman and Rousseeuw.³⁹

In comparison with CS, patients with ALS in cluster 1 exhibited significantly lower values of both PreCT and ParaCT and MOv ($P < .001$ for all). Patients with ALS in cluster 2 had lower values of MOv compared with CS ($P < .001$), whereas patients with ALS in cluster 3 showed significantly lower PreCT and ParaCT values ($P = .001$), but no differences in MOv (Fig 1).

Patients with ALS in cluster 1 showed significantly lower PreCT and ParaCT values compared with those in cluster 2 ($P < .001$ for both), but not patients in cluster 3. Furthermore, the patients with ALS in cluster 1 had lower MOv values than those in cluster 3 ($P < .001$), but not patients in cluster 2. On the other hand, patients with ALS in cluster 2 exhibited significantly lower values of MOv ($P < .001$) compared with those in cluster 3, and in turn, this latter cluster had lower values of both PreCT and ParaCT than cluster 2 ($P = .001$ for both) (Fig 1).

Clinical and Demographic Features of the 3 Clusters

The Table shows the cluster-associated ALS clinical and demographic features.

The 3 clusters differed in age and sex: specifically, patients with ALS in cluster 1 were older than those in cluster 2 and cluster 3 ($P = .045$ and $P = .001$, respectively), while no differences were found between these latter 2 groups (Table). Male prevalence was 57% and 82% in clusters 2 and 3, respectively, while female prevalence was 68% in cluster 1 ($P = .035$ and $P = .005$, respectively).

No statistically significant differences were found in the ODI among the 3 groups. A spinal onset of the disease was found in all patients with ALS in cluster 3 and in about 70% of patients with ALS in both clusters 1 and 2. Patients with ALS in cluster 1 also had a higher diagnostic certainty, expressed by a higher percentage of “definite ALS” according to the El Escorial-revised criteria, compared with those in cluster 2 (43% versus 16%, $P < .001$) and cluster 3 (43% versus 18%, $P = .017$).

Patients with ALS in cluster 1 had an overall higher disease severity, expressed by lower ALSFRS-r scores than patients in both cluster 2 and cluster 3 ($P = .001$ and $P < .001$, respectively), while no differences were found between these latter 2 groups. Furthermore, patients with ALS in cluster 1 showed a higher progression rate compared with those in cluster 2 and cluster 3 ($P = .002$ and $P = .02$, respectively).

Survival Analysis

Among our study cohort, 26 patients were included in the long survivors’ group with a median time of observation of 57 months (IQR = 45–80 months), and none of them reached the composite

Association between MR imaging clusters and clinical features in patients with ALS^a

	ALS Population (n = 90)	Cluster 1 (n = 28)	Cluster 2 (n = 51)	Cluster 3 (n = 11)	P Value
Age at onset (median) (IQR) (yr)	57 (50–65)	67 (62–70)	41 (44–54)	46 (45–54)	<i>P</i> = .045 ^b <i>P</i> = .001 ^c <i>P</i> = ns ^d
Sex (No. of patients) (male/female)	47:43	9:19	29:22	9:2	<i>P</i> = .035 ^b <i>P</i> = .005 ^c <i>P</i> = ns ^d
Site of onset (spinal/bulbar) (No. of patients)	67/23	20/8	36/15	11/0	<i>P</i> = ns ^b <i>P</i> = .047 ^c <i>P</i> = .039 ^d
ALS phenotypes: classic/bulbar/flail arm/flail leg/pyramidal/respiratory/ PLMN/PUMN (No. of patients)	68/7/0/0/0/0/ 15/0	25/2/0/0/0/0/ 0/1/0	34/5//0/0/0/0/ 0/12/0	9/0//0/0/0/0/ 0/2/0	<i>P</i> = ns ^b <i>P</i> = ns ^c <i>P</i> = ns ^d
El Escorial-revised, categories: definite/ probable/possible (No. of patients)	22/36/32	12/14/2	8/18/25	2/4/5	<i>P</i> < .001 ^b <i>P</i> = .017 ^c <i>P</i> = ns ^d
ODI (median) (IQR) (mo)	10.07 (6.08–19.27)	9.18 (6.08–14.32)	11.73 (6.23–19.53)	8.97 (4.07–19.27)	<i>P</i> = ns ^b <i>P</i> = ns ^c <i>P</i> = ns ^d
ALSFRS-r (median score) (IQR)	38 (34–42)	34 (31–37)	40 (35–43)	40 (38–43)	<i>P</i> = .001 ^b <i>P</i> < .001 ^c <i>P</i> = ns ^d
Progression rate (median) (IQR)	0.83 (0.45–1.38)	1.26 (0.68–2.84)	0.70 (0.29–1.20)	0.80 (0.45–1.12)	<i>P</i> = .002 ^b <i>P</i> = .022 ^c <i>P</i> = ns ^d
Long/short survivors (No. of patients)	26/64	3/25	17/34	6/5	<i>P</i> = .032 ^b <i>P</i> = .008 ^c <i>P</i> = ns ^d
Survival time from symptom onset to composite outcome (median) (estimated median) (95% CI) (mo)	46.63 (37.95–55.31)	34.5 (22.39 –46.6)	46.63 (35.4–57.87)	72.73 (42.98–102.47)	<i>P</i> = .043 ^b <i>P</i> = .004 ^c <i>P</i> = ns ^d

Note:—ns indicates not significant; PLMN, prevalent lower motor neuron; PUMN, prevalent upper motor neuron.

^a Group differences in the demographic and clinical variables were evaluated using a Mann-Whitney *U* test for continuous variables and χ^2 tests for discrete variables. Log-rank tests were used to test for differences in survival between different radiologic clusters.

^b Cluster 1 versus cluster 2.

^c Cluster 1 versus cluster 3.

^d Cluster 2 versus cluster 3.

outcome at the censoring date (Table). The short survivors' group was characterized by 64 patients with a median time of observation of 36 months (IQR = 24–52 months), and all of them reached the composite outcome. Patients in cluster 1 showed a 4- and 10-fold risk of belonging to the short survivors' group compared with those in clusters 2 and 3, respectively (*P* = .036 with hazard risk: 4.17 and a 95% CI, 1.11–15.87 and *P* = .007 with hazard risk: 10 and a 95% CI, 1.85–52.63, respectively).

Kaplan-Meier survival curves revealed that patients with ALS in cluster 1 showed a worse prognosis compared with patients in cluster 2 (log-rank: 4.10, *P* = .043) and cluster 3 (log-rank: 8.22, *P* = .004). No significant differences in overall survival from the onset of symptoms were detected between patients in these latter 2 groups (Table and Fig 2).

DISCUSSION

In the present study, we performed a data-driven analysis to identify the radiologic clustering of newly diagnosed patients with ALS, in relation to 3 well-known neuroanatomic loci involved in ALS disease, namely the PreCT²² and ParaCT²² and the medulla oblongata.²⁰ Our data suggested that already at the time of diagnosis, patients with ALS showed specific patterns of neurodegeneration, with a prevalent impairment of the motor

and extramotor cortex, cluster 3; MOv, cluster 2; or all 3 MR imaging measures, cluster 1. This latter group of patients was characterized by older age, higher female prevalence, greater disease severity expressed by lower ALSFRS-r scores, a higher progression rate, and lower median survival.

MR imaging data-driven approaches potentially have several advantages in clinical practice because they do not require a previous integration of clinical data. Unlike in interesting previous studies that first applied this approach,^{26,27} we focused our cluster-based analysis on CNS-selected areas that are already found to be associated with survival^{20,22} and disease severity.^{17,21,40} Restricting the cluster-based analysis to the motor cortical areas and medulla oblongata, we first found that a considerable proportion (57%) of patients with ALS (belonging to cluster 2) showed greater involvement of the medulla already at the time of diagnosis. Second, a small subgroup of the ALS cohort (cluster 3, 12%) had early involvement of the motor and extramotor cortices with relative preservation of the medulla oblongata. Finally, 31% of those with ALS (cluster 1) showed wider and more prominent involvement of both cortical regions and medulla oblongata volume. These results appear in line with previous neuropathologic and neuroradiologic studies. Indeed, the earlier brainstem involvement found in 88% of our patients (clusters 1 and 2)

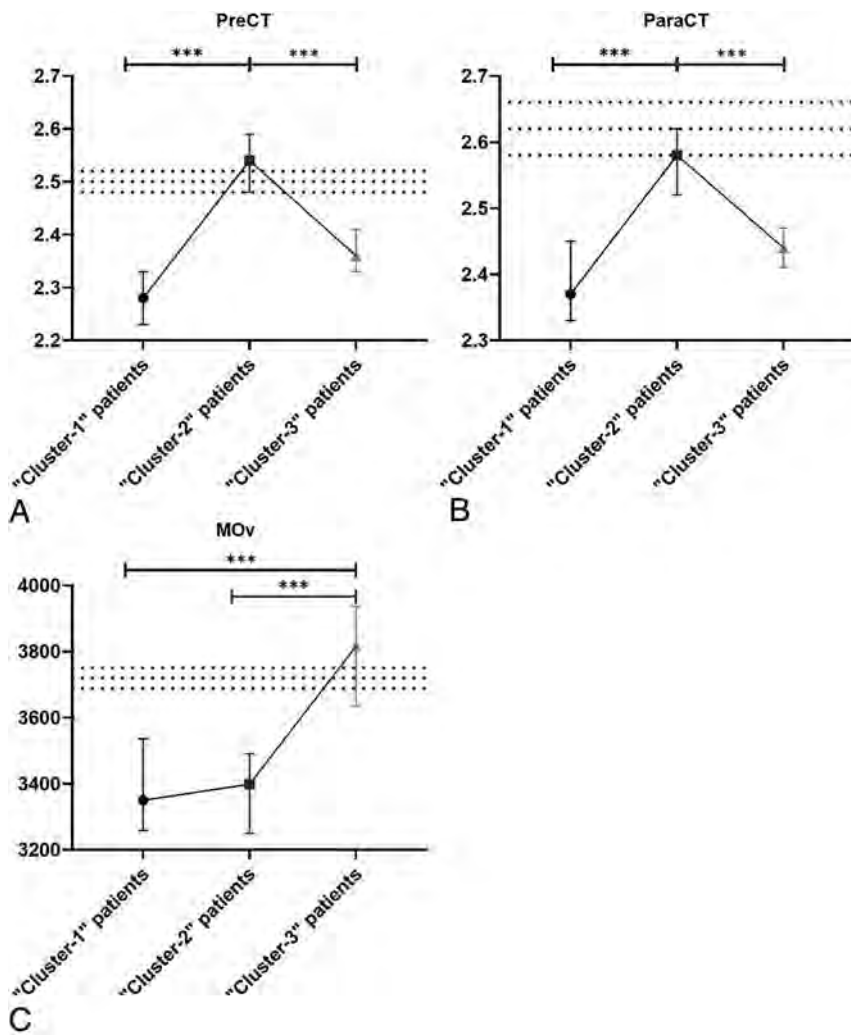


FIG 1. Estimated marginal means with SDs of the PreCT (A), ParaCT (B), and MOv (C) are plotted for each radiologic cluster adjusted for age and sex. Estimated marginal means and SDs of the CS are reported in the black dotted lines. The asterisk indicates $P < .001$.

agrees with the findings of Brettschneider et al,⁴¹ who reported that brainstem involvement represents “stage 1” in ALS pathology. Nonetheless, the early involvement of cortical motor neurons with subsequent spread along contiguous neuroanatomic regions in fewer patients (43% belonging to clusters 1 and 3) may support the role of these brain regions in the onset of ALS disease, as recently postulated by a radiologic study of Schito et al.⁴²

Finally, to explain the simultaneous and early involvement of both cortical regions and the medulla oblongata volume in patients with ALS in cluster 1, we referred to the most accredited model of ALS disease propagation reported in the literature.⁴³ Indeed, also in these latter patients, the onset of the disease could have been focal in the cortical and/or the brainstem motor neurons, as postulated by Ravits,⁴³ but a rapid spread of the disease along the neuroaxis would not allow us to detect the first neuroanatomic region involved, even at the onset of the disease in these patients. Alternatively, the onset of disease could have been due to “multifocal hits” with simultaneous involvement of cortical and brainstem motor neurons as recently postulated and demonstrated through an elegant neurophysiologic study by Sekiguchi et al.⁴⁴

In addition, we observed that patients with ALS with wider impairment of both cortical and medulla oblongata regions (cluster 1) were characterized by an older age at onset and higher female prevalence. The effect of both age at onset and sex on MR imaging metrics was previously and extensively reported.^{37,45-47} On the basis of previous literature data, older age at symptom onset might provide a vulnerable substrate for faster and more severe disease propagation,⁴⁵ while ALS sex-related brain functional and structural changes have been reported with controversial results.^{37,48}

According to a very recent study, there is increasing evidence that ALS disease follows different patterns of neurodegeneration that are age- and sex-specific. Tan et al²⁷ found a cluster of patients with ALS characterized by predominant involvement of the PreCT, younger age, and higher male prevalence. In addition, the authors described another cluster characterized by female prevalence and older age with wide posterior cingulate, parietal, cerebellar motor, temporal, and corpus medullare neurodegeneration.²⁷ Overall, all these findings agreed with a previous population-based study that reported the interaction between age and female sex, with women more affected than men at older ages.⁴⁹

The most intriguing findings of our study were the clinical consequences of the radiologic clustering of patients with ALS. Indeed, patients with ALS in cluster 1 with a wider impairment of both cortical and medulla oblongata regions were characterized by overall higher disease severity (expressed as lower scores of the total ALSFRS-r score), higher progression rate, and worse outcome, compared with patients in clusters 2 and 3. As stated above, several previous studies have underlined how PreCT, ParaCT and MOv could be used singularly as indicators of ALS disease aggressiveness.^{14,17,20,21,40} Nevertheless, these latter approaches relied invariably on the interpretation of clinical data that could somehow be misleading. An example of this limitation was recently aroused by Ferrea et al,²⁵ who demonstrated through a discriminant analysis that patients with ALS with prevalent upper and lower motor neuron impairment could be differentiated by specific MR imaging metrics of the motor and extramotor regions. However, the same authors reported that the clinical distinction between ALS phenotypes (prevalent upper and prevalent lower motor neurons and classic ALS) is somewhat heterogeneous; therefore, they included this concept as a limit of their study.²⁵ Instead, using a cluster-based approach without a priori clinical categorization of patients with ALS, we overcame the

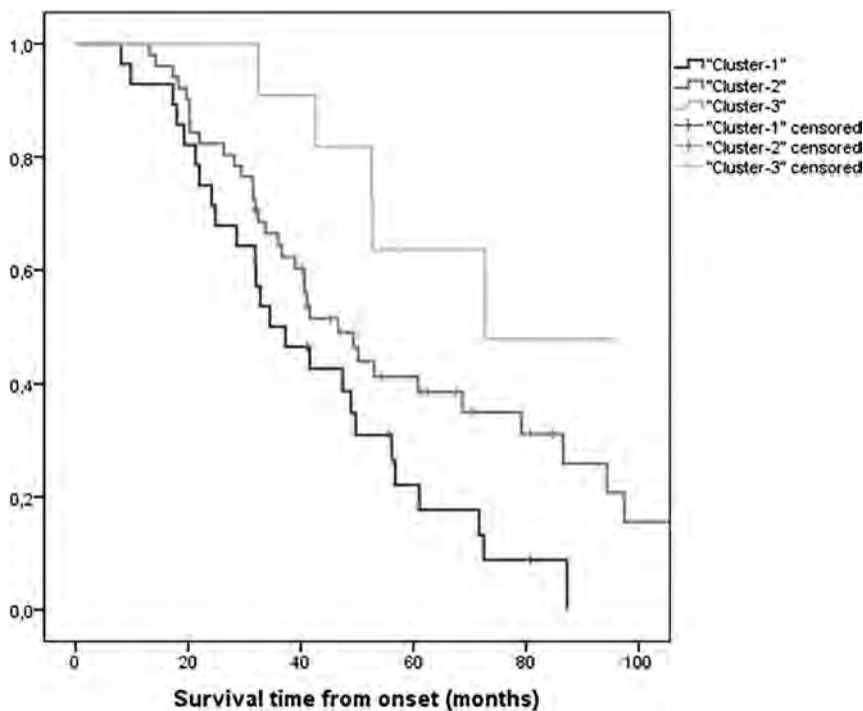


FIG 2. Kaplan Mayer survival curves in patients with ALS stratified according to radiologic clusters.

intrinsic limitation of investigating the correlation between clinical characteristics and each neuroanatomic structure, and we demonstrated that both the impairment of cortical and medullar regions corresponded simultaneously with the severity, rate of progression, and survival in ALS disease. Furthermore, a data-driven analysis could also overcome the potentially subjective interpretation of reported symptoms, which could be biased by “recall error,” especially in patients with a long-lasting disease.

The main limitation of our study is the lack of a longitudinal MR imaging analysis, which, instead, would have better defined the trajectories of the disease burden and the rate of decline of MR imaging metrics according to different clusters. Another limitation is the lack of neuropsychological assessment, which would guarantee a better characterization of cognitive profiles among radiologic clusters. Last, in our study, we included only patients with a definite, probable, or possible diagnosis of ALS. The inclusion of patients with ALS with pure lower motor neuron impairment, as well as progressive muscular atrophy or progressive lateral sclerosis, may be of potential interest to evaluate whether these subtypes segregate from ALS on the basis of their radiologic profiles.^{50,51}

CONCLUSIONS

We demonstrated that radiologic clustering of newly diagnosed patients with ALS could have clinical and prognostic implications and could unravel some aspects of the extreme phenotypic heterogeneity of ALS disease. Patients with undoubtedly more advanced and extended disease burdens (cluster 1) should be carefully evaluated to propose therapeutic interventions, such as timely positioning of percutaneous endoscopic gastrostomy or tracheostomy.

ACKNOWLEDGMENT

We are grateful to the patients with ALS and their families.

Disclosure forms provided by the authors are available with the full text and PDF of this article at www.ajnr.org.

REFERENCES

- Chio A, Calvo A, Moglia C, et al. **Phenotypic heterogeneity of amyotrophic lateral sclerosis: a population based study.** *J Neurol Neurosurg Psychiatry* 2011; 82:740–46 CrossRef Medline
- Fang T, Al Khleifat A, Stahl DR, et al. **Comparison of the King’s and MiToS staging systems for ALS.** *Amyotroph Lateral Scler Frontotemporal Degener* 2017;18:227–32 CrossRef Medline
- Tramacere I, Dalla Bella E, Chio A, et al. **The MITOS system predicts long-term survival in amyotrophic lateral sclerosis.** *J Neurol Neurosurg Psychiatry* 2015;86:1180–85 CrossRef Medline
- Brooks BR, Miller RG, Swash M, et al; World Federation of Neurology Research Group on Motor Neuron Diseases. **El Escorial revisited: revised criteria for the diagnosis of amyotrophic lateral sclerosis.** *Amyotroph Lateral Scler Motor Neuron Disord* 2000;1:293–99 CrossRef Medline
- Strong MJ, Abrahams S, Goldstein LH, et al. **Amyotrophic lateral sclerosis: frontotemporal spectrum disorder (ALS-FTSD)—revised diagnostic criteria.** *Amyotroph Lateral Scler Frontoporal Degener* 2017;18:153–74 CrossRef Medline
- Balendra R, Jones A, Jivraj N, et al; UK-MND LiCALS Study Group, Mito Target ALS Study Group. **Use of clinical staging in amyotrophic lateral sclerosis for phase 3 clinical trials.** *J Neurol Neurosurg Psychiatry* 2015;86:45–49 CrossRef Medline
- Introna A, Milella G, Morea A, et al. **King’s College progression rate at first clinical evaluation: a new measure of disease progression in amyotrophic lateral sclerosis.** *J Neurol Sci* 2021;431:120041 CrossRef Medline
- Balendra R, Al Khleifat A, Fang T, et al. **A standard operating procedure for King’s ALS clinical staging.** *Amyotroph Lateral Scler Frontoporal* 2019;20:159–64 CrossRef Medline
- Bakers JN, de Jongh AD, Bunte TM, et al. **Using the ALSFRS-R in multicentre clinical trials for amyotrophic lateral sclerosis: potential limitations in current standard operating procedures.** *Amyotroph Lateral Scler Frontoporal* 2021;23:500–07 CrossRef Medline
- Gaiani A, Martinelli I, Bello L, et al. **Diagnostic and prognostic biomarkers in amyotrophic lateral sclerosis: neurofilament light chain levels in definite subtypes of disease.** *JAMA Neurol* 2017;74:525–32 CrossRef Medline
- Scarafino A, D’Errico E, Introna A, et al. **Diagnostic and prognostic power of CSF Tau in amyotrophic lateral sclerosis.** *J Neurol* 2018;265:2353–62 CrossRef Medline
- Verber NS, Shepheard SR, Sassani M, et al. **Biomarkers in motor neuron disease: a state of the art review.** *Front Neurol* 2019;10:291 CrossRef Medline
- Grolez G, Moreau C, Danel-Brunaud V, et al. **The value of magnetic resonance imaging as a biomarker for amyotrophic lateral sclerosis: a systematic review.** *BMC Neurol* 2016;16:155 CrossRef Medline
- Agosta F, Valsasina P, Riva N, et al. **The cortical signature of amyotrophic lateral sclerosis.** *PLoS One* 2012;7:e42816 CrossRef Medline

15. Schuster C, Kasper E, Machts J, et al. **Focal thinning of the motor cortex mirrors clinical features of amyotrophic lateral sclerosis and their phenotypes: a neuroimaging study.** *J Neurol* 2013;260:2856–64 CrossRef Medline
16. Walhout R, Westeneng H-J, Verstraete E, et al. **Cortical thickness in ALS: towards a marker for upper motor neuron involvement.** *J Neurol Neurosurg Psychiatry* 2015;86:288–94 CrossRef Medline
17. Mezzapesa DM, D'Errico E, Tortelli R, et al. **Cortical thinning and clinical heterogeneity in amyotrophic lateral sclerosis.** *PLoS One* 2013;8:e80748 CrossRef Medline
18. Distaso E, Milella G, Mezzapesa DM, et al. **Magnetic resonance metrics to evaluate the effect of therapy in amyotrophic lateral sclerosis: the experience with edaravone.** *J Neurol* 2021;268:3307–15 CrossRef Medline
19. Senda J, Kato S, Kaga T, et al. **Progressive and widespread brain damage in ALS: MRI voxel-based morphometry and diffusion tensor imaging study.** *Amyotroph Lateral Scler* 2011;12:59–69 CrossRef Medline
20. Milella G, Introna A, Ghirelli A, et al. **Medulla oblongata volume as a promising predictor of survival in amyotrophic lateral sclerosis.** *Neuroimage Clin* 2022;34:103015 CrossRef Medline
21. Li H, Zhang Q, Duan Q, et al. **Brainstem involvement in amyotrophic lateral sclerosis: a combined structural and diffusion tensor MRI analysis.** *Front. Neurosci* 2021;15:675444 CrossRef Medline
22. Schuster C, Hardiman O, Bede P. **Survival prediction in amyotrophic lateral sclerosis based on MRI measures and clinical characteristics.** *BMC Neurol* 2017;17:73 CrossRef Medline
23. Finegan E, Li Hi Shing S, Chipika RH, et al. **Widespread subcortical grey matter degeneration in primary lateral sclerosis: a multimodal imaging study with genetic profiling.** *Neuroimage Clin* 2019;24:102089 CrossRef Medline
24. Consonni M, Dalla Bella E, Contarino VE, et al. **Cortical thinning trajectories across disease stages and cognitive impairment in amyotrophic lateral sclerosis.** *Cortex* 2020;131:284–94 CrossRef Medline
25. Ferrea S, Junker F, Korth M, et al. **Cortical thinning of motor and non-motor brain regions enables diagnosis of amyotrophic lateral sclerosis and supports distinction between upper- and lower-motor neuron phenotypes.** *Biomedicines* 2021;9:1195 CrossRef Medline
26. Bede P, Murad A, Lope J, et al. **Clusters of anatomical disease-burden patterns in ALS: a data-driven approach confirms radiological subtypes.** *J Neurol* 2022;268:4404–13 CrossRef Medline
27. Tan HH, Westeneng HJ, Nitert AD, et al. **MRI clustering reveals three ALS subtypes with unique neurodegeneration patterns.** *Ann Neurol* 2022;92:1030–45 CrossRef Medline
28. Cedarbaum JM, Stambler N, Malta E, et al. **The ALSFRS-R: a revised ALS functional rating scale that incorporates assessments of respiratory function—BDNF ALS Study Group (Phase III).** *J Neurol Sci* 1999;169:13–21 CrossRef Medline
29. Kimura F, Fujimura C, Ishida S, et al. **Progression rate of ALSFRS-R at time of diagnosis predicts survival time in ALS.** *Neurology* 2006;66:265–67 CrossRef Medline
30. Grachev ID, Berdichevsky D, Rauch SL, et al. **A method for assessing the accuracy of intersubject registration of the human brain using anatomic landmarks.** *Neuroimage* 1999;9:250–68 CrossRef Medline
31. Hutton C, Draganski B, Ashburner J, et al. **A comparison between voxel-based cortical thickness and voxel-based morphometry in normal aging.** *Neuroimage* 2009;48:371–80 CrossRef Medline
32. Iglesias JE, Van Leemput K, Bhatt P, et al; Alzheimer's Disease Neuroimaging Initiative. **Bayesian segmentation of brainstem structures in MRI.** *NeuroImage* 2015;113:184–95 CrossRef Medline
33. Pintzka C, Hansen TI, Evensmoen H, et al. **Marked effects of intracranial volume correction methods on sex differences in neuroanatomical structures: a HUNT MRI study.** *Front Neurosci* 2015;9:238 CrossRef Medline
34. Steinbach R, Prell T, Gaur N, et al. **Patterns of grey and white matter changes differ between bulbar and limb onset amyotrophic lateral sclerosis.** *Neuroimage Clin* 2021;30:102674 CrossRef Medline
35. Zhang Q, Mao C, Jin J, et al. **Side of limb-onset predicts laterality of gray matter loss in amyotrophic lateral sclerosis.** *BioMed Res Int* 2014;2014:e473250 CrossRef Medline
36. Fabiano AJ, Horsfield MA, Bakshi R. **Interhemispheric asymmetry of brain diffusivity in normal individuals: a diffusion-weighted MR imaging study.** *AJNR Am J Neuroradiol* 2005;26:1089–94 Medline
37. Bede P, Elamin M, Byrne S, et al. **Sexual dimorphism in ALS: exploring gender-specific neuroimaging signatures.** *Amyotroph Lateral Scler Frontotemporal Degener* 2014;15:235–43 CrossRef Medline
38. Chiu T, Fang D, Chen J, et al. **A robust and scalable clustering algorithm for mixed type attributes in large database environment.** In: *Proceedings of the seventh ACM SIGKDD international conference on knowledge discovery and data mining.* New York, New York, August 2001:263–68 CrossRef
39. Kaufman L, Rousseeuw PJ. **Finding groups in data: an introduction to cluster analysis.** *Biometrics* 1991;47:788 CrossRef
40. Spinelli EG, Riva N, Rancoita PMV, et al. **Structural MRI outcomes and predictors of disease progression in amyotrophic lateral sclerosis.** *Neuroimage Clin* 2020;27:102315 CrossRef Medline
41. Brettschneider J, Del Tredici K, Toledo JB, et al. **Stages of pTDP-43 pathology in amyotrophic lateral sclerosis.** *Ann Neurol* 2013;74:20–38 CrossRef Medline
42. Schito P, Spinelli EG, Malvaso A, et al. **Primary lateral sclerosis presenting with focal onset spreading through contiguous neuroanatomic regions.** *Neurology* 2022;98:503–04 CrossRef Medline
43. Ravits J. **Focality, stochasticity and neuroanatomic propagation in ALS pathogenesis.** *Exp Neurol* 2014;262:121–26 CrossRef Medline
44. Sekiguchi T, Kanouchi T, Shibuya K, et al. **Spreading of amyotrophic lateral sclerosis lesions—multifocal hits and local propagation?** *J Neurol Neurosurg Psychiatry* 2014;85:85–91 CrossRef Medline
45. Ferraro PM, Cabona C, Meo G, et al. **Age at symptom onset influences cortical thinning distribution and survival in amyotrophic lateral sclerosis.** *Neuroradiology* 2021;63:1481–87 CrossRef Medline
46. Angenstein F, Niessen HG, Goldschmidt J, et al. **Age-dependent changes in MRI of motor brain stem nuclei in a mouse model of ALS.** *Neuroreport* 2004;15:2271–74 CrossRef Medline
47. Ferraro PM, Campi C, Miceli A, et al. **18F-FDG-PET correlates of aging and disease course in ALS as revealed by distinct PVC approaches.** *Eur J Radiol Open* 2022;9:100394 CrossRef Medline
48. Trojsi F, Di Nardo F, Caiazzo G, et al. **Between-sex variability of resting state functional brain networks in amyotrophic lateral sclerosis (ALS).** *J Neural Transm (Vienna)* 1996;2021;128:1881–97 CrossRef Medline
49. Chiò A, Moglia C, Canosa A, et al. **ALS phenotype is influenced by age, sex, and genetics: a population-based study.** *Neurology* 2020;94:e802–10 CrossRef Medline
50. Finegan E, Chipika RH, Li Hi Shing S, et al. **The clinical and radiological profile of primary lateral sclerosis: a population-based study.** *J Neurol* 2019;266:2718–33 CrossRef Medline
51. Tahedl M, Li H, Shing S, Finegan E, et al. **Propagation patterns in motor neuron diseases: Individual and phenotype-associated disease-burden trajectories across the UMN-LMN spectrum of MNDs.** *Neurobiol Aging* 2022;109:78–87 CrossRef Medline

Comparison between Dual-Energy CT and Quantitative Susceptibility Mapping in Assessing Brain Iron Deposition in Parkinson Disease

Y. Chen, M. Ge, J.J. Kang, Y.C. Ding, Y.C. Chen, and Z.Z. Jia



ABSTRACT

BACKGROUND AND PURPOSE: Both dual-energy CT and quantitative susceptibility mapping can evaluate iron depositions in the brain. The purpose of this study was to compare these 2 techniques in evaluating brain iron depositions in Parkinson disease.

MATERIALS AND METHODS: Forty-one patients with Parkinson disease (Parkinson disease group) and 31 age- and sex-matched healthy controls (healthy control group) were included. All participants underwent brain dual-energy CT and quantitative susceptibility mapping. ROIs were set bilaterally in the globus pallidus, substantia nigra, red nucleus, caudate nucleus, and putamen. CT values and magnetic susceptibility values were obtained in each ROI. Differences in CT values and magnetic susceptibility values between the Parkinson disease and healthy control groups were compared, followed by analysis of receiver operating characteristic curves. Correlations between CT values and magnetic susceptibility values were then evaluated.

RESULTS: The CT values of the bilateral globus pallidus, substantia nigra, and red nucleus were higher in the Parkinson disease group ($P < .05$). The magnetic susceptibility values of the bilateral globus pallidus and substantia nigra were higher in the Parkinson disease group ($P < .05$). The CT value of the right globus pallidus in linear fusion images had the highest diagnostic performance (0.912). Magnetic susceptibility values of the bilateral globus pallidus in the Parkinson disease group were positively correlated with CT values at the level of 80 kV(peak), linear fusion images, and SNI50 kV(p) ($r = 0.466\sim 0.617$; all, $P < .05$).

CONCLUSIONS: Both dual-energy CT and quantitative susceptibility mapping could assess excessive brain iron depositions in Parkinson disease, and we found a positive correlation between CT values and magnetic susceptibility values in the bilateral globus pallidus.

ABBREVIATIONS: AALv3 = Anatomical Automatic Labeling Version 3; AUC = area under curve; CA = caudate nucleus; DECT = dual-energy CT; GP = globus pallidus; HC = healthy control; MNI = Montreal Neurological Institute; MSV = magnetic susceptibility values; PD = Parkinson disease; PU = putamen; QSM = quantitative susceptibility mapping; RN = red nucleus; ROC = receiver operating characteristic; SN = substantia nigra

Parkinson disease (PD) is a neurodegenerative disease that causes progressive death of dopaminergic neurons, with excessive iron deposition within the nigrostriatal system being a main factor.¹⁻³ Therefore, assessment and monitoring of iron deposition in the brain are particularly vital for patients with PD. Both postmortem investigations and animal studies have confirmed the correlation between brain iron deposition and magnetic

susceptibility.⁴ Quantitative susceptibility mapping (QSM), a newly developed MR imaging technique, is based on the correspondence between phase data and the magnetic field, which can quantitatively assess brain iron deposition by measuring magnetic susceptibility values (MSV). Some studies have demonstrated brain iron accumulation in patients with PD by QSM to validate QSM as a method of tracking brain iron, which can be used as a biomarker and therapeutic target for the disease.⁵⁻⁷ Thus, QSM can be used as a guide in the early diagnosis of PD.

However, as an fMRI technique, QSM has some limitations in its application. Therefore, to address this problem, dual-energy CT (DECT) has recently been introduced. DECT has the ability to simultaneously capture images at different energy levels, creating the potential to gauge iron deposition without the disadvantages of energy-dependent CT attenuation of tissue.⁸⁻¹¹ Furthermore, the continuous development of CT reconstruction algorithms and detector technology has helped to significantly reduce the radiation dosage, making CT quicker and safer.⁸⁻¹²

Received September 1, 2022; accepted after revision February 20, 2023.

From the Department of Medical Imaging, Affiliated Hospital of Nantong University, Nantong, China.

Y. Chen and M. Ge contributed equally to this work.

This work was supported by the Jiangsu Provincial Health Commission (No. H2019089).

Please address correspondence to Z.Z. Jia, MD, PhD, Department of Medical Imaging, Affiliated Hospital of Nantong University, Medical School of Nantong University, No. 20 Xisi Rd, Nantong 226001, China; e-mail: jzz2397@163.com

Indicates open access to non-subscribers at www.ajnr.org

Indicates article with online supplemental data.

<http://dx.doi.org/10.3174/ajnr.A7822>

Demographics and clinical status of the study participants

	No. (Female/Male)	Age (mean) (yr)	Disease Duration (mean)	H-Y (Stage)
Patients with PD	41 (18:23)	65.0 (SD, 7.5)	4.5 (SD, 2.7)	1.9 (SD, 1.1)
H-Cs	31 (20:11)	62.4 (SD, 7.5)		

Note:—H-Y indicates Hoehn and Yahr stage.

Few studies have combined these imaging techniques to explore the relationship between CT values and the MSV of paramagnetic substances such as iron in the brain. Previous studies have demonstrated the efficiency of DECT in measuring liver iron,¹¹ and a recent study found that it was possible to estimate CT values using QSM of the brain.¹³ Therefore, we hypothesized that CT values from DECT could assess QSM-based MSV when measuring brain iron deposition and that these 2 parameters may be correlated in patients with PD.

MATERIALS AND METHODS

Study Population

This study was approved by the Ethics Committee of Nantong University Affiliated Hospital. All participants provided written consent as required by institutional guidelines. We selected 52 patients from a cohort of patients with clinically proved PD receiving treatment in our hospital from October 2020 to December 2021. After we applied inclusion and exclusion criteria, 41 eligible patients (PD group, 23 men; average age, 63.96 [SD, 8.27] years; 18 women; average age, 66.28 [SD, 6.47] years) were included. In addition, 31 age- and sex-matched healthy controls (HC group) were recruited. Their clinical characteristics are summarized in the Table. All participants underwent DECT and QSM. The interval between DECT and the MR imaging examination was <1 week.

The inclusion criteria were as follows: 1) Patients must have been diagnosed by a neurologist according to PD diagnostic criteria; 2) patients underwent DECT and QSM; 3) patients had no history of brain surgery; 4) patients had not received iron supplementation (eg, blood products, ferrous citrate, and so forth) or any dopamine medication within 1 week of testing; and 5) patients had no concurrent diseases that could lead to abnormal iron deposition (eg, intracerebral hemorrhage, renal failure, cerebral infarction, amyotrophic lateral sclerosis, and so forth) and no increased gastrointestinal iron absorption.

The exclusion criteria were as follows: 1) incomplete imaging data, which excluded 9 participants; 2) image artifacts, which excluded 2 participants due to motion artifacts.

DECT Scan

Participants underwent a third-generation DECT head scan (Somatom Force; Siemens). The dual-energy mode was run in different kilovolt settings (tube A: 80 kV[peak]; tube B: Sn150 kV[p]) with a dual energy scanning scheme (rotation time, 1.0 second; pitch, 0.7; layer thickness, 5 mm; layer spacing, 1 mm; collimation, 64 × 0.6 mm; FOV, 200 mm; volume CT dose index, 27.72 mGy). By means of automatic attenuation-based tube current modulation, the cross-sectional images were reconstructed using a kernel (Qr40; Siemens) (layer thickness, 1.0 mm; layer spacing, 0.7 mm).

A linear virtual hybrid image was generated by simulating a standard 120 kV(p) data set with a linear combination of the originally acquired 80-kV and Sn150-kV(p) image data. Final images with high and low kilovolts and their linear fusion were derived.

MRI

A 3T MR imaging scanner (Signal 750w; GE Healthcare) with a 24-channel head matrix coil was used to obtain MR images. Foam pads and earplugs were used to prevent head movement and reduce scanner noise. The QSM sequence was based on the gradient-echo sequence for multivoxel cross-sectional scans. The scan parameters of QSM were as follows: TR/TE, 32.5/3.3 ms; flip angle, 20°; layer thickness, 1 mm; acceptance bandwidth, 62.50 Hz/Px; FOV, 256 × 256 mm; matrix, 256 × 256 mm; imaging time, 3 minutes 42 seconds. The scan range of QSM was the substantia nigra (SN) area and the basal ganglia area, symmetric on both sides. Influences of the skull base, sinus gas, skull, blood vessels, and CSF were avoided to the greatest extent. Scanning started when the automatic shimming reached >98% of the half-height line width. In addition, routine brain scans were obtained before QSM to rule out various brain diseases.

Data Acquisition and ROI Extraction

MR imaging data were analyzed using Matlab R2019a (Version 9.6.0; MathWorks). QSM images were generated using the STI Suite toolbox (<https://people.eecs.berkeley.edu/~chunlei.liu/software.html>, Version 3.0) reconstruction. Image alignment and normalization of MR images were performed in SPM 12 (<http://www.fil.ion.ucl.ac.uk/spm/software/spm12>). Alignment of CT and MR images was performed using 3D Slicer software (Version 4.10.2; <http://www.slicer.org>), and processing was handled automatically by the program.

Image processing included the following 5 steps (Fig 1):

- 1) QSM reconstruction: Enhanced T2*-weighted angiography sequence images consisted of a magnitude map and a phase map. After we imported ESWAN into the STI Suite, the corresponding amplitude and QSM maps were generated after decoherence.
- 2) MR image normalization: The magnitude map was aligned with the T1 structure image to generate T1-cor. The magnitude map was then aligned with the corresponding structural image position. The T1-cor was normalized and aligned to the Montreal Neurological Institute (MNI) standard space to generate T1-MNI, and the transformation function (T-matrix) in this normalization process was recorded.
- 3) DECT image normalization: The DECT images were aligned with T1-cor, performing exactly the same transformation as T1-MNI aligned to the standard space.
- 4) QSM normalization: The T-matrix was applied to transform the QSM to the MNI standard space.
- 5) ROI extraction: After we matched the normalized MRI, QSM, and CT images with the Anatomical Automatic Labeling Version 3 (AALv3) template, we extracted the MSVs and CT values (average values) of the corresponding 3D ROIs. The

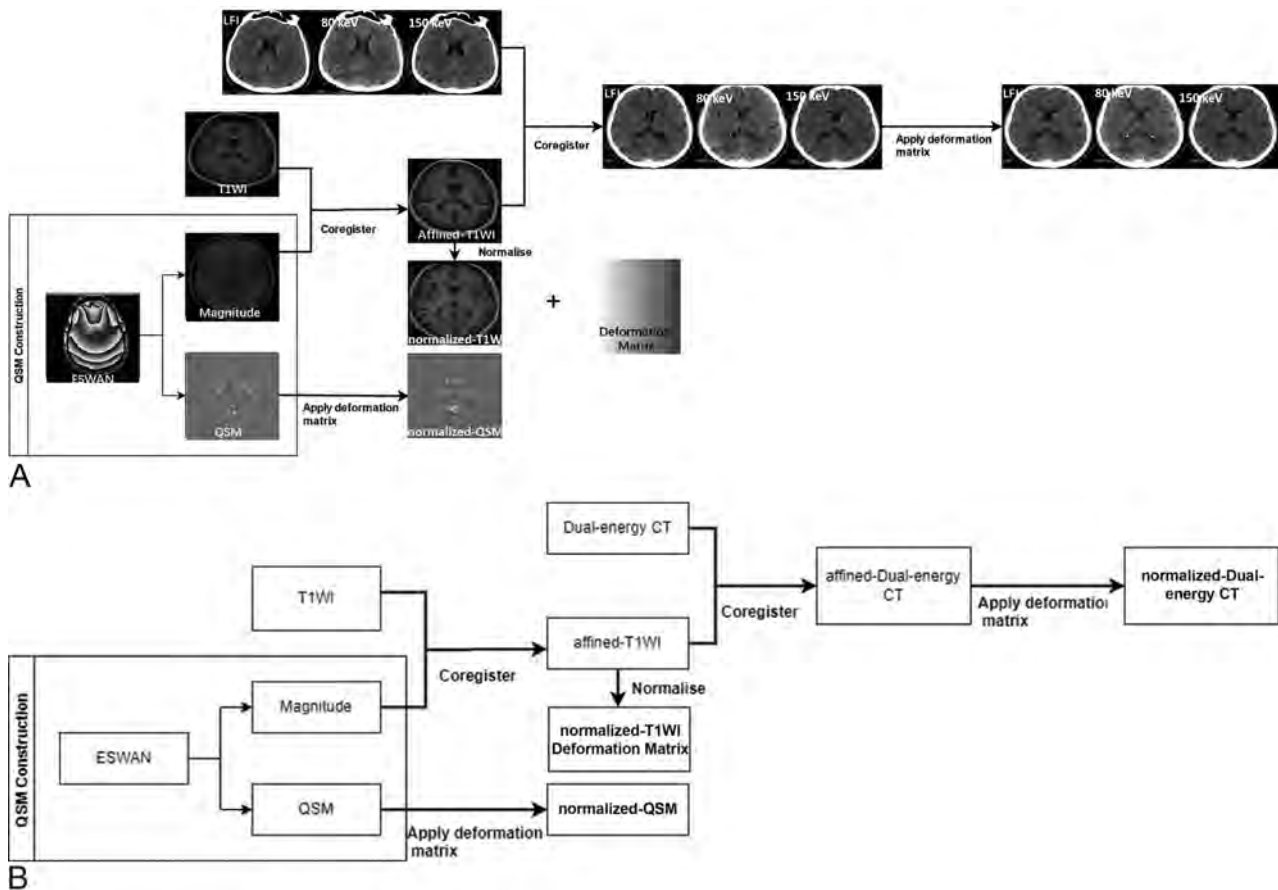


FIG 1. Main flow chart. *A*, The specific process of image registration. *B*, The process description: First, the QSM image was reconstructed and the magnitude map was normalized to the MNI standard space using the T1 structure image to obtain the T1-MNI, and the transformation matrix was recorded. DECT images were aligned with T1-MNI; and finally, QSM was transformed to the standard space using the same transformation matrix. After we matched the normalized MR imaging, QSM, and CT images with the AALv3 template, we extracted the MSV and CT values (average values) of the corresponding 3D ROIs using enhanced T2*-weighted angiography (ESWAN). LFI indicates linear fusion image.

extracted ROIs were set bilaterally in the globus pallidus (GP), SN, red nucleus (RN), caudate nucleus (CA), and putamen (PU) (Fig 2).

Statistical Analysis

The Kolmogorov-Smirnov test was applied to check the normality of each set of data. The mean (SD) was used to represent normally distributed data. The *t* test was used to compare differences in CT values and MSVs between the PD and HC groups. Receiver operating characteristic (ROC) curves were implemented to assess the diagnostic performance for PD. The Pearson correlation analysis was used to evaluate correlations between CT values and MSV for data with normal distributions. The false discovery rate was used to correct *P* values for multiple comparisons, and $P < .05$ was considered statistically significant. Statistical analyses were performed using SPSS 25.0 (IBM).

RESULTS

Participant Demographics

There were no significant differences in age or sex between the PD and HC groups (both, $P > .05$; Table).

Differences in CT Values and MSV between the PD and HC Groups

The CT values of the bilateral GP, SN, and RN were significantly higher in the PD group than in the HC group (all $P < .05$; Online Supplemental Data). The MSV of the bilateral GP and SN were significantly higher in the PD group than in the HC group (all, $P < .05$; Online Supplemental Data). However, there were no significant differences in CT values and MSV between the 2 groups in other ROIs (Fig 3).

ROC Curve Analysis of CT Values and MSV for Diagnosing PD

The ROC curve analysis showed that the CT values in the bilateral GP, SN, and RN at the level of 80 kV(p), linear fusion images, and Sn150 kV(p) could distinguish the PD group from the HC group (all, $P < .05$). The area under curve (AUC) of CT values was highest for the right GP in the linear fusion images (0.912).

The ROC curve analysis showed that the MSV in the bilateral GP and SN could distinguish the PD group from the HC group (all $P < .05$). The MSV of the right SN had the highest AUC (0.732) (Fig 4 and Online Supplemental Data).

Correlations between CT Values and MSV in the PD Group

MSV of the left GP in the PD group were positively correlated with CT values at the levels of 80 kV(p), linear fusion images, and Sn150 kV(p) ($r = 0.617, P < .001$; $r = 0.563, P < .001$; $r = 0.511, P < .001$). MSV of the right GP in the PD group were positively correlated with CT values at the levels of 80 kV(p), linear fusion images, and Sn150 kV(p) ($r = 0.550, P < .001$; $r = 0.524, P < .001$; $r = 0.466, P = .002$). There were no correlations between CT

values and MSV in the PD group in other ROIs (Fig 5 and Online Supplemental Data).

DISCUSSION

Studies have shown that iron metabolism is present during the aging process in healthy participants, while abnormal iron deposition has been observed in some neurodegenerative diseases.^{14,15}

QSM is the most commonly used method for MR imaging of iron quantification. Some previous studies used QSM to quantitatively assess iron deposition in the brains of patients with PD, not only for early detection and diagnosis but also for assessing neurologic impairment of cognitive and motor function and guiding neurosurgical treatment, making it a feasible noninvasive test for PD.^{7,16-22} Although MR imaging has advantages in iron quantification for patients with high iron content, previous studies have shown that its signal decays rapidly with increasing iron concentration. High iron content can indirectly lead to inaccuracies in the subsequently generated magnetization maps due to transverse signal attenuation and the possibly insufficient number of measurements. Moreover, MR



FIG 2. ROI settings. The ROIs used to extract MSV and CT values (average values) were set in the bilateral CA (blue), PU (purple), GP (orange), SN (red), and RN (yellow).

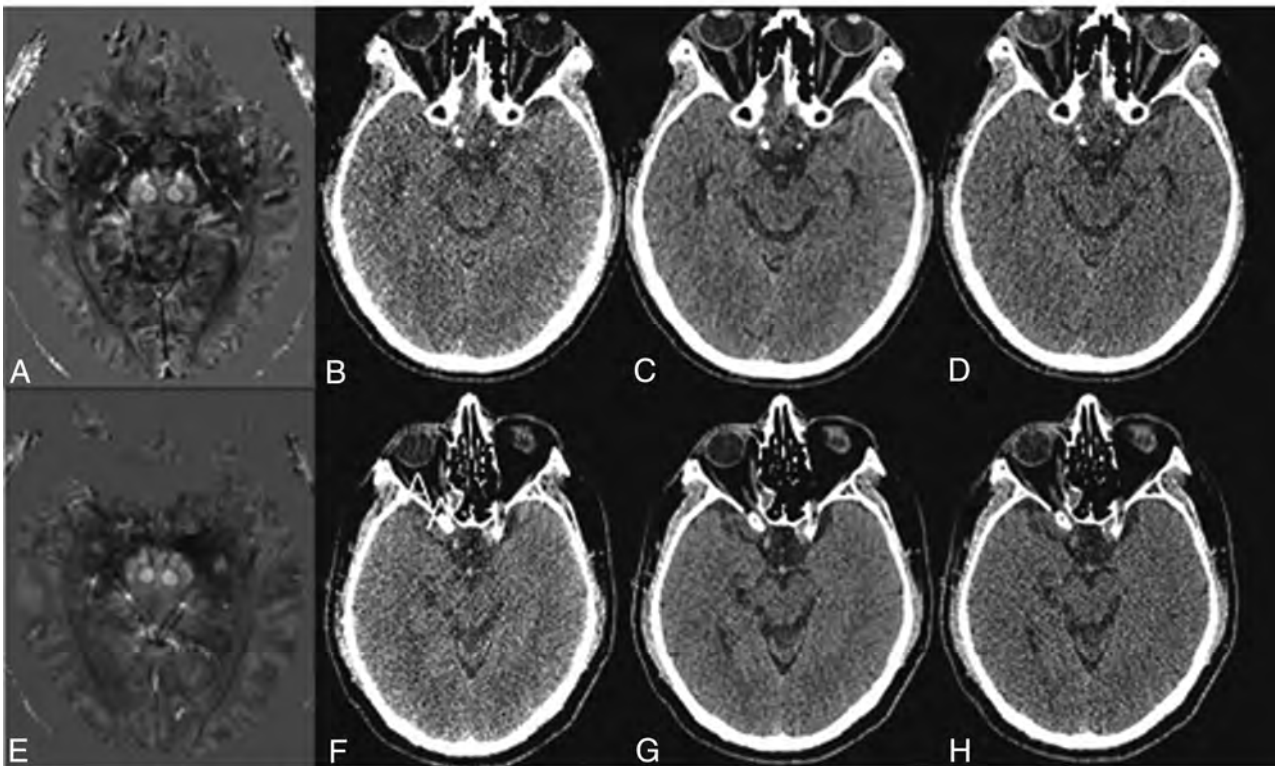


FIG 3. Comparison of QSM and CT images of patients with PD and HC groups. A–D, A 67-year-old female patient with PD. A, QSM image of a patient with PD showing the increased signal in the bilateral SN, suggesting increased iron deposition; B–D, CT images of a patient with PD at 80 kV(p), linear fusion, and Sn150 kV(p) levels, respectively. E–H, A 68-year-old healthy woman. E, QSM image of a healthy person showing no obvious abnormal signal changes in the bilateral SN. F–H, CT images of a healthy person at the level of 80 kV(p), linear fusion, and Sn150 kV(p), respectively.

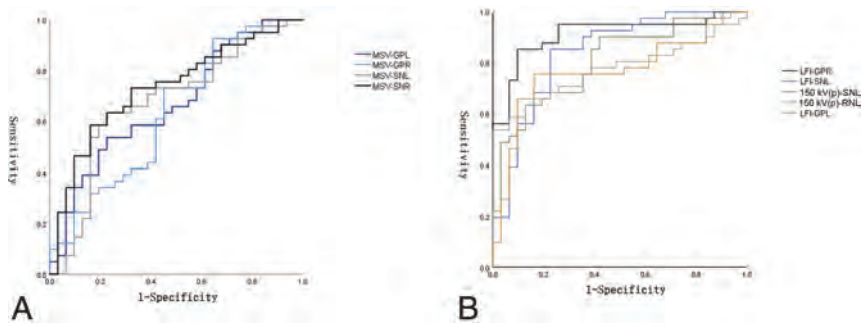


FIG 4. ROC curves of MSV and CT values. A, The MSV in the left GP has the highest diagnostic performance (black). B, The LFI-based CT value in GPR had the highest diagnostic performance (black). GPL indicates globus pallidus left; GPR, globus pallidus right; SNL, substantia nigra left; SNR, substantia nigra right; LFI, linear fusion image; RNL, red nucleus left.

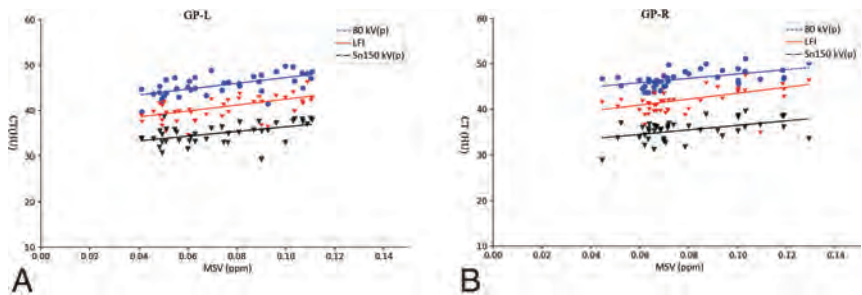


FIG 5. Correlations between MSV and CT values of the bilateral GP of patients with PD. MSV of the left (A) and right GPs (B) in the PD group were positively correlated with CT values at the 80 kV(p) level, linear fusion images, and Sn150 kV(p) values. GP-L indicates globus pallidus left; LFI, linear fusion image; GP-R, globus pallidus right.

imaging is expensive, with long scan times and some contraindications. Therefore, finding an alternative quantification method is necessary. Previous studies have investigated the accuracy of DECT for quantifying liver iron content.¹¹ DECT provides a simple and easy method for iron quantification with diagnostic performance similar to that of MR imaging.^{11,23} Therefore, we aimed to explore and compare the use of DECT and QSM for measuring iron deposition in the brain in patients with PD and to verify whether DECT could be a cost-saving and alternative method for examining patients with PD.

DECT is performed by a weighted linear combination of 2 acquisition images (80 kV[p] and Sn150 kV[p]) to generate a dual-energy-simulated standard 120 kV(p) image.^{24,25} If one adjusts the weights, the dual-energy-simulated standard CT images can have the characteristics of standard 120 kV(p) images in terms of pixel noise and CT values.²⁵ Thus, the dual-energy-simulated standard CT images can be used alternatively for diagnosis. Compared with MR imaging, CT is widely used due to lower cost, shorter examination time, and relatively simple image acquisition methods. Furthermore, DECT is effective for patients with possible motor impairment and metal dentures.

In the present study, the MSV of the bilateral GP and SN were found to be apparently higher in the PD group than in the HC group, suggesting that patients with PD had increased iron deposition in these regions. Guan, Chen and Lewis et al²⁶⁻²⁸ found that MSV from QSM in patients with PD were significantly

higher than those in healthy patients in the GP, RN, SN, and thalamus. These findings were consistent with the pathogenesis of PD and in agreement with the results of the present study. However, the present study measured not only the MSV in these regions but also CT values from DECT. Our results demonstrated that the CT values of the PD group in the GP, SN, and RN at 80 kV(p), linear fusion, and Sn150 kV(p) were higher than those in the HC group, indicating that increased iron deposition in these regions led to elevated CT values. The CT values and MSVs of different ROIs had a different diagnostic efficacy for PD. The area under the ROC curve of the CT values of the linear fusion images in the right GP and the AUC of the MSV in the right SN were significantly higher than in other ROIs. It is possible that this finding is because the main lesional areas in PD are the SN and GP. Unlike previous studies, the present study measured CT values from DECT to complement the diagnostic performance of QSM. We also performed a correlation analysis between MSV and CT values at different levels in patients with PD. At 80 kV(p), linear fusion, and Sn150 kV(p), the CT values detected in the bilateral GP were positively correlated with the MSV.

The GP is the most iron-rich structure in the brain, and patients with PD have increased iron deposition in the GP.²⁹ Because iron (ferritin and hemosiderin) is paramagnetic, it can cause local magnetic field inhomogeneity, resulting in an increase in MSVs. At the same time, as a metal, iron can also lead to an increase in CT values. In addition, by using DECT scanning, we found that a smaller kilovolt (peak) led to better correlation and greater tissue attenuation at a low kilovolt (peak) compared with a high kilovolt (peak), leading to higher CT values. Thus, larger differences in tissue contrast improved the correlation between CT values and MSV. This evidence provided the basis for subsequent low-dose studies. There was no strong increase in susceptibility within the GP of patients with PD compared with the SN. Although calcification of the GP leads to negative magnetization in QSM, this may be overlooked due to the strong paramagnetic properties of iron.³⁰ Previous studies have shown that iron is usually distributed in the anterior part of the GP externus;³¹ however, the present study targeted the entire GP, contradicting former research on the iron content of the GP.

Previously, increased iron deposition in the SN was studied as the most representative pathologic feature in patients with PD. Still, no correlation between MSV and CT values of the SN was found in the present study, which may be related to the specific site of iron deposition in the SN, because iron often accumulates

in the dorsal-caudal region and the SN is very small. Another factor that should not be overlooked is the comparatively smaller sample size. Thus, when one quantifies the magnetic induction intensity of the whole SN, the results here may be biased. This issue could explain why there was no correlation between MSV and CT values in the SN.

A previous study by Dimov et al³² found that the MSV of bone correlated with CT values due to the antimagnetic susceptibility and high CT values from calcification. Although abnormal iron deposition has also been observed in several deep brain nuclei in other studies,^{21,33,34} we found no correlation between MSV and CT values in the CA, PU, and RN. This could be the result of low iron deposition and the absence of calcification in these regions, causing the amount of iron deposited at these sites to be insufficient to produce a correlation, in agreement with previous findings.¹³ Future studies are needed to thoroughly evaluate these sites.

In this study, DECT and QSM were equivalent in objectively assessing brain iron deposition in patients with PD. There was a positive correlation between MSVs and CT values of the GP. These results suggest that both DECT and QSM can detect brain iron deposition. In most cases, QSM remains the technique of choice to assess brain iron deposition in patients with PD. However, when some patients have contraindications to MR imaging or movement disorders that are not suitable for examination with QSM, DECT can be used to measure brain iron deposition. Moreover, with the development of new technologies, the amount of radiation exposure is decreasing. Thus, QSM and CT could substitute for each other in evaluating iron deposition in the brain. It is beneficial to provide different imaging options for patients that can provide an essential reference for the clinical diagnosis of PD.

There were several limitations to the present study. First, the small sample size may lead to uncertainty in the analysis. However, our participants would have received radiation doses as a result of the CT examinations. Second, other metals may also contribute to an increase in MSV, though these effects are weaker than those of iron.

CONCLUSIONS

The present study showed increased brain iron deposition in patients with PD using DECT and QSM imaging analyses. MSV correlated with CT values in the bilateral GP, suggesting that DECT and QSM are equally valuable for assessing brain iron deposition and can be used interchangeably.

Disclosure forms provided by the authors are available with the full text and PDF of this article at www.ajnr.org.

REFERENCES

- Acosta-Cabronero J, Cardenas-Blanco A, Betts MJ, et al. **The whole-brain pattern of magnetic susceptibility perturbations in Parkinson's disease.** *Brain* 2017;140:118–31 CrossRef Medline
- An H, Zeng X, Niu T, et al. **Quantifying iron deposition within the substantia nigra of Parkinson's disease by quantitative susceptibility mapping.** *J Neurol Sci* 2018;386:46–52 CrossRef Medline
- Ghassaban K, He N, Sethi SK, et al. **Regional high iron in the substantia nigra differentiates Parkinson's disease patients from healthy controls.** *Front Aging Neurosci* 2019;11:106 CrossRef Medline
- Langkammer C, Schweser F, Krebs N, et al. **Quantitative susceptibility mapping (QSM) as a means to measure brain iron? A post mortem validation study.** *Neuroimage* 2012;62:1593–99 CrossRef Medline
- Li KR, Vecillas-Chasin J, Nguyen TD, et al. **Quantitative evaluation of brain iron accumulation in different stages of Parkinson's disease.** *J Neuroimaging* 2022;32:363–71 CrossRef Medline
- Aggarwal M, Li X, Gröhn O, et al. **Nuclei-specific deposits of iron and calcium in the rat thalamus after status epilepticus revealed with quantitative susceptibility mapping (QSM).** *J Magn Reson Imaging* 2018;47:554–64 CrossRef Medline
- Kang JJ, Chen Y, Xu GD, et al. **Combining quantitative susceptibility mapping to radiomics in diagnosing Parkinson's disease and assessing cognitive impairment.** *Eur Radiol* 2022;32:6992–7003 CrossRef Medline
- Tsai YS, Chen JS, Wang CK, et al. **Quantitative assessment of iron in heart and liver phantoms using dual-energy computed tomography.** *Exp Ther Med* 2014;8:907–12 CrossRef Medline
- Luo XF, Yang Y, Yan J, et al. **Virtual iron concentration imaging based on dual-energy CT for noninvasive quantification and grading of liver iron content: an iron overload rabbit model study.** *Eur Radiol* 2015;25:2657–64 CrossRef Medline
- Ibrahim EH, Bowman AW. **Characterization of myocardial iron overload by dual-energy computed tomography compared to T2* MRI; a phantom study.** *Annu Int Conf IEEE Eng Med Biol Soc* 2014;2014:5133–36 CrossRef Medline
- Ma Q, Hu J, Yang W, et al. **Dual-layer detector spectral CT versus magnetic resonance imaging for the assessment of iron overload in myelodysplastic syndromes and aplastic anemia.** *Jpn J Radiol* 2020;38:374–81 CrossRef Medline
- Fischer MA, Reiner CS, Raptis D, et al. **Quantification of liver iron content with CT-added value of dual-energy.** *Eur Radiol* 2011;21:1727–32 CrossRef Medline
- Oshima S, Fushimi Y, Okada T, et al. **Brain MRI with quantitative susceptibility mapping: relationship to CT attenuation values.** *Radiology* 2020;294:600–09 CrossRef Medline
- Arisaka O, Ichikawa G, Imataka G, et al. **Iron, ketone bodies, and brain development.** *J Pediatr* 2020;222:262–63 CrossRef Medline
- Thirupathi A, Chang YZ. **Brain iron metabolism and CNS diseases.** *Adv Exp Med Biol* 2019;1173:1–19 CrossRef Medline
- Azuma M, Hirai T, Yamada K, et al. **Lateral asymmetry and spatial difference of iron deposition in the substantia nigra of patients with Parkinson disease measured with quantitative susceptibility mapping.** *AJNR Am J Neuroradiol* 2016;37:782–88 CrossRef Medline
- Fedeli MP, Contarino VE, Siggillino S, et al. **Iron deposition in parkinsonisms: a quantitative susceptibility mapping study in the deep grey matter.** *Eur J Radiol* 2020;133:109394 CrossRef Medline
- Guan JJ, Feng YQ. **Quantitative magnetic resonance imaging of brain iron deposition: comparison between quantitative susceptibility mapping and transverse relaxation rate (R2*) mapping [in Chinese].** *Nanfang yi ke da xue xue bao* 2018;38:305–11 CrossRef Medline
- Li DT, Hui ES, Chan Q, et al. **Quantitative susceptibility mapping as an indicator of subcortical and limbic iron abnormality in Parkinson's disease with dementia.** *Neuroimage Clin* 2018;20:365–73 CrossRef Medline
- Mazzucchi S, Frosini D, Costagli M, et al. **Quantitative susceptibility mapping in atypical Parkinsonisms.** *Neuroimage Clin* 2019;24:101999 CrossRef Medline
- Shahmaei V, Faeghi F, Mohammadbeigi A, et al. **Evaluation of iron deposition in brain basal ganglia of patients with Parkinson's disease using quantitative susceptibility mapping.** *Eur J Radiol Open* 2019;6:169–74 CrossRef Medline
- Uchida Y, Kan H, Sakurai K, et al. **Magnetic susceptibility associates with dopaminergic deficits and cognition in Parkinson's disease.** *Mov Disord* 2020;35:1396–405 CrossRef Medline
- Luo XF, Xie XQ, Cheng S, et al. **Dual-energy CT for patients suspected of having liver iron overload: can virtual iron content imaging accurately quantify liver iron content?** *Radiology* 2015;277:95–103 CrossRef Medline

24. Hamid S, Nasir MU, So A, et al. **Clinical applications of dual-energy CT.** *Korean J Radiol* 2021;22:970–82 CrossRef Medline
25. Naruto N, Itoh T, Noguchi K. **Dual energy computed tomography for the head.** *Jpn J Radiol* 2018;36:69–80 CrossRef Medline
26. Guan X, Xuan M, Gu Q, et al. **Regionally progressive accumulation of iron in Parkinson's disease as measured by quantitative susceptibility mapping.** *NMR Biomed* 2017;30:e3489 CrossRef Medline
27. Chen Q, Chen Y, Zhang Y, et al. **Iron deposition in Parkinson's disease by quantitative susceptibility mapping.** *BMC Neurosci* 2019;20:23 CrossRef Medline
28. Lewis MM, Du G, Kidacki M, et al. **Higher iron in the red nucleus marks Parkinson's dyskinesia.** *Neurobiol Aging* 2013;34:1497–503 CrossRef Medline
29. Jaggi S, Khandelwal N, Sahni D, et al. **In vitro study of iron deposition in normal human brains: an Indian scenario.** *Clin Anat* 2018;31:275–81 CrossRef Medline
30. Jang J, Nam Y, Jung SW, et al. **Paradoxical paramagnetic calcifications in the globus pallidus: an ex vivo MR investigation and histological validation study.** *NMR Biomed* 2021;34:e4571 CrossRef Medline
31. De Barros A, Arribarat G, Lotterie JA, et al. **Iron distribution in the lentiform nucleus: a post-mortem MRI and histology study.** *Brain Struct Funct* 2021;226:351–64 CrossRef Medline
32. Dimov AV, Liu Z, Spincemaille P, et al. **Bone quantitative susceptibility mapping using a chemical species-specific R2* signal model with ultrashort and conventional echo data.** *Magn Reson Med* 2018;79:121–28 CrossRef Medline
33. Chen J, Cai T, Li Y, et al. **Different iron deposition patterns in Parkinson's disease subtypes: a quantitative susceptibility mapping study.** *Quant Imaging Med Surg* 2020;10:2168–76 CrossRef Medline
34. Guan X, Bai X, Zhou C, et al. **Serum ceruloplasmin depletion is associated with magnetic resonance evidence of widespread accumulation of brain iron in Parkinson's disease.** *J Magn Reson Imaging* 2021;54:1098–106 CrossRef Medline

Incidental Findings from 16,400 Brain MRI Examinations of Research Volunteers

 P.A. Rowley,  M.J. Paukner,  L.B. Eisenmenger,  A.S. Field,  R.J. Davidson,  S.C. Johnson, S. Asthana,  N.A. Chin,  V. Prabhakaran,  B.B. Bendlin,  B.R. Postle,  H.H. Goldsmith,  C.M. Carlsson, M.A. Brooks,  N.H. Kalin,  L.E. Williams, and  H.A. Rowley



ABSTRACT

BACKGROUND AND PURPOSE: Incidental findings are discovered in neuroimaging research, ranging from trivial to life-threatening. We describe the prevalence and characteristics of incidental findings from 16,400 research brain MRIs, comparing spontaneous detection by nonradiology scanning staff versus formal neuroradiologist interpretation.

MATERIALS AND METHODS: We prospectively collected 16,400 brain MRIs (7782 males, 8618 females; younger than 1 to 94 years of age; median age, 38 years) under an institutional review board directive intended to identify clinically relevant incidental findings. The study population included 13,150 presumed healthy volunteers and 3250 individuals with known neurologic diagnoses. Scanning staff were asked to flag concerning imaging findings seen during the scan session, and neuroradiologists produced structured reports after reviewing every scan.

RESULTS: Neuroradiologists reported 13,593/16,400 (83%) scans as having normal findings, 2193/16,400 (13.3%) with abnormal findings without follow-up recommended, and 614/16,400 (3.7%) with “abnormal findings with follow-up recommended.” The most common abnormalities prompting follow-up were vascular (263/614, 43%), neoplastic (130/614, 21%), and congenital (92/614, 15%). Volunteers older than 65 years of age were significantly more likely to have scans with abnormal findings ($P < .001$); however, among all volunteers with incidental findings, those younger than 65 years of age were more likely to be recommended for follow-up. Nonradiologists flagged <1% of MRIs containing at least 1 abnormality reported by the neuroradiologists to be concerning enough to warrant further evaluation.

CONCLUSIONS: Four percent of individuals who undergo research brain MRIs have an incidental, potentially clinically significant finding. Routine neuroradiologist review of all scans yields a much higher rate of significant lesion detection than selective referral from nonradiologists who perform the examinations. Workflow and scan review processes need to be carefully considered when designing research protocols.

ABBREVIATIONS: CHS = Cardiovascular Health Studies; NPV = negative predictive value; PI = principal investigator; PPV = positive predictive value; SE = standard error

Brain MRIs are performed for research and even commercial purposes. In addition to supporting primary research objectives, neuroimaging can uncover incidental findings. Incidental

findings herein refer to previously unknown abnormalities of potential clinical significance discovered during MRIs that are both unrelated to the purpose of the research examination and distinct from the clinical history of the volunteer.¹ It is estimated that incidental findings are found in approximately 4% of research brain MRIs;^{1,2} however, further examination is warranted, given that past studies have used small sample sizes, homogeneous

Received December 16, 2022; accepted after revision February 20, 2023.

From the University of Wisconsin School of Medicine and Public Health (P.A.R., L.B.E., A.S.F., R.J.D., S.C.J., S.A., V.P., B.B.B., B.R.P., H.H.G., C.M.C., M.A.B., N.H.K., L.E.W., H.A.R.), Departments of Radiology (P.A.R., L.B.E., A.S.F., V.P., H.A.R.), Statistics (M.J.P.), and Psychology (R.J.D., B.R.P., H.H.G.), Wisconsin Alzheimer’s Disease Research Center (S.C.J., S.A., B.B.B., C.M.C.), and Departments of Medicine (S.C.J., S.A., N.A.C., B.B.B., C.M.C.), Orthopedics (M.A.B.), and Psychiatry (N.H.K., L.E.W.), University of Wisconsin–Madison, Madison, Wisconsin.

This work was supported, in part, by the Grand Alliance Concussion Assessment, Research and Education Consortium, funded, in part, by the National Collegiate Athletic Association and the Department of Defense. The US Army Medical Research Acquisition Activity is the awarding and administering acquisition office. This work was also supported by the Office of the Assistant Secretary of Defense for Health Affairs through the Psychological Health and Traumatic Brain Injury Program under award No. W81XWH-14-2-0151 and by grants from the National Institute of Mental Health: R21MH092581 (N.H. Kalin), R01MH107563 (N.H. Kalin, L.E. Williams), and U01MH12913 (N.H. Kalin, L.E. Williams). Other funding sources include R01AG062285, R01AG037639, UFIAG051216, P30AG062715, R01MH064498.

Opinions, interpretations, conclusions, and recommendations are those of the authors and are not necessarily endorsed by the Department of Defense (Defense Health Program funds).

Please address correspondence to Paul Rowley, MD, University of Wisconsin School of Medicine and Public Health, Department of Radiology, 600 Highland Ave, Madison, WI 53792-3252; e-mail: prowley@wisc.edu

 Indicates open access to non-subscribers at www.ajnr.org

 Indicates article with online supplemental data.
<http://dx.doi.org/10.3174/ajnr.A7821>

population-based cohorts across narrow age ranges, and specialty MRI protocols limiting external validity and/or having problematic methods for identifying incidental findings.²⁻⁶

There is poor consensus on whether the baseline prevalence of clinically significant brain abnormalities in the general population justifies the routine use of neuroradiologists to review research MRIs. Standard practices for research MRI interpretation differ by institution and by country, but budgetary and workflow constraints have historically limited expert review solely to scans flagged by scanning technologists and research personnel. These nonradiologists have variable experience and, in most circumstances, lack formal training in diagnostic MR imaging reporting; nonetheless, they are tasked with screening and referring concerning findings for further review, leaving most scans without formal interpretation.

In this prospective cross-sectional study, we describe the prevalence and characteristics of incidental findings and assess the detection rate of abnormalities of nonradiologists compared with neuroradiologists from a series of 16,400 consecutive research brain MRIs collected at a single institution across 18 years.

MATERIALS AND METHODS

All research activities performed and described were conducted in accordance with an institutional review board–approved protocol at the University of Wisconsin-Madison.

Population Recruitment and Inclusion

Brain MRIs were collected from 17,010 consecutive volunteers from research studies conducted at the University of Wisconsin-Madison from April 2002 to March 2020. The final study population included 16,400 scans (7782 males, 8618 females; younger than 1 year of age to 94 years; median age, 38 years) after excluding 610 whose participant intake forms lacked age and/or sex. The overall study data base compiled neuroimaging from volunteers in >300 research protocols and 73 principal investigator (PI) groups. All volunteers or their guardians provided informed consent before participation. Participants were recruited by each individual PI on the basis of eligibility criteria for their respective studies. Most studies recruited healthy age-matched control volunteers, while a minority recruited individuals with pre-existing conditions such as stroke, MS, and dementia.

Each scan was treated as a unique case, though some participants were scanned more than once. We are unable to quantify how many participants were serially scanned because of the research scan anonymization, a code that sometimes changed with time for the same individual. Typical workflow required that all scans be read unless a prior MRI in the same protocol had been read within the past year, in which case the PI was not required to submit the scan for radiologist interpretation. We encountered significant abnormalities on follow-up scans in some previously healthy subjects, justifying review of new studies. Most important, volunteers with known pre-existing medical conditions, including those with disease-related neuroimaging findings, were not excluded. Therefore, volunteers with known conditions were considered to have either normal or abnormal findings, or no follow-up was recommended unless other previously unknown brain abnormalities were discovered. If a

volunteer had previously been informed of a clinically significant finding and this was seen again at follow-up, this duplicate was placed in the “abnormal, no follow-up” category unless there had been clear-cut interval worsening. Volunteers with normal anatomic variants and common incidental findings of doubtful significance were categorized as having normal findings.

Brain MRI Acquisition and Analysis

MRIs were performed on GE Healthcare MRI scanners at multiple research sites. Most scans were performed at 3T (15,888/16,400, 97%). Each PI chose pulse sequences on the basis of individual study needs, leading to a heterogeneous variety of scan protocols. Virtually all included T1-weighted images (mostly volumetric acquisitions) and additional sequences were included for most protocols, particularly in those older than 45 years of age for aging and dementia research. Examinations containing brain anatomy and already postprocessed parameter maps (eg, perfusion if available) were sent to the PACS for neuroradiologist interpretation. Advanced imaging techniques and raw data files including PET, 4D flow MRA, fMRI, and diffusion tensor maps were not interpreted.

MRI Interpretation and Reporting

Nonradiologists including scanning staff (MRI technologists and nurses) and research personnel (PhD scientists and neuropsychologists) were instructed to document concerns at the time of scanning using the same Web-based intake form they had used to upload cases to the reading queue of neuroradiologists. All scanning technicians were certified for MRI safety and technical proficiency, as verified by more senior technicians and ultimately the PI. The technicians in our neuroscience centers were specialty research personnel, most without a radiologic technologist degree, typically with 3–15 years of experience. The technicians in our combined clinical/research site were mostly formally certified radiologic technologists with 2–20 years of experience. Excluding the 202/16,400 scans for which scanner location was unspecified on the intake form, 9944/16,198 (61%) scans were obtained on scanners designated for research only, while 6254/16,198 (39%) scans were acquired on clinical scanners. All scans were anonymously coded, sent to the PACS, and formally interpreted by a neuroradiologist. Intake forms provided readers with volunteers’ age and sex, study diagnosis, and known medical conditions. Each neuroradiologist (H.A.R. with >30 years of experience, A.S.F. with >20 years of experience; V.P. with >20 years of experience, L.E.W. with >10 years of experience) independently reviewed scans and generated reports using a structured form linked to the volunteer’s research examination on the PACS (Online Supplemental Data). In each report, the neuroradiologist classified each examination finding as 1) normal, 2) abnormal, no follow-up, or 3) abnormal, follow-up recommended.

Our main aim while categorizing scans was to identify the full range of incidental findings in our population, but to only recommend follow-up for potentially clinically significant abnormalities. A clinically significant abnormality was defined as an unexpected MRI finding the radiologist considered serious enough to prompt notification of the research subject and review by their medical practitioner. Trivial changes, normal variants, and lesions within

Table 1: Characteristics of study volunteers

	Male	Female	P Value
Sample size	7782	8618	<.001
Age (mean) (yr)	39 (SD, 24)	41 (SD, 23)	<.001
No history of brain lesion (ie, typical control)	6155	6995	<.001
Recruited due to known condition	1627	1623	<.001

expectation were not recommended for follow-up or notification to limit anxiety and potential expense of follow-up, while identifying clear-cut concerning findings with potential clinical implications. The normal/normal variant scans included commonly encountered conditions in the general population such as inflammatory changes of the paranasal sinus, reactive-appearing cervical lymph nodes, small pineal and arachnoid cysts, uncomplicated developmental venous abnormalities, mild WM changes in the elderly, and slightly low cerebellar tonsils. Examples of “abnormal/no follow-up” would include lesions related to known conditions listed on the intake form (eg, MS, prior trauma, or stroke), excess hippocampal atrophy in a volunteer with dementia, or concerning-but-stable conditions for which the volunteer was already notified on the basis of earlier abnormal findings on a research scan. The “abnormal, follow-up recommended” scans contained more concerning lesions that we thought the volunteer should be aware of, even if there were no immediate treatment implications.

Follow-up on Incidental Findings

All volunteers or their guardians signed informed consent/assent under an institutional review board–approved protocol in which they addressed disclosure of incidental findings. On categorizing a scan as abnormal, follow-up recommended, the neuroradiologist informed the PI team, who unblinded the file and referred to the volunteer’s informed-consent document to determine the volunteer’s preference. The lead investigator would either directly communicate the finding to the volunteer, ask the neuroradiologist to contact the volunteer to disclose the findings, or respect the wishes of the volunteer not to be informed of incidental findings. All clinically relevant findings were communicated to both the participant and his or her physician if requested.

Statistical Analysis

After we acquired and interpreted 17,010 brain MRIs, those without documented age and/or sex were excluded, resulting in a final study population of 16,400. Examinations marked abnormal with follow-up recommended were further subcategorized on the basis of abnormality type using information in each structured report (Online Supplemental Data).

Descriptive Statistical Analysis

Most variables are either categoric or binary. Variables are summarized by the percentage of volunteers in each group. Correlations between categoric or binary variables were evaluated using χ^2 tests. Continuous variables are presented as mean (SD) and compared using ANOVA for multiple groups and the Student *t* test for 2 groups. The association between scans with abnormal findings and those with normal findings was determined by univariate

logistic regression adjusted for age and sex. All analyses were performed using R statistical and computing software (Version 3.5.2; <http://www.r-project.org/>), and *P* values < .05 were considered statistically significant.

We compared written initial concerns by nonradiologist reviewers with the neuroradiologist’s scan classification. Our other descriptive analyses divide scans with abnormal findings on the basis of whether follow-up was recommended; however, this analysis treated all scans with abnormalities as 1 classification because we intended to determine the ability of nonradiologist reviewers to classify scans as having abnormal-versus-normal findings on the basis of whether they perceived at least 1 incidental finding to be present or absent, respectively. Initial concerns were considered relevant to the analysis if the text described a presumptive abnormality (eg, “cyst,” “meningioma”) and were excluded if it listed known lesions or these were irrelevant (eg, “subject motion,” “anxiety meds given before scan”). Relevant initial concerns were compared with the final neuroradiologist classification (normal versus abnormal) and were presented in terms of sensitivity, specificity, positive predictive value (PPV), and negative predictive value (NPV).

Inferential Statistical Analysis

An ordinal logistic regression model was constructed to investigate how sex and age affect scan classification. Results of this analysis are presented in log order with standard error (SE) and 95% CIs. An increase in log order represents an increased likelihood of a scan having abnormal findings if a given variable was present.

RESULTS

Study Characteristics

This study comprised 16,400 research volunteers enrolled in studies for which brain MRIs were acquired at the University of Wisconsin-Madison and included both typical volunteers (ie, those without previously identified intracranial abnormalities) as well as individuals with a known brain lesion or congenital predisposition to neuropathology detectable by imaging (eg, excess mineralization in trisomy 21). Study demographic characteristics are shown in Table 1.

Descriptive Results

In 16,400 consecutive brain MRI examinations from research volunteers, 13,593/16,400 (83%) had normal findings, 2193/16,400 (13.3%) had abnormal findings but no follow-up was recommended, and 614/16,400 (3.7%) had abnormal findings with follow-up recommended (Fig 1). Among the 3250 volunteers recruited due to a known medical condition, 1948/3250 (60%) had normal findings, 1149/3250 (35%) had “abnormal findings without follow-up recommended,” and 153/3250 (5%) had abnormal findings with follow-up recommended.

Except as detailed below, changes commonly encountered in the general population were placed into the “normal/normal variant” category. This included paranasal sinus mucosal changes (*n* = 2891, 17.6%), prominent perivascular spaces (*n* = 2857,

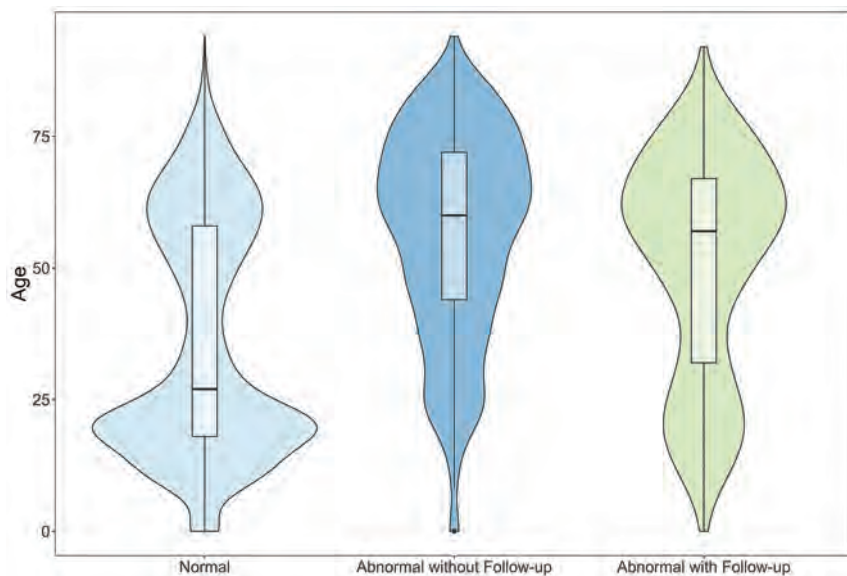


FIG 1. Violin plots stratified by scan category. Boxplots within each plot have medians and interquartile ranges. The median age and interquartile range of volunteers with normal examination findings were 28 and 42 years, respectively. The median age and interquartile range of volunteers with abnormal examination findings for which follow-up was not recommended were 61 and 27 years, respectively. The median age and interquartile range of volunteers with abnormal examinations for which follow-up was recommended were 58 and 37 years, respectively.

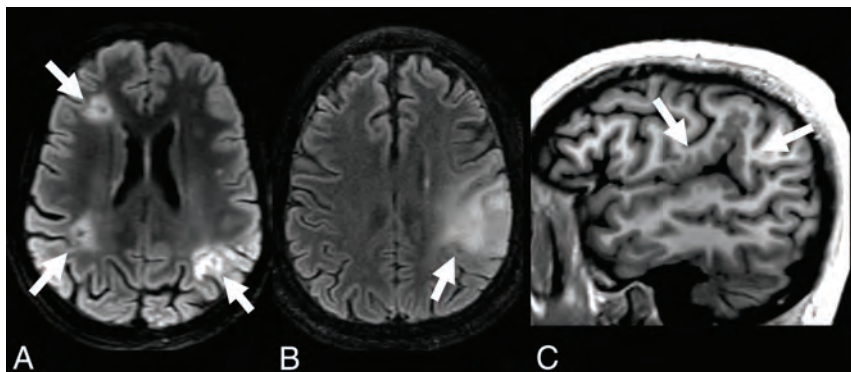


FIG 2. Illustrative cases of incidental findings for which clinical follow-up was recommended. Case examples of the 3 most frequently encountered abnormality categories, lesions marked by arrows, all reportedly asymptomatic at the time of scan. A, Vascular: a 38-year-old participant with trisomy 21 and normal scan findings 2 years earlier and found to have bihemispheric ischemic lesions, suspected to be cardioembolic versus Moyamoya vasculopathy (axial T2-FLAIR). B, Neoplastic: a 68-year-old participant with normal research scan findings 3 years earlier now has an infiltrative left parietal mass, later proven to be a glioblastoma (axial T2-FLAIR). C, Congenital: a 29-year-old participant with extensive left posterior Sylvian polymicrogyria (sagittal T1).

17.4%), pineal cysts ($n = 721$, 4.4%), arachnoid cysts ($n = 550$, 3.4%), uncomplicated developmental venous anomalies ($n = 509$, 3.1%), and low cerebellar tonsils that did not meet the Chiari I malformation criteria ($n = 358$, 2.2%).

WM changes were assessed with each volunteer's age and known risk factors in mind but were quantified only for some aging studies using the 10-point Cardiovascular Health Studies (CHS) score.⁷ Overall, 5089/16,400 (31%) volunteers were noted to have WM changes. Although most volunteers with WM changes were not prospectively scored using CHS methods, we

retrospectively estimated that most volunteers (4116/5089, 81%) had mild disease (CHS 2–4). A minority (973/5089, 19%) had moderate-to-severe WM disease (CHS 5–9); of these patients, 95/5089 (2%) were considered to have abnormal findings with follow-up recommended to assess treatable vascular risk factors. Developmental venous anomalies were considered abnormal only if they showed adjacent parenchymal changes including gliosis or cavernoma.

Scans recommended for follow-up were subcategorized by 2 independent reviewers on the basis of the most concerning finding in each examination (Online Supplemental Data). Vascular pathologies were most common (43%), and of these, WM hyperintensities were the leading cause for referral. Examples of scans with abnormal findings with follow-up recommended are shown in Fig 2. A detailed breakdown of findings is found in the Online Supplemental Data.

Disclosure of Potentially Serious Abnormalities

Reports were released only for abnormal scans with follow-up recommended. With rare exceptions, volunteers in the abnormal, follow-up category were first informed by telephone. Most “cold calls” were made by one of the neuroradiologists (H.A.R.) who is also board-certified in neurology. Volunteers were provided a brief, written report containing selected images. Results, reports, and recommendations were communicated to the participant's physician if requested in writing. Original data files were not released.

Abnormality Detection Analysis of Nonradiologists

Initial concerns at the time of scanning were noted for 133/16,400 (<1%) scans (Table 2). Overall, nonradiologists showed very low sensitivity to abnormalities, flagging only 52/2807 (2%) scans later considered to have abnormal findings by a neuroradiologist, regardless of whether follow-up was recommended. Among scans flagged by nonradiologists and confirmed to contain an abnormality, 22/52 (42%) contained an abnormality warranting further clinical evaluation. Therefore, nonradiologists detected 22/2807 (<1%) scans in which a clinically significant abnormality was confirmed and recommended for follow-up. Under the assumption that

Table 2: Comparison between concerns of nonradiologists about initial imaging versus impressions of neuroradiologists^a

	Incidental Finding Present	Incidental Finding Absent	
Nonradiologist concern present	52 (TP)	81 (FP)	PPV = 0.39
Nonradiologist concern absent	2807 (FN)	13,593 (TN)	NPV = 0.83
	Sensitivity = 0.02	Specificity = 0.99	

Note:—TP indicates true-positive; FP, false-positive; TN, true-negative; FN, false-negative.

^a PPV = TP/(TP + FP). NPV = TN/(FN + TN). Sensitivity = TP/(TP + FN). Specificity = TN/(TN + FP).

nonradiologist reviewers omitted comments if they considered a scan to have normal findings, nonradiologist reviewers demonstrated high specificity for examinations with normal finding (99%). Furthermore, nonradiologist reviewers demonstrated modest positive predictive value (39%) for examinations with confirmed abnormalities and good negative predictive value (83%) for examinations with normal findings.

Inferential Analysis

χ^2 tests for independence were performed to identify categorical variables significantly associated with scan category classification. The nominal level of significance $\alpha = .05$ was used as a threshold for statistical significance. Sex was not significantly associated with category classification ($P = .37$), while age dichotomized as “younger than 65” and “65 or older” was associated with category classification ($P < .001$). The Cramer V statistic was computed to determine the effect size of this association ($V = 0.16$), indicating a small effect. The highly statistically significant result from the χ^2 test most likely results from sample size versus the effect of age on category classification.

An ordinal logistic regression model was constructed to understand how sex and age affect scan classification. Male volunteers were more likely to be classified as having normal findings than female volunteers (log odds = -0.201 ; SE = 0.07; 95% CI, -0.34 to -1.14). Considering those with abnormal findings, young volunteers (younger than 65 years of age) were more likely to be recommended for follow-up than volunteers older than 65 years of age (log odds = 1.014; SE = 0.06; 95% CI, 0.89–1.14).

DISCUSSION

Incidental findings are previously unknown abnormalities of potential clinical significance discovered on research brain examinations that are unrelated to the research study aims and distinct from a volunteer’s clinical history. There is significant public interest in knowing the baseline prevalence of brain abnormalities, yet routine screening of brain MRIs for asymptomatic individuals has not been recommended.⁸ Furthermore, it is unclear whether expert review of research brain imaging examinations is prudent or if, instead, nonradiologists can detect abnormalities to facilitate expert review. Therefore, in 2002, the neuroradiology section at the University of Wisconsin Department of Radiology implemented a system for documenting incidental findings in research brain MRIs. As part of this initiative, nonradiologists were instructed to report any concerns at the time of scanning before formal interpretation by a neuroradiologist.

Consistent with other studies examining incidental findings in research MRIs, our study found about 4% of volunteers had at least 1 potentially serious brain abnormality.⁴ In a study examining incidental findings in 1867 healthy young adults, a

similar prevalence of potentially serious brain abnormalities was reported.⁶ However, we consider that the approach of the study for the detection of abnormalities was insufficient because some scans were screened only by nonexperts viewing only T1- and T2-weighted images; only after being flagged during this initial screening step would a scan undergo expert review by an experienced clinical neuroradiologist reviewing all acquired sequences. In contrast, in our study, every research volunteer underwent expert review of all sequences acquired per each specific study protocol.

Similar to the results of our study, an analysis of 2000 individuals older than 55 years of age from the Rotterdam Study (a prospective, population-based cohort study of age-related brain changes) found that the most common incidental findings were subclinical vascular pathologies and that the prevalence of abnormalities increased with age.² In contrast, while potential malignancies represented roughly half of incidental findings in a meta-analysis of studies with incidental findings,⁴ in our study, neoplastic phenomena were found in only 21% of MRIs recommended for follow-up. This discrepancy may be due to the emphasis on aging research at our institution, which could bias results toward nonspecific, age-associated WM hyperintensities.⁷ The authors of the Rotterdam Study claimed that a major strength of their study was its uniform MRI protocol, which indeed strengthens its internal validity. However, our study has greater external validity because of the variety of brain MRI protocols used across studies at our institution as well as the age range from infancy to elderly, reflecting the realistic heterogeneity of research neuroimaging protocols.

This study also examined and compared detection rates of abnormalities for all brain MRIs between nonradiologist reviewers and neuroradiologists. We prospectively collected this information to estimate how a workflow system using a selective “flag and refer” approach would compare with the “read every scan” approach. Our study found that nonradiologists flagged <2% of scans containing abnormalities, regardless of whether follow-up was recommended. However, among scans flagged and later confirmed to contain an abnormality, 22/52 (42%) were recommended for further clinical evaluation, demonstrating a poor PPV (22/133, 0.16) for flagging scans containing abnormalities warranting further evaluation. Nonradiologists were more likely to detect large abnormalities of variable clinical significance (eg, cystlike lesions, ventriculomegaly) and miss subtle, potentially serious abnormalities (eg, aneurysms, infiltrative gliomas) and virtually all head and neck pathology (eg, parotid tumors, pathologic cervical adenopathy). There were several cases flagged for innocuous findings (eg, cerebellar vermis cyst) and normal variant anatomy (eg, mega cisterna magna) that contained additional

undetected abnormalities (eg, ICA aneurysm). These results are expected on the basis of training and experience and particularly because the neuroradiologists' interpretations were considered ground truth. Ultimately, the results offer insight into the prevalence and characteristics of significant lesions that would be potentially missed by using a flag and refer screening approach alone.

In the United Kingdom Biobank study, a large-scale, multimodal (abdominal, cardiac, and brain MRI) population-based cohort study of adults 40–69 years of age examining incidental findings, radiographers were trained and tasked with identifying “incidental findings that might be clinically serious or life-threatening” for referral to a specialist radiologist to review.⁹ The workflow for detection of incidental findings was examined by comparing study findings with those in the systematic radiologist review of the first 1000 imaged participants. This study found that radiographers flagged 179/1000 (18%) scans for further review by a radiologist. Radiographers detected fewer overall incidental findings than the radiologists performing systematic review (18/1000, 1.8%, versus 179/1000, 17.9%, respectively) but a relatively greater percentage with serious final diagnoses (5/18, 28%, versus 21/179, 12%). Radiographers also missed 16/21 serious final diagnoses (false-negatives), whereas a systematic radiologist review led to many final diagnoses of doubtful clinical significance (158/179, false-positives).

There are 3 crucial caveats when comparing the United Kingdom Biobank study with our study. First, only the first 1000 participants' scans were systematically reviewed by radiologists and compared with radiographer impressions, whereas nonradiologist reviewers in our study had the opportunity to flag every scan and a neuroradiologist reviewed every scan regardless of whether it was flagged. Second, the multimodal nature of the United Kingdom Biobank study enables comparison of the abnormality detection rate for incidental findings throughout the body, whereas our study focused solely on those detectable by brain MRI. Last, our research protocols prevent verification of final diagnoses via supplemental diagnostic studies. When comparing studies, nonradiologist reviewers in the United Kingdom Biobank study flagged scans at greater rates (179/1000, 17.9%) versus our study (33/16,400, <1%). They also flagged scans in which abnormalities were detected and confirmed by radiologists at similar rates (21/179, 12%, versus 22/133, 16%). Overall, both studies demonstrated that nonradiologists flagged few scans with potentially serious abnormalities.

Our study has several limitations. First, we could not verify provisional neuroradiologic diagnoses on the basis of research brain scans, but these were, nonetheless, considered the ground truth. This issue is because subsequent clinical evaluations prompted by incidental findings were separate institutional review board–approved study activities and the anonymized research protocol forbade follow-up communication with participants receiving follow-up. Second, some participants were scanned more than once, potentially leading to overrepresentation of findings in any given volunteer. However, the authors estimated that fewer than 2000 participants were serially scanned. In the context of 16,400 volunteers, it is unlikely that serially scanned participants had a statistically significant impact

on summary results, and some serial scans revealed new significant findings, justifying independent analysis of all scans. Third, research brain MRIs are not performed for diagnostic purposes. Although acquired on high-quality MR imaging scanners and interpreted by neuroradiologists, research brain MRIs contain only the sequences necessary to suit the purpose of each study. Therefore, it is likely that some clinically significant brain abnormalities went undetected due to limited research imaging protocols.

Few protocols included MRA, resulting in a lower-than-expected detection rate for aneurysms in this large population. Conversely, “soft calls,” or provisional diagnoses based on limited information and/or with low confidence were more likely to occur out of caution on the part of the neuroradiologist interpreting each scan. Last, our discovery that nonradiologists showed very low sensitivity to abnormalities compared with neuroradiologists may be biased because nonradiologists knew that every scan underwent expert review. Accordingly, initial appraisals of scans by nonradiologists may have been more cursory and thus less sensitive compared with a scenario in which scans are expertly interpreted only on request. We emphasize that the comparison of nonradiologists with neuroradiologists was performed not to compare diagnostic performance per se but to help quantify the effect on discovery of significant lesions using either approach.

CONCLUSIONS

Incidental findings are previously unknown lesions of potential clinical significance found in brain MRIs performed for research volunteers. In a large series of research volunteers, incidental findings were found in roughly 4% of brain MRIs. The most common type of incidental finding was vascular disease followed by neoplastic and congenital lesions. When asked to note any concerning lesions on the initial image acquisition, scanning staff and research personnel flagged <2% of scans later found to contain at least 1 significant finding by neuroradiologists. Given the frequency of clinically relevant abnormalities coupled with a low abnormality detection rate by nonradiologists, routine neuroradiologist review of all research brain MRI scans should be considered to ensure that potentially serious abnormalities are detected.

ACKNOWLEDGMENTS

The authors gratefully acknowledge the other principal investigators whose studies contributed to the overall study population, including Drs Abercrombie, Busse, Dempsey, Afifi, Green, Ahearn, Ferrazzano, Lainhart, Oknowko, Alexander, Hermann, Li, Christian, Fleming, Herringa, Peppard, Rokers, Barnes, Cisler, Hubbard, Meyerand, Tononi, Gallagher, Travers, Cook, Pollak, Sanders, Nitschke, Whalen, and Fost. The authors also acknowledge the staff and research personnel at the Wisconsin Alzheimer Disease Research Center, Waisman Center, and the Lane Neuroimaging Laboratory. Most of all, the authors thank the research volunteers for their contributions to this work.

Disclosure forms provided by the authors are available with the full text and PDF of this article at www.ajnr.org.

REFERENCES

1. Illes J, Kirschen MP, Karetsky K, et al. **Discovery and disclosure of incidental findings in neuroimaging research.** *J Magn Reson Imaging* 2004;20:743–47 CrossRef Medline
2. Vernooij MW, Ikram MA, Tanghe HL, et al. **Incidental findings on brain MRI in the general population.** *N Engl J Med* 2007;357:1821–28 Medline
3. Li S, Fang F, Cui M, et al. **Incidental findings on brain MRI among Chinese at the age of 55–65 years: the Taizhou Imaging Study.** *Sci Rep* 2019;9:1–9 CrossRef Medline
4. Gibson LM, Paul L, Chappell FM, et al. **Potentially serious incidental findings on brain and body magnetic resonance imaging of apparently asymptomatic adults: systematic review and meta-analysis.** *BMJ* 2018;363:k4577 CrossRef Medline
5. Li Y, Thompson WK, Reuter C, et al; ABCD Consortium. **Rates of incidental findings in brain magnetic resonance imaging in children.** *JAMA Neurol* 2021;78:578–87 CrossRef Medline
6. Soumaré A, Beguedou N, Laurent A, et al. **Prevalence, severity, and clinical management of brain incidental findings in healthy young adults: MRI-Share Cross-Sectional Study.** *Front Neurol* 2021;12:675244 CrossRef Medline
7. Bryan RN, Manolio TA, Schertz LD, et al. **A method for using MR to evaluate the effects of cardiovascular disease on the brain: the Cardiovascular Health Study.** *AJNR Am J Neuroradiol* 1994;15:1625–33 Medline
8. Komotar RJ, Starke RM, Connolly ES. **Brain magnetic resonance imaging scans for asymptomatic patients: role in medical screening.** *Mayo Clin Proc* 2008;83:563–65 CrossRef Medline
9. Littlejohns TJ, Holliday J, Gibson LM, et al. **The UK Biobank imaging enhancement of 100,000 participants: rationale, data collection, management and future directions.** *Nat Commun* 2020;11:2624 CrossRef Medline

Phenotyping Superagers Using Resting-State fMRI

 L.L. de Godoy,  A. Studart-Neto,  D.R. de Paula,  N. Green,  A. Halder,  P. Arantes,  K.T. Chaim,  N.C. Moraes,  M.S. Yassuda,  R. Nitri,  M. Dresler,  C. da Costa Leite,  J. Panovska-Griffiths,  A. Soddu, and  S. Bisdas



ABSTRACT

BACKGROUND AND PURPOSE: Superagers are defined as older adults with episodic memory performance similar or superior to that in middle-aged adults. This study aimed to investigate the key differences in discriminative networks and their main nodes between superagers and cognitively average elderly controls. In addition, we sought to explore differences in sensitivity in detecting these functional activities across the networks at 3T and 7T MR imaging fields.

MATERIALS AND METHODS: Fifty-five subjects 80 years of age or older were screened using a detailed neuropsychological protocol, and 31 participants, comprising 14 superagers and 17 cognitively average elderly controls, were included for analysis. Participants underwent resting-state-fMRI at 3T and 7T MR imaging. A prediction classification algorithm using a penalized regression model on the measurements of the network was used to calculate the probabilities of a healthy older adult being a superager. Additionally, ORs quantified the influence of each node across preselected networks.

RESULTS: The key networks that differentiated superagers and elderly controls were the default mode, salience, and language networks. The most discriminative nodes (ORs > 1) in superagers encompassed areas in the precuneus posterior cingulate cortex, prefrontal cortex, temporoparietal junction, temporal pole, extrastriate superior cortex, and insula. The prediction classification model for being a superager showed better performance using the 7T compared with 3T resting-state-fMRI data set.

CONCLUSIONS: Our findings suggest that the functional connectivity in the default mode, salience, and language networks can provide potential imaging biomarkers for predicting superagers. The 7T field holds promise for the most appropriate study setting to accurately detect the functional connectivity patterns in superagers.

ABBREVIATIONS: ASSET = array spatial sensitivity encoding technique; BOLD = blood oxygen level-dependent; DMN = default mode network; ECN-L = executive control network left; ECN-R = executive control network right; EN = elastic net; ICA = independent component analysis; IPAT = integrated parallel acquisition technique; rs-fMRI = resting-state fMRI; OLS = ordinary least squares; SN = salience network

Ageing is an increasingly global phenomenon, usually accompanied by cognitive decline, with direct implications for the health care system and individuals' lives.¹ In this setting, subjects with superior memory performance in late life (80 years of age or older) stand out because they have a model capable of clarifying the brain mechanisms underlying cognitive resilience. These subjects have been identified as "superagers" in the literature.² To date, it is known that superagers show selective cortical preservation

in particular regions of the default mode network (DMN) and salience network (SN), overlapped by stronger functional connectivity, highlighting possible key hubs for memory and cognition.³⁻⁵ However, these studies included subjects from 60 years of age, which may be biased to obtain meaningful assertions about "youthful" memory performance in late life (80 years of age and older).⁶

Cognitive maintenance in older adults may reflect intrinsic functional integrity as a neurobiologic substrate.⁷ fMRI can play an important role in detecting key brain hubs sustaining youthful cognition, thereby contributing to understanding the most resilient brain areas in superagers. Moreover, alterations in the brain functional connectome were previously reported to provide biomarkers for age-related cognitive decline and Alzheimer disease.⁸

Received July 28, 2022; accepted after revision February 19, 2023.

From the Departments of Radiology and Oncology (L.L.d.G., P.A., K.T.C., C.d.C.L.) and Neurology (A.S.-N., N.C.M., M.S.Y., R.N.), Hospital das Clinicas, Faculdade de Medicina da Universidade de Sao Paulo, Universidade de Sao Paulo, Sao Paulo, Brazil; Lysholm Department of Neuroradiology (L.L.d.G., S.B.), The National Hospital of Neurology and Neurosurgery, and Department of Statistics (N.G.), University College London, London, UK; Donders Institute for Brain Cognition and Behavior (D.R.d.P., M.D.), Radboud University Medical Centre, Nijmegen, the Netherlands; Departments of Medical Biophysics (A.H.), and Physics and Astronomy (A.S.), University of Western Ontario, London, Ontario, Canada; The Big Data Institute and the Pandemic Sciences Institute (J.P.-G.), and The Queen's College (J.P.-G.), University of Oxford, Oxford, UK. Sotirios Bisdas, Andrea Soddu, and Jasmina Panovska-Griffiths contributed equally to this work.

Please address correspondence to Laiz Laura de Godoy, MD, Department of Radiology, Perelman School of Medicine at the University of Pennsylvania, 3400 Spruce St, Philadelphia, PA 19104; e-mail: laiz.godoy@penmedicine.upenn.edu; @SBisdas

 Indicates article with online supplemental data.
<http://dx.doi.org/10.3174/ajnr.A7820>

Resting-state fMRI (rs-fMRI) focuses on the temporal characteristics and spatial organization of spontaneous fluctuations of the blood oxygen level–dependent (BOLD) signal and is powerful for characterizing brain organization and its abnormalities. Because the discrepancies between superagers and cognitively average elderly controls may be modest-but-important to detect early changes in brain function, using an ultra-high-field rs-fMRI with increased spatial and temporal resolution may allow study of more subtle disruption.⁹ This is the first time that older adults with superior memory performance have been investigated at a 7T field.

In this study, we compared the differences in the resting-state functional connectivity between superagers and cognitively average elderly controls (elderly controls) in a range of neural networks with the aim of identifying the most discriminative networks and within-network nodes for predicting superagers. We additionally examined differences in the prediction probability of being a superager between the rs-fMRI data at 3T and 7T magnetic fields. We hypothesized that hub regions are critical to predicting youthful cognitive function in superagers, and the measurements of functional connectivity would be improved at a higher magnetic field.

MATERIALS AND METHODS

Selection of Participants

Initially, 55 participants were recruited from different centers in the city of Sao Paulo, Brazil, as detailed previously by de Godoy et al,¹⁰ and the neuropsychological tests were performed at the Department of Neurology of Hospital das Clinicas (Medical School of the University of Sao Paulo). Informed consent was obtained from each participant and the research project was approved by the Ethics Committee of the University of Sao Paulo (#62047616.0.0000.0068). The study was designed and conducted according to the Declaration of Helsinki.

The inclusion criteria for the participants were the following: 1) 80 years of age and older; 2) education of ≥ 4 years; 3) Mini-Mental State Examination scores normal for the individuals' education;^{11,12} 4) Functional Activity Questionnaire score of ≤ 4 ;¹³ 5) Clinical Dementia Rating score equal to zero; and 6) a result of the 15-question version of the Geriatric Depression Scale of ≤ 5 .

The exclusion criteria included the following: 1) a diagnosis of dementia or mild cognitive impairment according to the National Institute on Aging and Alzheimer's Association criteria;^{14,15} 2) a diagnosis of a major psychiatric disorder by the *Diagnostic and Statistical Manual of Mental Disorders, Fifth Edition*; 3) a history of alcohol or psychoactive drug abuse; 4) current or previous diagnosis of diseases of the CNS (ie, stroke or seizure); 5) the presence of structural lesions in the CNS on imaging that could distort the brain parenchyma (ie, tumor or brain malformation); and 6) visual and/or auditory limitations that impair the performance of cognitive tests.

The flow charts of participant selection and the neuropsychological tests performed are shown in Fig 1 and the Online Supplemental Data, respectively.

Neurocognitive Screening

The first assessment consisted of a semistructured interview with the collection of sociodemographic data; cognitive assessment

using the Mini-Mental State Examination, Montreal Cognitive Assessment, and the Brief Cognitive Screening Battery;¹⁶ screening for depressive symptoms and anxiety using the Geriatric Depression Scale-15 and the Geriatric Anxiety Inventory, respectively; and functional assessment with the Functional Activity Questionnaire and Clinical Dementia Rating.

Subsequently, the subjects who met the inclusion criteria underwent neuropsychological tests. The tests included the Forward and Backward Digit Span, Trail-Making A and B, Verbal Fluency (animals) and Letter Verbal Fluency tests, Rey-Osterrieth Complex Figure (copy and delayed recall), Logical Memory of the Wechsler Memory Scale, Rey Auditory Verbal Learning Test, 60-item version of the Boston Naming Test, and Estimated Intelligence Quotient measured with the Wechsler Adult Intelligence Scale, Third Edition. Those who performed equal or less than -1.5 SDs from average normative values adjusted by age and education for any cognitive test aforementioned were excluded.

Healthy Older Adult Grouping

Participants were separated into 2 groups: superagers ($n = 14$; mean age, 82.93 [SD, 3.47] years) and cognitively average elderly controls ($n = 17$; mean age, 84.47 [SD, 4.29] years). Superagers were defined as the participants who presented with a delayed recall score (30 minutes) in the Rey Auditory Verbal Learning Test, used as a measure of episodic memory, equal to or greater than average normative values for individuals 50–60 years of age (≥ 9 words), according to the criteria established by the Northwestern SuperAging research program.² In addition, to conform with these criteria, they had to perform at or above 1 SD of the average for their age and demographics for cognitive function in the non-memory domains tests, including Forward and Backward Digit Span, 60-item version of the Boston Naming Test, Trail-Making A, Trail-Making B, Rey-Osterrieth Complex Figure, and Verbal Fluency (animals) and Letter Verbal Fluency tests.^{17,18} The cognitively average elderly controls performed in memory and non-memory domains within 1 SD of the average range for their age and demographics, which means that they were average-performing older adults according to their cognitive status.

Imaging Data Acquisition

We acquired MR imaging data of 31 participants (14 superagers and 17 elderly controls) on a 3T scanner, whereas 21 of them (12 superagers and 9 elderly controls) were also imaged on a 7T scanner. The fewer subjects scanned at the 7T field were due to MR imaging safety concerns (eg, the presence of ferromagnetic aneurysm clips, pacemakers, and stents)¹⁹ and the safety measures in place during the coronavirus disease 2019 (COVID-19) pandemic.

The 3T MR imaging session was scheduled <1 month after the clinical and neuropsychological assessments. We used a Signa PET/MR imaging 3T scanner (GE Healthcare) with a 32-channel head coil. An anatomic whole-brain 3D T1-weighted scan was acquired with the parameters as follows: TR = 8 ms, TE = 3.2 ms, flip angle = 80° , array spatial sensitivity encoding technique (ASSET) factor = 1.5, FOV = 240×240 , matrix = 240×240 , and 180 slices of 1 mm each yielding a voxel size = $1 \times 1 \times 1$ mm during 5 minutes 16 seconds. rs-fMRI was acquired with a T2*-

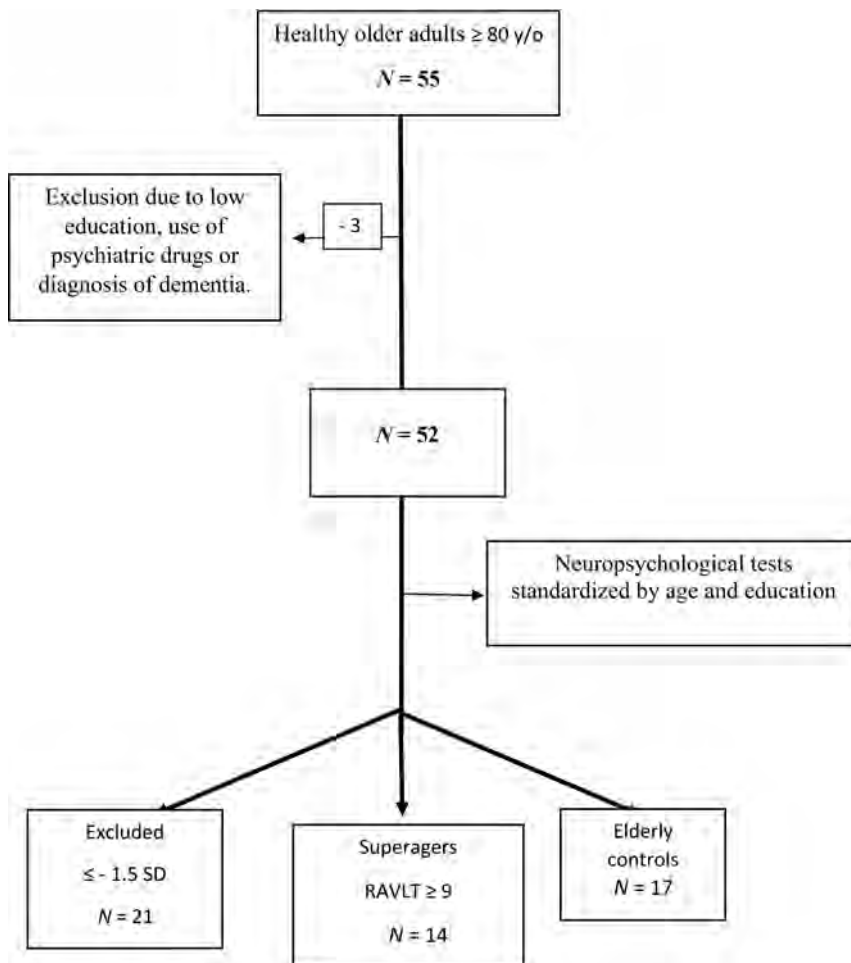


FIG 1. Flow chart of participant selection. RAVLT indicates the Rey Auditory Verbal Learning Test; y/o, years of age.

weighted echo-planar imaging sequence with the following parameters: TR = 2000 ms, TE = 30 ms, flip angle = 90°, FOV = 240 × 240, matrix = 80 × 80, section thickness = 3.6 mm (voxel size = 3 × 3 × 3.6 mm), number of slices = 36, gap = 0.4 mm, ASSET factor = 2.5. Although 208 volumes were acquired during 6 minutes 56 seconds, the first 4 volumes were discarded, so we had 204 volumes per subject.

The 7T MR imaging was performed after acquiring all the data on the 3T scanner and within 6 months after the clinical evaluation. We used a Magnetom 7T scanner (Siemens) with a 32-channel coil (Nova Medical). The 3D T1 image was acquired by the MP2RAGE technique with the following parameters: TR = 6000 ms, TE = 2.25 ms, flip angle = 4°/5°, TI = 800/2700 ms, integrated parallel acquisition technique (IPAT) = 3, FOV = 240 × 240, matrix = 320 × 320, and 256 slices, yielding an isotropic voxel size of 0.75 mm³ during 9 minutes 36 seconds. rs-fMRI was acquired with a T2*-weighted EPI multiband sequence, provided by the Center for Magnetic Resonance Research, with the following parameters: TR = 1500 ms, TE = 24 ms, flip angle = 70°, FOV = 210 × 210, matrix = 120 × 120, section thickness = 1.75 mm (isotropic voxel size = 1.75 mm³), number of slices = 81, no gap, multiband accel factor 3, IPAT = 2, and 250 volumes were acquired in 6 minutes 38 seconds.

During the rs-fMRI at 3T and 7T, participants were told to keep their eyes open while looking at a fixation cross. No cognitive tasks or tests were administered before the MR imaging session.

Brain Connectivity Analysis

rs-fMRI Preprocessing. The MR imaging DICOM files were entered into an automatic pipeline in GraphICA (<https://www.brainet.ca/>) (Online Supplemental Data).²⁰ Anatomic and functional images were kept in native space and preprocessed using FSL 6.03 (<http://www.fmrib.ox.ac.uk/fsl>).²¹ Preprocessing steps of the T1-weighted anatomic images included bias field correction, brain extraction, tissue-type segmentation (CSF, gray matter, white matter), and subcortical segmentation. On the functional data, we performed skull stripping, motion correction, section-timing correction, spatial smoothing (ceiling of 1.5 × voxel size), independent component analysis (ICA)-based Automatic Removal Of Motion Artifacts, high-pass filtering of 100 seconds, and nuisance regression of white matter and CSF.

Extraction of the Functional Networks. Graphica performs ICA with dual regression implemented in FSL.²¹ As a part of this process, a set of independent component maps were identified for each network, and dual regression

was implemented to identify subject-specific spatial maps using 11 resting-state network masks: auditory, DMN, executive control network left (ECN-L), executive control network right (ECN-R), hippocampal, language, SN, sensorimotor, visual lateral, visual medial, and visual occipital.

Regional Parcellation. Each subject's T1-weighted image was automatically segmented with a pipeline implemented in FreeSurfer (Version 7.1.0; <http://surfer.nmr.mgh.harvard.edu>). Further parcellation was performed with Graphica using a gradient-weighted Markov Random Field Model procedure described in Schaefer et al.²² The procedure yielded 832 parcellated brain regions, which were included as network nodes for further analyses.

Functional Network Construction and Thresholding. After we coregistered each of the functional resting-state networks to the subject, a mean *z* value was calculated by averaging the scalar map values of the voxel belonging to each one of the 832 ROIs. The resulting *z*-standardized correlation coefficients describe the loading of each nodal time course on the respective resting-state networks. To remove spurious or weak *z* values, for instance, due to noise, the loadings were thresholded with a data-driven mixture modeling approach at a single-subject level.²³

Global Properties. Global properties include the number of found, missing, and extra regions. These properties were calculated on the basis of template masks created and separated by sex for each one of the functional networks using healthy controls to create a baseline for the quality index and to exclude or keep the subjects on the basis of their motion. The data from healthy controls came from the Human Connectome Project²⁴ and Openneuro,²⁵ comprising 319 female subjects (mean age, 22.18 [SD, 25.19] years) and 482 male subjects (mean age, 25.05 [SD, 28.26] years). The number of found regions was defined as the regions with z values different from zero that survived the thresholding process. Missing regions were defined as the regions that have not been identified but do belong to the specific functional template mask. The number of extra regions was defined as regions that do not belong to the respective functional network template mask but were found.

$$\begin{aligned} \text{Regions (Belong Template Mask)} &= \text{Regions (Found)} \\ &+ \text{Regions (Missing)} - \text{Regions (Extra)}. \end{aligned}$$

Statistical Analysis

Classification Analysis. The whole-brain connectivity parcellation comprises 832 ROIs. To avoid overfitting in the regression model, we selected 6 key networks for successful aging,³⁻⁵ encompassing 397 distinct ROIs, with some ROIs overlapping the networks, including the DMN, SN, ECN-L, ECN-R, hippocampal, and language networks. Penalized regression analysis used these networks and within-network nodes to determine brain regions with statistical differences between superagers and cognitively average elderly controls.

Each of the ROIs, grouped within the specific 6 networks, was considered as a covariate in the penalized regression modeling in the following way: For a set of predictors $X = X_1, \dots, X_N$ with p measurements taken on each, and the response variable y , regression allows estimation of the coefficients β_i in the following linear regression model:

$$y = x_1\beta_1 + \dots + x_N\beta_N = X\beta.$$

The ordinary least squares (OLS) regression finds a set of β_i that minimize the sum-squared approximation error $(y - x\beta)^2$. However, in general, OLS solutions are often unsatisfactory because there is not a unique solution when $p \gg n$, and it is difficult to pinpoint which predictors are most relevant to the response. Various regularization approaches have been proposed in order to handle “large- p , small- n ” data sets and to avoid overfitting, such as LASSO (Least Absolute Shrinkage and Selection Operator) and ridge regression, or a combination of both. Elastic Net (EN) addresses these shortcomings since variable selection is embedded into their model-fitting process. These methods were previously applied to a similar problem, with results suggesting that the EN regression was a more robust approach to extreme correlations among the predictors.²⁶ Briefly, sparse regularization methods include the L1-norm regularization on the coefficients, which is known to produce sparse solutions, ie, solutions with many zeros, thus eliminating predictors that are not essential.

For the analysis here, we used the EN regression that finds an optimal solution to the OLS problem objective, augmented with

additional regularization terms that include the sparsity-enforcing. Specifically, there are 2 types of regularizations that EN allows: L1-norm constraint on the regression coefficients that penalizes the absolute size and “shrinks” some coefficients to zero, and a “grouping” L2-norm constraint, which penalizes the squared size of the coefficients and enforces similar coefficients on predictors that are highly correlated with each other, which L1-constraint alone does not provide. Formally, EN regression optimizes the following function,

$$L(\lambda_1, \lambda_2; \beta) = (y - x\beta)^2 + \lambda_1\|\beta\|_1 + \lambda_2\|\beta\|_2,$$

where λ_1 is L1-penalty term and λ_2 is the quadratic penalty term.

In our case, for each of the networks, we let y be a binary outcome of either being a superager or an elderly control and X consisted of 397 covariate measurements representing the regions (nodes) across the 6 neural networks. We modeled the relationship as,

$$\text{logit}(p^i) = X^i\beta^i, \quad i = 1, 2, \dots, n.$$

Model Prediction and Classification. Using these models, we calculated the expected probabilities of an individual being a superager predicted from the penalized regression model using the measurements of the network and plotted this as an outcome (on the y -axis) versus the binary observed values of the individual being either an elderly control or superager to evaluate the prediction performance of the model (Fig 2). The diagonal lines in Fig 2 represent the mean difference between predicted probabilities for superagers and elderly controls. The prediction model can be thought of as an OLS linear regression,

$$\underline{p}_{control} + (\underline{p}_{superager} - \underline{p}_{control})^s,$$

where s is the observed data superager indicator variable, \underline{p}_x is the mean predicted probability of being a superager for the observed group (either control or superager), and $\underline{p}_{superager} - \underline{p}_{control}$ is the slope of the line, which indicates the discriminatory ability of the model. Larger values demonstrate better performance (steeper lines), and zero corresponds to no predictive ability with a horizontal line for that network.

Quantification of Regression Analysis Results. We used the regression models in Equation $\text{logit}(p^i) = X^i\beta^i, \quad i = 1, 2, \dots, n$ to infer the ORs describing the difference between the odds of exposure in each network and region (node) among superagers and elderly controls. In our study, they can be interpreted as a measure of the relative influence of a network and region within on the likelihood of being a superager. We obtained the ORs using the fitted models to give an average comparison between individuals with or without a unit increase in a particular region j ; if p is the probability of being a superager then,

$$\text{OR}_j = \frac{p_j/(1-p_j)}{p/(1-p)} = \exp(\beta_j).$$

We used the ORs to quantify the influence of each region within each of the 6 networks. We identified the regions with the

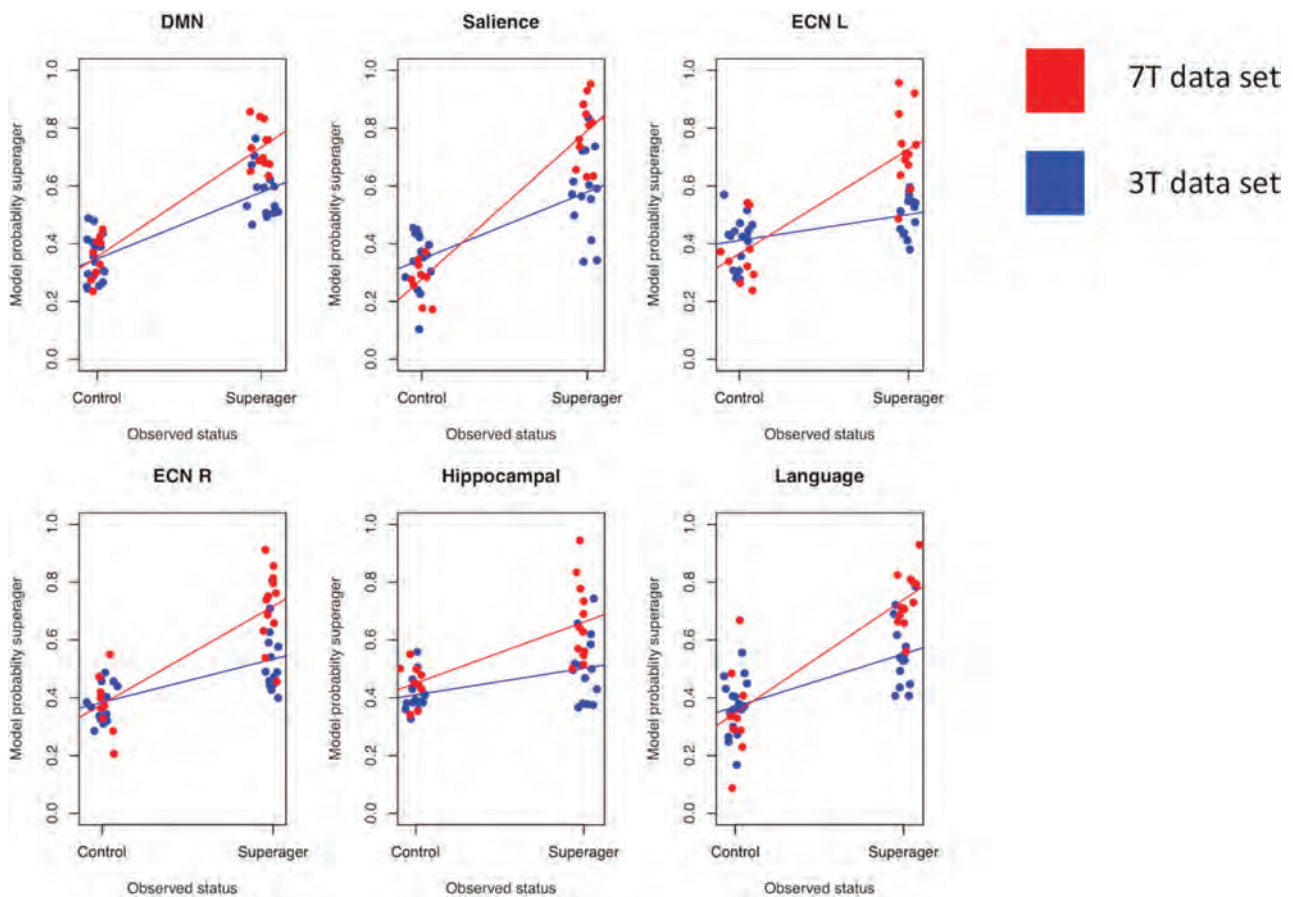


FIG 2. Plots showing the classification results for superagers across several networks examined on 3T and 7T fields. These plots show the observed superager status for each participant (*blue and red dots*) plotted against the probability of being a superager predicted from the fitted model. The *diagonal lines* represent the mean difference between predicted probabilities for superagers and elderly controls. The steeper the gradient of the lines, the higher the superagers' prediction.

ORs that are >1 to be the regions that are most differentiable/discriminative between superagers and elderly controls. If the OR values were equal to 1 ($OR = 1$), there was no discrimination in the examined regions between groups. Finally, if the OR values were <1 , the regions negatively discriminated the examined region as characteristic for a superager. We noted that the P value was not generated from this analysis but the significance of the influence from a network/region could be inferred from the 95% CI for an OR.²⁷

Because the number of variables in the model was very large, the maximum number of nonzero variables was limited to 10. For the analyses, we used the statistical programming language R (<https://cran.r-project.org/web/packages/glmnet>) and the package `glmnet`.²⁶

RESULTS

Demographics and Neuropsychological Performance Scores

Superagers and elderly controls did not differ in terms of age ($P = .304$), education ($P = .299$), or sex distribution ($P = .224$). Superagers had statistically significantly better performance compared with elderly controls in the Montreal Cognitive Assessment ($P = .003$) and some episodic memory tests, including the Delayed-Recall Brief Cognitive Screening Battery ($P = .036$), Delayed-Recall Rey Auditory Verbal Learning Test ($P < .001$), and

Logical Memory Delayed-Recall ($P = .01$) (Online Supplemental Data).

Discriminative Networks and Brain Nodes for Predicting Superagers

The lollipop plots (as an alternative to bar charts) in Fig 3 show the magnitude (dot) and the range (line) of the nodes within each network that are discriminative between superagers and elderly controls. Here $ORs > 1$ suggest nodes that are more likely to be different in superagers (ie, larger influence on the predicted probability of being a superager) and are illustrated by lollipops in green. Conversely, nodes with $ORs < 1$ are less likely to be different in superagers (ie, these regions are negatively discriminated as a characteristic of a superager) and are illustrated by lollipops in red.

When we used the 3T and 7T data sets, though all networks were overall distinct in superagers compared with elderly controls (Fig 2), some of them were more differentiable and predictive of superagers than others. For example, for the 3T data (Fig 3A), the ORs for the SN and language networks were >1 across some regions, with relatively good predictive performance (Fig 2), suggesting that these regions were discriminative in superagers. In contrast, the ECN-L presented only a few regions of $ORs > 1$ and others with $ORs < 1$, showing a poor predictive performance. For the 7T data analysis (Fig 3B), the lollipop plots in most

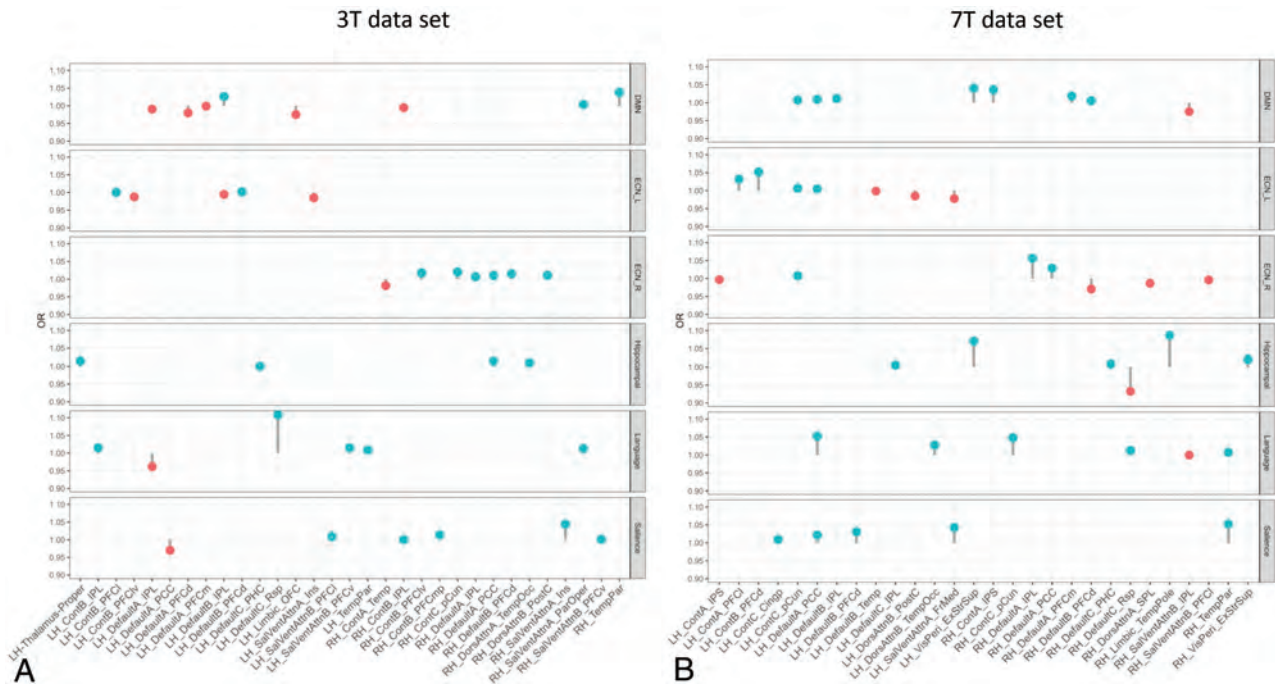


FIG 3. The lollipop plots in the 3T data set (A) and the 7T data set (B) indicate the nodes within networks that can differentiate superagers from elderly controls. Within the plots, we show the magnitude (dot) and the range (line) of the difference between superagers and elderly controls. ORs of >1 ($OR > 1$) suggest a larger influence on the predicted probability of being a superager (lollipops in green). ORs of < 1 indicate regions negatively discriminated as characteristic of a superager (lollipops in red). Cingp indicates posterior cingulate cortex; ContA, control A; ContB, control B; ContC, control C; DorsAttnA, dorsal attention A; DorsAttnB, dorsal attention B; ExStrSup, extrastriate superior cortex; FrMed, frontal medial cortex; Ins, insula; IPL, inferior parietal lobule; IPS, intraparietal sulcus; LH, left hemisphere; OFC, orbital frontal cortex; ParOper, parietal operculum; PCC, precuneus posterior cingulate cortex; pCun, precuneus; PHC, parahippocampal cortex; PFCd, dorsal prefrontal cortex; PFCl, lateral prefrontal cortex; PFCvl, lateral ventral prefrontal cortex; PFCm, medial prefrontal cortex; PFCmp, medial posterior prefrontal cortex; PFCv, ventral prefrontal cortex; PostC, postcentral cortex; RH, right hemisphere; Rsp, retrosplenial cortex; SalVentAttnA, salience/ventral attention A; SalVentAttnB, salience/ventral attention B; SPL, superior parietal lobule; Temp, temporal cortex; TempPar, temporoparietal junction; TempPole, medial temporal pole; TempOcc, temporo-occipital junction; VisPeri, peripheral visual.

networks had $ORs > 1$ across several nodes and great predictive performance, characterized by a steeper slope of the diagonal lines in Fig 2. The DMN, SN, hippocampal, and language networks were the most discriminative networks in our model prediction classifier for the 7T data set. In addition, for the 7T magnetic field, we had improved sensitivity in detecting a higher number of essential regions within each network. Therefore, on the basis of the classification algorithm, when differentiating superagers from elderly controls, we were more confident using the model fit from the 7T rather than the 3T scanner.

The Online Supplemental Data delineate the anatomic space of each network studied (networks masks). Figures 4, 5, and 6 illustrate the nodes within each network in brain maps, with OR values > 1 , which predict superagers for the 3T and 7T data sets (Online Supplemental Data). We used Montreal Neurological Institute coordinates to plot the nodes and heatmaps, varying from dark blue to dark red (OR values furthest away from 1 have higher superager prediction), to demonstrate the discriminative power of each node. The Online Supplemental Data show the elastic model results for the 3T and 7T data sets for all ROIs included.

DISCUSSION

In this study, we identified functional networks showing that superagers exhibited distinct intrinsic connectivity compared with

elderly controls in a range of brain networks and the core networks predicting a superager were the DMN, SN, and language. Areas in the precuneus posterior cingulate cortex, prefrontal cortex, temporoparietal junction, temporal pole, extrastriate superior cortex, and insula were the most discriminative nodes within these networks. By exploring the 7T and the 3T data sets separately, we could demonstrate higher prediction task confidence in rs-fMRI data sets acquired with the 7T rather than with the 3T scanner.

During the past years, clinical fMRI at 7T has gained traction²⁸ because it offers a beneficial increased SNR and BOLD contrast over conventional 1.5T and 3T MR imaging scanners,^{29,30} translated into a greatly enhanced spatial resolution of functional activity, the main clinical advantage of 7T fMRI.^{31,32} A prior study³³ demonstrated up to 300% improvement in the temporal SNR and resting-state functional connectivity coefficients provided by ultra-high-field 7T fMRI compared with 3T, indicating enhanced power for the detection of functional neural architecture. We have shown that the higher BOLD contrast-to-noise ratio available at 7T yielded improved sensitivity in detecting differences in the activity across all networks compared with the 3T field, reflected by a steeper gradient of the lines in the prediction classification algorithm. Moreover, higher ORs ($OR > 1$) were observed across several nodes for the 7T compared with the 3T data set. These differences imply that 7T scanners may facilitate

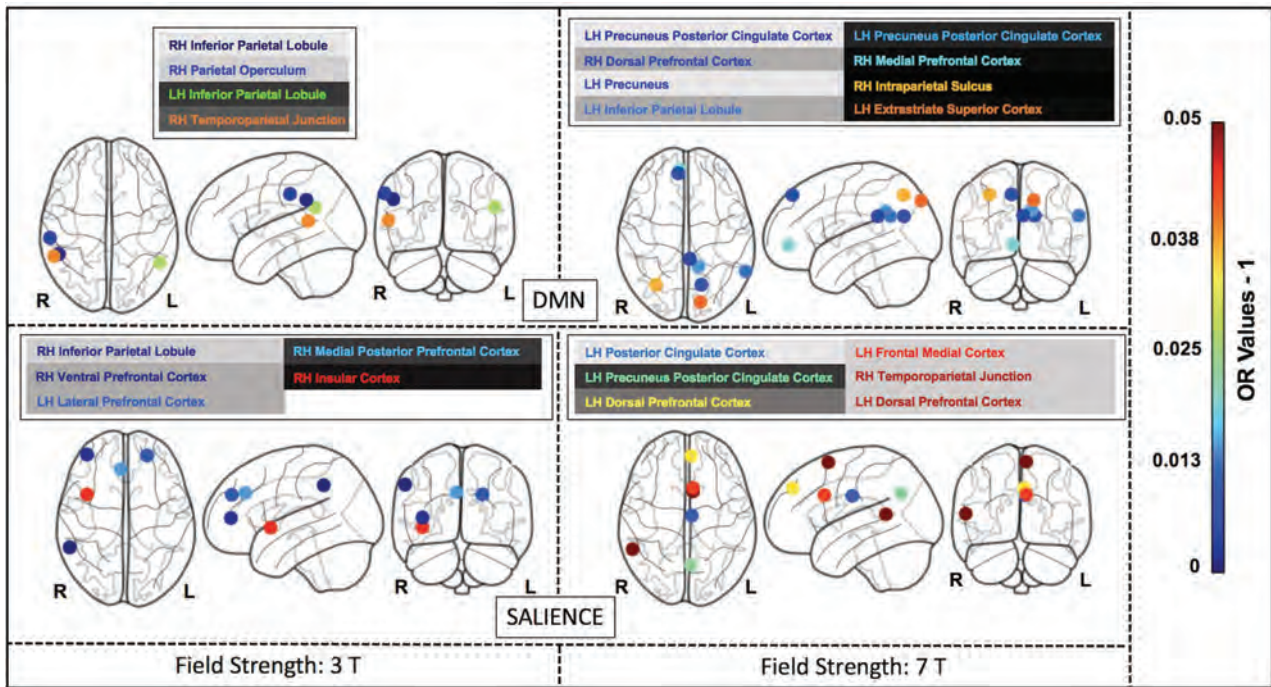


FIG 4. The most discriminative nodes among the DMN and SN in superagers compared with elderly controls. The heatmap varies from dark blue to dark red (denoting a higher prediction rate for classification as a superager using ORs). RH indicates right hemisphere; LH, left hemisphere; L, left; R, right.

high-quality connectivity measurements capturing stronger evoked rs-fMRI responses, hence offering potentially greater group-level power. This possibility raises our confidence for the results of the within-network nodes and overall model fit from the 7T scanner. Therefore, in the discussion below, the discriminatory nodes for identifying superagers at the 7T data set are emphasized more.

In line with previous studies including successful agers from 60 years of age,^{4,34} we have found important features for predicting superagers in the DMN and SN. The DMN is implicated in memory encoding, storage, and retrieval, while the SN is believed to be associated with executive processes and detecting emotionally relevant stimuli, as well as alerting.⁵ In parallel, normal aging is associated with decreased signal complexity within the DMN and SN nodes,³⁵ and there is a disrupted variability in these networks in mild cognitive impairment and Alzheimer disease.³⁶ It stands to reason that the DMN and SN hubs may potentially provide valid and reliable biomarkers for early age-related cognitive decline.

Beyond the classic hubs of the DMN and SN, we also found discriminative nodes within the ECN-L/R, language, and hippocampal networks for predicting a superager among elderly controls. The ECN is generally involved in tasks relying on executive functions, such as the control process and working memory.³⁷ The hippocampal network plays an important role in the consolidation of short-term memory and spatial memory.³⁸ The language network, a critical connectome in our model, encompasses regions of the Broca (inferior frontal) and Wernicke (superior temporal with extension into the inferior parietal cortex) areas³⁹ and has not been previously investigated in understanding the superior preservation of cognitive abilities. Although our groups did not show significant differences in verbal fluency tests,

modifications in the language functional connectivity may anticipate changes in language performance in healthy older adults. Moreover, it is well-known that the language network can accurately discriminate patients with mild cognitive impairment from healthy controls⁴⁰ and is also known to demonstrate weaker functional connectivity in Alzheimer disease.⁴¹

The nodes with superior importance for predicting superagers encompassed areas in the extrastriate superior cortex, precuneus posterior cingulate cortex in both hemispheres; inferior parietal lobule, the temporoparietal junction, intraparietal sulcus, and medial temporal pole in the right brain hemisphere; and the prefrontal/dorsal prefrontal cortex, temporo-occipital junction, and retrosplenial cortex in the left hemisphere. Most interesting, most of these cortical nodes presented with stronger intrinsic functional connectivity^{4,34} and volumetric preservation,^{5,42,43} akin to features of younger adults in previous studies.³ These nodes also have been considered as key brain functional hubs for diverse cognitive functions and information integration among segregated functional networks.⁴⁴

Our results indicate that the posterior cingulate cortex, a region mainly engaged in episodic memory,⁴⁵ plays a crucial role. Our previous study on superagers¹⁰ showed a higher total NAA concentration in superagers than in elderly controls in the posterior cingulate cortex, reflecting a metabolically active brain region contributing to superior cognition in late life. Therefore, the functional and metabolic features of this structure observed in our cohort may underlie the superagers' significantly higher scores in the episodic memory tests. The prefrontal cortex, one of the most discriminative nodes in our cohort, is known to be associated with executive functions (planning, decision-making) and

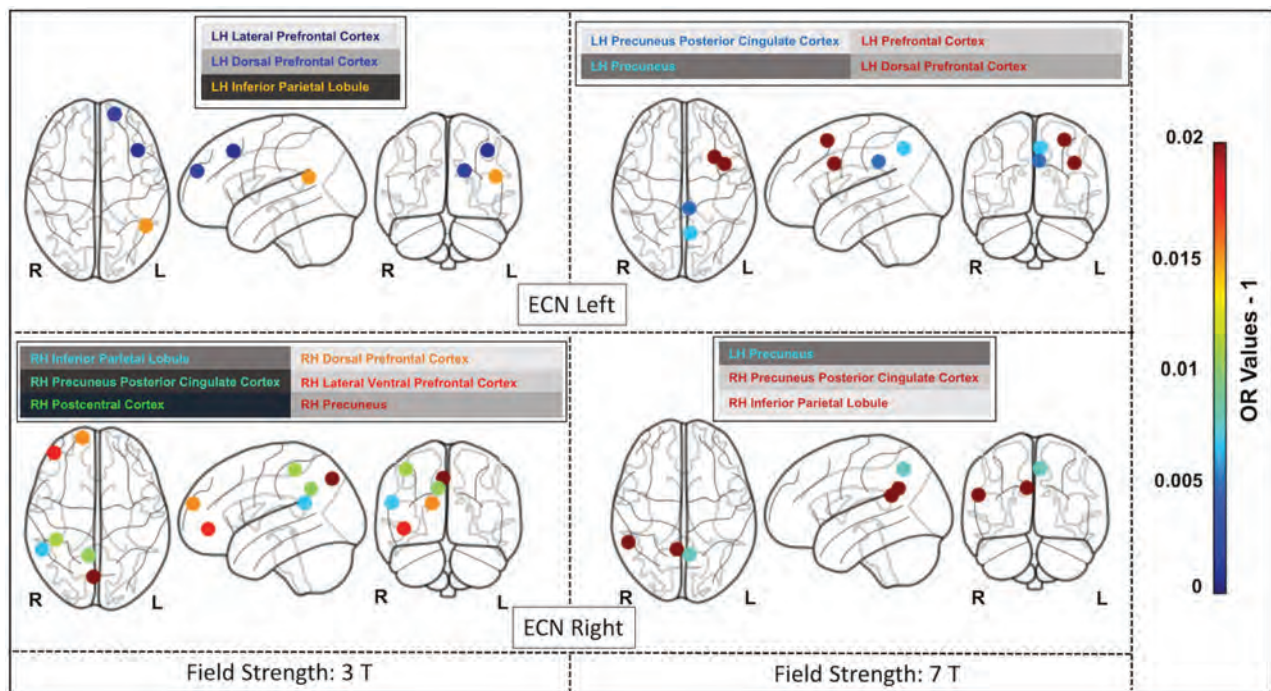


FIG 5. The most discriminative nodes among the ECN-L and ECN-R in superagers compared with elderly controls. The heatmap varies from dark blue to dark red (denoting a higher prediction rate for classification as a superager using ORs). RH indicates right hemisphere; LH, left hemisphere; L, left; R, right.

social-cognitive processes.⁴⁶ Another powerful discriminatory node, the right temporoparietal junction, is engaged in the social domain (empathy, sympathy) and self-evaluating behavior.⁴⁷ It was previously observed that superagers present with an increased level of positive relations with others, defined by truthfulness and satisfaction, and they manage stress better.⁴⁸

Among the discriminative nodes from the classifier, the inferior parietal cortex is known to be involved in semantic processing and attention.⁴⁹ The insula contributes to various brain functions through the integration of sensory, emotional, and cognitive information.⁵⁰ Moreover, the extrastriate superior cortex, involved in visual-processing information, plays an important role in the DMN and hippocampal networks.⁵¹ These nodes highlight how structures not directly involved with memory can contribute to superior memory performance.

Our study has a number of limitations. Our cohort was small due to the constraints in data collection and for prioritizing a rigorous selection protocol, preventing splitting the data set into training and validation samples. Also, the individuals scanned at 7T were a subset of those scanned at 3T due to patient contraindication heightened at 7T. Because for each individual, there were hundreds of measurements introducing a risk of overfitting, the penalized regression methodology was selected. The results should be seen as a contribution to the field and not definitive, because we aimed to investigate the signal that can be found in the data set in the presence of a low number of subjects and possible measurement error. The regression method used did not generate significant *P* values; however, even if we used standardized methodologies, these would have to be caveated. Moreover, we compared superagers with cognitively healthy older adults, reflecting early and subtle age-related cognitive functional changes; therefore, remarkable differences would not be expected.

The increased spatial resolution of BOLD on 7T and secondary higher detection of intrasubject variability can overestimate the intragroup differences in a small sample size.⁵² There are also problems concerning B_0 and B_1 inhomogeneity created by higher field strengths, resulting in geometric distortion and drop-out, respectively, demanding advanced shimming and specialized pulse sequence designs.⁵³ The shorter TE (7T: 24 ms versus 3T: 30 ms), thinner slices (7T: 1.75 mm versus 3T: 3.6 mm), and parallel imaging can avoid some of these issues by reducing intravoxel inhomogeneity and through-plane dephasing.^{53,54} The present study also had constraints regarding differences in acquisition protocols between the 3T and 7T scanners. First, the voxel size was different in 7T (isotropic voxel size = 1.75 mm³) compared with 3T (voxel size = 3 × 3 × 3.6 mm). The precision of the whole-brain functional connectivity maps shown in this study may have been impacted by the smaller voxel size of the 7T protocol compared with 3T.⁵⁵ The TR was also longer at 3T (TR = 2000 ms) compared with 7T (TR = 1500 ms), indicating that the number of frames was higher for 7T for the same scan time. The higher number of frames is expected to improve the temporal resolution of the 7T scan compared with 3T. Ultimately, the acceleration factor was higher at 7T (multiband acceleration factor 3, IPAT 2) compared with 3T (ASSET factor 2.5), which can reduce signal distortion, signal drop-out, and partial volume effects but can also increase motion sensitivity and reduce the SNR.^{29,56} Even though we highlight advancements in numerous metrics, including temporal SNR, sensitivity to detect connectivity measurements, and whole-brain connectivity maps for the data set at 7T compared with 3T, some results may be affected by differences in acquisition protocols and different scanners.

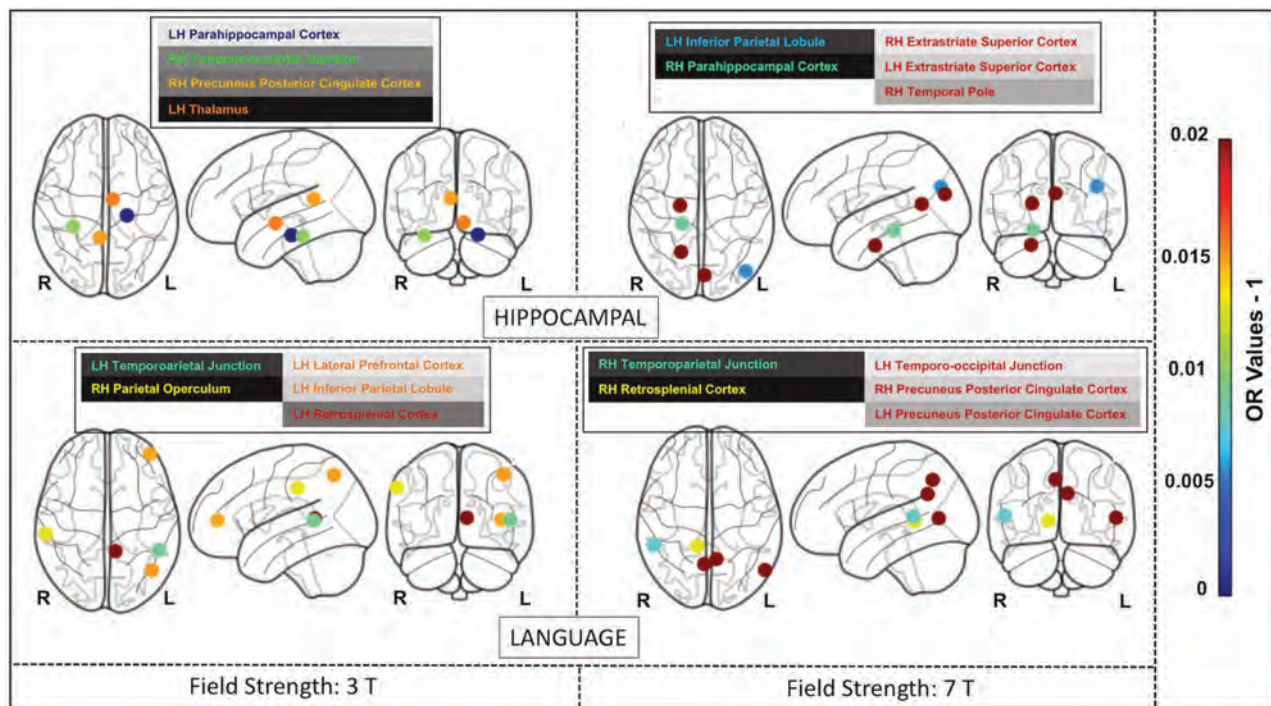


FIG 6. The most discriminative nodes among the hippocampal and language networks in superagers compared with elderly controls. The heatmap varies from dark blue to dark red (denoting a higher prediction rate for classification as a superager using ORs). RH indicates right hemisphere; LH, left hemisphere; L, left; R, right.

CONCLUSIONS

Our findings indicated that rs-fMRI may be a useful technique in assessing youthful memory performance in late life and identifying potential superagers, particularly in nodes among the DMN, SN, and language network. Our results highlight the benefit of 7T over the 3T magnetic field scanners for this diagnostic and classification task and warrant further validation in larger prospective studies.

ACKNOWLEDGMENTS

We thank Camila de Godoy Carneiro, MSc; Artur M. Coutinho, MD, PhD; and Carlos A. Buchpiguel, MD, PhD, for the collaboration in the development of this project.

Disclosure forms provided by the authors are available with the full text and PDF of this article at www.ajnr.org.

REFERENCES

- Onoda K, Ishihara M, Yamaguchi S. Decreased functional connectivity by aging is associated with cognitive decline. *J Cogn Neurosci* 2012;24:2186–98 CrossRef Medline
- Rogalski EJ, Gefen T, Shi J, et al. Youthful memory capacity in old brains: anatomic and genetic clues from the Northwestern SuperAging Project. *J Cogn Neurosci* 2013;25:29–36 CrossRef Medline
- de Godoy LL, Alves CA, Saavedra JS, et al. Understanding brain resilience in superagers: a systematic review. *Neuroradiology* 2021;63:663–83 CrossRef Medline
- Park CH, Kim BR, Park HK, et al. Predicting superagers by machine learning classification based on the functional brain connectome using resting-state functional magnetic resonance imaging. *Cereb Cortex* 2022;32:4183–90 CrossRef Medline
- Sun FW, Stepanovic MR, Andreano J, et al. Youthful brains in older adults: preserved neuroanatomy in the default mode and salience

- networks contributes to youthful memory in superaging. *J Neurosci* 2016;36:9659–68 CrossRef Medline
- Rogalski EJ. Don't forget—age is a relevant variable in defining SuperAgers. *Alzheimers Dement (Amst)* 2019;11:560–61 CrossRef Medline
- Wang X, Ren P, Baran TM, et al; Alzheimer's Disease Neuroimaging Initiative. Longitudinal functional brain mapping in supernormals. *Cereb Cortex* 2019;29:242–52 CrossRef Medline
- Mevel K, Chételat G, Eustache F, et al. The default mode network in healthy aging and Alzheimer's disease. *Int J Alzheimers Dis* 2011;2011:1–9 CrossRef Medline
- Raimondo L, Oliveira LAF, Heij J, et al. Advances in resting state fMRI acquisitions for functional connectomics. *Neuroimage* 2021;243:118503 CrossRef Medline
- de Godoy LL, Studart-Neto A, Wylezinska-Arridge M, et al. The brain metabolic signature in superagers using in vivo ¹H-MRS: a pilot study. *AJNR Am J Neuroradiol* 2021;42:1790–97 CrossRef Medline
- Folstein MF, Folstein SE, McHugh PR. Mini-Mental State: a practical guide for grading the mental state of patients for the clinician. *J Psychiatr Res* 1975;12:189–98 CrossRef Medline
- Brucki S, Nitrini R, Caramelli P, et al. Suggestions for utilization of the Mini-Mental State Examination in Brazil [in Portuguese]. *Arq Neuropsiquiatr* 2003;61:777–81 CrossRef Medline
- Pfeffer RI, Kurosaki TT, Harrah CH Jr, et al. Measurement of functional activities in older adults in the community. *J Gerontol* 1982;37:323–29 CrossRef Medline
- McKhann GM, Knopman DS, Chertkow H, et al. The diagnosis of dementia due to Alzheimer's disease: recommendations from the National Institute on Aging-Alzheimer's Association workgroups on diagnostic guidelines for Alzheimer's disease. *Alzheimers Dement* 2011;7:263–69 CrossRef Medline
- Albert MS, DeKosky ST, Dickson D, et al. The diagnosis of mild cognitive impairment due to Alzheimer's disease: recommendations from the National Institute on Aging-Alzheimer's Association workgroups on diagnostic guidelines for Alzheimer's disease. *Alzheimers Dement* 2011;7:270–79 CrossRef Medline

16. Nittrini R, Caramelli P, Porto CS, et al. **Brief cognitive battery in the diagnosis of mild Alzheimer's disease in subjects with medium and high levels of education.** *Dement Neuropsychol* 2007;1:32–36 CrossRef Medline
17. Heaton RK, Miller SW, Taylor MJ, et al. **Revised comprehensive norms for an expanded Halstead-Reitan Battery: demographically adjusted neuropsychological norms for African American and Caucasian adults.** *PAR*. 2004. <https://www.parinc.com/Products/Pkey/357>. Accessed April 10, 2022
18. Shirk SD, Mitchell MB, Shaughnessy LW, et al. **A web-based normative calculator for the uniform data set (UDS) neuropsychological test battery.** *Alzheimers Res Ther* 2011;3:32 CrossRef Medline
19. Kraff O, Quick HH. **7T: Physics, safety, and potential clinical applications.** *J Magn Reson Imaging* 2017;46:1573–89 CrossRef Medline
20. Ribeiro de Paula D, Ziegler E, Abeyasinghe PM, et al. **A method for independent component graph analysis of resting-state fMRI.** *Brain Behav* 2017;7:e00626 CrossRef Medline
21. Nickerson LD, Smith SM, Öngür D, et al. **Using dual regression to investigate network shape and amplitude in functional connectivity analyses.** *Front Neurosci* 2017;11:115 CrossRef Medline
22. Schaefer A, Kong R, Gordon EM, et al. **Local-global parcellation of the human cerebral cortex from intrinsic functional connectivity MRI.** *Cereb Cortex* 2018;28:3095–114 CrossRef Medline
23. Bielczyk NZ, Llera A, Buitelaar JK, et al. **Increasing robustness of pairwise methods for effective connectivity in magnetic resonance imaging by using fractional moment series of BOLD signal distributions.** *Netw Neurosci* 2019;3:1009–37 CrossRef Medline
24. Van Essen DC, Smith SM, Barch DM, et al; WU-Minn HCP Consortium. **The WU-Minn Human Connectome Project: an overview.** *Neuroimage* 2013;80:62–79 CrossRef Medline
25. Snoek L, van der Miesen M, van der Leij A, et al. **AOMIC-PIOP1.** *Openneuro*. July 21, 2020. <https://doi.org/10.18112/OPENNEURO.DS002785.V2.0.0>. Accessed December 10, 2022
26. Friedman J, Hastie T, Tibshirani R. **Regularization paths for generalized linear models via coordinate descent.** *J Stat Softw* 2010;33:1–22 Medline
27. Bland JM, Altman DG. **Statistics notes: the odds ratio.** *BMJ* 2000;320:1468 CrossRef Medline
28. Isaacs BR, Mulder MJ, Groot JM, et al. **3 versus 7 Tesla magnetic resonance imaging for parcellations of subcortical brain structures in clinical settings.** *PLoS One* 2020;15:e0236208 CrossRef Medline
29. Beisteiner R, Robinson S, Wurnig M, et al. **Clinical fMRI: evidence for a 7T benefit over 3T.** *Neuroimage* 2011;57:1015–21 CrossRef Medline
30. van der Zwaag W, Francis S, Head K, et al. **fMRI at 1.5, 3 and 7 T: characterising BOLD signal changes.** *Neuroimage* 2009;47:1425–34 CrossRef Medline
31. Colizoli O, de Gee JW, van der Zwaag W, et al. **Comparing fMRI responses measured at 3 versus 7 Tesla across human cortex, striatum, and brainstem.** May 14, 2020. *bioRxiv*. <https://doi.org/10.1101/2020.05.12.090175>. Accessed April 15, 2022
32. Hale JR, Brookes MJ, Hall EL, et al. **Comparison of functional connectivity in default mode and sensorimotor networks at 3 and 7T.** *MAGMA* 2010;23:339–49 CrossRef Medline
33. Morris LS, Kundu P, Costi S, et al. **Ultra-high field MRI reveals mood-related circuit disturbances in depression: a comparison between 3-Tesla and 7-Tesla.** *Transl Psychiatry* 2019;9:94 CrossRef Medline
34. Zhang J, Andreano JM, Dickerson BC, et al. **Stronger functional connectivity in the default mode and salience networks is associated with youthful memory in superaging.** *Cereb Cortex* 2020;30:72–84 CrossRef Medline
35. Grady C, Sarraf S, Saverino C, et al. **Age differences in the functional interactions among the default, frontoparietal control, and dorsal attention networks.** *Neurobiol Aging* 2016;41:159–72 CrossRef Medline
36. Zhang L, Zuo XN, Ng KK, et al. **Distinct BOLD variability changes in the default mode and salience networks in Alzheimer's disease spectrum and associations with cognitive decline.** *Sci Rep* 2020;10:6457 CrossRef Medline
37. Wu L, Soder RB, Schoemaker D, et al. **Resting state executive control network adaptations in amnesic mild cognitive impairment.** *J Alzheimers Dis* 2014;40:993–1004 CrossRef Medline
38. Aertsen A. **Insights into hippocampal network function.** *Nat Comput Sci* 2021;1:782–83 CrossRef
39. Tomasi D, Volkow ND. **Resting functional connectivity of language networks: characterization and reproducibility.** *Mol Psychiatry* 2012;17:841–54 CrossRef Medline
40. Mueller KD, Kosciak RL, Turkstra LS, et al. **Connected language in late middle-aged adults at risk for Alzheimer's disease.** *J Alzheimers Dis* 2016;54:1539–50 CrossRef Medline
41. Montembeault M, Chapleau M, Jarret J, et al. **Differential language network functional connectivity alterations in Alzheimer's disease and the semantic variant of primary progressive aphasia.** *Cortex* 2019;117:284–98 CrossRef Medline
42. Harrison TM, Maass A, Baker SL, et al. **Brain morphology, cognition, and β -amyloid in older adults with superior memory performance.** *Neurobiol Aging* 2018;67:162–70 CrossRef Medline
43. Gefen T, Peterson M, Papastefan ST, et al. **Morphometric and histologic substrates of cingulate integrity in elders with exceptional memory capacity.** *J Neurosci* 2015;35:1781–91 CrossRef Medline
44. van den Heuvel MP, Sporns O. **Network hubs in the human brain.** *Trends Cogn Sci* 2013;17:683–96 CrossRef Medline
45. Schneider F, Bermpohl F, Heinzel A, et al. **The resting brain and our self: self-relatedness modulates resting state neural activity in cortical midline structures.** *Neuroscience* 2008;157:120–31 CrossRef Medline
46. Amodio DM, Frith CD. **Meeting of minds: the medial frontal cortex and social cognition.** *Nat Rev Neurosci* 2006;7:268–77 CrossRef Medline
47. Krall SC, Rottschy C, Oberwelland E, et al. **The role of the right temporoparietal junction in attention and social interaction as revealed by ALE meta-analysis.** *Brain Struct Funct* 2015;220:587–604 CrossRef Medline
48. Cook Maher A, Kielbaso S, Loyer E, et al. **Psychological well-being in elderly adults with extraordinary episodic memory.** *PLoS One* 2017;12:e0186413 CrossRef Medline
49. Binder JR, Desai RH, Graves WW, et al. **Where is the semantic system? A critical review and meta-analysis of 120 functional neuroimaging studies.** *Cereb Cortex* 2009;19:2767–96 CrossRef Medline
50. La Corte V, Sperduti M, Malherbe C, et al. **Cognitive decline and reorganization of functional connectivity in healthy aging: the pivotal role of the salience network in the prediction of age and cognitive performances.** *Front Aging Neurosci* 2016;8:204 CrossRef Medline
51. Orban GA. **Higher order visual processing in macaque extrastriate cortex.** *Physiol Rev* 2008;88:59–89 CrossRef Medline
52. Jones SE, Lee J, Law M. **Neuroimaging at 3T vs 7T: is it really worth it?** *Magn Reson Imaging Clin N Am* 2021;29:1–12 CrossRef Medline
53. Balchandani P, Naidich TP. **Ultra-high-field MR neuroimaging.** *AJNR Am J Neuroradiol* 2015;36:1204–15 CrossRef Medline
54. Sladky R, Baldinger P, Kranz GS, et al. **High-resolution functional MRI of the human amygdala at 7 T.** *Eur J Radiol* 2013;82:728–33 CrossRef Medline
55. Newton AT, Rogers BP, Gore JC, et al. **Improving measurement of functional connectivity through decreasing partial volume effects at 7 T.** *Neuroimage* 2012;59:2511–17 CrossRef Medline
56. Vu AT, Jamison K, Glasser MF, et al. **Tradeoffs in pushing the spatial resolution of fMRI for the 7T Human Connectome Project.** *Neuroimage* 2017;154:23–32 CrossRef Medline

Infarct Evolution in Patients with Anterior Circulation Large-Vessel Occlusion Randomized to IV Alteplase and Endovascular Treatment versus Endovascular Treatment Alone

J.W. Hoving, H. van Voorst, M. Kappelhof, M. Tolhuisen, K.M. Treurniet, N.E. LeCouffe, L.A. Rinkel, M.S. Koopman, F. Cavalcante, P.R. Konduri, I.R. van den Wijngaard, E. Ghariq, F.J. Anton Meijer, J.M. Coutinho, H.A. Marquering, Y.B.W.E.M. Roos, B.J. Emmer, and C.B.L.M. Majoie; for the MR CLEAN-NO IV Investigators



ABSTRACT

BACKGROUND AND PURPOSE: Infarct evolution after endovascular treatment varies widely among patients with stroke and may be affected by baseline characteristics and procedural outcomes. Moreover, IV alteplase and endovascular treatment may influence the relationship of these factors to infarct evolution. We aimed to assess whether the infarct evolution between baseline and follow-up imaging was different for patients who received IVT and EVT versus EVT alone.

MATERIALS AND METHODS: We included patients from the Multicenter Randomized Clinical Trial of Endovascular Treatment for Acute Ischemic Stroke in the Netherlands (MR CLEAN)-NO IV trial with baseline CTP and follow-up imaging. Follow-up infarct volume was segmented on 24-hour or 1-week follow-up DWI or NCCT. Infarct evolution was defined as the follow-up lesion volume: CTP core volume. Substantial infarct growth was defined as an increase in follow-up infarct volume of >10 mL. We assessed whether infarct evolution was different for patients with IV alteplase and endovascular treatment versus endovascular treatment alone and evaluated the association of baseline characteristics and procedural outcomes with infarct evolution using multivariable regression.

RESULTS: From 228 patients with CTP results available, 145 patients had follow-up imaging and were included in our analysis. For patients with IV alteplase and endovascular treatment versus endovascular treatment alone, the baseline median CTP core volume was 17 (interquartile range = 4–35) mL versus 11 (interquartile range = 6–24) mL. The median follow-up infarct volume was 13 (interquartile range, 4–48) mL versus 17 (interquartile range = 4–50) mL. Collateral status and occlusion location were negatively associated with substantial infarct growth in patients with and without IV alteplase before endovascular treatment.

CONCLUSIONS: No statistically significant difference in infarct evolution was found in directly admitted patients who received IV alteplase and endovascular treatment within 4.5 hours of symptom onset versus patients who underwent endovascular treatment alone. Collateral status and occlusion location may be useful predictors of infarct evolution prognosis in patients eligible for IV alteplase who underwent endovascular treatment.

ABBREVIATIONS: EVT = endovascular treatment; eTICI = expanded treatment in cerebral ischemia; FIV = follow-up infarct volume; IQR = interquartile range; IVT = IV alteplase; mAOL = modified arterial occlusive lesion; RCT = randomized controlled trial

Endovascular treatment (EVT) preceded by administering IV alteplase (IVT) is the current standard of care and is effective in patients with acute ischemic stroke.¹

A first meta-analysis of 3 Asian randomized controlled trials (RCTs) comparing EVT alone with IVT before EVT suggested non-inferiority of EVT alone.² However, 4 following RCTs, including

Received October 3, 2022; accepted after revision January 31, 2023.

From the Departments of Radiology and Nuclear Medicine (J.W.H., H.v.V., M.K., M.T., K.M.T., M.S.K., H.A.M., B.J.E., C.B.L.M.M.), Biomedical Engineering and Physics (H.v.V., M.T., F.C., P.R.K., H.A.M.), and Neurology (N.E.L., L.A.R., J.M.C., Y.B.W.E.M.R.), Amsterdam University Medical Centers, University of Amsterdam, Amsterdam, the Netherlands; Department of Radiology (K.M.T., I.R.v.d.W., E.G.), The Hague Medical Centers, The Hague, the Netherlands; and Department of Radiology (F.J.A.M.), Radboud University Medical Center, Nijmegen, the Netherlands.

B.J. Emmer and C.B.L.M. Majoie are shared last authors.

The MR CLEAN-NO IV trial was part of the Collaboration for New Treatments of Acute Stroke (CONTRAST) consortium. The CONTRAST consortium acknowledges the support from the Netherlands Cardiovascular Research Initiative, an initiative of the Dutch Heart Foundation (CVON2015-01: CONTRAST) and from the Brain Foundation Netherlands (HA2015.01.06). The collaboration project is additionally financed by the

Ministry of Economic Affairs by means of the public-private partnerships allowance made available by Top Sector Life Sciences & Health to stimulate public-private partnerships (LSHM17016). This work was funded, in part, through unrestricted funding by Stryker, Medtronic, and Cerenovus.

The funding sources were not involved in study design, monitoring, data collection, statistical analyses, interpretation of results, or manuscript writing.

Please address correspondence to Jan W. Hoving, MD, Amsterdam University Medical Centers, University of Amsterdam, Department of Radiology and Nuclear Medicine, Office G1-229, Meibergdreef 9, 1105 AZ Amsterdam, the Netherlands; e-mail: j.w.hoving@amsterdamumc.nl

Indicates open access to non-subscribers at www.ajnr.org

Indicates article with online supplemental data.

<http://dx.doi.org/10.3174/ajnr.A7826>

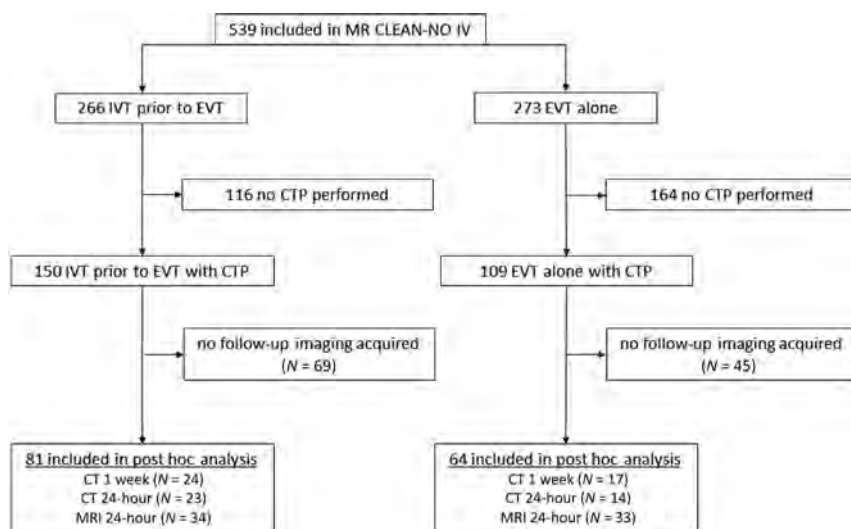


FIG 1. Flow chart of patient selection.

the Multicenter Randomized Clinical Trial of Endovascular Treatment for Acute Ischemic Stroke in the Netherlands (MR CLEAN)-NO IV trial (ISRCTN80619088), demonstrated neither superiority nor noninferiority of EVT alone with regard to functional outcome at 90 days after stroke.³⁻⁶ A recent expedited guideline from the European Stroke Organization and the European Society for Minimally Invasive Neurologic Therapy, a meta-analysis of all 6 RCTs, recommended IVT before EVT over EVT alone.⁷ While there were no large differences in clinical outcome between the overall study groups in the RCTs, individual variations in infarct evolution might still be present.^{5,6,8,9} These are clinically relevant because infarct evolution and infarct growth in particular are associated with functional outcome after EVT and differ from patient to patient.¹⁰⁻¹⁸ The following factors affect subacute infarct evolution: collateral status, occlusion location, onset-to-reperfusion time, reperfusion rate, total attempts, and early re-occlusion of the target artery.¹⁹⁻²¹ These factors may be influenced by IVT before EVT.

CTP acquisition allows quantification of the CBF to estimate the brain tissue viability and ischemic core volume on baseline imaging.²² The estimated ischemic core may still evolve in the first days to weeks after stroke onset, despite timely and adequate endovascular treatment.^{17,23-25} To our knowledge, infarct evolution has not yet been compared between patients with endovascularly treated acute ischemic stroke who were randomized for IVT and EVT versus those with EVT alone.

In this post hoc analysis of the MR CLEAN-NO IV trial, we aimed to assess whether the infarct evolution between baseline and follow-up imaging was different for patients who received IVT and EVT versus EVT alone. Additionally, we aimed to identify which clinical and procedural outcomes are associated with infarct evolution in patients with acute ischemic stroke who received IVT and EVT versus EVT alone.

MATERIALS AND METHODS

Patient Selection

We included patients with baseline CTP and follow-up DWI or NCCT from the MR CLEAN-NO IV trial.⁵ The MR CLEAN-NO

IV trial included patients with acute ischemic stroke due to an intracranial proximal occlusion of the anterior circulation who were directly admitted to an EVT-capable center between January 2018 and October 2020. If eligible for EVT and IVT administration within 4.5 hours, patients were randomly assigned to receive either EVT alone or IVT followed by EVT. Analyses were performed in the as-treated population. Details of the trial protocol were previously published.²⁶ A flow chart explaining the inclusion criteria of this study is provided in Fig 1.

Image Acquisition and Postprocessing

Baseline CTP images were acquired according to site-specific baseline CT acquisition protocols. CTP data were centrally postprocessed by an independent core lab using syngo.via (Version VB40; Siemens). The ischemic core was estimated using a CBV of $<1.2/100$ mL, and the penumbra was estimated using a CBF of $<27/100$ mL/min.²⁷ A smoothing filter (smoothing strength, 10 mm) was applied.²⁷ Expert visual-quality assessment of the CTP results was performed by 2 experienced neuroradiologists (with >10 and >15 years of experience), and craniocaudal cropping was allowed to remove obvious artifacts at the level of the skull base.²⁸ Follow-up imaging was acquired at a median of 24- to 48-hour DWI, 24-hour NCCT, or 5- to 7-day NCCT. DWI was the preferred technique for determining the follow-up infarct volume (FIV). If DWI was not available, follow-up NCCT was used to segment the FIV using a semiautomated segmentation method,²⁹ with subsequent expert visual-quality assessment (>15 years of experience). In case both 24-hour and 5- to 7-day NCCT were available, the 5- to 7-day NCCT was used to assess the FIV. If hemorrhagic transformation was present, the hemorrhagic regions were included in the segmentation volume. Hemorrhagic transformation was scored by an independent core lab and defined according to the Heidelberg Bleeding Classification.³⁰ Recanalization on follow-up imaging was assessed on either CTA or MRA using the modified arterial occlusive lesion (mAOL) score.³¹

Infarct Evolution and Imaging Assessment

We compared the infarct evolution and occurrence of substantial lesion growth between patients who received IVT and EVT versus patients who underwent EVT alone. Infarct evolution was calculated by subtracting the CTP core volume from the FIV. Overestimation of the FIV by CTP was defined as CTP core volume of $>FIV$. Substantial infarct growth was defined as an increase in FIV of >10 mL. All imaging data were assessed by an independent core laboratory of neuroradiologists or radiologists. Postprocedural reperfusion was assessed on postprocedural DSA. Successful reperfusion was defined as extended TICI (eTICI) 2b-3, and complete reperfusion was defined as eTICI 3. Recanalization

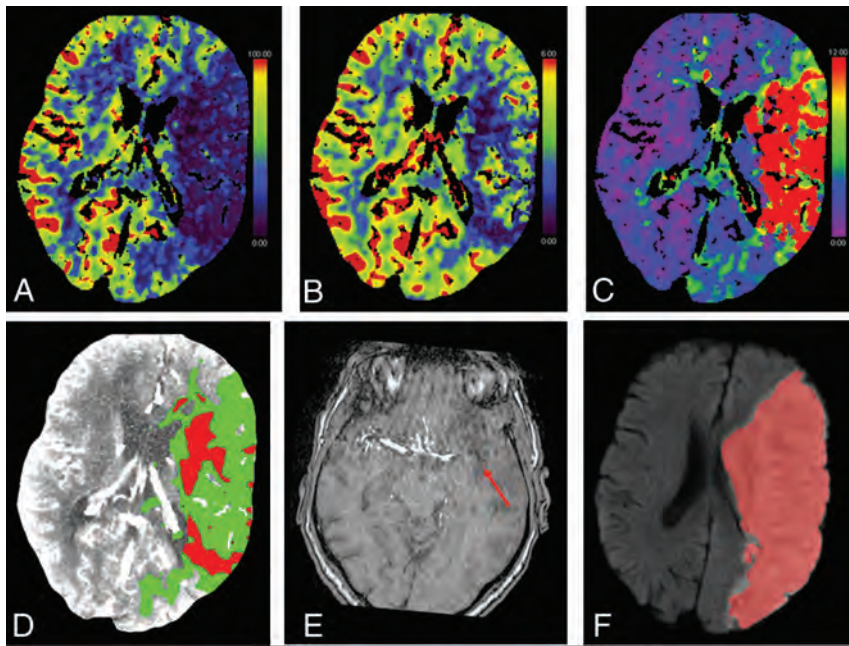


FIG 2. Baseline CTP of a patient with a left-sided M1 occlusion with substantial infarct growth with complete reperfusion (eTICI 3) after 5 attempts within 195 minutes of onset. The collateral score at baseline CTA (not shown) was zero. The CBF, CBV, and time-to-maximum parameter maps are shown in panels A–C. D, Ischemic core (red) and penumbra (green) estimations. E, Follow-up MRA shows a re-occluded M1 with visible calcified embolus (red arrow, mAOL = 0). F, Follow-up DWI acquired at 15 hours after baseline imaging with FIV segmentation (red).

of the target artery was assessed on 24-hour follow-up CTA or MRA. Incomplete patency of the target artery on follow-up imaging was defined as mAOL 0–1.³²

Statistical Analysis

Baseline clinical and imaging variables were compared between patients with IVT prior to EVT versus EVT alone using the Mann-Whitney *U* or χ^2 test. The primary outcome in this study was infarct evolution in milliliters. To assess the association of IVT before EVT with substantial infarct growth (ie, positive infarct evolution of >10 mL), we performed uni- and multivariable logistic regression analysis adjusted for the following potential confounders: ASPECTS, CTA collateral score, onset-to-reperfusion time, reperfusion rate (scored on the eTICI scale), occlusion location, total attempts, occurrence of any hemorrhagic transformation, and re-occlusion rates on follow-up CTA or MRA (scored on the mAOL scale). We checked our model for multicollinearity by determining the variance inflation factor values of all variables included in the model. Infarct evolution between patients with successful reperfusion versus unsuccessful reperfusion was compared using Mann-Whitney *U* tests. We performed a sensitivity analysis for patients who underwent 24-hour follow-up DWI and NCCT imaging to evaluate whether including 1-week follow-up NCCT FIVs would affect our findings. We performed a sensitivity analysis for patients with tandem lesions because tandem lesions (ie, occlusion or stenosis of the ICA with a concomitant intracranial occlusion) are known to be associated with lower reperfusion rates and, therefore, may show different infarct evolution.³³ Furthermore, we explored whether our results were consistent in a subgroup of patients without hemorrhagic transformation because

large hemorrhages between baseline and follow-up imaging can strongly affect the FIV assessment. Both sensitivity analyses are reported in the Online Supplemental Data.

Protocol Approval and Patient Consent

The MR CLEAN-NO IV trial protocol was approved by national central ethics committees and by research boards at each participating center. The final versions of the trial protocol and statistical analysis plan are both available at www.nejm.org. The MR CLEAN-NO IV trial was conducted in accordance with the revised Helsinki guidelines.

Data Availability

Individual patient data cannot be made available under Dutch law because we did not obtain patient approval for sharing individual patient data. All syntax files and output of statistical analyses are available on reasonable request.

RESULTS

From 539 patients included in the MR CLEAN-NO IV trial, 228 had available

CTP results. Of these 228 patients, follow-up imaging was performed in 145 patients, and they were included in our post hoc analysis. Eighty-one (56%) patients received IVT and EVT. Baseline characteristics such as age, sex, and baseline NIHSS were comparable for patients who received IVT and EVT versus patients who underwent EVT alone. Median baseline CTP-estimated ischemic core volume was 17 (interquartile range [IQR] = 4–35) mL versus 11 (IQR = 6–24) mL ($P = .5$). The median FIV was 13 (IQR = 4–48) mL versus 17 (IQR = 4–50) mL ($P = 1.0$). CTP ischemic core overestimation of >10 mL occurred in 17/81 (21%) versus 9/64 (14%) patients and occurred primarily in the white matter. The time between baseline CTP and follow-up imaging was comparable (27 versus 33 hours, $P = .3$). Good functional outcome occurred in 45/81 (56%) patients who received IVT and EVT versus in 37/64 (58%) patients who received EVT alone (OR = 0.86; 95% CI, 0.42–1.73; $P = .7$). Four (3%) patients showed early recanalization (ie, recanalization before EVT). Two patients with early recanalization received IVT before EVT. An example of a patient with a left-sided M1 occlusion and a baseline CTP-estimated core of 65 mL is shown in Fig 2. This patient underwent successful EVT alone (eTICI 3) with an onset-to-reperfusion time of 195 minutes. Follow-up CTA showed a visible calcified embolus in the left M1 (mAOL 0). Follow-up DWI showed substantial infarct growth (384 mL). See the Online Supplemental Data for a complete description of baseline, procedural, and outcome characteristics stratified per study subgroup.

Association of Baseline Characteristics and Procedural Outcomes with Infarct Evolution

Univariable analyses showed that better collateral status was negatively associated with substantial infarct growth, and early

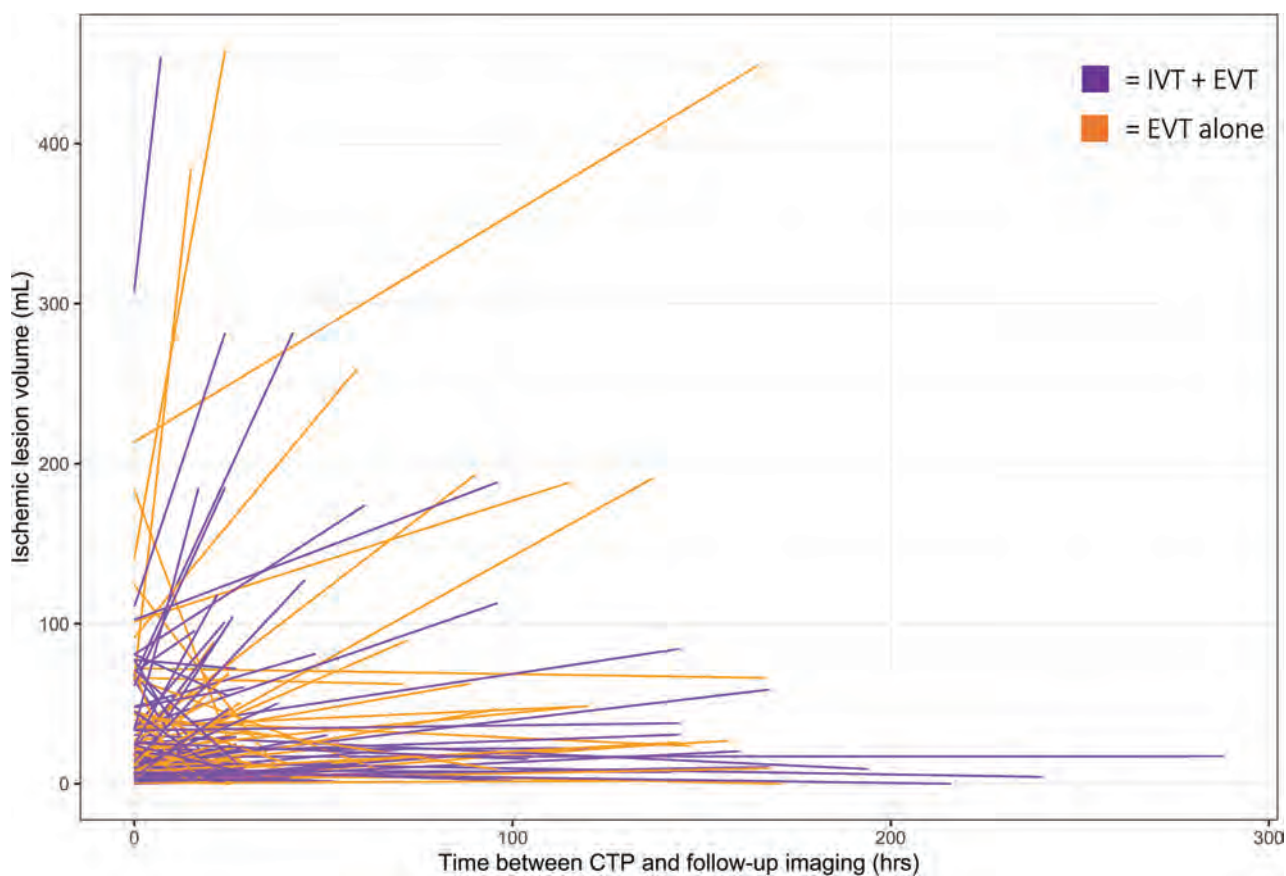


FIG 3. Infarct evolution between baseline CTP and follow-up imaging on either DWI or NCCT for patients who received IVT and EVT (purple) and patients who underwent EVT alone (orange). A, The left panel shows data for all included patients.

re-occlusion of the target artery at 24-hour follow-up imaging was positively associated with substantial infarct growth. In addition, the number of attempts during EVT and the occurrence of any hemorrhage were positively associated with substantial infarct growth (Online Supplemental Data). Notably, reperfusion (eTICI) was not associated with infarct evolution. The distribution of infarct evolution stratified by reperfusion subgroup is shown in Fig 3.

After adjustment for confounders, better collateral status and a more distal occlusion location were negatively associated with substantial infarct growth. The number of attempts during EVT and the occurrence of any hemorrhage were positively associated with substantial infarct growth. Early re-occlusion of the target artery was not associated with substantial infarct growth in multivariable analysis. For all included variables, the variance inflation factors were <1.5 , indicating no correlation between the included independent variables (Online Supplemental Data). An exploratory analysis in a subgroup of patients without any hemorrhagic transformation ($n = 103$) consistently showed that better collateral status and more distal occlusion location were negatively associated with substantial infarct growth.

Infarct Evolution for Patients Who Received IVT and EVT versus EVT Alone

Substantial infarct growth (ie, infarct growth of >10 mL) occurred in 27/81 (33%) patients with IVT and EVT versus 27/64 (42%)

patients who underwent EVT alone ($P = .3$). After adjustment for confounders, substantial infarct growth was not significantly associated with the administration of IVT and EVT (adjusted OR = 0.63; 95% CI, 0.30–1.32; $P = .2$). Boxplots showing the infarct growth per subgroup are provided in Fig 4.

Infarct Evolution for Patients with and without Successful Reperfusion

One hundred twelve (84%) patients achieved successful reperfusion after EVT. Patients with successful reperfusion showed lower median infarct evolution rates compared with patients without successful reperfusion (1 [IQR = 7–20] mL versus 15 [IQR = 2–71] mL), though this difference was not statistically significant ($P = .2$). From 59 patients with complete reperfusion (ie, eTICI 3), 20 (34%) showed substantial infarct growth.

Effect of Follow-up CTA or MRA Recanalization Status on Infarct Evolution

Follow-up CTA or MRA was available for 132 patients and showed incomplete patency of the target artery in 10% of patients receiving IVT and EVT versus in 15% of patients receiving EVT alone. However, this difference was not statistically significant ($P = .3$). In multivariable analysis, early re-occlusion of the target artery, assessed on follow-up CTA or MRA, was not associated with infarct growth (adjusted OR = 1.48; 95% CI, 0.28–7.83).

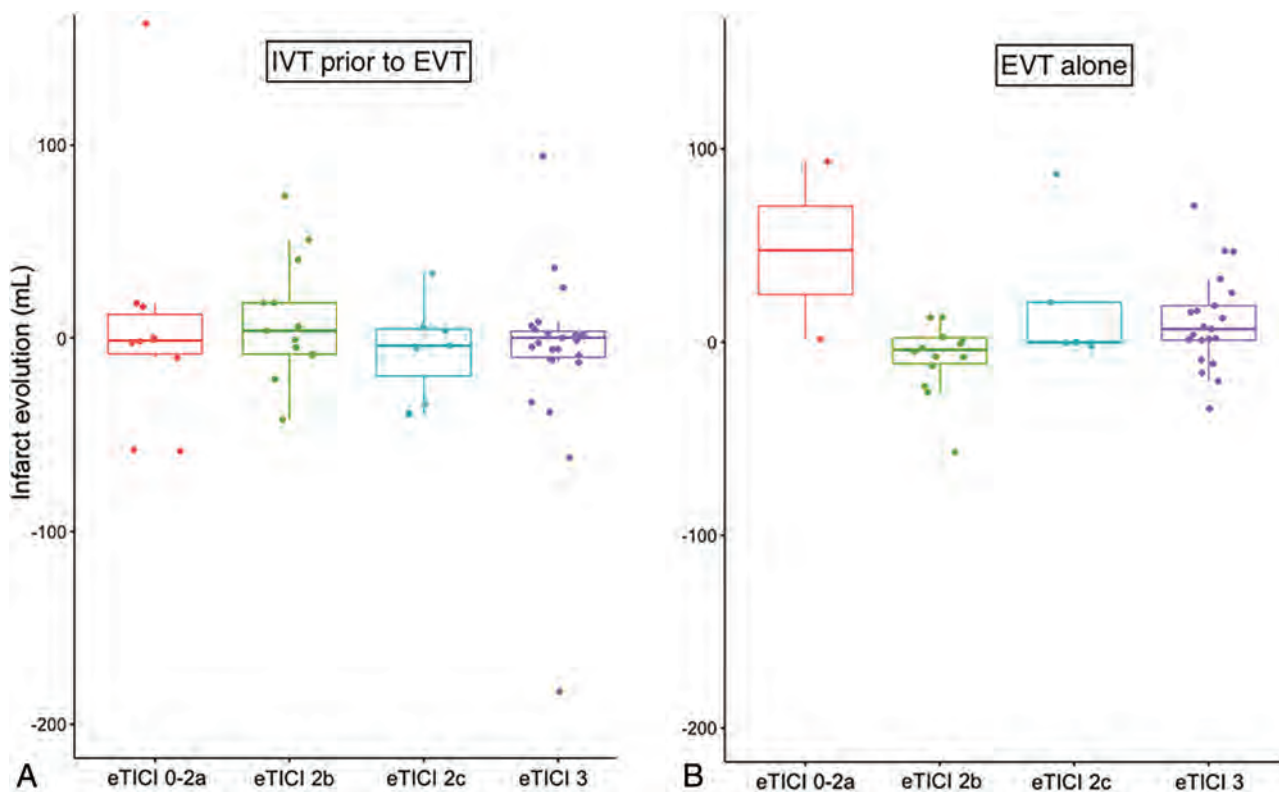


FIG 4. Boxplots showing infarct evolution (milliliters) for patients who received IVT and EVT (A) and patients who underwent EVT alone (B), with eTICI 0-2a versus eTICI 2b versus eTICI 2c versus eTICI 3 reperfusion.

DISCUSSION

In this post hoc analysis of the MR CLEAN-NO IV trial, we did not observe a statistically significant difference in infarct evolution between directly admitted patients who received IVT and EVT versus patients who underwent EVT alone within 4.5 hours after symptom onset. Overall, successful reperfusion rates were similar in patients who received IVT and EVT versus EVT alone. Furthermore, our results demonstrated that collateral status, occlusion location, the number of attempts during EVT, and occurrence of any hemorrhage were statistically significantly associated with substantial infarct growth in patients who received IVT and EVT or EVT alone within 4.5 hours after symptom onset.

Our results showed that re-occlusion on follow-up imaging was not uncommon. However, frequencies of re-occlusion were comparable between both groups. Most interesting, re-occlusion on follow-up imaging was not statistically significantly associated with substantial infarct growth after adjusting for potential confounders. However, this nonintuitive finding might be explained by the fact that our sample size was limited and, therefore, potentially underpowered to detect a clear association. The observed rates of re-occlusion on follow-up imaging are in line with a previous study assessing vessel patency at 24-hour follow-up imaging using the mAOL score.³⁴ Other studies assessing re-occlusion after EVT reported rates of early re-occlusion ranging from 3% to 9%. However, these studies used different imaging techniques and grading systems to assess the vessel patency on follow-up imaging (eg, 24-hour follow-up angiography using the Qureshi grading scheme).^{35,36}

Our results showed that substantial infarct growth was associated with the number of attempts during EVT, which is in line with a previous large prospective study from multiple stroke registries.²⁰ In addition, our results suggested that in the hyperacute (0–4.5 hour) time window, patients with poor collaterals have a higher likelihood of substantial infarct growth compared with patients with good collaterals. This finding is also in concordance with previous research in patients with stroke who underwent EVT within 6 hours of symptom onset.^{19,21}

If replicated, the relatively high frequency of re-occlusion within 24 hours after endovascular treatment could imply that there might be a potential added benefit of thrombolytic therapy in addition to EVT to improve functional outcome after stroke. This possibility would also be in line with the preliminary findings from the Chemical Optimization of Cerebral Embolectomy (CHOICE) trial, which showed that adjunct intra-arterial alteplase in patients with large-vessel occlusion stroke resulted in a greater likelihood of excellent neurologic outcome at 90 days.³⁷ Also, the authors showed that additional intra-arterial thrombolysis was associated with an increased likelihood of achieving excellent angiographic reperfusion (ie, eTICI 2c–3). However, the proportion of patients with infarct growth between baseline and follow-up imaging was not statistically significantly different between both study groups. This result could imply that additional factors such as, for example, microvascular perfusion may also contribute to functional outcome at 90 days and that these factors might be affected by additional thrombolytic therapy in patients treated with EVT.

Several limitations to our study should be noted. First, selection bias may have been introduced because CTP was not mandatory for inclusion in the MR CLEAN-NO IV trial and CTP was performed according to local imaging protocols. Of note, not all centers routinely performed CTP in every admitted patient with suspected stroke. A total of 228 (41%) patients in the MR CLEAN-NO IV had CTP available from 17 participating centers. Of these 228 patients, 145 (64%) patients had baseline CTP with follow-up NCCT or MR imaging available, leading to a relatively small sample size. However, the baseline, imaging, and outcome characteristics of patients without follow-up imaging were comparable with those in the overall MR CLEAN-NO IV population. Second, the MR CLEAN-NO IV trial had no standardized CTP acquisition protocol, and CTP data were acquired according to local acquisition protocols per site, possibly introducing differences in CTP ischemic core volume estimations.³⁸ However, all CTP data were centrally processed using a previously described single postprocessing protocol.²⁷

Furthermore, differences in CTP results that are caused by differences in acquisition protocols are commonly largely driven by differences in contrast medium injection protocols,³⁸ and because the particular contrast medium injection protocols from centers in the MR CLEAN-NO IV were similar, we expect that the effect of using data from different acquisition protocols is limited. Third, FIV was measured on both 24-hour and 1-week follow-up NCCT and MR imaging. This practice could have affected the accuracy of our FIV assessments because it is known that edema affects the FIV on NCCT after stroke, and it can be challenging to distinguish edema from infarcted tissue on NCCT.³⁹ However, the FIVs were not different for patients who received a median 24-hour follow-up DWI versus patients with 24-hour follow-up NCCT. In addition, it has been demonstrated that FIV assessed on 24-hour NCCT is equally strongly associated with functional outcome as the FIV measured on 1-week NCCT, regardless of the fact that infarct growth between 24-hour and 1-week imaging is common.²⁴

Fourth, hemorrhagic regions were included in the final infarct lesion, possibly affecting our results. An exploratory analysis in a subgroup of patients without any hemorrhagic transformation ($n = 103$) consistently showed that collateral status and occlusion location were associated with substantial infarct growth. Excluding all patients with hemorrhagic transformation from our analyses could potentially introduce bias because it is not well-known how infarct growth changes with time and what the tempo of blood-brain barrier disruption and development of hemorrhagic transformation is.⁴⁰

It is known that CTP may overestimate the FIV (ie, the “ghost infarct core concept”), especially in patients with successful reperfusion in the early time window.⁴¹ However, rates of overestimation of >10 mL were comparable with rates previously reported in a post hoc analysis of the Highly Effective Reperfusion evaluated in Multiple Endovascular Stroke (HERMES) trials collaboration.⁴² Similarly, we found that CTP ischemic core overestimation by syngo.via predominantly occurred in the white matter. Because previous studies have shown that ischemic core thresholds might differ between gray and white matter,⁴³ future studies focusing on improving white matter ischemic core estimation by syngo.via should consider this difference.

Finally, the timing of follow-up scans had a wide range (1–288 hours posttreatment). Because we showed that infarct growth was common in our population, the timing of follow-up imaging could have affected the accuracy of FIV measurements. A pooled analysis on this topic from all trials investigating the noninferiority of EVT alone is warranted for confirmation of whether infarct growth differs between patients who received IVT and EVT versus patients who underwent EVT alone. Ideally, follow-up imaging should be acquired at similar time points using a single technique.

CONCLUSIONS

No statistically significant difference in infarct evolution was found in patients who received IVT and EVT versus patients who underwent EVT alone. Collateral status, occlusion location, and number of attempts during EVT are significantly associated with substantial infarct growth in IVT-eligible patients who undergo EVT.

Disclosure forms provided by the authors are available with the full text and PDF of this article at www.ajnr.org.

REFERENCES

1. Sarraj A, Hassan AE, Grotta J, et al; SELECT Investigators. **Early infarct growth rate correlation with endovascular thrombectomy clinical outcomes: analysis from the SELECT Study.** *Stroke* 2021;52:57–69 CrossRef Medline
2. Katsanos AH, Turc G, Psychogios M, et al. **Utility of intravenous alteplase prior to endovascular stroke treatment.** *Neurology* 2021;97:e777–84 CrossRef Medline
3. Fischer U, Kaesmacher J, Strbian D, et al; SWIFT DIRECT Collaborators. **Thrombectomy alone versus intravenous alteplase plus thrombectomy in patients with stroke: an open-label, blinded-outcome, randomised non-inferiority trial.** *Lancet* 2022;400:104–15 CrossRef Medline
4. Mitchell PJ, Yan B, Churilov L; DIRECT-SAFE Investigators, et al. **DIRECT-SAFE: a randomized controlled trial of DIRECT endovascular clot retrieval versus standard bridging therapy.** *J Stroke* 2022;24:57–64 CrossRef Medline
5. LeCouffe NE, Kappelhof M, Treurniet KM, et al; MR CLEAN-NO IV Investigators. **A randomized trial of intravenous alteplase before endovascular treatment for stroke.** *N Engl J Med* 2021;385:1833–44 CrossRef Medline
6. Zi W, Qiu Z, Li F, et al; DEVT Trial Investigators. **Effect of endovascular treatment alone vs intravenous alteplase plus endovascular treatment on functional independence in patients with acute ischemic stroke: the DEVT Randomized Clinical Trial.** *JAMA* 2021;325:234 CrossRef Medline
7. Turc G, Tsivgoulis G, Audebert HJ, et al. **European Stroke Organisation (ESO)-European Society for Minimally Invasive Neurological Therapy (ESMINT) expedited recommendation on indication for intravenous thrombolysis before mechanical thrombectomy in patients with acute ischemic stroke and anterior circulation large vessel occlusion.** *J Neurointerv Surg* 2022;14:209 CrossRef Medline
8. Yang P, Zhang Y, Zhang L, et al; DIRECT-MT Investigators. **Endovascular thrombectomy with or without intravenous alteplase in acute stroke.** *N Engl J Med* 2020;382:1981–93 CrossRef Medline
9. Suzuki K, Matsumaru Y, Takeuchi M, et al; SKIP Study Investigators. **Effect of mechanical thrombectomy without vs with intravenous thrombolysis on functional outcome among patients with acute ischemic stroke: the SKIP Randomized Clinical Trial.** *JAMA* 2021;325:244 CrossRef Medline

10. Yoo AJ, Chaudhry ZA, Nogueira RG, et al. **Infarct volume is a pivotal biomarker after intra-arterial stroke therapy.** *Stroke* 2012;43:1323–30 CrossRef Medline
11. Zaidi SF, Aghaebrahim A, Urrea X, et al. **Final infarct volume is a stronger predictor of outcome than recanalization in patients with proximal middle cerebral artery occlusion treated with endovascular therapy.** *Stroke* 2012;43:2338–44 CrossRef Medline
12. Albers GW, Goyal M, Jahan R, et al. **Relationships between imaging assessments and outcomes in Solitaire with the intention for thrombectomy as primary endovascular treatment for acute ischemic stroke.** *Stroke* 2015;46:2786–94 CrossRef Medline
13. Al-Ajlan FS, Goyal M, Demchuk AM, et al; ESCAPE Trial Investigators. **Intra-arterial therapy and post-treatment infarct volumes: insights from the ESCAPE randomized controlled trial.** *Stroke* 2016;47:777–81 CrossRef Medline
14. Boers AMM, Jansen IGH, Beenen LFM, et al. **Association of follow-up infarct volume with functional outcome in acute ischemic stroke: a pooled analysis of seven randomized trials.** *J Neurointerv Surg* 2018;10:1137–42 CrossRef Medline
15. Boers AM, Jansen IG, Brown S, et al. **Mediation of the relationship between endovascular therapy and functional outcome by follow-up infarct volume in patients with acute ischemic stroke.** *JAMA Neurol* 2019;76:194 CrossRef Medline
16. Bala F, Ospel J, Mulpur B, et al. **Infarct growth despite successful endovascular reperfusion in acute ischemic stroke: a meta-analysis.** *AJNR Am J Neuroradiol* 2021;42:1472–78 CrossRef Medline
17. Simonsen CZ, Mikkelsen IK, Karabegovic S, et al. **Predictors of infarct growth in patients with large vessel occlusion treated with endovascular therapy.** *Front Neurol* 2017;8:574 CrossRef Medline
18. Regenhardt RW, Etherton MR, Das AS, et al. **Infarct growth despite endovascular thrombectomy recanalization in large vessel occlusive stroke.** *J Neuroimaging* 2021;31:155–64 CrossRef Medline
19. Campbell BC, Christensen S, Tress BM, et al; EPITHET Investigators. **Failure of collateral blood flow is associated with infarct growth in ischemic stroke.** *J Cereb Blood Flow Metab* 2013;33:1168–72 CrossRef Medline
20. Ben Hassen W, Touloupas C, Benzakoun J, et al. **Impact of repeated clot retrieval attempts on infarct growth and outcome after ischemic stroke.** *Neurology* 2021;97:e444–53 CrossRef Medline
21. Man S, Aoki J, Hussain MS, et al. **Predictors of infarct growth after endovascular therapy for acute ischemic stroke.** *J Stroke Cerebrovasc Dis* 2015;24:401–47 CrossRef Medline
22. Demeestere J, Wouters A, Christensen S, et al. **Review of perfusion imaging in acute ischemic stroke: from time to tissue.** *Stroke* 2020;51:1017–24 CrossRef Medline
23. Konduri P, van Voorst H, Buckner A, et al; MR CLEAN Trial Investigators. **Posttreatment ischemic lesion evolution is associated with reduced favorable functional outcome in patients with stroke.** *Stroke* 2021;52:3523–31 CrossRef Medline
24. Buckner A, Boers AM, Bot JJC, et al; MR CLEAN Trial Investigators (Multicenter Randomized Clinical Trial of Endovascular Treatment for Acute Ischemic Stroke in the Netherlands). **Associations of ischemic lesion volume with functional outcome in patients with acute ischemic stroke: 24-hour versus 1-week imaging.** *Stroke* 2017;48:1233–40 CrossRef Medline
25. Krongold M, Almekhlafi MA, Demchuk AM, et al. **Final infarct volume estimation on 1-week follow-up MR imaging is feasible and is dependent on recanalization status.** *Neuroimage Clin* 2015;7:1–6 CrossRef Medline
26. Treurniet KM, LeCouffe NE, Kappelhof M, et al; for the MR CLEAN-NO IV Investigators. **MR CLEAN-NO IV: intravenous treatment followed by endovascular treatment versus direct endovascular treatment for acute ischemic stroke caused by a proximal intracranial occlusion—study protocol for a randomized clinical trial.** *Trials* 2021;22:141 CrossRef Medline
27. Koopman MS, Berkhemer OA, Geuskens RR, et al; MR CLEAN Trial Investigators. **Comparison of three commonly used CT perfusion software packages in patients with acute ischemic stroke.** *J Neurointerv Surg* 2019;11:1249–56 CrossRef Medline
28. Koopman MS, Hoving JW, Kappelhof M, et al; the MR CLEAN Registry Investigators. **Association of ischemic core imaging biomarkers with post-thrombectomy clinical outcomes in the MR CLEAN Registry.** *Front Neurol* 2022;12:77136 CrossRef Medline
29. Kamnitsas K, Ledig C, Newcombe VF, et al. **Efficient multi-scale 3D CNN with fully connected CRF for accurate brain lesion segmentation.** *Med Image Anal* 2017;36:61–78 CrossRef Medline
30. von Kummer R, Broderick JP, Campbell BC, et al. **The Heidelberg Bleeding Classification: classification of bleeding events after ischemic stroke and reperfusion therapy.** *Stroke* 2015;46:2981–86 CrossRef Medline
31. Zaidat OO, Yoo AJ, Khatri P, et al; Cerebral Angiographic Revascularization Grading (CARG) Collaborators; STIR Revascularization Working Group; STIR Thrombolysis in Cerebral Infarction (TICI) Task Force. **Recommendations on angiographic revascularization grading standards for acute ischemic stroke: a consensus statement.** *Stroke* 2013;44:2650–63 CrossRef Medline
32. Khatri P, Neff J, Broderick JP, et al. **Revascularization end points in stroke interventional trials: recanalization versus reperfusion in IMS-I.** *Stroke* 2005;36:2400–03 CrossRef Medline
33. Nolan NM, Regenhardt RW, Koch MJ, et al. **Treatment approaches and outcomes for acute anterior circulation stroke patients with tandem lesions.** *J Stroke Cerebrovasc Dis* 2021;30:105478 CrossRef Medline
34. Millán M, Remollo S, Quesada H, et al. **Vessel patency at 24 hours and its relationship with clinical outcomes and infarct volume in REVASCAT Trial (Randomized Trial of Revascularization with Solitaire FR Device Versus Best Medical Therapy in the Treatment of Acute Stroke Due to Anterior Circulation Large Vessel Occlusion Presenting Within Eight Hours of Symptom Onset).** *Stroke* 2017;48:983–89 CrossRef Medline
35. Qureshi AI, Hussein HM, Abdelmoula M, et al. **Subacute recanalization and reocclusion in patients with acute ischemic stroke following endovascular treatment.** *Neurocrit Care* 2009;10:195–203 CrossRef Medline
36. Mosimann PJ, Kaesmacher J, Gautschi D, et al. **Predictors of unexpected early reocclusion after successful mechanical thrombectomy in acute ischemic stroke patients.** *Stroke* 2018;49:2643–51 CrossRef Medline
37. Renu A, Millan M, San Roman L, et al; CHOICE Investigators. **Effect of intra-arterial alteplase vs placebo following successful thrombectomy on functional outcomes in patients with large vessel occlusion acute ischemic stroke: the CHOICE Randomized Clinical Trial.** *JAMA* 2022;327:826 CrossRef Medline
38. Peerlings D, Bennink E, Dankbaar JW, et al; DUTch acute STroke (DUST) Study Investigators. **Variation in arterial input function in a large multicenter computed tomography perfusion study.** *Eur Radiol* 2021;31:8317–25 CrossRef Medline
39. Konduri P, van Kranendonk K, Boers A, et al; MR CLEAN Trial Investigators (Multicenter Randomized Clinical Trial of Endovascular Treatment for Acute Ischemic Stroke in the Netherlands). **The role of edema in subacute lesion progression after treatment of acute ischemic stroke.** *Front Neurol* 2021;12:705221 CrossRef Medline
40. Goyal M, McTaggart R, Ospel JM, et al. **How can imaging in acute ischemic stroke help us to understand tissue fate in the era of endovascular treatment and cerebroprotection?** *Neuroradiology* 2022;64:1697–707 CrossRef Medline
41. Boned S, Padroni M, Rubiera M, et al. **Admission CT perfusion may overestimate initial infarct core: the ghost infarct core concept.** *J Neurointerv Surg* 2017;9:66–69 CrossRef Medline
42. Hoving JW, Marquering HA, Majoie CB, et al. **Volumetric and spatial accuracy of computed tomography perfusion estimated ischemic core volume in patients with acute ischemic stroke.** *Stroke* 2018;49:2368–67 CrossRef Medline
43. Chen C, Bivard A, Lin L, et al. **Thresholds for infarction vary between gray matter and white matter in acute ischemic stroke: a CT perfusion study.** *J Cereb Blood Flow Metab* 2019;39:536–46 CrossRef Medline

Direct Aspiration versus Combined Technique for Distal Medium-Vessel Occlusions: Comparison on a Human Placenta Model

J. Burel, E. Gerardin, C. Papagiannaki, E. Shotar, N. Sourour, C. Laporte, P.-L. Hermet, K. Premat, J.-N. Dacher, and F. Clarençon



ABSTRACT

BACKGROUND AND PURPOSE: Mechanical thrombectomy appears to be a promising option for distal medium-vessel occlusions, for which intravenous thrombolysis is effective but may be insufficient when used alone. This study aimed to determine the optimal technique for these distal mechanical thrombectomies using the human placenta model.

MATERIALS AND METHODS: Twenty-four procedures were performed, allowing comparison of direct aspiration ($n = 12$) versus the combined technique ($n = 12$). Two positions of the aspiration catheter were tested for each of these techniques: in direct contact with the clot and at a distance from it (5–10 mm). Two types of clots were tested: red blood cell–rich clots and fibrin-rich clots. First-pass recanalization and induced arterial collapse and traction were assessed.

RESULTS: The first-pass recanalization was less frequent for direct aspiration than for the combined technique, without reaching statistical significance (41.7% versus 75.0%, $P = .098$). Full collapse ($P < .001$) and extended arterial traction ($P = .001$) were significantly less frequent for direct aspiration. For direct aspiration with the aspiration catheter not in direct contact with the clot, there was not a single first-pass recanalization and there was systematic arterial collapse, resulting in a no-flow in the aspiration syringe.

CONCLUSIONS: The combined technique appears to be more harmful, and although direct aspiration has a lower rate of first-pass recanalization, it seems appropriate to try direct aspiration as a first-line procedure. However, if the aspiration catheter cannot reach the clot, it is not useful or even risky to try aspiration alone. These results need to be confirmed by clinical studies.

ABBREVIATIONS: ACS = arterial collapse score; ATS = arterial traction score; DA = direct aspiration; DMVO = distal medium-vessel occlusion; FPR = first-pass recanalization; HP = human placenta; MT = mechanical thrombectomy; PLVO = proximal large-vessel occlusion; RBC = red blood cell

Randomized controlled trials on acute ischemic stroke due to proximal large-vessel occlusion (PLVO) established the superiority of mechanical thrombectomy (MT) in addition to the best medical management, including IV thrombolysis, over the best medical management alone within 6 hours from symptom onset.¹ More recent trials have demonstrated that the time window for MT can be extended up to 16² or 24 hours³ from the last time the patient was known well, when the selection is based on neuroimaging evaluation showing a salvageable penumbra² or a mismatch

between clinical deficit and infarct size.³ Different techniques are currently used to perform these procedures, including stent retriever alone, the direct aspiration (DA) technique, and the combined techniques (ie, using different techniques such as stent retriever and an aspiration catheter at the same time). However, there is no consensus on the optimal technique for thrombectomy.

Although IV thrombolysis is more effective for the small clots of distal medium-vessel occlusions (DMVOs) than for the large clots of PLVOs,^{4,5} IV thrombolysis alone is sometimes insufficient for DMVOs, recanalizing only one-third to one-half of the occluded vessels.^{6,7} With the iterative advances in device technology, MT is emerging as a promising solution for these DMVOs for several reasons:⁸ First, the considerable benefit of MT for PLVOs suggests that MT would also be beneficial for DMVOs; second, the advent of MT for PLVOs has led to rapid advances in catheter technology, leading to more navigable and smaller devices capable of reaching more distal and narrower vessels; third, an adverse event during MT for PLVOs is thrombus fragmentation with emboli in the distal arteries (thus, for maximum benefit from MT for PLVOs, rescue endovascular treatment of these distal

Received December 5, 2022; accepted after revision February 23, 2023.

From the Departments of Radiology (J.B., E.G., C.P., P.-L.H., J.-N.D.) and Obstetrics and Gynecology (C.L.), Rouen University Hospital, Rouen, Normandie, France; Groupe de Recherche Clinique BioFast (J.B., F.C.), Sorbonne University, Paris, France; and Department of Neuroradiology (E.S., N.S., K.P., F.C.), Assistance Publique–Hôpitaux de Paris, Sorbonne University, Pitié-Salpêtrière Hospital, Paris, France.

Please address correspondence to Frédéric Clarençon, MD, PhD, Pitié-Salpêtrière Hospital, Interventional Neuroradiology, 47, Bd de l'Hôpital, Paris, Île-de-France, 75013, France; e-mail: frederic.clarencon@aphp.fr

Indicates article with online supplemental data.

Indicates article with supplemental online videos.

<http://dx.doi.org/10.3174/ajnr.A7831>

emboli is desirable). Evaluation of Mechanical Thrombectomy in Acute Ischemic Stroke Related to a Distal Arterial Occlusion (DISCOUNT⁹) (NCT05030142) is a multicenter open, randomized controlled trial that is currently recruiting. The main objective of this trial is to assess the efficacy of MT in addition to the best medical treatment compared with the best medical treatment alone in acute ischemic stroke related to a DMVO.

The more tortuous access route and greater mobility of DMVOs, combined with thinner arterial walls, potentially increase the risk of complications, especially hemorrhages. Arterial collapse and traction induced by thrombectomy devices, particularly by avulsion of the cortical arteries or perforating branches, are phenomena thought to be responsible for these hemorrhagic complications.¹⁰ It is, therefore, necessary to study which techniques are the least harmful and most effective, especially between the DA technique and the combined technique, which are commonly used for this indication.¹¹

The human placenta (HP) is a validated vascular model for interventional neuroradiology, using either the veins or arteries of the chorionic plate.¹²⁻¹⁵ The HP model has many advantages, including its relatively low cost, minimal infrastructure requirements, and ease of preparation and setup, with fewer ethical concerns compared with animal models. The aim of this translational study was to determine the optimal technique for these distal MTs by assessing first-pass recanalization (FPR), induced arterial collapse, and induced arterial traction, using this HP model.

MATERIALS AND METHODS

Angiogram Procedures, HP Model, and Clots

All procedures were performed with a monoplane angiographic system (Azurion; Philips Healthcare), allowing the acquisition of posterior-anterior 2D projections and 3D rotational angiography after injection of iodinated contrast medium. Iodixanol, 320-mg iodine/mL (Visipaque 320; GE Healthcare), was diluted to 70% with saline and injected manually (8 mL for 2D projections and 20 mL for 3D rotational angiography). All acquired images were converted to internationally compatible DICOM files.

After written consent was obtained from the mothers, 2 placentas were prepared with the methods previously described by our group,¹⁵ using the antiphysiologic direction (ie, using the chorionic plate veins as intracranial arteries). Briefly, the guidewire provided with an 8F introducer sheath was placed in the umbilical vein up to the chorionic plate veins, allowing positioning the introducer sheath with its dilator on this guidewire. The same strategy was used to catheterize each of the umbilical arteries up to the chorionic plate with 5F introducer sheaths. A suture was then placed around each umbilical vessel to avoid fluid reflux along them. A pressure bag was used to deliver a heparinized saline solution via an IV line into the venous introducer, dilating the vessels and removing the intraluminal clots. Another IV line was connected to each arterial introducer, and the other ends were placed in a tray, as the end of the circuit. To avoid any confusion and to allow the use of common terms, we will consider these chorionic plate veins as arteries for the remainder of this article.

Twenty-four clot analogs were generated using the methodology described by Duffy et al¹⁶ to obtain 2 types of clots: red blood

cell (RBC)-rich clots, formed after spontaneous coagulation of ovine whole blood, and fibrin-rich clots, formed by mixing citrated plasma with RBCs in a 19:1 ratio (ie, 5% RBCs), which were subsequently coagulated.

MT

According to Saver et al,⁸ the intermediate, “medium vessels” can be defined as cerebral arteries with lumen diameters between 0.75 and 2.0 mm. To study the induced arterial collapse and traction on DMVOs produced by the different MT techniques, we therefore performed MTs on vessels of <2.0 mm in diameter. To ensure having vessels with a diameter of <2.0 mm and taking into account the potential random errors induced by the operator and the software, we used only vessels with diameters between 1.5 and 1.7 mm.

Revascularization was conducted by the following: 1) a DA technique with an aspiration catheter (3MAX; Penumbra), and 2) the combined technique with a 3 × 15 mm stent retriever (Catch Mini; Balt Extrusion) and an aspiration catheter (Fargomax; Balt Extrusion). Aspiration was generated by a 60-mL locking syringe (VacLok; Merit Medical). For the DA technique, the aspiration catheter was pushed close to the clot without crossing it with a microwire or microcatheter. We studied 2 positions of the aspiration catheter: in direct contact with the clot and at a distance from it (5–10 mm), simulating cases in which the clot cannot be reached by the aspiration catheter due to the tortuosities of the vessels or angulation. Ten seconds after the start of the manual aspiration, the aspiration catheter was removed. With the distal inner diameter of the 3MAX aspiration catheter being 0.89 mm, the vessel-to-catheter ratio was 1.7 to 1.9. For the combined technique, a microwire (Traxcess 14; MicroVention) and microcatheter (Headway 17; MicroVention) were directed through the clots. The stent was then loaded into the microcatheter and deployed across the clot using the unsheathing technique, with approximately two-thirds of the stent distal to the clot. The aspiration catheter was then guided coaxially along the microcatheter and the stent. In addition, for the combined technique, we studied 2 positions of the aspiration catheter: in direct contact with the clot and at a distance from it (5–10 mm). The stent was allowed to deploy for 5 minutes before removal using the Solumbra technique. An example of MT using the combined technique is shown in Fig 1.

FPR, Arterial Collapse, and Arterial Traction

FPR was defined as achieving a complete recanalization with a single thrombectomy device pass. Failure of FPR was defined by an inability to mobilize the clot or by distal embolization (ie, fragmentation of a primary clot downstream of the primary occlusion).

Possible arterial collapse induced during MT procedures was graded according to the arterial collapse score (ACS) described by Liu et al:¹⁷ ACS 0 when arteries remained unchanged; ACS 1 for indentation (ie, focal inward movement of 1 side of the arterial wall closest to the catheter tip); ACS 2 for flutter (ie, reciprocal cycles of focal collapse and re-expansion of the complete arterial lumen circumference distal to the catheter tip); ACS 3 for focal collapse (ie, sustained collapse of a short segment of the whole arterial lumen into the catheter tip); and ACS 4 for full

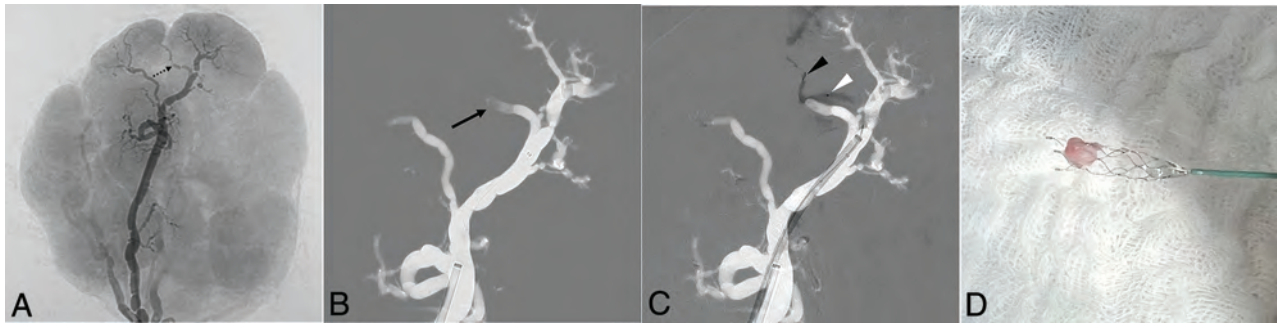


FIG 1. MT of a fibrin-rich clot by the combined technique with the aspiration catheter at 5–10 mm from the clot. *A*, 3D acquisition after injection of iodinated contrast medium by the introducer. The *black dotted arrow* indicates the branch where the occlusion will be located. *B*, Snapshot of the roadmap performed at the beginning of the procedure, showing the branch occluded by the clot (*black arrow*). *C*, Stent retriever unsheathed across the clot. The distal markers of the stent are indicated by the *black arrowhead*. The tip of the microcatheter is indicated by the *white arrowhead*. Note that the stent is not yet fully deployed because this snapshot was taken immediately after unsheathing. *D*, Fibrin-rich clot removed.

collapse (ie, complete collapse of a long segment of the artery extending away from the catheter tip).

Arterial traction was divided into 3 grades: arterial traction score (ATS) 0 for no arterial traction; ATS 1 for local arterial traction (ie, mobilization of the thrombectomized arterial segment only); and ATS 2 for important extended arterial traction with or without avulsion.

Statistical Analysis

Categoric variables are presented as count (percentage). Statistical comparisons were performed by the χ^2 and Fisher exact tests for categoric data. A P value $< .05$ was considered statistically significant. The data were analyzed using the Statistical Package for the Social Sciences (Version 28.0.1.1; IBM).

RESULTS

Two techniques (DA and combined technique), 2 clot types (RBC-rich and fibrin-rich clots), and 2 aspiration catheter positions (direct contact with the clot and at a distance from it [5–10 mm]) were tested with different combinations for a total of 24 procedures. The overall FPR rate was 58.3% ($n = 14$). Arterial collapse of any type occurred in 87.5% of the cases, with 50.0% ACS 3 ($n = 12$) and 37.5% ACS 4 ($n = 9$). We observed no indentation (ACS 1) or flutter (ACS 2). Arterial traction of any type also occurred in 87.5%, with 54.2% ATS 1 ($n = 13$) and 33.3% ATS 2 ($n = 8$). A detailed table of the results for each procedure is provided in the Online Supplemental Data. Examples of arterial collapse and arterial traction are shown in Fig 2. No contrast media extravasation was observed during the procedures.

DA versus Combined Technique

The main results are summarized in the Table. The FPR was less frequent for DA than for the combined technique, without reaching statistical significance (41.7% versus 75.0%, $P = .098$). ACSs were as follows: 25.0% ACS 0, 75.0% ACS 3, and 0.0% ACS 4 for DA; and 0.0% ACS 0, 25.0% ACS 3, and 75.0% ACS 4 for the combined technique. Full collapse (ACS 4) was significantly less frequent for DA ($P < .001$). ATSs were as follows: 25.0% ATS 0, 75.0% ATS 1, and 0.0% ATS 2 for DA; and 0.0% ATS 0, 33.3%

ATS 1, and 66.7% ATS 2 for the combined technique. Extended arterial traction (ATS 2) was significantly less frequent for DA ($P = .001$).

Aspiration Catheter Position

The FPR was more frequent when the aspiration catheter was in direct contact with the clot than when it was at 5–10 mm from the proximal end of the clot, but it did not reach statistical significance (75.0% versus 41.7%, $P = .098$). ACSs were as follows: 25.0% ACS 0, 33.3% ACS 3, and 41.7% ACS 4 when the aspiration catheter was in direct contact with the clot; and 0.0% ACS 0, 66.7% ACS 3, and 33.3% ACS 4 when it was at 5–10 mm from the proximal end of the clot. Full collapse (ACS 4) was not significantly more frequent for either position of the aspiration catheter. ATSs were as follows: 25.0% ATS 0, 41.7% ATS 1, and 33.3% ATS 2 when the aspiration catheter was in direct contact with the clot; and 0.0% ATS 0, 66.7% ATS 1, and 33.3% ATS 2 when it was at 5–10 mm from the proximal end of the clot. Extended arterial traction (ATS 2) was not significantly more frequent for either position of the aspiration catheter.

For DA, when the aspiration catheter was in direct contact with the clot and the clot completely obstructed the tip of the catheter after the start of the aspiration ($n = 3$), there was neither collapse nor arterial traction, and in these cases, FPR was always successful (Fig 3). Conversely, when the aspiration catheter was not in direct contact with the proximal aspect of the clot, there was not a single FPR and there was a systematic arterial collapse, resulting in no-flow in the aspiration syringe and a systematic arterial traction. For the combined technique, when the aspiration catheter was at 5–10 mm from the proximal aspect of the clot, FPR occurred in 5 of 6 cases (83.3%), and when the catheter was in direct contact with the clot, FPR occurred in 4 of 6 cases (66.7%).

Types of Clots

The FPR was more frequent for fibrin-rich clots than for RBC-rich clots, without reaching statistical significance (75.0% versus 41.7%; $P = .098$). Of the failed FPRs, fragmentation occurred in 2 cases, with an RBC-rich clot in both cases.

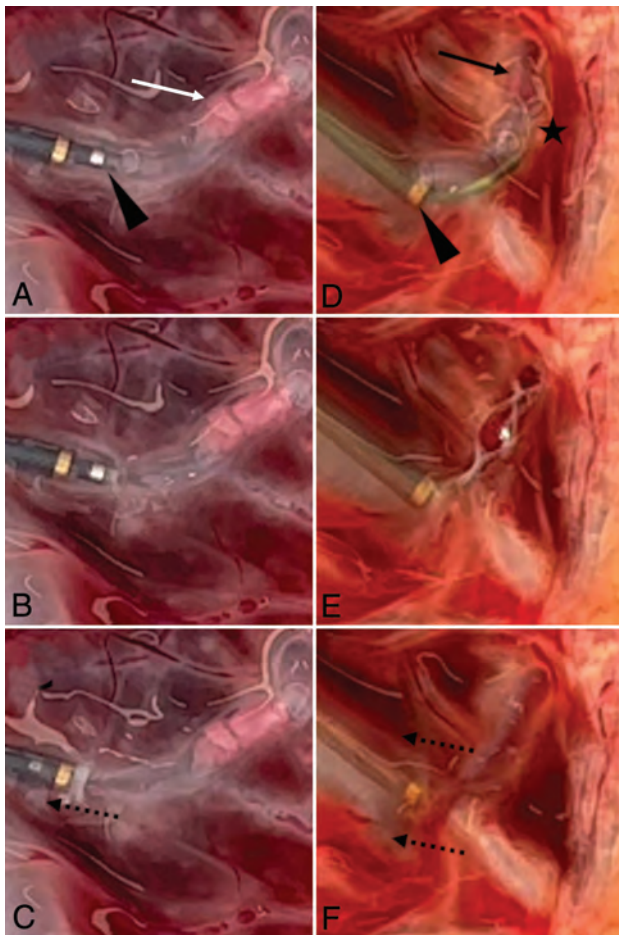


FIG 2. MTs of a fibrin-rich clot (*white arrow*) by DA (A–C), and of an RBC-rich clot (*black arrow*) by the combined technique (D–F); both aspiration catheters (*black arrowheads*) are at 5–10 mm from the clot. The *black star* indicates the stent retriever for the combined technique. A, Before the start of the aspiration. B, After the start of the aspiration, focal collapse (ACS 3) at the tip of the catheter. C, When the aspiration catheter is removed, local arterial traction (ATS 1), the artery is pulled into the aspiration catheter. This is illustrated by the *dotted black arrow*. It was an FPR failure. D, Before the start of the aspiration. E, After the start of the aspiration, full collapse (ACS 4) of the proximal artery and both distal branches. The collapse extends away from the catheter tip; the stent-retriever is molded by the vessel wall. F, When the stent is being retrieved, note extended arterial traction (ATS 2) of all regional branches. This is illustrated by the *dashed black arrows*. It was an FPR success. Both cases are available in the Online Supplemental Data and Online Supplemental Videos 1 and 2.

DISCUSSION

The risk of complications, particularly hemorrhagic ones, is increased for MTs of DMVOs. Arterial collapse and traction induced by thrombectomy devices are phenomena considered potentially responsible for these hemorrhagic complications.¹⁰ However, because DMVOs can be debilitating in some locations, it seems that some distal MTs might be useful for well-selected patients. It is, therefore, necessary to study which techniques are effective and which are the least harmful, especially between DA and the combined technique, which are commonly used for this indication.¹¹ The HP model is particularly well-suited for these investigations regarding MTs of DMVOs.¹⁵

The FPR rate was 58.3% in this study, which is consistent with the modified first-pass effect (ie, TICI 2b-3 after a single pass) rates found in the literature (52.4%).¹⁸ In our study, DA was associated with a lower FPR rate than the combined technique, without reaching statistical significance ($P = .098$). This finding is similar to what is found in the literature. Abbasi et al¹⁸ published a meta-analysis regarding PLVOs in 2021, which showed that the modified first-pass effect rates were 48% (1653/3191) for DA and 58% (193/333) for the combined technique. As in our study, these rates were not significantly different ($P = .22$).

In our study dedicated to distal thrombectomies, we observed no indentation (ACS 1) or flutter (ACS 2). Focal or full arterial collapse (ACS 3 or 4) occurred in 87.5% of cases. This result is consistent with the findings of Liu et al,¹⁷ who initially defined 4 stages of arterial collapse for PLVOs but observed ACS 3 or 4 in 98% of cases in the M2 branches. DA was associated with significantly less full arterial collapse ($P < .001$) and extended arterial traction ($P = .001$) than the combined technique. Arterial collapse, especially if full, and arterial traction, especially if extended, are possibly responsible for the high rates of SAH seen during MTs of DMVOs.¹⁰ Thus, because the combined technique appears to be more harmful and even though DA has a probable lower rate of FPR, it seems relevant to try DA as the first-line procedure in thrombectomies of DMVOs.

There was not a single FPR for DA when the aspiration catheter was not in direct contact with the proximal aspect of the clot. The usual way to recognize clot engagement in the aspiration catheter is to activate aspiration and wait until there is no flow in the canister or the aspiration syringe. We have found that arterial collapse also results in a no-flow situation, which can be misinterpreted as clot engagement. Moreover, the aspiration catheter being withdrawn while the arterial wall is being aspirated can cause arterial traction, which can lead to intracranial hemorrhage, without any chance of recanalization. This issue suggests that if the clot cannot be reached with the aspiration catheter, there is little point in trying aspiration alone. For the combined technique, the FPR rates were good regardless of the position of the aspiration catheter (83.3% and 66.7%). Therefore, contrary to DA, it appears relevant to use aspiration in addition to the stent retriever, even if the aspiration catheter cannot reach the clot.

We found that the FPR was more frequent for fibrin-rich clots than for RBC-rich clots, a finding not consistent with findings in the literature.¹⁹⁻²¹ We hypothesized that this finding was due to less interaction between the arterial wall and the clot in this HP model compared with real-world conditions, whereas this interaction in real-world conditions might be more important with fibrin-rich clots compared with RBC-rich clots. This lack of interaction is one of the inherent limitations. In addition, for our experiments, the clots were removed within minutes after placement, whereas in real patients, clot removal is usually performed after several hours. This delay most likely allows greater interaction between the clot and the arterial wall.

While initial stent retrievers had radial diameters of 6 and 4 mm, smaller devices have recently been developed to be more suitable for distal thrombectomies, including 3-mm-diameter devices (eg, the Catch Mini; pREset LITE, phenox; Trevo NXT ProVue, Stryker Neurovascular; and, more recently, Solitaire X, Medtronic) and a 2.5-mm diameter device (eg, the Tigertriever 13; Rapid Medical).⁸ For the combined technique in this study,

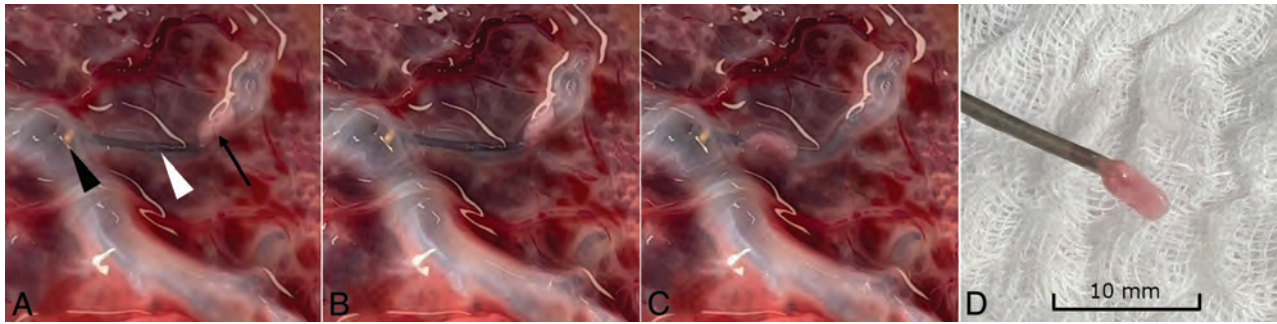


FIG 3. MT of a fibrin-rich clot by DA with the aspiration catheter in contact with the clot. **A**, The small aspiration catheter (*white arrowhead*) is placed in contact with the clot (*black arrow*) using a distal access catheter (the *black arrowhead* indicates the tip of this catheter). **B**, After the start of the aspiration, the clot is drawn toward the tip of the aspiration catheter, without any arterial collapse. **C**, When the aspiration catheter is removed, there is still no collapse and no arterial traction is observed. **D**, Removed fibrin-rich clot at the tip of the aspiration catheter. The case is available in Online Supplemental Data and Online Supplemental Video 3.

Comparison of FPR, full collapse, and extended arterial traction induced by DA and the combined technique

	DA (n = 12)	Combined Technique (n = 12)	P Value
FPR	41.7%	75.0%	P = .098 ^a
Full collapse	0.0%	75.0%	P < .001 ^b
Extended arterial traction	0.0%	66.7%	P = .001 ^b

^a χ^2 test.

^b Fisher exact test.

we used the Catch Mini stent retriever, which has the important advantage of being usable with the 0.017- and 0.013-inch microcatheters.²²

One limitation of this study is that the results might have been different with any of the other commercially available stent retrievers. Unfortunately, to the best of our knowledge, there are no studies comparing these devices in terms of safety and effectiveness.

There are a few other limitations we would like to acknowledge. First, in this model, there is no collateral circulation as in the human brain, and extrapolation to human cerebral arteries must be done with caution because arterial collapse might be overestimated. Second, the semitransparent nature of the chorionic plaque is a definite advantage of this model because it allows macroscopic observation of clots and device behavior, but it also allows improved positioning of the aspiration catheter and stent retriever compared with real-world conditions, which may have increased the FPR rate. Third, the ACS (developed by Liu et al¹⁷) and ATS scales were developed on the basis of testing in ex vivo models and may not be translatable to patients. Techniques to monitor the mechanical response of arteries in living patients are needed.

CONCLUSIONS

The combined technique appears to be more harmful, and although DA has a lower rate of FPR, it seems appropriate to try DA as a first-line procedure. However, if the clot cannot be reached by the aspiration catheter, it is not useful and is even risky to try aspiration alone. Conversely, for the combined technique, it seems relevant to use aspiration, even if the aspiration catheter cannot reach the clot. These results need to be confirmed by clinical studies.

ACKNOWLEDGMENTS

We would like to thank Mr Denis Biaussat and Balt Extrusion for their valuable assistance, particularly in obtaining the Catch Mini stent retrievers and Fargomax catheters. We would also like to thank Mrs Fabienne Santini and Penumbra for their valuable assistance, particularly in obtaining the 3MAX aspiration catheters. We would also like to thank Mr Mahmood Mirza, Mrs Sarah

Johnson, and Cerenovus for their valuable assistance, particularly in obtaining the clot analogues.

Disclosure forms provided by the authors are available with the full text and PDF of this article at www.ajnr.org.

REFERENCES

- Goyal M, Menon BK, van Zwam WH, et al; HERMES Collaborators. Endovascular thrombectomy after large-vessel ischaemic stroke: a meta-analysis of individual patient data from five randomised trials. *Lancet* 2016;387:1723–31 CrossRef Medline
- Albers GW, Marks MP, Kemp S, et al; DEFUSE 3 Investigators. Thrombectomy for stroke at 6 to 16 hours with selection by perfusion imaging. *N Engl J Med* 2018;378:708–18 CrossRef Medline
- Nogueira RG, Jadhav AP, Haussen DC, et al; DAWN Trial Investigators. Thrombectomy 6 to 24 hours after stroke with a mismatch between deficit and infarct. *N Engl J Med* 2018;378:11–21 CrossRef Medline
- Kim YD, Nam HS, Kim SH, et al. Time-dependent thrombus resolution after tissue-type plasminogen activator in patients with stroke and mice. *Stroke* 2015;46:1877–82 CrossRef Medline
- Yoo J, Baek JH, Park H, et al. Thrombus volume as a predictor of nonrecanalization after intravenous thrombolysis in acute stroke. *Stroke* 2018;49:2108–15 CrossRef Medline
- Seners P, Turc G, Maier B, et al. Incidence and predictors of early recanalization after intravenous thrombolysis: a systematic review and meta-analysis. *Stroke* 2016;47:2409–12 CrossRef Medline
- Menon BK, Al-Ajlan FS, Najm M, et al; INTERRSeCT Study Investigators. Association of clinical, imaging, and thrombus characteristics with recanalization of visible intracranial occlusion in patients with acute ischemic stroke. *JAMA* 2018;320:1017–26 CrossRef Medline
- Saver JL, Chapot R, Agid R, et al; Distal Thrombectomy Summit Group. Thrombectomy for distal, medium vessel occlusions: a

consensus statement on present knowledge and promising directions. *Stroke* 2020;51:2872–84 CrossRef Medline

9. Evaluation of mechanical thrombectomy in acute ischemic stroke related to a distal arterial occlusion (DISCOUNT). NCT number: NCT05030142. <https://clinicaltrials.gov/ct2/show/NCT05030142?term=discount&cond=stroke&draw=2&rank=1>
10. Liu Y, Gebrezgiabhier D, Reddy AS, et al. **Failure modes and effects analysis of mechanical thrombectomy for stroke discovered in human brains.** *J Neurosurg* 2022;136:197–204 CrossRef Medline
11. Brehm A, Maus V, Tsogkas I, et al. **Stent-retriever assisted vacuum-locked extraction (SAVE) versus a direct aspiration first pass technique (ADAPT) for acute stroke: data from the real-world.** *BMC Neurol* 2019;19:65 CrossRef Medline
12. Kwok JC, Huang W, Leung WC, et al. **Human placenta as an ex vivo vascular model for neurointerventional research.** *J Neurointerv Surg* 2014;6:394–99 CrossRef Medline
13. Ribeiro de Oliveira MM, Nicolato A, Santos M, et al. **Face, content, and construct validity of human placenta as a haptic training tool in neurointerventional surgery.** *J Neurosurg* 2016;124:1238–44 CrossRef Medline
14. Okada H, Chung J, Heiferman DM, et al. **Assessment of human placenta as an ex-vivo vascular model for testing of liquid embolic agent injections with adjunctive techniques.** *J Neurointerv Surg* 2018;10:892–95 CrossRef Medline
15. Burel J, Cornacchini J, Garnier M, et al. **The human placenta as a model for training and research in mechanical thrombectomy: clarifications and use of the chorionic plate veins.** *Front Neurol* 2022;13:925763 CrossRef Medline
16. Duffy S, Farrell M, McArdle K, et al. **Novel methodology to replicate clot analogs with diverse composition in acute ischemic stroke.** *J Neurointerv Surg* 2017;9:486–91 CrossRef Medline
17. Liu Y, Gebrezgiabhier D, Zheng Y, et al. **Arterial collapse during thrombectomy for stroke: clinical evidence and experimental findings in human brains and in vivo models.** *AJNR Am J Neuroradiol* 2022;43:251–57 CrossRef Medline
18. Abbasi M, Liu Y, Fitzgerald S, et al. **Systematic review and meta-analysis of current rates of first pass effect by thrombectomy technique and associations with clinical outcomes.** *J Neurointerv Surg* 2021;13:212–16 CrossRef Medline
19. Jolugbo P, Ariens RA. **Thrombus composition and efficacy of thrombolysis and thrombectomy in acute ischemic stroke.** *Stroke* 2021;52:1131–42 CrossRef Medline
20. Fennell VS, Setlur Nagesh SV, Meess KM, et al. **What to do about fibrin-rich “tough clots”? Comparing the Solitaire stent retriever with a novel geometric clot extractor in an in vitro stroke model.** *J Neurointerv Surg* 2018;10:907–10 CrossRef Medline
21. Johnson J, Srivatsan A, Chueh J, et al. **E-144 High clot red blood cell content is associated with first pass success in mechanical thrombectomy.** *J Neurointerv Surg* 2019;11(Suppl 1):A127.1 CrossRef
22. Piergallini L, Cervo A, Macera A, et al. **Distal trombectomy with Headway Duo 167 cm and Catchview Mini stent retriever: a technical note.** *World Neurosurg* 2020;137:425–28.e1 CrossRef Medline

Outcomes with Endovascular Treatment of Patients with M2 Segment MCA Occlusion in the Late Time Window

F. Bala, B.J. Kim, M. Najm, J. Thornton, E. Fainardi, P. Michel, K. Alpay, D. Herlihy, M. Goyal, I. Casetta, S. Nannoni, P. Ylikotila, S. Power, V. Saia, A. Hegarty, G. Pracucci, R. Rautio, A. Ademola, A. Demchuk, S. Mangiafico, K. Boyle, M.D. Hill, D. Toni, S. Murphy, B.K. Menon, and M.A. Almekhlafi; for the Selection of Late-window Stroke for Thrombectomy by Imaging Collateral Extent (SOLSTICE) Consortium



ABSTRACT

BACKGROUND AND PURPOSE: Randomized trials in the late window have demonstrated the efficacy and safety of endovascular thrombectomy in large-vessel occlusions. Patients with M2-segment MCA occlusions were excluded from these trials. We compared outcomes with endovascular thrombectomy in patients with M2-versus-M1 occlusions presenting 6–24 hours after symptom onset.

MATERIALS AND METHODS: Analyses were on pooled data from studies enrolling patients with stroke treated with endovascular thrombectomy 6–24 hours after symptom onset. We compared 90-day functional independence (mRS ≤ 2), mortality, symptomatic intracranial hemorrhage, and successful reperfusion (expanded TICI = 2b–3) between patients with M2 and M1 occlusions. The benefit of successful reperfusion was then assessed among patients with M2 occlusion.

RESULTS: Of 461 patients, 367 (79.6%) had M1 occlusions and 94 (20.4%) had M2 occlusions. Patients with M2 occlusions were older and had lower median baseline NIHSS scores. Patients with M2 occlusion were more likely to achieve 90-day functional independence than those with M1 occlusion (adjusted OR = 2.13; 95% CI, 1.25–3.65). There were no significant differences in the proportion of successful reperfusion (82.9% versus 81.1%) or mortality (11.2% versus 17.2%). Symptomatic intracranial hemorrhage risk was lower in patients with M2-versus-M1 occlusions (4.3% versus 12.2%, $P = .03$). Successful reperfusion was independently associated with functional independence among patients with M2 occlusions (adjusted OR = 2.84; 95% CI, 1.11–7.29).

CONCLUSIONS: In the late time window, patients with M2 occlusions treated with endovascular thrombectomy achieved better clinical outcomes, similar reperfusion, and lower symptomatic intracranial hemorrhage rates compared with patients with M1 occlusion. These results support the safety and benefit of endovascular thrombectomy in patients with M2 occlusions in the late window.

ABBREVIATIONS: eTICI = expanded thrombolysis in cerebral infarction; IQR = interquartile range; SICH = symptomatic intracranial hemorrhage

Treatment of medium-vessel occlusion with endovascular thrombectomy is gaining attention among the stroke community. In a recent survey of 366 physicians, 59.2% of participants were willing to treat such patients immediately with endovascular thrombectomy without waiting for the effect of

intravenous thrombolysis or the worsening of patient symptoms.¹ These preferences are partly based on evidence from observational studies and meta-analyses suggesting the safety and efficacy of endovascular thrombectomy among patients with medium-vessel occlusion treated within 6 hours from

Received October 29, 2022; accepted after revision February 23, 2023.

From the Calgary Stroke Program (F.B., M.N., M.G., A.D., M.D.H., B.K.M., M.A.A.), Departments of Clinical Neurosciences and Radiology, University of Calgary, Calgary, Alberta, Canada; Diagnostic and Interventional Neuroradiology Department (F.B.), University Hospital of Tours, Tours, France; Department of Neurology and Cerebrovascular Center (B.J.K.), Seoul National University Bundang Hospital, Seoul, Republic of Korea; Neuroradiology Department (J.T., D.H., S.P.) and Department of Geriatric and Stroke Medicine (K.B.), Beaumont Hospital, Dublin, Ireland; Royal College of Surgeons in Ireland (J.T., A.H.), Dublin, Ireland; Neuroradiology Unit (E.F.), Department of Experimental and Clinical Biomedical Sciences, University of Florence, Florence, Italy; Stroke Center (P.M., S.N.), Neurology Service, Lausanne University Hospital and University of Lausanne, Lausanne, Switzerland; Department of Radiology (K.A., R.R.), Turku University Hospital, Turku, Finland; Clinica Neurologica (I.C.), University of Ferrara, Ferrara, Italy; Stroke Unit (V.S.), Santa Corona Hospital, Pietra Ligure, Italy; Stroke Unit (G.P.), Careggi University Hospital, Florence, Italy; Neurocenter (P.Y.), Turku University

Hospital, University of Turku, Turku, Finland; Department of Community Health Sciences (A.A., M.D.H., B.K.M., M.A.A.), University of Calgary, Calgary, Alberta, Canada; Interventional Neuroradiology Unit (S. Mangiafico), Institute for Hospitalization and Healthcare Neuromed, Pozzilli, Italy; Emergency Department (D.T.), Stroke Unit, Sapienza University Hospital, Rome, Italy; Department of Geriatric and Stroke Medicine (S. Murphy), The Mater Misericordiae University Hospital, Dublin, Ireland; School of Medicine (S. Murphy), Royal College of Surgeons in Ireland, Dublin, Ireland; and School of Medicine (S. Murphy), University College Dublin, Dublin, Ireland.

Please address correspondence to Mohammed Almekhlafi, MD, MSc, FRCP, 1403 29th St NW, Calgary Stroke Program, Departments of Clinical Neurosciences and Radiology, University of Calgary, Calgary, Alberta, T2N 2T9, Canada; e-mail: mohammed.almekhlafi@ucalgary.ca; @FouzBala; @AlmekhlafiMa

Indicates article with online supplemental data.
<http://dx.doi.org/10.3174/ajnr.A7833>

symptom onset.²⁻⁵ The Highly Effective Reperfusion evaluated in Multiple Endovascular Stroke Trials (HERMES) collaboration included 130 patients with M2 occlusion and showed the benefit of endovascular thrombectomy compared with medical treatment.² In addition, multiple prior studies showed similar endovascular thrombectomy benefits among patients with M2 occlusions.^{3,4}

The safety and effectiveness of endovascular thrombectomy in patients with M2 occlusion in the late time window remain unknown. The late-window randomized trials that demonstrated the efficacy and safety of endovascular thrombectomy excluded patients with M2 occlusions. A recent individual patient data meta-analysis of randomized controlled trials of endovascular thrombectomy in the late window included only 15 patients with M2 occlusion of 505 patients.⁶ Therefore, current guidelines from the American Stroke Association⁷ recommend endovascular thrombectomy in the late window only in patients with large-vessel occlusions in the M1 segment and the ICA.^{8,9}

Using data from a multicenter international registry, we evaluated the safety and clinical outcomes of endovascular thrombectomy in patients with M2 occlusion presenting between 6 and 24 hours from symptom onset or last known well.

MATERIALS AND METHODS

Data were used from the Selection Of Late-window Stroke for Thrombectomy by Imaging Collateral Extent (SOLSTICE) Consortium, an individual-patient-level analysis of 2 randomized trials and 6 prospective registries from North America, Europe, and South Korea using collateral imaging to select patients eligible for endovascular thrombectomy between 6 and 24 hours after symptom onset or last known well.¹⁰ These include the Acute Stroke Registry and Analysis of Lausanne,¹¹ Lausanne, Switzerland; the National Thrombectomy Service Beaumont Hospital Registry,¹² Dublin, Ireland; the stroke registry of Turku University Hospital, Turku, Finland; the Endovascular Treatment for Small Core and Proximal Occlusion Ischemic Stroke (ESCAPE) trial,¹³ the Safety and Efficacy of Nerinetide in Subjects Undergoing Endovascular Thrombectomy for Stroke (ESCAPE-NA1) trial,¹⁴ the Italian Registry of Endovascular Thrombectomy,¹⁵ Italy; the Precise and Rapid Assessment of Collaterals Using Multiphase CTA in the Triage of Patients with Acute Ischemic Stroke for IV or IA Therapy (PROVE-IT) study;¹⁶ and the Seoul National University Bundang Hospital stroke registry.¹⁷ All included studies and registries were approved by local ethics review committees or analyzed only anonymized data as permitted by local legislation. Details regarding the included studies are summarized in the Online Supplemental Data. The pooled analysis of the main study was registered at PROSPERO (No. CRD42020222003).

All patients underwent collateral imaging and were treated with endovascular thrombectomy. Perfusion imaging was performed in a subset of patients according to local institutional protocols. All included studies were approved by the local review board at each participating center.

For this study, we included patients with MCA occlusion and compared patients with M1 occlusions with patients with M2 occlusions. The M2 segment was defined as the segment starting from the first bifurcation of the proximal MCA excluding the anterior temporal branch and ending at the circular sulcus.¹⁸

This study adheres to the Strengthening the Reporting of Observational Studies in Epidemiology guidelines (Online Supplemental Data).

Outcomes

The primary clinical outcome was functional independence defined as mRS ≤ 2 at 90 days. Secondary outcomes were mRS 0–1 at 90 days and safety outcomes, which included mortality within 90 days and the incidence of symptomatic intracranial hemorrhage (SICH) defined according to European-Australian Cooperative Acute Stroke Study 2 (ECASS2) definition.¹⁹ Successful reperfusion was defined as expanded TICI (eTICI) $\geq 2b$, corresponding to reperfusion of at least half of the affected arterial territory.

Statistical Analysis

Categorical data were presented as numbers (percentages), and continuous data, as median with interquartile range (IQR). We compared baseline characteristics and outcomes between M1 and M2 occlusion groups using the χ^2 test for categorical variables and the Mann-Whitney test for continuous variables. Mixed-effects logistic regression was then performed to determine whether M2 occlusion was associated with functional independence after adjusting for age, sex, and time from onset to reperfusion with the data source treated as a random-effects variable. To investigate the differential effect of time from onset to reperfusion on functional independence in patients with M2-versus-M1 occlusion, we performed interaction analyses by including the multiplicative interaction term in the regression model.

Furthermore, in patients with M2 occlusions, baseline characteristics were compared between patients who achieved successful reperfusion and those who did not. Because all patients in our data had undergone endovascular thrombectomy, we used successful reperfusion as a proxy for endovascular thrombectomy efficacy, similar to previously published studies.^{20,21} Mixed-effects logistic regression was attempted to determine the association between successful reperfusion and functional independence at 90 days in the M2 occlusion group after adjusting for age, sex, NIHSS score, and time from onset to reperfusion (“study ID” was included as a random-effects variable). No imputation was performed because missing data were minimal (<5%).

All statistical tests were 2-sided, and *P* values < .05 were considered significant. Statistical analysis was performed using STATA 17 (StataCorp).

RESULTS

Of 461 patients, 94 (20.4%) had M2 occlusion and 367 (79.6%) had M1 occlusion. The study flow chart is shown in Fig 1.

Baseline demographics, imaging parameters, and outcomes are summarized in Table 1. Compared with patients with M1 occlusion, patients with M2 occlusion were older (75 [median IQR = 63–82] years versus 69 [IQR = 58–78] years, *P* = .01) and had a lower median NIHSS score (10 versus 16, *P* < .001) and a higher median ASPECTS (9 versus 8, *P* < .001). Arterial puncture to reperfusion time was longer in patients with M2 occlusions (median, 45 versus 30 minutes, *P* = .001). Other workflow times were not significantly different between patients with M2 and M1

occlusion. Rates of successful reperfusion were similar between the M2 and M1 occlusion groups (82.9% versus 81.1%, $P = .77$). The 90-day follow-up was available in 438/461 (95%) patients. The proportion of patients achieving 90-day functional independence (mRS 0–2) was higher in patients with M2 compared with M1 occlusions (59.6% versus 45.0%, $P = .02$) (Table 1 and

Fig 2). Mortality rates in the patients with M2-versus-M1 occlusion were comparable (11.2% versus 17.2%, $P = .20$), while SICH occurred less frequently in the M2 occlusion group (4.3% versus 12.2%, $P = .03$) (Table 1). In multivariable analysis adjusting for age, sex, and time from onset to reperfusion, age (adjusted OR = 0.60 per decile increase; 95% CI, 0.51–0.71), time from onset to reperfusion (adjusted OR = 0.94 per 60-minute delay; 95% CI, 0.88–0.99), and M2 occlusion (adjusted OR = 2.13; 95% CI, 1.25–3.65) were independently associated with a higher likelihood of functional independence at 90 days. In the interaction analysis, there was no evidence of the heterogeneity of effect by time from onset to reperfusion when comparing patients with M2-versus-M1 occlusion ($p_{\text{interaction}} = 0.19$).

M2 Subgroup

Among the 94 patients with M2 occlusion, 89 (95%) had 90-day follow-up data. Functional independence (mRS 0–2) was achieved in 53/89 (59.6%) patients, and successful reperfusion (eTICI $\geq 2b$) was seen in 78/94 (83.0%). Patients with successful reperfusion had longer onset-to-reperfusion times (median, 762 [IQR = 586–968] minutes versus 540 [IQR = 511–663] minutes, $P = .03$) and higher ASPECTS scores (median 10 [IQR = 8–10] versus median 8

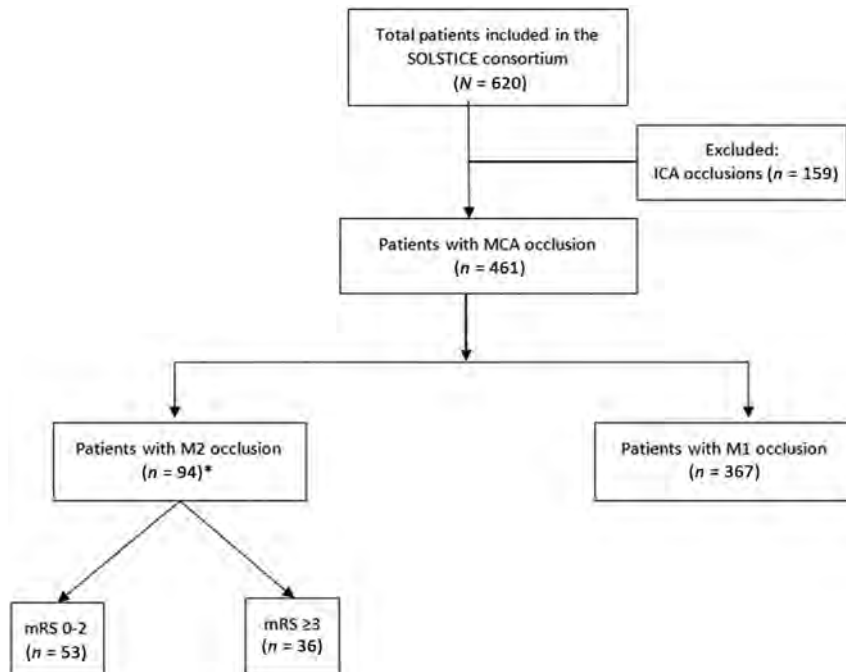


FIG 1. Study flow chart for SOLSTICE. The asterisk indicates that 5 patients did not have 90-day follow-up data.

Table 1: Patient baseline characteristics and outcomes stratified by MCA occlusion location^a

Characteristic	M2 Occlusion (n = 94)	M1 Occlusion (n = 367)	Missing
Age (median) (IQR) (yr) ^b	75 (63–82)	69 (58–78)	0
Female sex	51 (54.3)	193 (52.6)	0
Stroke presentation			
Wake-up stroke	49/93 (52.7)	187/349 (53.6)	19
Baseline NIHSS (median) (IQR) ^b	10 (7–15)	16 (11–20)	1
Tandem cervical occlusion	10 (10.6)	46 (12.5)	0
IV Alteplase	12 (12.8)	34 (9.3)	0
Time metrics (median) (IQR) (min)			
Time from onset to ED door	545 (368–730), [n = 91]	538 (405–692), [n = 342]	28
Time from onset to CT scan	579 (416–735), [n = 91]	551 (430–710), [n = 359]	11
Time from onset to puncture	744 (485–900), [n = 87]	631 (521–815), [n = 348]	26
Time from onset to reperfusion	762 (530–968), [n = 85]	671 (570–848), [n = 333]	26
Time from puncture to reperfusion ^b	45 (26–64), [n = 85]	30 (19–50), [n = 333]	25
Imaging factors			
ASPECTS ^b	9 (8–10)	8 (7–9)	2
Use of perfusion imaging	67 (71.3)	223 (60.7)	0
Outcomes			
Final TICI 2b–3	78 (82.9)	297 (81.1)	1
Final TICI 2c–3	29 (30.8)	119 (32.4)	1
SICH ^b	4/92 (4.3)	41/337 (12.2)	32
90-Day mRS (median) IQR)	2 (1–3) [n = 89]	3 (1–5) [n = 349]	23
90-Day mRS = 0–1	36/89 (40.4)	102/349 (29.2)	23
90-Day mRS = 0–2 ^b	53/89 (59.6)	157/349 (45.0)	23
90-Day mortality	10/89 (11.2)	60/349 (17.2)	23

Note:—ED indicates emergency department.

^a Values are expressed as median (IQR) or No. (%). Data are for the entire population unless otherwise specified in brackets.

^b Significant difference between groups.

90-day mRS

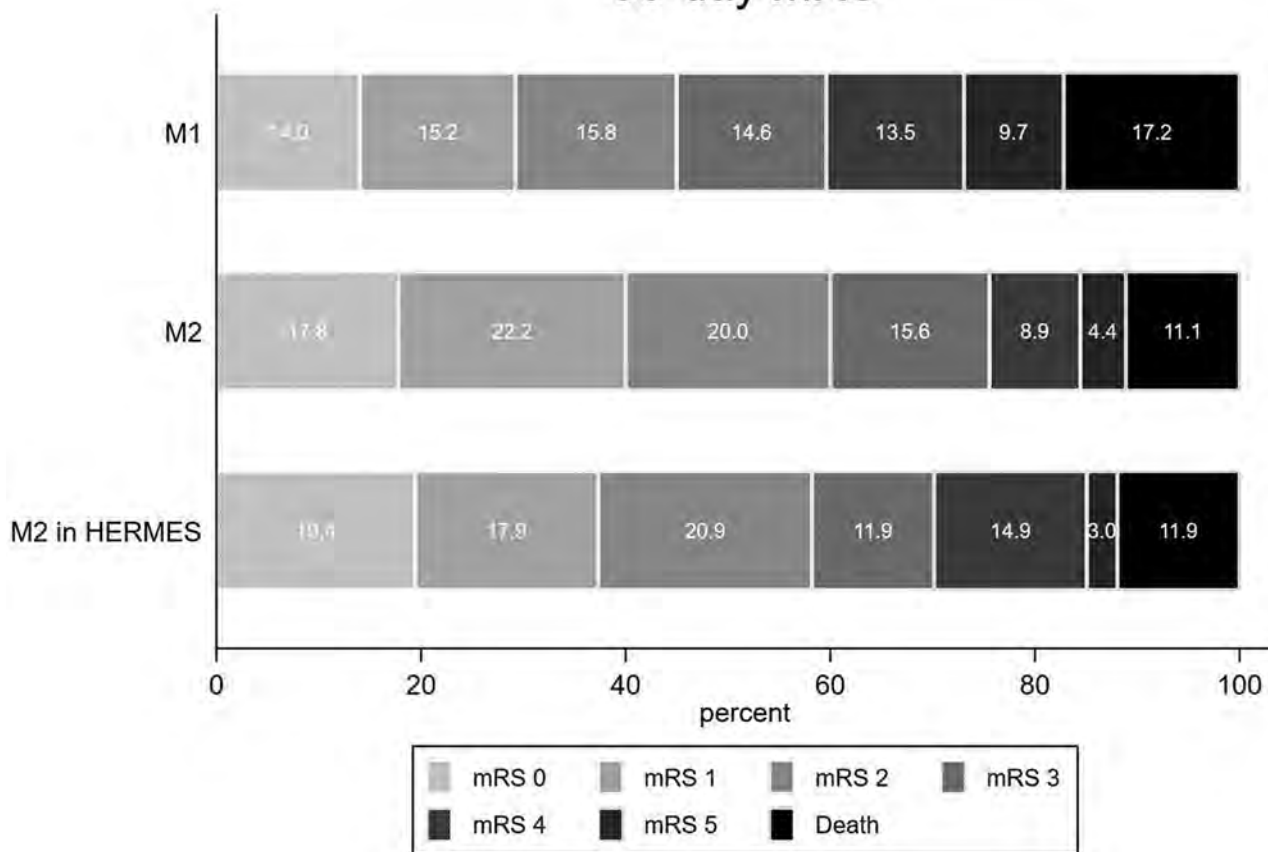


FIG 2. mRS distribution at 90 days in patients with M1 and M2 occlusion in this study versus patients with M2 occlusion treated with endovascular thrombectomy in the HERMES collaboration.

Table 2: Primary and secondary outcomes in patients with M2 occlusion stratified by successful reperfusion^a

	Successful Reperfusion (n = 75)	Unsuccessful Reperfusion (n = 14)	P Value	Unadjusted OR (95% CI)	Adjusted OR (95% CI)
90-Day mRS 0–2	48 (64.0)	5 (35.7)	.07	3.20 (0.97–10.52)	2.84 (1.11–7.29) ^b
90-Day mRS 0–1	33 (44.0)	3 (21.4)	.14	2.88 (0.74–11.17)	2.52 (0.82–7.67)
90-Day mortality	8 (10.7)	2 (14.3)	.65	0.72 (0.13–3.79)	0.13 (0.02–0.67) ^b
SICH	4 (5.3)	0 (0.0)	.99	–	–

Note:—En dash indicates that logistic regression was not performed because of the low number of events ($n < 10$).

^aData on 90-day mRS was missing for 5 patients. Regression analyses were not performed for SICH because the number of events was zero in the unsuccessful reperfusion group. Successful reperfusion was defined as a final eTICI 2b–3. The numbers in parentheses in columns 2 and 3 indicate percentages.

^bSignificant results.

[IQR = 7–9], $P = .03$). No significant difference was noted for the remaining baseline characteristics (Online Supplemental Data).

Effect of Successful Reperfusion in Patients with M2 Occlusion.

Patients with successful reperfusion more often achieved 90-day functional independence (48/78, 64.0%) than those with unsuccessful reperfusion (5/16, 35.7%; $P = .07$). Similarly, higher proportions of 90-day mRS 0–1 (44.0% versus 21.4%, $P = .14$) and reduced 90-day mortality (10.7% versus 14.3%, $P = .65$) were seen in successfully reperfused patients. Proportions of SICH were numerically higher but not significantly different in the successful reperfusion group (0% versus 5.3%, $P = .99$) (Table 2).

In multivariable regression analyses adjusting for age, sex, NIHSS score, and time from onset to reperfusion, successful reperfusion was significantly associated with functional independence (adjusted OR = 2.84; 95% CI, 1.11–7.29), 90-day mortality (adjusted OR = 0.13; 95% CI, 0.02–0.67), but not with 90-day mRS 0–1 (adjusted OR = 2.52; 95% CI, 0.82–7.67) (Table 2 and Online Supplemental Data). Regression analysis for SICH was not performed because there was no event in the unsuccessful reperfusion group.

DISCUSSION

In this multicenter international study of patients with stroke presenting in the late window and treated with endovascular

Table 3: Comparison of clinical outcomes in patients with M2 occlusions treated with endovascular thrombectomy in the current study versus the HERMES collaboration study^a

	Current Study (n = 94)	HERMES (n = 67)
Final TICl 2b–3	82.9% (78/94)	59.2% (40/67)
SICH	4.3% (4/92)	0.0% (0/67)
90-Day mRS = 0–1	40.4% (36/89)	37.3% (25/67)
90-Day mRS = 0–2	59.6% (53/89)	58.2% (39/67)
90-Day mortality	11.2% (10/89)	11.9% (8/67)

^aData are percentages (n/N).

thrombectomy, patients with M2 occlusion were more likely to achieve functional independence at 90 days and had a lower risk of SICH compared with patients with M1 occlusion. There were no differences in successful reperfusion rates between the 2 groups. Among patients with M2 occlusion receiving endovascular thrombectomy, successful reperfusion was independently associated with higher rates of functional independence and lower mortality at 90 days. While patients with M2 occlusions are predicted to have less severe initial stroke and therefore better outcomes compared with patients with M1 occlusions regardless of time window, it is relevant that we have empirically shown that there is no evidence of harm in this population of patients in the late window and, indeed, that the direction of effect on clinical outcomes is strongly positive.

There is some evidence supporting the safety and efficacy of endovascular thrombectomy in patients with M2 occlusion in the early window,^{3,22–26} with a patient-level meta-analysis from the HERMES collaboration showing a beneficial effect of endovascular thrombectomy over best medical care (adjusted OR = 2.39 for mRS 0–2 at 90 days).² Evidence regarding the benefit of endovascular thrombectomy in patients with M2 occlusions presenting late is, however, minimal. In this study, we noted higher proportions of successful reperfusion in patients with M2 occlusions than in those reported in the HERMES collaboration (82.9% versus 59.2%) (Fig 2 and Table 3).² This difference might be attributed to secular improvement in thrombectomy device technology across the years^{27,28} and the increased experience of neurointerventionalists since 2015, when endovascular thrombectomy became the standard of care.²⁹

Rates of functional independence were higher in patients with M2-versus-M1 occlusions in our study. This outcome is both predicted and concordant with a previous meta-analysis of 12 studies in the early time window comparing outcomes in patients with M2-versus-M1 segment occlusions.⁴ The rates of functional independence in our study were similar to those reported in patients with M2 occlusion in the HERMES collaboration (59.6% versus 58.2%). Additionally, mortality in patients with M2 occlusions was similar between this study and the HERMES collaboration (11.2% versus 11.9%) (Table 3),² suggesting that endovascular thrombectomy of M2 occlusion may be similarly effective and safe in the late window.

The risk of SICH in our patients with M2 occlusion was slightly higher compared with patients with M2 occlusion in the HERMES collaboration (4.3%, 4/92, versus 0.0%; 0/67). However, this risk was significantly lower than that of patients with M1 occlusion in this study. Prior studies in the early time window reported varying results. A meta-analysis of 1080 patients with

M2 occlusion found a higher risk of SICH compared with patients with M1 occlusion (15% versus 4.7%).⁴ Other studies described a similar or lower risk of SICH in patients with M2-versus-M1 occlusion.^{30,31} The endovascular thrombectomy procedure for M2 occlusions can be technically challenging, given the small size of the vessel, tortuous course, and distal location. This issue was reflected in the longer median procedural times in patients with M2-versus-M1 occlusion in this study (45 versus 30 minutes).³² However, this difference was not translated into a lower rate of successful reperfusion or 90-day functional independence.

Prior studies identified various predictors of favorable outcomes among patients with M2 occlusion presenting early.^{3,25,31,33} In a study by Jumaa et al,³ a history of hypertension, baseline NIHSS, prestroke mRS, and time from puncture to reperfusion were associated with functional outcome. In this study, age, baseline NIHSS, time from onset to reperfusion, and successful reperfusion were associated with functional outcomes among patients with M2 occlusion. Successful reperfusion was the strongest predictor of functional independence with an adjusted OR of 2.84. A previous multicenter French registry in the early time window showed similar results, with a comparable effect size of successful reperfusion (adjusted OR = 2.79), corroborating our results.³⁴

Our study has several limitations. First, we included studies from different centers with varying institutional protocols and inclusion criteria, potentially introducing sampling biases. Second, we did not have a control, non-endovascular thrombectomy arm and, therefore, cannot comment on the outcome of patients with M2 occlusions in the late time window if not treated with endovascular thrombectomy. It is likely that in this retrospective data, only patients with a high likelihood of benefit from endovascular thrombectomy judged by the treating physician were treated. However, our results of patients who were treated in prospective registries were similar to results of the HERMES collaboration, supporting the safety and good outcome among patients with M2 occlusion treated with endovascular thrombectomy in routine practice. Third, procedural techniques or associated complications were not collected in this study. The risk of SICH was, however, low overall. Fourth, information regarding the type of M2 occlusion (proximal-versus-distal, dominant-versus-nondominant) and procedural details such as the number of passes, the use of a stent retriever versus contact aspiration, and general anesthesia versus sedation were not collected in this study, possibly influencing our results. Fifth, the sample size of patients with M2 occlusion was relatively small, precluding subgroup analyses.

CONCLUSIONS

In this multicenter international analysis of patients treated with endovascular thrombectomy in the late time window, patients with M2 occlusion achieved better safety and functional outcomes than those with M1 occlusion. The rates of functional independence and mortality are similar to those in prior studies treating M2 occlusions in the earlier time window. These results provide some support for the safety of endovascular thrombectomy in patients with M2 occlusion presenting late after stroke onset or last known well.

Disclosure forms provided by the authors are available with the full text and PDF of this article at www.ajnr.org.

REFERENCES

1. Cimflova P, Kappelhof M, Singh N, et al. **Factors influencing thrombectomy decision making for primary medium vessel occlusion stroke.** *J Neurointerv Surg* 2022;14:350–55 CrossRef Medline
2. Menon BK, Hill MD, Davalos A, et al. **Efficacy of endovascular thrombectomy in patients with M2 segment middle cerebral artery occlusions: meta-analysis of data from the HERMES Collaboration.** *J Neurointerv Surg* 2019;11:1065–69 CrossRef Medline
3. Jumaa MA, Castonguay AC, Salahuddin H, et al. **Middle cerebral artery M2 thrombectomy in the STRATIS Registry.** *Stroke* 2021;52:3490–96 CrossRef Medline
4. Saber H, Narayanan S, Palla M, et al. **Mechanical thrombectomy for acute ischemic stroke with occlusion of the M2 segment of the middle cerebral artery: a meta-analysis.** *J Neurointerv Surg* 2018;10:620–24 CrossRef Medline
5. Sarraj A, Sangha N, Hussain MS, et al. **Endovascular therapy for acute ischemic stroke with occlusion of the middle cerebral artery M2 segment.** *JAMA Neurol* 2016;73:1291–96 CrossRef Medline
6. Jovin TG, Nogueira RG, Lansberg MG, et al. **Thrombectomy for anterior circulation stroke beyond 6 h from time last known well (AURORA): a systematic review and individual patient data meta-analysis.** *Lancet* 2022;399:249–58 CrossRef Medline
7. Powers WJ, Rabinstein AA, Ackerson T, et al. **Guidelines for the Early Management of Patients with Acute Ischemic Stroke: 2019 Update to the 2018 Guidelines for the Early Management of Acute Ischemic Stroke—A Guideline for Healthcare Professionals From the American Heart Association/American Stroke Association.** *Stroke* 2019;50:e344–18 CrossRef Medline
8. Albers GW, Marks MP, Kemp S, et al; DEFUSE 3 Investigators. **Thrombectomy for stroke at 6 to 16 hours with selection by perfusion imaging.** *N Engl J Med* 2018;378:708–18 CrossRef Medline
9. Nogueira RG, Jadhav AP, Haussen DC, et al; DAWN Trial Investigators. **Thrombectomy 6 to 24 hours after stroke with a mismatch between deficit and infarct.** *N Engl J Med* 2018;378:11–21 CrossRef Medline
10. Almekhlafi MA, Thornton J, Casetta I, et al; Selection Of Late-window Stroke for Thrombectomy by Imaging Collateral Extent (SOLSTICE) Consortium. **Stroke imaging prior to thrombectomy in the late window results from a pooled multicentre analysis.** *J Neurol Neurosurg Psychiatry* 2022;93:468–74 CrossRef Medline
11. Nannoni S, Strambo D, Sirimarco G, et al. **Eligibility for late endovascular treatment using DAWN, DEFUSE-3, and more liberal selection criteria in a stroke center.** *J Neurointerv Surg* 2020;12:842–47 CrossRef Medline
12. Motyer R, Thornton J, Power S, et al. **Endovascular thrombectomy beyond 12 hours of stroke onset: a stroke network's experience of late intervention.** *J Neurointerv Surg* 2018;10:1043–46 CrossRef Medline
13. Evans JW, Graham BR, Pordeli P, et al; ESCAPE Trial Investigators. **Time for a time window extension: insights from late presenters in the ESCAPE trial.** *AJNR Am J Neuroradiol* 2018;39:102–06 CrossRef Medline
14. Hill MD, Goyal M, Menon BK, et al; ESCAPE-NA1 Investigators. **Efficacy and safety of nerinetide for the treatment of acute ischaemic stroke (ESCAPE-NA1): a multicentre, double-blind, randomised controlled trial.** *Lancet* 2020;395:878–87 CrossRef Medline
15. Casetta I, Fainardi E, Saia V, et al; Italian Registry of Endovascular Treatment in Acute Stroke. **Endovascular thrombectomy for acute ischemic stroke beyond 6 hours from onset: a real-world experience.** *Stroke* 2020;51:2051–57 CrossRef Medline
16. Almekhlafi MA, Kunz WG, McTaggart RA, et al. **Imaging triage of patients with late-window (6-24 hours) acute ischemic stroke: a comparative study using multiphase CT angiography versus CT perfusion.** *AJNR Am J Neuroradiol* 2020;41:129–33 CrossRef Medline
17. Chung JW, Kim BJ, Jeong HG, et al. **Selection of candidates for endovascular treatment: characteristics according to three different selection methods.** *J Stroke* 2019;21:332–39 CrossRef Medline
18. Goyal M, Menon BK, Krings T, et al. **What constitutes the M1 segment of the middle cerebral artery? J Neurointerv Surg 2016;8:1273–77 CrossRef Medline**
19. Hacke W, Kaste M, Bluhmki E, et al; ECASS Investigators. **Thrombolysis with alteplase 3 to 4.5 hours after acute ischemic stroke.** *N Engl J Med* 2008;359:1317–29 CrossRef Medline
20. Groot AE, Treurniet KM, Jansen IG, et al; MR CLEAN Registry Investigators. **Endovascular treatment in older adults with acute ischemic stroke in the MR CLEAN Registry.** *Neurology* 2020;95:e131–39 CrossRef Medline
21. Salwi S, Cutting S, Salgado AD, et al. **Mechanical thrombectomy in patients with ischemic stroke with prestroke disability.** *Stroke* 2020;51:1539–45 CrossRef Medline
22. Alexander C, Caras A, Miller WK, et al. **M2 segment thrombectomy is not associated with increased complication risk compared to M1 segment: a meta-analysis of recent literature.** *J Stroke Cerebrovasc Dis* 2020;29:105018 CrossRef Medline
23. Almekhlafi M, Ospel JM, Saposnik G, et al. **Endovascular treatment decisions in patients with M2 segment MCA occlusions.** *AJNR Am J Neuroradiol* 2020;41:280–85 CrossRef Medline
24. Anadani M, Alawieh A, Chalhoub R, et al. **Mechanical thrombectomy for distal occlusions: efficacy, functional and safety outcomes: insight from the STAR Collaboration.** *World Neurosurg* 2021;151:e871–79 CrossRef Medline
25. de Havenon A, Narata AP, Amelot A, et al; ARISE II Investigators. **Benefit of endovascular thrombectomy for M2 middle cerebral artery occlusion in the ARISE II study.** *J Neurointerv Surg* 2021;13:779–83 CrossRef Medline
26. Salahuddin H, Ramaiah G, Slawski DE, et al. **Mechanical thrombectomy of M1 and M2 middle cerebral artery occlusions.** *J Neurointerv Surg* 2018;10:330–34 CrossRef Medline
27. Gupta R, Saver JL, Levy E, et al; TIGER Trial Investigators. **New class of radially adjustable Stentriever for acute ischemic stroke.** *Stroke* 2021;52:1534–44 CrossRef Medline
28. Haussen DC, Eby B, Al-Bayati AR, et al. **A comparative analysis of 3MAX aspiration versus 3 mm Trevo Retriever for distal occlusion thrombectomy in acute stroke.** *J Neurointerv Surg* 2020;12:279–82 CrossRef Medline
29. Zhu F, Ben Hassen W, Bricout N, et al; ETIS Registry and Study Collaborators. **Effect of operator's experience on proficiency in mechanical thrombectomy: a multicenter study.** *Stroke* 2021;52:2736–42 CrossRef Medline
30. Sweid A, Head J, Tjoumakaris S, et al. **Mechanical thrombectomy in distal vessels: revascularization rates, complications, and functional outcome.** *World Neurosurg* 2019;130:e1098–1104 CrossRef Medline
31. Nogueira RG, Mohammedan MH, Haussen DC, et al; Trevo Registry Investigators. **Endovascular therapy in the distal neurovascular territory: results of a large prospective registry.** *J Neurointerv Surg* 2021;13:979–84 CrossRef Medline
32. Nakano T, Shigeta K, Ota T, et al. **Efficacy and safety of mechanical thrombectomy for occlusion of the second segment of the middle cerebral artery.** *Clin Neuroradiol* 2020;30:481–87 CrossRef Medline
33. Shek K, Alcock S, Ghrooda E, et al. **Effectiveness and safety of endovascular thrombectomy for large versus medium vessel occlusions: a single-center experience.** *J Neurointerv Surg* 2022;14:neurintsurg-2021-017502 CrossRef Medline
34. Muszynski P, Anadani M, Richard S, et al; ETIS Registry Investigators. **Endovascular reperfusion of M2 occlusions in acute ischemic stroke reduced disability and mortality: ETIS Registry results.** *J Neurointerv Surg* 2022;14:444–49 CrossRef Medline

Diagnostic Performance of High-Resolution Vessel Wall MR Imaging Combined with TOF-MRA in the Follow-up of Intracranial Vertebrobasilar Dissecting Aneurysms after Reconstructive Endovascular Treatment

S. Tan, X. Zhou, X. Xu, Y. Lu, X. Zeng, Q. Wu, and Y. Wang



ABSTRACT

BACKGROUND AND PURPOSE: Few studies have reported the utility of high-resolution vessel wall MR imaging in the follow-up of endovascularly treated vertebrobasilar dissecting aneurysms. This study aimed to evaluate the diagnostic performance of high-resolution vessel wall MR imaging combined with TOF-MRA in the follow-up of intracranial vertebrobasilar dissecting aneurysms after reconstructive endovascular treatment.

MATERIALS AND METHODS: Patients with intracranial vertebrobasilar dissecting aneurysms with reconstructive endovascular treatment and followed up with TOF-MRA, high-resolution vessel wall MR imaging, and DSA were included. With DSA as the criterion standard, the diagnostic performance of TOF-MRA, high-resolution vessel wall MR imaging, and high-resolution vessel wall MR imaging combined with TOF-MRA in the evaluation of aneurysm occlusion status and parent artery patency was assessed. Visualization of the stented artery on TOF-MRA and high-resolution vessel wall MR imaging was rated on a 5-point scale.

RESULTS: Twenty-seven patients with 29 aneurysms were included. The sensitivity, specificity, positive predictive value, and negative predictive value of TOF-MRA, high-resolution vessel wall MR imaging, and high-resolution vessel wall MR imaging combined with TOF-MRA for diagnosing aneurysm remnants were 80.0%, 100.0%, 100.0%, and 82.4%; 53.3%, 100.0%, 100.0%, and 66.7%; and 93.3%, 100.0%, 100.0%, and 93.3%, respectively. For the visualization of the stented artery, the mean score of high-resolution vessel wall MR imaging was significantly higher than that of TOF-MRA (4.88 [SD, 0.32] versus 2.53 [SD, 1.25], $P < .001$). In the evaluation of parent artery patency (normal or pathologic), whereas TOF-MRA had a sensitivity, specificity, positive predictive value, and negative predictive value of 100.0%, 8.0%, 14.8%, and 100.0%, respectively, high-resolution vessel wall MR imaging was completely consistent with the DSA.

CONCLUSIONS: High-resolution vessel wall MR imaging combined with TOF-MRA at 3T showed good diagnostic performance in the follow-up of intracranial vertebrobasilar dissecting aneurysms after reconstructive endovascular treatment.

ABBREVIATIONS: EVT = endovascular treatment; HR-VW-MR imaging = high-resolution vessel wall MR imaging; IMH = intramural hematoma; SPACE = sampling perfection with application-optimized contrasts by using different flip angle evolutions; VBDA = vertebrobasilar dissecting aneurysm

Intracranial dissecting aneurysms are rare and are usually located at the vertebrobasilar artery. The treatment of intracranial vertebrobasilar dissecting aneurysms (VBDAs) is challenging and difficult. Compared with surgical treatment, endovascular treatment

(EVT) has less treatment-associated morbidity and mortality and has become the major treatment method for intracranial VBDAs.¹ However, for VBDAs treated with reconstructive EVT, imaging follow-up is imperative to detect recurrence in a timely manner.² DSA, the criterion standard for imaging follow-up, is invasive and has radiation exposure. Patients tend not to accept long-term repeat DSA follow-up examinations. Therefore, a noninvasive imaging technique is needed in clinical practice.

Received December 13, 2022; accepted after revision February 14, 2023.

From the Departments of Neurosurgery (S.T., Y.L., X. Zhou, Y.W.) and Radiology (X. Zeng, Q.W.), The First Affiliated Hospital of Nanchang University, Nanchang University, Nanchang, Jiangxi Province, China; Department of Neurosurgery (X.X.), The First People's Hospital of Zhaoqing City, Zhaoqing, Guangdong Province, China; and Department of Neurosurgery (Y.W.), Beijing Chaoyang Hospital, Capital Medical University, Beijing, China.

Yang Wang and Xiaobing Zhou contributed equally to this work.

Song Tan and Xiaobing Zhou would be designated as co-authors.

This study was funded by the National Natural Science Foundation of China (No. 8196070077), the Natural Science Foundation of Jiangxi Province (No. 20202BABL206053), and the National Key R&D program of China (No. 2016YFC1300802).

Please address correspondence to Yang Wang, MD, Department of Neurosurgery, Beijing Chaoyang Hospital, Capital Medical University, No. 8, South Gongti Rd, Chaoyang District, Beijing 100020, China; e-mail: wangyang7839@163.com

Indicates open access to non-subscribers at www.ajnr.org

<http://dx.doi.org/10.3174/ajnr.A7838>

Table 1: Imaging parameters of MR imaging sequences

Parameters	TOF-MRA	3D T1-Weighted SPACE
TR (ms)	21	900
TE (ms)	3.43	16
Flip angle	18°	—
FOV (mm)	180 × 180	200 × 200
Matrix	320 × 320	384 × 384
No. of excitations	1	1
Section thickness (mm)	0.55	0.53
No. of slices	162	256
Echo-train length	—	293
Scanning time (min)	4:05	9:18

Note:—The en dash indicates not applicable.

Because of the severe artifacts arising from stents or coils, CTA is seldom used in the follow-up of endovascularly treated intracranial aneurysms. As a noninvasive imaging technique without radiation exposure, TOF-MRA has been widely used in the follow-up of these aneurysms.³ In VBDA, compared with saccular aneurysms, the injury of the arterial wall is more complex, and greater attention must be paid to the repair of the injured vessel wall during the follow-up period. Both DSA and MRA depict only geometric shapes of the arterial lumen by blood flow signals but cannot visualize the vessel wall. In contrast, high-resolution vessel wall MR imaging (HR-VW-MR imaging) can reveal the arterial lumen and wall simultaneously by suppressing the flow signals. In our center (First Affiliated Hospital of Nanchang University), HR-VW-MR imaging combined with TOF-MRA has been the most common follow-up imaging technique for intracranial VBDA. Multiple studies have reported the utility of HR-VW-MR imaging in the diagnosis of intracranial VBDA.⁴⁻⁷ However, few studies have reported the utility of HR-VW-MR imaging in the follow-up of endovascularly treated VBDA to date. In this study, we aimed to evaluate the diagnostic performance of HR-VW-MR imaging combined with TOF-MRA in the follow-up of intracranial VBDA treated with reconstructive EVT.

MATERIALS AND METHODS

Ethics Approval

This study was approved by the ethics committee of First Affiliated Hospital of Nanchang University (Nanchang, China, No. 2020047).

Patient Cohort

The local institutional review board (First Affiliated Hospital of Nanchang University) approved this study. Because the study was retrospective, the requirement for written informed consent was waived. Between January 2016 and December 2021, patients with intracranial VBDA treated with reconstructive EVT and followed up with HR-VW-MR imaging, TOF-MRA, and DSA in our center were included. If the interval between HR-VW-MR imaging and the DSA examination was >2 weeks, the patient was excluded. Patients' baseline and treatment information was acquired from the medical record system.

Image Acquisition

The MR imaging examination was performed on a 3T system (Magnetom Skyra; Siemens) with a 20-channel head and neck

unit coil. A TOF-MRA was performed first. HR-VW-MR imaging included pre- and postcontrast 3D T1-weighted sampling perfection with application-optimized contrasts by using different flip angle evolutions (SPACE) sequences. Postcontrast images were obtained 5 minutes after venous injection of single-dose (0.1 mmol/kg) gadopentetate dimeglumine (Magnevist; Bayer HealthCare Pharmaceuticals) with the same parameters as for the precontrast T1-weighted images. The scanning range included the whole brain. The scan parameters are listed in Table 1.

With transfemoral catheterization, EVT and follow-up DSA were performed with the following angiographic systems: UNIQU FD20/15 (Philips Healthcare) or Axiom Artis dFA (Siemens).

Image Analysis

All images were reviewed blindly in random order by 2 interventional neuroradiologists with >10 years' experience. Only the locations of the treated aneurysms were provided to the reviewers. TOF-MRA and HR-VW-MR imaging were reviewed separately with an interval of 1 month. For TOF-MRA, both MIP images and source images were reviewed. For 3D T1 SPACE, MPRs were performed in the axial and oblique sagittal directions to visualize VBDA from different planes. The image quality of the stented artery on TOF-MRA and HR-VW-MR imaging was rated on the following 5-point scale:⁸ 1) not visible (the arterial structure was invisible, and strong artifacts were present); 2) poor (structures were slightly visible, and substantial artifacts or blurring was present); 3) acceptable (the diagnostic quality was acceptable, and moderate artifacts or blurring was present); 4) good (the images were of good quality, and minimal artifacts or blurring was present); or 5) excellent (the depiction was nearly equal to that of DSA). In cases of disagreement, the scores of the 2 reviewers were averaged. The patency of the parent artery was divided into 3 grades (normal, stenosis, or occlusion) or 2 grades on a simplified scale (normal or pathologic [stenosis or occlusion]). The aneurysm occlusion status was classified as complete or incomplete occlusion. Complete occlusion was defined by an absence of contrast agent in the aneurysmal sac observed on DSA, no flow signal in the aneurysmal sac on TOF-MRA, or no flow void in the aneurysmal sac on HR-VW-MR imaging. Otherwise, the aneurysm was considered incomplete occlusion. In cases of discrepancy, a consensus was reached between the reviewers by discussion.

After another month, the TOF-MRA and HR-VW-MR imaging findings were again reviewed together. After the diagnostic information from TOF-MRA and HR-VW-MR imaging was combined, the aneurysm occlusion status and parent artery patency were assessed. In cases of discrepancy, a consensus was reached by discussion.

DSA images were reviewed 1 month later by the same reviewers without knowledge of the MR imaging results. The evaluation included the aneurysm occlusion status and parent artery patency with the same classification standard used for the MR imaging examinations.

To investigate the vessel wall features of VBDA after procedures, the presence of an intimal flap, double lumen sign, or intramural hematoma was reviewed on HR-VW-MR imaging. An intimal flap was defined as a linear layer crossing the arterial lumen that extended to the sidewall. The double lumen sign was

Table 2: Evaluation of aneurysm occlusion status with different imaging modalities

	DSA			κ (95% CI)
	InCO	CO	Total	
TOF-MRA				0.794 (0.579–1.0)
InCO	12	0	12	
CO	3	14	17	
Total	15	14	29	
HR-VW-MR imaging				0.525 (0.255–0.794)
InCO	8	0	8	
CO	7	14	21	
Total	15	14	29	
TOF-MRA combined with HR-VW-MR imaging				0.931 (0.799–1.0)
InCO	14	0	14	
CO	1	14	15	
Total	15	14	29	

Note:—CO indicates complete occlusion; InCO, incomplete occlusion.

defined as 2 lumens represented as 2 jets of flow void within 1 vessel.⁵ An intramural hematoma was identified as a false lumen filled with hematoma.

Statistical Analysis

All statistical analyses were performed in SPSS 26.0 (IBM) and SAS 9.4 (SAS Institute). Quantitative variables are expressed as mean (SD) or median (interquartile range), and qualitative variables are presented as counts (percentages). The aneurysm size is expressed as (the Maximum Diameter Perpendicular to the Parent Artery) \times (the Length of Lesion along the Parent Artery) on preoperative DSA. Interobserver and intermodality consistency were evaluated with κ or weighted κ statistics. The κ value was interpreted as follows:⁹ 0.81–1.00, almost perfect agreement; 0.61–0.80, substantial agreement; 0.41–0.60, moderate agreement; 0.21–0.40, fair agreement; 0.00–0.20, slight agreement; and <0.00, poor agreement. The Wilcoxon signed-rank test was used to compare image quality between TOF-MRA and HR-VW-MR imaging. With DSA used as the criterion standard to assess the aneurysm occlusion status and parent artery patency, the accuracy, sensitivity, specificity, positive predictive value, and negative predictive value of TOF-MRA, HR-VW-MR imaging, and HR-VW-MR imaging combined with TOF-MRA were calculated. $P < .05$ was considered significant.

RESULTS

Patient and Aneurysm Characteristics

Twenty-seven patients (5 women, 22 men; mean age, 48.7 [SD, 10.3] years; range, 25–66 years) with 29 intracranial VBDA were included in this study. Among those patients, 25 patients had 1 aneurysm, and 2 patients had 2 aneurysms. Twelve (41.4%) aneurysms ruptured before the procedures. The distribution of these aneurysms was as follows: basilar artery, 3 (10.3%); left vertebral artery, 12 (41.4%); right vertebral artery, 13 (44.8%); and vertebrobasilar junction, 1 (3.4%). The average size of these aneurysms was 7.7 (SD, 2.2) \times 13.7 (SD, 5.3) mm. The 29 aneurysms were treated as follows: 24 with stent-assisted coiling (single LVIS, MicroVention, 17; single Enterprise, Codman & Shurtleff, 2; double LVIS, 1; double Enterprise, 2; LVIS + Enterprise, 2), 1 with double

LVIS without coils, 1 with single Tubridge (MicroPort Medical Company) with coiling, 2 with a single Pipeline (Medtronic) alone, and 1 with a double Pipeline without coils. All coils used in this study were bare platinum coils. Seven (24.1%) aneurysms were completely occluded, and 22 (75.9%) aneurysms were incompletely occluded immediately after treatment. The median interval between the procedures and MR imaging examinations was 191 days (range, 49–1128 days; interquartile range, 129–273 days).

Aneurysm Occlusion Status

The assessment of aneurysm occlusion status with different imaging modalities is summarized in Table 2. DSA showed 14 (48.3%) aneurysms with total occlusion and 15 (51.7%) with incomplete occlusion. TOF-MRA and DSA were discordant for 3 (10.3%) aneurysms that showed incomplete occlusion on DSA but were classified as complete occlusion with TOF-MRA ($\kappa = 0.794$). HR-VW-MR imaging and DSA were discordant for 7 (24.1%) aneurysms that showed incomplete occlusion on DSA but were classified as complete occlusion with HR-VW-MR imaging ($\kappa = 0.525$). However, only 1 (3.4%) aneurysm was discordant between HR-VW-MR imaging combined with TOF-MRA and DSA ($\kappa = 0.931$). One aneurysm treated with 2 Pipeline implantations, with small remnants visible on DSA, was classified as complete occlusion on HR-VW-MR imaging combined with TOF-MRA. Figures 1–3 show representative images.

The comparative diagnostic performance of different imaging modalities is shown in Table 3. Whereas TOF-MRA and HR-VW-MR imaging showed a sensitivity and specificity of 80.0% and 100.0% and 53.3% and 100.0%, respectively, HR-VW-MR imaging combined with TOF-MRA showed a sensitivity and specificity of 93.3% and 100.0%, respectively.

Patency of the Parent Artery

The mean image quality score of HR-VW-MR imaging was significantly higher than that of TOF-MRA (4.88 [SD, 0.32] versus 2.53 [SD, 1.25], $P < .001$). Although all HR-VW-MR images had good or excellent image quality (score, ≥ 4), only 31.0% (9/29) of the TOF-MRA images had good or excellent image quality. When the TOF-MRA and HR-VW-MR images were reviewed together, all assessments of the patency of the parent artery were made on the basis of the HR-VW-MR images in this study because the HR-VW-MR imaging provided a better view of the arterial lumen than TOF-MRA in all cases. Four (14.8%) patients showed mild motion artifacts on HR-VW-MR imaging, whereas no motion artifacts were found in TOF-MRA. The motion artifacts were presumed to have been caused by oral motion and had little influence on image quality.

DSA indicated that 25 (86.2%) patients had a normal parent artery, and 4 (13.8%) patients had mild parent artery stenosis (<50%). TOF-MRA indicated that 2 (6.9%) patients had a normal parent artery, 18 (62.1%) patients had parent artery stenosis, and 9 (31.0%) patients had parent artery occlusion. TOF-MRA and DSA were discordant for 23 (79.3%) patients ($\kappa = 0.088$): Nineteen normal parent arteries on DSA were classified as stenosis with TOF-MRA, and 4 other normal parent arteries on DSA were classified as occlusion with TOF-MRA. With the simplified 2-grade scale, the intermodality agreement between DSA and TOF-MRA was 0.023.

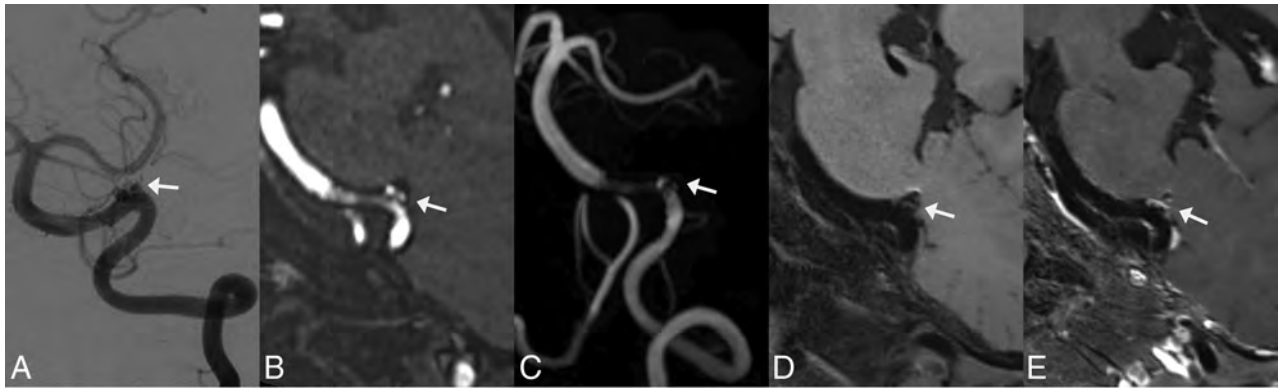


FIG 1. Follow-up images of a left vertebral artery dissecting aneurysm treated by LVIS stent-assisted coiling 6 months after the procedure. *White arrows* indicate the location of the aneurysm. *A*, DSA shows that the aneurysm involves incomplete occlusion and the stented artery is normal. *B* and *C*, MPR and MIP images of TOF-MRA show an aneurysm remnant. Moderate artifacts and a stenosis are observed at the stented artery on TOF-MRA. *D* and *E*, On pre- and postcontrast 3D T1-weighted SPACE, though no aneurysm remnant is observed, the stented artery is depicted well and indicates an absence of stenosis. The postcontrast image shows enhancement of the aneurysm wall, aneurysm lumen, and stented artery. The image quality score assigned by the 2 reviewers for TOF-MRA and 3D TIWI SPACE is 3/3 and 5/5, respectively.

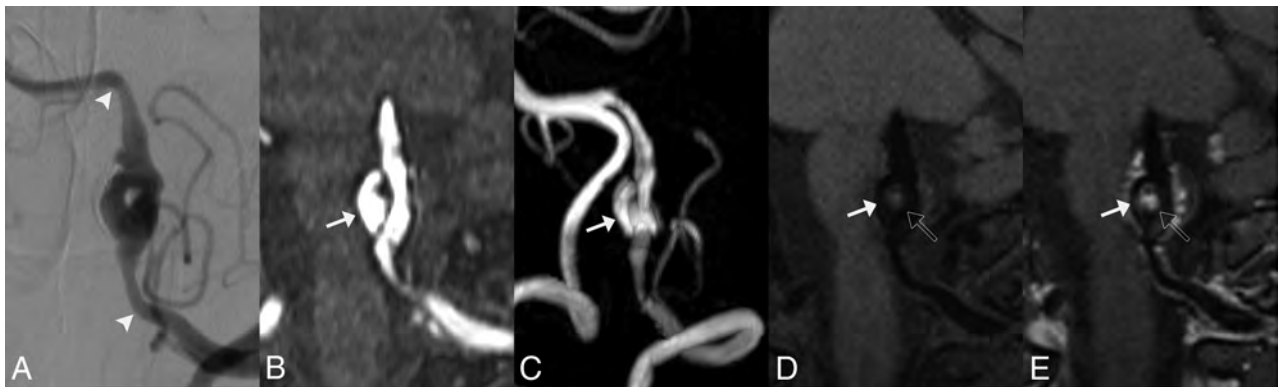


FIG 2. Follow-up images of a left vertebral artery dissecting aneurysm treated with LVIS stent-assisted coiling at the third month postoperatively. *A*, DSA shows recurrence of the aneurysm and mild stenosis of the proximal stented artery. *Arrowheads* indicate the stent edges. *B* and *C*, MPR and MIP images of TOF-MRA show the residual aneurysm lumen (*white arrow*) clearly. However, substantial artifacts and severe stenosis are observed at the proximal stented artery on TOF-MRA. *D* and *E*, On pre- and postcontrast 3D T1-weighted SPACE, the residual aneurysm lumen (*white arrow*) is depicted clearly, and an intramural hematoma (*outline arrow*) is observed. The depiction of the in-stent lumen is similar to that of DSA, with hardly any artifacts. The postcontrast image shows enhancement of the aneurysm wall, intramural hematoma, and stented artery. The image quality score assigned by the 2 reviewers for TOF-MRA and 3D TIWI SPACE is 2/2 and 5/5, respectively.

The sensitivity, specificity, positive predictive value, negative predictive value, and accuracy of TOF-MRA were 100.0%, 8.0%, 14.8%, 100.0%, and 20.7%, respectively. However, regardless of whether the simplified 2-grade scale or the 3-grade scale was used, the assessment results based on HR-VW-MR imaging were completely consistent with those based on DSA. Therefore, the intermodality agreement was 1.00.

Evaluation of the Vessel Wall

The presence of an intimal flap, double lumen sign, and intramural hematoma (IMH) was observed in 2 (6.9%), 3 (10.3%), and 17 (58.6%) patients, respectively. All intimal flaps and double lumen signs were observed in incompletely occluded aneurysms. Intramural hematomas were observed in 42.9% (6/14) of completely occluded aneurysms and 73.3% (11/15) of incompletely occluded aneurysms, respectively ($P = .139$). Contrast enhancement of the affected vessel wall and intimal flaps was observed in all the cases.

Interobserver Agreement

In the evaluation of the aneurysm occlusion status, the κ value of interobserver agreement for TOF-MRA, HR-VW-MR imaging, HR-VW-MR imaging combined with TOF-MRA, and DSA was 0.86, 0.83, 1.00, and 0.93, respectively.

In the assessment of the patency of the parent artery with the 3-grade scale, the κ value for TOF-MRA, HR-VW-MR imaging, HR-VW-MR imaging combined with TOF-MRA, and DSA was 0.88, 0.84, 0.84, and 0.84, respectively. With the simplified 2-grade scale, the κ value for TOF-MRA, HR-VW-MR imaging, HR-VW-MR imaging combined with TOF-MRA, and DSA was 0.65, 0.84, 0.84, and 0.84, respectively.

DISCUSSION

This study demonstrated that HR-VW-MR imaging combined with TOF-MRA at 3T had high concordance with DSA in the

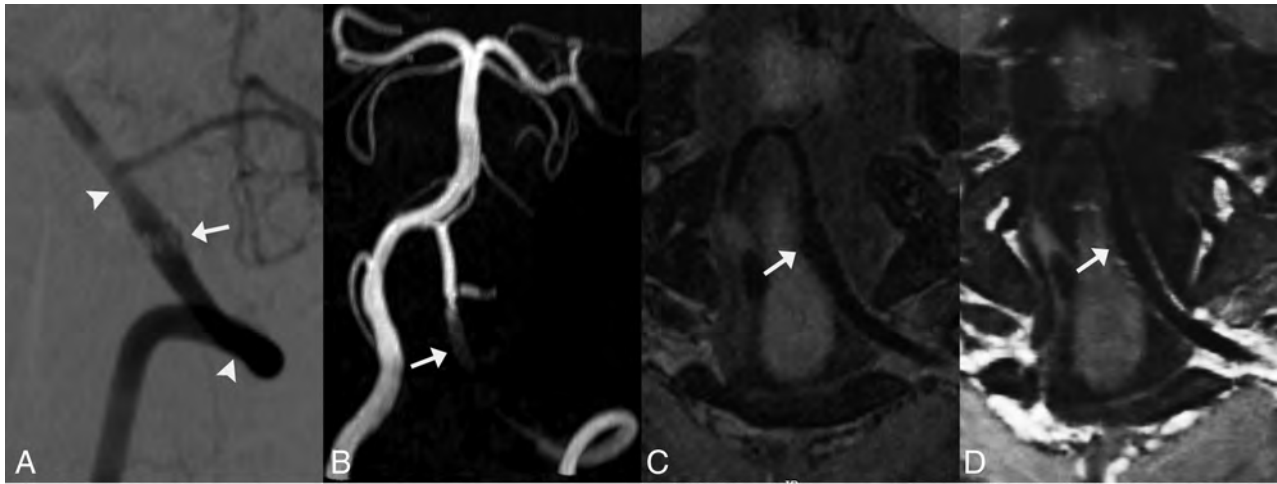


FIG 3. Follow-up images of a left vertebral artery dissecting aneurysm treated with Enterprise stent-assisted coiling at the sixth month postoperatively. A, DSA shows fusiform dilation (white arrows) of the left vertebral artery. The aneurysm is diagnosed as having incomplete occlusion. Arrowheads indicate the stent edges. B, The MIP image of TOF-MRA shows strong signal loss at the stented artery. The aneurysm remnant is not depicted. C and D, Pre- and postcontrast 3D T1-weighted SPACE shows a fusiform dilation of the parent artery, similar to the DSA findings. The aneurysm is classified as having incomplete occlusion on 3D T1-weighted SPACE. The postcontrast image shows mild enhancement of the stented artery. The image quality score for TOF-MRA and 3D T1-weighted SPACE is 1/1 and 5/5, respectively.

Table 3: Diagnostic performance of TOF-MRA, HR-VW-MR imaging, and HR-VW-MR imaging combined with TOF-MRA in the assessment of aneurysm occlusion status

	Sensitivity	Specificity	Positive Predictive Value	Negative Predictive Value	Accuracy
TOF-MRA	80.0%	100.0%	100.0%	82.4%	89.7%
HR-VW-MR imaging	53.30%	100.0%	100.0%	66.7%	75.9%
HR-VW-MR imaging combined with TOF-MRA	93.3%	100.0%	100.0%	93.3%	96.6%

evaluation of aneurysm occlusion status and the patency of the parent artery in the follow-up of intracranial VBDA after reconstructive EVT. For visualization of the stented artery, HR-VW-MR imaging provided obviously better image quality than TOF-MRA. The interobserver agreement in the image analysis for different imaging modalities ranged from substantial to almost perfect.

Aneurysm Occlusion Status

The aneurysm occlusion status and patency of the parent artery were the 2 major concerns in the follow-up of VBDA. Because TOF-MRA used bright-blood technology to depict the blood flow, the blood flow in the parent artery and residual aneurysm showed high signals, which were distinguishable from those of the surrounding tissues. In contrast, to depict the vessel wall and lumen directly, black-blood technology was used in HR-VW-MR imaging. Because the blood flow signals were suppressed in HR-VW-MR imaging, the residual aneurysm was sometimes difficult to distinguish from surrounding tissues (Fig 1). In general, TOF-MRA was superior to HR-VW-MR imaging in the evaluation of aneurysm occlusion status in our study. However, HR-VW-MR imaging was less sensitive to the susceptibility artifacts caused by stents and coils than TOF-MRA, and the vessel wall features on HR-VW-MR imaging might be helpful in assessing aneurysm occlusion status. Figure 3 shows the follow-up images of a

vertebral artery dissecting aneurysm treated with Enterprise stent-assisted coiling. Whereas the residual aneurysm and most of the stented artery were invisible on TOF-MRA because of artifacts, the HR-VW-MR imaging showed a fusiform dilation of the parent artery, similar to the DSA findings. The aneurysm was classified as incomplete occlusion on DSA and HR-VW-MR imaging. Therefore, the combination of TOF-MRA and HR-VW-MR imaging improved the diagnostic accuracy in the evaluation of aneurysm occlusion status.

In this study, the overall sensitivity and specificity of TOF-MRA in the assessment of aneurysm occlusion status were 80.0% and 100.0%, respectively. Except for 4 aneurysms treated with flow diverters, TOF-MRA had a sensitivity and specificity of 84.6% and 100.0%, respectively, in the rest of the aneurysms treated with stent placement with or without coils. In the largest prospective study on the diagnostic performance of TOF-MRA in the follow-up of treated intracranial aneurysms to date, Xiang et al³ reported a sensitivity and specificity of 0.67 and 0.95, respectively, for aneurysms treated with stent-assisted coiling, and 0.92 and 1.00, respectively, for aneurysms treated with flow diverters. TOF-MRA showed a better diagnostic performance in this study than in previous studies of aneurysms treated with stent placement,^{3,10} possibly because of the use of different treatment concepts for dissecting aneurysms and saccular aneurysms. Because the dissecting aneurysmal wall might be more fragile than the wall of a saccular aneurysm, the

VBDAs may pose greater risk than saccular aneurysms in embolization with coils. The relatively looser coil packing resulted in fewer susceptibility artifacts caused by coils.

Patency of the Parent Artery

The image quality of the stented artery on TOF-MRA was disappointing because TOF-MRA was sensitive to the susceptibility artifacts and radiofrequency shielding artifacts of implanted stents or flow diverters. Consequently, TOF-MRA often showed false stenosis or occlusion of the stented artery (Figs 1 and 3).^{11,12} In contrast, HR-VW-MR imaging showed significantly better image quality than TOF-MRA, with no or few artifacts. This result was consistent with findings from a previous study demonstrating that 3D T1-weighted SPACE was more accurate than TOF-MRA in the assessment of patency of the stented artery in 53 intracranial aneurysms treated with the Pipeline.¹³ In this study, regardless of whether the simplified 2-grade or 3-grade scale was used, the HR-VW-MR imaging had a 100% coincidence rate with DSA in the evaluation of the patency of the parent artery. Therefore, HR-VW-MR imaging is a good technique for assessing the patency of the parent artery in intracranial VBDAs treated with reconstructive EVT.

Evaluation of Vessel Walls

Beyond the aneurysm occlusion status and the patency of the parent artery, attention should also be paid to arterial wall evolution during the follow-up period. In this study, whereas an intimal flap and double lumen sign were observed only in incompletely occluded aneurysms, IMH was observed in both completely occluded and incompletely occluded aneurysms. Complete occlusion of the aneurysms indicated an absence of blood flow into the vessel wall through the ruptured internal elastic lamina but did not indicate that the affected vessel wall was healing well. Tian et al¹⁴ reported that persistent high signal intensity of IMHs may be associated with the progression of intracranial VBDAs after reconstructive EVT. Zhang et al¹⁵ reported 3 VBDAs that were confirmed to have total occlusion on DSA and showed IMH enlargement on MR imaging. Even if the parent arteries are sacrificed, the IMH might continue to enlarge; however, the mechanism is unclear in this circumstance.¹⁵ Some authors have speculated that the rupture of the vasa vasorum in the arterial wall results in IMH recurrence.^{16,17} Therefore, for patients with treated VBDAs whose symptoms persist or worsen, an HR-VW-MR imaging examination is recommended even if the DSA shows that the aneurysms involve total occlusion.

Zhang et al¹⁸ have reported that aneurysm wall enhancement of unruptured VBDAs on HR-VW-MR imaging before procedures might predict an unstable state and can be used to predict aneurysm progression after reconstructive EVT. A study including 53 intracranial saccular aneurysms has reported that aneurysm wall enhancement is commonly observed after embolization and decreases with time.¹⁹ However, no study on affected vessel wall enhancement in VBDAs after reconstructive EVT has been reported. In our study, the affected vessel wall enhancement was observed in all cases. The association between the degree of affected vessel wall enhancement and the stability of VBDAs after reconstructive EVT and the change in vessel wall enhancement with time will be explored in our future studies.

Imaging Protocol

Although HR-VW-MR imaging can be acquired with both 2D and 3D sequences, only the 3D T1-weighted SPACE sequence was performed in this study. The 2D sequences can provide high spatial resolution and a good SNR but require longer acquisition times than 3D sequences when the VBDAs are large.⁴ In contrast, 3D T1-weighted SPACE using isotropic volume scanning can cover a large scope in a relatively short scanning time. In addition, the vessel wall and lumen can be observed from different projections through MPR of 3D SPACE. The major limitation of HR-VW-MR imaging is its relatively long scanning time. The total examination time in our study was nearly 20 minutes. Therefore, the HR-VW-MR imaging examination is not suitable for patients with claustrophobia or postoperative restlessness. To decrease the examination time, we changed the imaging protocol of HR-VW-MR imaging from 2022: First, TOF-MRA was performed to define the location of the vertebrobasilar artery; then, the scanning scope of 3D T1-weighted SPACE was limited to the location of the vertebrobasilar artery. This imaging protocol decreased the examination time by nearly half.

Owing to the high signal intensity of the contrast agent, contrast-enhanced MRA has been reported to be superior to TOF-MRA in the assessment of aneurysmal occlusion status for endovascularly treated intracranial aneurysms.^{11,20} In recent years, Silent MRA (GE Healthcare) and pointwise encoding time reduction with radial acquisition subtraction-based MRA (PETRA; Siemens), both using an arterial spin-labeling combined with an ultrashort TE technique, have been demonstrated to be superior to TOF-MRA in the evaluation of aneurysm occlusion status for endovascularly treated aneurysms.^{10,20-22} Given that most treated intracranial aneurysms in these previous studies were saccular aneurysms, the diagnostic performance of these MRA techniques should be compared in intracranial VBDAs treated with reconstructive EVT in future studies. Because all MRA techniques are unable to provide a precise assessment of the affected arterial wall, HR-VW-MR imaging is always recommended in the follow-up of treated VBDAs.

Limitations

This article had several limitations: First, it was a retrospective study with a small sample size. Second, the exact sizes of dissecting aneurysms should be measured on the 3D SPACE images. Because some patients did not undergo HR-VW-MR imaging before their procedures, the aneurysmal size was measured on the DSA images during their procedures. The exact size of the VBDAs might have been larger because the IMHs could not be visualized on DSA images. Finally, the interval between the procedures and MR examinations varied widely among patients.

CONCLUSIONS

In the follow-up of intracranial VBDAs after reconstructive EVT, HR-VW-MR imaging combined with TOF-MRA at 3T showed good diagnostic performance in the evaluation of aneurysm occlusion status and patency of the parent artery. As a noninvasive imaging technique, the combination of HR-VW-MR imaging and TOF-MRA may be an ideal option for repeat

examinations in patients with intracranial VBDA after reconstructive EVT.

Disclosure forms provided by the authors are available with the full text and PDF of this article at www.ajnr.org.

REFERENCES

1. Sikkema T, Uyttenboogaart M, Eshghi O, et al. **Intracranial artery dissection.** *Eur J Neurol* 2014;21:820–26 CrossRef Medline
2. Catapano JS, Ducruet AF, Cadigan MS, et al. **Endovascular treatment of vertebral artery dissecting aneurysms: a 20-year institutional experience.** *J Neurointerv Surg* 2022;14:257–61 CrossRef Medline
3. Xiang S, Fan F, Hu P, et al. **The sensitivity and specificity of TOF-MRA compared with DSA in the follow-up of treated intracranial aneurysms.** *J Neurointerv Surg* 2021;13:1172–79 CrossRef Medline
4. Sui B, Bai X, Gao P, et al. **High-resolution vessel wall magnetic resonance imaging for depicting imaging features of unruptured intracranial vertebrobasilar dissecting aneurysms.** *J Int Med Res* 2021;49:30006052097738 CrossRef Medline
5. Zhu X, Qiu H, Hui FK, et al. **Practical value of three-dimensional high resolution magnetic resonance vessel wall imaging in identifying suspicious intracranial vertebrobasilar dissecting aneurysms.** *BMC Neurol* 2020;20:199 CrossRef Medline
6. Wang Y, Lou X, Li Y, et al. **Imaging investigation of intracranial arterial dissecting aneurysms by using 3 T high-resolution MRI and DSA: from the interventional neuroradiologists' view.** *Acta Neurochir (Wien)* 2014;156:515–25 CrossRef Medline
7. Wu Y, Wu F, Liu Y, et al. **High-resolution magnetic resonance imaging of cervicocranial artery dissection: imaging features associated with stroke.** *Stroke* 2019;50:3101–07 CrossRef Medline
8. Takano N, Suzuki M, Irie R, et al. **Usefulness of non-contrast-enhanced MR angiography using a silent scan for follow-up after y-configuration stent-assisted coil embolization for basilar tip aneurysms.** *AJNR Am J Neuroradiol* 2017;38:577–81 CrossRef Medline
9. Landis JR, Koch GG. **The measurement of observer agreement for categorical data.** *Biometrics* 1977;33:159–74 CrossRef Medline
10. Kim YN, Choi JW, Lim YC, et al. **Usefulness of silent MRA for evaluation of aneurysm after stent-assisted coil embolization.** *Korean J Radiol* 2022;23:246–55 CrossRef Medline
11. Attali J, Benaissa A, Soize S, et al. **Follow-up of intracranial aneurysms treated by flow diverter: comparison of three-dimensional time-of-flight MR angiography (3D-TOF-MRA) and contrast-enhanced MR angiography (CE-MRA) sequences with digital subtraction angiography as the gold standard.** *J Neurointerv Surg* 2016;8:81–86 CrossRef Medline
12. Akkaya S, Akca O, Arat A, et al. **Usefulness of contrast-enhanced and TOF MR angiography for follow-up after low-profile stent-assisted coil embolization of intracranial aneurysms.** *Interv Neuroradiol* 2018;24:655–61 CrossRef Medline
13. Shao Q, Wu Q, Li Q, et al. **Usefulness of 3D T1-SPACE in combination with 3D-TOF MRA for follow-up evaluation of intracranial aneurysms treated with Pipeline embolization devices.** *Front Neurol* 2020;11:542493 CrossRef Medline
14. Tian Z, Chen J, Zhang Y, et al. **Quantitative analysis of intracranial vertebrobasilar dissecting aneurysm with intramural hematoma after endovascular treatment using 3-T high-resolution magnetic resonance imaging.** *World Neurosurg* 2017;108:236–43 CrossRef Medline
15. Zhang Y, Wang Y, Sui B, et al. **Magnetic resonance imaging follow-up of large or giant vertebrobasilar dissecting aneurysms after total embolization on angiography.** *World Neurosurg* 2016;91:218–27 CrossRef Medline
16. Nakatomi H, Segawa H, Kurata A, et al. **Clinicopathological study of intracranial fusiform and dolichoectatic aneurysms: insight on the mechanism of growth.** *Stroke* 2000;31:896–900 CrossRef Medline
17. Ono H, Nakatomi H, Tsutsumi K, et al. **Symptomatic recurrence of intracranial arterial dissections: follow-up study of 143 consecutive cases and pathological investigation.** *Stroke* 2013;44:126–31 CrossRef Medline
18. Zhang Y, Sui B, Liu J, et al. **Aneurysm wall enhancement on magnetic resonance imaging as a risk factor for progression of unruptured vertebrobasilar dissecting aneurysms after reconstructive endovascular treatment.** *J Neurosurg* 2018;128:747–55 CrossRef Medline
19. Larsen N, Flüh C, Madjidyar J, et al. **Visualization of aneurysm healing: enhancement patterns and reperfusion in intracranial aneurysms after embolization on 3T vessel wall MRI.** *Clin Neuroradiol* 2020;30:811–15 CrossRef Medline
20. You SH, Kim B, Yang KS, et al. **Ultrashort echo time magnetic resonance angiography in follow-up of intracranial aneurysms treated with endovascular coiling: comparison of time-of-flight, pointwise encoding time reduction with radial acquisition, and contrast-enhanced magnetic resonance angiography.** *Neurosurgery* 2021;88: E179–89 CrossRef Medline
21. Tan S, Lu Y, Li B, et al. **Usefulness of silent magnetic resonance angiography in the follow-up of endovascular-treated intracranial aneurysm: a prospective study.** *J Stroke Cerebrovasc Dis* 2022;31:106256 CrossRef Medline
22. Oishi H, Fujii T, Suzuki M, et al. **Usefulness of Silent MR angiography for intracranial aneurysms treated with a flow-diverter device.** *AJNR Am J Neuroradiol* 2019;40:808–14 CrossRef Medline

Malpractice Litigation Related to Diagnosis and Treatment of Intracranial Aneurysms

 A. Khan,  M. Khunte,  X. Wu,  S. Bajaj,  S. Payabvash,  M. Wintermark,  C. Matouk,  D.J. Seidenwurm,  D. Gandhi,  P. Parizel,  J. Mezrich, and  A. Malhotra



ABSTRACT

BACKGROUND AND PURPOSE: Approaches to management of intracranial aneurysms are inconsistent, in part due to apprehension relating to potential malpractice claims. The purpose of this article was to review the causes of action underlying medical malpractice lawsuits related to the diagnosis and management of intracranial aneurysms and to identify the factors associated and their outcomes.

MATERIALS AND METHODS: We consulted 2 large legal databases in the United States to search for cases in which there were jury awards and settlements related to the diagnosis and management of patients with intracranial aneurysms in the United States. Files were screened to include only those cases in which the cause of action involved negligence in the diagnosis and management of a patient with an intracranial aneurysm.

RESULTS: Between 2000 and 2020, two hundred eighty-seven published case summaries were identified, of which 133 were eligible for inclusion in the analysis. Radiologists constituted 16% of 159 physicians sued in these lawsuits. Failure to diagnose was the most common medical malpractice claim referenced (100/133 cases), with the most common subgroups being “failure to include cerebral aneurysm as a differential and thus perform adequate work-up” (30 cases), and “failure to correctly interpret aneurysm evidence on CT or MR imaging” (16 cases). Only 6 of these 16 cases were adjudicated at trial, with 2 decided in favor of the plaintiff (awarded \$4,000,000 and \$43,000,000, respectively).

CONCLUSIONS: Incorrect interpretation of imaging is relatively infrequent as a cause of malpractice litigation compared with failure to diagnose aneurysms in the clinical setting by neurosurgeons, emergency physicians, and primary care providers.

ABBREVIATION: IA = intracranial aneurysm

The natural history of intracranial aneurysms (IAs) is poorly understood, and there is significant variability in their management.¹⁻³ Increasing use of noninvasive, cross-sectional imaging leads to frequent diagnosis of incidental, small unruptured aneurysms. Unfortunately, their rupture risk is not well-known, and there are no clear guidelines regarding which aneurysms should be treated or the optimal frequency and duration of subsequent surveillance studies.^{4,5} In addition, recommendations

for screening high-risk populations for IAs should take into consideration the higher baseline prevalence suggested in more recent studies compared with historical publications.^{6,7} Ruptured aneurysms, however, are associated with very high morbidity and mortality.⁸ Lack of timely diagnosis and treatment can be a source of poor outcome and, potentially, malpractice claims.⁹

Fear of litigation and rising malpractice premiums may encourage defensive medicine practices, including administration of superfluous tests or aggressive use of preventive treatments.¹⁰ In a 2012 survey of >1000 practicing neurosurgeons in the United States, 72% reported ordering additional imaging studies in an effort to reduce the perceived risk of medical malpractice claims.¹¹ This approach has huge health and economic implications and may lead to increased physician frustration and burnout.¹² An estimated \$60 billion of the nearly \$3 trillion annual health care expenditure in the United States is attributed to defensive medicine practices.⁹

The high financial and emotional costs of lawsuits create a need to understand the medicolegal risks associated with IAs. This requires an awareness of previous lawsuits associated with

Received January 2, 2023; accepted after revision February 23.

From the Departments of Radiology and Biomedical Imaging (A.K., M.K., S.B., S.P., C.M., J.M., A.M.), and Neurosurgery (C.M.), Yale School of Medicine, New Haven, Connecticut; Department of Radiology (X.W.), University of California at San Francisco, San Francisco, California; Department of Radiology (M.W.), MD Anderson Cancer Center, Houston, Texas; Department of Neuroradiology (D.J.S.), Sutter Health, Sacramento, California; Departments of Interventional Neuroradiology, Radiology, and Nuclear Medicine (D.G.), Neurology (D.G.), and Neurosurgery (D.G.), University of Maryland School of Medicine, Baltimore, Maryland; and Department of Radiology (P.P.), University of Western Australia, Perth, Australia.

Please address correspondence to Ajay Malhotra, MD, MMM, Department of Radiology and Biomedical Imaging, Yale School of Medicine, Box 208042, Tompkins East 2, 333 Cedar St, New Haven, CT 06520-8042; e-mail: ajay.malhotra@yale.edu



Indicates article with online supplemental data.

<http://dx.doi.org/10.3174/ajnr.A7828>

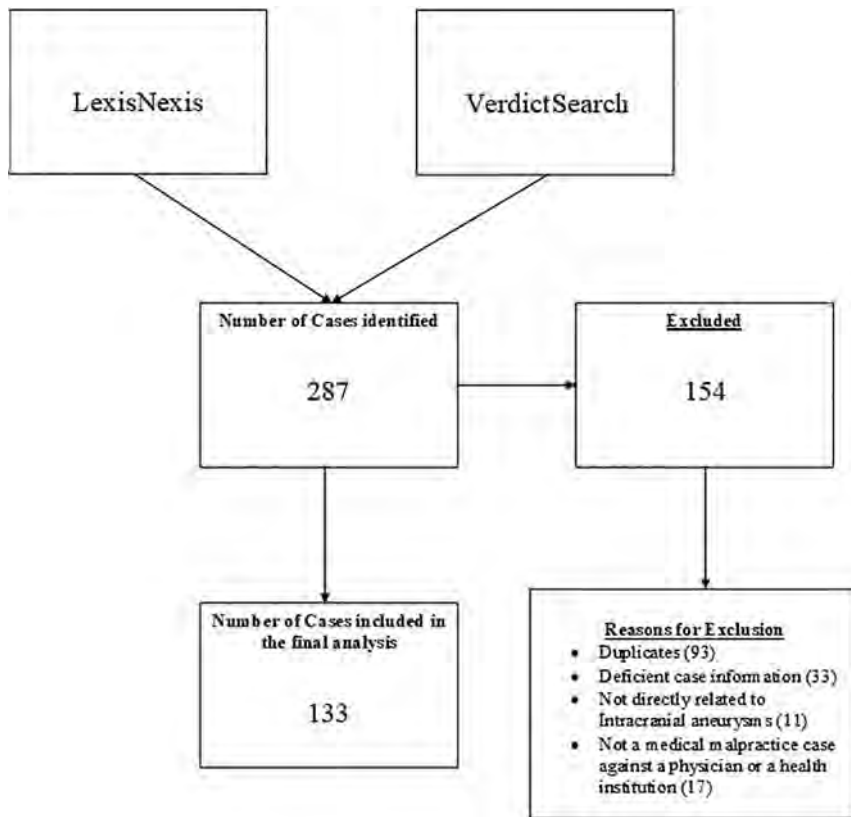


FIG 1. Flow chart illustrating the search strategy.

the diagnosis and management of IAs and the clinical settings in which they are most likely to arise. This study aimed to characterize the causes, distribution, and nature of malpractice litigation related to the diagnosis and treatment of IAs in the United States.

MATERIALS AND METHODS

No ethics approval was required for this study because no sensitive data were used and all materials were collected from open, published sources. Two online legal data repositories, VerdictSearch (American Lawyer media; <https://www.linkedin.com/company/the-american-lawyer>) and LexisNexis (RELX; <https://www.relx.com/our-business/market-segments/legal>) were screened to identify jury awards and settlements related to medical malpractice involving patients with IAs. Information was collected from all jurisdictions, ie, all 50 states and Washington, DC, from January 1, 2000, to December 31, 2020, and the most recently available published court determinations were included. These 2 legal research platforms collectively contain >1.1 million published summaries of jury awards and settlements.¹³ Furthermore, they both provide detailed information regarding plaintiff and defendant characteristics, causes of action, list of plaintiff and defendant experts, injury reports, award breakdowns, and other facts of the case. Claims that were dismissed before proceeding to trial or settled out of court, however, are not available in these databases. Both databases were queried using the terms “cerebral” and “aneurysm,” and only those cases categorized as “medical malpractice” or “wrongful death” were included. Only those cases in which claims of negligence

were made against a doctor and/or a health care institution (including clinics, privately owned hospitals, private radiology firms, and university hospitals) were included. Claims were further categorized as failure to diagnose despite reasonable suspicion, failure to treat, failure to transfer, complications during the treatment of aneurysms, and failure in acquiring proper informed consent. Cases against corporations or doctors prescribing over-the-counter medications that may have indirectly led to aneurysmal rupture were not included (eg, prescription of antihistamines with phenylpropanolamine leading to hypertension and eventual aneurysmal rupture). Cases in which there was a claim made against paramedics or firemen for inappropriate diagnoses or treatments were not included. Finally, claims of negligence and indirect causes of aneurysmal rupture by health care professionals were not included (ie, a nurse practitioner assaulted a patient in the head leading to aneurysmal rupture).

Relevant factors were identified and collected after analysis of each case summary. Such factors included the

year of publication of the trial, location of the trial, defendant and plaintiff characteristics, health care setting, case outcomes, award amounts, reasons for the lawsuit/claim, and category of negligence or medical malpractice, eg, failure to diagnose. There were a few cases in which the method of resolution was mixed when multiple parties were involved, ie, 1 plaintiff victory and 1 case dismissal; in such cases, it was counted as 1 plaintiff victory. Descriptive statistics were used for data analysis when appropriate.

RESULTS

Case Details

Case Characteristics. LexisNexis and VerdictSearch returned 287 published case summaries. After screening for inclusion and exclusion criteria and removal of duplicate studies, 133 unique case summaries were identified and included in the analysis (Fig 1). Twenty-seven states were represented, with most of the cases coming from New York (31, 23%), California (15, 11%), and Pennsylvania (11, 8%). Jurisdictions at the federal and state level were included (Online Supplemental Data).

Plaintiff Characteristics. The average age of the plaintiff at the time of the judgment was 47 years (range, 2 weeks to 76 years of age). Only 2 pediatric cases were noted.

Defendant Characteristics. Of 133 case summaries, 159 physicians were sued for medical malpractice, of which 125 (79%) were men, 12 (7%) were women, and 22 (14%) were unidentified. In 60/133 (45%) cases, claims were made against at least 1 doctor

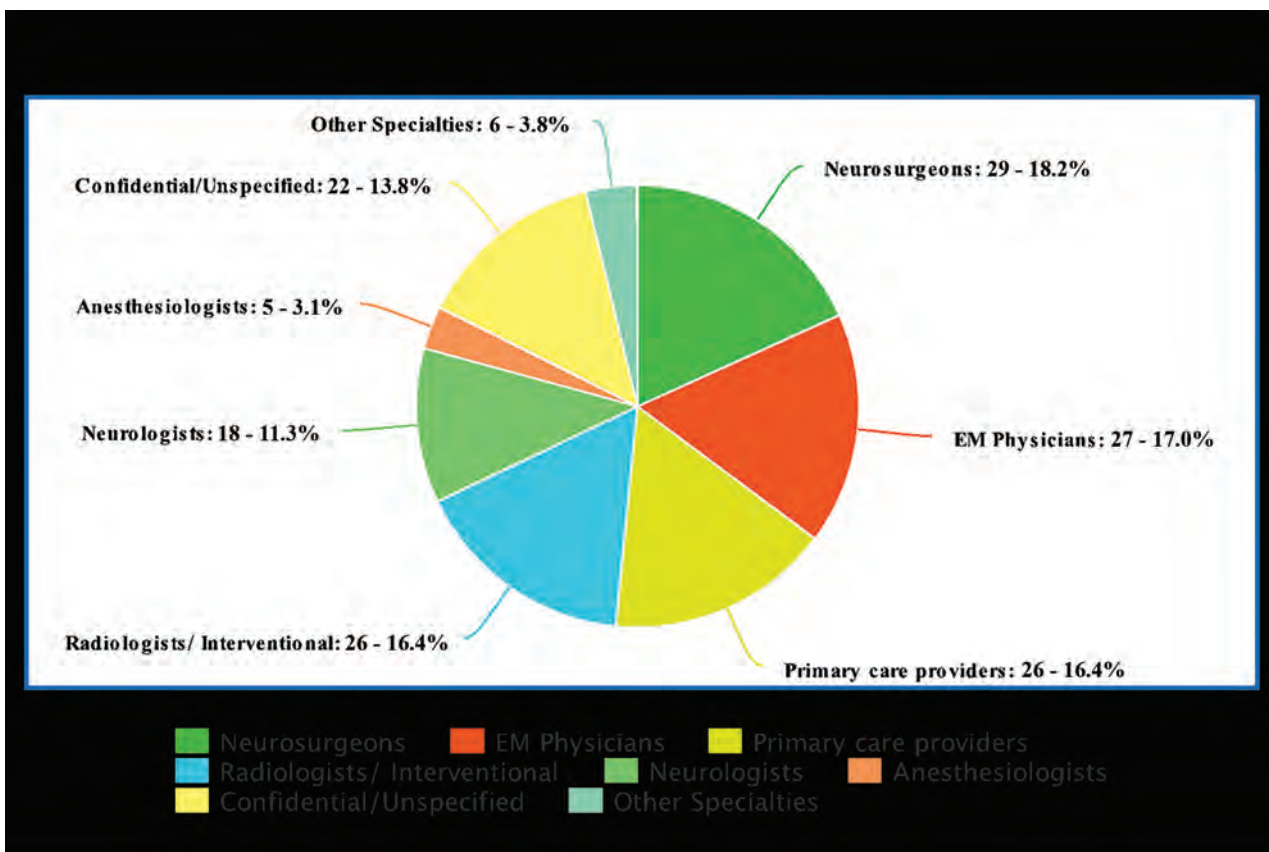


FIG 2. Pie chart showing specialties of physicians involved.

Table 1: Cause of action by specialty

	Diagnostic Radiologists	Neuro-interventional Radiologists	Emergency Medicine Physicians	Internists and Family Medicine Physicians	Neurosurgeons
Nonspecific failure to diagnose	0	1	18	16	2
Failure to include cerebral aneurysm as a differential and failure to perform adequate work-up	0	0	14	12	0
Failure to correctly interpret aneurysm evidence on CT or MR imaging	17	0	0	0	0
Procedural complications	0	6	0	0	18
Failure to timely treat	0	1	2	0	9
Failure to timely transfer	2	0	2	0	0
Failure to refer	0	0	0	4	0

and no health care facility. In another 60/133 (45%) cases, claims were made against both a physician and a health care facility. In 13/133 (10%) cases, claims were made against a health care facility only.

Defendant Specialties. After analysis of the case summaries, physicians from several specialties were found to be involved in litigation. Claims of malpractice were made against neurosurgeons (29/159, 18%), emergency medicine physicians (27/159, 17%), primary care providers (26/159, 16%), diagnostic/nonspecified radiologists (18/159, 11%), interventional neuroradiologists (7/159, 4%), a diagnostic neuroradiologist (1/159, 0.6%), neurologists (18/159, 11%), and anesthesiologists (5/159, 3%). Less frequently named specialists included ophthalmologists, otolaryngologists, and vascular surgeons. The defendant specialties are presented in Fig 2,

and a summary of the malpractice allegations against the 5 most common specialties is presented in Table 1.

Health Care Facility Involvement. There were 75 unique health care facilities involved in 73 cases. Forty-five of 75 (60.0%) health care facilities were identified as private hospitals/clinics, 22/75 (30%) were identified as university-affiliated or university hospitals, 7/75 (9%) were identified as private radiology clinics, and there was 1 claim made against the Office of Veteran Affairs.

Radiology-Specific Analysis. Twenty-six radiologists were involved in a malpractice suit. Eighteen of 26 (69%) were diagnostic/nonspecified radiologists, 7/26 (27%) were neurointerventional radiologists, and there was 1 (4%) neuroradiologist. Sixteen of 18 (89%) diagnostic radiologists and 1 neuroradiologist

Table 2: Settlement and trial outcomes for radiologists

	Settlements	Trials Won	Trials Lost	Dismissals
Diagnostic radiologists	9	4	3	2
Neurointerventional radiologists	5	2	0	0
Neuroradiologist	0	0	1	0

**FIG 3.** A, Award amounts in failure-to-treat cases resolved by trial. B, Award amounts in failure-to-treat cases resolved by settlement.

allegedly “failed to correctly interpret aneurysm evidence on CT or MR imaging.” Two of 18 (11%) diagnostic radiologists allegedly “failed to timely schedule a patient for imaging.” Six of 7 (86%) neurointerventional radiologists allegedly “failed to adequately treat due to procedural error during a diagnostic or treatment intervention.” Procedural errors included 5/6 (83%) cases of an attempted coiling with resultant perforation and rupture of an unruptured aneurysm, and 1 (17%) case of “misdiagnosis of an aneurysm as a junctional dilation on cerebral arteriography and failure to treat that aneurysm.” Last, 1/7 neurointerventional radiologists allegedly “failed to timely treat and unnecessarily delay a neuro-interventional procedure.” A summary of the malpractice allegations against the 5 most common specialties and a summary of the settlement and trial outcomes for radiologists is presented in Tables 1 and 2, respectively.

Causes of Action

Failure to Diagnose. Failure to diagnose was by far the most common medical malpractice cause of action referenced (100 cases). This was further subcategorized into failure to include cerebral aneurysm as a differential and thus perform adequate work-up (30/100, 30%) and “failure to correctly interpret aneurysm evidence on CT or MR imaging” (17/100, 17%). The remainder of the claims were designated as nonspecific failure to diagnose (53/100 cases).

Twenty of 30 (66%) cases in the “failure to work-up” category went to trial, with 12/20 (60%) judgments for the defense and 8/20 (40%) for the plaintiff. Eight of 30 (27%) cases settled, of which 5/8 (63%) cases settled for a specific dollar amount and 3/8 (37%) settled for a confidential/undisclosed amount.

In the failure to correctly interpret a CT or MR imaging category, 16/17 (94%) cases involved diagnostic/nonspecified radiologists and 1/17 (6%) physicians was specified as a neuroradiologist. Fifteen of 17 (88%) incorrect interpretation cases were on CT, and

2/17 (12%) were on MR imaging. Five of 17 (29%) cases occurred in the outpatient setting, and 2/17 (12%), in the emergency setting; the rest of the cases (10/17, 59%) did not specify the radiology setting. Nine of 17 cases (53%) were resolved by settlements, and 5/9 (55%) settlements specified the amount awarded to the plaintiff, while 4/9 (45%) settlements were confidential/undisclosed. Six of 17 (35%) cases went to trial, with 4/6 (67%) trials resulting in judgments for the defense and 2/6 (33%) trials resulting in judgments for the plaintiff. The plaintiffs were awarded \$4,000,000 and \$43,000,000, respectively. Last, 2/17 (12%) cases were dismissed.

Failure to Treat. Failure to treat was the next most common medical malpractice claim recorded (37 cases). Thirteen of 37 (35%) cases were attributed to failure to timely treat a case of a diagnosed IA resulting in rupture and SAH. Seven of 13 (54%) cases were resolved at trial (Fig 3A), with 3/7 (43%) judgments for the plaintiff and 4/7 (57%) for the defendant. The plaintiffs were awarded \$1,500,000, \$9,000,000, and \$7,200,000, respectively. Six of 13 (46%) cases were resolved by settlement (Fig 3B). Four of 6 (67%) cases were settled for a specified amount, ie, \$4,000,000, \$1,300,000, \$450,000, and \$150,000; and 2/6 (33%) cases were settled for unspecified amounts. Other claims of failure to treat did not provide specific details beyond failure to treat (24 cases).

Failure to Timely Transfer. There were 4 medical malpractice claims relating to the inability or failure to timely transfer a patient for a procedure or imaging that was necessary for diagnosis/work-up of an IA. In most of these cases, there was a high suspicion of IA rupture. In 1/4 (25%) cases, there was a failure to schedule imaging due to a delay in finding an oversized MR imaging machine for a morbidly obese patient. In another case, the plaintiffs claimed that there was a failure to properly triage, and an inappropriate delay in imaging. In 2/4 (50%) cases, there was an inability to transfer a

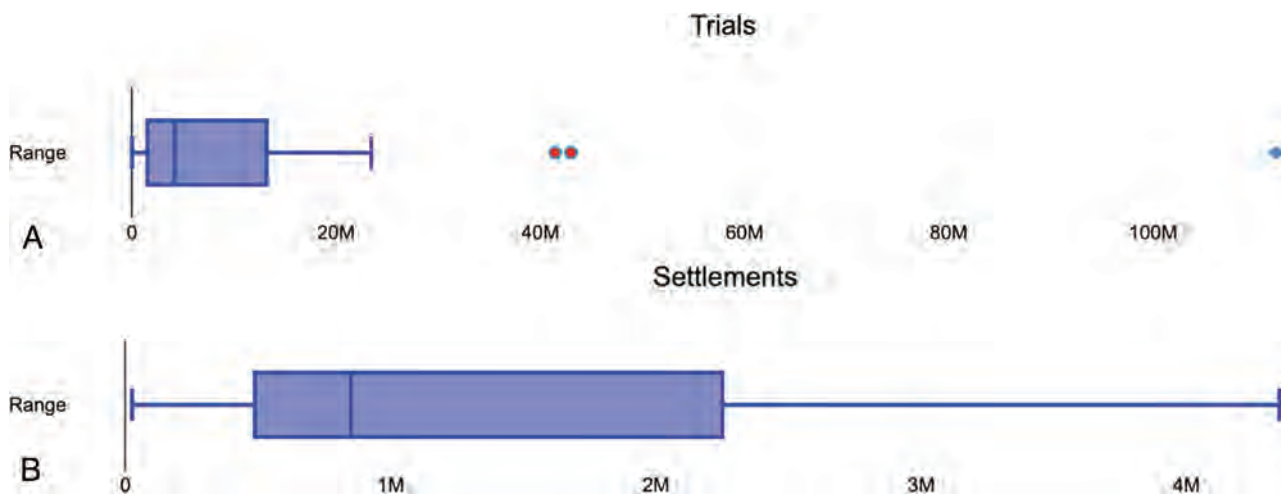


FIG 4. A, Award amounts in cases resolved by trial. B, Award amounts in cases resolved by settlement.

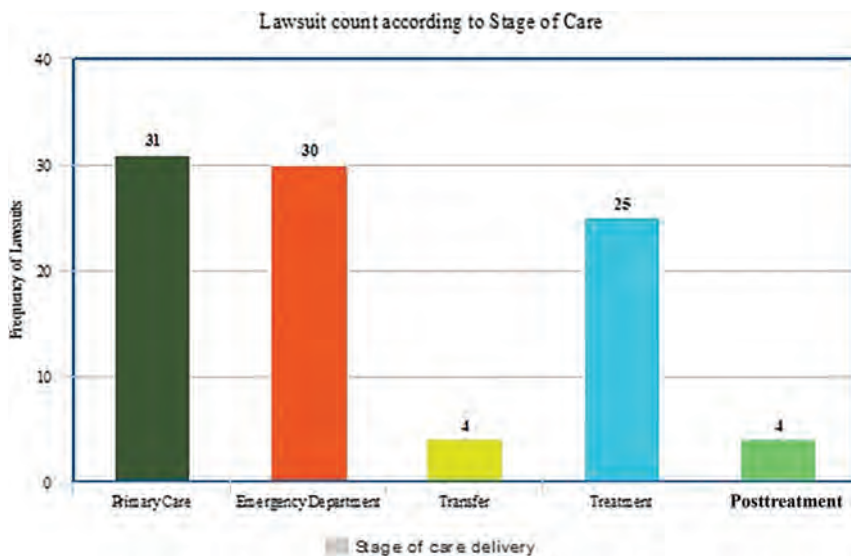


FIG 5. Incidence of lawsuits relative to the stage of care delivery.

patient due to unavailable beds caused by patient overflow. Three of 4 (75%) cases went to trial, resulting in awards for the plaintiff of \$9,000,000, \$8,000,000, and \$112,000,000, respectively. There was 1 case that was settled for \$450,000.

Failure to Refer. Last, there were 4 medical malpractice claims made against primary care providers and their inability to timely refer the patient to a neurology specialist. Primary care providers included internal medicine physicians and family medicine practitioners. Two of 4 (50%) were resolved at trial with 1 judgment for the defense and 1 for the plaintiff, with an award of \$1,500,000. Two of 4 (50%) cases were resolved by settlement, in the amounts of \$3,600,000 and \$450,000, respectively.

The causes of action related to treatment of aneurysms are detailed in the Online Supplemental Data.

There were 37 cases related to failure to treat an IA and 24 that were related to surgical procedures or postoperative complications

(4 of these were for ruptured IAs and 9 for unruptured IAs, and 11 were non-specific). There were 3 cases in which the defendant physicians diagnosed an unruptured cerebral aneurysm and scheduled follow-up for a procedure or further imaging at a later date. However, in all 3 cases, the diagnosed aneurysm ruptured before the scheduled follow-up. Two of these cases were settled when plaintiffs were awarded \$150,000 and \$3,600,000, respectively.

Judgment Awards and Settlements

One hundred thirty-three cases were identified from 2000 to 2020. Fifty-two of 133 (39%) of these cases resulted in settlement, and 70/133 (53%) cases went to trial. Nine of 133 (7%) cases were dismissed without a trial, and there were 2/133 (1.5%) cases in which

the method of resolution was mediation. There was only 1 case in which the awarded amount had to be reduced to the statutory cap (\$7,000,780 reduced to \$2,050,000).

Of the cases that went to trial (Fig 4A), 44/70 (63%) cases resulted in a judgment for the defendant and 26/70 (37%) cases resulted in a judgment for the plaintiff, with an average award of \$12,620,953 (range, \$0–\$112,000,000). Of the 52 cases that were settled (Fig 4B), 35/52 (67%) cases were settled for an undisclosed or confidential dollar amount. Seventeen of 52 (33%) cases provided specific information regarding settlement amounts. The average settlement amount was \$1,491,928 (range, \$25,000–\$4,350,000).

Incidence of Lawsuits Relative to the Stage of Care Delivery

The highest incidence of lawsuits occurred in the primary and emergency care settings (Fig 5). We identified 31/133 (23%) claims of medical malpractice occurring in the primary care

setting; the most common cause of action consisted of a nonspecific failure to diagnose (14/31, 45%) or a failure on the part of a primary care provider to include unruptured or ruptured IA as one of the differential diagnoses for vague presentations, thus a failure to perform further work-up (12/31, 39%). We also found 5/31 (16%) cases of failure to correctly identify an unruptured intracranial aneurysm in an outpatient setting by a radiologist, with subsequent rupture of the aneurysm.

Thirty of 133 (22%) claims of medical malpractice were in the emergency care setting; almost all the claims were against emergency medicine physicians (26/30, 87%). Only 2/28 (7%) cases in the emergency setting were due to failure on the part of the radiologist to identify a ruptured IA in an emergency setting.

DISCUSSION

Our review of 2 large legal databases resulted in 133 unique malpractice claims between 2000 and 2020 filed in 27 states in the United States relating to patients with IAs. One hundred fifty-nine physicians were sued in 120/133 cases, most frequently involving neurosurgeons (18.2%, 29/159), emergency medicine physicians (17%, 27/159), and primary care physicians (16.4%, 26/159). Radiologists were sued in 26 cases.

Failure to diagnose in a timely manner (75%, 100/133) was the most frequent cause of action for malpractice litigation. More than two-thirds of cases were due to failure to include cerebral aneurysm as a differential and thus perform adequate work-up or due to failure on the part of the primary care physician to refer or transfer the patient in a timely manner for neurologic consult/imaging. Management of patients with thunderclap headache and the utility/effectiveness of CTA versus lumbar puncture after negative findings on a CT of the head study are areas of active debate.¹⁴⁻¹⁶ Unfortunately, the legal case summaries did not provide adequate details to analyze these issues further in this study.

Of 30 claims of medical malpractice in the emergency care setting, only 2 were due to failure on the part of the radiologist to identify a ruptured IA in an emergency setting. In 1 case of a fall at home, CT of the brain was allegedly erroneously interpreted as having negative findings by a radiologist. The patient returned a day later with new neurologic deficits that were ascribed to barbiturates the patient had recently taken. Repeat CT at a different local hospital showed evidence of a ruptured aneurysm. A facilitated settlement was reached among all parties of \$4,000,000. The other case was nonspecific and only mentioned a failure to diagnose ruptured aneurysms and SAH, which went to trial and resulted in a judgment for the defense. The sensitivity of noncontrast CT for SAH decreases after 6 hours of the onset of thunderclap headache.¹⁷

Of 31 claims of medical malpractice in the primary care setting, we found 5 cases of failure to correctly identify an unruptured IA in an outpatient setting by a radiologist, with subsequent rupture of the aneurysm. Increasing use of noninvasive imaging has shown the prevalence of IAs to be >7% in the general population, and most of these incidental aneurysms are small. Artificial intelligence has also been proposed to facilitate the detection of IAs.¹⁸ However, the role and medicolegal implications of the incorporation of artificial intelligence have not yet been fully determined.¹⁹

Of the 17 cases in the failure to correctly interpret the CT or MR imaging category, 6 went to trial and only 2 resulted in judgments in favor of the plaintiff. In 1 case of blunt head trauma presenting as headache, findings of MR imaging of the brain were normal, but a subsequent CT showed SAH from a ruptured aneurysm. In this case, the plaintiff was awarded \$43,000,000. The second case presented with syncope and severe headache in which CT of the head was read as an “unremarkable study.” The patient was discharged and had worsening symptoms but did not have further imaging until 2 weeks later when a CT showed a large intracranial bleed. The plaintiff was awarded \$4,000,000.

Limitations

Various factors influence a plaintiff's decision to file a claim, including the relationship with the physician and/or hospital or perceived financial incentives, which may influence cases going to trial but cannot be assessed in this analysis.

The legal databases used in the study do not contain a comprehensive list of all litigation filed across the United States. Cases that are resolved privately in the prelitigation setting before reaching trial would not be included in these data sets. Previous studies have reported that up to 85% of malpractice cases may be dropped, dismissed, or settled before trial.^{9,20} The available content varies by jurisdiction; some jurisdictions are more robust in sharing litigation materials with legal databases than others. However, these legal data sets are frequently used as a representation of legal precedent in outcome and value.

Case details within the database were not consistently clearly presented, making it difficult to accurately characterize some cases. There were multiple cases in which there were claims made against >1 party. There were also a handful of cases in which the method of resolution was mixed; ie, one party went to trial while another claim was dismissed. In such cases, the case was counted as 1 trial. A number of trials and settlements reported an undisclosed award amount, making it difficult to find accurate associations between award amounts and types of malpractice claims.

CONCLUSIONS

A review of the malpractice lawsuits in 2 major legal databases suggests a failure to clinically consider IA or do adequate imaging/work-up and failure to treat as the most frequent cause of action. Failure to correctly interpret imaging studies was a less frequent claim but may lead to significant financial liability. Although detection and treatment of IAs have increased in the past 2 decades, we did not see a corresponding increase in the frequency of lawsuits.

Disclosure forms provided by the authors are available with the full text and PDF of this article at www.ajnr.org.

REFERENCES

1. Malhotra A, Wu X, Forman HP, et al. **Management of tiny unruptured intracranial aneurysms: a comparative effectiveness analysis.** *JAMA Neurol* 2018;75:27-34 CrossRef Medline
2. Malhotra A, Wu X, Forman HP, et al. **Growth and rupture risk of small unruptured intracranial aneurysms: a systematic review.** *Ann Intern Med* 2017;167:26-33 CrossRef Medline

3. Malhotra A, Wu X, Geng B, et al. **Management of small unruptured intracranial aneurysms: a survey of neuroradiologists.** *AJNR Am J Neuroradiol* 2018;39:875–80 CrossRef Medline
4. Wu X, Matouk CC, Mangla R, et al. **Cost-effectiveness of computed tomography angiography in management of tiny unruptured intracranial aneurysms in the United States.** *Stroke* 2019;50:2396–403 CrossRef Medline
5. Malhotra A, Wu X, Forman HP, et al. **Management of unruptured intracranial aneurysms in older adults: a cost-effectiveness analysis.** *Radiology* 2019;291:411–17 CrossRef Medline
6. Malhotra A, Seifert K, Wu X, et al. **Screening for intracranial aneurysms in patients with thoracic aortic aneurysms.** *Cerebrovasc Dis* 2019;47:253–59 CrossRef Medline
7. Malhotra A, Wu X, Matouk CC, et al. **MR angiography screening and surveillance for intracranial aneurysms in autosomal dominant polycystic kidney disease: a cost-effectiveness analysis.** *Radiology* 2019;291:400–08 CrossRef Medline
8. Wardlaw JM, White PM. **The detection and management of unruptured intracranial aneurysms.** *Brain* 2000;123:205–21 CrossRef Medline
9. Gupta R, Griessenauer CJ, Moore JM, et al. **An analysis of malpractice litigation related to the management of brain aneurysms.** *J Neurosurg* 2017;127:1077–83 CrossRef Medline
10. Saint S, Vaughn VM, Chopra V, et al. **Perception of resources spent on defensive medicine and history of being sued among hospitalists: results from a national survey.** *J Hosp Med* 2018;13:26–29 CrossRef Medline
11. Nahed BV, Babu MA, Smith TR, et al. **Malpractice liability and defensive medicine: a national survey of neurosurgeons.** *PLoS One* 2012;7:e39237 CrossRef Medline
12. Williams PL, Williams JP, Williams BR. **The fine line of defensive medicine.** *J Forensic Leg Med* 2021;80:102170 CrossRef Medline
13. Haslett JJ, Genadry L, Zhang X, et al. **Systematic review of malpractice litigation in the diagnosis and treatment of acute stroke.** *Stroke* 2019;50:2858–64 CrossRef Medline
14. Malhotra A, Wu X, Kalra VB, et al. **Cost-effectiveness analysis of follow-up strategies for thunderclap headache patients with negative noncontrast CT.** *Acad Emerg Med* 2016;23:243–50 CrossRef Medline
15. Wu X, Kalra VB, Forman HP, et al. **Cost-effectiveness analysis of CTA and LP for evaluation of suspected SAH after negative non-contrast CT.** *Clin Neurol Neurosurg* 2016;142:104–11 CrossRef Medline
16. Malhotra A, Wu X, Gandhi D, et al. **The patient with thunderclap headache.** *Neuroimaging Clin N Am* 2018;28:335–51 CrossRef Medline
17. Dubosh NM, Belloio MF, Rabinstein AA, et al. **Sensitivity of early brain computed tomography to exclude aneurysmal subarachnoid hemorrhage: a systematic review and meta-analysis.** *Stroke* 2016;47:750–55 CrossRef Medline
18. Marasini A, Shrestha A, Phuyal S, et al. **Role of artificial intelligence in unruptured intracranial aneurysm: an overview.** *Front Neurol* 2022;13:784326 CrossRef Medline
19. Mezrich JL. **Is artificial intelligence (AI) a pipe dream? Why legal issues present significant hurdles to AI autonomy.** *AJR Am J Roentgenol* 2022;219:152–56 CrossRef Medline
20. Jena AB, Seabury S, Lakdawalla D, et al. **Malpractice risk according to physician specialty.** *N Engl J Med* 2011;365:629–36 CrossRef Medline

Aneurysm Treatment with Woven EndoBridge-17: Angiographic and Clinical Results at 12 Months from a Retrospective, 2-Center Series

 P. Pagano,  J. Cortese,  S. Soize,  J. Caroff,  P.F. Manceau,  J. Moret,  L. Spelle, and  L. Pierot



ABSTRACT

BACKGROUND AND PURPOSE: This retrospective, 2-center study investigated the feasibility, safety, and efficacy at 12-month follow-up of the treatment of ruptured, unruptured, and recurrent intracranial aneurysms using the latest generation of the Woven EndoBridge (WEB) device, the WEB-17 system.

MATERIALS AND METHODS: Aneurysms treated with WEB-17 were extracted from the databases of 2 neurovascular centers. Patients, aneurysm characteristics, complications, and clinical and anatomic results were analyzed.

RESULTS: From February 2017 to May 2021, two hundred twelve patients with 233 aneurysms (181/233, 77.7%, unruptured-recurrent, and 52/233, 22.3%, ruptured) were included. High treatment feasibility (95.3%) was reported and was similar in ruptured aneurysms (94.2%) and unruptured-recurrent aneurysms (95.6%) ($P = .71$) and in typical (95.4%) and atypical (94.7%) locations ($P = .70$), but it was lower in aneurysms with an angle between the parent artery and main aneurysm axis of $\geq 45^\circ$ (90.2%) compared with those with an angle of $< 45^\circ$ (97.1%) ($P = .03$). Global mortality and morbidity were 1.9% and 3.8% at 1 month, respectively, and 4.4% and 1.9% at 12 months, respectively. One-month morbidity ($P = .02$) and mortality ($P = .003$) were higher in the ruptured group (10.0% and 8.0%, respectively) compared with unruptured-recurrent group (1.9% and 0.0%, respectively). Overall adequate occlusion (complete occlusion and neck remnant) was 86.3%. The percentage of adequate occlusion was higher ($P = .05$) in the unruptured-recurrent group (88.5%) compared with the ruptured group (77.5%).

CONCLUSIONS: The WEB-17 system showed high feasibility for ruptured and unruptured aneurysms, typical and atypical locations, and some aneurysms with an angle of $\geq 45^\circ$. As the most recent generation device, the WEB-17 also demonstrates high safety and good efficacy.

ABBREVIATIONS: AcoA = anterior choroidal artery; AcomA = anterior communicating artery; EVT = endovascular treatment; FD = flow diverter; IA = intracranial aneurysm; WEB = Woven EndoBridge; WEB-DL = Woven EndoBridge Dual-Layer; WEB-SL/SLS = Woven EndoBridge Single-Layer and Single-Layer Sphere; WFNS = World Federation of Neurosurgical Societies

During the past 10 years, the intrasaccular Woven EndoBridge (WEB; MicroVention) device has completely changed endovascular treatment (EVT) of wide-neck intracranial aneurysms (IAs). After its introduction in Europe for clinical use,¹ the WEB

device evolved from the initial dual-layer (DL) version (WEB-DL) to the 2 single-layer (SL) versions (WEB-SL and WEB-SLS [single layer spherical]) and finally the enhanced visualization version that introduced drawn filled tubing technology to improve device fluoroscopy visibility.² In parallel, WEB-specific microcatheters (VIA microcatheters; Sequent Medical) were designed to facilitate WEB deployment (VIA -33, VIA -27, and VIA -21). The most recent advance of the WEB device is the 17 system that permits delivery of small WEB devices (width = ≤ 7 mm) through a 0.017-inch microcatheter. Additional WEB sizes have also been introduced, including a small device (width = 3 mm), half sizes (widths = 3.5 and 4.5 mm), and shallow devices with a 2-mm height.

The WEB was initially developed to treat wide-neck bifurcation aneurysms, specifically located at the MCA bifurcation, basilar artery tip, ICA terminus, and anterior communicating artery

Received November 10, 2022; accepted after revision February 23, 2023.

From the Department of Neuroradiology (P.P., S.S., P.F.M., L.P.), Hôpital Maison Blanche, Centre Hospitalier Universitaire, Reims, France; Faculty of Medicine (P.P., S.S., L.P.), Champagne-Ardenne University, Reims, Grand-Est, France; NEURI Brain Vascular Center (J. Cortese, J. Caroff, J.M., L.S.), Bicêtre Hospital Interventional Neuroradiology, Le Kremlin-Bicêtre, France; and Faculty of Medicine (J. Cortese, L.S.), Paris-Saclay University, L'Institut National de la Santé et de la Recherche Médicale U1195, Le Kremlin-Bicêtre, France.

Please address correspondence to Paolo Pagano, MD, Department of Neuroradiology, Hôpital Maison-Blanche, 45 rue Cognacq-Jay, 51092 Reims cedex, France; e-mail: paolopagano6@gmail.com

 Indicates open access to non-subscribers at www.ajnr.org

 Indicates article with online supplemental data.

<http://dx.doi.org/10.3174/ajnr.A7830>

(AcomA).²⁻¹⁰ Because the device is strictly endosaccular, there is no need for dual-antiplatelet treatment after WEB treatment, making it possible to treat unruptured and recurrent aneurysms as well as ruptured aneurysms.¹¹⁻²⁰

The Clinical Assessment of the WEB Device in the Ruptured Aneurysms (CLARYS) study recently confirmed the effectiveness of the WEB device in preventing aneurysm re-rupture in ruptured aneurysms.¹⁸ In parallel to the technical evolution of the WEB device, its indications progressively enlarged to distal and sidewall aneurysms.¹¹⁻¹³

Several multicenter prospective series, including WEB Clinical Assessment of Intracranial Aneurysm Therapy (WEBCAST),³ WEBCAST 2,⁵ French Observatory,⁶ WEB Intracranial Aneurysm Therapy (WEB-IT),¹⁰ and CLARYS,²¹ have demonstrated favorable safety and efficacy of EVT with the WEB device; however, these studies were conducted before the introduction of the 17 system.

Given the limited data available regarding the safety and efficacy of the WEB-17 device,^{14,22-27} this retrospective 2-center study aimed to evaluate the feasibility, safety, and efficacy at mid-term follow-up (12 months) after the treatment of ruptured, unruptured, and recurrent IAs using WEB-17 system.

MATERIALS AND METHODS

Study Design

This retrospective, observational study included patients from 2 French neurovascular centers (Centre Hospitalier Universitaire, Reims and NEURI brain Vascular Center, Le Kremlin-Bicetre). Both centers maintain an institutional prospective database that includes all patients treated with EVT for IA. From these databases, all patients treated with the WEB-17 until May 2021 were enrolled in the study.

The Comité d’Ethique pour la Recherche en Imagerie Médicale of Collège des Enseignants de Radiologie de France approved this retrospective study and waived written informed consent due to the retrospective study design (Institutional Review Board No. CRM-2207-293).

WEB Device

The WEB device consists of self-expanding, retrievable, electrothermally detachable, intrasaccular implants developed for the treatment of wide-neck bifurcation aneurysms.^{1,10,22-25,27} The WEB-17 is available in 2 configurations: WEB-SL (size range, 3 × 2 to 7 × 4 mm) and a more spherical WEB-SLS (size range, 4–7mm).²⁷ The WEB-17 system debuted in Europe in December 2016²² and is available in a small size (3 × 2 mm), in half sizes for the smallest size (with widths of 3.5 and 4.5 mm), and for shallow devices (with a 2-mm height for devices with a width between 3 and 5 mm). It is compatible with a straight or preshaped 0.017-inch microcatheter (VIA-17).²⁵

Procedure

In the 2 centers, the decision for EVT was reached by consensus with neurosurgeons and neuroradiologists. Pre-, intra-, and postoperative antiplatelet therapy was similar in the 2 centers. For unruptured and recurrent aneurysms, dual-antiplatelet treatment with 75 or 160 mg of aspirin and 180 mg of ticagrelor per day

was given 1 or 2 days preprocedure; if no stent was placed, ticagrelor was discontinued after the intervention and aspirin was maintained for 1 month. For ruptured aneurysms, aspirin, 250 mg IV, was administered during the procedure followed by oral aspirin for 1 month.

All procedures were performed on a biplane angiographic system (AlluraClarity; Philips Healthcare) with the patient under general anesthesia and systemic heparinization with triaxial access. The distal tip of VIA-17 microcatheter was always shaped with steam. The WEB size was selected according to measurements performed on 3D DSA: The WEB is typically oversized by 1 mm in width and undersized in height by 1 mm.

Follow-up

Follow-up was similar in both centers with 3- to 6-month and 12- to 18-month clinical and anatomic follow-up.

Data Collection

The following data were collected for each patient:

- Demographics: age and sex
- Aneurysm: location, status (ruptured, unruptured, and recurrent), and size (mean width, maximal width, maximal height, and maximal neck size); dome-to-neck ratio; angle between parent artery and main aneurysm axis
- Procedure: date, type (SL/SLS), and dimension of WEB used; additional device used; intra- and postprocedural complications;
- Retreatment of target aneurysm before the 12-month follow-up
- Angiographic and clinical follow-up at 12 months.

Data Analysis

Data analysis was performed by an interventional neuroradiologist (P.P.) independently of the procedures and clinical evaluations.

According to the initial WEB treatment indications, aneurysm location was classified into 2 groups:

- Typical location: AcomA, MCA bifurcation, ICA terminus, and basilar tip
- Atypical location: other ICA locations (ophthalmic, posterior communicating artery, anterior choroidal artery [AchoA]), A1-A2 segment, anterior-inferior cerebellar artery, posterior-inferior cerebellar artery, and superior cerebellar artery.

Aneurysms were dichotomized as wide-neck (neck of ≥ 4 mm or dome-to-neck ratio of <2) and narrow-neck. Aneurysms were also classified in 2 groups according to the angle (α) between the parent artery and the neck-to-fundus axis ($\alpha < 45^\circ$ and $\alpha \geq 45^\circ$). The α was measured with 3D-DSA images.

For patients with ruptured aneurysms, the World Federation of Neurosurgical Societies (WFNS) grade before aneurysm treatment was collected. For all patients, pre- and postoperative clinical status was evaluated using the mRS. In patients with SAH, the mRS was evaluated on the basis of patient, family, or caregiver reports.

All complications were reviewed and classified into 4 categories: intraprocedural thromboembolic, intraprocedural hemorrhagic, site of puncture, and postoperative (postprocedure and before 1 month). Complications were classified into 4 groups: no

symptoms, transitory deficit (when the duration of symptoms was <7 days), permanent deficit (when the duration of symptoms was ≥7 days), and death.

Morbidity was defined as mRS > 2 when the preoperative mRS was ≤2 and as an increase of 1 point when the preoperative mRS was >2. Morbidity and mortality were classified as procedure-related (related to all steps and all devices used during the procedure, including the WEB), SAH-related, and related to another disease.

Feasibility was evaluated in the global population and in relation to aneurysm status, to α ($\alpha < 45^\circ$ and $\alpha \geq 45^\circ$), and to location (typical and atypical). Aneurysm occlusion was evaluated with 12-month DSA using a 3-point scale: complete aneurysm occlusion, neck remnant, and aneurysm remnant. Clinical and angiographic results were evaluated in the global population and in 2 subgroups: unruptured-recurrent and ruptured aneurysms.

Statistical Analysis

Distribution normality was assessed using the Shapiro-Wilk test. Continuous variables were described as mean (SD) or median and interquartile range and were compared using the Student *t* test or Mann-Whitney *U* test. Categorical variables were presented as counts and compared using the χ^2 or Fisher exact test. ORs and their 95% CIs were calculated. A *P* value < .05 was considered statistically significant. Analyses were performed using MedCalc for Windows (Release 18.2; MedCalc Software).

RESULTS

Patients and Aneurysms

From February 2017 to May 2021, two hundred sixty patients with 281 aneurysms were treated with the WEB. During 224 procedures, 212/260 (81.5%) patients with 233/281 (82.9%) aneurysms were treated with the WEB-17, of whom 133/212 (62.7%) were women (Online Supplemental Data). The mean age was 55.2 (SD, 11.4) years. In 50/212 (23.6%) patients, 52/233 (22.3%) aneurysms were ruptured (WFNS score I for 25 patients, II for 12 patients, III for 4 patients, IV for 5 patients, and V for 4 patients). Three of 233 aneurysms (1.3%) were recurrent. Due to the small number, recurrent aneurysms were analyzed with the unruptured group.

Treatment Feasibility

The WEB was successfully implanted in 222/233 (95.3%) aneurysms, including 173/181 (95.6%) unruptured-recurrent and 49/52 (94.2%) ruptured (*P* = .71) aneurysms. Aneurysms were treated with the WEB-SL (188/222, 84.7%) or WEB-SLS (34/222, 15.3%). Feasibility was higher in the $\alpha < 45^\circ$ group (167/172, 97.1%) compared with the $\alpha \geq 45^\circ$ group (55/61, 90.2%) (*P* = .03) but was similar for aneurysms in typical locations (186/195, 95.4%) and atypical locations (36/38, 94.7%) (*P* = .70). Adjunctive devices (including balloons) were used in 42/222 (18.9%) aneurysms (Table).

A remodeling balloon, with or without an implantable device (flow diverter [FD], stent, or coils) was inflated in 25/220 (11.4%) WEB aneurysm treatments: 6/220 (2.7%) in aneurysms with $\alpha \geq 45^\circ$ and 3/220 (1.3%) in atypical locations.

A stent or FD, with or without a balloon, was used in 19/222 (8.5%) procedures, all of them for unruptured-recurrent

aneurysms (19/173, 10.9%). In 4/222 (1.8%) procedures, the WEB aneurysm treatment was performed with coils (2/173, 1.2%, unruptured-ruptured, and 2/49, 4.1%, ruptured), and in 1 procedure (1/222, 0.5%) using the WEB, coils and balloon were used to treat a ruptured aneurysm (1/49, 2.0%).

Treatment failed in 11/233 (4.7%) aneurysms (8/181 unruptured-recurrent, 4.4%; 3/52 ruptured, 5.8%): in 2 cases, the smallest WEB (WEB-SL, 3 × 2 mm) was too large; in 1 recurrent aneurysm initially treated with coiling, the WEB-SL was unstable in the aneurysm sac; in 8 procedures, 2 different WEB devices were deployed but did not adequately close the neck.

Complications were encountered in 2 of these 11 failed WEB treatments: In 1 patient treated with balloon-assisted coiling (BAC) for an unruptured AcomA aneurysm, perforation occurred during aneurysm coiling, leading to a small SAH without clinical worsening (mRS 0 at discharge); in the second situation 7 days posttreatment of an MCA bifurcation aneurysm with an FD, the patient experienced intrastent thrombosis with clinical worsening (the mRS at discharge and 12 months was 4).

Complications and Morbidity-Mortality at 1 Month

Complications are detailed in the Online Supplemental Data. Among 224 procedures, 15 (6.7%) thromboembolic intraprocedural events occurred. In 10 procedures, distal emboli were treated with intra-arterial administration of antiplatelet treatment (abciximab or tirofiban) in 8 procedures and no additional treatment in 2 procedures. mRS at discharge was 0 in 6 patients, 1 in 3 patients, and 2 in 1 patient. Four patients treated for ruptured AcomA aneurysms had thrombosis of the pericallosal artery treated by intra-arterial administration of aspirin and/or tirofiban. In 2 patients, the clot was successfully dissolved, but the patients died due to SAH (WFNS = V and WFNS = IV). In 2 other patients, the clot was not dissolved and clinical evolution was deleterious (death at 45 days and mRS 4 at discharge and 12 months, respectively). Finally, 1 patient treated for an unruptured MCA aneurysm with the WEB and a stent had intrastent thrombosis successfully treated with intra-arterial tirofiban (mRS 1 at discharge).

A hemorrhagic intraprocedural complication occurred in 3/224 (1.3%) procedures. One patient treated with the WEB and a balloon for an unruptured A2 aneurysm experienced aneurysm rupture during balloon inflation (producing a large SAH leading to death 50 days later). In 1 patient treated for an unruptured AcomA aneurysm, WEB treatment failed and a minor hemorrhagic complication occurred during aneurysm coiling (see above). In a patient with an unruptured MCA aneurysm, a sac perforation occurred during catheterization with a microwire and was managed by WEB deployment. Postoperative CT showed limited SAH with slight clinical worsening (mRS 1 at discharge and 0 at 12 months).

In 2/224 (0.8%) procedures, there were complications at the puncture site, treated with surgery or endovascularly. In both cases, no clinical consequences at discharge were reported.

Postprocedural complications were reported in 16/224 (7.1%) procedures. No delayed hemorrhagic complication (including bleeding/rebleeding of the aneurysm) was observed. Twelve patients experienced slight motor deficits a few days postprocedure with DWI- detected lesions in only 4 patients.

Treatment modalities^a

	Total (n = 222)	Unruptured and Recurrent Aneurysms (n = 173)	Ruptured Aneurysms (n = 49)	P Value
WEB alone	180 (81.1)	136 (78.6)	44 (89.8)	.08
WEB + another device (No.) (%)	42 (18.9)	37 (21.4)	5 (10.2)	
WEB-coils	4 (1.8)	2 (1.2)	2 (4.1)	
WEB-stent	11 (4.9)	11 (6.4)	0 (0)	
WEB-balloon	18 (8.1)	16 (9.2)	2 (4.1)	
WEB-FD	2 (0.9)	2 (1.2)	0 (0)	
WEB-stent-balloon	5 (2.2)	5 (2.9)	0 (0)	
WEB-coils-balloon	1 (0.5)	0 (0)	1 (2.0)	
WEB-FD-balloon	1 (0.5)	1 (0.5)	0 (0)	
WEB type (No.) (%)				.26
WEB-SL	188 (84.7)	144 (83.2)	44 (89.8)	
WEB-SLS	34 (15.3)	29 (16.8)	5 (10.2)	

^aCategoric variables are described as a number (percentage).

All 12 patients were treated medically (oral or IV antiplatelet medication) and had good clinical outcomes (mRS at discharge 0 in 10 patients and 1 in 2 patients). A patient treated for an ICA-AchoA unruptured aneurysm with the WEB only had an ischemic stroke 5 days postprocedure related to a WEB protrusion. One stent was placed in front of the neck during a second procedure, but intrastent thrombosis and a pericallosal embolic complication occurred and were unresolved at the procedure end despite the administration of an intra-arterial antiplatelet drug. The mRS at discharge and at 12 months was 4. Two patients experienced non-neurologic complications: pneumonia and acute lower limb ischemia in 1 patient (mRS 4 at discharge, stable compared with preoperative status) and pneumonia in 1 patient (mRS at discharge was 2, and it was 0 at 12 months).

In 1 case of WEB failure, one patient was treated with an FD but experienced an intrastent thrombosis 7 days after the treatment (see above).

Finally, 36/212 (16.9%) patients had intraprocedural or postprocedural complications: no symptoms in 10/212 (4.7%), transitory symptoms in 16/212 (7.5%), permanent deficit in 6/212 (2.8%), and death in 4/212 (1.8%). Two of these 4 patients died after 1 month and were not included in mortality at 1 month but were included in the mortality at 12-month evaluation (both considered procedure-related deaths). The other 2 patients had a thromboembolic intraprocedural complication and died 2 days posttreatment due to the severity of SAH (WFNS = V and WFNS = IV); these deaths were considered SAH-related and were included in the mortality at 1-month evaluation.

The overall morbidity and mortality at 1 month were 8/212 (3.8%) and 4/212 (1.9%), respectively. Morbidity was higher in patients with ruptured aneurysms than in those with unruptured-recurrent aneurysms (5/50, 10.0%, versus 3/162, 1.9%, respectively) ($P = .02$). Morbidity was procedure-related in 5/212 (2.4%; 2 of them WEB-related, 2/212, 1.0%) and SAH-related in 3/212 (1.4%). Mortality was higher in patients with ruptured aneurysms than in those with unruptured or recurrent aneurysms (4/50, 8.0%, versus 0/162, 0.0%, respectively) ($P = .003$). Mortality was related to SAH in all patients.

Angiographic and Clinical Results at 12 Months

The Figure illustrates the participant flow chart for safety and efficacy analysis. Among the baseline population of 212 patients and 233 aneurysms, 205 patients (96.7%) and 197 aneurysms (84.5%) had 12-month follow-up (mean for 12-month DSA, 12.6 [SD, 4.9] months).

Safety at 12 Months. The overall morbidity was 4/205 (1.9%), and no statistical difference was reported between the unruptured-recurrent group (2/156, 1.2%) and the ruptured group (2/49, 4.0%) ($P = .24$). Morbidity was procedure-related in 3/205 (1.4%; 1 was WEB-related, 1/205, 0.5%) and SAH-related in 1/205 (0.5%).

The overall mortality rate was 9/205 (4.4%) and was significantly higher in the ruptured group (7/49, 14.3%) compared with unruptured-recurrent group (2/156, 1.2%) ($P = .0008$). Mortality was procedure-related in 2/205 (1.0%; 1 was WEB-related, 1/205, 0.5%), SAH-related in 6/205 (2.9%), and due to unrelated disease in 1/205 (0.5%).

Efficacy. Complete occlusion was reported in 133/197 (67.5%) aneurysms; neck remnant, in 37/197 (18.8%); and aneurysm remnant, in 27/197 (13.7%). In the unruptured-recurrent group, 108/157 (68.8%), 31/157 (19.7%), and 18/157 (11.5%) aneurysms had complete occlusion, neck remnant, and aneurysm remnant, respectively, and in the ruptured group, they were 25/40 (62.5%), 6/40 (15.0%), and 9/40 (22.5%), respectively.

Adequate occlusion (complete occlusion and neck remnant) in the overall population was 170/197 (86.3%). The percentage of adequate occlusion was higher ($P = .05$) in the unruptured-recurrent group (139/157, 88.5%) versus the ruptured group (31/40, 77.5%).

There were 4/197 aneurysms (2.0%) retreated before 12 months: 2/157 (1.3%) in the unruptured-recurrent group and 2/40 (5.0%) in the ruptured group ($P = .18$). Two aneurysms were treated with an FD; 1, with coiling; and 1, with stent-assisted coiling. At the time of retreatment, occlusion status was aneurysm remnant in the 4 aneurysms. Retreatments took place 5.2, 6.0, 8.5, and 9.6 months after the initial WEB procedure.

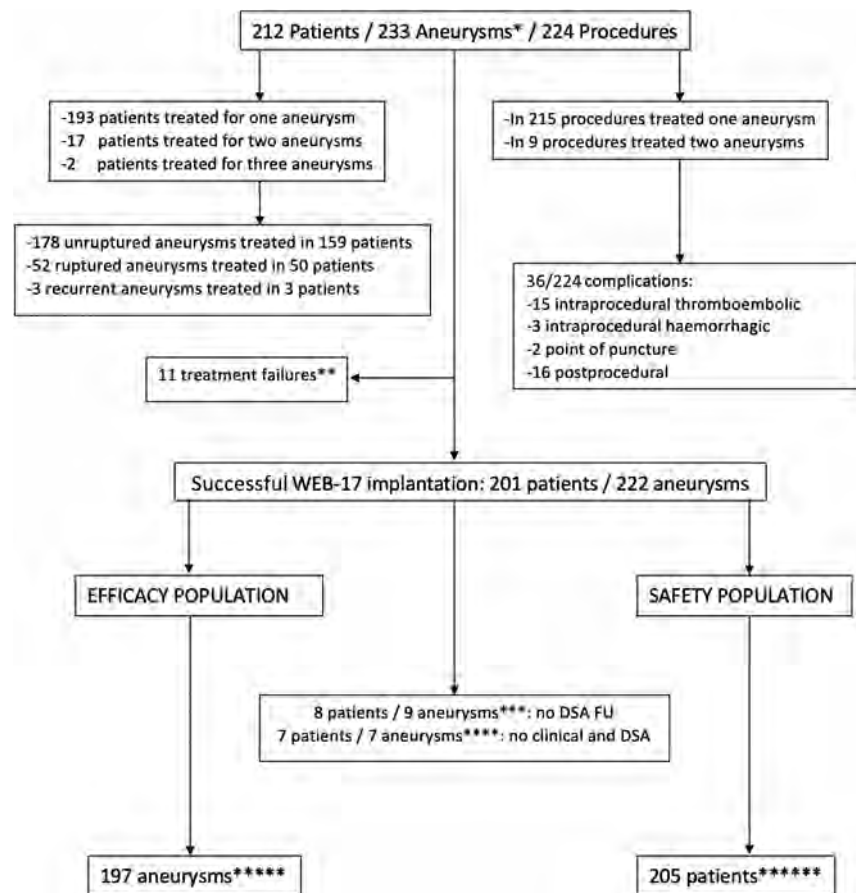


FIGURE Study flow chart. *All aneurysms treated with WEB-17 system. **See Treatment Feasibility in the text ***Seven patients refused DSA, and 1 patient had a comorbidity that prevented DSA; all 8 patients had clinical FU. ****Seven patients were lost to FU. *****Nine patients with 9 aneurysms died. Four were described in the mortality at 1-month evaluation (SAH-related); 4/9 patients died >1 month posttreatment (2 related to complications and 2 related to SAH severity); 1/9 patients died due to unrelated disease (hepatic carcinoma). *****Safety was assessed for 11 treatment failures. FU indicates follow-up.

DISCUSSION

This analysis of aneurysm treatment with the WEB-17 system shows its high feasibility (95.3%), with a complication rate of 16.9% (36/212 patients), most of them associated with no or transient clinical worsening. Global mortality and morbidity rates were 1.9% (4/212 patients) and 3.8% (8/212 patients) at 1 month, respectively, and 4.4% (9/205 patients) and 1.9% (4/205 patients) at 12 months, respectively. All deaths at 1 month were related to SAH, and most deaths (7/9, 77.8%) at 12 months were related to SAH or unrelated disease. Finally, the anatomic results at 12 months confirm the high efficacy of WEB treatment with complete aneurysm occlusion in 67.5% (133/197 aneurysms), neck remnant in 18.8% (37/197), and aneurysm remnant in 13.7% (27/197).

Mortality at 1 month was 1.9% (all SAH-related) compared with 0.0% in the 3 European Good Clinical Practice studies (WEBCAST, WEBCAST-2, and the French Observatory) or WEB-IT,^{3,5-7,10} in which the percentage of ruptured aneurysms was much lower (8.3% and 6.0%, respectively) compared with this series (22.3%). Similarly, at 12 months, most deaths (7/9, 77.8%) were related to SAH or unrelated disease. Morbidity at 1 and 12 months was also partially related to SAH: in 3/8 patients (37.5%) at 1 month and 1/4 patients (25.0%) at 12 months. Aneurysm

treatment with the WEB was associated with a high feasibility (95.3%) with similar results in ruptured aneurysms (94.2%), unruptured-recurrent aneurysms (95.6%) ($P = .71$), and in typical (95.4%) and atypical (94.7%) locations ($P = .70$). In contrast, feasibility was lower in aneurysms with an angle of $\geq 45^\circ$ (90.2%) compared with those with an angle of $< 45^\circ$ (97.1%) ($P = .03$). These data must be carefully interpreted because they relate to indications for aneurysm treatment with the WEB in the 2 centers of these studies (see Limitations). Our findings show that the WEB-17 system permits treatment of atypical and typical locations in the same percentage of cases, whereas some aneurysms with an angle of $\geq 45^\circ$ remain difficult or impossible to treat.

Among the 11 WEB-treated failures reported in this series, in 8 procedures, 2 different WEB devices were deployed but did not adequately close the neck; especially in 2 procedures, the WEB SL 6×3 mm and WEB SL 5×2 were too large or too small, while the unavailable WEB SL 6×2 mm would have been useful. These 2 situations showed that at the moment, in some aneurysms with limited height, treatment with the WEB device is not a good option. Anyway, as WEB indication for aneurysm treatment progressively increasing, our results could suggest the existence of limitation of WEB sizing, especially for height dimension and that shallow WEB device is a really necessity in the current clinical scenario.

In this series, adjunctive implants (stent, FD, or coils), with or without balloon inflation, were used in 19/222 (8.6%) aneurysm treatments. This rate is in line with the WEBCAST (8.3%) and the French Observatory (11.3%) studies but higher compared with WEBCAST 2 (1.9%).

The rate of procedural and postprocedural complications was 16.9%; however, a permanent deficit was observed in only 6/212 (2.8%) patients, and 2 of these 6 patients had non-neurologic complications.

The percentage of thromboembolic complications was lower (7.1%) compared with what has been reported in the European Good Clinical Practice series (14.4%) or WEB-IT (10.0%). Several factors may explain this difference: 1) The European and US series were conducted at the beginning of clinical experience with the WEB; 2) the patients included in this series were treated with the most recent WEB generation, while the patients in the European Good Clinical Practice studies were treated with the first WEB generation (WEB-DL) and second generation (WEB-SL and SLS); 3) antiplatelet protocols have evolved, and not all patients were premedicated with dual-antiplatelet treatment in the European and US series; 4) the microcatheter used in this series has the smallest size (VIA-17) compared with microcatheters used in the European and US series (including VIA-33, VIA-27, and VIA-21); and 5) most aneurysms included in this series were small.

Other recent retrospective series showing the results of aneurysm treatment with the WEB-17 device reported a rate of thromboembolic complications similar to ours: in van Rooij et al,²² 5.0%; in Pagano et al,²⁵ 5.5%; in Maurer et al,²³ 4.2%; in König et al,²⁶ 5.7%; in Mihalea et al,²⁴ 4.0%; in Goertz et al,²⁷ 5.3%; and in Zimmer et al,¹⁴ 6.4%.

In contrast to thromboembolic complications, the rate of procedural hemorrhagic complications was similar in this series (1.4%), the European series (1.2%), and WEB-IT (1.3%). Since beginning of clinical practice with WEB, it has been clearly shown that the rate of intraoperative rupture is very low. In the present series, only 1 patient died (50 days after the procedure) due to an intraprocedural rupture, related to balloon use and not to the WEB device.

The rate of delayed complications was not low (7.5%). None were hemorrhagic, and a few were infectious (2/16 patients). Most delayed complications were likely ischemic or hemodynamic, were treated with antiplatelet medication, and had good clinical outcome.

Anatomic results in this series were slightly better compared with previous series. The rate of complete aneurysm occlusion at 12 months was 67.5% compared with 52.9% in the European studies and 53.8% in WEB-IT. However, the rate of adequate occlusion was only slightly superior in the present series (86.3%) compared with European studies (79.1%) and WEB-IT (84.6%). These results are probably explained by the factors noted above regarding thromboembolic complications.

In this series, feasibility was similar in ruptured aneurysms (94.2%) and unruptured-recurrent aneurysms (95.6%) ($P = .71$). The complication rate was also similar in both groups (20.0% in ruptured and 16.0% in unruptured-recurrent aneurysm) ($P = .52$). Of note, the rate of intraprocedural thromboembolic complications was significantly higher in ruptured (18.0%) than in

unruptured aneurysms (3.7%) ($P = .001$). Moreover, due to SAHs in all cases, mortality at 1 month was significantly higher in ruptured aneurysms (8.0%) compared with unruptured-recurrent (0.0%) ($P = .003$) aneurysms. Morbidity was also higher in the ruptured group (10.0%) compared with the unruptured-recurrent group (1.9%) ($P = .02$). Finally, anatomic results were not significantly different, but adequate occlusion was more frequent in unruptured-recurrent aneurysms (88.5%) compared with ruptured aneurysms (77.5%) ($P = .05$).

In the CLARYS study,²¹ 12-month anatomic results were slightly different compared with the present series, with a lower rate of complete aneurysm occlusion (41.3%) and higher rates of neck (45.7%) and aneurysm (13.0%) remnants. However, the rate of adequate occlusion was higher (87.0%). Because all aneurysms were treated with the WEB-21 system in the CLARYS study, it is likely that the characteristics of the WEB-17 system (smaller system profile, half sizes, shallow devices) were responsible for the higher rate of complete aneurysm occlusion.

The rate of aneurysm retreatment at 12 months was globally low (4/197, 2.0%). The rate of retreatment was statistically not different between the unruptured-recurrent (2/157, 1.3%) and the ruptured (2/40, 5.0%) ($P = .18$) groups.

Limitations

This study has several limitations. First, our results are based on a retrospective analysis. This limitation is partially mitigated by all patients treated with WEB-17 being prospectively included in the database from 2 neurovascular centers. Second, the feasibility of WEB-17 aneurysm treatment was evaluated on the basis of the initial indication for WEB aneurysm treatment by the teams. Some aneurysms were likely not treated with the WEB on the basis of the team's decisions due to anticipated treatment complexity. These decisions could potentially have biased some results regarding feasibility.

CONCLUSIONS

The most recent generation of the WEB device (WEB-17 system) is associated with high feasibility of the treatment (95.3%), high safety (with 1-month morbidity and mortality 3.8% and 1.9%, respectively), and good efficacy (12-month adequate occlusion in 86.3%). Moreover, our findings indicate similar feasibility in unruptured-recurrent (95.6%) and ruptured (94.2%) aneurysms and in typical (95.4%) and atypical locations (94.7%); however, feasibility is slightly lower in aneurysms with an angle of $\geq 45^\circ$ (90.2%) compared with aneurysms with an angle of $< 45^\circ$ (97.1%). Ruptured aneurysms are associated with higher morbidity and mortality rates (4.0% and 14.3%, respectively), mostly due to the consequences of SAH. Finally, 12-month adequate occlusion was more frequent in the unruptured-recurrent group (88.5%) compared with the ruptured group (77.5%).

Disclosure forms provided by the authors are available with the full text and PDF of this article at www.ajnr.org

REFERENCES

1. Goyal N, Hoit D, Dinitto J, et al. **How to WEB: a practical review of methodology for the use of the Woven EndoBridge.** *J Neurointerv Surg* 2020;12:512–20 CrossRef Medline

2. Pierot L, Szikora I, Barreau X, et al. **Aneurysm treatment with the Woven EndoBridge (WEB) device in the combined population of two prospective, multicenter series: 5-year follow-up.** *J Neurointerv Surg* 2022 July 8 [Epub ahead of print] CrossRef Medline
3. Pierot L, Costalat V, Moret J, et al. **Safety and efficacy of aneurysm treatment with WEB: results of the WEBCAST study.** *J Neurosurg* 2016;124:1250–56 CrossRef Medline
4. Papagiannaki C, Spelle L, Januel AC, et al. **WEB intrasaccular flow disruptor-Prospective, multicenter experience in 83 patients with 85 aneurysms.** *AJNR Am J Neuroradiol* 2014;35:2106–11 CrossRef Medline
5. Pierot L, Gubucz I, Buhk JH, et al. **Safety and efficacy of aneurysm treatment with the WEB: results of the WEBCAST 2 study.** *AJNR Am J Neuroradiol* 2017;38:1151–55 CrossRef Medline
6. Pierot XL, Moret J, Turjman F, et al. **WEB French observatory.** *AJNR Am J Neuroradiol* 2016;37:655–59 CrossRef Medline
7. Pierot L, Moret J, Barreau X, et al. **Safety and efficacy of aneurysm treatment with WEB in the cumulative population of three prospective, multicenter series.** *J Neurointerv Surg* 2018;10:556–62 CrossRef Medline
8. Pierot L, Szikora I, Barreau X, et al. **Aneurysm treatment with WEB in the cumulative population of two prospective, multicenter series: 3-year follow-up.** *J Neurointerv Surg* 2021;13:363–68 CrossRef Medline
9. Fiorella D, Molyneux A, Coon A, et al. **Demographic, procedural and 30-day safety results from the WEB Intra-saccular Therapy Study (WEB-IT).** *J Neurointerv Surg* 2017;9:1191–96 CrossRef Medline
10. Arthur AS, Molyneux A, Coon AL, et al. **The safety and effectiveness of the Woven EndoBridge (WEB) system for the treatment of wide-necked bifurcation aneurysms: final 12-month results of the pivotal WEB Intrasaccular Therapy (WEB-IT) study.** *J Neurointerv Surg* 2019;11:924–30 CrossRef Medline
11. Pierot L, Biondi A, Narata AP, et al. **Should indications for WEB aneurysm treatment be enlarged? Report of a series of 20 patients with aneurysms in “atypical” locations for WEB treatment.** *J Neuroradiol* 2017;44:203–09 CrossRef Medline
12. Aguiar G, Caroff J, Mihalea C, et al. **WEB device for treatment of posterior communicating artery aneurysms.** *J Neurointerv Surg* 2022;14:362–65 CrossRef Medline
13. Adeeb N, Dibas M, Diestro JDB, et al. **Multicenter study for the treatment of sidewall versus bifurcation intracranial aneurysms with use of Woven EndoBridge (WEB).** *Radiology* 2022;304:372–82 CrossRef Medline
14. Zimmer S, Maus V, Maurer C, et al. **Widening the indications for intrasaccular flow disruption: WEB 17 in the treatment of aneurysm locations different from those in the Good Clinical Practice Trials.** *AJNR Am J Neuroradiol* 2021;42:524–29 CrossRef Medline
15. Gawlitza M, Soize S, Januel AC, et al. **Treatment of recurrent aneurysms using the Woven EndoBridge (WEB): anatomical and clinical results.** *J Neurointerv Surg* 2018;10:629–33 CrossRef Medline
16. Liebig T, Kabbasch C, Strasilla C, et al. **Intrasaccular flow disruption in acutely ruptured aneurysms: a multicenter retrospective review of the use of the WEB.** *AJNR Am J Neuroradiol* 2015;36:1721–27 CrossRef Medline
17. Popielski J, Berlis A, Weber W, et al. **Two-center experience in the endovascular treatment of ruptured and unruptured intracranial aneurysms using the WEB device: a retrospective analysis.** *AJNR Am J Neuroradiol* 2018;39:111–17 CrossRef Medline
18. Spelle L, Herbretreau D, Caroff J, et al. **CLinical Assessment of WEB device in Ruptured aneurYSms (CLARYS): results of 1-month and 1-year assessment of rebleeding protection and clinical safety in a multicenter study.** *J Neurointerv Surg* 2022;14:80714 CrossRef Medline
19. Al Saiegh F, Hasan D, Mouchtouris N, et al. **Treatment of acutely ruptured cerebral aneurysms with the Woven EndoBridge device: experience post-FDA approval.** *Neurosurg* 2020;87:E16–22 CrossRef Medline
20. Youssef PP, Dornbos D, Peterson J, et al. **Woven EndoBridge (WEB) device in the treatment of ruptured aneurysms.** *J Neurointerv Surg* 2021;13:443–46 CrossRef Medline
21. Spelle L, Herbretreau D, Caroff J, et al. **CLinical Assessment of WEB device in Ruptured aneurYSms (CLARYS): 12-month angiographic results of a multicenter study.** *J Neurointerv Surg* 2022 Jul 26 CrossRef Medline
22. Van Rooij SBT, Peluso JP, Sluzewski M, et al. **The new low-profile WEB 17 system for treatment of intracranial aneurysms: first clinical experiences.** *AJNR Am J Neuroradiol* 2018;39:859–63 CrossRef Medline
23. Maurer C, König I, Berlis A, et al. **Two-center experience in the endovascular treatment of intracranial aneurysms using the Woven EndoBridge-17 device including midterm follow-up results: a retrospective analysis.** *AJNR Am J Neuroradiol* 2019;40:1517–22 CrossRef Medline
24. Mihalea C, Caroff J, Pagiola I, et al. **Safety and efficiency of the fifth generation Woven EndoBridge device: technical note.** *J Neurointerv Surg* 2019;11:511–15 CrossRef Medline
25. Pagano P, Paiusan L, Soize S, et al. **Intracranial aneurysm treatment with intrasaccular flow disruption: comparison of WEB-21 and WEB-17 systems.** *J Neurointerv Surg* 2022;14:904–09 CrossRef Medline
26. König I, Maurer C, Berlis A, et al. **Treatment of ruptured and unruptured intracranial aneurysms with WEB 17 versus WEB 21 systems: comparison of indications and early angiographic outcomes.** *Clin Neuroradiol* 2021;31:691–97 CrossRef Medline
27. Goertz L, Liebig T, Siebert E, et al. **Low-profile intra-aneurysmal flow disruptor WEB 17 versus WEB predecessor systems for treatment of small intracranial aneurysms: comparative analysis of procedural safety and feasibility.** *AJNR Am J Neuroradiol* 2019;40:1766–72 CrossRef Medline

The FRESH Study: Treatment of Intracranial Aneurysms with the New FRED X Flow Diverter with Antithrombotic Surface Treatment Technology—First Multicenter Experience in 161 Patients

 D.F. Vollherbst,  H. Lücking,  J. DuPlessis,  M. Sonnberger,  C. Maurer,  N. Kocer,  M. Killer-Oberpfalzer,  R. Rautio,  L. Valvassori,  A. Berlis, S. Gasser,  S. Gatt,  A. Dörfler,  M. Bendszus, and  M.A. Möhlenbruch



ABSTRACT

BACKGROUND AND PURPOSE: Flow diverters with antithrombotic coatings are increasingly used to improve the safety of flow diverter treatments of intracranial aneurysms. This study aimed to investigate the safety and short-term efficacy of the new FRED X flow diverter.

MATERIALS AND METHODS: Medical charts and procedural and imaging data of a consecutive series of patients with intracranial aneurysms who were treated with the FRED X at 9 international neurovascular centers were retrospectively analyzed.

RESULTS: One hundred sixty-one patients (77.6% women; mean age, 55 years) with 184 aneurysms (11.2% acutely ruptured) were included in this study. Most aneurysms were located in the anterior circulation (77.0%), most frequently at the ICA (72.7%). The FRED X was successfully implanted in all procedures. Additional coiling was performed in 29.8%. In-stent balloon angioplasty was necessary in 2.5%. The rate of major adverse events was 3.1%. Thrombotic events occurred in 7 patients (4.3%) with 4 intra- and 4 postprocedural in-stent thromboses, respectively (1 patient had both peri- and postprocedural thrombosis). Of these thrombotic events, only 2 (1.2%) led to major adverse events (ischemic strokes). Postinterventional neurologic morbidity and mortality were observed in 1.9% and 1.2%, respectively. The rate of complete aneurysm occlusion after a mean follow-up of 7.0 months was 66.0%.

CONCLUSIONS: The new FRED X is a safe and feasible device for aneurysm treatment. In this retrospective multicenter study, the rate of thrombotic complications was low, and the short-term occlusion rates are satisfactory.

ABBREVIATIONS: ASA = acetylsalicylic acid; BA = basilar artery; FD = flow diverter; HH = Hunt and Hess; OKM = O'Kelly-Marotta; PcomA = posterior communicating artery; RROC = Raymond-Roy occlusion classification

The treatment of intracranial aneurysms with flow diverters (FDs) has emerged as an established treatment option for a considerable number of aneurysms.¹⁻⁴ The functional principle of FDs is based on a dense mesh of stent struts, which diverts the

flow within the target vessel past the aneurysm, eventually leading to the occlusion of the aneurysm. This relatively high metal coverage of the vessel wall, which is higher compared with conventional intracranial stents, can trigger thrombosis within the FD, which is a feared complication during and after FD treatments because it can lead to distal emboli and stent occlusion, eventually causing ischemic stroke.^{5,6} An emerging trend in the field of FD treatment of intracranial aneurysms is the use of FDs with specific antithrombotic coatings, which aim to reduce the risk of this potentially harmful complication.^{7,8} The Flow-Redirection Intraluminal Device (FRED; MicroVention) is one of the most frequently used FDs worldwide. Its safety and efficacy were demonstrated in numerous studies during the past years.^{2,9-11} After the publication of the FRED pivotal trial, it received FDA approval in the United States in 2020.¹² The FRED X, which was introduced only recently, is a new version of the FRED. The novelty of this successor product is the X-technology, a specific antithrombotic surface treatment that is applied to the stent.

The aim of this multicenter study was to investigate the peri- and postprocedural safety and the short-term efficacy of the

Received November 25, 2022; accepted after revision February 23, 2023.

From the Department of Neuroradiology (D.F.V., M.B., M.A.M.), Heidelberg University Hospital, Heidelberg, Germany; Department of Neuroradiology (H.L., A.D.), University of Erlangen-Nuremberg, Erlangen, Germany; Department of Clinical Neurosciences (J.D., S. Gatt), Royal Infirmary of Edinburgh, Edinburgh, UK; Department of Neuroradiology (M.S., S. Gasser), Johannes Kepler University Linz, Linz, Austria; Department of Diagnostic and Interventional Neuroradiology (C.M., A.B.), University Hospital Augsburg, Augsburg, Germany; Department of Radiology (N.K.), Division of Neuroradiology, Istanbul University-Cerrahpasa, Cerrahpasa Faculty of Medicine, Istanbul, Turkey; Department of Neurology (M.K.-O.), Institute of Neurointervention, Paracelsus Medizinische Privatuniversität, Salzburg, Austria; Department of Interventional Radiology (R.R.), Turku University Hospital, Turku, Finland; and Department of Neuroradiology (L.V.), San Carlo Borromeo Hospital, Milano, Lombardia, Italy.

Please address correspondence to Markus A. Möhlenbruch, MD, Department of Neuroradiology, Heidelberg University Hospital, INF 400, 69120 Heidelberg, Germany; e-mail: markus.moehlenbruch@med.uni-heidelberg.de

 Indicates article with online supplemental data.
<http://dx.doi.org/10.3174/ajnr.A7834>

new FRED X FD for the treatment of ruptured and unruptured intracranial aneurysms. The participating centers received the FRED X as part of a limited market release.

MATERIALS AND METHODS

Study Design

The FRESH study - Treatment of Intracranial Aneurysms with the New FRED X Flow Diverter with Antithrombotic Surface Treatment Technology - is a retrospective, multicentric, observational study at 9 international high-volume neurovascular centers. A survey, which was specifically designed for this study, was completed by the physicians who performed the treatments with the FRED X. On the basis of these surveys, the clinical, radiologic, and procedural parameters of patients with ruptured and unruptured intracranial aneurysms who were treated with the FRED X between January 2020 and March 2022 were systematically analyzed. The observation period, including the assessment of postprocedural events and the degree of occlusion at the latest imaging, was from January 2020 until June 2022. A part of this patient cohort was also included in the FRED/FRED Jr/FRED X Intracranial Aneurysm Treatment Study (FRITS; not yet published, ClinicalTrials.gov Identifier: NCT03920358). The institutional ethics committees approved this study.

Patient Data

The patient data included age, sex, and the initial clinical presentation. The pre- and posttreatment clinical statuses of the patients were assessed using the mRS. For patients with an acutely ruptured aneurysm, the clinical status was assessed according to the Hunt and Hess (HH) scale.

Aneurysm Data

The assessed characteristics of the treated aneurysms included the location of the aneurysm, the aneurysm type (saccular, fusiform, blister-like, or dissecting), the size of the aneurysm (maximal diameter), and the diameter of its neck. The diameter of the parent vessel proximal and distal to the aneurysm was also assessed. Wide-neck aneurysms were defined as those with a neck diameter of ≥ 4 mm or aneurysms with a dome-to-neck ratio of < 2 .

FRED X: Device Characteristics

As mentioned in the beginning of the article, the novelty of the FRED X is a specific antithrombotic surface treatment. The X-technology, which is applied to the new FRED X device, is based on the material poly-2-methoxyethyl acrylate. The nanopolymer surface treatment is derived from the Xcoating surface treatment (Terumo), which has also been applied in other cardiovascular devices, such as oxygenators and arterial filter lines for > 30 years.^{13,14} The surface treatment comprises an amphiphilic polymer with a hydrophobic part toward the device and a hydrophilic part toward the vessel lumen (and blood) or vessel wall, leading to a boundary layer adjacent to the stent struts, which aims to reduce protein denaturation and thus platelet adhesion. Apart from the X-technology surface treatment, the FRED X is identical to the FRED and FRED Jr with its specific dual-layer design, comprising a low-porosity inner mesh and a high-porosity outer stent. However, there was a change in the designation of

the devices. For its precursor, the larger devices with a diameter of ≥ 3.5 mm, which featured a distal tip and had to be delivered with a 0.027-inch microcatheter, were named "FRED," and the smaller devices with a diameter of ≤ 3.0 mm, which did not have a distal tip and could be delivered with a 0.021-inch microcatheter, were named "FRED Jr." In contrast, all sizes of the new device are named FRED X, while the design of the larger (≥ 3.5 mm) and smaller (≤ 3.0) devices (distal tip, microcatheter compatibility) remained unchanged.

Procedural Parameters

The assessed procedural parameters included the peri-interventional antithrombotic medication, as well as treatment characteristics, such as the procedure duration, the number of implanted devices, additional coiling, and the need for in-stent balloon angioplasty.

Ease of deployment, vessel wall apposition, and radiopacity of the device were rated overall by the treating interventionalist for each treatment, using a 5-point scale (1, very poor; 2, poor; 3, intermediate; 4, good; 5, very good). Additionally, the general performance of the FRED X was compared with its precursor, FRED/FRED Jr, also using a 5-point scale (1, worse; 2, slightly worse; 3, equivalent; 4, slightly better; 5, better) for each treatment.

Periprocedural technical difficulties as well as peri- and postinterventional adverse events were assessed. The severity of adverse events was defined as described previously:¹⁵ A minor adverse event was defined as an event that resolved within 7 days without any clinical sequelae, while a major adverse event was defined as an ongoing clinical deficit at 7 days following the event. Clinical evaluation was performed before the procedure, immediately after the procedure, 24 (± 6) hours after the procedure, at discharge, and at follow-up visits.

Follow-up

Clinical and imaging follow-up was performed according to the individual protocol of the respective centers. At the follow-up visits, the clinical condition of the patients was assessed, and imaging was performed. In follow-up imaging, the degree of in-stent stenosis was assessed and categorized as "not present," "mild" (defined as $\leq 50\%$ stenosis, compared with the immediate postinterventional diameter), "moderate" (50%–75%), "severe" ($> 75\%$), or "complete occlusion."

Assessment of the Degree of Occlusion

The grade of aneurysm occlusion immediately after the procedure was reported according to the O'Kelly-Marotta (OKM) scale.¹⁶ Because invasive angiography was not available for all follow-ups, the grade of occlusion at the latest follow-up was reported according to the Raymond-Roy occlusion classification (RROC) for all patients.¹⁷ Adequate occlusion was defined as complete occlusion or residual neck (OKM C and D and RROC I and II).

RESULTS

One hundred sixty-one consecutive patients with 184 aneurysms treated with the FRED X device were included in this study. Patient and aneurysm characteristics are summarized in Table 1.

Table 1: Patient and aneurysm characteristics^a

Characteristics							
Patient age (mean) (range) (yr)	55 (SD, 12) (27–79)						
Clinical presentation	Incidental	Regrowth/persistent aneurysm ^b	SAH	Headache	Co-incidental ^c	Diplopia	Other
	100 (62.1%)	20 (12.4%)	18 (11.2%)	9 (5.6%)	6 (3.7%)	3 (1.9%)	5 (3.1%)
Aneurysm location		ICA	BA	MCA	VA	Other	
		117 (72.7%)	13 (8.1%)	10 (6.2%)	9 (5.6%)	12 (7.5%)	
Aneurysm size ^d (mean) (range) (mm)	7.8 (SD, 6.3) (1.0–46.0)						
Neck diameter (mean) (range) (mm)	4.7 (SD, 3.8) (1.0–36.0)						
Dome-to-neck ratio (mean) (range)	1.7 (SD, 0.9) (0.4–7.5)						
Diameter of the parent artery proximal and distal to the aneurysm mean (range) (mm)		Proximal				Distal	
		3.5 (SD, 0.8) (1.5–7.0)				3.1 (SD, 0.7) (1.2–5.2)	
Aneurysm type		Saccular	Blister-like	Fusiform	Dissecting		
		131 (81.4%)	14 (8.7%)	11 (6.8%)	5 (3.1%)		
Sidewall or bifurcation aneurysm		Sidewall				Bifurcation	
		136 (84.5%)				25 (15.5%)	

^a Data are as mean (minimum–maximum) or absolute number of cases (relative frequency in %).

^b Persistent aneurysm after previous treatment.

^c Aneurysm diagnosed because of a ruptured intracranial aneurysm elsewhere.

^d Maximal diameter.

Table 2: Treatment parameters^a

Parameters					
	1		2	3	4
Aneurysms treated in the respective treatment session	144 (89.4%)		13 (8.1%)	2 (1.2%)	2 (1.2%)
Ease of deployment ^b	Very poor	Poor	Intermediate	Good	Very good
	0 (0%)	1 (0.6%)	1 (0.6%)	12 (7.5%)	147 (91.3%)
Vessel wall apposition ^b	Very poor	Poor	Intermediate	Good	Very good
	0 (0%)	0 (0%)	2 (1.2%)	8 (5.0%)	151 (93.8%)
Radiopacity ^b	Very poor	Poor	Intermediate	Good	Very good
	0 (0%)	0 (0%)	0 (0%)	59 (36.7%)	102 (63.4%)
Performance compared with FRED/FRED Jr ^b	Worse	Slightly worse	Equivalent	Slightly better	Better
	0 (0%)	0 (0%)	154 (96.3%)	6 (3.8%)	0 (0%)
Additional coiling			48 (29.8%)		
In-stent balloon angioplasty			4 (2.5%)		

^a Data are absolute number of cases (relative frequency in %).

^b Rated as an overall score for each treatment (not for each implanted FD).

Results subdivided into unruptured and ruptured aneurysms are summarized in the Online Supplemental Data.

Patient Characteristics

The mean age of the patients was 55.1 years, and 77.6% were women. The median pretreatment mRS was 0 (first quartile; third quartile, 0; 0) (mRS 0 in 126 patients [78.3%], mRS 1 in 24 [14.9%], and mRS 4 in 1 [0.6%]). The patient with mRS 4 presented with a subacute brainstem infarction caused by a large, fusiform, unruptured aneurysm of the basilar artery (BA). Of the 18 patients (11.2%) who presented with an acutely ruptured aneurysm, the HH scale was 1 (first quartile; third quartile, 1; 2.5) (HH 1 in 8 patients [53.3%], HH 2 in 3 patients [20.0%], HH 3 in 2 patients [13.3%], and HH 5 in 2 patients [13.3%]). In 100 patients (62.1%), the aneurysm was incidental and asymptomatic.

Aneurysm Characteristics

Most patients (89.4%) had only 1 aneurysm treated with the FRED X, while in 8.1%, 2 aneurysms, and in 1.2%, 3 aneurysms were treated. The most frequent aneurysm location was the ICA (72.7%),

followed by the BA (8.1%) and the MCA (6.2%). The mean aneurysm size was 7.8 mm, ranging from 1-mm blister-like to 46-mm giant aneurysms. Most aneurysms had a wide neck (90.1%), a saccular shape (81.4%), and were sidewall aneurysms (84.5%).

Antiplatelet Therapy

Pre-, intra-, and postprocedural platelet inhibition and testing of the thrombocyte aggregation response were managed according to local standards of the respective institutions. Platelet reactivity testing was performed in 91.9% of the patients. The most common antiplatelet medications were acetylsalicylic acid (ASA) plus clopidogrel (62.4%), ASA plus prasugrel (21.0%), and ASA plus ticagrelor (6.4%). Patients with acute aneurysmal SAH received periprocedural tirofiban, followed by double-antiplatelet therapy after the treatment.

Treatment

The treatment characteristics are summarized in Table 2 and the Online Supplemental Data. Two example cases are illustrated in Figs 1 and 2.

Table 3: Adverse events and complications^a

Adverse event	Adverse events/complications				
	Technical periprocedural adverse event	Minor adverse event	Major adverse event	Neurological morbidity	Mortality
	5 (3.1%)	21 (13.0%)	5 (3.1%)	3 (1.9%)	2 (1.2%)

^a Data are absolute number of cases (relative frequency in %).

Table 4: Occlusion rates^a

Occlusion rates			
Occlusion at latest follow-up ^b	I: Complete occlusion	II: Residual neck	III: Residual aneurysm
	94 (66.2%)	24 (16.9%)	24 (16.9%)

^a Data are absolute number of cases (relative frequency in %).

^b Imaging follow-up was available for 142/161 patients with a mean follow-up period of 7.0 months, reported according to the RROC.

One hundred sixty-seven FRED X devices were implanted in 161 treatment sessions (1 FD was implanted in 155 treatments, and 2 FDs in 6 treatments) with a mean duration of 80.2 [SD, 47.5] minutes. A FRED X FD could be successfully implanted as planned in all treatments. Recapturing or repositioning of the device was required in 14.3% of the treatments. Additional coiling of the aneurysm was performed in 29.8%. The reasons for additional coiling were large aneurysm size, irregular aneurysm shape, and aneurysmal hemorrhage. In-stent balloon angioplasty to improve the vessel wall apposition was performed in 2.5%.

The ease of deployment was rated “good” or “very good” in 98.8%. It was rated “poor” in 1 case (0.6%) in which the stent kinked at a sharp curve in the vessel. Vessel wall apposition was rated good or very good in 98.8%. Radiopacity was rated good or very good in all cases (100%). When we compared the FRED X with its precursor, it was rated “equivalent” in 96.3% and “slightly better” in 3.8%.

Adverse Events and Complications

Asymptomatic and symptomatic adverse events are presented in detail in the Online Supplemental Data and summarized in Table 3.

Intraprocedural technical adverse events occurred in 5 treatments (3.1%) and consisted of 2 cases of inadvertent stent shortening, as well as stent kinking, insufficient stent opening, and coil migration in 1 case, respectively. All of these adverse events were asymptomatic.

Most (95.8%) of recorded symptomatic adverse events occurred postinterventionally. Minor adverse events occurred in 13.0% of the patients. Nine of 21 of these events were neurologic, resulting in a minor neurologic adverse event rate of 5.6%. Major adverse events (2 ischemic strokes, 1 intracerebral hemorrhage, 1 mass effect of the aneurysm, and 1 case of vasospasms caused by a preinterventional aneurysmal SAH) were observed in 5 patients (3.1%), leading to neurologic morbidity in 3 (1.9%) and death in 2 patients (1.2%). All these major adverse events were neurologic complications. One of the major adverse events was a major ischemic stroke, which occurred 2 weeks after an uneventful treatment of an unruptured posterior communicating artery (PcomA) aneurysm, due to severe in-stent thrombosis, leading to hemodynamic cerebral infarctions. This patient had a good response to ASA and clopidogrel in the reactivity testing before treatment. Treatment in this case was performed with tirofiban, which led to a resolution of the thrombus, followed by oral medication with ASA in

combination with prasugrel. The patient was discharged with mRS 3 and recovered to mRS 2 at 6 months after treatment. The second patient who had neurologic morbidity presented with a large BA aneurysm causing brainstem infarctions, which increased after the FD treatment (worsening of pre-existing stroke), without any evidence of thrombus formation. Of the patients who died, 1 patient with an enlarging giant BA aneurysm died due to increasing mass effect despite the treatment. The second case of mortality occurred in a patient with aneurysmal SAH, who developed an intracerebral hemorrhage located adjacent to the external ventricular drainage. Consequently, tirofiban had to be stopped, which led to occlusion of the stent in the ICA, eventually leading to cerebral infarction and death.

Postinterventional visual disturbances occurred in 5 patients (3.1%). In all of these patients, an aneurysm of the ICA was treated with an FD, which covered the ophthalmic artery.

A total number of 8 thrombotic events was reported in 7 patients (4.3%). In 4 of these, slight in-stent thrombosis was observed during treatment, which was immediately treated with tirofiban, leading to complete resolution of the thrombus in all cases without any clinical sequelae. Postinterventional in-stent thrombosis occurred in 1 of the 4 patients with intraprocedural thrombosis (despite complete intraprocedural thrombus resolution after tirofiban administration and after discontinuation of ticagrelor intake by the patient) and in 3 further patients with an uneventful treatment procedure. One of these patients developed an asymptomatic stent occlusion. Another stent thrombosis occurred after stopping tirofiban due to an intracerebral hemorrhage as described above. Apart from this patient, only 1 thrombotic event resulted in a major adverse event: the case of a major stroke that is described in more detail above.

Clinical Follow-up

Two patients died during the follow-up (listed under adverse events and complications), resulting in a mortality rate of 1.2%. The mean mRS at the latest follow-up, which was available for 133 patients, was 0.4 (SD, 1.0) (mRS 0 in 102 patients [76.7%], mRS 1 in 18 [13.5%], mRS 2 in 8 [6.0%], mRS 3 in 4 [3.0%], and mRS 6 in 2 [1.5%]). Deterioration of the mRS (compared with the preinterventional scale) was observed in 11 patients; 4 deteriorations were related to the procedure or the underlying disease (see adverse events and complications). For the remaining patients, mRS deterioration was caused by non-neurologic conditions.

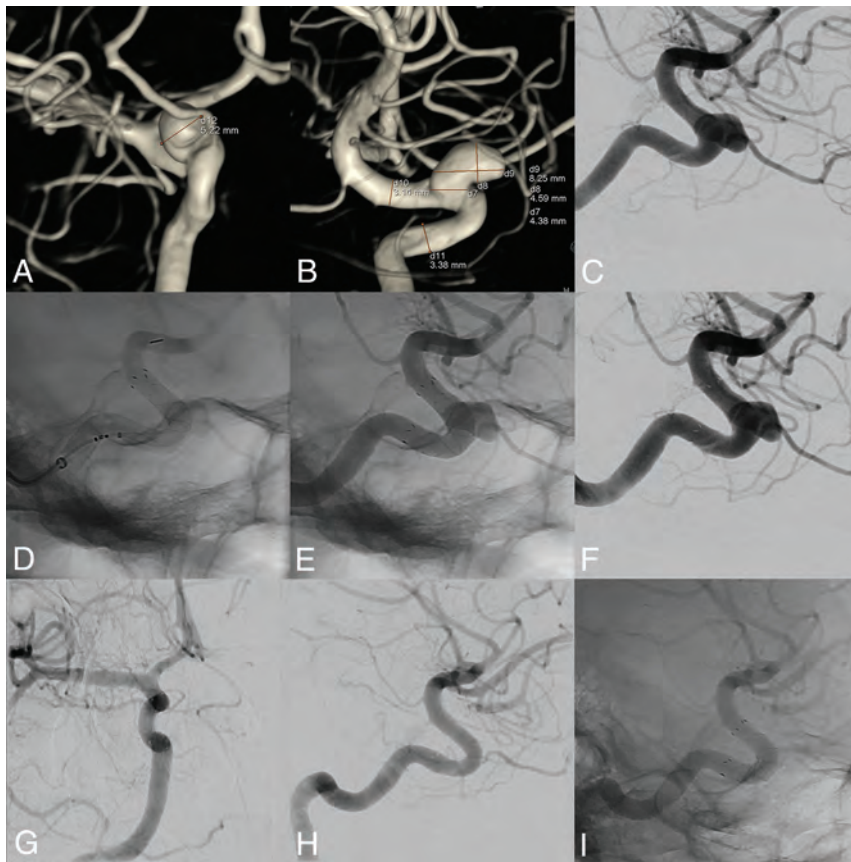


FIG 1. Treatment of an incidental aneurysm of the ICA with the FRED X. The preinterventional angiography including 3D reconstructions (A–C) showed a saccular sidewall aneurysm of the right ICA in an asymptomatic patient. A FRED X FD was placed in the parent artery, covering the aneurysm neck (D–F). On the angiography 13 months after the treatment (G–I), the aneurysm was completely occluded.

Imaging Follow-up

Imaging follow-up was available for 145 of the 161 patients (90.1%), with a mean imaging follow-up period of 7.0 (SD, 4.3) months. The patients without follow-up imaging refused further imaging, were lost to follow-up, or died.

The imaging technique was invasive conventional angiography and MR imaging in 22.1%, conventional angiography alone in 14.5%, MR imaging and flat panel CT in 28.3%, MR imaging only in 30.3%, and flat panel CT only in 4.8%.

During follow-up, in-stent stenosis or stent occlusion was observed in 17 patients (10.6%). Most of these cases (14/17, 82.4%) were only mild stenoses. There were 2 cases of moderate in-stent stenosis and 1 case of complete stent occlusion. Of all these cases, only 1 patient was symptomatic: the above-mentioned patient with major stroke due to in-stent thrombosis. The moderate in-stent stenosis persisted in the latest follow-up imaging.

Aneurysm Occlusion

The aneurysm occlusion rates are summarized in Table 4. The immediate postinterventional occlusion rates were as follows: OKM A1 in 19.9%, A2 in 23.0%, A3 in 20.5%, B1 in 2.5%, B2 in 5.6%, B3 in 13.7%, C1 in 1.2%, C2 in 5.0%, C3 in 4.4%, and D in 4.4%.

At the latest follow-up, aneurysm occlusion rates were as follows: RROC I in 66.2%, RROC II in 16.9% and RROC III in 16.9%, resulting in a rate of adequate aneurysm occlusion of 83.1%.

DISCUSSION

FDs have increasingly become a treatment option for cerebral aneurysms with the drawback of a higher metal density being potentially more thrombogenic than conventional stents. In this multicenter cohort, the first study reporting on the new FRED X with antithrombotic surface treatment, the FD showed a satisfactory safety profile and proved to be effective judged by short-term aneurysm occlusion.

As explained, the only modification of the FRED X toward its precursor is the new antithrombotic surface treatment. In this study, thrombotic complications occurred in 7 of 161 patients, resulting in a thrombotic complication rate of 4.3%, of which only 2 led to a major adverse event (one occurring after a necessary discontinuation of antiplatelet therapy because of an intracerebral hemorrhage). This low but still considerable number of thrombotic events indicates that even when using devices with antithrombotic coatings, high awareness is still mandatory for both peri- and postprocedural thromboses.

In recent studies on the FRED and FRED Jr, the rate of thrombotic complications was slightly higher. In the Safety and Efficacy Analysis of FRED Embolic Device in Aneurysm Treatment (SAFE) study, the pivotal study for the FRED in France (published in 2019),¹⁸ thromboembolic complications occurred in 7/103 patients (6.8%). In the US pivotal trial (2022), device thrombosis was reported in 12/145 patients (8.3%).¹⁹ These thrombotic events rates are also in line with reported data for other FDs, such as the Pipeline Embolization Device (PED; Medtronic). A meta-analysis, comprising data of 1110 patients, focusing on thrombotic complications after PED treatment reported an overall rate of 7.0% thrombotic events.²⁰ The new antithrombotic surface treatment might serve as an explanation for the slightly lower thrombotic complication rate in this study. However, the FRESH study was based on a retrospective, self-adjudicated analysis, the cohort in our study was heterogeneous, and there was no control group consisting of patients treated with the precursor devices, preventing a direct comparison of these studies and the devices regarding thrombogenicity. Prospective trials are warranted to further assess the safety of the FRED X and its potential to reduce the rate of thrombotic complications compared with conventional FDs.

The nonthrombotic complications in this study (minor adverse events in 13.0% and major adverse events in 3.1%) are

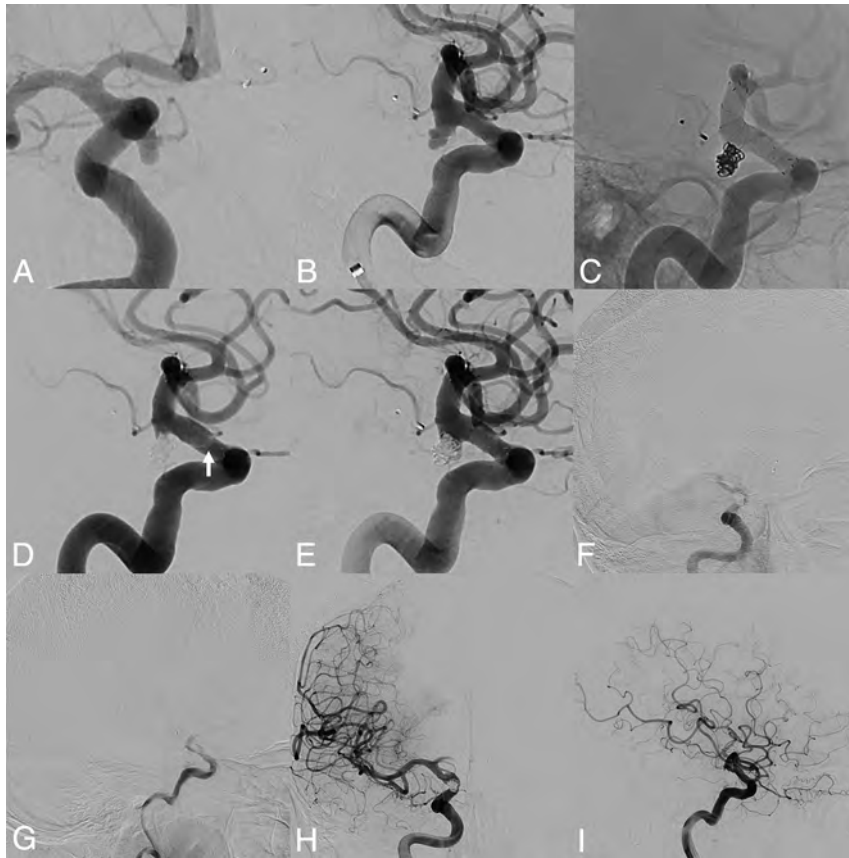


FIG 2. Treatment of an incidental PcomA aneurysm with the FRED X and coiling with intra- and postprocedural thrombosis. This patient, who had an incidental BA aneurysm treated with a Woven EndoBridge device (WEB; MicroVention) previously, presented with an incidental, irregularly shaped aneurysm of the ICA adjacent to the PcomA (A and B). After an uneventful treatment with FRED X implantation and coiling with a jailing technique (C), intraprocedural thrombus formation at the proximal part of the flow-diverting section of the stent was observed (white arrow in D). Tirofiban was instantly administered for 30 minutes, which led to a complete resolution of the thrombosis (E). Seven days after the treatment, after discontinuation of her ticagrelor medication, the patient presented with complete occlusion of the FD (F and G) with good collateralization via the contralateral side. Recanalization of the stent was achieved by tirofiban administration for 48 hours (H and I). The patient was neurologically asymptomatic the entire time.

similar to those reported in previous studies for the FRED and FRED Jr. In the largest study reporting on the FRED, the European Flow-Redirection Intraluminal Device Study, comprising data of 531 patients, the rate of complications and adverse events was 14%.⁹ In the above-mentioned US pivotal trial, the composite primary safety end point of major stroke or death within 30 days or major ipsilateral stroke or neurologic death after 30 days was met by 6.2% of the patients.

Because the FRED X is technically identical to the FRED and FRED Jr, despite the antithrombotic surface treatment, it is consistent that the occlusion rates in this study are similar to those reported for its precursor. The rate of complete occlusion at a mean follow-up of 7.0 months was 66.2% in our cohort. In the European Flow-Redirection Intraluminal Device Study, the complete occlusion rate was 82.5% at 6 months and 91.3% at 1 year. For the above-mentioned pivotal trials, the complete occlusion rate was 61.1% at 6 months and 73.3% at 1 year for the French study¹⁸ and 62.9% at 1 year for the US study.¹⁹ Occlusion rates of

studies reporting on the PED are also in line with those of our study. A recent work reported a 77.9% complete occlusion rate for the new Pipeline Vantage,²¹ while in the Pipeline for Uncoilable or Failed Aneurysms (PUFs) trial, the early rate of complete occlusion was 73.6% at 180 days,²² reaching 95.2% at 5 years.²³ The relatively high rate of additional coiling in our study (30.0%) must be considered when comparing our results with those in other studies. Future studies with long-term follow-up are needed to further assess the efficacy of the FRED X.

We acknowledge that this work has several limitations. This study was performed retrospectively and was based on a survey that was completed by the treating physicians, without data or imaging analysis by an independent core lab, indicating an inherent selection and reporting bias. Despite the relatively high number of patients in this study, the data are quite heterogeneous (eg, different aneurysm locations, high rate of additional coiling). However, the use of the FRED X in this study reflects a real-world experience, not being limited to a certain aneurysm location or rupture status. The treatments in this study were performed in the context of a limited market release to a few high-volume neurovascular centers that were selected by the manufacturer. The results may vary when the device is available freely to other centers. Furthermore, the rate of patients with follow-up conventional angiography was only 36.6%, and the

follow-up period in this study was relatively short, due to the novelty of the device.

CONCLUSIONS

The FRED X is a safe and feasible FD for treatment of ruptured and unruptured intracranial aneurysms. With its new antithrombotic surface treatment, the rate of thrombotic complications was relatively low, and the short-term efficacy is promising.

Disclosure forms provided by the authors are available with the full text and PDF of this article at www.ajnr.org.

REFERENCES

1. Lv X, Yang H, Liu P, et al. **Flow-diverter devices in the treatment of intracranial aneurysms: a meta-analysis and systematic review.** *Neuroradiol J* 2016;29:66-71 CrossRef Medline
2. Mohlenbruch MA, Kizilkilic O, Killer-Oberpfalzer M, et al. **Multicenter experience with FRED Jr Flow Re-Direction Endoluminal Device for**

- intracranial aneurysms in small arteries. *AJNR Am J Neuroradiol* 2017;38:1959–65 CrossRef Medline
3. Kallmes DF, Brinjikji W, Boccardi E, et al. **Aneurysm Study of Pipeline in an Observational Registry (ASPIRe).** *Interv Neurol* 2016;5:89–99 CrossRef Medline
 4. Brinjikji W, Murad MH, Lanzino G, et al. **Endovascular treatment of intracranial aneurysms with flow diverters: a meta-analysis.** *Stroke* 2013;44:442–47 CrossRef Medline
 5. Fiehler J, Ries T. **Prevention and treatment of thromboembolism during endovascular aneurysm therapy.** *Klin Neuroradiol* 2009;19:73–81 CrossRef Medline
 6. Ihn YK, Shin SH, Baik SK, et al. **Complications of endovascular treatment for intracranial aneurysms: management and prevention.** *Interv Neuroradiol* 2018;24:237–45 CrossRef Medline
 7. Marosfoi M, Clarencon F, Langan ET, et al. **Acute thrombus formation on phosphorilcholine surface modified flow diverters.** *J Neurointerv Surg* 2018;10:406–11 CrossRef Medline
 8. King RM, Langan ET, Ughi GJ, et al. **Acute thrombus burden on coated flow diverters assessed by high frequency optical coherence tomography.** *Cardiovasc Intervent Radiol* 2020;43:1218–23 CrossRef Medline
 9. Killer-Oberpfalzer M, Kocer N, Griessenauer CJ, et al. **European multicenter study for the evaluation of a dual-layer flow-diverting stent for treatment of wide-neck intracranial aneurysms: the European Flow-Redirection Intraluminal Device Study.** *AJNR Am J Neuroradiol* 2018;39:841–47 CrossRef Medline
 10. Mohlenbruch MA, Herweh C, Jestaedt L, et al. **The FRED flow-diverter stent for intracranial aneurysms: clinical study to assess safety and efficacy.** *AJNR Am J Neuroradiol* 2015;36:1155–61 CrossRef Medline
 11. Pierot L, Spelle L, Berge J, et al. **SAFE study (Safety and efficacy Analysis of FRED Embolic device in aneurysm treatment): 1-year clinical and anatomical results.** *J Neurointerv Surg* 2019;11:184–89 CrossRef Medline
 12. McDougall CG, Diaz O, Boulos A, et al. **Safety and efficacy results of the Flow Redirection Endoluminal Device (FRED) stent system in the treatment of intracranial aneurysms: US pivotal trial.** *J Neurointerv Surg* 2022;14:577–84 CrossRef Medline
 13. Gunaydin S, Farsak B, Kocakulak M, et al. **Clinical performance and biocompatibility of poly(2-methoxyethylacrylate)-coated extracorporeal circuits.** *Ann Thorac Surg* 2002;74:819–24 CrossRef Medline
 14. Nutter BT, Stammers AH, Schmer RG, et al. **The rheological effects of X-Coating with albumin and hetastarch on blood during cardiopulmonary bypass.** *J Extra Corpor Technol* 2004;36:36–43 Medline
 15. Kallmes DF, Hanel R, Lopes D, et al. **International retrospective study of the Pipeline embolization device: a multicenter aneurysm treatment study.** *AJNR Am J Neuroradiol* 2015;36:108–15 CrossRef Medline
 16. O'Kelly CJ, Krings T, Fiorella D, et al. **A novel grading scale for the angiographic assessment of intracranial aneurysms treated using flow diverting stents.** *Interv Neuroradiol* 2010;16:133–37 CrossRef Medline
 17. Mascitelli JR, Moyle H, Oermann EK, et al. **An update to the Raymond-Roy occlusion classification of intracranial aneurysms treated with coil embolization.** *J Neurointerv Surg* 2015;7:496–502 CrossRef Medline
 18. Pierot L, Spelle L, Berge J, et al. **SAFE study (Safety and efficacy Analysis of FRED Embolic device in aneurysm treatment): 1-year clinical and anatomical results.** *J Neurointerv Surg* 2019;11:184–189 CrossRef Medline
 19. McDougall CG, Diaz O, Boulos A, et al. **Safety and efficacy results of the Flow Redirection Endoluminal Device (FRED) stent system in the treatment of intracranial aneurysms: US pivotal trial.** *J Neurointerv Surg* 2022;14:577–584 CrossRef Medline
 20. Skukalek SL, Winkler AM, Kang J, et al. **Effect of antiplatelet therapy and platelet function testing on hemorrhagic and thrombotic complications in patients with cerebral aneurysms treated with the Pipeline embolization device: a review and meta-analysis.** *J Neurointerv Surg* 2016;8:58–65 CrossRef Medline
 21. Vollherbst DF, Cekirge HS, Saatci I, et al. **First clinical multicenter experience with the new Pipeline Vantage flow diverter.** *J Neurointerv Surg* 2023;15:63–69 CrossRef Medline
 22. Becks T, Kallmes DF, Saatci I, et al. **Pipeline for uncoilable or failed aneurysms: results from a multicenter clinical trial.** *Radiology* 2013;267:858–68 CrossRef Medline
 23. Becks T, Brinjikji W, Potts MB, et al. **Long-term clinical and angiographic outcomes following Pipeline Embolization Device treatment of complex internal carotid artery aneurysms: five-year results of the Pipeline for Uncoilable or Failed Aneurysms Trial.** *Neurosurgery* 2017;80:40–48 CrossRef Medline

CT and MR Imaging Appearance of the Pedicled Submandibular Gland Flap: A Potential Imaging Pitfall in the Posttreatment Head and Neck

 D.A. Zander,  D.L. Gursahaney,  C. Oliver,  A.L. Callen, and  V.L. Potigailo

ABSTRACT

SUMMARY: Pedicled locoregional submandibular gland reconstruction flaps are increasingly used in oncologic head and neck surgery and have unique imaging characteristics that can mimic locally recurrent tumor. In this clinical report, 23 posttreatment imaging studies were evaluated in 19 patients who had undergone submandibular gland flap reconstructions after resection of a primary head and neck tumor. Submandibular gland flaps were most commonly mobilized into the parapharyngeal space or parotid bed, with others located inferior to the mandibular body and within marginal mandibulectomy defects. The original shape of the gland was typically not preserved. Identifying the submandibular gland hilum, vascular pedicle, glandular texture, and absence of submandibular gland in the orthotopic location was most useful in recognizing a flap. The interpreting radiologist must be familiar with the unique submandibular gland flap imaging characteristics to accurately differentiate normal postoperative appearance and recurrent tumor.

ABBREVIATIONS: SCC = squamous cell carcinoma; SMG = submandibular gland

Surgical flaps are commonly encountered during surveillance imaging following oncologic resection in the head and neck, particularly as advancements in microvascular surgical techniques have facilitated the widespread use of free flaps. The resultant complex postoperative anatomy can make imaging interpretation challenging. To aid the interpreting radiologist, multiple studies have characterized the typical postoperative imaging appearance of various fasciocutaneous and myocutaneous flap reconstructions in the head and neck.¹⁻³ To our knowledge, existing studies have not characterized the imaging appearance of pedicled locoregional glandulofascial flaps involving the submandibular gland (SMG).

First described by Mozolewski et al⁴ for laryngeal reconstruction, the SMG flap has since been described for the reconstruction of small-to-medium defects that cannot be closed primarily yet may not necessitate the additional risk and surgical complexity of free flaps.⁵ From a surgical perspective, the benefits of a pedicled regional SMG flap include an abundant blood supply from the facial artery, the option to include surrounding adipose tissue for bulk, and a relatively long arc of rotation, thereby allowing mobilization to sites as far as the infratemporal fossa or parotid bed.^{6,7} Furthermore, in instances when level 1 nodes will be dissected, no additional incision or secondary surgical defect is required, unlike

the temporalis myofascial or pectoralis flaps.⁵⁻⁷ In comparison with myocutaneous flaps, an SMG flap retains greater bulk across time, therefore obviating surgical overestimation of tissue volume necessary to reconstruct a defect.⁶ This feature may more accurately restore a desired facial contour after parotidectomy or preserve mucosal volume of an oropharyngeal defect in which the swallowing function could be eventually impaired by flap atrophy. Of note, SMG transfer to the submental space with the intent of avoiding the high-dose radiation field to avoid xerostomia is a distinct entity and not included herein.⁸ A key difference between these entities is that SMG transfer is performed on the SMG contralateral to the site of disease, whereas SMG flap reconstruction is performed ipsilaterally.

As previously described in the literature, the postlaryngectomy imaging appearance of a mobilized thyroid gland can simulate recurrent tumor.⁹ Likewise, the postoperative appearance of an SMG flap reconstruction may consist of hyperattenuating, nodular tissue in the primary resection site, whereby an interpreting radiologist who is unfamiliar with this technique may easily mischaracterize normal flap reconstruction for recurrent tumor (Fig 1). The purpose of this study was to characterize the normal CT and MR imaging postoperative appearance of SMG flaps to avoid this pitfall in the posttreatment setting.

Case Series

In this institutional review board–exempt and Health Insurance Portability and Accountability Act–compliant study, we retrospectively reviewed the records of a tertiary oncologic otolaryngology

Received June 11, 2022; accepted after revision February 21, 2023.

From the Departments of Radiology (D.A.Z., D.L.G., A.L.C., V.L.P.) and Otolaryngology-Head and Neck Surgery (C.O.), University of Colorado School of Medicine, Aurora, Colorado.

Please address correspondence to David A Zander, MD, 12401 E 17th Ave, MS L954, Aurora, CO 80045; e-mail: David.zander@cuanschutz.edu; @dave_zander

<http://dx.doi.org/10.3174/ajnr.A7825>



FIG 1. SMG flap misdiagnosed as recurrent tumor. Axial contrast-enhanced CT performed as the first posttreatment surveillance scan following resection of an SCC involving the lateral oral tongue, retromolar trigone, and lateral oropharynx. The enhancing nodular masslike lesion of the lateral oropharynx was mistakenly interpreted as recurrent tumor (*arrow*). After discussion with the otolaryngologist, this was determined to represent an SMG flap reconstruction of the lateral oropharynx.

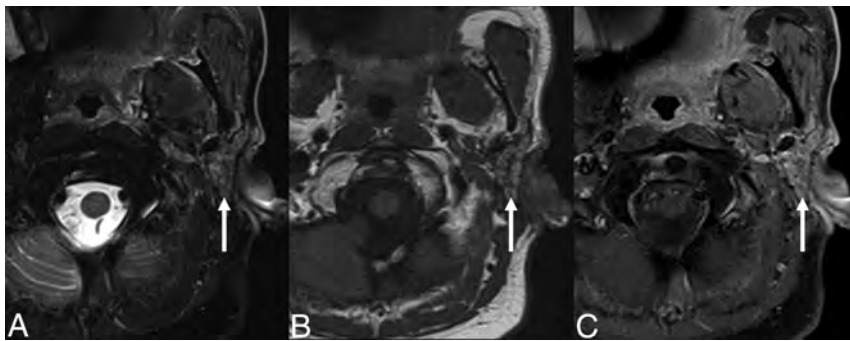


FIG 2. SMG flap of the parotid bed. Axial T2-weighted fat-suppressed (A), T1-weighted (B), and T1-weighted postcontrast fat-suppressed (C) MR images demonstrating facial contour reconstruction with an SMG flap in the parotid bed (*arrow*), after total parotidectomy for a poorly differentiated carcinoma.



FIG 3. Typical SMG flap appearance. A, Axial contrast-enhanced CT of an SCC involving the left lateral oropharynx (*dashed arrow*). Axial (B) and coronal (C) contrast-enhanced CT images obtained 6 months after resection and reconstruction with an SMG flap show an enhancing, nodular, masslike lesion in the operative bed (*solid arrow*). The glandular heterogeneous enhancement, the semblance of a preserved hilum, and the absence of the native SMG in its orthotopic location in the submandibular space are useful in differentiating a normal SMG flap from recurrent tumor.

surgical practice performing pedicled locoregional glandulofascial flap reconstruction during 2014–2022, yielding 37 patients. We excluded all patients with no postoperative imaging and any patients in whom glands other than the SMG were used for the flap reconstruction (eg, thyroid glands mobilized to bolster the pharyngeal closure following laryngectomy). Nineteen patients met the inclusion criteria. All patients underwent an SMG flap operation with the intent of reconstruction and not transfer of the gland to shield it from high-dose radiation (ie, Seikaly and Jha submandibular transfer procedure).⁸

In total, 23 studies of SMG flaps were characterized, including 16 CTs and 7 MR images. Preoperative imaging was available for 14 patients, consisting of 12 CTs and 3 MR images. All CTs were performed with IV iodinated contrast and included multiplanar reconstructions. Of these, CT examinations performed at our institution included administration of 100 mL of iopamidol (Isovue; Bracco) using a split bolus technique of 60 mL contrast at 2.5 mL/s, a 35-second pause, 40 mL of contrast at 2.5 mL/s, 40 mL of saline at 2.5 mL/s, and scanning at 90 seconds after start of the injection. All MR imaging was performed without and with IV gadolinium-based contrast and consisted of, at a minimum, T1-weighted, T2-weighted fat-suppressed, DWI, and T1-weighted fat-suppressed postcontrast sequences. Of these, MR imaging examinations performed at our institution included administration of gadobenate dimeglumine (MultiHance; Bracco) per weight-based dosing.

RESULTS

In 19 patients, SMG flaps were used for reconstruction following primary resection of squamous cell carcinoma (SCC) of the oral cavity ($n = 7$), SCC of the oropharynx ($n = 3$), poorly differentiated carcinoma of the parotid ($n = 2$), parapharyngeal synovial cell sarcoma ($n = 2$), 1 case of metastatic SCC of unknown primary (p16 negative), and individual cases of mandibular ameloblastoma, deep lobe parotid pleomorphic adenoma, parotid adenoid cystic carcinoma, and parotid salivary ductal carcinoma. The time between the operation and imaging ranged from 1 month to 9 years, with a median follow-up of 7 months. SMG flaps were mobilized into the parapharyngeal space ($n = 10$), parotid bed ($n = 4$), marginal mandibulectomy defect ($n = 3$), and inferior to the mandibular body ($n = 2$). Once mobilized, the glands typically did not retain their usual glandular shape ($n = 2$), instead becoming distorted ($n = 17$) with triangular, fusiform, and overall ill-defined morphologies. There was variable CT enhancement, MR imaging enhancement, and MR imaging T2

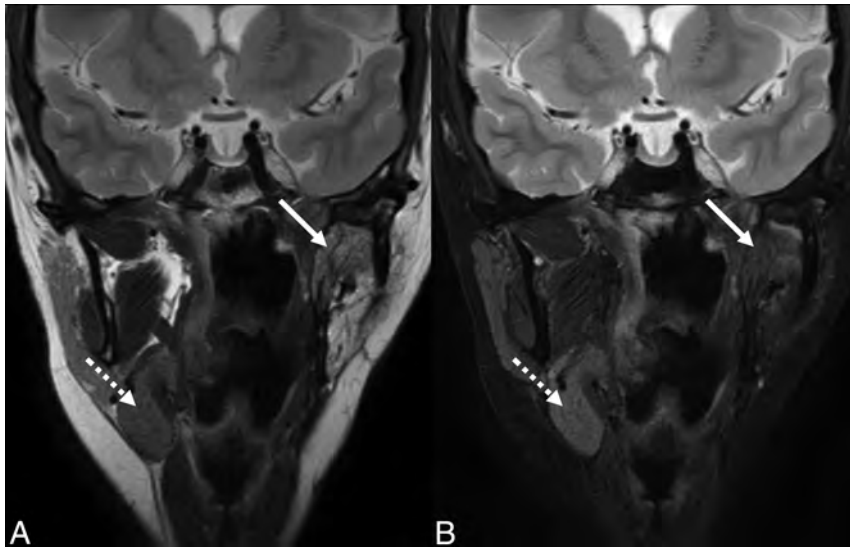


FIG 4. T2 signal intensity of an SMG flap. Coronal T2-weighted (A) and T2-weighted fat-suppressed (B) MR images of an SMG flap within the parapharyngeal space (solid arrow) for reconstruction following resection of a synovial cell sarcoma. MR imaging characteristics of SMG flaps are variable compared with the contralateral gland. Due to atrophy in this case, the mobilized gland is increased in signal intensity relative to the contralateral gland in the orthotopic location (dashed arrow) in the first image, but decreased in signal intensity in the fat-suppressed image.

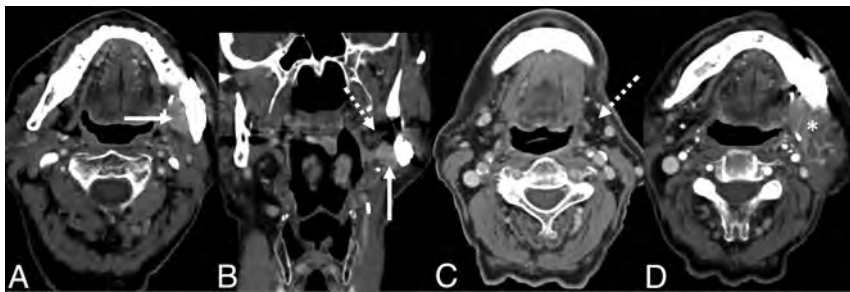


FIG 5. A potential interpretation pitfall of SMG flaps. Axial (A) and coronal (B) contrast-enhanced CT images of a patient undergoing a first postoperative surveillance scan following marginal mandibulectomy and internal fixation for resection of an SCC of the retromolar trigone. The patient declined adjuvant chemoradiation. After reviewing the operative report, an enhancing masslike lesion medial to the mandible was presumed to represent the SMG flap (solid arrow). However, this enhancing tissue was later retrospectively revealed to be recurrent tumor adjacent to the SMG flap with an atrophic, fatty gland (dashed arrow). C, Axial contrast-enhanced CT from the preoperative staging study shows that the gland was originally low in attenuation due to fat content (dashed arrow). D, Axial contrast-enhanced CT of the second postoperative surveillance scan shows heterogeneous enhancement of progressive tumor (asterisk).

signal intensity of the SMG flaps compared with the contralateral gland on postoperative studies or the preoperative ipsilateral gland. Most mobilized glands in the 23 studies had a heterogeneous appearance consistent with a subjective glandular texture ($n = 14$). The most common feature was a preserved glandular hilum, defined as visible ducts and/or a vascular pedicle contiguous with the gland ($n = 19$). In all cases, no distinct glandular tissue could be discerned at the orthotopic location of the SMG in the submandibular space.

DISCUSSION

Imaging interpretation of the postoperative head and neck can be challenging for the radiologist, in part due to the diverse and

complex surgical techniques encountered. To aid in interpretation, previous studies have described in detail the mobilization of glandular tissue, including the thyroid gland during laryngectomy and the SMG for glandular transfer. Therefore, this clinical report aimed to characterize the imaging appearance of the reconstructive SMG flap. In the surgical literature, the SMG flap has been described as an elegant reconstruction to facilitate closure of oropharyngeal defects or restore facial contour following parotidectomy (Fig 2) in instances in which primary closure may result in too much tension of the tissues, while a larger free flap would introduce further complexity of a microvascular operative technique.

The primary pitfall in imaging of SMG flaps in the postsurgical head and neck is that enhancing glandular tissue may be easily mistaken for recurrent tumor (Fig 1). In fact, this mistake was how such a surgical flap was brought to our attention, when a SMG mobilized to the lateral oropharynx was mistakenly interpreted as recurrent tumor. Certainly, in this setting, no adage is more appropriate than that no head and neck imaging interpretation is complete without a priori knowledge of the clinical and surgical history; knowledge of the existence of an SMG flap is of utmost importance for the radiologist. Preoperative imaging is also crucial to differentiate the intermediate enhancement typical of primary tumors from often hyperenhancing glandular tissue. However, recognizing the instances when our interpretations may be bereft of specific, relevant clinical information, we offer these characteristics that may aid the radiologist in recognizing the presence of such a flap (Fig 3).

It may be logical to presume that a gland mobilized for a flap would maintain some semblance of its original imaging characteristics or similarity to the contralateral nonoperative gland. However, enhancement and T2 signal intensity in this series were unpredictable and, therefore, unreliable for gland identification (Fig 4). This issue is due to a variety of opposing factors. Edema and inflammation (eg, postsurgical, immediate postradiation, or localized sialadenitis) increase T2 signal intensity and enhancement. On the contrary, progressive atrophy (eg, long-term postradiation, postinflammatory, or sequelae of chronic ductal obstruction) decreases signal intensity on T2-weighted fat-suppressed and T1-weighted fat-suppressed postcontrast sequences. One notable exception was those glands that were atrophic and replaced by fat preoperatively



FIG 6. Distortion of the SMG flap into a fusiform shape. Axial contrast-enhanced CT following marginal mandibulectomy for resection of an ameloblastoma. The SMG flap appears as a fusiform enhancing nodule inferior to the operative bed (*arrow*). While similar in imaging appearance to a SMG transfer, this gland was mobilized for reconstruction of the ipsilateral surgical defect rather than to shield the contralateral gland away from the high-dose radiation treatment field.

and were invariably fatty in the postoperative period. A fat-replaced gland may introduce a countervailing interpretive pitfall, whereby nodular locally recurrent tumor may be falsely characterized as a normal SMG flap (Fig 5).

To the surgeon, the SMG flap is mobile and pliable, permitting placement in a wide range of useful locations. Thus, the radiologist can anticipate that the gland will largely conform to the surgical defect, depending on the volume of surrounding adipose tissue that is mobilized with the gland. For example, in this series, glands often conformed to the triangular shape of the parapharyngeal space, and those inferior to the mandible were elongated into a fusiform shape (Fig 6). The latter shape is similar to that described in the SMG transfer, yet it is the ipsilateral gland that is mobilized in a SMG flap, and the contralateral gland, for a SMG transfer.⁸ While it may seem intuitive, the absence of glandular tissue at the expected orthotopic location of the SMG may be the first clue to the radiologist that the gland has been manipulated, whether mobilized for reconstruction as in the case of the SMG flap or removed as part of the more frequently encountered neck dissection. Otherwise, features of a glandular hilum such as identifiable ducts and/or a vascular pedicle (Fig 7) and heterogeneous hyperenhancement of a glandular texture (Fig 8) are most useful in identifying a SMG flap and therefore differentiating it from recurrent tumor. As with any reconstructive flap, the margins should be closely evaluated as a site of potential recurrence, with care to differentiate tumor from the gland.

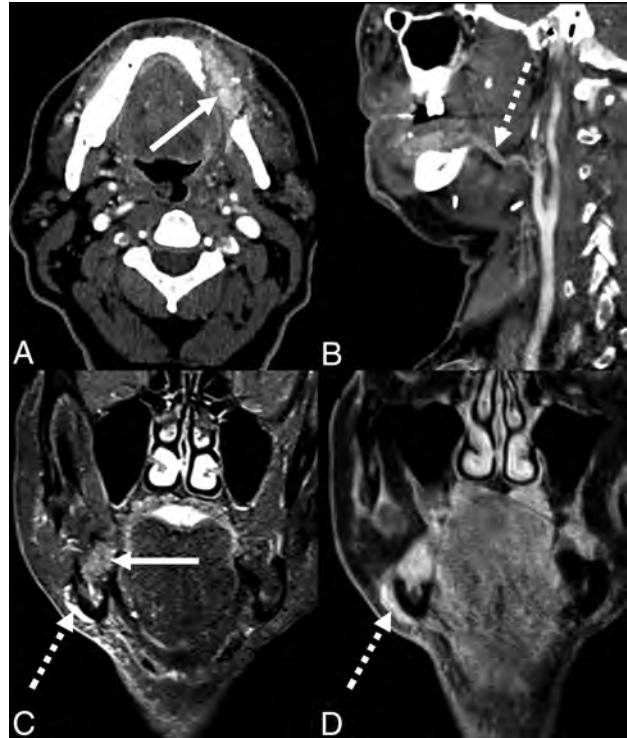


FIG 7. SMG flaps and vascular pedicles in 2 patients following marginal mandibulectomy and SMG flap reconstruction for primary resection of an SCC of the oral cavity. Axial (A) and sagittal (B) contrast-enhanced CT images reveal the hyperenhancing, heterogeneous, glandular texture of the SMG flap (*solid arrow*) with a vascular pedicle including the facial artery coursing medial to the mandibular ramus (*dashed arrow*). Coronal STIR (C) and coronal T1-weighted fat-suppressed (D) postcontrast MR images show an SMG flap in the mandibulectomy defect (*solid arrow*) and vascular pedicle, including the facial vein coursing lateral to the mandibular body (*dashed arrows*).

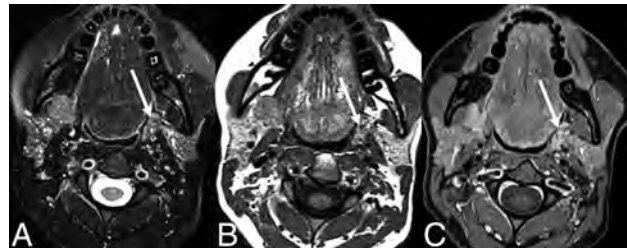


FIG 8. SMG flap glandular texture. Axial T2-weighted fat-suppressed (A), T1-weighted (B), and T1-weighted postcontrast fat-suppressed (C) MR images in a patient with a pleomorphic adenoma of the parapharyngeal space following resection and reconstruction with an SMG flap (*arrow*). The gland conforms to the triangular shape of the parapharyngeal space, while maintaining a glandular heterogeneity similar to that in the adjacent parotid gland.

CONCLUSIONS

The SMG flap is a pedicled locoregional reconstruction flap occasionally used following oncologic resection within the head and neck. This feature presents a potential pitfall to the radiologist interpreting posttreatment head and neck examinations because an enhancing SMG flap can be confused with recurrent tumor.

To reduce misdiagnosis, this clinical report raises awareness of this surgical technique and offers a description of the appearance of the SMG flap on CT and MR imaging.

Disclosure forms provided by the authors are available with the full text and PDF of this article at www.ajnr.org.

REFERENCES

1. Chong J, Chan LL, Langstein HN, et al. **MR imaging of the muscular component of myocutaneous flaps in the head and neck.** *AJNR Am J Neuroradiol* 2001;22:170–74 Medline
2. McCarty JL, Corey AS, El-Deiry MW, et al. **Imaging of surgical free flaps in head and neck reconstruction.** *AJNR Am J Neuroradiol* 2019;40:5–13 CrossRef Medline
3. Saito N, Nadgir RN, Nakahira M, et al. **Posttreatment CT and MR imaging in head and neck cancer: what the radiologist needs to know.** *Radiographics* 2012;32:1261–82 CrossRef Medline
4. Mozolewski E, Maj P, Kordowski J, et al. **Vascular pedicle flap of the thyroid or submandibular gland in the reconstruction following partial laryngectomy** [in Polish]. *Otolaryngol Pol* 1999;53:387–96 Medline
5. Mashrah MA, Zhou SH, Abdelrehem A, et al. **Oropharyngeal reconstruction with a pedicled submandibular gland flap.** *Br J Oral Maxillofac Surg* 2016;54:388–93 CrossRef Medline
6. Liang KY, Breen MS, Tracy JC, et al. **Submandibular gland flap for reconstruction after parotidectomy.** *Laryngoscope* 2020;130:E157–62 CrossRef Medline
7. Yang B, Su M, Li H, et al. **Use of submandibular gland flap for repairing defects after tumor resection in the infratemporal region.** *J Craniomaxillofac Surg* 2015;43:87–91 CrossRef Medline
8. Wu X, Yom SS, Ha PK, et al. **Submandibular gland transfer: a potential imaging pitfall.** *AJNR Am J Neuroradiol* 2018;39:1140–45 CrossRef Medline
9. Weissman JL, Curtin HD, Johnson JT. **Thyroid gland after total laryngectomy: CT appearance.** *Radiology* 1998;207:405–09 CrossRef Medline

Application of Automatic Segmentation on Super-Resolution Reconstruction MR Images of the Abnormal Fetal Brain

T. Deprest, L. Fidon, F. De Keyzer, M. Ebner, J. Deprest, P. Demaerel, L. De Catte, T. Vercauteren, S. Ourselin, S. Dymarkowski, and M. Aertsen



ABSTRACT

BACKGROUND AND PURPOSE: Fetal brain MR imaging is clinically used to characterize fetal brain abnormalities. Recently, algorithms have been proposed to reconstruct high-resolution 3D fetal brain volumes from 2D slices. By means of these reconstructions, convolutional neural networks have been developed for automatic image segmentation to avoid labor-intensive manual annotations, usually trained on data of normal fetal brains. Herein, we tested the performance of an algorithm specifically developed for segmentation of abnormal fetal brains.

MATERIALS AND METHODS: This was a single-center retrospective study on MR images of 16 fetuses with severe CNS anomalies (gestation, 21–39 weeks). T2-weighted 2D slices were converted to 3D volumes using a super-resolution reconstruction algorithm. The acquired volumetric data were then processed by a novel convolutional neural network to perform segmentations of white matter and the ventricular system and cerebellum. These were compared with manual segmentation using the Dice coefficient, Hausdorff distance (95th percentile), and volume difference. Using interquartile ranges, we identified outliers of these metrics and further analyzed them in detail.

RESULTS: The mean Dice coefficient was 96.2%, 93.7%, and 94.7% for white matter and the ventricular system and cerebellum, respectively. The Hausdorff distance was 1.1, 2.3, and 1.6 mm, respectively. The volume difference was 1.6, 1.4, and 0.3 mL, respectively. Of the 126 measurements, there were 16 outliers among 5 fetuses, discussed on a case-by-case basis.

CONCLUSIONS: Our novel segmentation algorithm obtained excellent results on MR images of fetuses with severe brain abnormalities. Analysis of the outliers shows the need to include pathologies underrepresented in the current data set. Quality control to prevent occasional errors is still needed.

ABBREVIATIONS: CNN = convolutional neural network; DC = Dice coefficient; IQR = interquartile range

MR imaging of the fetal brain is an important adjunct to ultrasound in the detection and characterization of abnormalities at an early stage of development.¹ High-resolution imaging is essential to accurately diagnose and follow up the evolution of these pathologies. New techniques have allowed the development of isotropic motion-corrected volume reconstructions based on the acquired 2D image stacks, including the so-called super-resolution reconstruction method.² These types of volumetric reconstruction

methods combine several stacks of 2D slices in different planes to construct a single isotropic volume, removing individual section artifacts and interslice inconsistencies,^{2–6} as well as providing a volume with the same high resolution between slices as within a section. The segmentation of different parts and tissue types of the fetal brain should provide more accurate and more reproducible information regarding the evolution in certain pathologies, such as ventriculomegaly, malformations of cortical development, and tumors.

Performing such segmentation manually requires a high level of expertise and is time-consuming and prone to human error and variability; therefore, accurate automatic segmentation is essential for routine clinical use. Segmentation of the fetal brain is challenging because of the complex and rapidly changing anatomy during fetal life and is further complicated by variable image quality and a variety of artifacts.⁷

In medical image analysis, deep learning methods have recently proved to be very competitive, often outperforming conventional

Received February 6, 2022; accepted after revision February 6, 2023.

From the Departments of Radiology (T.D., F.D.K., P.D., S.D., M.A.) and Gynaecology and Obstetrics (J.D., L.D.C., T.V.), University Hospitals Leuven, Belgium; School of Biomedical Engineering and Imaging Sciences (L.F., M.E., T.V., S.O.), King's College London, London, UK; and Institute for Women's Health (J.D.) and Department of Medical Physics and Biomedical Engineering (M.E., T.V.), University College London, London, UK.

Please address correspondence to T. Deprest, MD, Pastoor Paquaylaan 129, 3550 Heusden-Zolder, Belgium; e-mail: tdeprest@gmail.com



Indicates article with online supplemental data.

<http://dx.doi.org/10.3174/ajnr.A7808>

machine learning and model-based methods,⁸ including MR imaging of the adult and normal perinatal brain.^{9,10} Deep neural networks have the major advantage of being able to retrieve specific features for the task at hand directly from the data. The networks learn to extract and interpret features related to the segmentation task without the need to first derive a collection of handcrafted features from the image as input to a classifier or model. The state-of-the-art deep neural networks for segmentation are based on convolutional neural networks (CNNs). The use of automatic segmentation of fetal brain tissues by CNNs has been shown to be effective in normal cases¹¹ and more recently in cases with spinal dysraphism as well for the ventricles.¹² Developing automated segmentation tools for normal brains may be a good starting point, but in clinical practice, MR imaging is used to assess fetuses with pathology, rather than as a screening tool.¹³ Currently, there is a need for robust methods to segment fetal brain structures in the presence of varying severe abnormalities, which are common in the fetal period and can substantially affect the performance of developed techniques.¹⁰

One of the downsides of using CNNs is that they require large sets of training data.¹¹ These data also have to be diverse enough for the CNN to be robust to pathologies. Typically, CNNs are trained by using empirical risk minimization to maximize the average segmentation performance. This can cause errors when pathologies are underrepresented in the training data set, as is typically the case with the available abundance of healthy control cases in contrast to the ones with abnormal findings. To address this problem, we specifically developed an algorithm that is more robust to anatomic abnormalities. This algorithm trains a CNN with distributionally robust optimization,¹⁴⁻¹⁷ which automatically reweighs the training samples with lower performance, encouraging the CNN to perform more consistently on all cases. This method has been shown to be more robust than conventional CNNs trained with empirical risk minimization.¹⁸ This algorithm was validated earlier using 197 fetal brain volumes from 4 different centers, including both normal brains and those with various CNS abnormalities. Using data from multiple centers with MR imaging machines from different vendors with various CNS abnormalities present during testing ensures us that this method of training is especially robust to different data input. This algorithm has since been updated to segment even more brain structures and was validated on a larger data set.¹⁹ The robustness of the algorithm allows the user to input a variety of new cases with abnormal findings with excellent overall generalization results, as is key for the clinical implementation of the algorithm. The acquired segmentations aid in the detection and characterization of fetal pathologies, which could be considered the most important goal of these automatic segmentations.¹⁰

The algorithm we use automatically segments the cerebellum, ventricular system, and white matter. To ensure the clinical usefulness of this algorithm with distributionally robust optimization, one must evaluate its performance and robustness against the criterion standard, ie, manual segmentation. Therefore, we compared automatic and manual segmentations of different brain structures on a series of super-resolution reconstruction fetal MR imaging volumes of fetal brain malformations.

MATERIALS AND METHODS

The education-support committee of the KU Leuven approved this study.

Data

This was a single-center retrospective study on fetal brain MR imaging, which was performed between October 1, 2016, and February 1, 2020, for CNS anomalies detected on prenatal ultrasound or for an increased risk of CNS anomalies (for diagnosis of included cases, see the Online Supplemental Data). All cases were selected from our data base on fetuses who were assessed because they were at increased risk for/suspected of having CNS abnormalities. Criteria for selection were severe brain malformations of different origins (eg, infectious, destructive, vascular, developmental, and so forth.) In addition, these cases could not have been included in the training data set. If multiple cases of the same pathology were present in the data base, the more severe one was selected. Images were acquired on a clinical 1.5T MR imaging system using a routine clinical protocol, without maternal sedation. This protocol includes T2-weighted single-shot turbo spin-echo sequences of the fetal brain in 3 orthogonal planes (see the Online Supplemental Data for MR imaging parameters), with repetition because of fetal motion when deemed necessary by the attending radiologist (M.A.). 2D slices were reconstructed to isotropic 3D volumes (resolution $0.8 \times 0.8 \times 0.8$ mm) using the super-resolution reconstruction algorithm on a server in the hospital network.²

Method

Automatic Segmentation. Isotropic 3D volumes of 16 fetuses were used as input of a CNN, which was trained using distributionally robust optimization for the fully automatic segmentations of the cerebellum, ventricular system, and white matter on both normal and abnormal brains.¹⁹ When we trained the algorithm, it was agreed that the segmentation of the ventricular system would include the lateral, third, and fourth ventricles with the cerebral aqueduct, cavum septum pellucidum, and cavum vergae, when present. The term “white matter” used throughout this article is for ease of use. What eventually becomes white matter consists, during fetal development, of multiple transient layers.²⁰ Both the automatic and manual segmentations of what is referred to as white matter included these transient layers, more specifically the intermediate zone, cortical subplate, and ventricular zones.

There was no overlap between testing and training data in terms of subjects. The original training data set included 162 patients (124 controls without CNS abnormalities, 28 with spinal dysraphism, and 10 with other CNS abnormalities; see the Online Supplemental Data for more detailed information), with a gestational age range between 21 and 37 weeks.

Manual Segmentation. The reference standard was set by manual segmentation of the selected brain structures, using the automatic segmentations as a starting point. Manual segmentations were performed using the software application ITK-SNAP (Version 3.8.0; www.itksnap.org).²¹ These structures were first segmented by a radiology resident (T.D.) and then reviewed and corrected by an experienced fetal radiologist (M.A.).

Table 1: Evaluation of automatic segmentations for the 14 volumes of abnormal fetal brains^a

	WM	V	C
DC (%)			
Mean	96.2	93.7	94.7
SD	9.0	7.8	4.4
Median	99.5	97.4	96.8
IQR	0.8	6.5	8.3
Hausdorff 95% (mm)			
Mean	1.1	2.3	1.6
SD	2.4	2.7	0.9
Median	0.0	1.5	1.5
IQR	0.8	1.9	0.9
Volume difference (mL)			
Mean	1.6	1.4	0.3
SD	3.7	1.6	0.4
Median	0.4	0.7	0.2
IQR	0.5	1.7	0.3
Total volume (mL)			
Mean	62.3	25.7	5.3
SD	27.0	52.2	4.0
Median	57.1	10.1	3.9
IQR	46.1	7.0	4.6
Relative volume difference (%)			
Mean	7.4	11.4	7.6
SD	23.2	17.0	6.8
Median	0.7	3.5	4.8
IQR	1.0	10.4	8.4

Note:—V indicates ventricular system; C, cerebellum.

^aVolume difference is calculated by subtracting the manual from automatic segmentations. Total volume (based on manual segmentations) and relative volume difference are added as a reference for volume difference.

Evaluation. To compare the automatic and manual segmentations, we used quantitative methods and a descriptive discussion with reference to the underlying pathology. Quantitative comparison was performed with the Dice coefficient (DC) for volume overlap and the Hausdorff distance at the 95th percentile (Hausdorff 95%) between manual and automatic segmentation, because these were also the 2 metrics that were previously used in the original evaluation of the adopted CNN. We additionally calculated the volume difference between automatic and manual segmentations as an absolute value in Euclidean space. The volume difference was added because of the clinical relevance of volume measurements.

As is common in medical imaging analysis, for a surface-distance parameter, Hausdorff 95% was chosen (rather than at percentile 100).²² This makes more sense in our study because of the inevitable minor manual segmentation errors, as well as the few stray voxels that are rarely segmented by the CNN, which can even be located outside the skull. These result in a few extreme outliers that do not accurately represent the overall performance. We were particularly interested in measuring the statistical dispersion of the results as a way to evaluate the robustness of the algorithm, as well as to identify outlier values. To this end, we used the SD that is sensitive to outliers and the interquartile range (IQR) that is robust to outliers.²²

Statistical analysis was performed using Python (<https://www.python.org/>) and Excel 2016 (Microsoft). To detect outliers, we defined these metric cutoff values as either lower than $Q1 - (1.5 \times IQR)$ or higher than $Q3 + (1.5 \times IQR)$, with $Q1$ and $Q3$ being the first and third quartiles. These outliers were descriptively discussed in the context of the underlying anomalies on a case-by-case basis.

RESULTS

In 2 cases, the super-resolution reconstruction algorithm failed due to severe motion corruption; thus, these images were excluded. The gestational age in the remaining 14 cases was between 21.6 and 39.7 weeks (mean, 27.5 [SD, 4.4] weeks). For each of the 14 cases, the DC, Hausdorff 95%, and volume difference were calculated for the white matter, ventricle system, and cerebellum. Thus, 9 measurements were obtained per case, resulting in 126 measurements. The results of the comparison of automatic-to-manual segmentations are shown in Table 1; total volume and relative volume difference were added as a reference for the volume difference. The median DC for the white matter was 99.5%, which ranged between 64.5% and 99.8%. For the ventricular system, the median DC was 97.4% (range, 75.3%–99.3%). For the cerebellum, the median DC was 96.8% (range, 87.4%–99.1%). The median Hausdorff 95% of the white matter was 0.0 mm (range, 0.0–9.3 mm). For the ventricular system, the median Hausdorff 95% was 1.5 mm (range, 0.0–8.2 mm). For the cerebellum, the median Hausdorff 95% was 1.5 mm (range, 0.8–4.3 mm). The median volume difference for the white matter was 0.4 mL (range, 0.2–14.7 mL); for the ventricular system, it was 0.7 mL (range, 0.1–5.0 mL); and for the cerebellum, it was 0.2 mL (range, 0.0–1.9 mL). Note that the relative volume difference metrics based on all individual data (as in Table 1) is not necessarily the same as the relative comparison of the metrics of volume difference and total volume.

Of the above 126 measurements, there were 16 outliers in 5 fetuses as illustrated in the boxplots of the Figure.

DISCUSSION

In this data set of fetuses scanned for CNS abnormalities, we found an overall excellent correlation of automatic and manual segmentations of the white matter, ventricular system, and the cerebellum. This was supported by the high DC, low Hausdorff 95%, and small volume difference. On the basis of our own evaluation of the algorithm, using our data set with abnormal fetal brains, we additionally compared the performance of the CNN with results reported earlier using other methods and data sets (Table 2). DC values of >70% are usually considered consistent with a satisfactory level of agreement between 2 segmentations.²³ This comparison obviously provides only an indication because those studies were performed on other data sets with either healthy fetuses and/or fetuses with different pathologies.

Of the 126 measurements, there were 13% outliers ($n = 16$); and artifacts such as the partial volume effect could account for only a minor contributing factor. Conversely, most of these outliers were present in fetuses with very specific anatomic changes. Thus, the outliers are further descriptively discussed on the basis of the underlying condition, hereby identifying when the algorithm makes segmentation errors. This feature emphasizes the limitation of our study, because the number of cases of each pathology is rather small (Online Supplemental Data). As a hypothesis for further research to improve the algorithm, one would need to train the algorithm with additional images with fetal pathologies similar to those in the erroneous cases and at a similar gestational age, to rule out the effect of brain development. This hypothesis is possibly strengthened by the finding that none of the automatic segmentations of the 2 Chiari II cases had outlier

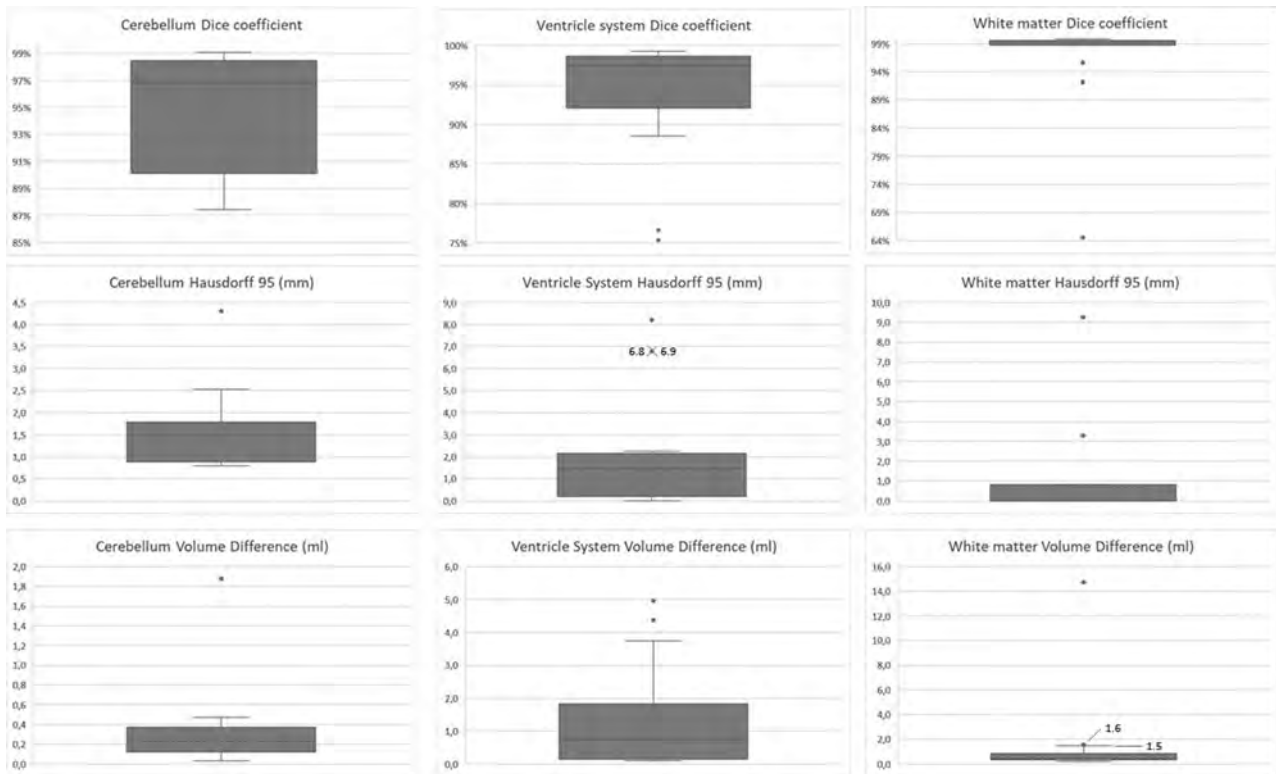


FIGURE. Results of the automatic segmentations compared with the manual references for the cerebellum, ventricular system, and white matter in our data set of fetuses with severe CNS anomalies. The metrics used are the DC, Hausdorff 95, and volume difference. Outliers are represented by dots in the boxplots. Note that different scales are used for optimal visualization.

values, possibly due to the large portion of spinal dysraphism cases in the training data set (28 of the 162 cases).

When we looked at the outlier values of our metrics, we found the most extreme outliers for the white matter and ventricular system in a case of an intracranial hemorrhage, which happened to have a signal intensity similar to that of the developing white matter at the time of imaging. The hemorrhage followed the convexity of the skull bilaterally, deviating the parenchyma medially, thus occupying the space where the white matter is typically found (Online Supplemental Data). This change caused errors in the automatic segmentations, which was to be expected because there were no cases with hemorrhages in the training data set. Because we had a postmortem scan available at the time of manual segmentation, we could verify our manual segmentation and determine that the automatic segmentation algorithm included parts of the hemorrhage in the segmentation of the white matter (see Online Supplemental Data for MR imaging parameters). In the same case, the CNN erroneously included parts of the hemorrhage, extra-axial CSF, as well as porencephalic changes in the segmentation of the ventricular system (Online Supplemental Data). These oversegmentations correspond to the outliers of the DC, Hausdorff 95%, and volume difference for both white matter and the ventricular system.

There was only 1 case with outliers in the segmentation of the cerebellum. This can be explained by the inherent changes due to the pathology present in this case, ie, an aqueductal stenosis. Due to the stenosis, there is a dilation of the supratentorial ventricular system with accompanying mass effect, which, in turn, alters the

configuration of the posterior fossa. More precisely, this scenario leads to a redistribution of the pericerebellar CSF and a reduced space between the cerebellum and the tentorium. Presumably, this altered configuration causes undersegmentation of the anterior lobe by the CNN (Online Supplemental Data). The cerebellar folia in the region of the vermis were also undersegmented, due to the partial volume effect brought on by the different distribution of the surrounding CSF. This feature translated into outlier values in Hausdorff 95% and volume difference.

In the same fetus, there were also outliers for the white matter segmentation (both for DC and Hausdorff 95%). The aqueductal stenosis caused dilation of the supratentorial ventricular system and secondary white matter thinning. This result created a thin and irregular segmentation that caused variable DCs, because the DC is inherently highly susceptible to these irregularities (Online Supplemental Data). In addition, this fetus was an outlier due to its advanced gestational age (39.7 weeks), at which time there is advanced gyration and a decrease in the subcortical plate tissue throughout the brain, with physiologic remnants in different areas. The combination of both physiologic processes makes the white matter more heterogeneous and probably more difficult for the CNN trained algorithm to segment correctly. The algorithm we used was trained on younger fetuses (21–37 weeks) because these are more commonly scanned; therefore, it had no prior experience with fetuses of that advanced age.

There were also outliers for the ventricular system segmentation in 2 of the 3 cases with (partial) corpus callosum agenesis, in which the CNN makes an oversegmentation of the extraventricular

Table 2: Automatic segmentation performance on our testing data set (trained using distributionally robust optimization) compared with other methods trained and evaluated with different data sets^a

	Our Data Set	Habas et al ²⁶	Serag et al ²⁷	Khalili et al ¹¹	Gholipour et al ⁴
Fetal data set	Abnormal	Normal	Normal	Not specified	Both normal and abnormal
WM	96.2 (9.0)	90.0 (2.0)	90.0 (6.0)	91.9	
V	93.7 (7.8)	90.0 (2.0)	92.0 (4.0)	87.4	88.0 (6.7)
C	94.7 (4.4)			79.4	

Note:—V indicates ventricular system; C, cerebellum.

^a We report the mean DC (%). SD is noted in parentheses (when available). Performance of previous methods is taken from the literature. Hence, this comparison can be used as an indication only. Whether the test data set contains normal and/or abnormal fetal brains is specified in the row "Fetal data set."

CSF in the interhemispheric cistern (Online Supplemental Data). This finding is likely due to the algorithm falsely assuming the presence of a cavum septum pellucidum. This structure is present in healthy fetuses, but absent in corpus callosum agenesis. As mentioned earlier, it was agreed in advance to include the cavum septum pellucidum in the segmentation of the ventricular system (both when training the CNN, as well as for the manual segmentation comparison). This inclusion was because the cavum septum pellucidum is a normal structure in normal fetal brains, though we acknowledge it is not part of the ventricular system. Furthermore, in the training data set, we included several cases with spinal dysraphism in which the cavum septum pellucidum can be absent or incomplete.^{24,25} In corpus callosum agenesis, the lateral ventricles are generally more widely spaced and the third ventricle is dilated and may communicate with the interhemispheric fissure. Therefore, we hypothesize that the algorithm recognizes the fluid-filled space or associated cyst between the hemispheres as the cavum septum pellucidum. In one of these 2 cases, a borderline outlier was also seen in the white matter volume difference, presumably because of the partial volume effect in the narrow parts of the lateral ventricles, in turn causing lower-signal-intensity voxels of the CSF to be wrongfully included (Online Supplemental Data).

Finally, there was an outlier in the DC of the white matter in a case with idiopathic dilation of the lateral ventricles. We attribute this to the previously mentioned factors of thin and irregular white matter due to ventriculomegaly (Online Supplemental Data). We have focused on the outliers because they are the most interesting for further development of segmentation algorithms. For completion, we have also added an example of a case in which the algorithm performs well; thus, there is a good correlation of the automatic and the manual segmentations (Online Supplemental Data).

Note that the commissures were not added to the white matter segmentation, even though we acknowledge that commissural fibers are white matter. This decision was due to additional brain structures being added in later versions of the algorithm, which include commissural fibers such as the corpus callosum.

Another potential limitation is that the manual segmentation was performed using the automatic segmentation as a starting point. This step was to simultaneously identify potential errors in the automatic segmentation, being important to the engineers involved in the development and further optimization of the algorithm. To minimize the potential effect on the statistical results, we reviewed the manual segmentations and an experienced fetal radiologist (M.A.) corrected them after the initial manual segmentation by a radiology resident (T.D.). As a final limitation, we

acknowledge the small number of cases of each pathology, which has been mentioned before in this section.

CONCLUSIONS

We demonstrated an overall excellent correlation between the automatic segmentation by the CNN and the ground truth manual segmentations in a new clinical data set, consisting exclusively of cases with a variety of severe brain abnormalities. Additionally, our results suggest the need to include enough cases with a diverse spectrum of pathologies and a broad age range when training these algorithms to prevent errors. The remaining errors emphasize the need to perform a manual check and look for occasional faults of the algorithm due to severe or rare abnormalities or induced by artifacts. Nevertheless, the vast time savings would suggest that this algorithm is very useful for managing clinical data sets with a variety of pathologies.

Disclosure forms provided by the authors are available with the full text and PDF of this article at www.ajnr.org.

REFERENCES

1. Pugash D, Brugger PC, Bettelheim D, et al. **Prenatal ultrasound and fetal MRI: the comparative value of each modality in prenatal diagnosis.** *Eur J Radiol* 2008;68:214–26 CrossRef Medline
2. Ebner M, Wang G, Li W, et al. **An automated framework for localization, segmentation and super-resolution reconstruction of fetal brain MRI.** *Neuroimage* 2020;206:116324 CrossRef Medline
3. Jiang S, Xue H, Glover A, et al. **MRI of moving subjects using multi-slice snapshot images with volume reconstruction (SVR): application to fetal, neonatal, and adult brain studies.** *IEEE Trans Med Imaging* 2007;26:967–80 CrossRef Medline
4. Gholipour A, Estroff JA, Warfield SK. **Robust super-resolution volume reconstruction from slice acquisitions: application to fetal brain MRI.** *IEEE Trans Med Imaging* 2010;29:1739–58 CrossRef Medline
5. Kuklisova-Murgasova M, Quaghebeur G, Rutherford MA, et al. **Reconstruction of fetal brain MRI with intensity matching and complete outlier removal.** *Med Image Anal* 2012;16:1550–64 CrossRef Medline
6. Kainz B, Steinberger M, Wein W, et al. **Fast volume reconstruction from motion corrupted stacks of 2D slices.** *IEEE Trans Med Imaging* 2015;34:1901–13 CrossRef Medline
7. Prayer D, Kasprian G, Krampfl E, et al. **MRI of normal fetal brain development.** *Eur J Radiol* 2006;57:199–216 CrossRef Medline
8. Litjens G, Kooi T, Bejnordi BE, et al. **A survey on deep learning in medical image analysis.** *Med Image Anal* 2017;42:60–88 CrossRef Medline
9. Akkus Z, Galimzianova A, Hoogi A, et al. **Deep learning for brain MRI segmentation: state of the art and future directions.** *J Digit Imaging* 2017;30:449–59 CrossRef Medline
10. Makropoulos A, Counsell SJ, Rueckert D. **A review on automatic fetal and neonatal brain MRI segmentation.** *Neuroimage* 2018;170:231–48 CrossRef Medline

11. Khalili N, Lessmann N, Turk E, et al. **Automatic brain tissue segmentation in fetal MRI using convolutional neural networks.** *Magn Reson Imaging* 2019;64:77–89 CrossRef Medline
12. Wang Q, Gomez A, Hutter J, et al. *Smart Ultrasound Imaging and Perinatal, Preterm and Paediatric Image Analysis.* Springer-Verlag International Publishing; 2019
13. Aertsen M, Diogo MC, Dymarkowski S, et al. **MRI for dummies: what the fetal medicine specialist should know about acquisitions and sequences.** *Prenatal Diagnosis* 2020;40:6–17 CrossRef Medline
14. Chouzenoux E, Gérard H, Pesquet JC. **General risk measures for robust machine learning.** *arXiv* [Internet] May 24, 2019. <http://arxiv.org/abs/1904.11707>. Accessed March 13, 2021
15. Duchi J, Glynn P, Namkoong H. **Statistics of robust optimization: a generalized empirical likelihood approach.** *arXiv* [Internet] October 11, 2016. <http://arxiv.org/abs/1610.03425>. Accessed April 13, 2021
16. Namkoong H, Duchi JC. **Stochastic gradient methods for distributionally robust optimization with f-divergences.** In: *Proceedings of the Thirtieth Conference on Neural Information Processing Systems*, Barcelona, Spain. December 5–10, 2016
17. Rafique H, Liu M, Lin Q, et al. **Non-convex min-max optimization: provable algorithms and applications in machine learning.** *arXiv* October 4, 2018. <http://arxiv.org/abs/1810.02060>. Accessed April 13, 2021
18. Fidon L, Ourselin S, Vercauteren T. **Distributionally robust deep learning using hardness weighted sampling.** *arXiv* July 14, 2022, <http://arxiv.org/abs/2001.02658>. Accessed November 5, 2020
19. Fidon L, Aertsen M, Mufti N, et al. **Distributionally robust segmentation of abnormal fetal brain 3D MRI.** In: Sudre CH, Licandro K, Baumgartner C, et al, eds. *Uncertainty for Safe Utilization of Machine Learning in Medical Imaging, and Perinatal Imaging, Placental and Preterm Image Analysis.* 2021;12959:263–73 CrossRef
20. Bystron I, Blakemore C, Rakic P. **Development of the human cerebral cortex: Boulder Committee revisited.** *Nat Rev Neurosci* 2008;9:110–22 CrossRef Medline
21. Yushkevich PA, Piven J, Hazlett HC, et al. **User-guided 3D active contour segmentation of anatomical structures: significantly improved efficiency and reliability.** *Neuroimage* 2006;31:1116–28 CrossRef Medline
22. Bakas S, Reyes M, Jakab A, et al. **Identifying the best machine learning algorithms for brain tumor segmentation, progression assessment, and overall survival prediction in the BRATS Challenge.** *arXiv* July 14, 2019. <http://arxiv.org/abs/1811.02629>. Accessed December 22, 2020
23. Zijdenbos AP, Dawant BM, Margolin RA, et al. **Morphometric analysis of white matter lesions in MR images: method and validation.** *IEEE Trans Med Imaging* 1994;13:716–24 CrossRef Medline
24. Trigo L, Eixarch E, Bottura I, et al. **Prevalence of supratentorial anomalies assessed by fetal magnetic resonance in fetuses with open spina bifida.** *Ultrasound Obstet Gynecol* 2022;59:804–12 CrossRef Medline
25. Fidon L, Viola E, Mufti N, et al. **A spatio-temporal atlas of the developing fetal brain with spina bifida aperta.** *Open Research Europe* 2021;1:123 CrossRef
26. Habas PA, Kim K, Rousseau F, et al. **Atlas-based segmentation of developing tissues in the human brain with quantitative validation in young fetuses.** *Hum Brain Mapp* 2010;31:1348–58 CrossRef Medline
27. Serag A, Kyriakopoulou V, Rutherford MA, et al. **Multi-channel 4D probabilistic atlas of the developing brain: application to fetuses and neonates.** *Ann Br Mach Vis Assoc* 2012;2012:1–14

Temporal Characteristics of CSF-Venous Fistulas on Digital Subtraction Myelography

I. Mark, A. Madhavan, M. Oien, J. Verdoorn, J.C. Benson, J. Cutsforth-Gregory, W. Brinjikji, and P. Morris



ABSTRACT

BACKGROUND AND PURPOSE: CSF-venous fistula can be diagnosed with multiple myelographic techniques; however, no prior work has characterized the time to contrast opacification and the duration of visualization. The purpose of our study was to evaluate the temporal characteristics of CSF-venous fistula on digital subtraction myelography.

MATERIALS AND METHODS: We reviewed the digital subtraction myelography images of 26 patients with CSF-venous fistulas. We evaluated how long the CSF-venous fistula took to opacify after contrast reached the spinal level of interest and how long it remained opacified. Patient demographics, CSF-venous fistula treatment, brain MR imaging findings, CSF-venous fistula spinal level, and CSF-venous fistula laterality were recorded.

RESULTS: Eight of the 26 CSF-venous fistulas were seen on both the upper- and lower-FOV digital subtraction myelography, for a total of 34 CSF-venous fistula views evaluated on digital subtraction myelography. The mean time to appearance was 9.1 seconds (range, 0–30 seconds). Twenty-two (84.6%) of the CSF-venous fistulas were on the right. The highest fistula level was C7, while the lowest was T13 (13 rib-bearing vertebral bodies). The most common CSF-venous fistula levels were T6 (4 patients) followed by T8, T10, and T11 (3 patients each). The mean age was 58.3 years (range, 31.7–87.6 years). Sixteen patients were women (61.5%).

CONCLUSIONS: This is the first study to report the temporal characteristics of CSF-venous fistulas using digital subtraction myelography. We found that on average, the CSF-venous fistula appeared 9.1 seconds (range, 0–30 seconds) after intrathecal contrast reached the spinal level.

ABBREVIATIONS: CTM = CT myelography; CVF = CSF-venous fistula; DSM = digital subtraction myelography; SIH = spontaneous intracranial hypotension

Spontaneous intracranial hypotension (SIH), a misnomer better characterized as low CSF volume from a spinal cause, can be a debilitating disease and commonly presents with orthostatic headache.¹ Spontaneous spinal CSF leaks can be classified as ventral dural tears (type 1a), posterolateral CSF leaks (type 1b), ruptured meningeal diverticular (type 2), or CSF-venous fistula (CVF) (type 3).² CVFs are challenging to diagnose because they are occult on spine MR imaging and are rarely seen on conventional CT myelography (CTM). Thus, myelographic techniques with high spatial and temporal resolution are necessary. Myelography technique varies widely but most commonly includes dynamic CTM³ or digital subtraction myelography (DSM),^{4,5} both of which acquire images immediately after the injection of intrathecal contrast and both of which are performed with the patient in the

lateral decubitus position when assessing a CVF. The timing of when CVFs are first visible on myelography and for how long they remain opacified has not been studied. The purpose of this article was to evaluate CVF temporal characteristics on DSM.

MATERIALS AND METHODS

We retrospectively reviewed an internal database following institutional review board clearance for patients with DSM-proved CVF from January to September 2022 at a single institution. All DSMs were performed by neuroradiologists in our spine practice who specialize in SIH and CVF evaluation. All images were reviewed for CVF temporal characteristics by a single neuroradiologist in our spine practice (I.M.). DSM images were reviewed for CVF laterality and spinal level. The time to appearance was measured as the time from when intrathecal contrast reached the CVF spinal level to when the CVF was first seen. The duration of time that the fistula was visible was also determined. All DSM images were reviewed, including the upper run focusing on the thoracic spine and the lower run focusing on the thoracolumbar

Received November 15, 2022; accepted after revision February 6, 2023.

From the Departments of Radiology (I.M., A.M., M.O., J.V., J.C.B., W.B., P.M.) and Neurology (J.C.-G.), Mayo Clinic, Rochester, Minnesota.

Please address correspondence to Ian Mark, MD, Department of Radiology, Mayo Building, 3-72W, Rochester, MN 55905; e-mail: Mark.Ian@mayo.edu; @iantmark
<http://dx.doi.org/10.3174/ajnr.A7809>

Individual CVF information that includes the laterality, spinal level, and temporal characteristics

Side	Level	Upper: Time to	Lower: Time to
		Appear/Duration (sec)	Appear/Duration (sec)
R	C7	12/37+	–
R	T1	10/46+	–
R	T2	3/27+	–
L	T2	12/28+	–
R	T3	3/59+	–
R	T4	1/54	–
R	T4	6/72+	N
R	T5	2/51+	N
R	T5	5/52	–
L	T6	5/41	–
L	T6	7/67+	–
R	T6	11/68	7/67
R	T6	24/35	7/45
L	T7	3/60	0/58
R	T7	16/24	10/38
R	T8	4/51+	–
R	T8	6/49+	11/36+
R	T8	18/38+	N
R	T9	12/54+	14/50+
R	T10	15/54+	N
R	T10	–	5/44+
R	T10	30/34	14/36
R	T11	4/50	3/49+
R	T11	–	14/38+
R	T11	22/73+	N
R	T13	–	6/42+

Note:—The en dash indicates not in the FOV; N, not seen but in the FOV; +, the CVF is opacified on the last image; R, right; L, left.

spine. When the CVF was seen in both the upper and lower DSM images on the same patient, the temporal characteristics were averaged. In cases in which the CVF was no longer visualized before the last image, we also noted whether intrathecal contrast remained at that spinal level.

Additional patient information such as sex, age, and treatment were recorded. Pre-DSM brain MR imaging was evaluated by a neuroradiologist (A.M.) for signs of SIH using a previously described quantitative scale (Bern score).⁶

DSM Technique

All DSMs were performed with the patient under moderate sedation in the lateral decubitus position on a tiltable table with or without a wedge to elevate the patient’s hips to achieve approximately 4°–8° of spinal tilt.⁷ Imaging was performed at a rate of 1 frame/second. The thecal sac was accessed at L2–L3 or below with a 20- or 22-ga needle, with the intrathecal needle position confirmed by 0.5 mL of iohexol (Omnipaque 300; GE Healthcare). Approximately 5–10 mL of normal saline was slowly infused into the thecal sac for pressurization followed by a hand injection of 6 mL of Omnipaque, while imaging from the cervicothoracic junction to the lower thoracic spine; the caudal FOV depended on the patient’s body habitus. We used 5–10 mL of normal saline to flush the line. Then, a second bolus of 5 mL of contrast was injected while imaging from the needle access site and extending cranially, normally extending to the mid-thoracic spine. The connecting tube and needle were cleared with sterile saline, but we did not routinely pressurize the thecal sac with saline after this contrast injection. The duration of image acquisition was determined by

the individual proceduralist. This variability was 1 factor that led to our desire to study CVF temporal characteristics.

RESULTS

Patient Demographics and Brain MR Imaging Findings

Twenty-six patients with CVF on DSM were included in this study. The mean age was 58.3 years (range, 31.7–87.6 years). Sixteen patients were women (61.5%). The mean Bern score was 4.2 (SD, 2.6) (range, 0–8). The occurrence of SIH findings was as follows: suprasellar cistern effacement of ≤4 mm (61.5%), pachymeningeal enhancement (57.7%), venous sinus engorgement (15.4%), subdural fluid collection (7.7%), prepontine cistern effacement of ≤5 mm (80.8%), and mamillopontine distance of ≤6.5 mm (80.8%). None of the patients had been treated with transvenous catheter embolization, epidural blood patch, fibrin glue injection, or surgical ligation before DSM. All patients underwent transvenous catheter embolization with Onyx (Medtronic) for treatment after DSM.

CVF Level and Laterality

The highest fistula level was C7, while the lowest was T13 (13 rib-bearing vertebral bodies). The most common CVF levels were T6 (4 patients) followed by T8, T10, and T11 (3 patients each). Twenty-two (84.6%) CVFs were on the right side. Patient-specific details are listed in the Table.

CVF Temporal Characteristics

Of the 26 patients, 8 had CVFs that were seen on the upper and lower runs. The mean time from contrast reaching the spinal level to the time of CVF appearance was 9.1 seconds (range, 0–30 seconds). The mean duration of CVF opacification was 48.1 seconds (range, 24–73 seconds). An imaging example of the CVF temporal characteristics on DSM is shown in the Figure. Of the 34 CVFs, 18 CVFs remained opacified on the last DSM image acquired, so we could not assess further duration of contrast opacification beyond the final acquired image. Sixteen CVFs disappeared before the last DSM image, with a mean CVF duration of 49.8 seconds (range, 24–68 seconds). Of the 16 CVFs that disappeared before the last image, 14 (87.5%) had intrathecal contrast at the CVF level (6 of which were faint) and 2 (12.5%) no longer had intrathecal contrast at the CVF level.

CVF Temporal Characteristics by Location

Thirteen CVFs were in the cervical or upper thoracic spine (C7–T6), with a mean time to appearance of 7.0 seconds (range, 1–15.5 seconds), a mean duration of contrast opacification of 49.3 seconds (range, 27–72 seconds), and a mean combined time of 56.3 seconds. The 13 CVFs in the lower thoracic spine (T7–T13) had a similar mean combined time of 58.0 seconds, but a slightly longer mean time to appearance (11.2 seconds) and a shorter mean duration (46.8 seconds).

DSM Upper-versus-Lower Runs

The spinal level of the CVF was within the FOV in both the upper and lower runs in 13 patients. All were seen on the upper run, compared with only 8 (61.5%) on the lower run. All cases

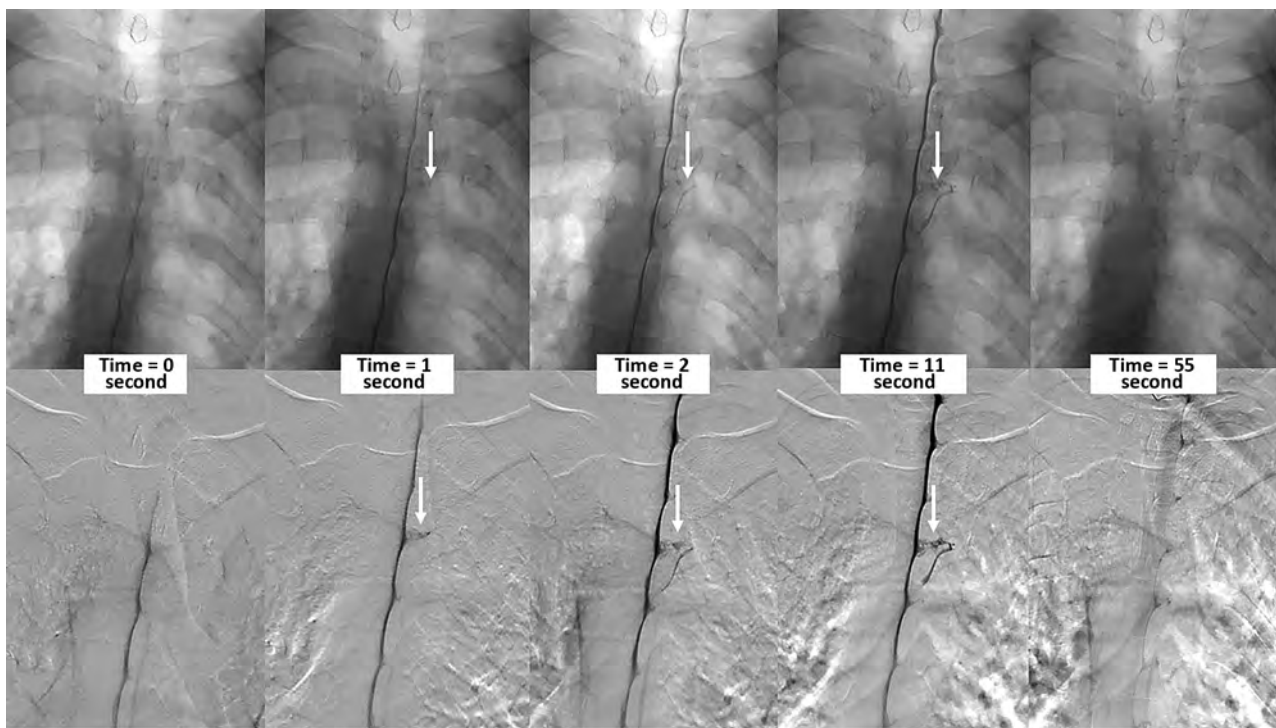


FIGURE. Multiple imaging timepoints of a right (DSM laterality is opposite conventional radiographs) T4 CVF (arrows) in a single patient. The upper row shows nonsubtracted fluoroscopy images, and the lower row shows DSM images. At time = 0, the contrast column reaches the level of the CVF. One second after, intrathecal contrast starts to fill the CVF, which is better seen at the 2- and 11-second images. The CVF is no longer visible 54 seconds after the initial appearance.

followed our standard technique, with the upper run acquired before the lower run.

DISCUSSION

In the current study, we evaluated the temporal characteristics of CVF on DSM. We found that CVFs take 9.1 seconds to appear once contrast reaches the spinal level of the CVF and remain visible for an additional 48.1 seconds. Because CVFs are challenging to diagnose, multiple modalities (DSM, CTM, MR myelography) and image-acquisition timing (dynamic-versus-nondynamic) have been used. The variety of myelographic techniques is due, in part, to resource availability as well as lack of understanding of how and when CVFs opacify with contrast. This is the first study to evaluate CVF temporal characteristics and could help to improve future myelographic techniques in the evaluation of CVF.

CVFs were first described with DSM.⁸ Since that discovery, multiple modalities have been used for CVF diagnosis.^{7,9,10} DSM has the advantage of higher temporal resolution because our technique acquires images at a rate of 1 frame per second. One challenge with DSM lies in the uncertainty of knowing how long to image. The dilemma of when to image and for how long could also apply to CTM. Prior work describing ultrafast dynamic CTM reported approximately 15 seconds per acquisition of the cervical and thoracic spine.¹¹ The acquisition time would be longer when including the lumbar spine.

Depending on the table tilt, spine curvature, and CSF dynamics, our practice observes intrathecal contrast flowing at various rates during DSM. Therefore, we measured the time of CVF

appearance from when the contrast reached the spinal level. We found that on average, CVFs opacify with contrast 9.1 seconds after intrathecal contrast reaches the CVF level. Twelve of 33 (36.4%) CVFs opacified within the first 5 seconds, while 5 (18.2%) took at least 15 seconds to appear. On average, the CVF remained opacified for 48.1 seconds. Only 3 (9.1%) CVFs disappeared before 30 seconds, while 18 (52.9%) remained opacified on the final image. If the spine were imaged 30 seconds after the contrast reached a particular spinal level, all cases of CVF from our cohort would be seen on at least 1 frame.

Prior work has suggested that respiratory techniques during myelography could help opacify the CVF. Amrhein et al¹² described increased conspicuity of the CVF at end-inspiration. Other work has shown that the CSF-to-venous pressure gradient can be increased with resisted inspiration.¹³ It is unknown how resisted inspiration would affect the temporal characteristics of CVF, but it could conceivably decrease the time to appearance and duration. The duration of CVF opacification should depend, in part, on the venous outflow, with most CVFs draining into the azygos system and, in turn, into the superior vena cava (SVC). Prior work has shown that the SVC-azygos junction can have efferent flow depending on the cardiac cycle,¹⁴ which could further delay emptying of the azygos system. The effect of general anesthesia and positive pressure ventilation are unknown, but increased intrathoracic pressure could pressurize the azygos system and contribute to delayed opacification and emptying of the CVF. While general anesthesia would optimize motion control, we did not find that motion obscured CVF visualization in our cases.

Thirteen of our patients had CVFs at a spinal level that was within the FOV on both the upper and lower runs of the DSM. The CVF was visualized on the upper run in all cases. Most interesting, only 61.5% of CVFs were also seen on the lower run, despite being within the FOV. In each of these cases, the upper run was acquired first, and the lower run, second. This result could be attributed to the use of a postcontrast saline chaser for the upper run but not the lower run. Work by Caton et al¹⁵ suggests that a CVF may need a certain pressure to open; likewise, there may be a subsequent pressure drop. With our technique, the contrast from the lower run and the lack of a saline chaser may not provide the necessary pressure to open the CVF seen on the upper run. The ideal saline chaser size and rate of infusion are not known, but theoretically, a more robust chaser could make the CVF appear sooner. Further study comparing the DSM yield with and without positive pressurization of the thecal sac could better elucidate these observations.

Our study has limitations. Our sample size is small, just 26 patients, yet this represents one of the largest studies on CVF using DSM. A larger sample size may help to categorize the temporal characteristics by spinal level. Second, the CVF was opacified on the last image in more than one-half of our patients; therefore, we do not know the true duration of opacification. This limitation falsely decreases the calculated duration of opacification. Also, we imaged patients for only a short duration after the injection of contrast. Prior work has used a delayed image acquisition with conventional nondynamic CTM¹⁶ and MR myelography^{17,18} to evaluate CVFs. Therefore, it would be difficult to apply our findings to those cases of delayed imaging. Additionally, dynamic myelography technique can differ at each institution (modality, saline chaser, contrast amount, breathing instructions) and, therefore, limits the generalization of these results. Finally, we were unable to detail the time between the injection of contrast and the time of first image acquisition. While our typical procedure has a 5- to 7-second delay, this is variable and it cannot be measured retrospectively.

CONCLUSIONS

This is the first study to report on the temporal characteristics of CVF using DSM. We found that on average, the CVF appeared 9.1 seconds after the intrathecal contrast reached the CVF spinal level.

Disclosure forms provided by the authors are available with the full text and PDF of this article at www.ajnr.org.

REFERENCES

- Kranz PG, Gray L, Malinzak MD, et al. **Spontaneous intracranial hypotension: pathogenesis, diagnosis, and treatment.** *Neuroimaging Clin N Am* 2019;29:581–94 CrossRef Medline
- Schievink WI, Maya MM, Jean-Pierre S, et al. **A classification system of spontaneous spinal CSF leaks.** *Neurology* 2016;87:673–79 CrossRef Medline
- Luetmer PH, Mokri B. **Dynamic CT myelography: a technique for localizing high-flow spinal cerebrospinal fluid leaks.** *AJNR Am J Neuroradiol* 2003;24:1711–14 Medline
- Schievink WI, Moser FG, Maya MM, et al. **Digital subtraction myelography for the identification of spontaneous spinal CSF-venous fistulas.** *J Neurosurg Spine* 2016;24:960–64 CrossRef Medline
- Schievink WI, Maya MM, Moser FG, et al. **Lateral decubitus digital subtraction myelography to identify spinal CSF-venous fistulas in spontaneous intracranial hypotension.** *J Neurosurg Spine* 2019 Sep 13. [Epub ahead of print] CrossRef Medline
- Dobrocky T, Grunder L, Breiding PS, et al. **Assessing spinal cerebrospinal fluid leaks in spontaneous intracranial hypotension with a scoring system based on brain magnetic resonance imaging findings.** *JAMA Neurol* 2019;76:580–87 CrossRef Medline
- Kim DK, Brinjikji W, Morris PP, et al. **Lateral decubitus digital subtraction myelography: tips, tricks, and pitfalls.** *AJNR Am J Neuroradiol* 2020;41:21–28 CrossRef Medline
- Schievink WI, Moser FG, Maya MM. **CSF-venous fistula in spontaneous intracranial hypotension.** *Neurology* 2014;83:472–73 CrossRef Medline
- Callen AL, Timpone VM, Schwertner A, et al. **Algorithmic multimodality approach to diagnosis and treatment of spinal CSF leak and venous fistula in patients with spontaneous intracranial hypotension.** *AJR Am J Roentgenol* 2022;219:292–301 CrossRef Medline
- Mamlouk MD, Ochi RP, Jun P, et al. **Decubitus CT myelography for CSF-venous fistulas: a procedural approach.** *AJNR Am J Neuroradiol* 2021;42:32–36 CrossRef Medline
- Thielen KR, Sillery JC, Morris JM, et al. **Ultrafast dynamic computed tomography myelography for the precise identification of high-flow cerebrospinal fluid leaks caused by spiculated spinal osteophytes.** *J Neurosurg Spine* 2015;22:324–31 CrossRef Medline
- Amrhein TJ, Gray L, Malinzak MD, et al. **Respiratory phase affects the conspicuity of CSF-venous fistulas in spontaneous intracranial hypotension.** *AJNR Am J Neuroradiol* 2020;41:1754–56 CrossRef Medline
- Mark IT, Amans MR, Shah VN, et al. **Resisted inspiration: a new technique to aid in the detection of CSF-venous fistulas.** *AJNR Am J Neuroradiol* 2022;43:1544–47 CrossRef Medline
- Morita S, Suzuki K, Masukawa A, et al. **Identification of efferent flow in the superior vena cava and azygos vein confluence using cine phase-contrast MRI: speculation of the role of the azygos arch valves.** *Magn Reson Imaging* 2010;28:1306–10 CrossRef Medline
- Caton MT Jr, Laguna B, Soderlund KA, et al. **Spinal compliance curves: preliminary experience with a new tool for evaluating suspected CSF venous fistulas on CT myelography in patients with spontaneous intracranial hypotension.** *AJNR Am J Neuroradiol* 2021;42:986–92 CrossRef Medline
- Clark MS, Diehn FE, Verdoorn JT, et al. **Prevalence of hyperdense paraspinous vein sign in patients with spontaneous intracranial hypotension without dural CSF leak on standard CT myelography.** *Diagn Interv Radiol* 2018;24:54–59 CrossRef Medline
- Chazen JL, Robbins MS, Strauss SB, et al. **MR myelography for the detection of CSF-venous fistulas.** *AJNR Am J Neuroradiol* 2020;41:938–40 CrossRef Medline
- Madhavan AA, Carr CM, Benson JC, et al. **Diagnostic yield of intrathecal gadolinium MR myelography for CSF leak localization.** *Clin Neuroradiol* 2022;32:537–45 CrossRef Medline